Honda R&D

Technical Review



October 2002

Comment on the Cover

ASIMO the humanoid robot,
with its unique style that gives a feeling of intimacy,
has become a popular character.

What if ASIMO became a work partner?
Did drawings and development testing, gave presentations,
and other things like that?

I look forward to seeing the kinds of places
where ASIMO goes to take an active role in the times ahead.

Takamaru HOSHINO
Asaka R&D Center

Development of GX25 4-Stroke Engine for Handheld Equipment

Keita ITO* Yasutake RYU* Shingo YONEDA*
Makoto WARASHINA* Shigeki EDAMATSU*

ABSTRACT

The multi-position 4-stroke engine, GX25, was developed for handheld equipment such as string trimmers and brush cutters. The purpose of the development was to achieve weight and acceleration levels equivalent to 2-stroke engines with better startability than the current GX22/31. Further refinement was made to the Rotary Slinger Pump Lubrication system developed for the GX22/31. To achieve lightweight composition, an OHC structure with an in-oil micro timing belt was adopted. A new one piece Rocker Arm Assembly and sintered cam were adopted in order to fit the valve train in the limited space of the oil tank. As a result of above the improvements, the GX25 has 13% less weight, 13% more displacement, and 30% more power-weight ratio when compared to the GX22. Furthermore, the improved decompression system has reduced the pull load and enhanced startability. A newly developed acceleration pump has achieved the 2-stroke level acceleration. In addition, matched with the UMK425 brush cutter, the reduced inertial moment of a lighter engine makes it easier to operate the equipment.

1. Introduction

Approximately 12 million portable, handheld engines (1.8 kW or less) are sold yearly around the world and sales have been showing a slight upward trend.

2-stroke engines are less expensive and have simpler configurations than 4-stroke engines, and are also able to be operated in multiple-positions, making them extremely widely used in handheld equipment such as brush cutters. Exhaust emissions are, however, a serious issue with these engines.

In 1997, Honda responded to this issue by developing and marketing the GX22/31, the world's first multi-positioned 4-stroke engine[(1)].

Since then, small engine manufacturers have examined various methods in their efforts to reduce exhaust emissions, some of which have been utilized in products on the market. These methods have included the transition to 4-stroke engines, the use of 2-stroke engines with exhaust gas after-treatment or scavenging control, and the development of 4-stroke engines using oil mixed fuels.

The GX25 handheld 4-stroke engine, which will be introduced in this paper, was developed against this market background to improve on the GX22/31.

* Asakahigashi R&D Center

2. Development Concept

The development concept for this engine was “the lightest handheld 4-stroke engine in its class”.

Development targets were as follows:

- 360°–inclinable operation equivalent to the GX22/31
- 30% improvement in power-weight ratio
- Acceleration performance equivalent to a 2-stroke engine
- Able to be started with less pull load on the starter rope than the GX22/31

3. Main Specifications

The external design features a full cover to prevent the engine from catching on branches and the like when the machine is in use. Ease of maintenance has been considered, and the engine cover can be removed and reattached by removal of one bolt.

Extensive reexamination of the configuration of the GX22 led to the adoption of a belt drive OHC valve mechanism to decrease the size and weight of the engine. An external view of the GX25 is shown in Fig. 1; Figure 2 shows a comparison of engine size between the GX25 and the GX22.



Fig. 1 External view of GX25

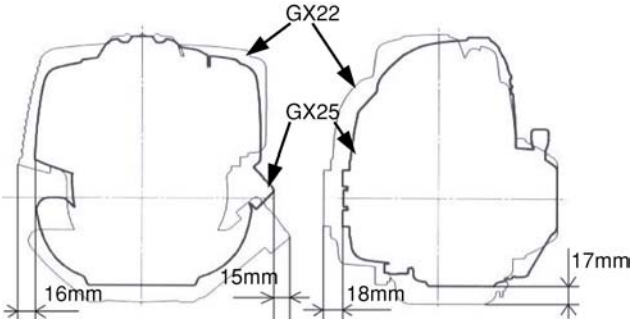


Fig. 2 Comparison of engine size between GX25 and GX22

The main specifications are shown in Table 1. Despite the fact that the new engine has a displacement of 25 cc, a 13% increase over the previous engine, its dry mass is 2.78 kg and its power-weight ratio is 0.29 kW/kg, putting it at the top of the 4-stroke handheld engine class. Figure 3 shows a comparison of power and weight for different models.

Table 1 Engine specifications

Model	GX25
Engine type	Air cooled 4-stroke OHC Single-cylinder
Bore × Stroke [mm]	35 × 26
Displacement [cm^3]	25
Compression ratio	8.0 : 1
Maximum power [kW/s^{-1}]	0.81/116.7
Maximum torque [Nm/ s^{-1}]	1.25/83.3
PTO shaft rotation	Counterclockwise
Fuel type	Unleaded gasoline
Fuel tank capacity [cm^3]	550
Fuel consumption [g/kWh]	340
Engine oil capacity [cm^3]	80
Oil consumption [cm^3/hr]	2
Ignition system	Transistorized magneto
Starting system	Recoil
Lubrication	Crankcase pressure driven
Dry mass [kg]	2.78
Dimensions (L × W × H) [mm]	192 × 221 × 230

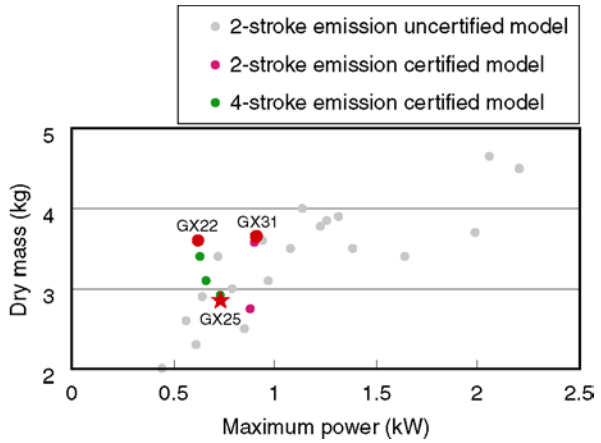


Fig. 3 Power/weight relation

4. Weight-saving Technology

4.1. Placement of Valve System

In the GX22/31, valve housing equipment such as push rods and cam gears (components of the OHV mechanism) were positioned between the cylinder and the cooling fan. An OHC configuration has been adopted for the GX25, and the valve housing has therefore been positioned on the opposite side of the cooling fan, close to both the cylinder and the

cooling fan. This configuration enables the new engine to equal the cooling performance of the GX22 with a 15% reduction in the area of the cooling fins. In addition, the length from the center of the engine to the power axis located at the tip of the cooling fan has been reduced from 100 mm to 83 mm, enabling size and weight reductions with no loss of overall engine rigidity. Figure 4 shows comparative cross-sections of the GX22 and GX25.

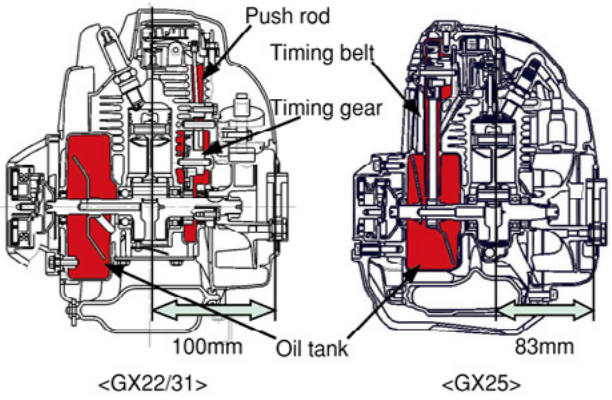


Fig. 4 Structural differences between GX22 and GX25

4.2. High-rigidity Block

Rigidity and strength are required in the support ribs for the attachment joint, because the attachment joint supports the entire weight of these small engines. In the GX25, support ribs have been located in six positions from the crank support and cylinder bore towards the fastening boss, balancing weight savings with rigidity. Block weight has been reduced by 25% against the GX22, from 967 g to 720 g, while up-down rigidity is 3.9 times higher and left-right rigidity is 2.4 times higher in the new engine. Figure 5 shows a three-dimensional image of the cylinder block and the attachment joint support ribs.

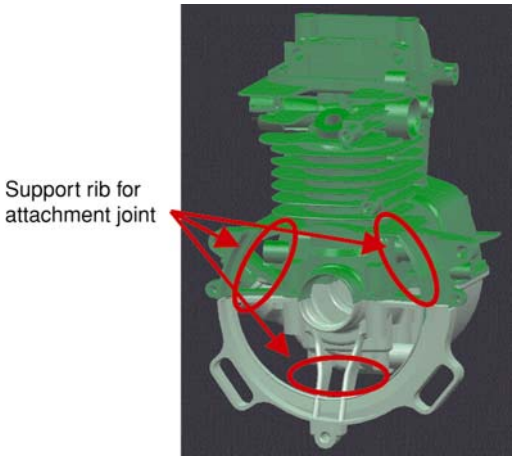


Fig. 5 Cylinder block

5. Lubrication Breather System

The following requirements were placed on the lubrication system of the new handheld engine:

- Able to be operated in any position.
- Able to be stored in any position when engine is stopped.
- As simple a configuration as possible, to achieve weight savings and cost reductions.

The rotary slinger pumping lubrication system developed for the GX22/31 was utilized in the GX25 to enable these requirements to be satisfied.

The salient points of the rotary slinger pumping lubrication system are as follows:

- It is a dry sump lubrication system with a separate oil tank provided with an oil slinger (oil agitator) directly connected to the crank, enabling oil flow to the combustion chamber to be prevented.
- Crankcase pressure rather than an oil pump is used to supply and return oil, enabling simplification of configuration and consequent weight savings and cost reductions.

Because blowby gases and oil mist were separated and oil was collected in the cam case and rocker arm chamber, the GX22/31 had a complex oil path. The adoption of an OHC mechanism in which the timing belt is located in the oil tank for the GX25 has resulted in a simplified lubrication path in which oil mist separation and collection can be conducted in the rocker arm chamber alone. Figure 6 shows a comparison between the lubrication paths of the GX22/31 and the GX25. This configuration minimizes delay in lubrication of the cam sliding parts which experiences severe lubrication conditions when the engine is started. Figure 7 shows the lubrication path in the GX25.

In addition, the following modifications were made to the rocker arm chamber to enable breather function (blowby gas and oil mist separation) and oil collection in any engine position:

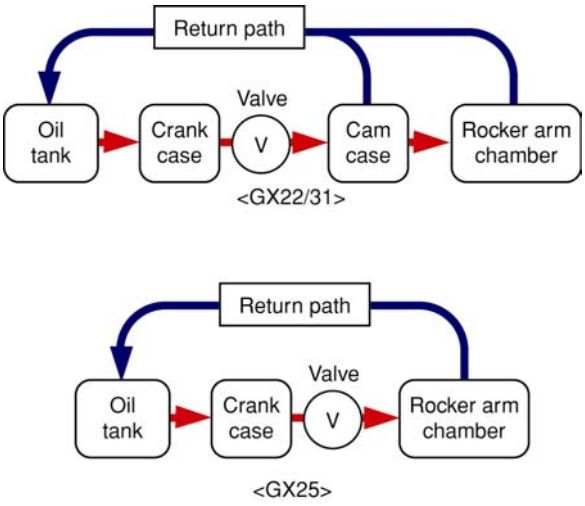


Fig. 6 Differences in oil path between GX22/31 and GX25

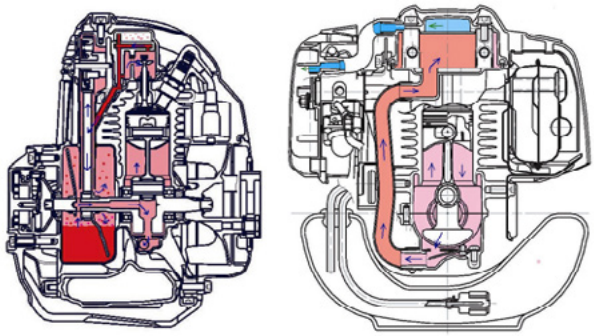


Fig. 7 Lubrication system

- A negative pressure chamber for oil collection was positioned close to the center of the rocker arm chamber.
- The first separator chamber, rocker arm chamber and breather chamber were positioned around this negative pressure chamber.
- Twelve oil suction holes were placed in the negative pressure chamber to enable oil to be collected regardless of engine position.

These modifications have enabled stable oil collection and return regardless of engine position, and the lightweight and simple configuration enables continuous multi-position operation. Figure 8 shows a cross-section of the rocker arm chamber.

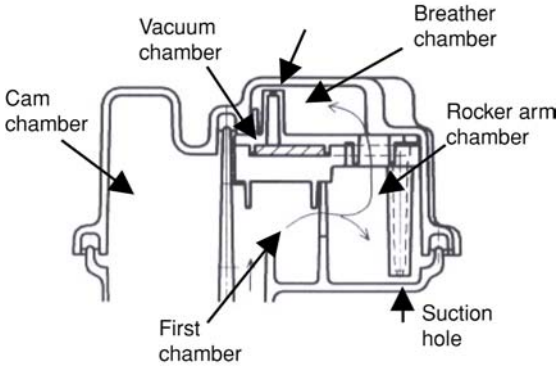


Fig. 8 Rocker arm chamber

6. Valve System

An OHC configuration driven by a timing belt has been utilized in the GX25. The layout is shown in Fig. 9.

6.1. Small, High-speed Oil-immersed Timing Belt

The specifications of the timing belt are shown in Table 2. An oil-immersible timing belt was adopted to drive the valve train to enable integration of the oil tank and valve chamber.

An oil-immersible timing belt was also utilized in the GC/GCV160[(2)]. The rubber material, canvas, core wire, etc., remain unchanged in the new belt, but the following points have changed in the new engine, affecting the conditions of belt use:



Fig. 9 Valve train layout

Table 2 Belt specifications

Model	GX25	GCV160
Belt length [mm]	320.6	533.4
Belt width [mm]	6	7
Maximum speed [s^{-1}]	200	60
Drive pulley diameter [mm]	20.6	39.3

- The new engine is high-speed and high-rpm, running from a normal operating speed of 116.7 s^{-1} (7,000 rpm) to a maximum engine speed of 200 s^{-1} (12,000 rpm).
- Drive pulley diameter has been reduced to contribute to the reduction of overall engine size.

These conditions of use significantly increase the damage caused to the core wire by polygonal behavior of the belt, and it was therefore necessary to increase bending fatigue resistance against the GC/GCV160. The dimensions of the teeth were accordingly reduced to achieve a balance between the level of bending fatigue induced and teeth jumping. The flexibility of the core wire was increased by reducing the diameter, and bending fatigue resistance in oil was increased by utilizing an adhesion treatment with superior oil resistance properties.

6.2. Assembled Rocker Arm

It was necessary to separate the rocker arm chamber and the valve housing (oil tank) to ensure the necessary pressure differential for oil return in the multi-position lubrication system. To achieve this, the rocker arm utilized in the new engine is assembled from two parts connected by a pin. The valve lifter, which slides across the cam surface, and the rocker arm, which pushes the valve head, are positioned in different chambers. The components of the rocker arm are



Fig. 10 Rocker arm

assembled by press fitting, and the pin is knurled to ensure slip torque after fitting. Sintered steel is used for the valve lifter and rocker arm, because of its superior strength, formability, and performance in sliding parts. An external view of a rocker arm is shown in Fig. 10.

6.3. Sintered Cam Integrated with Pulley

The driven pulley in the new engine has been integrated with a cam drive, as shown in Fig. 11.

To enable a biaxial tensionless belt drive to be used for the pulleys, they are formed from phenol resin, because of its ability to maintain its dimensions at high temperatures, and a mechanical decompression mechanism has been built in. Sintered steel has been integrated with phenol resin to produce the sliding parts of the cam and the bearings to increase durability given the high speeds and low diameters.

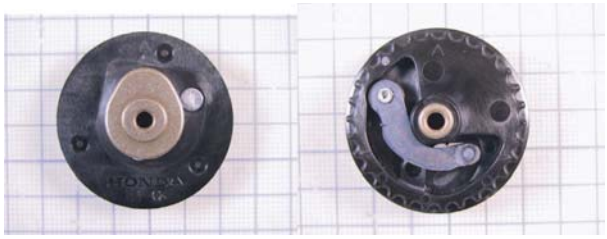


Fig. 11 Timing pulley

7. Improvements to Starting and Acceleration

7.1. Technology for Reduction of Recoil Pull Load

The GX22/31 utilized a decompression mechanism to open the inlet valve when the engine was started. The GX25 utilizes a decompression mechanism in the exhaust valve.

The GX25 is mainly used in brush cutters, and in these machines the throttle is normally closed when the engine is started. Because of this, decompression is more effective if pressure escapes via the exhaust valve when the engine is started. Lift timing has been set within a range which will minimize its effect on starting performance while enabling decompression, thus reducing recoil pull load. Figure 12 shows a three-dimensional model of the exhaust decompression.

Recoil starters with power spring have recently begun to be commercially utilized to reduce recoil pull load; the GX25 pull load is equivalent to that of an engine utilizing a power spring starter. Figure 13 shows a comparison of recoil pull loads in engines of identical displacement. Figure 14 shows recoil pull load waveforms when the engine is started. The engine utilizing a power spring averages a high load over an extended period, requiring a considerable amount of work; the GX25 can be started with just half the effort.

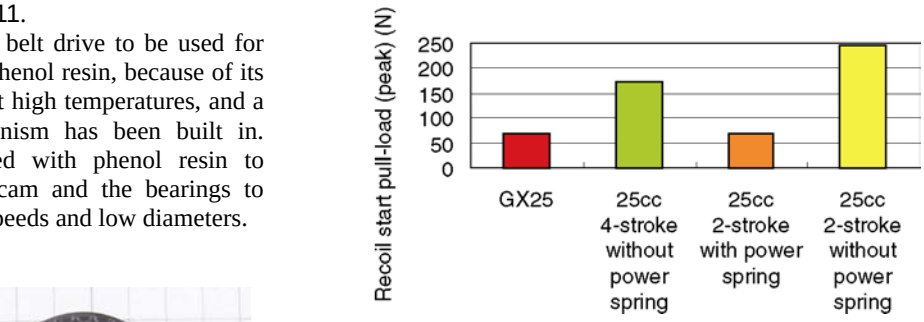


Fig. 13 Comparison of recoil pull-load (peak load)

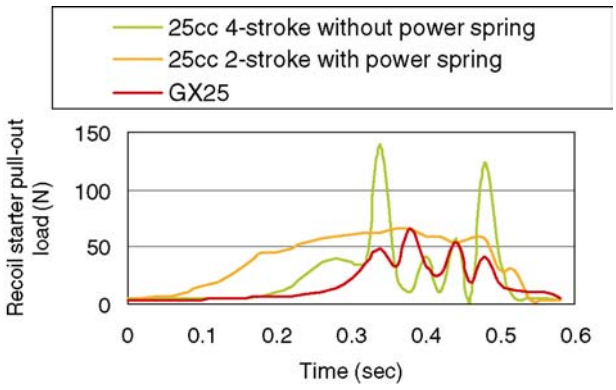


Fig. 14 Comparison of recoil pull-load



Fig. 12 Exhaust decompression

7.2. Diaphragm Carburetor with Acceleration Pump

The GX25 is provided with a newly developed carburetor with a built-in acceleration pump. The pump mechanism is a piston type synchronized with the throttle; size reductions have been achieved by constructing the pump from four components. Figure 15 shows the acceleration pump built in to the carburetor.

In this configuration, the path producing the main jet is pressurized by the cam, which is synchronized with the throttle, enabling fuel output to respond to throttle speed. This has improved acceleration at low temperatures.

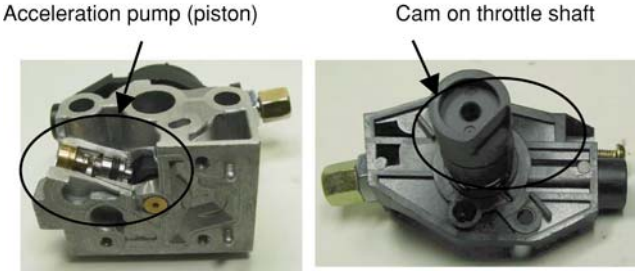


Fig. 15 Acceleration pump on carburetor

Figure 16 shows the operation mechanism of the acceleration pump. When the throttle is opened, the cam section of the throttle shaft pushes the piston, delivering fuel to the engine.

This configuration has greatly improved throttle response directly after the engine is started, which had previously been a point of concern in the development of 4-stroke handheld engines, and has enabled the achievement of operation with no feeling of stress in the engine. Figure 17 shows a comparison of engine speed response when the throttle is suddenly opened for several engines.

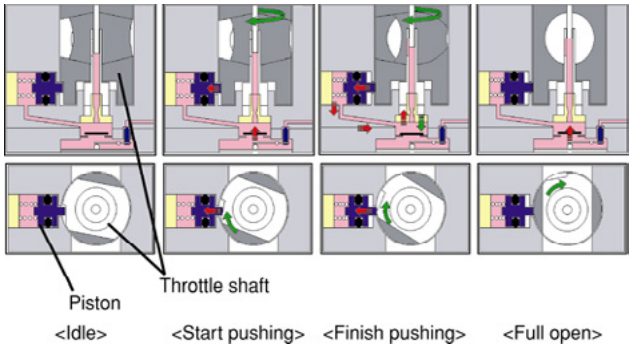


Fig. 16 Acceleration pump operation mechanism

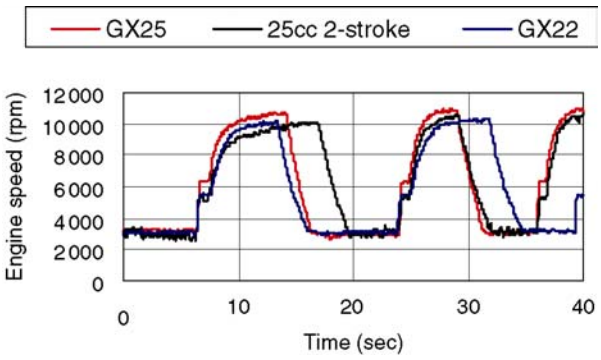


Fig. 17 Throttle response

8. Practical Application

The main application of the GX25 is in the UMK425 4-stroke brush cutter, the lightest in its class.

The main characteristic customers demand from a brush cutter is lightness, and the various companies in the field have continued to reduce the weight of their products. The UMK425 is made up of the lightweight GX25 and a lightweight frame, and is 20% lighter than the previous model, the UMK422, making it equivalent to the lightweight 2-strokes of the same displacement, despite its 4-stroke engine.

The operator of a brush cutter cuts weeds, grass, etc. by swinging the machine's pole to the left and right, moving the cutting blades at the tip. This swinging motion therefore has a significant effect on operator fatigue. Because the center of gravity is normally constant with respect to the operator, the moment of inertia of the completed machine is an important element in operator fatigue. The moment of inertia has been reduced by 20% in the UMK425 against the previous UMK422, enabling the achievement of an ease of swing equivalent to that of lighter brush cutters. Figure 18 shows a photograph of the UMK425 in operation, and Fig. 19 shows a comparison of the moment of inertia of various models.



Fig. 18 UMK425 in operation

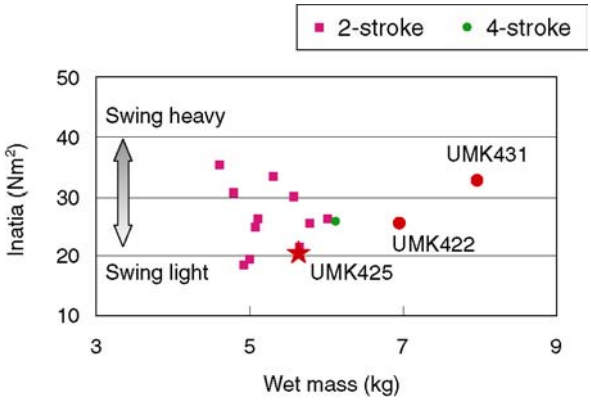


Fig. 19 Relation between swing light and inertia

In addition to the benefits of ease of starting and fuel economy achieved by using a 4-stroke engine, the UMK425 is lightweight and therefore easy for the operator to carry and to swing. This product has done away with the conventional image of 4-stroke brush cutter as being heavy.

9. Conclusion

The GX25 engine was developed as an engine for handheld equipment.

(1) Improved valve placement and the adoption of an OHC mechanism with an oil-immersed belt has enabled a 30% improvement in power-weight ratio against the GX22.
(2) The utilization of an exhaust valve decompression mechanism and an acceleration pump integrated with the carburetor has enabled improvement of acceleration when the engine is started.
(3) The moment of inertia of the completed UMK425 has been reduced by 20% against the UMK422, and ease of swing has been increased.

10. Afterword

The authors hope this engine will increase the recognition and evaluation of 4-stroke engines in the handheld market, currently dominated by 2-strokes, and help to increase the level of use of cleaner engines in the future.

In closing, the authors wish to sincerely thank all those who contributed so extensively and generously to the development of this engine.

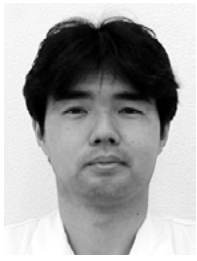
References

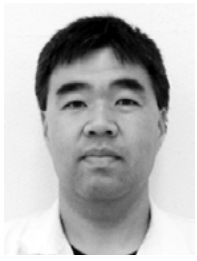
(1) Shiga, M., Nishida, T., Ryu, Y., Tsugega, T., Azuma, K.: Development of Small, Multi Position 4-stroke Engine, HONDA R&D Technical Review, Vol. 9, pp. 44-50 (1997)

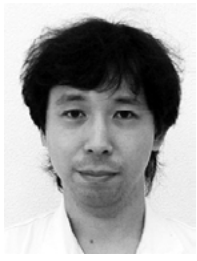
(2) Suzuki, S., Hojo, H., Inoue, S., Moriyama, H., Fujinaga, Y.: Development of General Purpose OHC Engines with Internal Timing Belts, HONDA R&D Technical Review, Vol. 10, pp. 122-127 (1998)

■ Authors ■


Keita ITO


Yasutake RYU


Shingo YONEDA


Makoto WARASHINA


Shigeki EDAMATSU

Development of the Compact FG201 Tiller

Masayuki SASAOKA* Takashi IKEDA*
Nobuchika KATAGIRI* Takayuki SATOH*

ABSTRACT

The FG201 tiller was developed to realize the highest level of work performance among compact tillers while also achieving low weight. This tiller utilizes a specially-designed 4-stroke OHV engine equipped with a mechanical governor that maintains optimum rotor speed. This keeps the engine speed from falling off even when tilling hard soil, thus producing excellent tilling performance. The tiller is designed to keep the center of gravity low and near the tiller blade axis. The blades are newly designed to match the lightweight body. Special attention was given to the shape of the drag bar, and tine shaft rotation was set at an optimum speed. These measures achieved a low weight of 17 kg, making this the lightest tiller in the 4-stroke engine class, and also made it possible to achieve top class work efficiency for compact tillers. In terms of operability, the recoil starter force has been reduced 40% over conventional tillers by utilizing optimum decompressor valve lift and valve timing settings. A centrifugal clutch was adopted so that the throttle lever alone could be used to start and stop operation. This produces simplicity of operation, making the tiller easy to use for beginners and elderly people. This model was also made to easily carry around and stow in a passenger vehicle, with a folding handle for compact storage and a single handed carrying handle. In terms of environmental conformity, this model meets the EPA Phase II and CARB Tier II regulation levels, as well as European EN noise regulations for 2006 Stage 2.

1. Introduction

In recent years, there has been a global increase in the number of people planting domestic gardens. Accordingly, there has been a growing demand for suitable and diverse tiller features. Furthermore, there has been a notable change in the type of user with an increasing number of beginners and elderly. Also, there has been a significant change in the domestic garden environment brought on by an increase in the number of residences. The current trend in the domestic garden market is for small 2-horsepower or under tillers configured with 2-stroke engines. Nowadays, in response to an increased sense of environmental preservation, a growing number of users are looking for an environmentally ‘friendlier’ tiller that embodies a high level of work performance and operability. The current domestic tiller market has an estimated 100,000 tillers, of which, Honda holds a 20% market share. These tillers typically weigh less than 40 kg and yield a tilling width of less than 600 mm. This report introduces the FG201, which has been designed to create a new market from this increasing global garden trend.

* Asakahigashi R&D Center

2. Aim of Development

It is generally held that increasing the overall weight of the tiller unit will improve the depth of cultivation and overall working performance. In designing the FG201, the developers abandoned all preconceptions and returned to the basics in consideration of what is required in a tiller for the typical person who enjoys domestic gardening. From there, it was determined that the development design should embody a 4-stroke engine configuration of the lightest class possible and be easy to handle. Additionally, it should be easy to transport while providing adequate tilling functionality. Figure 1 shows the external view of the FG201 and its unique design features.

3. Basic Structure and Main Specifications

Table 1 lists the main specifications for the FG201, classified as a tiller within the category of walk-along plows. The FG201 is different from conventional power driven tiller units that incorporate both a drive unit and tiller rotor to perform tilling work. The FG201 utilizes only a tiller rotor to provide both forward movement and tilling work[(1)]. The unit adopts a drag bar and handle bar, which are attached behind the rotor to control the propulsion speed and regulate the tilling depth.

Additionally, the FG201 has been configured with the engine mass mounted directly above the rotor. This effectively reduces the soil reaction force that naturally occurs during tilling.

The power generated from the vertical crankshaft type engine is directed 90° to propel the machine in the forward direction. This vertical crankshaft engine drives the tine shaft via a transmission fitted with a centrifugal clutch and worm reduction gear assembly.

The operator is able to control the tilling depth and propulsion speed by adjusting the height of the handle as required.

Table 1 Major specifications

Items	Specifications
Engine model name	GXV50
Engine type	Air cooled 4-stroke OHV single cylinder
Engine displacement (cm^3)	49
Maximum power (kW)	1.4
Rated power (kW/rpm)	1.1/4 600
Maximum torque (Nm/rpm)	2.56/4 600
Compression ratio	8.0
Minimum specific fuel consumption (g/kWh)	367
Fuel tank capacity (cm^3)	400
Overall length (mm)	1 050
Overall width (mm)	475
Overall height (mm)	995
Dry weight (kg)	16.5
Tine speed (rpm)	135
Tilling width (mm)	450
Tine diameter (mm)	φ 260
Starting system	Recoil starter
Main clutch type	Centrifugal clutch
Transmission speeds	1Forward

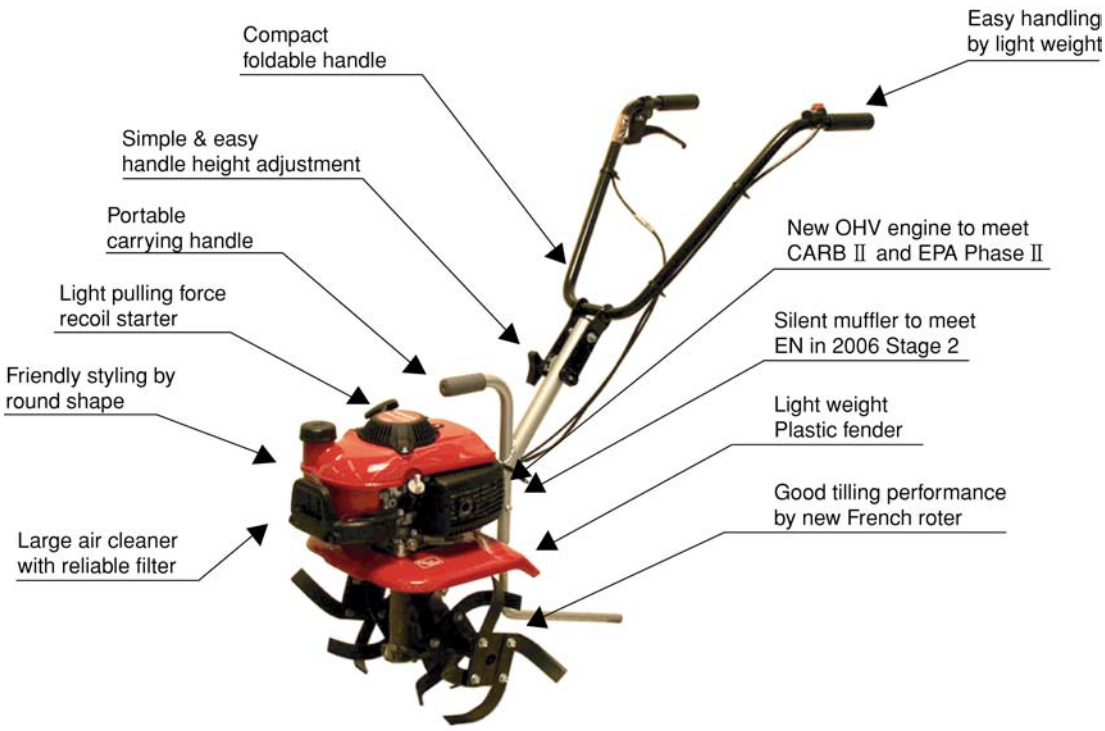


Fig. 1 External view and features

3.1 Engine

To facilitate ease of handling and transportability, a domestic tiller must be lightweight.

The FG201 has been configured with a 50 cc displacement overhead valve (OHV) engine to achieve such weight reduction. Also, by adopting a fan cover and fuel tank assembly made of lightweight plastic, 12 parts that were implemented in previous models have been eliminated in the FG201 thereby achieving an overall weight reduction. Figure 2 shows the layout of the FG201 engine.

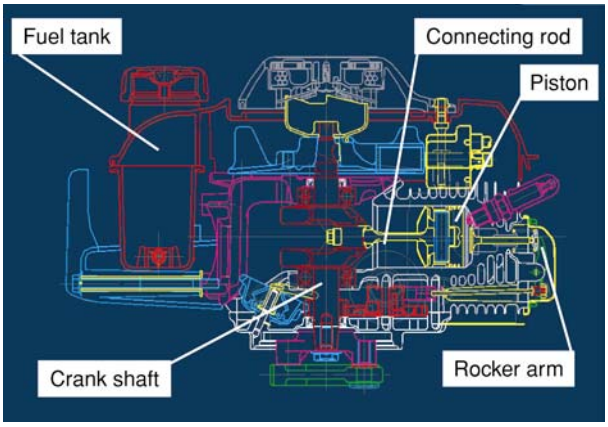


Fig. 2 Layout of engine

The FG201 engine has been configured with an OHV engine with a more compact combustion chamber, achieving a high compression ratio. This improves thermal efficiency and is compatible with EPA Phase II and California Air Resource Board (CARB) Tier II regulation levels for engine exhaust systems. The implementation of uniblock cylinders[(2)] with reduced cylinder strain reduces oil consumption and contributes significantly to the reduction of carbon build up in the combustion chamber.

Ease of operation and maintenance are another important aspect of domestic garden tillers. The FG 201 recoil force has been reduced to provide for easy starting, which was achieved through optimal decompressor valve lift and valve timing settings. Longer maintenance-free intervals were achieved as well, with use of an oversized air cleaner.

This design also meets Stage 2 level EN noise regulations set for 2006 thereby allowing the FG201 to be used for tilling within typical neighborhood settings.

3.2 Transmission

The basic design of the power train follows that used in the previously released FG200 and operates via a clutch which is attached to the power train output (PTO) crankshaft mounted on the vertical engine. The transmission drives the rotor via the tine shaft, which is controlled by a couple of worm gears, in a forward direction. See Fig. 3 for an illustration of the FG201 transmission power train construction.

The adoption of a centrifugal clutch in conjunction with the vertical engine design has contributed to the simplicity of operation and overall compactness of the tiller unit.

The tine rotor has been enlarged to improve tiller performance. The rotor diameter has been enlarged from ϕ 220 mm to ϕ 260 mm and the tilling width from 300 mm to 450 mm. Also, the screw gear used on the previous FG200 has been replaced with a new worm gear. This has contributed to the greatly reduced rotation speed (1/34), low noise level, and compact design.

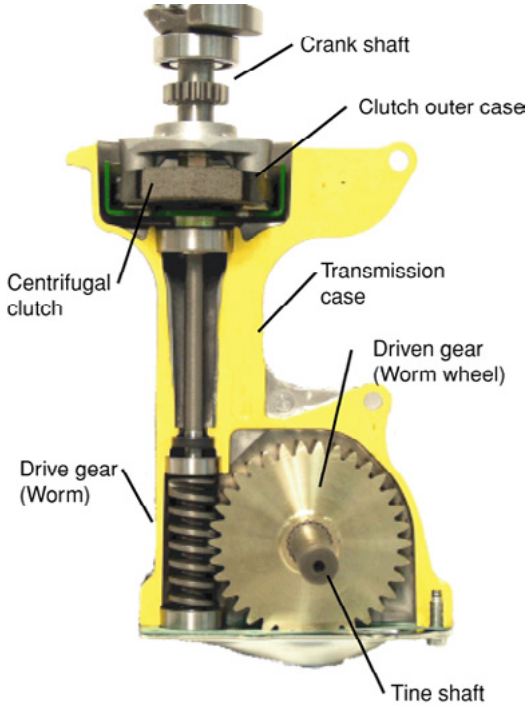


Fig. 3 Transmission of FG201

A barricade has been built around the transmission case to prevent stones, which tend to be kicked up by the rotor activity, from getting lodged in between the plastic fender bolts and rotor while the tiller is being used. See Fig. 4 for an illustration of the transmission case barricade. The barricade is designed to stop flying stones and protect surrounding components. The barricade also allows the transmission to be placed at a lower position, contributing to an overall compact design.

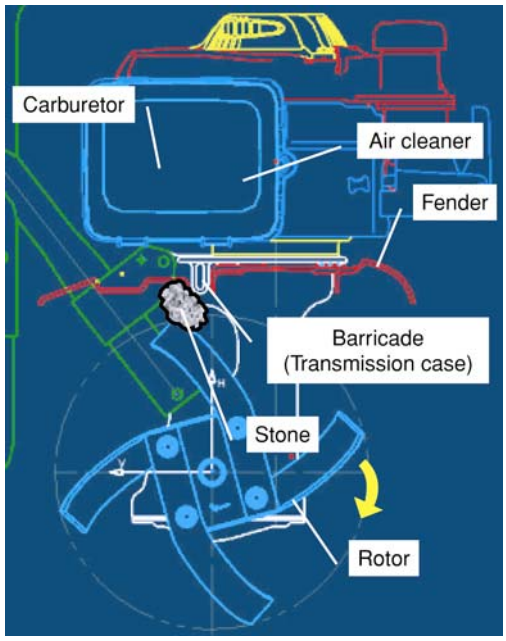


Fig. 4 Barricade of transmission case

3.3 Handle Operation

The handle unit has been fitted with a newly designed 3-level setting. The adjustable drag bar enables the user to adjust the handle bar height from 757 mm to 1,050 mm as required. Each height setting has been designed to provide the most natural posture for the respective work task. The Y-shaped handle was designed to provide firmness and is 450 mm wide, approximate shoulder width, to provide stability during operation.

The handle is constructed to fold easily without the need of any additional tools. It provides added flexibility for transporting and stowing the tiller in small passenger vehicles. A carrying handle is positioned at the center of the unit to enable easy transport with one hand. The FG201 small tiller has been designed to provide the user with maximum benefits.

3.4 Attachments

The FG201 can also handle additional garden maintenance such as ground ridging, cultivation and weeding. Ridging is the process of turning the earth to facilitate lighting, respiration of roots, and to increase water drainage. Cultivation is when air and fertilizer are mixed into the earth as it is being lightly turned. Depending on which attachments are used and the positioning of the operating posture, users can set the ideal leg position spacing according to the tasks at hand thus providing the small tiller with comfortable working space. There are 16 different attachment settings possible and users can select the attachment as required. For example, the side disks can be attached to minimize vibration to further ease tilling work for the elderly and female users. Figure 5a shows the spiral rotor, 5b shows the steel blade and ridger, and 5c shows the side disk attachments.

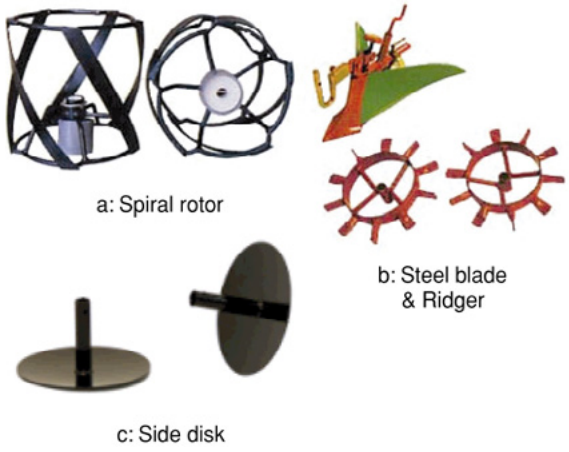


Fig. 5 Attachments

4. Characteristics

4.1 Combining Weight Reduction and Superior Tilling Performance

By using lightweight plastic parts and adopting a lightweight OHV engine, the FG201 has successfully achieved an extremely lightweight configuration of 17 kg, making it very competitive in the dominant over 20 kg tiller class. Generally, as a tiller's performance is improved, the soil reaction force increases, further pushing the tiller in a forward diagonal direction. To counter the increased force, weight needs to be applied. Conversely, as the weight of the tiller unit is reduced, the vertical load exerted on the ground surface becomes insufficient against the soil reaction force resulting in inadequate tiller performance. By applying the following design points, the FG201 has successfully achieved a desirable degree of weight reduction while attaining excellent tiller performance.

1) Optimization of weight distribution

The number of parts surrounding the handle unit has been reduced, and the center of gravity is positioned in close approximation above the rotor shaft. The shift in weight distribution has produced a rotor to drag bar weight balance ratio of 9:1 while achieving a desirable weight loading of 14.7 kg exerted on the tilling blade and still maintaining a vertical load equal to that of existing 2 horse-power class tillers. The optimization of weight distribution and vertical load on the rotor provides sufficient tilling depth and a stable working process.

2) Reconsideration of the drag bar shape

The drag bar is fitted to tilling machines to adjust handle height and fine-tune propulsion force on the tilled soil. The heavier the unit's weight, the larger the torque exerted on the tine shaft. This can often cause the drag bar on 2 horsepower or higher classed tiller machines to jab the soil. Since the area where the drag bar collides directly with the soil is small, the drag bar can be disrupted by the fluctuating soil consistency making smooth tilling work difficult.

As shown in Fig. 6, the drag bar for the FG201 has only one bend point with an obtuse angle. In previous drag bar designs that incorporated 2 bend points, the soil resistance was concentrated on one point. In contrast, the FG201 drag bar has a larger contact area that reduces surface pressure and provides less resistance fluctuation due to changes in soil consistency.

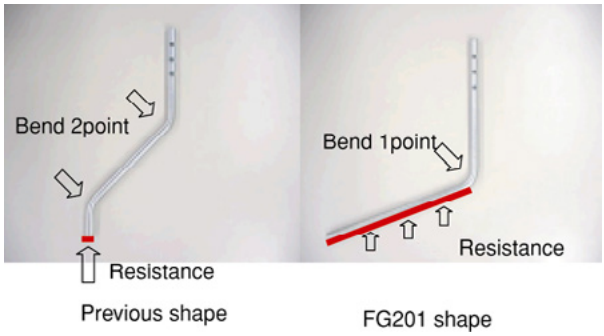


Fig. 6 Drag bar

3) Adoption of a new shaped French rotor

The plate shaped rotor type blade used in the previous FG200 tiller unit has been replaced with the French blade design in which each blade functions independently. The French rotor is lighter and provides better soil biting functionality and improved propulsion.

The bite of the French rotor is improved by increasing the trailing angle of the tilling blade, which helps to reduce the amount of pressure exerted when the tilling blade cuts the soil. Also, the increased bending angle of the blades has reduced the amount of soil that tends to accumulate beneath the transmission case. This has solved the issue of poorer propulsion caused by soil accumulation under the transmission case. The French blade has contributed to the overall lightweight feature of the tiller unit while providing effective penetration of even the hardest ground conditions. Figure 7 shows the French rotor used on the FG201.

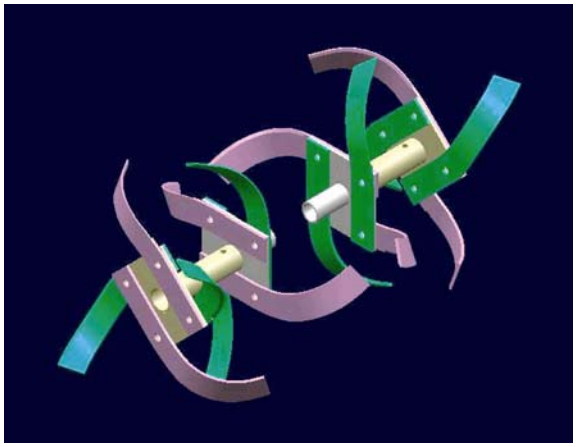


Fig. 7 French rotor of FG201

4) Optimized axial rotation

The rotor diameter and tilling width has been enlarged to 260 mm and 450 mm, respectively, for improved work performance. In comparison with the previous FG200 model, the rotor diameter of the new FG201 has been increased by 30 mm and the tilling width by 150 mm thereby causing a tine shaft torque increase of 1.5 times, from 19.6 N•m to 29.4 N•m. The load factor has been kept at the same level as the previous FG200 model by increasing the rotation speed to 135 rpm and increasing tine shaft torque capacity 1.5 times.

The blade rotation has been increased to 135 rpm to provide stable performance and good work results as well as prevent scattering of soil due to variations in its consistency.

The above listed characteristics have made the FG201 the lightest model in the small tiller class while providing the highest level of work performance. Figure 8 provides a comparative weight analysis and Fig. 9 provides a comparative analysis of work performance for the new FG201 and other current tiller models.

4.2 Reduced Operation Force and Improved Operability

To minimize the recoil starter operation load required to start the engine, the decompressor, which was previously set to the inlet on the FG200 model, has been reconfigured to the exhaust. Also, the angle of decompressor has been adjusted from 240° to 275°. This has reduced the compression exerted when initiating the recoil starter by 40%, from 0.5 Mpa to 0.28 Mpa, achieving a low-effort sure start. Figure 10 shows a comparative analysis of the recoil starter operation load.

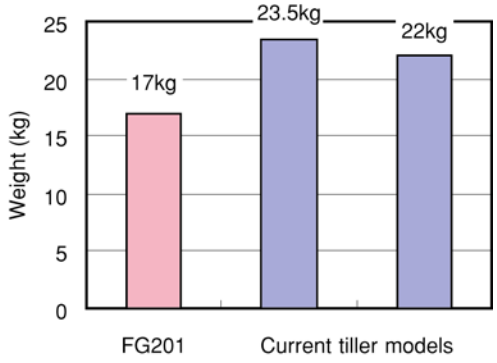


Fig. 8 Comparison of weight

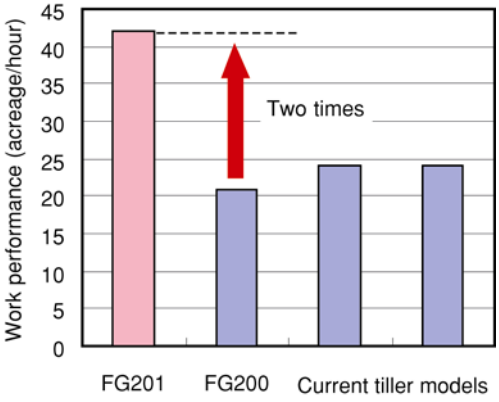


Fig. 9 Comparison of work performance

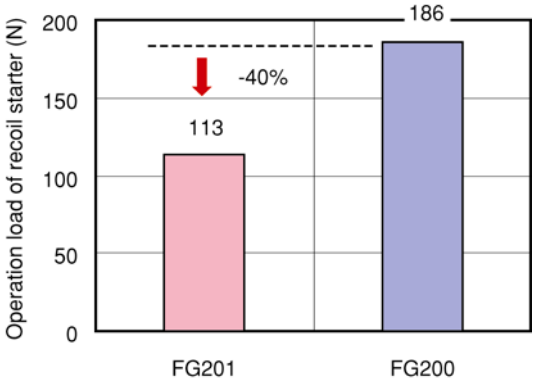


Fig. 10 Operation load of recoil starter

The tiller control is a single lever that incorporates throttle and rotor control, its function is made possible with the use of a centrifugal clutch. This combined control system is responsible for both engine speed and rotor engagement. The operator simply grips the lever to start the rotor and releases the lever to stop it, making this tiller easy and safe to use.

The lever operation load is 14.7 N and the holding load has been set at a low level of 11.8 N. Accordingly, the lever shape is designed so the operator experiences no discomfort after prolonged use, ultimately resulting in minimal operator effort.

4.3 Improved Handling and Transportability

As shown in Fig. 11, the center of gravity on the FG201 has been positioned closer to the tine shaft in comparison with that on the FG200 model. This reduces the operation load for raising and lowering the handle while tilling by 20%. The adjustment in the center of gravity position was made in line with the overall weight reduction of the unit to improve the handle maneuverability when turning the tiller.

This model has been equipped with a convenient folding handle for compact storage and a carrying handle for easy transport as standard features. The handle can be easily folded without the need of any additional tools. The handle can be folded forward or backward as required to enable storage into the most compact locations. The carry handle has been positioned at the unit's center of gravity to provide excellent balance when lifted and makes it easy to carry or change the tiller's direction when used in the garden. Figure 12 provides a comparative analysis of the handle lift operation load. Figure 13 shows the FG201 being transported by the carrying handle and Fig. 14 shows the storing capacity of the FG201.

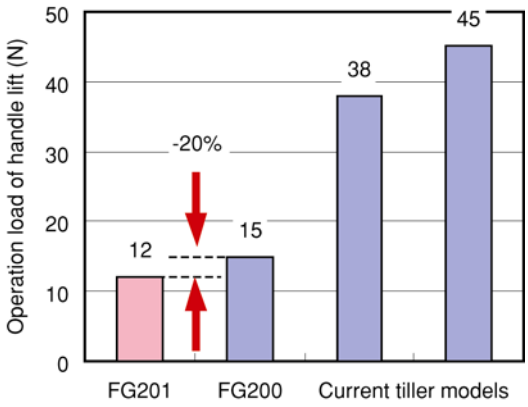


Fig. 12 Operation load of handle lift

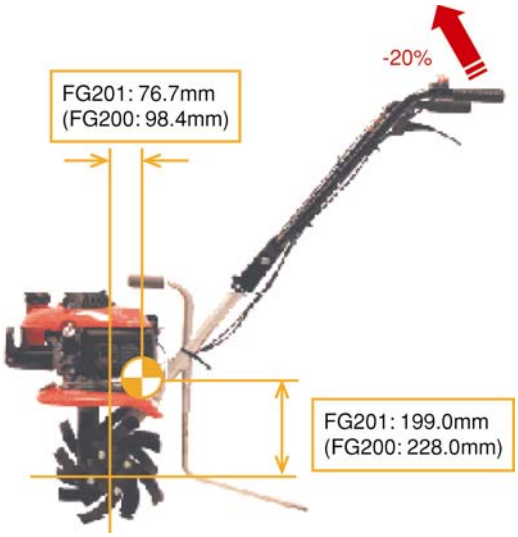


Fig. 11 Center of gravity



Fig. 13 Carrying handle

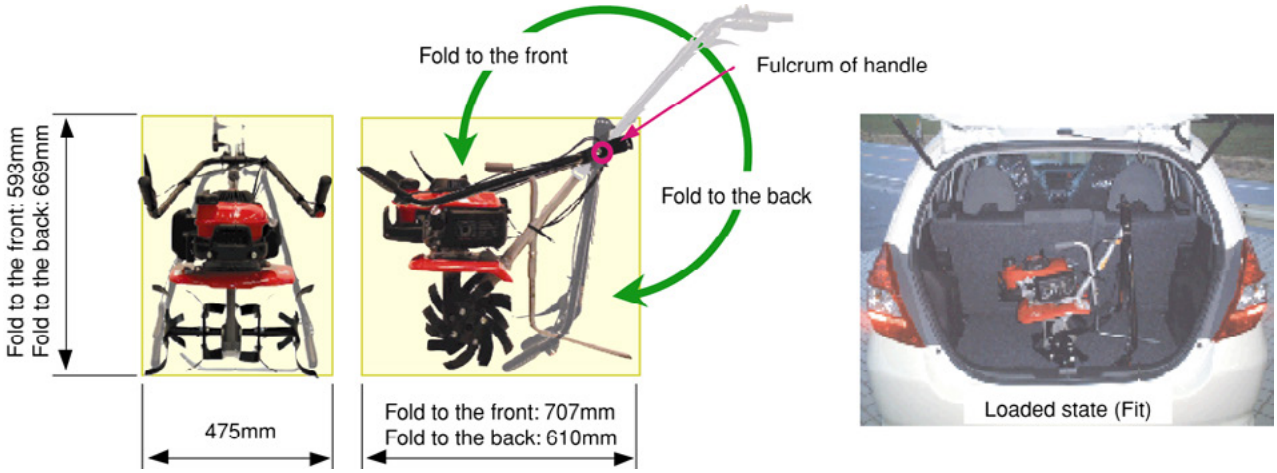


Fig. 14 Storing capacity of FG201

4.4 Improved Maintenance Features

As dust is easily produced during tiller operation, a key criterion in the design of the FG201 was to allow for longer intervals between air cleaner maintenance. The FG201 air cleaner element is a large dry type element that is sufficient for use on a standard engine with 160 cc displacement. The additional surface area enables the FG201 to function well despite large deposits of dust being on the air cleaner. The mouth of the airflow channel has been connected to the inside of the air cleaner case to help prevent dust from being easily pulled into it. This also improves the air cleaner purification performance under normal user conditions by 100 hours, or 5 times that of the 20 hours normally associated with the previous FG200 model. Figure 15 shows the layout of the FG201 air cleaner assembly, and Fig. 16 shows the external view of the air cleaner.

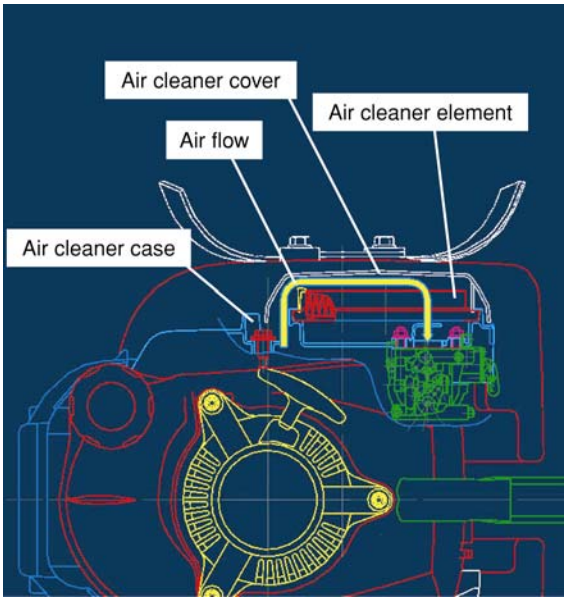


Fig. 15 Layout of air cleaner



Fig. 16 External view of air cleaner

5. Conclusion

The FG201 has been developed as an easy and fun to use compact tiller offering domestic users practical features to provide enjoyment in the cultivation of domestic gardens.

In meeting user demands for a lightweight, easier-to-use tiller offering advanced features and tilling performance, this tiller has been configured with an engine having the same displacement normally found in higher ranked cultivator machines while still maintaining a lightweight design. The transmission has been modified, and optimal tiller blades fitted to satisfy all functional and design requirements.

The FG201 offers the domestic user an easier-to-use set of features achieved through a less complex design, improved workability and improved maintenance features.

Members of the development team hope that this product will bring enjoyment and satisfaction to many domestic users.

The authors would like to express their gratitude to the many people within the organization that have made the development of this product a success.

References

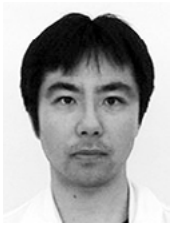
(1) Masuda, S., et al.: III. 4 Small Tractors, III. 5 Power Tillers pp. 78-86 (1975)

(2) Suzuki, S., et al.: Development of General Purpose OHC Engines with Internal Timing Belts, HONDA R&D Technical Review, Vol. 10, pp. 122-127 (1998)

■ Authors ■



Masayuki SASAOKA



Takashi IKEDA



Nobuchika KATAGIRI



Takayuki SATOH

Development of a Four-stroke Engine with Turbocharger for Personal Watercraft

Takaharu KUROSAKI* Kazunori OKADA* Hitoshi YOKOTANI*

ABSTRACT

Recently, there is a movement to apply emission control in marine engines in the United States. Environmental measures for marine engines have become severe. Honda has developed a three seat personal watercraft with a 4-stroke engine installed in consideration of environmental suitability and the future. Using the motorcycle CBR1100XX in-line 4-cylinder 4-stroke engine, with a displacement of 1,100 cm^3 as the base engine, the specifications were modified for marine use to satisfy such areas as engine performance, function, and corrosion resistance, as a PWC engine. Moreover, the turbocharger was employed to obtain a power/weight ratio greater than that of PWCs with 2-stroke engines. Driveability and durability exceeding conventional PWCs with 2-stroke engine were achieved. Emission performance of the engine satisfied EPA2006 and CARB2004 regulations, while fuel economy also improved by 16 % compared to conventional 2-stroke engine models.

1. Introduction

Personal watercrafts (PWC) are widely used as marine leisure craft in Japan, the US and numerous other countries. However, increasing concern over environmental issues has led to emission regulations being applied to marine engines, including outboard motors and PWC, since 1994 in the US. Honda has given consideration to the future, and developed a 4-stroke engine for PWC, which satisfies the requirements of these emission regulations. The remainder of this section will discuss the current trend of emission regulations and the concept behind the new engine.

1.1. Trend of Emission Regulations

The US is a major market for large outboard motors. The comparatively large numbers of these engines and their high level of emissions against power make them the main targets of marine emission regulations. The number of PWC is low in comparison, but they show similarly high levels of emissions against power, and have therefore become the target of emission regulations.

1.1.1. U.S. Environmental Protection Agency (EPA) emission regulations

The U.S. EPA marine emission regulations, as Fig. 1 shows, stipulate a step-by-step reduction from 1998 levels,

* Asaka R&D Center

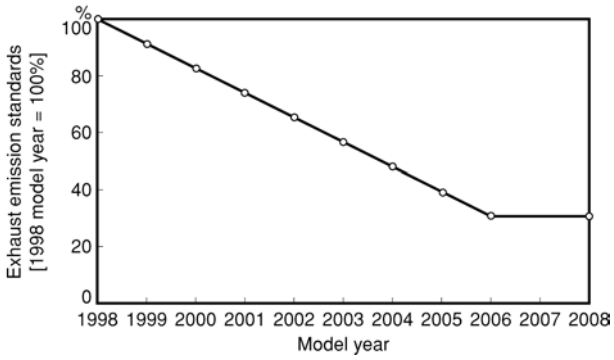


Fig. 1 EPA exhaust emission standards

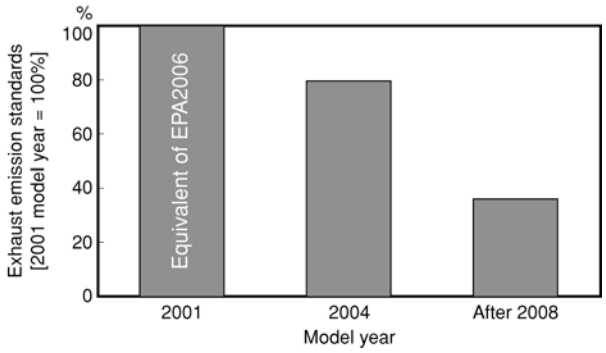


Fig. 2 CARB exhaust emission standards

considered as 100%, to 25% in 2006. Table 1 shows emission measurement modes and their weighting factors. There are five modes based on the power peaks established by the International Council of Marine Industry Associations (ICOMIA). The modes cover idling to full power with wide-open throttle, and almost exactly correspond to running resistance peaks during actual operation. The target for measurements is the combined value of HC and NOx emissions; CO emissions fall outside the scope of these measurements. Five years or 350 hours of operation are required for a PWC to receive assurance for emission deterioration. The regulation values are extremely strict. One of the modes measures emissions with a wide-open throttle; in addition, it has proven to be very difficult to modify conventional 2-stroke engines which were designed as marine engines and do not utilized exhaust gas after-treatment technology to satisfy the regulations. Because of this, design changes such as the incorporation of direct injection have become necessary.

1.1.2 California air resources board (CARB) marine emission regulations

California is an extremely important market for marine products, prompting the CARB to announce emission regulation values stricter than those of the EPA. Figure 2 shows CARB emissions values, with EPA 2006 values shown as 100% of CARB 2001 values. The CARB regulations stipulate reduction to 80% of EPA 2006 values by 2004, and 35% of EPA 2006 values by 2008. The 2008 emission values can be cleared by current 4-stroke outboard motors with a specific power of 50 kW/L, but has proven to be difficult for conventional 2-stroke engines. The California Department of Water Resources has also commenced a program of water analysis to determine the effect of marine engines on water quality, focusing in particular on pollution by unburned oil from the mixed lubrication utilized in 2-stroke engines.

Table 1 Test procedure specified in ICOMIA

Mode number	Engine speed as a percentage of engine rated speed	Engine torque as a percentage of maximum torque at rated speed	Mode weighting factor
1	100	100	0.06
2	80	71.6	0.14
3	60	46.5	0.15
4	40	25.3	0.25
5	IDLE	0	0.40

1.2. Engine Development Concept

Various engine types were studied to provide a new PWC engine, including 2-stroke direct injection and stratified scavenging and 4-stroke engines. However, the increasing stringency of the environmental regulations applied to marine engines prioritized considerations of environmental friendliness and adaptability to future regulations. For this reason it was decided to develop a 4-stroke engine for PWC use. The selection of a 4-stroke engine enables the EPA 2006 emission level to be met, and prevents water pollution caused by the combustion of mixed oils. The following design concepts were established to develop a 4-stroke engine which could compete with 2-stroke engines mainly used in PWC:

(1) A high level of environmental friendliness combined with sportiness and ease of handling;
(2) Superior specific power and power-weight ratio to a 2-stroke engine to achieve class-topping power performance;
(3) Use of a mass-production engine as the base engine, to enable existing facilities to be used for production; this would control cost increases occasioned by a new engine design, and allow the product to be offered to purchasers at a reasonable price;
(4) Superior durability and reliability in marine use to that of a 2-stroke engine.

2. Engine Technologies

2.1. Selection of Engine Configuration

Motorcycle, automobile and outboard motor engines were examined to provide the base engine. The CBR1100XX motorcycle engine was finally selected due to weight considerations, compactness and specific power capable of competing with the 2-stroke engines already on the market. The stroke of the engine was extended 5 mm, and the displacement increased to 1,235 cm^3. Figures 3 and 4 show cutaway views of the base engine and the newly developed PWC engine respectively. Table 2 shows the main specifications of both engines. Despite their numerous advantages, 4-stroke engines are generally inferior to 2-strokes in specific power. Increasing engine speed,



Fig. 3 Based motorcycle model

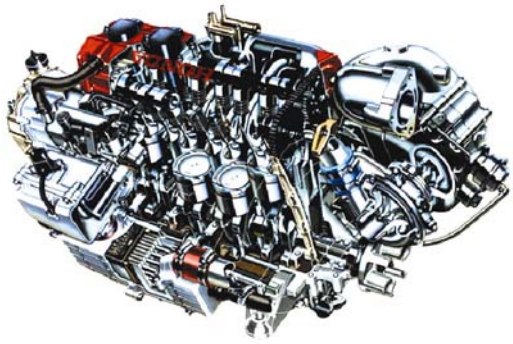


Fig. 4 Developed turbochaged model

supercharging, and increasing displacement were examined as methods of increasing power in the new engine. Increasing the cruising engine speed would cause cavitation to occur in the water jet pump, reducing its efficiency. Engine speed reduction was studied as a method of preventing the engine from exceeding the impeller application limit revolutions, but this caused a feeling of over revving and was rejected to maintain the inherent quietness of the 4-stroke engine. A large increase in displacement would increase weight, affecting the power-weight ratio. These considerations led to the development of an engine fitted with an exhaust turbocharger to meet target performance requirements.

2.2. Configuring the Motorcycle Engine for Marine Use

The configuration of PWC engines is simple, without water pumps, transmissions, etc. However, certain other features are indispensable to a marine engine; configuration changes necessary to convert a motorcycle engine to marine use are discussed below.

2.2.1. Lubrication system

In PWC engines, the jet pump and crankshaft are generally directly connected by a damper. The engine layout locates the crank center in the lowest possible position, bringing the jet pump as close to the bottom of the craft, as possible, thereby increasing pump efficiency. The new engine has been provided with a dry sump lubrication system, with a thin oil pan located at the bottom of the crankcase. The crank center has therefore been lowered 93 mm from the bottom of the engine in comparison to the base model. The oil tank has been re-positioned to the front end of the front cover, and is integrated with the engine. The oil pump is built in and is directly driven from the ACG flywheel boss by means of a semi-Oldham's coupling. This has simplified the structure, dispensing with the need for chains and drive gears.

Table 2 Specification of based motorcycle model and developed turbocharged model

Items		Based motorcycle model	Developed turbocharged model
Engine type		4 stroke inline 4 cylinder	4 stroke inline 4 cylinder
Valve train		DOHC 16 valve	DOHC 16 valve
Displacement	(cm^3)	1 137	1 235
Bore × stroke	(mm)	79 × 58	79 × 63
Compression ratio		11.0	8.5
Cooling system		Liquid cooled, closed loop	Water cooled, open loop
Lubricating system		Wet sump	Dry sump
Fuel supply system		Programmed fuel injection	Programmed fuel injection
Intake system		–	Turbocharger and intercooler
Balancer shaft		Applied	Applied
Max. power / ne	(kW/rpm)	105.6 / 9 500	121.4 / 6 100
Max. torque / ne	(N·m/rpm)	111.9 / 7 250	191.8 / 5 500

Ruffling of the engine oil level generated by extremely high acceleration such as when a PWC jumps or spins can cause air to mix with the oil. To prevent this, the oil tank in the new engine is positioned vertically so that the oil level is consequently high. The oil tank is separated into front and rear chambers by a metal gasket. The scavenging pump discharges into the rear chamber. The front defoaming chamber features four baffle plates to prevent ruffling of the oil level. By positioning the oil pump suction opening at the bottom of the tank, aeration has been prevented even during hard spins or when the craft hits the water after a jump, causing impact acceleration in excess of 400 m/s^2.

The new engine is provided with oil pressure warning switches for both high and low pressures. When the oil pressure falls below the pressure required to maintain engine revolutions at normal craft speed, the switch issues a warning, controls engine speed, and signals the need for an oil check to the user. The low pressure switch shuts off the engine when there is no oil, or when it judges that the craft has overturned. These switches ensure that warnings are issued in advance of engine trouble caused by low oil due to the user having forgotten to check, etc.

Because a PWC can overturn while in operation, measures have to be taken to prevent outflow of oil. In a 4-stroke engine in particular, it is essential to prevent oil flow from the breather system when the engine is overturned. A vertical breather chamber was therefore built into the vertical oil tank, positioned at the side of the engine and the oil tank, as shown in Fig. 5. When the engine is overturned, the oil level is lower than the height of the separate line of the both breather chambers. This system ensures that even if the craft remains in an overturned position, oil will not flow into the breather hose. This is a simple structure with no special accessories, ensuring a high level of reliability.

2.2.2. Cooling system

PWC are not fitted with water pumps, and are generally provided with direct cooling systems using jet pump water pressure. The layout is the same in the new engine. A branched orifice is positioned behind the jet pump cooling water intake, providing water to the oil cooler, which cools the engine system, and the intercooler, which cools the exhaust system. Figure 6 shows the operation of these systems. Because jet pump water pressure reaches up to 490 kPa at the craft's top speed, if a thermostat is positioned at the engine cooling water outlet, the cooling system reaches an almost equivalent pressure to the jet pump before the thermostat valve opens. For this reason, outboard motors are usually provided with a spring-operated relief mechanism. However, this causes the thermostat to stop functioning to control water temperature. In addition, when flushing the system with fresh water after use on the sea, it is difficult to ensure a sufficient volume of water if water pressure is low. Because jet pump water pressure in the new engine is proportional to engine speed, water volume has been adjusted by optimization of the diameter of the orifice without a thermostat. The temperature range was established for a target area spanning from low-speed planning to high-speed operation. Chromate treatment and resin top coating were adopted to increase corrosion resistance on the inner surfaces of the cooling system because of the proven record of this treatment in outboard motors.

2.2.3. Exhaust system

Apart from the turbocharger, the exhaust system is constructed of aluminum with a water-cooled jacket, enabling cost reductions and weight savings. To prevent exhaust energy loss to the turbocharger as much as possible, the system has been provided with the shortest isometric collecting type exhaust manifold available. Because melting damage can easily occur if insufficient cooling water is supplied to the aluminum exhaust manifold, body temperature is monitored by a contact type thermo-switch. This system enables trouble to be prevented by issuing warnings before overheating occurs when the cooling system is blocked or is being flushed. The cooling system in most marine engines operates by injecting cooling water into the exhaust system. In PWC, this necessitates measures to control reverse flow. Measures to prevent reverse flow of

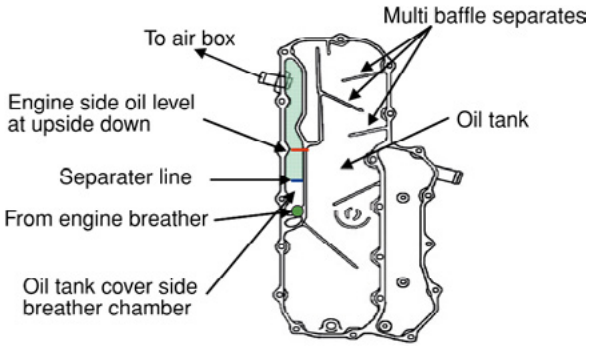


Fig. 5 Engine breather system

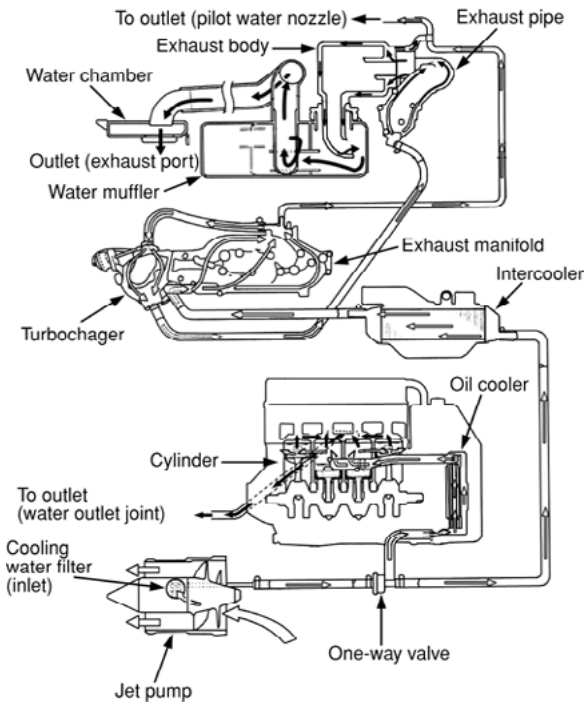


Fig. 6 Cooling system

cooling water when the new engine overturns are shown in Fig. 7. The water level inside the water muffler remains below the exhaust inlet even when the craft is upside-down. Even if a little water gets past this system, a water trap volume in the upper section of the exhaust body prevents reverse flow, therefore preventing inundation of the exhaust turbocharger and the engine itself.

2.3. Engine Performance

2.3.1. Power performance

One development concept behind the PWC to be fitted with the new engine was the achievement of natural turning performance with a lean angle similar to a motorcycle's. To achieve this, a deep-V hull was adopted for the bottom of the craft. Because this hull shape has a high running resistance, the power requirement for the craft was higher than the maximum power of conventional PWC with 2-stroke engines. This level of power was achieved by providing the engine with an exhaust turbocharger. Figure 8 shows the power performance of the newly developed PWC turbocharged engine, developed by changing the specifications of the CBR1100XX motorcycle engine. Figure 9 shows the indicated mean effective pressure for the engine speeds shown in Fig. 8. The new engine has a specific power of 98.3 kW/L, and a power-weight ratio of 0.78 kg/kW; this figure rises to 2.77 kg/kW in the completed craft, the top level for a three-person PWC. Engine speed at maximum power has been kept down to 6,100 rpm, and users will therefore have no concern about excessive engine speed when operating the craft continuously at maximum power with WOT, experiencing a smooth sense of acceleration due to the effectiveness of the turbo.

2.3.2. Turbocharger specifications

The exhaust turbocharger was specifically designed for the new engine, and is exclusively manufactured by Ishikawajima-Harima Heavy Industries Co., Ltd. It is the first direct-water-cooled turbocharger with a waste gate of this size in the world. The layout of the turbocharger is shown in Fig. 10. The turbine housing is constructed of niresist cast iron, a material with superior seawater corrosion resistance, and has a replaceable anode to prevent stray current

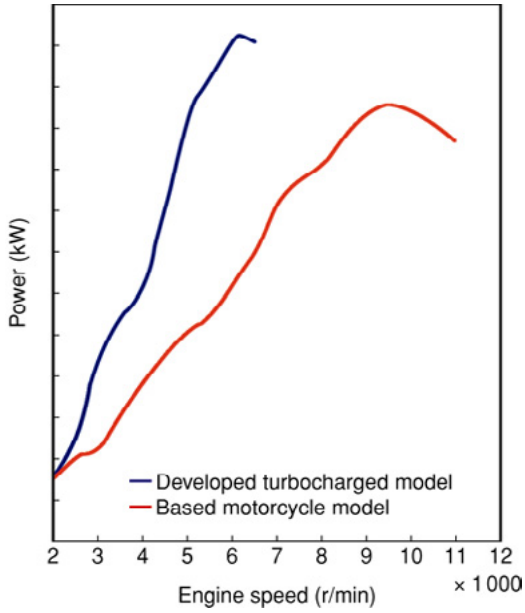


Fig. 8 Engine performance of based motorcycle model and developed model

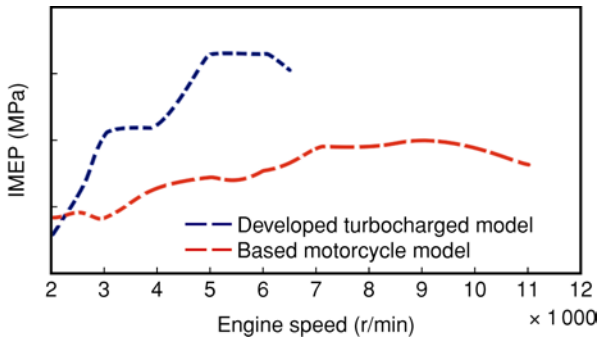


Fig. 9 IMEP of based motorcycle model and developed model

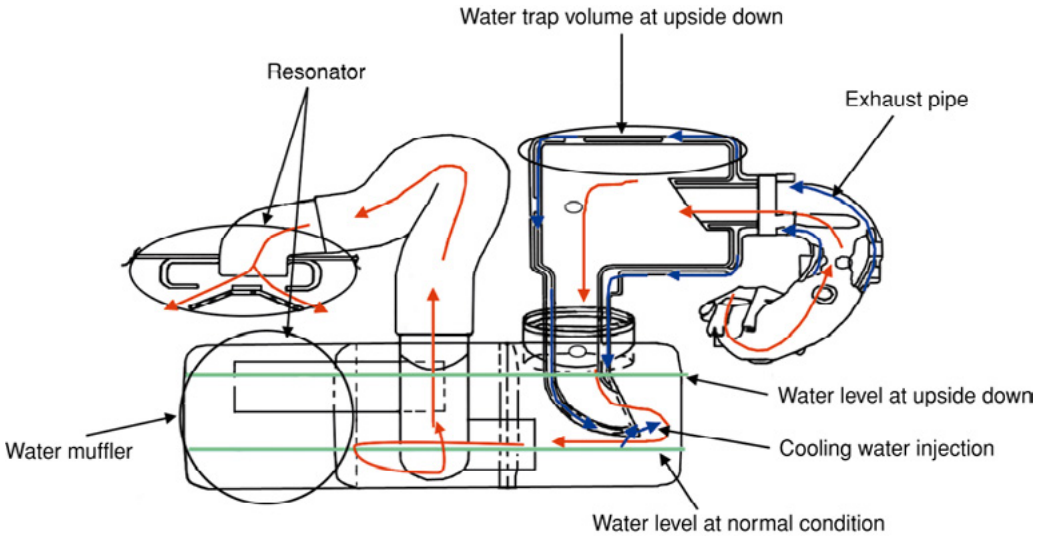


Fig. 7 Layout of exhaust system

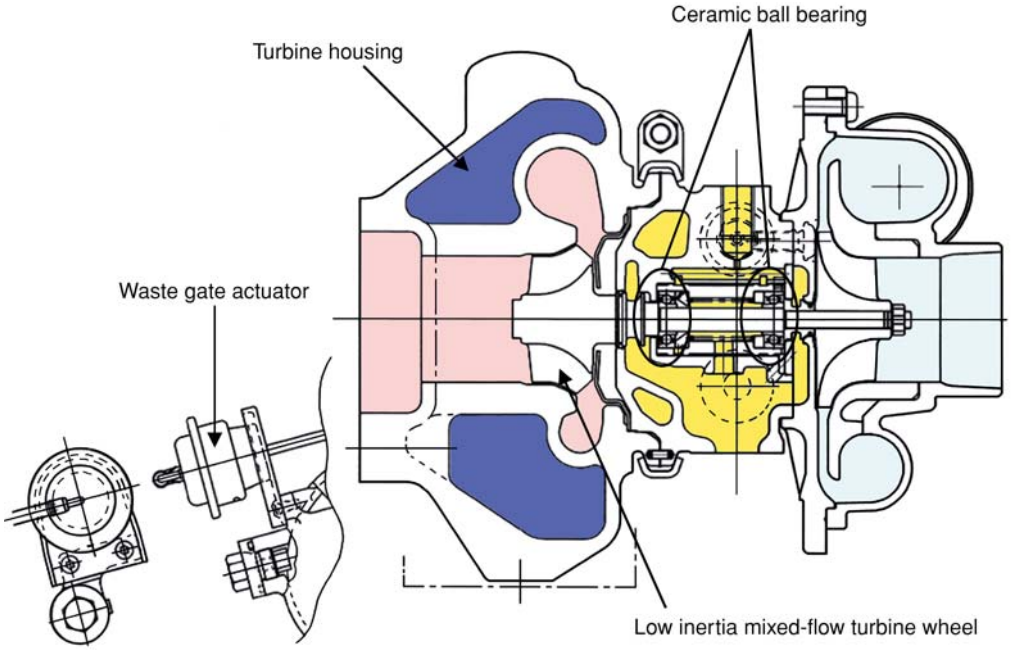


Fig. 10 Layout of the turbo charger

corrosion. The housing is exposed to high-temperature exhaust gas, but water cooling ensures that the surface temperature remains under 85 °C even at full power with WOT. To achieve the high level of throttle response required from PWC engines, a low-inertia mixed-flow turbine wheel has been adopted. As Fig. 11 shows, turbine weight has been reduced 22%, and acceleration performance has been increased 20%. In addition, turbo lag has been significantly reduced. Matching torque characteristics to this turbocharger has enabled the achievement of a unique feeling of acceleration. As Fig. 12 shows, the fineness of the exhaust pulse characteristic of turbos has reduced the acceleration noise level by 21% against a natural aspiration model, ensuring quiet and comfortable cruising.

The turbine speed of exhaust turbochargers normally increases when atmospheric pressure declines in high areas, to prevent over-run, the turbine speed at sea level was reduced. In the new turbocharger system, the craft's altitude is detected from the atmospheric pressure when the engine is started. Target supercharging pressures have been established up to different altitudes; the pressure setting is lowered if it is judged that the craft is at an altitude where turbine over-run will occur. This system has enabled the engine to demonstrate the same power and maximum speed performance at 1,500 m as at sea level, leading to considerable speed differences between the new model and a craft with naturally aspirated engines in which power drops due to lower atmospheric pressure. It has therefore been possible to maintain performance levels with the adoption of a turbocharger.

2.3.3. Engine parts specifications for high power

The addition of a turbocharger to the new engine has increased IMEP by more than 40% against a naturally aspirated engine. To cope with this increase, various changes have been made to engine components. The pistons are cold-forged, and temperature is controlled by oil injection cooling to the backsides of the pistons to increase reliability at continuous high load use. High-rigidity fully rounded pistons have been utilized to prevent increased friction or

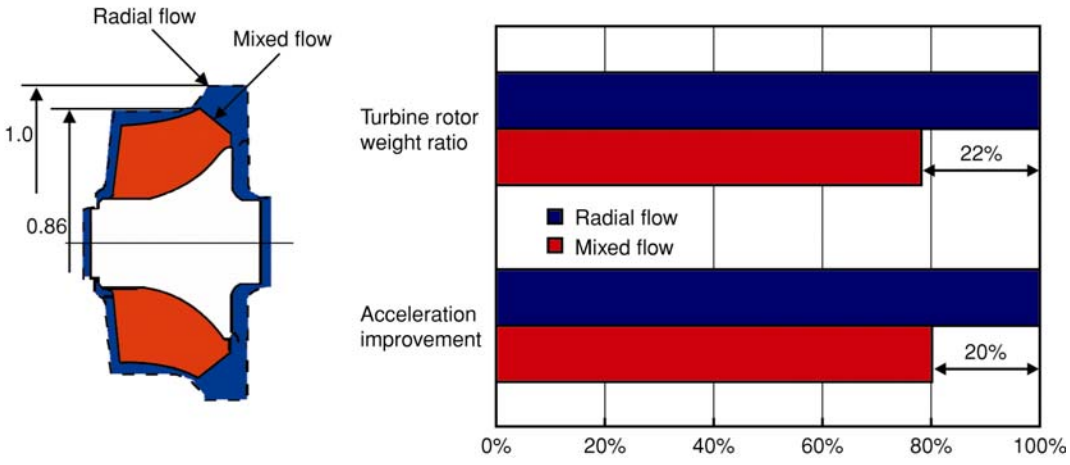


Fig. 11 Improvement of acceleration

temperature increases caused by deformation. Compression height has been increased as much as possible and sufficient land thickness ensured, enabling reduction of the ring groove temperature. The ring grooves receive hard alumite treatment. Figure 13 shows a comparison of the pistons in the newly developed model with the pistons in the base motorcycle model. Short, thick, high-strength connecting rods have been utilized; because the engine speed is low, the connecting rod lambda ratio has been reduced, consequently reducing the height of the engine and enabling the seat to be lowered. Figure 14 shows a comparison of the connecting rods used in the new model and the base motorcycle model. Surface treatment has been applied to the piston pins, and changes to the diameter and length of the pins have increased rigidity. This has increased durability and reliability under high loads, including that of the piston pin bosses.

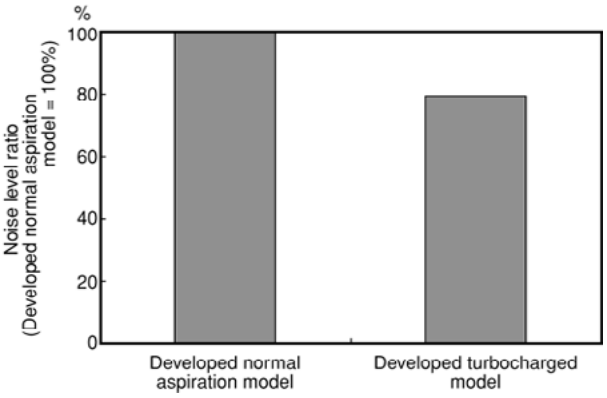


Fig. 12 Noise level of acceleration

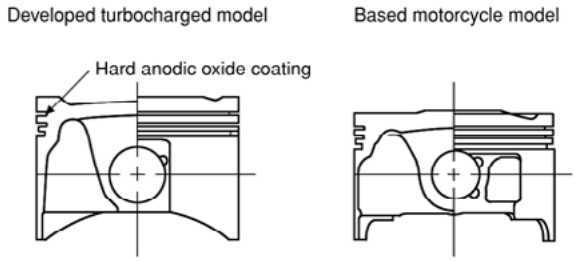


Fig. 13 Shapes of piston

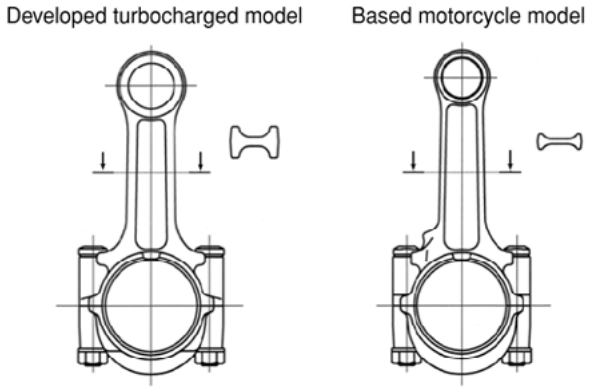


Fig. 14 Shapes of connecting rod

The new turbocharger-fitted engine has a volumetric efficiency of more than 180%, and the volume and temperature of exhaust gases place a severe load on the exhaust valves. To cope with this, SUH751 has been adopted as the material for the valves, to increase high-temperature oxidation resistance and prevent air leakage from the valve sheet. To reduce engine vibration and increase cruising comfort, a bi-axial secondary balancer has been fitted, necessitating increases to the durability and reliability of the turbocharger bearings.

3. Emission Performance

Figure 15 shows a comparison between CARB 2004 emission regulation values and family emission levels (FEL) calculated from power for the newly developed engine and a 2-stroke 3-cylinder 1,200 cc engine used for test purposes. Intensive study of valve timing and fuel injection timing have enabled the achievement of high power in the turbocharged engine while satisfying the CARB 2004 regulation values. Both the turbocharged and normal aspiration engines have received two star labels.

4. Fuel Consumption in Actual Running

Table 3 shows specific fuel consumption at each load level in the EPA marine emission measurement modes measured during bench tests. The newly developed model represents a significant improvement over the 2-stroke, 3-cylinder 1,200 cm^3 model used in tests. However, fuel consumption during actual running changes depending on the running resistance of the craft. The hull of the PWC in which the newly developed engine is fitted has a high level of drag. Increasing power to counteract this has meant that the improvements in fuel consumption during actual running cannot match the specific fuel consumption improvements measured in tests, and when running the craft at full speed with WOT, there is only a small fuel consumption improvement against existing 2-stroke models. On the other hand, Fig. 16 shows that the newly developed engine demonstrates a 16% improvement in fuel economy over approximately a month of idling, towing and ordinary running, and the same results can be expected in ordinary use.

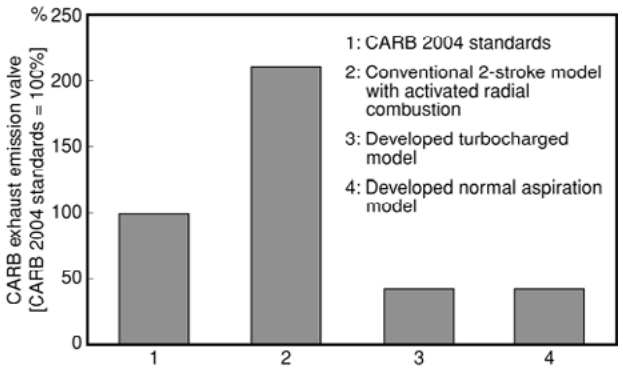


Fig. 15 CARB exhaust emission values

(g/kW h)

ICOMIA Mode Number	Conventional 2-stroke model with activated radical combustion	Developed turbocharged model	Developed normal aspiration model
1	389	310	286
2	343	307	305
3	330	329	341
4	350	418	421
5	(No load)	(No load)	(No load)

Table 3 Specific fuel consumption of emission test mode

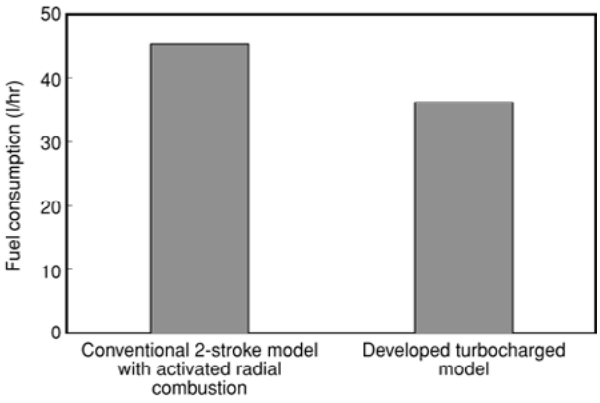


Fig. 16 Fuel consumption of actual riding

5.Conclusion

To develop the engine discussed in this paper, various changes were made to a base motorcycle engine to adapt it to marine use. These changes, and the addition of a turbocharger, have increased performance to a level higher than that of conventional 2-stroke models. This has enabled the development of a 4-stroke PWC which is both sporty and easy to handle, and which demonstrates a superior level of performance.

(1) A motorcycle engine was adapted to PWC engine requirements such as ability to be overturned and direct seawater cooling. These adaptations enabled the development of a marine 4-stroke engine.

(2) The new engine has cleared both the EPA 2006 and the CARB 2004 emission regulations. It does not cause water pollution due to unburned oils like 2-stroke models, and improvements to fuel consumption during actual running have contributed to reducing environmental impacts.

(3) The fitting of an exhaust turbocharger has enabled the achievement of specific power and power-weight ratios equivalent to those of 2-stroke engines. In addition, control of turbocharger pressure has ensured optimal power characteristics with little change due to the altitude at which the craft is used.

(4) Restricting the exhaust pulse with the turbocharger and controlling engine speed at maximum power has reduced exhaust noise, and enabled a balance of quietness and speed. Lowering engine speed at maximum power has improved the feeling of acceleration, and increased the potential of the craft to provide enjoyable marine leisure to users.

6. Acknowledgments

The team at Ishikawajima-Harima Heavy Industries Co. Ltd. accepted the challenge of achieving a world first, and together with the Honda development team overcame difficult design issues in developing an exhaust turbocharger for exclusive use with the PWC discussed in this paper. The authors would like to take this opportunity to offer their sincere thanks to everyone concerned.

References

(1) Shogase, H., et al.: Honda's New Personal Watercraft – The AquaTrax F12/F12X, Honda R&D Technical Review, Vol. 14, No. 1, pp. 1-10 (2002)

■ Authors ■


Takaharu KUROSAKI


Kazunori OKADA


Hitoshi YOKOTANI

Development of the Motor for the Civic Hybrid

Hirohisa OGAWA* Kenji FUKUDA*

ABSTRACT

A thin DC brushless motor was developed as auxiliary power for the Civic Hybrid, which is positioned to take the world lead in fuel consumption for five-passenger automobiles. The concept was to create a hybrid car using an existing mass-produced engine in an existing mass-produced car body. This raised more issues than the Insight, which was made with an engine and body specifically designed for that purpose. The Civic has a heavier body than the Insight. In order to assure its power performance and increase the energy regenerated during deceleration the engine displacement had to be increased and the regenerative performance of the motor had to be improved. However, the Civic body has the same width as the Insight, so it was not possible to increase the motor width in correspondence with the regenerative performance. The objective in development of the motor, therefore, was to improve performance while keeping the motor the same width. The methods used to achieve this objective were to increase the torque constant and to reduce the losses in all parts involved. Specifically, the space gained in the axial direction by functional integration of parts made it possible to increase the cumulative stator thickness, and the adoption of new coil winding methods made it possible to enlarge the coil diameter and the width of the teeth. As a result, the motor regenerative torque was improved approximately 30% while maintaining the same motor width, and the average efficiency of the motor in the practical use area was improved approximately 3%.

1. Introduction

In response to the demand for automobiles that are clean and consume less fuel, Honda began to market an ultra-low fuel consumption hybrid 2-seater car fitted with an IMA (Integrated Motor Assist) system in 1999 – the INSIGHT[(1)]. In 2001, the CIVIC Hybrid was marketed, giving the 5 passenger, 4-door CIVIC an improved IMA system. The motor in the IMA system provides assistance during acceleration and energy recovery during deceleration, and also provides for rapid engine start so that there is no feeling of uneasiness with the Idle Stop System. The motor fitted to the CIVIC Hybrid was developed to improve regenerative performance and at the same time be light weight and compact for productivity improvements. This paper introduces the motor technologies used to achieve these aims.

* Tochigi R&D Center

2. Aims of Development

The developmental aims for the CIVIC Hybrid motor were the following three items and the realization of new functions.

2.1. Increase in Regenerative Torque and Improved Efficiency in the Practical Use Range

In comparison with the INSIGHT, due to an increase in car body weight and a reduction in engine friction through the adoption of a cylinder idling system, etc., there is an increase in deceleration energy that the motor can recover. This means it is necessary to improve the corresponding regenerative torque. Improving regenerative torque while leaving motor efficiency as it is would lead to an increase in loss. Furthermore, natural air-cooling would not be feasible, so in this case a new cooling system would be required. A new cooling system would cause other problems in terms of space, weight, and overall efficiency, eliminating some of the advantages of the hybrid system. This means it is necessary to increase motor regenerative torque while simultaneously improving efficiency in the wide practical use range. It is particularly important to reduce losses on the high load side.

2.2. More Compact

In comparison with the INSIGHT that had a specially designed engine and car body, the target for the CIVIC Hybrid was to use a compact mass produced engine and mass produced car body, meaning that a compact motor was essential. Specifically, the development targets were to improve efficiency and regeneration performance corresponding to the increase in deceleration energy without changing motor width dimensions, so that, in comparison with the INSIGHT's 3-cylinder 1.0 L engine, a 4-cylinder 1.3 L engine, having the same 1,695 mm width as the INSIGHT, could be fitted in the CIVIC car body.

2.3. Lighter Weight and Productivity Improvements

In order to achieve the improved fuel economy that was the target for the CIVIC Hybrid, efforts were made for overall vehicle weight reduction, and at the same time, weight reduction of the motor. In addition, to expand the potential use of the 5-passenger, 4-door CIVIC Hybrid body, it was necessary to make further productivity improvements.

The following sections of the paper explain the specific technologies developed to achieve these aims.

3. Increase in Regenerative Torque and Improved Efficiency in the Practical Use Range

In order to achieve the above aims, efforts were made to increase torque constant, in comparison with conventional motors, and at the same time to reduce energy loss in each part. Increasing torque constant is not simply a matter of improving regenerative torque, but also contributes to improving efficiency in the practical use range. Generally, when the torque constant is increased, it is possible to move the motor's high efficiency range towards the lower engine speed side. With a conventional motor applied to the CIVIC as it is, the motor's high efficiency range is slightly to the high engine speed side of the practical use range, as shown in Fig. 1. Therefore, increasing torque constant also leads to improvements in the practical use range efficiency.

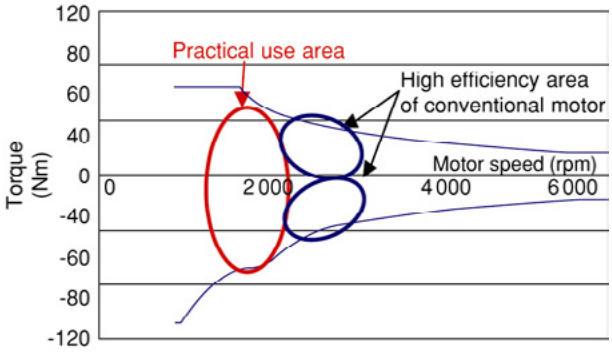


Fig. 1 10-15 Mode traveling area

3.1. Torque Constant Increase

An increase in torque constant is mainly accomplished by increasing the cumulative stator layer thickness (referred to as stator cumulative thickness hereafter). However, with a conventional structure, it is not possible to maintain axial direction space, so increasing the stator cumulative thickness was not possible. As explained in the paragraph below, thanks to functional integration of the parts inside the motor, it is now possible to maintain axial direction space, and so, as shown in Fig. 9, stator cumulative thickness has been increased by 13%. Mainly due to these modifications, torque constant could be increased by approximately 16% over the conventional model.

3.2 Reduction in Copper Loss, and Improved Saturation Flux Density

In order to reduce copper loss, the wire diameter was increased from 1.3 mm to 1.5 mm, reducing wire resistance by 33%. In addition, as shown in Fig. 2, the teeth width was increased, thereby improving saturation flux density, and by improving magnetic saturation during high torque generation, there is a reduction in loss in the high torque range.

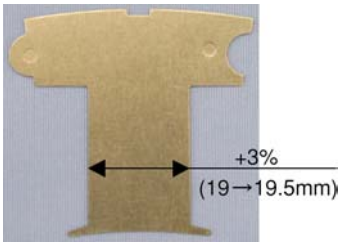


Fig. 2 Width of teeth

Here, if magnetic wire diameter enlargement and teeth width extension were carried out using conventional method, the thicker wire must be used in reduced space. Therefore, there would be a drastic reduction in the number of coils, causing a drop in performance. However, here we have applied a new winding method, as outlined below.

3.3. Asymmetric Winding

As shown in Fig. 3(a), if the wire is wound on teeth covered with a completely uniform insulator thickness, the coil becomes thicker in the middle, and will contact the adjoining coils. By taking countermeasures so that the winding does not accumulate in the center, even when using

wire with a thicker diameter the number of coils can be maintained. Specifically, the method is, as shown in Fig. 3(b), to have asymmetric insulator thickness, so that the thick part of the coil is not in the center, and that the coils are offset so that they don't come in contact each other. This means that it is possible to increase the wire diameter and widen teeth diameter without causing a drop in performance.

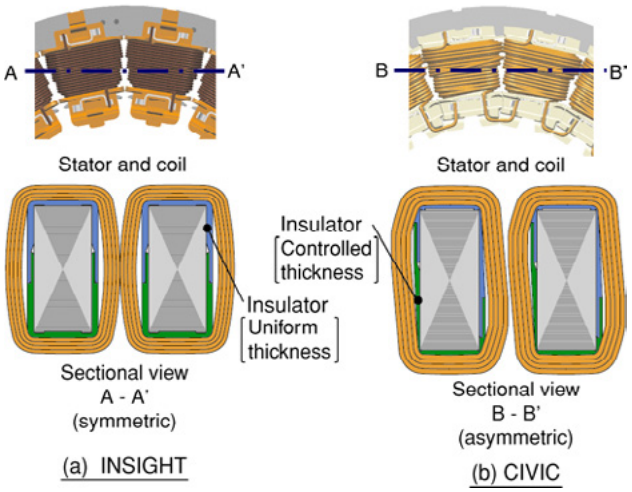


Fig. 3 Comparison of stator and coil

3.4. Revision of Silicon Steel Stamping Direction

Revision of silicon steel stamping direction was carried out to further improve performance. Generally, when non-directional silicon steel is used, there is no difference in properties due to direction, so stamping is carried out giving priority to yield. In addition, with a separated stator, in particular the teeth part and the back yoke part magnetic flux flow directions are straight so there are no restrictions in stamping direction.

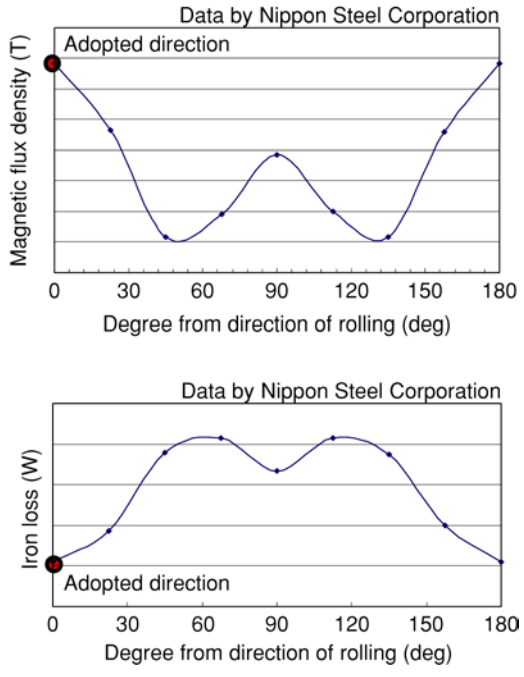


Fig. 4 Magnetic flux density and iron loss

However, even with non-direction silicon steel, as shown in Fig. 4[(2)], there are small differences in properties due to direction. A detailed analysis was made of the amount of magnetic flux in each part of the stator for this motor, and of direction, as shown in Fig. 5, to determine optimum stamping direction. From the results of this study, priority is given to the flow of magnetic flux in the teeth, and as shown in Fig. 6, it is clearly best that the motor diameter direction and rolling direction match, so this was adopted. As a result, it is possible to improve, by approximately 1.5% over the conventional design, efficiency that leads to improvements in electromagnetic saturation in the low engine speed high torque range, and to a reduction in iron loss.

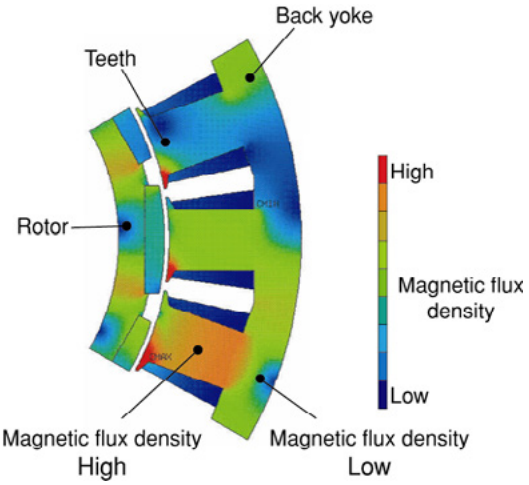


Fig. 5 Simulation of magnetic circuit

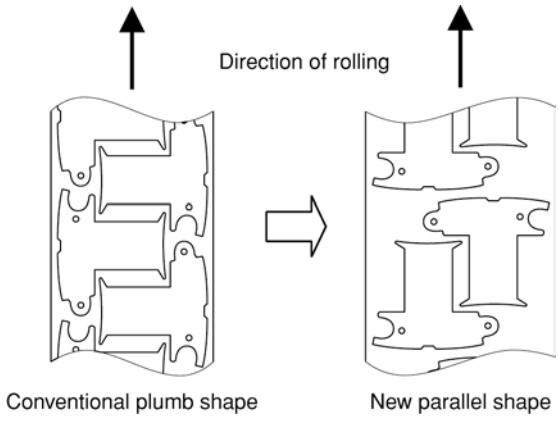


Fig. 6 Shape of stamp working

3.5. Summary of Increases in Regenerative Torque and Improvements in the Practical Use Range Efficiency

By carrying out the measures outlined above, as shown in Fig. 7, maximum regenerative torque is 30% better than with the conventional model, and with motor efficiency improvements (Fig. 8), average motor efficiency in the practical use range was improved by approximately 3%.

Major motor specifications are given in Table 2.

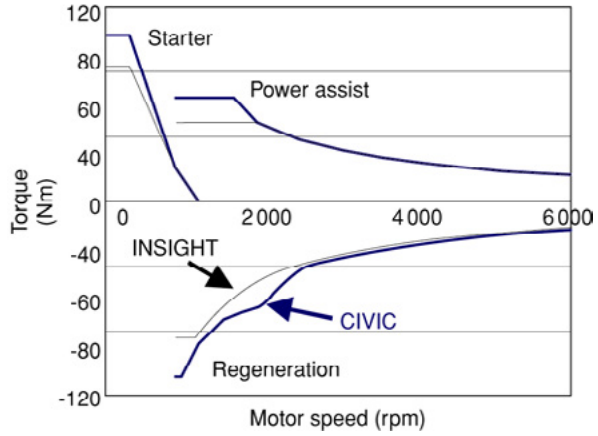


Fig. 7 Motor performance curve

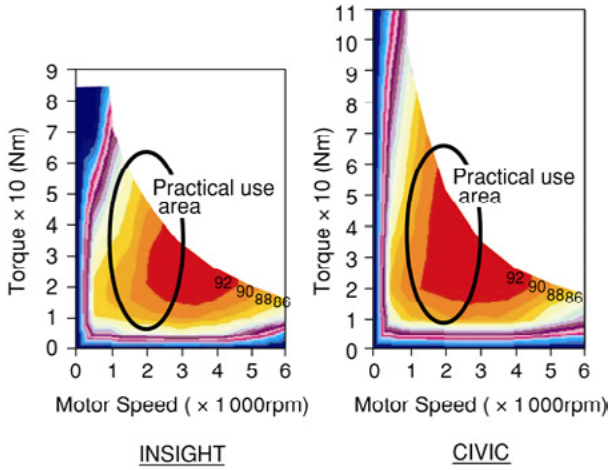


Fig. 8 Motor efficiency

Table 2 Motor specification

Motor type	DC brushless	
	(1) Power assist	(2) Regeneration
Max power	10kW	12.4kW
Max torque	49Nm (103Nm at engine Start)	108Nm

4. More Compact

In order to maintain motor width while making regenerative torque and efficiency improvements, functional integration of parts inside the motor was carried out, and axial direction space was reviewed. Space was created by eliminating the resin cover that, in the conventional structure, functions to hold the bus ring and the silicon plastic injection-molding frame for the coil connected insulation. When the resin was eliminated, as for bus ring holding, the structure was changed so that each separate part is an integrated part, able to support itself. As for the injection-molding frame function, the clearance with the adjoining insulator was created so that the silicon plastic cannot flow in, and a framework was formed by the bus ring around the outside and insulator around the inside.

Due to these measures, as shown in Fig. 10, motor width was not changed but stator cumulative thickness was increased by approximately 13%.

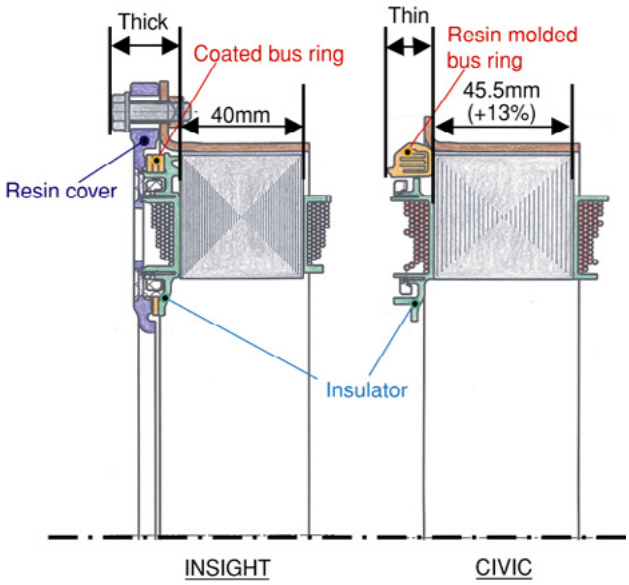


Fig. 9 Cutaway view of stator

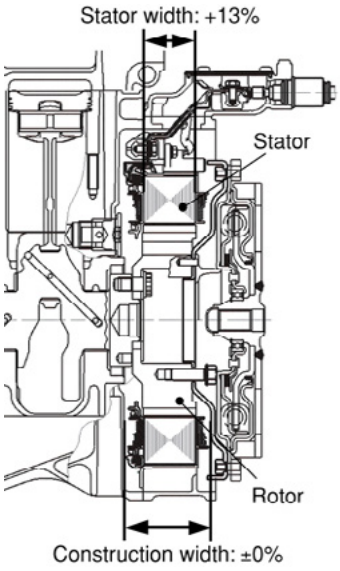


Fig. 10 Cutaway view of motor

5. Weight Reduction and Productivity Improvements

5.1. Sinter Diffusion Bonded Rotor

As shown in Fig. 11, the rotor has two functions – the outside functions to hold the magnets and create the magnetic circuit, while the inside functions to transfer torque between the crank and the transmission. Conventionally, carbon steel is selected, to make the torque transfer function feasible. The lost wax manufacturing method is adopted as the most appropriate when using this material. In contrast, the adoption of sinter diffusion bonding, which makes it possible to combine two materials having different properties that are

necessary for the functions on the inside and the outside, means that it is possible to use a high strength material on the inside, while using a soft magnetic material on the outside. While material density drops and connection strength is maintained, saturation flux density is improved by 30%. This leads to improved performance and a 15% reduction in weight.

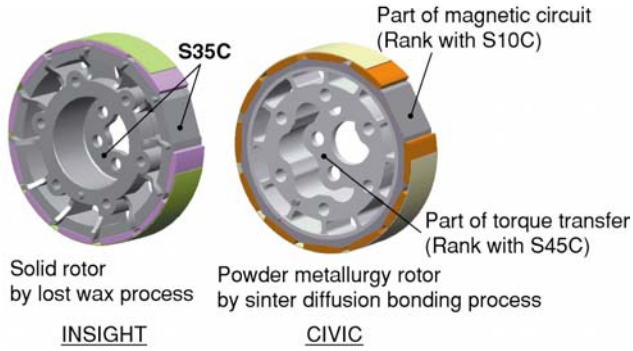


Fig. 11 Rotor construction

5.2. Resin Molded Bus Ring

The performance demanded of a bus ring is to make the distribution of electricity to each layer feasible, while providing insulation between each layer and GND insulation. As shown in Fig. 12, a conventional bus ring is coated with insulation in each layer, and during stator assembly, the structure deals with each one individually. In contrast, by using float-molded resin molding technology, it is possible to integrate all three parts into one, dramatically improving productivity.

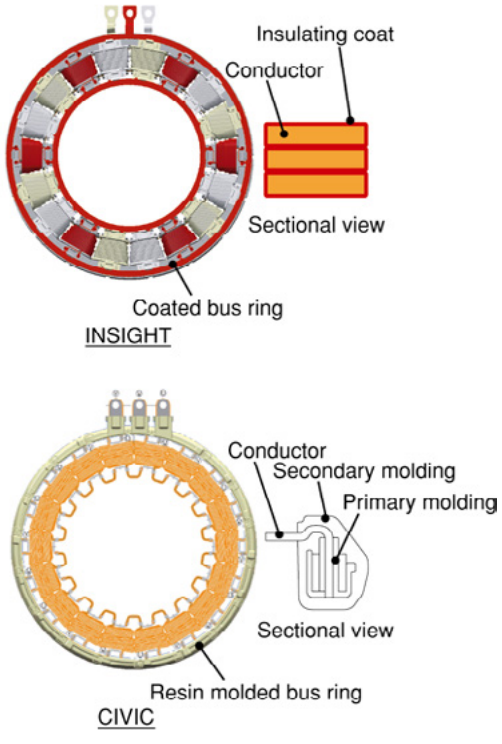


Fig. 12 Bus ring construction

This bus ring structure maintains the mutual insulation function with the primary molded body, and maintains GND insulation with the secondary molded resin. For this reason, it is necessary that the secondary molded resin completely envelop the primary molded body. The primary molded body floats in the mold on a support pin which is removed according to the resin hardening timing, and the resin completely fills the mold, so that no signs of the pin remain. By adopting this technology, insulation performance is maintained, and at the same time, manufacturing and assembly time is reduced by approximately 50%, achieving a dramatic improvement in productivity.

5.3. Neutral Point Direction Wiring

Conventionally, as shown in Fig. 13, a neutral point bus ring was used for each part, and these were connected. In contrast, without using a special bus ring, the structure is such that neutral points are formed with the wires. Specifically, using a salient-pole concentrated winding method on the separate teeth, it is possible to maintain a wire length the same as the distance to the adjoining neutral point, and when fusing to the bus ring, on the neutral point side, too, there is fusing between neutral points. Through this, the neutral point bus ring is eliminated, the structure is simplified, and weight is reduced.

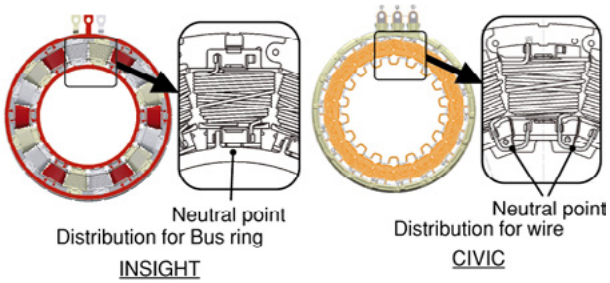


Fig. 13 Neutral point construction

6. New Function

With the CIVIC Hybrid, one developmental target is to achieve smooth driving by utilizing a motor assist function. The following is an explanation of newly applied functions to actualize that smooth driving.

6.1. Reduction in Vibration during Deceleration by Employing Motor Control

In order to achieve smooth driving, the vibration control technology used in the INSIGHT during idling has been more widely applied to deceleration. Specifically, the vibration reduction technology reduces vibration by utilizing a direct crankshaft to motor connection that is a feature of the IMA system, generating phase torque in the motor that is the reverse of the engine torque generated during deceleration. At this time, the amount of torque generated is determined by engine speed and load, and based on the crank position signal the torque phase is determined from engine speed and load.

The effectiveness of this control is shown in Table 1 and Fig. 14.

Table 1 Effect of damping control

Measuring point	Effect
Floor vibration	-6dB
Engine vibration	-4dB

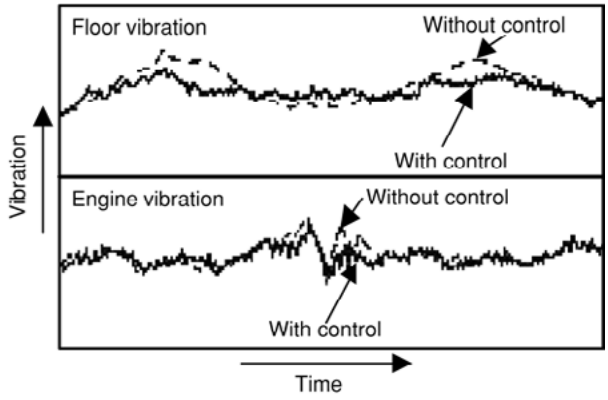


Fig. 14 Vibration in deceleration

6.2. Reduction in the Car Body Jerky Feeling through Motor Control

As another new function, the motor control is used to reduce the car body jerky feeling through throttle control when driving a manual transmission equipped car in low gear. Specifically, as a method of reducing vibration and utilizing the direct motor connection to the crankshaft in the same way as in the vibration control system, motor torque is applied at an appropriate time in response to car body longitudinal vibration generated according to throttle opening changes, and the jerky feeling is restricted. At this time, assistance or regeneration is determined from the direction of throttle change, and the amount of applied torque and the timing is determined from the amount of change in engine speed. The effect when this control is applied is shown in Fig. 15.

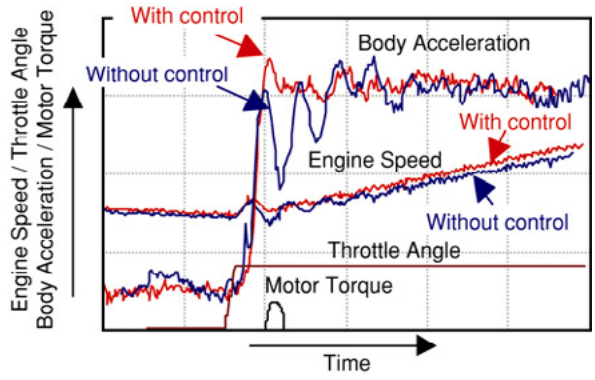


Fig. 15 Effect of smoothing control

7. Summary

In order to achieve the target performances set for the CIVIC Hybrid's motor, the torque constant was increased, and loss was reduced for each part. Specifically, maintaining axial direction space through the functional integration of parts made possible an increase in stator cumulative thickness. Furthermore, by adopting a new winding method, both wire diameter and teeth width were also increased. As a result, the developmental targets to improve drivability became possible, and at the same time, motor regenerative torque was improved by approximately 30% while retaining the same motor width, leading to an average efficiency improvement of 3% in the practical use range.

References

(1) Fukuo, K., Fujimura A., Saito, M., Kadota, K., Takiguchi, S.: Development of the Ultra-low Fuel Consumption Hybrid Car "INSIGHT", HONDA R&D Technical Review, Vol. 11, No. 2, pp. 1-8 (1999)

(2) Wakisaka, T., Kubota, T., Kaido, R.: Reduction in Rotor Iron Loss through the Optimum Selection of Electromagnetic Steel Sheet, The Institute of Electrical Engineers of Japan, Rotor Research Conference, No. 126 (1999)

■ Authors ■



Hirohisa OGAWA



Kenji FUKUDA

Development of High Power Energy Storage for the CIVIC Hybrid

Kazuya OHZONO* Morio KAYANO*

ABSTRACT

An attempt was made to improve the power density of a conventional nickel metal-hydride battery for installation of a hybrid system in the limited space available in a heavier vehicle. The plates were extended by 12%, the negative collector tab was eliminated, and the number of welds joining plate and collector was increased. These measures reduced the internal resistance by 19%. As a result, the power density during regeneration improved by 27%, making it possible to deal with increased regeneration energy without increasing the cubic volume of energy storage installed.

1. Introduction

Today, with an ever growing awareness of environmental issues such as global warming, etc., the demand for automobiles with reduced exhaust emissions, starting with carbon dioxide, has become stronger. Honda, in response to this demand, has made modifications to its gasoline engines, focusing on VTEC (Variable Valve Timing and Lift Electrical Control)[(1)]. In addition, Honda has developed a hybrid vehicle, leading to further possibilities, refining Honda's proprietary technology, the IMA (Integrated Motor Assist) system[(2)], and fitting it to the INSIGHT in 1999 with which it entered the market.

Now, in order to promote wider dissemination of the hybrid vehicle, Honda has developed the CIVIC Hybrid, based on the concept of fitting the IMA system to a mass produced vehicle without major changes to the vehicle body. Due to an increase in vehicle weight in comparison with the INSIGHT and the addition of a cylinder idling system[(3)], there is an increase in input and output electricity to and from the energy storage, and a demand for performance improvements.

This report explains the aims of the development of a new energy storage system (referred to as D2 hereafter) for the CIVIC Hybrid, and the performance it has achieved.

* Tochigi R&D Center

2. Aims of Development

In developing D2, a nickel metal-hydride battery (referred to as Ni-MH battery hereafter) was used, similar to that used for energy storage in the INSIGHT (referred to as D1 hereafter). As shown in Table 1, some reasons for the use of a Ni-MH battery are that Ni-MH batteries, in comparison with lead batteries used in conventional automobiles, have a higher power output density per unit of weight[(4)], have high energy density and a long life, among other features.

Table 1 Constitution and power density of secondary batteries

	Positive electrode	Negative electrode	Electrolyte	Power density
Ni-MH	NiOOH	MH	KOH	Over 500W/kg
Li-ion	$LiMnO_4$	C	Organic electrolyte	Over 1 000W/kg
Ni-Cd	NiOOH	Cd	KOH	170W/kg
Pb-acid	PbO_2	Pb	H_2SO_4	300W/kg

With the CIVIC Hybrid, due to the increase in vehicle weight and the cylinder idling system, there is a marked increase in input to the energy storage system, particularly during regeneration, over that of the INSIGHT, by approximately 80%. (See Fig. 1.) If D1 were used in the CIVIC Hybrid, there would be the possibility that not all of the regeneration energy could be recovered, reducing the fuel economy benefits of the IMA.

There are two ways the problem with D1 could be addressed in the CIVIC Hybrid.

(1) Increase the number of batteries installed in the vehicle.
(2) Improve the maximum charge energy for each cell in the battery.

If the first option were selected, with the increase in the number of cells installed, it leads to the increase in weight and installation volume, which is in direct conflict with the basic concept. In addition, voltage would rise and it would become necessary to change the set voltage for other components included in the IMA system. For these reasons, the second option was selected.

Specifically, the target for maximum charge energy was set at 27%, carrying out a simulation of regenerated energy increase due to increased vehicle weight and the cylinder idling system.

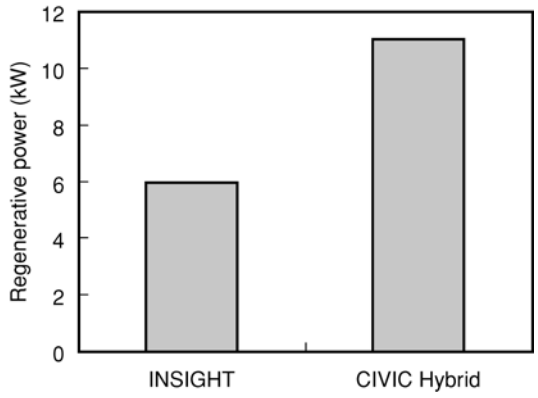


Fig. 1 Regenerative power

3. The Battery

The Ni-MH negative electrode is metal-hydride, and when charging and discharging the hydrogen is absorbed or released respectively. As for metal-hydrides, many are based on rare earth metals $LaNi_5$, and there are also those based on the Laves $TiMn_{1.5}$ or $ZrMn_2$. At present, considering the service life of the product, the use of rare earth metals is most common, and so the Ni-MH battery for the IMA, uses rare earth metals as well.

The reactions when charging the Ni-MH battery are shown below.

Positive electrode $Ni(OH)_2 + OH^- \rightarrow NiOOH + H_2O + e^-$ $(E_0 = +0.49V)$

Negative electrode $M + H_2O + e^- \rightarrow MH + OH^-$ $(E_0 = -0.823V)$

Total Reaction $Ni(OH)_2 + M \rightarrow NiOOH + MH$ $(E_0 = 1.318V)$

E_0 = Equilibrium potential

In this way, with Ni-MH batteries, consumption of electrolyte is restricted because there is no water directly applied in the charge or discharge reactions. Therefore, the battery service life is longer than with a lead battery or nickel cadmium battery. In addition, unlike Li-ion batteries, no organic solvents are used in the electrolyte, so even when the electrodes are excessively charged or excessively discharged, there is no possibility of spontaneous combustion, and therefore safety is not compromised.

4. Power Output Improvements

4.1. Causes of Power Output Reduction

When the battery is charged or discharged, the electrodes shift from the equilibrium state to the transient state, and so cell voltage is a different voltage from that of the equilibrium state. This phenomenon is called polarization, and when an electrical current flows, the size of the resulting polarization is called overvoltage. There are two major factors in overvoltage – one is called the activation overvoltage, which is the overvoltage needed for the material relating to electrode reaction (hydrogen ions in the case of Ni-MH) to move to the electrode across the solvent absorbing layer called the electrical double layer of the plate surface (see Fig. 2) and, the other is called the concentration overvoltage, which is generated according to the concentration gradient that occurs in the reaction of adjoining electrode surfaces.

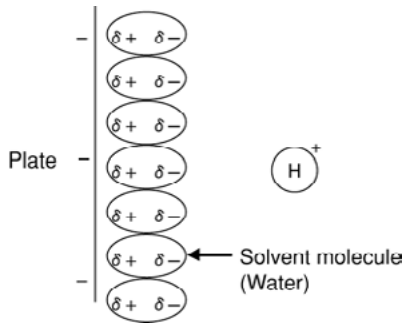


Fig. 2 Electrical double layer

The relationship between these overvoltages, and cell voltage at the time of charge and discharge (cell closed circuit voltage) E are as shown in Eq. (1).

$$E = E_0 - [(\eta ct)_a + (\eta c)_a] - [(\eta ct)_c + (\eta c)_c] - I \cdot R_i \quad (1)$$

E_0 : Cell open circuit voltage
ηct : Activation overvoltage
ηc : Concentration overvoltage
a : Negative electrode (anode)
c : Positive electrode (cathode)
I : Cell load current
R_i : Cell internal resistance

The overvoltage η which is a total of ηct and ηc is determined, in an ordinary battery, according to the Butler-Volmer formula, as shown below.

$$i = i_0 [- exp (- \alpha \cdot n \cdot F/(R \cdot T) \cdot \eta) + exp ((1 - \alpha) n \cdot F/(R \cdot T) \cdot \eta)]$$

R : Gas constant
T : Absolute temperature
n : Number of electrons involved in the electrode reaction
α : Mobility coefficient
F : Faraday constant
i_0 : Exchange current density
i : Current density

When overvoltage is low, developing the above index, items from the third can be ignored. So, looking at the first two items, it becomes as follows.

$$\eta = R \cdot T /(i_0 \cdot F) \cdot i \quad (2)$$

Then Eq. (1) can be simplified.

$$E = E_0 - (R_\eta + R_i) \cdot I \quad (3)$$

This R_η is known as polarization resistance, and is expressed as follows.

$$R_\eta = R \cdot T /(i_0 \cdot F \cdot A) \quad (4)$$

A : Electrode surface area

In the case of the Ni-MH battery actually used in the IMA, cell voltage against current in the use range, as shown in Eq. (3), is confirmed to change linearly. Figures 3 and 4 give examples.

Because the cell voltage when the electrical current is flowing is determined according to Eq. (3), Power output P at that time is expressed as below.

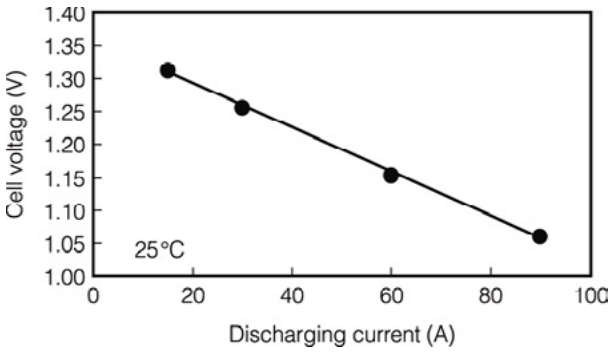


Fig. 3 Cell voltage and discharging current

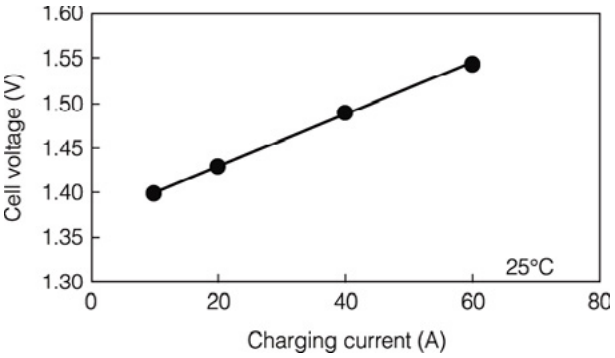


Fig. 4 Cell voltage and charging current

$$P = E \cdot I = E_0 \cdot I - R_T \cdot I \cdot I \quad (5)$$

$R_T : R_\eta + R_i$

From the above, by reducing the battery direct current resistant components R_η and R_i, battery output can be improved.

4.2. Battery Power Output Calculation Method

Equation (5) shows the relationships between P, E and I when a particular power is being charged or discharged. Using Eq. (3), P and E are as follows.

$$P = E \cdot I = E \cdot (E_0 - E)/R_T \quad (6)$$

This relationship between P and E can be expressed as a schematic diagram, and is shown in Fig. 5. However, this relationship is only feasible when overvoltage is low and is in the range where Eq. (2) applies.

In addition, when Ni-MH battery is used, if the battery is over-charged and/or excessively discharged, there are secondary reactions, such as water decomposition and additive material reactions, leading to deterioration in the Ni-MH battery. Therefore, an upper limit voltage E_U is established in order to prevent over-charging, and a lower limit voltage E_L is established in order to prevent excessive discharge. Because generally these values are set in the overvoltage range where Eq. (2) is feasible, it is possible to apply Eq. (6).

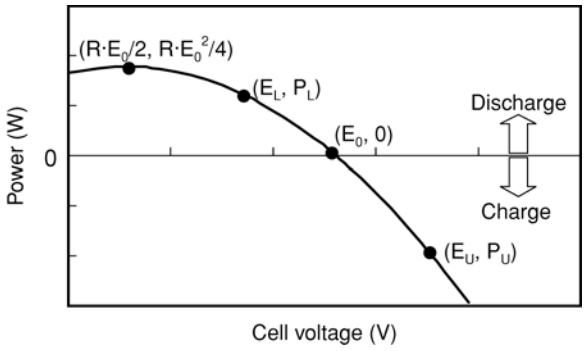


Fig. 5 Change of the electric power by cell voltage

Establishing the upper and lower limit voltage in this way, the maximum absolute values of the discharge power and charge energy can clearly be seen from Fig. 5, and is the P_L value at the time of E_L, and is $|P_U|$ at the time of E_U. Expressing charging as usual and P_U as an R_T function gives the following.

$$E_U = E_0 - R_T \cdot I_U \quad (7)$$

I_U : Current when it becomes E_U

$$\therefore I_U = (E_0 - E_U)/R_T \quad (8)$$

$$/P_U / = /E_U \cdot I_U / = /E_U \cdot (E_0 - E_U)/R_T / \quad (9)$$

Maximum charging power is determined using Eq. (9). In order to determine the R_T reduction target necessary to improve P_U by 27%, E_U is upper limit voltage sub-reaction constraint and E_0 is a unique value for the battery system,

using Eq. (9) as a fixed value, $|P_U|$ varying rate against the R_T reduction rate is determined. Here, taking D1's R_T and P_U as R_T0 and P_U0 respectively, and D2's R_T and P_U as R_T1, P_U1 respectively, the relationship between R_T1/R_T0 and $|P_U1/P_U0|$ is shown in Fig. 6.

From the above, the R_T1 reduction target was set at 19% or above in order to improve maximum charge power by 27%.

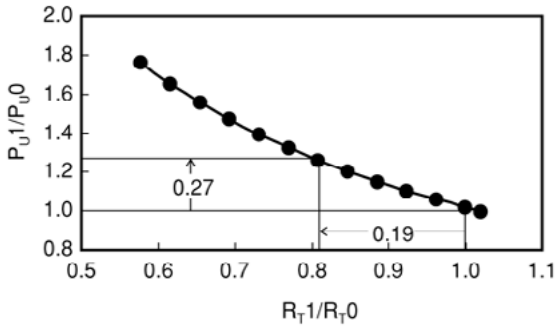


Fig. 6 Relation of regenerative electric power and cell resistance

4.3. Specific Means of R_T1 Reduction

The two elements that make up R_T1 are, as noted earlier, cell internal resistance R_i and polarization resistance R_η due to overvoltage. R_i is the resistance in the case of electrical flow through the conductive parts inside the cell, and as shown in Fig. 7, is composed of conduction resistance of the positive and negative plates, conduction resistance of positive and negative collectors, and connection resistance, etc. On the other hand, R_η is expressed in Eq. (4), and the elements that can be changed are exchange current density i_0 and electrode surface area A. Here, i_0 can be expressed as the following.

$$i_0 = n \cdot F \cdot A \cdot k \cdot C_o^{(1-\alpha)} \cdot C_R^{\alpha} \qquad (10)$$

k : Speed constant
C_O : Oxidant density
C_R : Reductant density

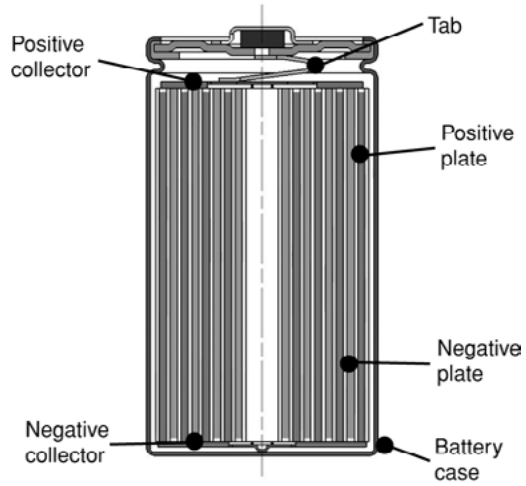


Fig. 7 Structure of cell

As it is dependent on electrode surface area A, it is clear that an increase in A will lead to a drop in R_η.

In this project, a study was carried out, looking at two means of improving maximum charge power.

1) R_i reduction
2) Expansion of electrode surface area.

As means of reducing R_i, in order to reduce current flow part resistance, the following are possibilities.

i) Positive and negative collector current flow resistance reduction
   - Increase thickness of collectors
   - Revise shape

ii) Positive and negative plate current flow resistance reduction
   - Increase thickness of plates
   - Increase length of plate

iii) Collector and plate connection resistance reduction
   - Increase spot surface area for weld bonded parts
   - Increase number of weld points

iv) Tab current flow resistance reduction
   - Increase thickness of tabs
   - Increase tab length

As it is well known that item iv) concerning tab current flow resistance reduction gives little contribution, items i) through iii) were studied.

First, shape of collectors were changed for item i) positive and negative collector current flow resistance reduction, simultaneously for item iii) collector and plate connection resistance reduction. Concerning the collector thickness increase, because the gap between the positive collector and the battery case was insufficient, there was the danger of a short between positive and negative electrodes, so those items were set aside.

The shape change details are shown in Fig. 8.

The main points of the changes were first that by lengthening the positive and negative collector slits, the number of weld points were increased by 27%and 55% respectively, thereby increasing the contacting area between plate and collector; and secondly that by eliminating the negative collector tab, current running is eliminated, and a current density drop is achieved. From the above measures, cell internal resistance could be reduced by 14%.

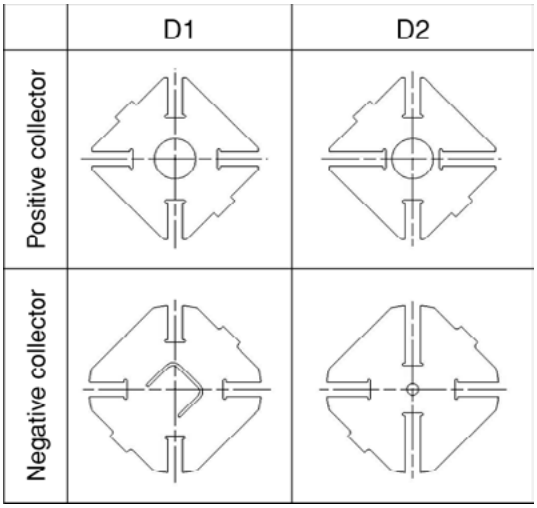


Fig. 8 Form of collector

Next, was an examination of item ii) – the plate current flow resistance reduction. With an increase in thickness, there was a marked reduction in volume of the reaction substances – the nickel hydroxide and the hydrogen storage alloys – which led to a drop in capacity. On the other hand, changing the length of the plates led to an improvement in electrode surface area in (2), and because it also led to a reduction in R_η, further study was made of extending the length of the plates.

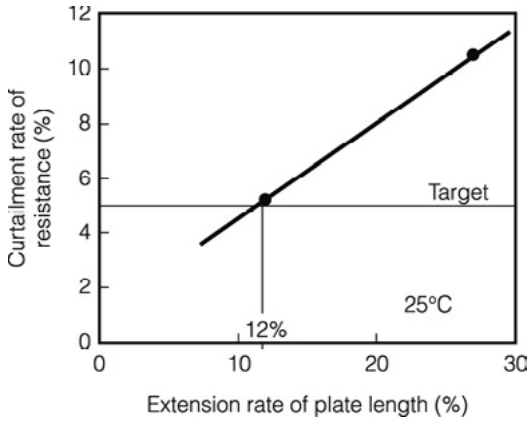


Fig. 9 Effect of plate length on resistance

Figure 9 shows the effect of plate length on resistance reduction. Against the ultimate resistance reduction target of 19%, a resistance reduction of 14% was possible by changing the shape of the collector, so the target for resistance reduction by lengthening the plate is the remaining 5%. From Fig. 9 it can be seen that the plate should be extended 12% in order to achieve the resistance reduction target.

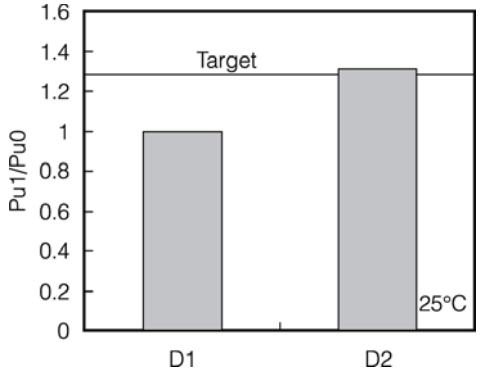


Fig. 10 Ratio of charging power

4.4. Effect of the Countermeasures

The effect of the countermeasures outlined above is shown in Fig. 10.

As intended, it was possible to reduce internal resistance by 19%, giving a 27% improvement in maximum charging power, and so achieving the target.

In addition, because there is a reduction in resistance, discharge power, too, was improved by approximately 10%, as shown in Fig. 11.

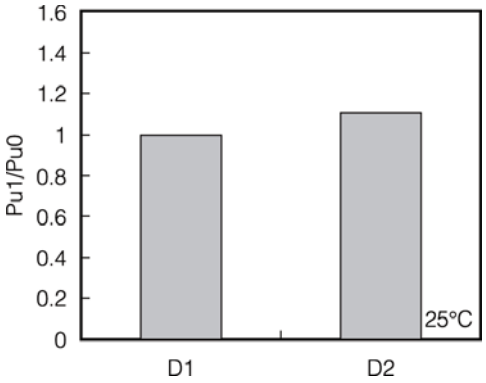


Fig. 11 Rate of discharging power

4.5. The Effect of Temperature

This report has outlined the principles of improving battery power output, measures taken, and their effect. These methods are effective at normal operating temperatures, where cell internal resistance greatly influences output power. However, when the temperature drops, Exchange current density's speed constant, as shown in Eq. (11), drops exponentially.

$$k = C_o^{\alpha} / C_R^{\alpha} \cdot k_f^0 \cdot exp((-\alpha n F E_e)/(R \cdot T)) \qquad (11)$$

k_f^0 : Standard speed constant
E_e : Equilibrium potential

As can be seen from Eq. (4) and Eq. (10), accompanying the above temperature drop, there is a dramatic rise in polarization resistance, so that it occupies the major portion of R_T, and becomes a dominant factor in power output drop. Therefore, at low temperatures, the resistance reducing effect of extending plate length, increasing the number of weld points, and changing the collector shape all drop relatively. As a result, at –25 °C, there is almost no improvement in maximum charging POWER, as shown in Fig. 12.

The contemplated means in this project have almost no effect on power output improvements at low ambient temperatures, so using a temperature control fan, as in a conventional system, to warm the battery leads to power output recovery. In order to improve low ambient temperature power output, it is necessary to increase electrode surface area to a level where it supplements the speed constant drop. The means of accomplishing this are as follows.

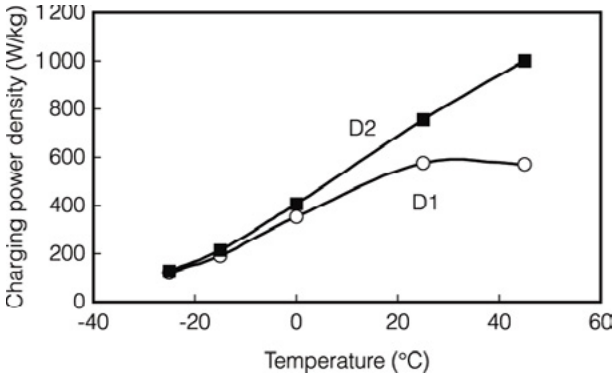


Fig. 12 Characteristic of charging power density by temperature

a. Change the type of electrode from a sinter type to a foam nickel.
b. Make the grain diameter of the hydrogen storage alloy smaller, or make the surface rougher.

5. Summary

For use in the CIVIC Hybrid's IMA System, a battery was developed that has a 27% improvement in maximum charging power during regeneration. This was done by reducing resistance by 19%, through the measures of dropping current density by eliminating the negative collector tab, by extending plate length by 12%, and by increasing the number of weld points between positive and negative collectors and plates.

At the same time, through this research the following was learned.

(1) Reduction in cell internal resistance is of great benefit in improving maximum charging power at normal operating temperatures.
(2) However, at low ambient temperatures, because polarization resistance is high, a drop in upper limit energy becomes dominant, and the benefits are lost.

References

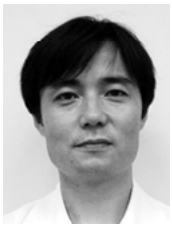
(1) Oura, S., Miura, K.: Making Gasoline Engines High-Efficiency through the Use of Variable Mechanisms, Automotive Technology, Vol. 45, No. 8, pp. 93-98 (1991)

(2) Ochiai, y., Uchibori, K., Hara, K., Tsurumi, T., Suzuki, M.: Development of a Motor Assist System for the Hybrid Car "INSIGHT", HONDA R&D Technical Review, Vol. 12, No. 1, pp. 7-14 (2000)

(3) Matsuki, M., Wakashiro, T., Kamiyama, T., Sato, T., Kaku, T., Kanda, M.: Development of a Power Train for the Hybrid Car "CIVIC Hybrid", Honda R&D Technical Review, Vol. 14, No. 1, pp. 39-48 (2002)

(4) Trends in Battery Application Product Development, Battery and Configured Material Market 1999, ~ Market Trends in First Generation Batteries, Second Generation Batteries, Fuel Cells, Solar Batteries, Capacitor and Battery Configured Mat erials ~ Tokyo, CMC, Ltd., p. 180 (1999)

■ Authors ■





Kazuya OHZONO Morio KAYANO

Development of a New Manual Transmission for a 3-Liter Class Vehicle

Shinji FUJIMOTO* Hideo UDOU* Kyouji KITAJIMA*
Shogo KOBAYASHI* Kouji OKAZAKI*

ABSTRACT

A new 6-speed manual transmission for 3 L class engines has been developed as Honda's top-of-the-line manual transmission. To be mounted on different models, this transmission was given the capability to employ a wide range of gear ratios and to handle high torque while keeping its total length equal to transmissions for 2 L class. Computer aided engineering (CAE) analysis was used to enhance the gear stiffness in order to cope with higher power outputs. The inside surface of the case was made smooth and a force feed lubrication system driven by an oil pump has been used to reduce oil agitation loss in order to curb a rise in oil temperature at high travel speeds. Much emphasis was put on reducing the weight of each component, which resulted in a 3 L class transmission with the weight equal to 2 L class. In order to realize the level of quality appropriate for our top-of-the-line vehicles, the transmission has been equipped with a constant-mesh reverse gear and a dual mass flywheel.

1. Development Concept

In North America, in recent years, there has been an increasing demand for manual transmission vehicles with 3 L displacement engines. Honda R&D has, in this project, developed a new 6-speed manual transmission (referred to as 6MT hereafter), to meet the following targets.

(1) Applicability to multiple models
(2) Have measures to handle high output and high torque
(3) While being in the 3 L class, actualize weight that is equivalent to that of the 2 L class
(4) Achieve high quality appropriate to luxury vehicles

This report introduces the major technologies used to achieve these targets.

2. Basic Structure

The gear train is a parallel dual shaft type with constant mesh type synchro-mesh structure from 1st to 6th and reverse gears. In addition, the case is a 2-piece structure – clutch case and transmission case. The major specifications of the 6MT developed in this project are given in Table 1, and Fig. 1 shows a vertical cross section diagram.

3. Applicability to Multiple Models

3.1. Change Control System

The change control system uses a cable control format. Its location is above the transmission giving more freedom to the layout of surrounding parts, such as the starter and wiring, and to fitting to the engine and vehicle body. In addition, in order to make wire layout easier, the structure is such that shift and selector cables are almost parallel making retrieval possible. Figure 2 shows the layout of the change control system.

* Tochigi R&D Center

Table 1 Specification of transmission

Transmission type		Manual 6-speed
Maximum speed (rpm)		7000
Transmissible torque (Nm)		317 over
Gear ratio	1st	3.933
	2nd	2.478
	3rd	1.700
	4th	1.250
	5th	0.975
	6th	0.770
	Reverse	4.008
	Final	3.285
Weight; Wet (kg)		67

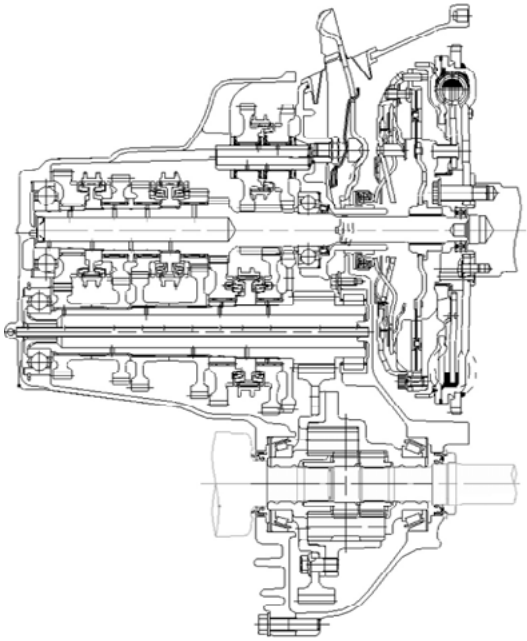


Fig. 1 Main section of transmission

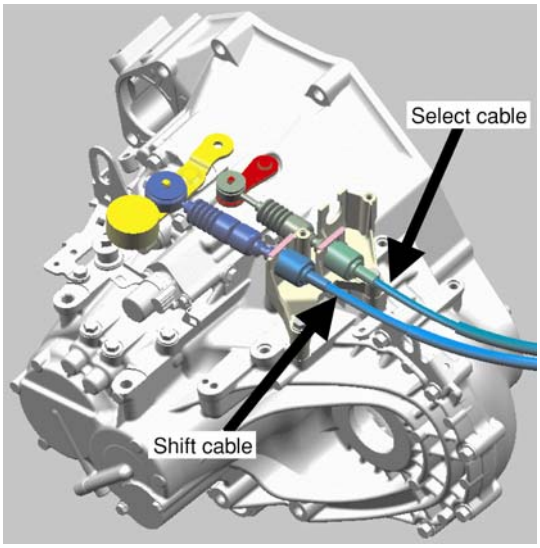


Fig. 2 Change cable layout

3.2. Gear Train

Widening the distance between the main shaft and the countershaft, the setting degrees of freedom are expanded from the sporty series' cross ratio to the sedan series' open ratio. It is possible to set final gear ratio across a wide range of gear ratio settings, from sedan series to SUVs. However, with conventional technology there has been the issue of a large increase in weight when taking measures for this. Therefore, measures have been taken utilizing the technologies described in sections 3.3, 4, and 5, to achieve the targets.

3.3. Shortening of Total Length

Utilizing the following technologies, the total length of the transmission has been shortened equivalent to that used in a 2 L class vehicle, while it is a 3 L class. Figure 3 shows total length relating to engine torque.

3.3.1. Clutch gear embedding structure

As shown in Fig. 4, concerning the counter 1st gear, while maintaining optimum synchronize capacity, the clutch gear which was formed on the conventional gear edge surface is embedded inside of the gear, and so the gear width is reduced. As a result, total length is reduced by 7 mm.

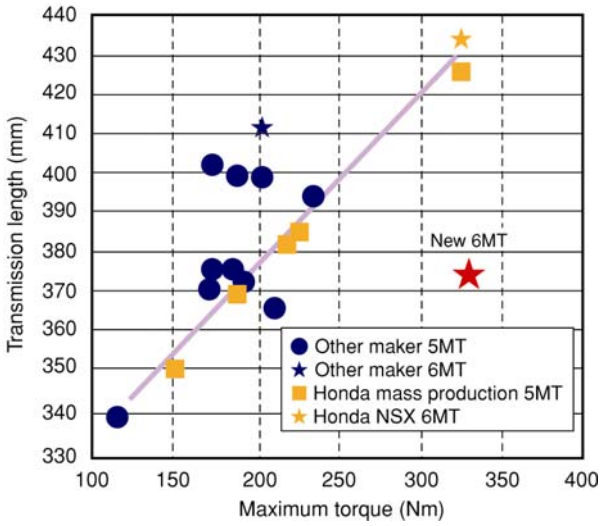


Fig. 3 Comparison of transmission length

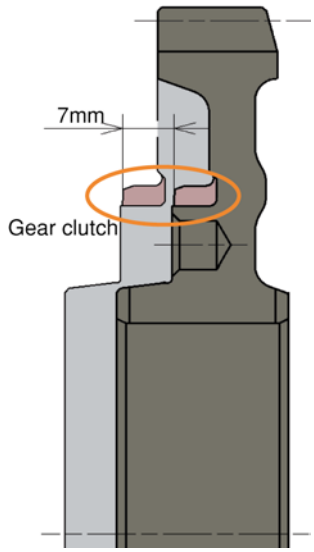


Fig. 4 Counter 1st gear

3.3.2. Self adjusting clutch system

The clutch uses an automatic wear adjustment system (self-adjusting clutch – referred to as SAC hereafter), and the system is designed such that the release bearing does not move back when it becomes worn. As a result, total length is shortened by 9 mm (Fig. 5).

3.3.3. Gear width shortening

Considering the 1st and 2nd gears, it is necessary to balance the issues of reducing tooth stress from impact load input while maintaining gear contact ratio, which greatly contributes to gear noise.

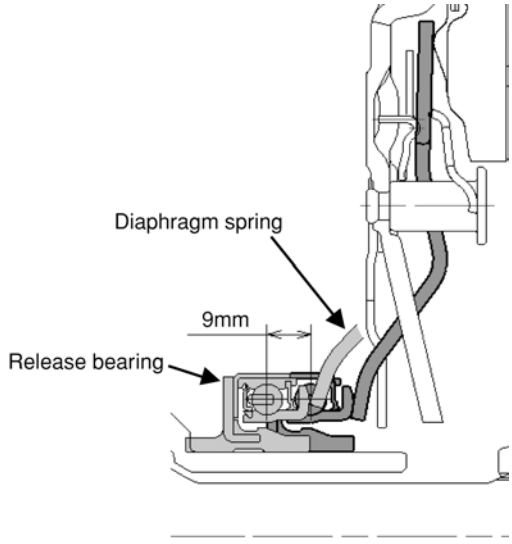


Fig. 5 Clutch

With this 6MT, at the same time as making it more compact, fully considering cost and weight, etc., and maintaining contact ratio with a small module, gear width is shortened by taking measures against high stress due to impact loads, including use of high strength gear material and shot peening treatment.

4. Technology for High Output and High Torque

4.1. Appropriate Case Stiffness

Development of the case was based on the concept of maintaining optimum stiffness and reducing oil agitation loss.

Conventionally, around the differential where high stress is generated, ribs have been created on the inside and outside of the case, thereby maintaining stiffness. In addition, because the differential is positioned below the transmission half in the oil, between the differential part ribs on the inside of the case and the final driven gear and differential, there is loss due to agitation, and in the high-speed range is a major factor in oil temperature rise. Focusing on this, as shown in Fig. 6, by smoothing the shape of the differential part ribs on the inside of the case and adding ribs outside the case, the stiffness required of the case was maintained. In addition, an oil chamber is formed by the ribs on the inside of the case, which also act as reinforcement, reducing oil agitation loss due to the gears.

The case shape was designed through CAE analysis, which allowed smoothing the shape of a differential part rib inside the case. When making the analysis, a clutch case and transmission case 3D model was connected by a simple model bolt, CAE analysis was made of the case as a whole, and the optimum shape designed for stress and stiffness. As a result, while it is a 3 L class transmission, the weight

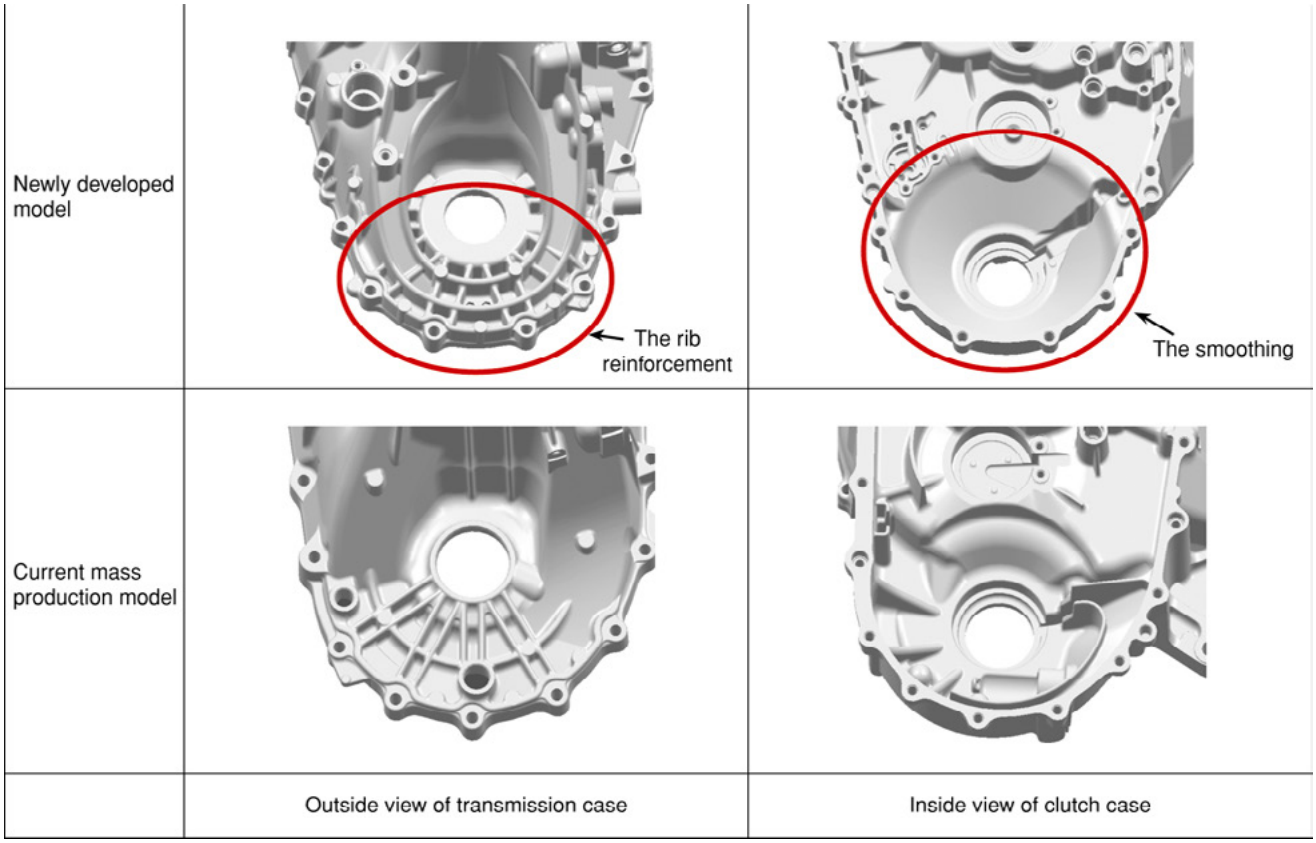


Fig. 6 Comparison roughness of differential

equivalent to that for a 2 L class vehicle was achieved. Figure 7 gives the analysis results, and Fig. 8 shows the relationship between case weight and engine torque.

4.2. Case Mating Surface Pressure

On the surface in which the clutch and transmission case join together, wear occurs due to the friction accompanying large load input. As a countermeasure to this, using CAE analysis, the surface pressure distribution is made uniform across the case mating surface improving durability. As a result, it is possible to reduce the sealed surface width of the clutch and transmission case making it possible to reduce the case weight together with the benefits described in section 4.1.

4.3. Optimization of Gear Stiffness

In the gears, by extending the distance between gear shafts and increasing input torque from the engine, large moment loads are generated. Therefore, gear part stiffness greatly affects tooth meshing errors and this is a major cause of tooth strength deterioration. It is possible to optimize gear part shape, fully considering gear meshing error and weight, by using CAE analyses. Figure 9 shows the results of tooth flank surface pressure analysis and the gear shape before and after measures were taken concerning counter 2nd gear. With the gear shape change, there is a reduction in tooth flank part meshing error and tooth flank surface pressure is reduced by 6.6%, thereby improving durability.

4.4. Lubrication

In order to have the appropriate oil distribution and effective oil supply for lubrication, a semi-dry sump structure (using both oil bath lubrication from gear agitation and force feed lubrication from an oil pump) was adopted. Figure 10 shows this lubrication structure.

As explained in section 4.1 on optimization of case stiffness, the oil chamber is created by the ribs of the transmission case. By locating the oil pump suction in this area, heat due to gear agitation and aeration in the high-speed range are prevented.

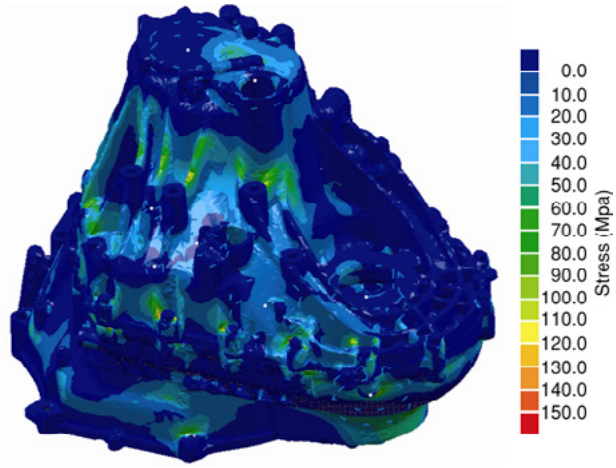


Fig. 7 Transmission case load analysis

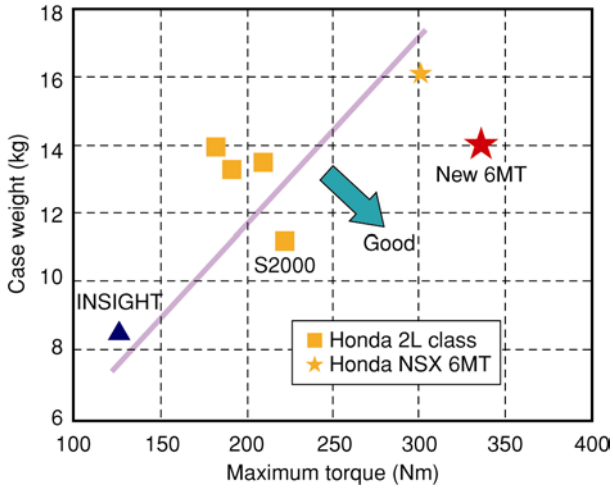


Fig. 8 Comparison of transmission case weight

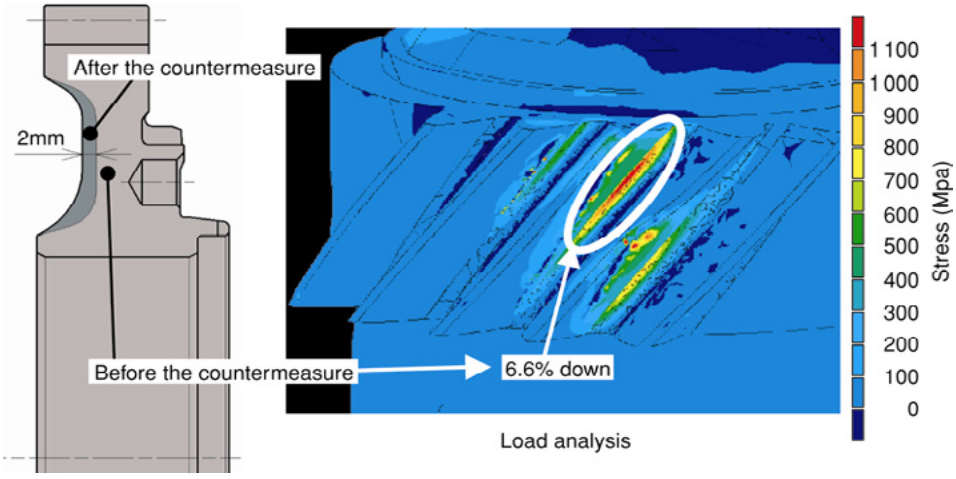


Fig. 9 Counter 2nd gear

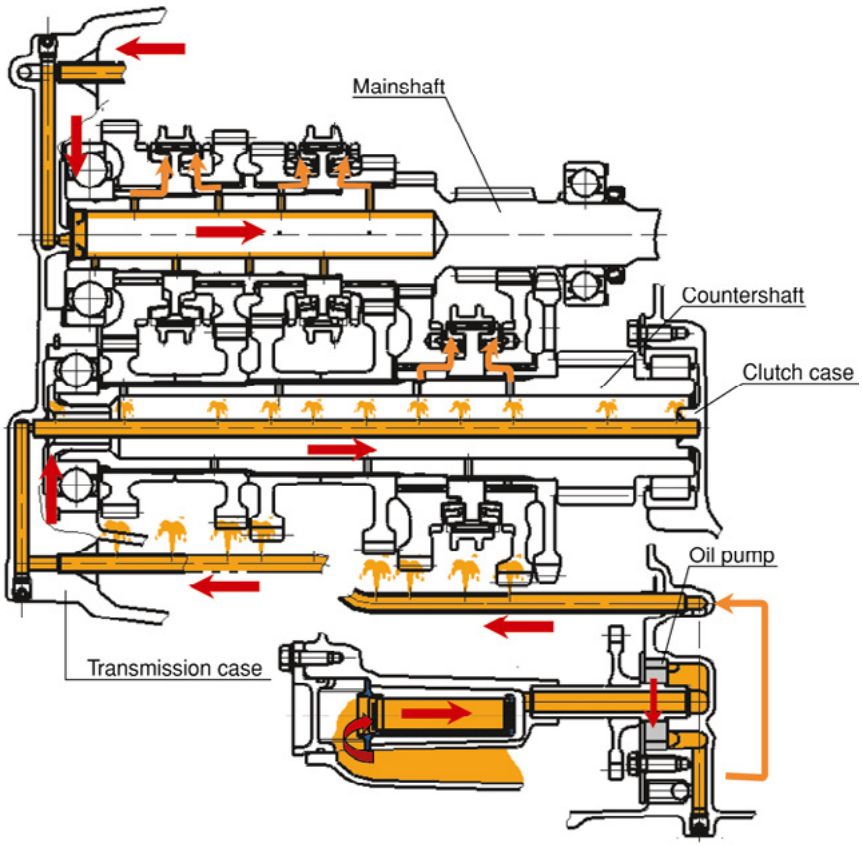


Fig. 10 Oil lubrication structure

In addition, the conventional countershaft lubrication structure is such that because oil is supplied from the edge of the transmission case, due to the effect of centrifugal force at high speeds, there is a large amount of lubricant on the transmission case side, while at the front edge of the clutch case it is difficult to maintain a sufficient amount of lubricant. As a countermeasure, piping is established within the countershaft to supply oil, the appropriate amount of lubricating oil required by the system, from holes in the piping.

Figure 11 shows a comparison of oil temperatures in the high-speed range. With the application of the technologies outlined above, there is a 15 °C drop in temperature, in comparison with conventional designs.

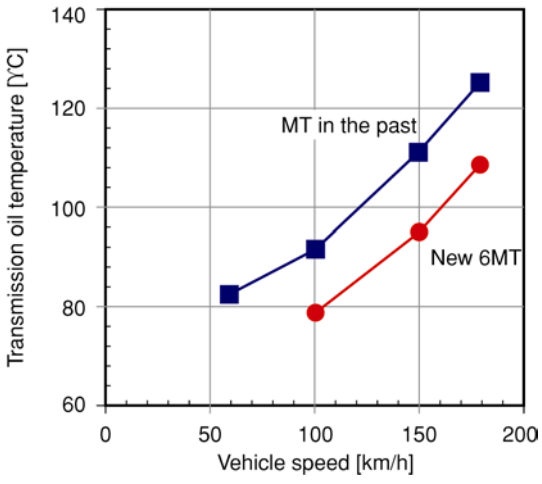


Fig. 11 Comparison of transmission oil temperature

5. Weight Reduction Technology

Together with the weight reduction of the frame part through total length reduction outlined in section 3.3, etc., weight reduction measures were taken for each part. The major technologies are introduced below.

5.1. Counter Reverse Gear Weight Reduction

The radial thickness of the gear flange part is determined by forging production limit dimensions. Furthermore, with hot forging, holes are made in the flange, and it is possible to reduce weight while maintaining the necessary rigidity (Fig. 12).



Fig. 12 Counter reverse gear

5.2. Hollow Countershaft

By making the external diameter of the countershaft large, the shaft's bending stiffness is maintained, and in order to reduce weight, the shaft's center hole diameter, which also acts as a lubricating oil supply path, is also made larger, thereby reducing weight.

5.3. Hollow Shaft and Pressed Shift Fork

A pressed fork was adopted for the shift fork and through CAE analysis the generated stress is equalized creating a lightweight, compact finished product that achieves stiffness balance of a shift fork, which is optimized to be almost symmetric. In addition, for a hollow shaft the welded shaft is used giving weight reduction.

Combining these technologies with frame weight reduction, a weight of a 3 L transmission was kept equivalent to that of a 2 L model. Figure 13 shows transmission weight against engine torque.

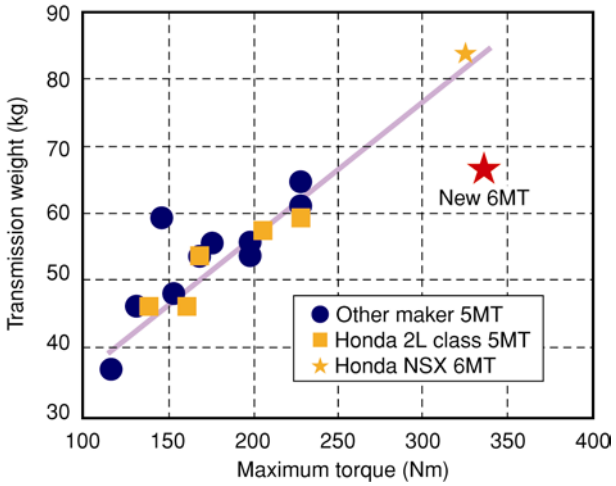


Fig. 13 Comparison of transmission weight

6. Technologies for Luxury

6.1. Shift Feeling

Shift feeling is an important element of a luxury vehicle, and development was carried out with the target being a nimble and smooth shift feeling as a high quality product.

In order to actualize a light shift feeling measures were taken to both shorten shift stroke and to reduce shift load. From 1st through 4th, a multi-cone synchronizer is used; and for 5th and 6th a high friction coefficient synchronizer is used. In addition, in 2nd, the triple-cone synchronizer, the largest developed in our company, is used to give it high capacity. A dual mass flywheel (referred to as DMFW hereafter) has been adopted leading to the elimination of a torsion spring mechanism on the friction disk making it possible to reduce the inertia moment on the synchronization side by 20%. However, increasing the synchronizer capacity (synchronization torque) increases the torsion generated during synchronization on the side being synchronized, and after synchronization is complete, that torsion is released generating a rotational difference. In this state, if the synchronizer sleeve advances when there is engagement with the clutch gear, the synchronizer sleeve bumps (as double bump) due to the rotational difference and the vibration generated is transmitted to the shift knob deteriorating the smooth shift feeling[(1)].

In order to solve this issue, the small diameter shape of the synchronizer sleeve that contacts the synchronizer spring was modified so that even after synchronization there is synchronization torque being generated by the synchronization spring, though it is very small. By reducing the rotational difference, shift knob vibration is reduced and shift feeling improved. Figure 14 shows a comparison of shift knob load and Fig. 15 shows synchronization operation state.

In addition, with our company's conventional

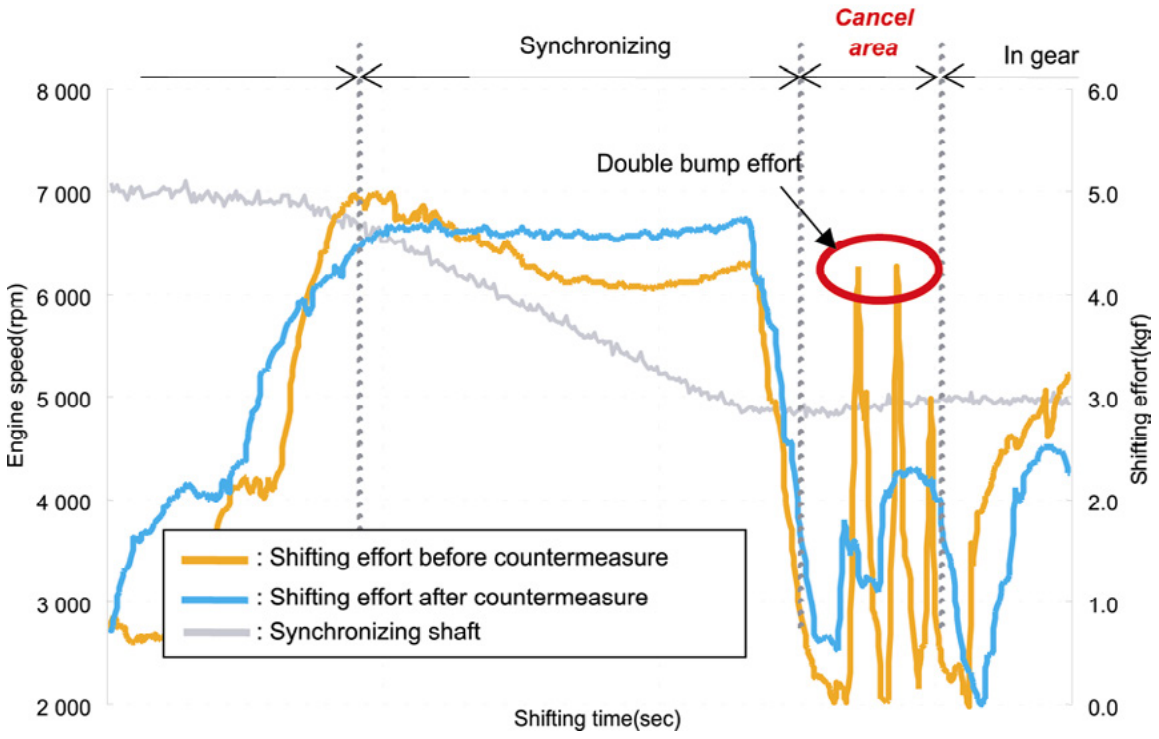


Fig. 14 Time chart of shifting

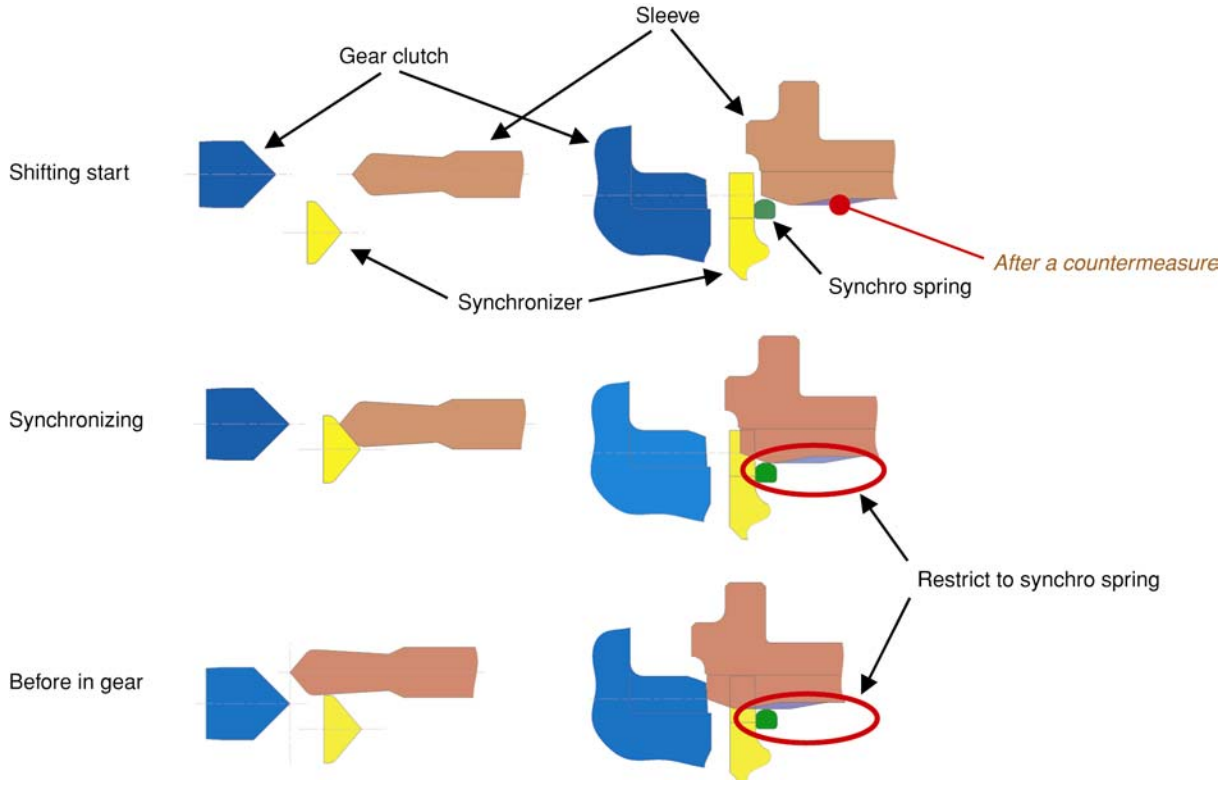


Fig. 15 Comparison of transmission length

transmission, to countermeasure rattling due to gear fluctuation of angular velocity when idling, a friction damper was used in counter low gear and counter 2nd gear.

In this new transmission, by adopting a DMFW, it is possible to establish wide-angle torsion properties, and by setting the spring constant low in the low torque range, fluctuation of angular velocity when idling is dramatically reduced. Through this, the friction dampers that were countermeasures for rattling were eliminated and the friction generated when the synchronization sleeve pushes its way through the clutch gear chamfer is reduced. Combined with the shift knob vibration reduction mentioned previously, shift feeling is improved and higher quality is achieved.

6.2. Reverse Structure

For the reverse structure, a constant mesh type synchro-mesh structure was adopted of the same type as for the drive gears. The purpose of a constant mesh type is to reduce gear noise when driving in reverse and the purpose of the synchro-mesh structure is to improve engagement during reverse shifting and to prevent abnormal noise from occurring.

Thanks to these measures engagement during reverse, which was 95% with the conventional sliding selection type, is dramatically improved.

6.3. Clutch Performance

Upon examination of clutch torsion properties, which greatly affect marketability of gear vibration and noise, it was found that by increasing idle gear count through the use of a constant mesh type for 6MT and reverse and by increasing idle gear rotation inertia accompanying an expansion of the distance between gear shafts, gear tooth contact energy is increased. Fully considering this, another company has adopted a DMFW for this class of vehicle, too. A DMFW has two large masses – one on the engine side and one on the transmission side. Between them are spring and hysteresis elements so fluctuation of angular velocity input from the engine is attenuated restraining fluctuation of angular velocity of the gear and reducing rattling noise.

A SAC was also adopted for the clutch, and in addition to the benefits outlined in 3.3.2, there is a reduction in clutch pedal force variation.

Conventionally, because there are changes to diaphragm spring usage position (set position) due to clutch disk wear a large change in load during use is generated. In contrast, with the adoption of SAC, it is possible to have the diaphragm spring operate in a fixed set position following the clutch disk wear, thereby reducing clutch pedal force variation. Figure 16 gives the results of a comparison between the conventional structure and SAC release load elapsed change.

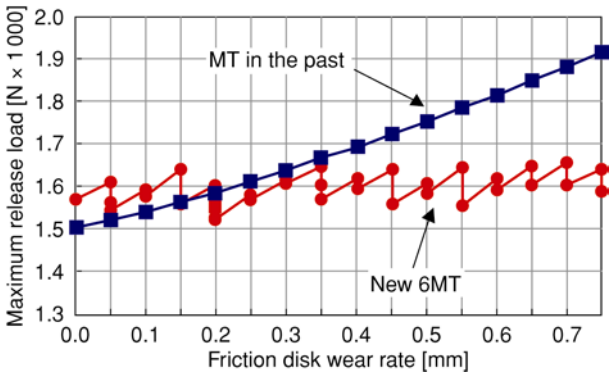


Fig. 16 Comparison of clutch release load

A new clutch disk facing material was adopted, which is environmentally friendlier.

7. Summary

Using the technologies outlined in this paper, the development targets for the transmission for Honda's luxury models were achieved through the following means.

(1) Wider gear ratio settings were made possible by extending the distance between shafts. By adopting a clutch gear embedded structure and clutch automatic wear adjusting structure, a compact size was realized. As a result, while at the same time handling high torque, total length was equivalent to that of the 2 L class, and it is possible to fit the transmission to multiple models.
(2) CAE analysis was carried out, enhancing gear stiffness and maintaining gear tooth flank durability. While maintaining case stiffness, case inner surface smoothness was implemented. In addition to the smooth case inner surface, by adopting a force feed lubrication structure, oil agitation loss was reduced and there was a 15 °C drop in oil temperature at high speeds. As a result, it is possible to deal with both high output and high torque.
(3) Weight reduction measures were taken for each part, including weight reduction of the frame parts and weight reduction by making holes in the gear flange through hot forging and making the countershaft center hole diameter larger. As a result, weight reduction was achieved while maintaining high capacity.
(4) Working towards shift feeling improvement, rattling noise reduction, and reduction in changes to clutch stepping force, a high quality product was achieved appropriate to a luxury sporty car.

8. Conclusion

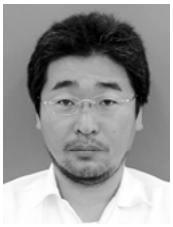
This 6MT is mounted to the ACURA 3.2CL TYPE S and has received favorable evaluations in the market. In addition, based on this 6MT and in response to the requirement for further weight reduction, a smaller size, or cost reduction, etc., this transmission can be fitted to multiple models.

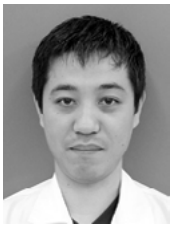
Finally, the authors would like to take this opportunity to express their deep gratitude to the many people both in Honda and in other companies, who gave their generous cooperation in the development of this 6MT.

References

(1) Murai, A., et al: Sporty Change Feeling in the S2000, HONDA R&D Technical Review, Vol. 11, No. 2, pp. 73-78 (1999)

■ Authors ■


Shinji FUJIMOTO


Hideo UDOU


Kyouji KITAJIMA


Shogo KOBAYASHI


Kouji OKAZAKI

Development of Electric Power Steering System for F-1 Race Car

Hideyuki FUJITA* Yutaka HORIUCHI* Hideki KUBONOYA*
Jun BABA** Katsuhiro SAKAI*

ABSTRACT

An electric power steering system for an F-1 car was developed and fitted into a 2000-2001 model F-1 car. The purpose of this development was to reduce steering effort, which can exceed 350 N during a race. The new system achieves the assist performance required for the F-1 car and is compact and lightweight, with low energy consumption. To achieve this, the motor, the motor control unit driving the motor, the torque sensor, the steering gear box containing the reduction gear and the control systems were all redesigned. During development, assist performance and response were evaluated on bench tests, and stroking durability and reliability were evaluated by simulation using actual car data. Final configuration was determined using track tests. As a result, a system was developed which meets assist performance targets and satisfies the F-1 car durability and reliability requirements.

1. Introduction

Current F-1 vehicles see a maximum steering effort of 350 N or more, equivalent to between 5 to 10 times that of mass produced vehicles. In a race that can last up to two hours, reducing the steering effort is essential to help the driver maintain both physical strength and concentration. Therefore, at present, all F-1 vehicles are fitted with power steering systems. Most other constructors use a hydraulic source, which is shared with the transmission control at approximately 18 MPa, and usually an electronically controlled flow control valve.

At Honda, during the initial spec study stage, a comparative study was made of hydraulic power steering system and electric power steering (EPS) system. The EPS system was selected for its low energy consumption. Figure 1 shows the energy consumption, calculated from steering torque according to actual running test data of hydraulic power steering and EPS. As shown in that graph, in circuit driving, EPS gives a 16% better average energy consumption.

This paper provides an overview of the F-1 EPS system, and its performance.

2. Regulations

In the 2001 FIA (Fédération Internationale de l'Automobile) regulations concerning F-1 vehicle steering it states, "Power assisted steering systems are permitted but may not carry out any function other than reduce the physical effort required to steer the car." That is to say, it is prohibited to control vehicle action with the purpose of assisting the driver's driving competency through power steering control. It states, "The only permissible inputs are steering torque, steering angle, and car speed," and it is also prohibited to use differential values or integrated values of these input signals as control inputs. In addition, if these inputs are filtered, the

* Tochigi R&D Center
** Honda Racing Development

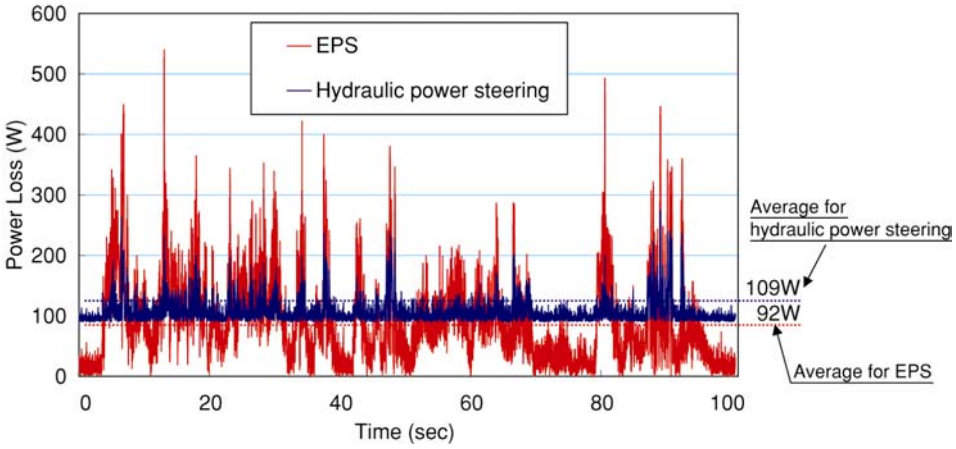


Fig. 1 Estimated power loss in hydraulic power steering and EPS; Suzuka circuit

cut-off frequencies must be approved and published by the FIA. That is to say, control that proceeds according to assist torque phase, using a band pass filter, is prohibited.

In 2002, the regulations were modified to state, “Power assisted steering systems may not be electronically controlled or electrically powered.” Therefore, from 2002 it is no longer possible to use EPS on F-1 vehicles.

3. Development Concepts and Target Performance

In the case of mass production vehicles, power steering assist performance settings are generally made with the focus on static steering. However, with F-1 vehicles the down force changes according to the vehicle’s designed aerodynamic characteristics. The steering holding effort has its greatest load during high speed cornering when the maximum tire vertical load is reached. Furthermore, there is a dynamic performance demand for power assistance in response to quick steering angle speeds when countersteering.

Currently, in the pursuit of aerodynamic performance, the F-1 vehicle body has become a sleek, spearhead-like mono-form shape. Therefore, it is essential that the EPS motor and reduction gear mechanism be as compact as possible to be compatible with the layout of the front suspension and brake system in the limited space available.

In addition, thorough weight reduction activity on the EPS unit is required to keep the weight increase due to installing the EPS unit as small as possible. Lastly, it is necessary to keep energy consumption to a minimum, yet have a design that makes a sufficient energy supply with the existing AC generator and battery.

To achieve this, the development concepts for the F-1 EPS were as follows.

- Compact and lightweight.
- Meet target assist torque and dynamic performance.
- No modification to the existing charge and discharge system.
- Meet durability and reliability levels so that there is no need to retire from the race due to an EPS failure.

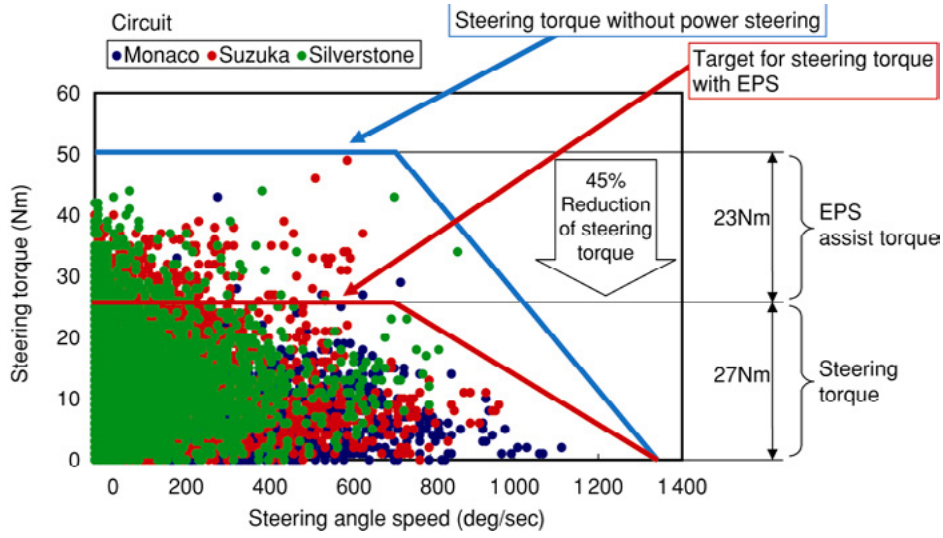


Fig. 2 Steering angle speed vs steering torque without power steering at each circuit

To set specific performance targets, a reference was made using results from trials of steering effort reduction using the EPS for mini-cars. This testing was carried out as part of past Japan Touring Car Championship (JTCC) race vehicle development. Based on these results, when steering effort is too light due to excessive assist, race vehicle controllability worsens. It was determined that steering effort of between 150 ~ 200 N is most appropriate. This level was used as the steering effort target in the current project. Through multiplication of the F-1 steering wheel diameter the target steering torque was then set at 20 ~ 27 Nm. Next, from track test data of past F-1 vehicles without power steering installed, a distribution of steering torque versus steering angle speed for each circuit was determined, as shown in Fig. 2. From this it was found that maximum steering torques of 50 Nm can occur at an angular steering rate of up to 720 deg/sec. Thus, in order to achieve the targeted steering torques, there must be a 45% reduction in steering effort over the whole range. Therefore, the maximum EPS assist torque target was 23 Nm, and dynamic performance targets required that this assist torque be generated at a maximum angular steering rate of 720 deg/sec.

As for charging and discharging feasibility, an estimation was taken of the generated current by the AC generators on the circuit with the highest assist load. The current that can be consumed by the EPS is then estimated from the difference from this level to the current consumption of the electrical systems other than the EPS. Based on these estimates, the target established was 5 A or less as the average current consumption allowed to the EPS system per circuit.

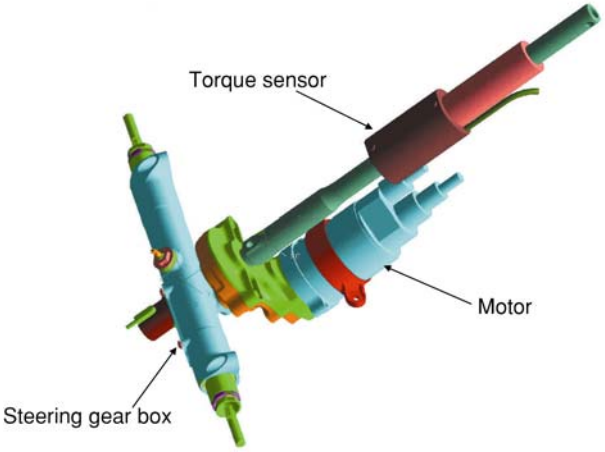


Fig. 3 EPS component for F-1 Car

4. System Overview

The components for the F-1 EPS are shown in Fig. 3. Figure 4 shows the EPS system block diagram.

The F-1 EPS system is comprised of the following.

- Torque sensor; detects the driver's steering torque and outputs the torque signal.
- ECU; receives the torque signal and outputs the assist torque instruction value.
- MCU; receives the assist torque instruction value from the ECU and controls motor torque.
- Steering gearbox; is integrated with a motor generating assist torque and a reduction gear mechanism which amplifies that drive torque.
- Vehicle speed sensor; detects vehicle speed.

4.1. Torque Sensor

In the case of a mass production vehicle's EPS, generally the torsion bar's torsion angle is mechanically converted to axial direction displacement. The differential transformer

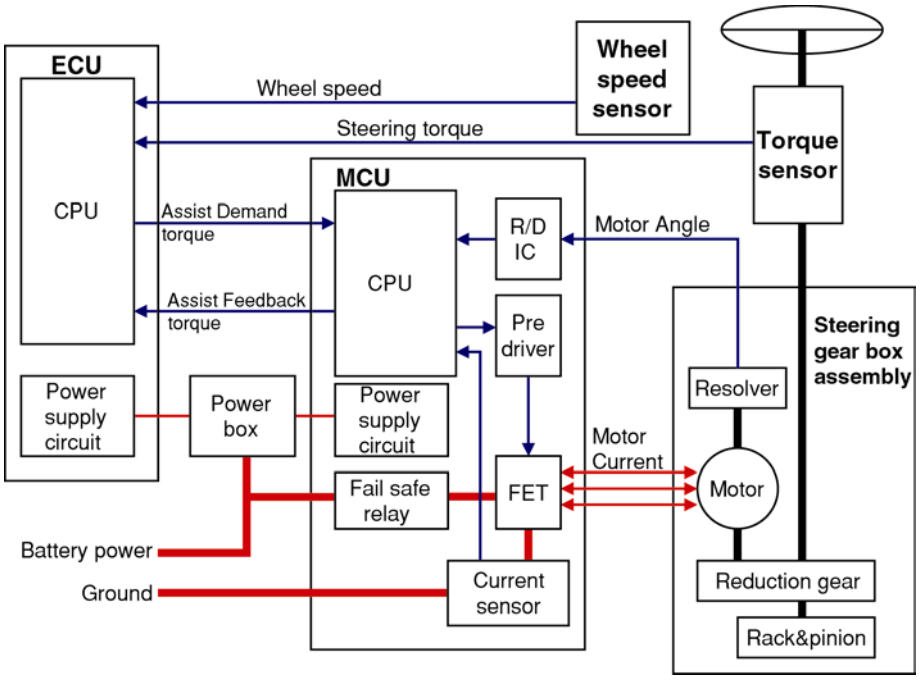


Fig. 4 EPs system block diagram

detects that displacement, then an electrical signal is output. With an F-1 EPS, as shown in Fig. 5, a strain gauge is directly mounted to the extension shaft that extends from the steering pinion, whereby the voltage of the bridge circuit, formed by the strain gauge, is detected – a simple structure with few parts. Focusing on ease of on-the-spot maintenance and ease of handling, there is only one component, a shaft with integrated strain gauge amp. In addition, in order to cope with the extreme vibrations generated by the F-1 vehicles which may reach as high as 30 G, the amp is mounted on floating rubber.

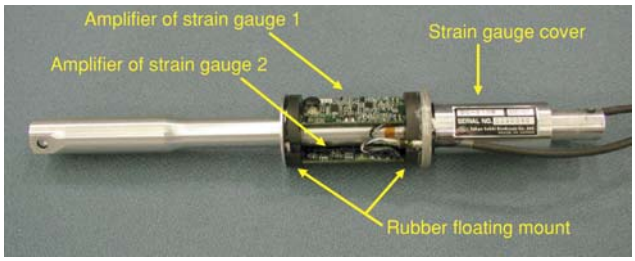


Fig. 5 Torque sensor

4.2. Motor

The motor selected was a specially developed DC brushless motor with advanced reliability and responsiveness. Figure 6 shows this motor. In order to make the motor smaller and more efficient, the magnets adopted were neodymium-based magnets. For ease of fitting to the F-1 vehicle, motor size was set at a diameter of 60 mm max with a length of 130 mm max. The aim was to achieve motor characteristics that satisfied both target assist performance and current consumption within these dimensions.



Fig. 6 EPS motor

4.3. Motor Control Unit (MCU)

At the same time, an MCU was developed to carry out torque control, through a drive circuit unique to the brushless motor. Figure 7 shows this MCU. In circuit driving mode, maximum assist torque frequently occurs, and a FET was selected that has sufficient capacity to withstand the generated heat. In addition, it has a motor control mechanism monitoring function and carries out mutual failure diagnosis through communication with the ECU.



Fig. 7 Motor control unit (MCU)

4.4. Steering Gearbox with Reduction Gear Mechanism

It was essential to make the reduction gear mechanism (that amplifies the motor torque) more compact, in order to maintain a layout inside the mono-form shape with the suspension and brake system parts. By using a titanium alloy helical gear in a double reduction gear mechanism, the external diameter shape can be reduced to 3/5 of that of a



Fig. 8 Steering gear box assembly

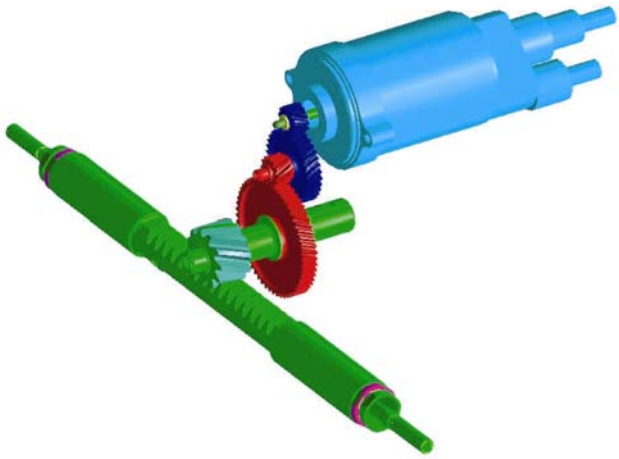


Fig. 9 Reduction gear

single reduction gear mechanism. Figure 8 shows the steering gearbox, and Fig. 9 shows the reduction gear mechanism. With this change, it is possible to fit the motor in parallel with the pinion shaft at the bottom of the gearbox, giving the vehicle a low center of gravity. In addition, two different types of reduction ratios have been designed, to match certain circuit characteristics. The actual rack and pinion steering mechanism itself is made of titanium alloy, and the gear housing is made from magnesium alloy, thereby reducing weight.

5. Control Specifications

With this F-1 EPS, the EPS assist torque as compared to the sum of the driver's steering torque and EPS assist torque, is set as the standard assist rate. However, in order to prevent system oscillation, a dead band was established in the steering torque neutral range. The standard assist rate Ra is defined as follows.

$$Ra = Ta/(Ts - Td + Ta) \quad (1)$$

Ts : Driver steering torque
Ta : EPS assist torque
Td : Dead band

In comparison with this standard assist rate, the assist rate is increased or decreased in response to vehicle speed according to coefficients specified in the speed control table. Final assist torque, Tv according to vehicle speed control is defined as follows.

$$Tv = Ra(Ts - Td)\cdot Kv/(1 - Ra) \quad (2)$$

Kv : Vehicle Speed Coefficient

A standard assist rate and vehicle speed control table, as shown in Fig. 10, establishes five types of standard assist rates (0, 30, 35, 40, 45%) for each circuit, and gives the vehicle speed control table in response to each. These assist modes are stored in the ECU. The driver selects the mode, using an EPS mode switch on the steering wheel, to match the course and the driving conditions. However, because the regulations prohibit changing power steering characteristics while driving, mode switching can only be carried out while the vehicle is stationary.

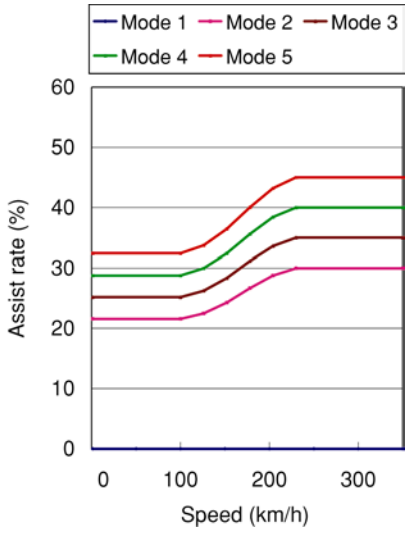


Fig. 10 Speed vs assist rate

6. System Reliability

The primary focus of the F-1 EPS system reliability is that an EPS malfunction must not be a cause of retiring from a race. Therefore, a feature was added so that the assist function stops within a specified time and manual steering function returns. Also, a switch was added so that the driver can interrupt the system at his/her discretion. Both are added in case a malfunction occurs or the appropriate assist function cannot be maintained.

In addition, there are instances where the assist torque demand exceeds the EPS estimated load, due to unpredictable changes in conditions. To maintain the assist function even in these situations, there is a protective function that monitors MCU drive circuit temperature and limits the amount of assist so that the tolerated temperature is not exceeded. There is also a protective function that limits the amount of assist in response to voltage drop, so that the power supply voltage can be maintained.

7. Durability and Reliability

With an F-1 vehicle, there are specified driving distances for which it is possible to use up a part, and replacement periods are managed correspondingly. For EPS, too, in order to establish the driving distance for which function can be guaranteed, stroke durability tests were carried out using a bench tester. This bench reproduces rack input loads and steering angles from actual running test data. Vibration resistance tests were also carried out, reproducing actual car vibration levels. The driving distance specified in these tests were verified with track tests in the end, and as long as there are no problems, the parts will be managed based on these specifications.

In addition, all EPS components are fitted inside the driver's cockpit. The EPS motor, sensors, and electrical units have all been given a waterproofing treatment, to protect them from water permeation into the cockpits when driving in rain.

8. Results

8.1. Weight

Shown in Table 1 are the results of a thorough weight reduction activity giving a total EPS weight of 4.09 kg, and a total weight increase due to adding EPS of 3.35 kg.

Table 1 Weight of EPS (kg)

	Original steering	EPS
Torque sensor	0.1	0.35
Motor		1.4
MCU		0.9
Harness		0.5
Steering gear box	0.64	0.94
Total weight	0.74	4.09

8.2. Performance

Table 2 gives the general specifications for the F-1 EPS.

Performance of the EPS fitted to the 2002 model realizes dynamic characteristics of maximum assist torque of 23.4 Nm up to a maximum steering angle speed of 720 deg/sec. It was possible to achieve both the F-1 required assist torque and the dynamic performance.

Table 2 Specifications of EPS

Type of EPS	Pinion assist type
Rated electric voltage	12V
Rated electric current	15A
Maximum assist torque	23.4Nm
Dynamics	4rev/sec
EPS reduction gear type	Double Helical gear
EPS reduction gear ratio	10.6
	13
Type of Motor	DC brushless Motor
Maximum Motor Torque	1.8Nm
Inertia of Motor	0.004g·m^2
Electric time constant	0.7msec
Type of Torque sensor	Strain gauge type

8.3. Current Consumption

Figure 11 shows the 2001 F-1 Japanese Grand Prix Suzuka circuit's actual running data.

In order to reduce the average EPS current consumption, an assist torque maximum value was established. The MCU carried out current consumption upper limit value control in response to motor speed, so that the maximum torque is not exceeded.

Actual running test results showed that on the Suzuka circuit with the largest assist torque load, the average consumed current for one circuit was kept to 3 A, which is below the target.

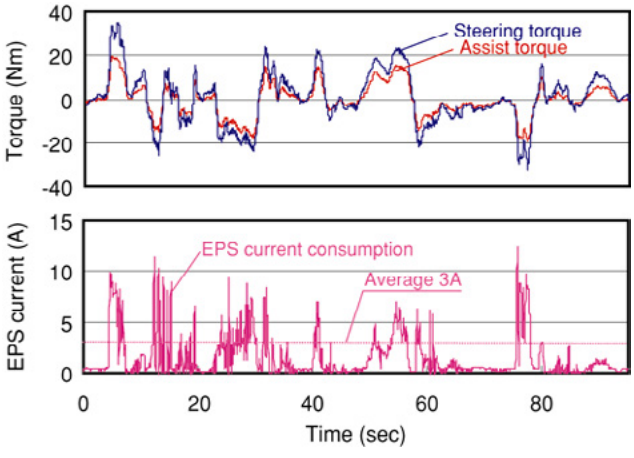


Fig. 11 Results for EPS current consumption (Suzuka)

9. Summary

A small, lightweight EPS system for F-1 vehicles was developed, which achieves both the required assist performance and energy consumption requirements. This EPS was fitted to the 2000 ~ 2001 model F-1 vehicle. With this EPS, it is possible for driver steering effort, in response to each circuit's characteristics, to be reduced by up to 45%.

10. Conclusion

By fitting an F-1 EPS system, it is possible to improve the ease of steering when cornering, to improve drivability, and, as noted by the drivers, to reduce physical exhaustion in a race, helping to maintain driver concentration. It is clear that this is an effective F-1 race vehicle system.

11. Acknowledgements

The authors would like to take this opportunity to offer their sincere appreciation to those within Honda who gave their support in the development of this EPS; those at Toshiba who gave their support in the development of the high performance motor and MCU; those at Tokyo's Measuring Instruments Laboratory Co., LTD who supplied the precision torque sensors; and those racing staff who supported the EPS operation during races.

References

(1) Shimizu, Y., et al: Development of Electric Power Steering, HONDA R&D Technical Review, Vol. 3, pp. 58-75 (1991)

(2) Suda, H., et al: Development of Steering Sensor for Electric Power Steering, HONDA R&D Technical Review, Vol. 3, pp. 83-91 (1991)

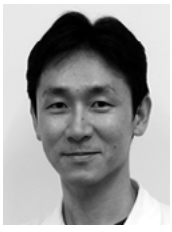
■ Authors ■


Hideyuki FUJITA


Yutaka HORIUCHI


Hideki KUBONOYA


Jun BABA


Katsuhiro SAKAI

Reduction of Engine Noise in the New Accord Using Hybrid CAE Technology

Tatsuhide SAKAI* Tetsuya MIYAHARA*
Tomonori NIIZATO* Hiromichi TSUSHIMA*

ABSTRACT

Hybrid CAE models were constructed for the 2003 Accord to reduce cabin noise induced from engine order vibration. The Hybrid CAE method utilizes a combination of two different approaches: numerical and experimental analysis. Targets for each system's contribution to cabin noise were established on the basis of tests of the prototype during the initial stage of development. The achievement of these targets has significantly reduced engine noise in the new Accord.

1. Introduction

Reductions in product development periods and in the number of prototypes have been constant matters of concern in recent years. Even if the number of experimental models is cut back and development periods are shortened, there will be no benefit if the end product does not perform well. Recently, dramatic improvements over previous models and various special features have been required to maintain a competitive edge and meet the demands of the evolutionary trends in the market.

A broad definition of 'product performance' includes many factors, from handling, acceleration performance, noise and vibration, ride comfort, to collision safety, cost, and weight. Many of these performance indicators stand in contradiction to each other. Performance goals are set by the product concept, but when elements conflict with each other it is essential to decide how to balance them. Those decisions have the potential to sidetrack development and could even result in a product with little resemblance to the initial concept.

The vibration and noise performance of a vehicle is determined by the interrelationship between various systems including the engine, subframe, body, bushings, and the suspension. Efforts to improve them can all too easily lead into the situation mentioned above. Therefore, throughout development, it is necessary to bear in mind which system is most efficient for handling issues and how to minimize the effects of elements that detract from other performance parameters.

Over a decade ago, the investigation of product performance was centered on a process of creation and analysis of prototypes; multiple prototypes were made in succession until the final one matched the product concept. Today, when the product must fulfill high performance requirements within a short period and research must be carried out to prevent features that compete with other desired performance parameters that may alter the product concept, it is vitally important to assure vehicle performance with a high degree of precision before any prototypes are made.

The object of this report is cabin noise caused by engine vibration, mainly that above 100 Hz. At present, it is not realistic to create numerical models of all the components affected by this region and attempt to analyze the aggregate vehicle model for highly precise predictions of performance. Consequently, a hybrid CAE technique tying numerical models to physical models has been employed; its superiority has been previously reported[(1), (2)]. In the developmental process presented here, good results were obtained when the technique was applied to the new 2003 model Accord (in-line 4-cylinder engine). The experimental results with this CAE technique are included in this report.

* Tochigi R&D Center

2. Determining Contributions to Cabin Noise and Setting System Targets

The targets for cabin noise in the new Accord and those assigned for each system are described below.

2.1. Targets for 2003 Models

The cabin noise levels and the reduced noise target for the basic mass-produced model (2.4 liter displacement, for U.S. market) are shown in Fig. 1. The aggressive goal of a reduction of about 5 dB under the previous model was set for the 2003 Accord. This was mandated in the concept so that a majority of users would notice the improvement.

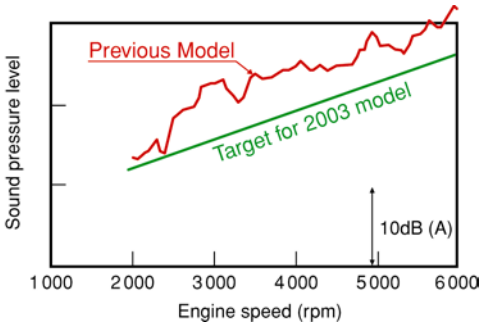


Fig. 1 Interior noise target for 2003 Accord compared with previous model

2.2. Determining Cabin Noise Contribution Levels and System Targets

The targets were studied for each system by analyzing the transfer paths for engine vibrations. Orders second through eighth were analyzed to include all the input in the structure borne noise frequency range (up to 800 Hz).

Equation (1) shows the components of noise S_i on each path due to the operational engine vibrations X_{Ei}, body vibrations X_{Bi}, engine mounting dynamic characteristics k_i, and body noise transfer function H_i, of engine mounting points i. Equation (2) shows the summation of the transfer path components to the total cabin noise S_{all}.

$$S_i = (X_{Ei} - X_{Bi}) \times k_i \times H_i \quad (1)$$

$$S_{all} = \sum_{i=1}^{All} S_i \quad (2)$$

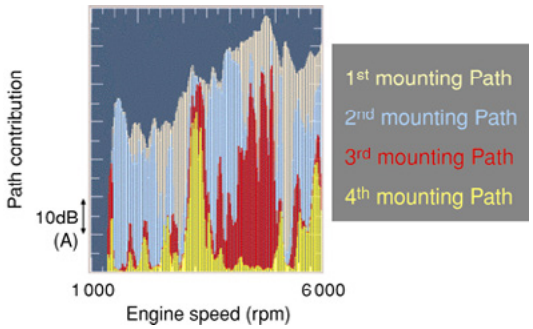


Fig. 2 Transfer path contribution in 1998 model

The transfer path contribution for the 6th order component of the cabin noise in the mass-production model (1998) is shown in Fig. 2. The paths with the highest contributions at the various engine RPM speeds are clear in this figure.

The second through the eighth orders were investigated in all 18 transfer paths (6 engine mounting points × 3 translational axes) prior to allocating the targets for the systems. Targets were set for the engine vibration inputs and for the body noise transfer function for each path. When calculating engine vibration inputs, body vibrations were assumed to be 20 dB lower than the engine vibrations.

Parameters for bushings such as those at the engine mounts and the subframe floating mounts were taken from component measurements. These known results were used as constraint conditions for establishing the hybrid model.

3. Verification of Engine Vibration

Engine vibration is expressed in Eq. (3) by the product of the forces F released inside the engine (engine interior forces) and the frequency response functions H^{EB} describing the transfer characteristics from the interior of the engine to the tips of the engine mounting brackets. These frequency response functions H^{EB} are again shown in Eq. (4) as being composed of distinct frequency response functions of the engine and brackets.

$$\{X_E\} = |H_i^{EB}| \cdot \{F_i\} \quad (3)$$

$$H_i^{EB} = H_{is}^{Brkt}(H_{ss}^{Eng} + H_{ss}^{Brkt} + k^{-1})^{-1} H_{si}^{Eng} \quad (4)$$

H^{Eng} :Frequency response function matrix of the engine (i, interior points; s, connection points)

H^{Brkt} :Frequency response function matrix of the brackets (t, bracket tips; s, connection points)

k :Stiffness matrix of connection structures

H^{EB} :Frequency response function matrix of the combination of the engine and brackets

F :Engine interior forces

The frequency response function matrix of the engine was constructed as an experimental model using the measured data, and the bracket frequency response matrices were made using finite element (FE) models. The engine interior forces were calculated using cylinder interior pressures and engine vibrations[1].

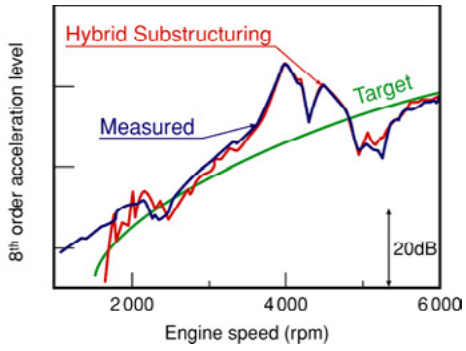


Fig. 3 Estimated 8th order vibration at 3rd engine mounting bracket

The test results at the 3rd engine mount for 8th order in the initial prototype are shown in Fig. 3. It is clear that the results of the hybrid calculations matched well with the measured data.

This was shown to be a good model, as nearly the same levels of precision were found for the second, fourth, sixth and eighth orders at the other mounting points. It was also clear that the prototype did not attain the targets set by allocating the transfer path contributions to cabin noise.

3.1. Experimental Model of Engine

An analysis of the frequency response matrix of the initial prototype revealed that the mating portions of the cylinder lower block and the transmission block were large factors in the failure to meet the targets in the region below 500 Hz. While the engine mount brackets connecting to the rear wall of the cylinder block were factors in the failure to meet the targets at frequencies above 500 Hz. Figure 4 shows the portions of the experimental engine model and of the blocks needing shape improvement, and Fig. 5 shows the corresponding portions on the rear wall of the cylinder block and the transmission case.

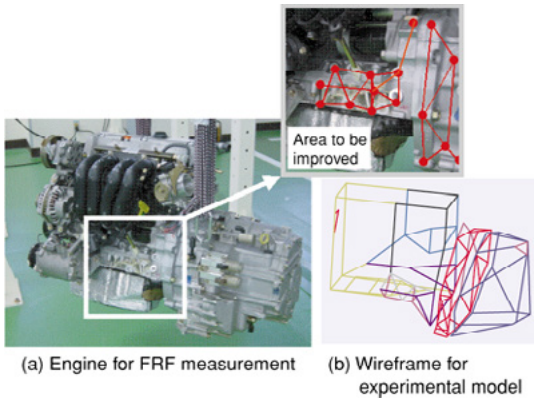


Fig. 4 Experimental engine model and improve section of powertrain block

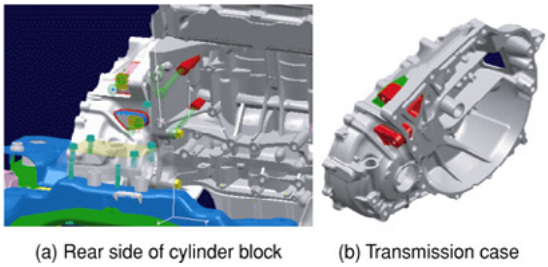


Fig. 5 Improved area for connecting points of engine mounting brackets

In addition to the component shape improvements just described, stiffeners were added in two patterns to see if they would improve the frequency response function matrix as well. Figure 6 shows the results of the proposed modifications to the cylinder block response function (excitation at the 5th journal). One of the stiffener designs proved effective for meeting the goal and was used.

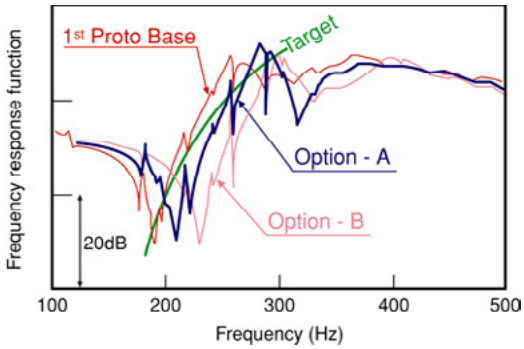


Fig. 6 Comparison of powertrain stiffness with two optional countermeasures

3.2. Finite element Model of Bracket

Figure 7 shows all of the engine mountings. All of the engine mounting brackets were updated as described in an earlier report by the authors[1]; this provided improved precision in calculation of the eigenmodes.

The number of fasteners in the first and second mounting brackets was changed from three in the previous model to four in the new model. The shapes of the tip and the attachment region were changed as suggested by an analysis of the transfer function and components were thinned to reduce weight. Other mounting brackets were modified accordingly and the material of four of the six brackets was changed to aluminum.

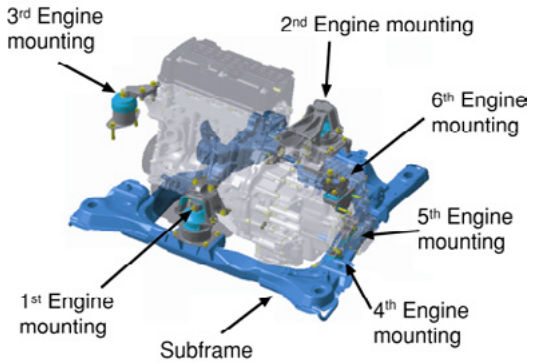


Fig. 7 Newly developed engine mounting system

3.3. Results on Engine Vibration

The engine vibration levels accomplished in the 2003 Accord are shown in Fig. 8. The goals were reached due to the measures taken in the various locations: the stiffening of

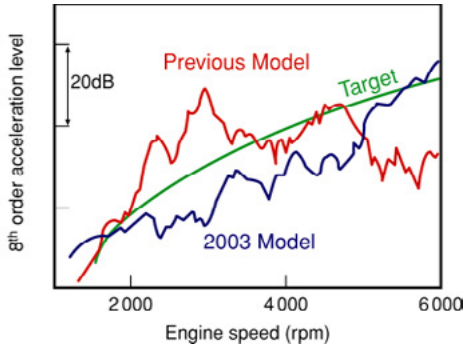


Fig. 8 Improvement of operational engine vibration-8th order at 2nd engine mounting bracket

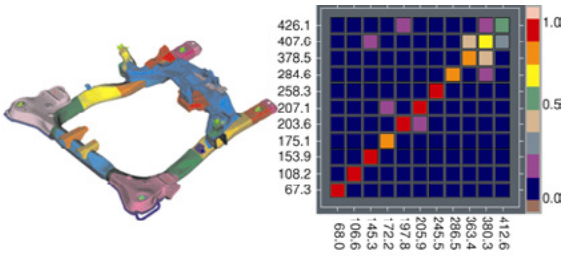
the power plant, of the block walls, and of the brackets. A large reduction in engine vibration of 5 – 20 dB was accomplished in relation to the previous model. Similar reductions in engine vibration (second through eighth orders) were seen in the other mounting locations.

4. Verification of Body Noise Transfer Function

The same process of modeling was carried out as for engine vibrations. Four vibration transfer paths through the subframe and two paths directly to the body were investigated.

4.1. Noise Transfer Path in Subframe

A frequency response matrix of the subframe was constructed from the FE model, and a frequency response function matrix of the body was constructed from experimental data. Figure 9 presents the model of the subframe. As in the brackets, the model was updated in order to improve the correlation with the experimental models.



(a) Subframe FE model (b) MAC with Experimental Mode

Fig. 9 Subframe FE Model

Table 1 shows the errors of the calculated eigenvalues in relation to the experimentally determined figures and the MAC values. The error stayed within about 5% up to the ninth mode. The MAC value remained above 0.8 or more, indicating a good correlation between the models.

The results obtained by combining the analytical subframe model with the experimental body model in the initial prototype are shown in Fig. 10. The Hybrid model showed a high correlation with the experimental model until

Table 1 Correlation of experimental subframe mode

No.	Experimental Mode Hz	FE Mode Hz	Difference Hz	Difference %	MAC
1	67.3	68.0	0.8	1.1	0.97
2	108.2	106.6	-1.7	-1.5	0.96
3	153.9	145.3	-8.6	-5.6	0.95
4	175.1	172.2	-2.9	-1.6	0.79
5	203.6	197.8	-5.8	-2.9	0.87
6	207.1	205.9	-1.3	-0.6	0.86
7	258.3	245.5	-12.9	-5.0	0.96
8	284.6	286.5	1.9	0.7	0.80
9	378.5	363.4	-15.1	-4.0	0.81
10	407.6	380.3	-27.3	-6.7	0.62
11	426.1	412.6	-13.5	-3.2	0.58

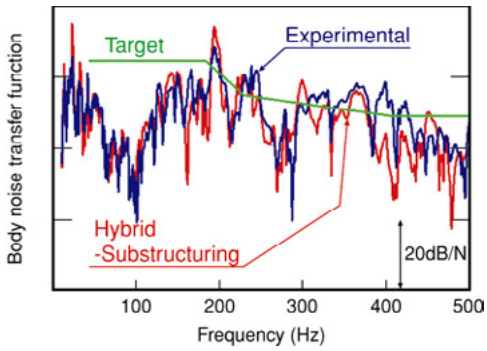


Fig. 10 Body noise transfer function of 2nd engine mounting point on subframe

the 380 Hz region, indicating that high precision had been maintained. In the vicinity of the tenth and eleventh modes, where the MAC value fell below 0.7, the hybrid calculations significantly underestimated the test results. This was noted for reference during later experiments.

It became clear when investigating the frequency response matrices for both the subframe and the body models that improvements in the subframe members, use of floating structures, and improvements to the attachment structures of the body would be necessary in order to attain the targets.

For the subframe, major structural modifications based on the use of a hydro form cradle allowed improvements of 84% in the bending mode and 29% in the torsional mode (compared to the previous model).

4.2. Noise Transfer Path in Body

The body frequency response matrix was found using a measurement setup similar to the one shown in Fig. 11. Figure 12 shows the results with the hybrid model composed of the physical model of the initial prototype and the FE model of the mounts; this indicates a good match with the prediction. It was evident that the frequency response matrices of both the body and the mounts would have to be improved in order for noise transmission through this path to meet the target.

The overall height of the 3rd engine mount was greatly reduced and it was changed to a low-CG (CG 40% lower than in the previous mount), high-stiffness hydraulic design, integrated with the body attachment bracket. The 6th mount was reconfigured to resin-steel design, which offered high dynamic stiffness. Both are shown in Fig. 13.



Fig. 11 Experimental trimmed body

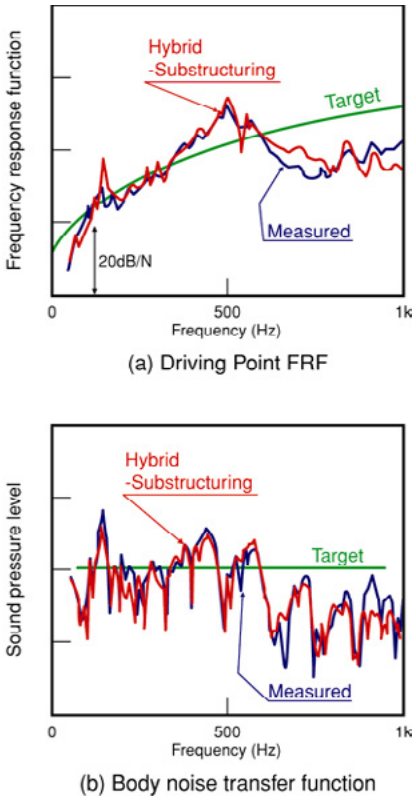


Fig. 12 Validation of sub-structuring for 3rd engine mounting FE model with experimental body

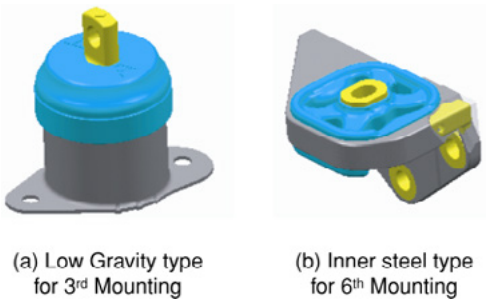


Fig. 13 3rd and 6th engine mounting

It was noted that, within this body frequency response function matrix, the dynamic stiffnesses at the mounting points had to be increased by factors of 6 to 10.

Experimental data was used in the frequency response function matrix, but FE models of the attachment structures were built and verified as valid for investigation of these structures. The trimmed body model is shown in Fig. 14 and the FE models of the attachment structures are shown in Fig. 15.

Since it was difficult to assure high accuracy in this frequency region at the body attachment points in the calculations required for this report, the flexibility of the hybrid model in permitting deletion of structure before performing experiments proved to be very useful.



Fig. 14 FE model of trimmed body

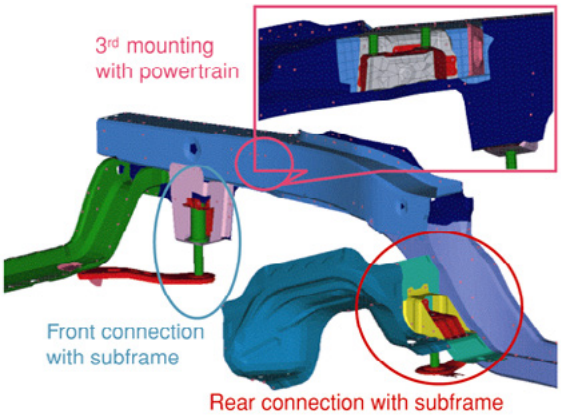


Fig. 15 Area for connection with subframe

4.3. Results on Body Noise Transfer Function

The body dynamic stiffness target was attained by shape improvements of both the collar structure at the body attachment bolts and the interior cross section of the bulkhead in addition to incorporation of the new engine mounts. Figure 16 shows the resulting dynamic stiffness levels of the low-CG 3rd engine mount body connection point.

The target for the body noise transfer function at the engine mounting points was achieved by structural improvements of the subframe, possible through hydro forming manufacturing, increasing isolation by making the subframe floating, and improvement of the dynamic stiffness at the body mounting points. The body noise transfer function at the 2nd engine mount on subframe is shown in Fig. 17.

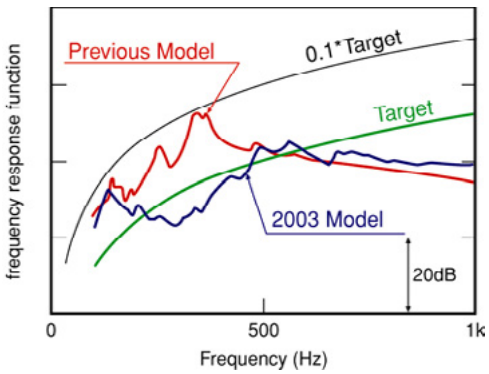


Fig. 16 Improvement of dynamic stiffness for 3rd engine mounting point on an actual body

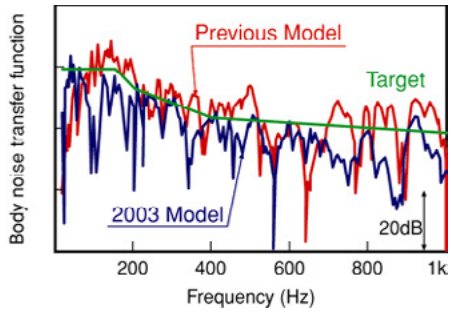


Fig. 17 Improvement of body noise transfer function at 2nd engine mounting point on a subframe

5. Cabin Noise Levels

As shown in Fig. 18, the goal for the 2003 Accord cabin noise was reached through this effort to achieve the targets for each system. A significant noise reduction compared to the previous model was accomplished.

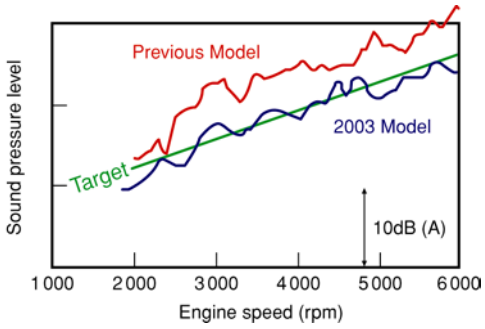


Fig. 18 Improvement of cabin noise

6. Summary

A hybrid CAE model was constructed for use in the development of the 2003 Accord. The target for each system of the model was set after its contribution had been quantitatively associated with the noise reduction target. As a result of the steps taken to achieve the targets set for each system, a large reduction in engine noise transmitted to the cabin was accomplished. The new Accord met the original vehicle performance objectives set at initiation of development.

References

(1) Sakai, T.: Development Procedure for Interior Noise Performance by Virtual Vehicle Refinement, Proceeding SAE Noise & Vibration Conference, 2001-01-1538 (2001)

(2) Sakai, T.: Development of Procedure for Interior Noise Estimation by Virtual Vehicle Analysis, Honda Technical Review, Vol. 13 No. 2, pp. 195-204 (2001)

(3) Wyckaert, K.: Flexible Substructuring Based on Mixed Finite Element and Experimental Models -A step ahead of Transfer Path Analysis, Proceedings 14th International Modal Analysis Conference, pp. 633-640 (1996)

(4) Wyckaert, K.: Hybrid Substructuring for Vibro-acoustical Optimisation – Application to suspension – Car Body Interaction, Proceedings International Noise & Vibration Conference, No. 971944 (1997)

■ Authors ■


Tatsuhide SAKAI


Tetsuya MIYAHARA


Tomonori NIIZATO


Hiromichi TSUSHIMA

A Configuration Evaluation Technique for CVT Metal Belt Rings

Mamoru ARIKAWA* Hirotoshi SHIMA*

ABSTRACT

A method for divided measurement of the lateral curvature of rings was developed for use in helping assure the quality of metal pushing V-belts for continuously variable transmissions (CVT). The method measures the lateral curvature without cutting the ring by dividing the full circumference into several partial segments that are measured separately. The data for the overlapping portions are cross-checked and the data starting point is then shifted over to calculate the peak-to-trough height automatically. The maximum quantity is taken as the lateral curvature for evaluation. The conventional method of lateral curvature measurement by cutting and expanding had shortcomings because that method could not be used for measurement prior to testing on actual transmissions and the lateral curvature varied depending on the point of cutting when measuring rings with points of curvature change. The present approach has resolved those issues.

1. Introduction

In 2001, Honda utilized original technologies to develop and mass-produce a metal belt for CVT. Details of the process of development and the specifications of this belt formed the subject of a previous paper in the *Honda R&D Technical Review*[(1)].

As shown in Fig. 1, the new metal belt is composed of elements and rings. The accuracy required in the production of these components is extremely high, even when compared to other automotive components, necessitating the development of new measurement methods to verify configuration. This paper provides an overview of the development of a new method for divided measurement of the lateral curvature of the rings utilized in these belts.

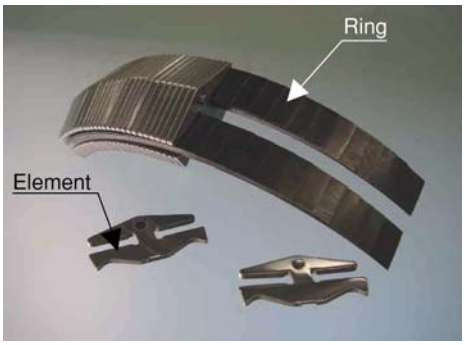


Fig. 1 Metal pushing V-belt

* Tochigi R&D Center

2. Development Aims

2.1. Directional Lateral Curvature of Ring Circumference

An example of the rings used in the CVT metal belt is shown in Fig. 2. Each ring is constructed from a thin cylindrical metal plate and is 0.18 mm thick.



Fig. 2 Ring

In the finished belt the rings are assembled in two layers of multiple rings. The rings guide the elements onto the pulley in the sections of the belt wrapped around the pulleys and control the trajectory of the elements between the drive and driven pulleys. Figure 3 shows a cross-section of the ring and element assembly when wrapped around a pulley. When the belt is in operation the ring assembly is normally centered on the saddle surface from the innermost to the outermost rings maintaining the ring edges in approximate alignment. This ensures that multiple ring edges make contact simultaneously if contact occurs with the elements and the pulley V-surfaces reducing the load on each individual ring.

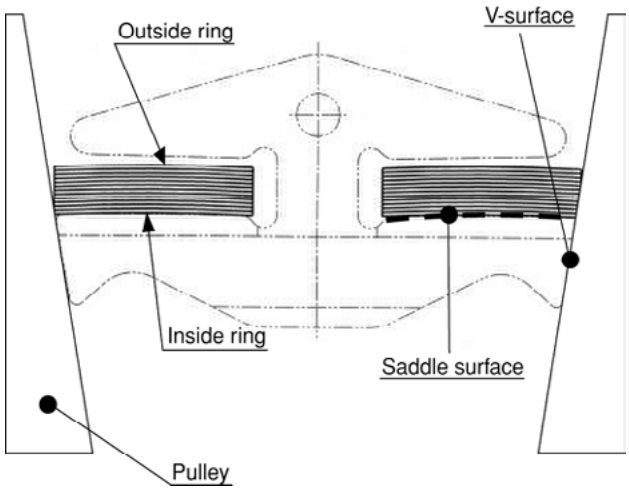


Fig. 3 Structure of V-belt assembly

However, as Fig. 4 shows, if deformed rings are included in the belt assembly the edges fall out of alignment with those of the cylindrical rings and protrude against the elements or the side of the pulley V-surface. When the metal belt is operated under these conditions the edges of the deformed rings make contact more easily with the elements and the pulley V-surfaces than those of the circular rings. This causes strong sectional loads in the ring assembly and can lead to early breakdown of the belt. It is therefore essential to control the degree of deformation of the rings within prescribed limits in the production process.

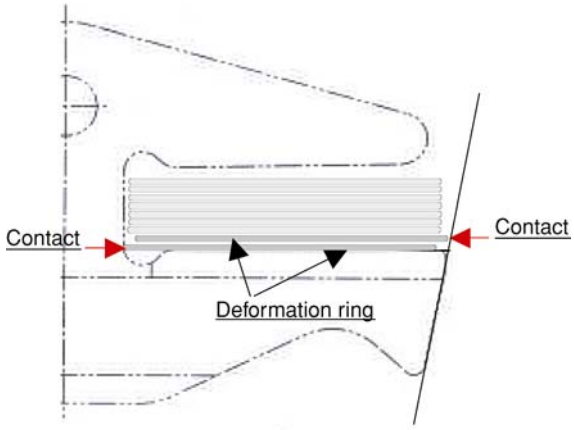


Fig. 4 Partial contact of ring assembly

Figure 5 shows the forms of normal and deformed rings and the shapes produced when they are cut and expanded. In Fig. 5, h, the degree of deviation from the straight line along the edge of an expanded circular ring, represents the lateral curvature of the ring. Figure 5(1) shows a ring with no deformation and therefore without lateral curvature. A ring that has a tapered deformation is shown in Fig. 5(2). When cut and expanded, this ring forms a U-shape. The ring shown in Fig. 5(3) has a parallel quadrilateral deformation producing an S-shape when cut and expanded.

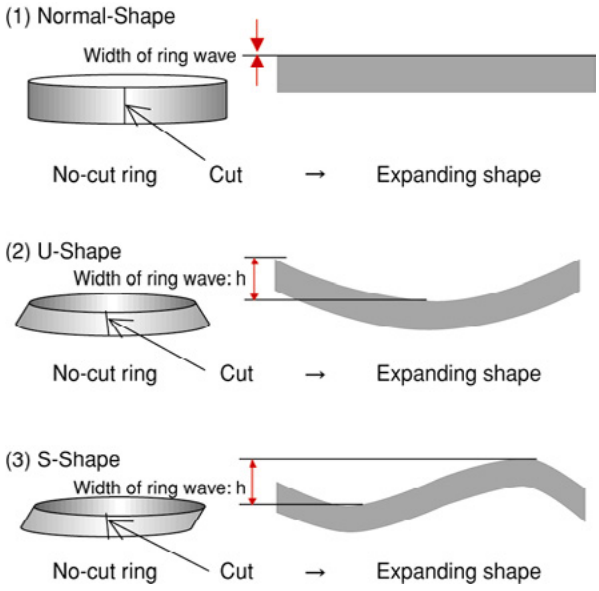


Fig. 5 Ring-wave

2.2. Conventional Measurement Method

Cutting and expanding the ring, as described above, is the conventional method for measurement of lateral curvature.

In this method, the rings are cut at an arbitrary point and expanded; the form of the resulting ring edge is measured, and the lateral curvature is found from the maximum deviation of the edge from a base point. Figure 6 shows an outline of the method.

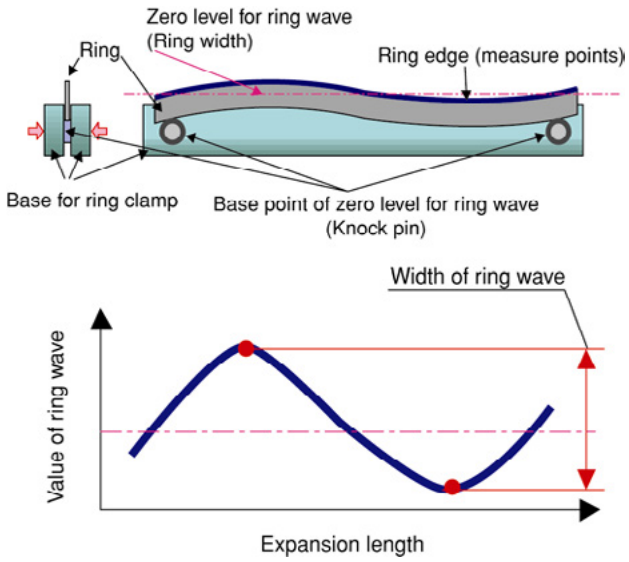


Fig. 6 Method for measurement of ring wave

The ring, after being cut and expanded is fixed in a ring clamp composed of two plates of approximately the same length as the circumference of the ring. When the ring is being fixed in the clamp, knock pins are put in place to hold the lower edge of the expanded ring on the base line for measurement. A cylindrical measuring probe is then used to trace the ring edge set in the clamp. The degree of wave of the ring edge is measured at fixed intervals and the values obtained at these points are plotted to reproduce the wave. Next, the amount of deviation of the reproduced wave from a straight line is determined over a fixed length and taken as the lateral curvature of the ring. However, because this method necessarily involves the destruction of the ring, it cannot, for example, be utilized to determine lateral curvature before a strength test. In addition, when the degree of lateral curvature of the ring changes at various points, measurements of lateral curvature differ with different starting points for measurement (the point at which the ring is cut).

Figure 7 shows a comparison of measurements of lateral curvature obtained from rings with various points of curvature change cut at different points. Figure 7 demonstrates that when rings are cut and expanded from the arbitrary points A-D around the circumference, the position of the points of curvature change differ. In addition, given this difference, the lateral curvatures h1, h2, h3 and h4 as measured over a fixed length also differ.

The aims for the development of a new measurement method for lateral curvature of CVT belt rings were therefore established as follows.

The measurement method should enable:

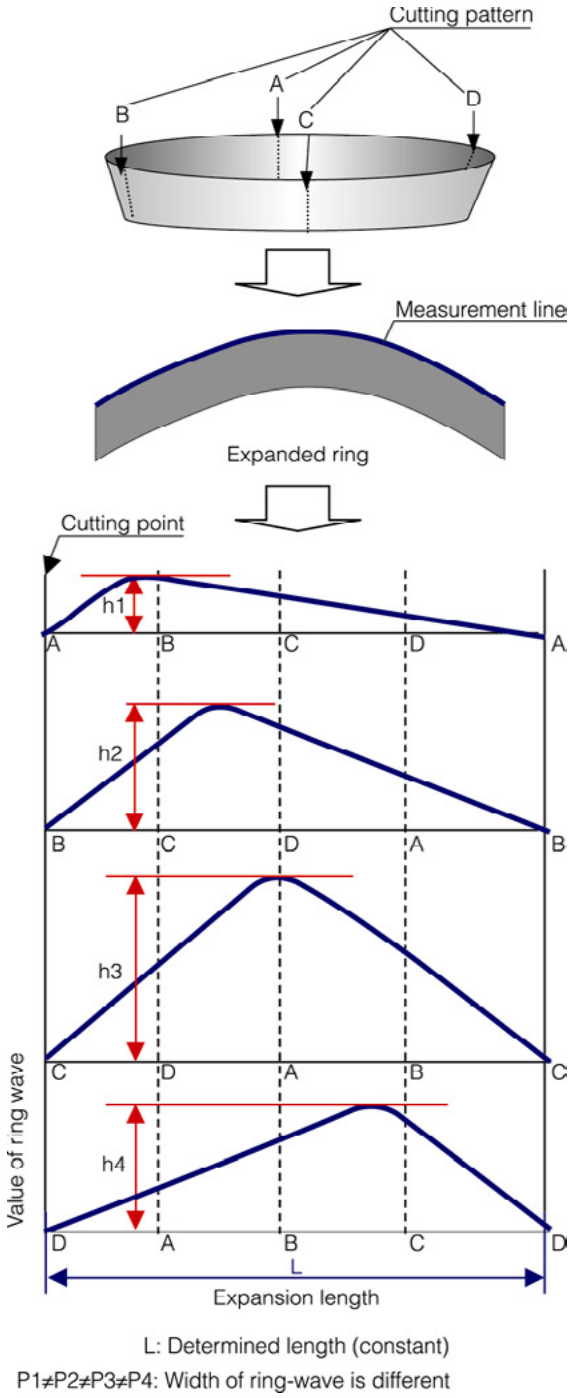


Fig. 7 Rings with points of extreme curvature change

(1) Measurement of any type of lateral curvature without cutting; and
(2) Accurate measurement of lateral curvature of rings with points of curvature change.

3. New Measurement Method

3.1. Divided Measurement of Lateral Curvature

Figure 8 shows a schematic of the new method and gives an outline of the basic principles used to solve the drawbacks of the conventional cutting and expansion method.

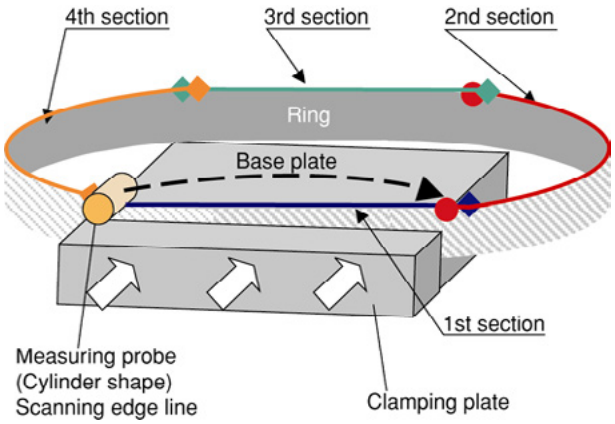


Fig. 8 Improved method (requires no cutting)

The ring clamp utilized in the divided measurement method is shorter than that used in the conventional method making it possible to position the clamp base plate against the inner circumference of the ring. The ring is fixed in the clamp at a specified clamping force. When the ring is clamped, the lower edge is placed against knock pins set at the base line for measurement. Next, a cylindrical measurement probe traces the ring edge fixed in the clamp and the amount of deviation from the base line is measured at fixed intervals along the circumference. The ring is then released from the clamp and moved enabling deviation from the base line to be measured in another segment. The starting point for measurement in this section is a point at approximately four-fifths the length of the first section, meaning that measurements overlap. Measurement proceeds in this way by dividing the overall circumference of the ring into several overlapping segments. The data for the overlapping sections is then cross-checked and a straight line drawn between the starting and finishing points. The maximum deviation occurring at a right angle to this line is taken as the lateral curvature for evaluation. Figure 9 shows a model of the procedure of cross-checking data for the overlapping sections in the divided measurement method.

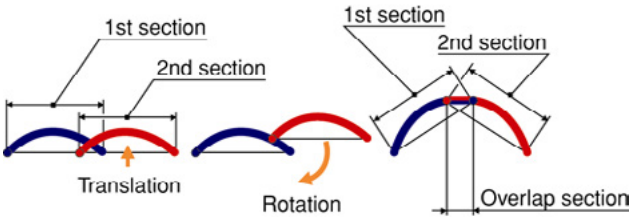


Fig. 9 Method for data overlapping

As previously discussed, measurements of lateral curvature taken using the cutting and expansion method differed depending on the point at which the ring was cut. This effect does not occur in the newly developed method because the starting point for evaluation of the combined data is shifted at fixed intervals over the circumference of the ring and the maximum deviation from the baseline that is calculated from this data is taken as the lateral curvature of the ring.

Figure 10 shows an image of this method.

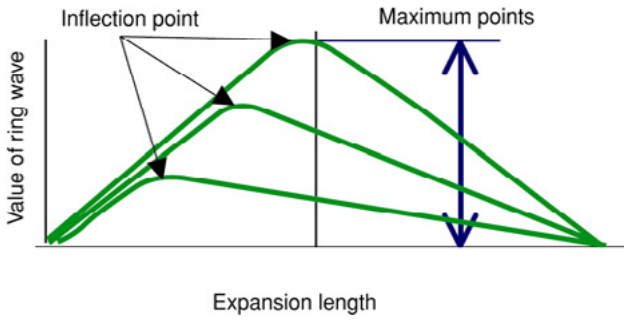


Fig. 10 Method for defining curvature

3.2. Verification of Reliability

Tests were conducted to determine the reliability of the results obtained for degree and form of lateral curvature by the combination of data obtained in various segments using the new method against the results obtained using the cutting and expansion method. These tests were conducted on a sample of 50 rings and involved comparison of measurement results obtained from both methods when identical starting points were used for measurements.

Figure 11 shows the results of these reliability tests as a scatter diagram.

The vertical axis shows results obtained using the divided measurement method and the horizontal axis shows results from the cutting and expansion method. The new method shows high reliability with a coefficient of correlation of 0.974.

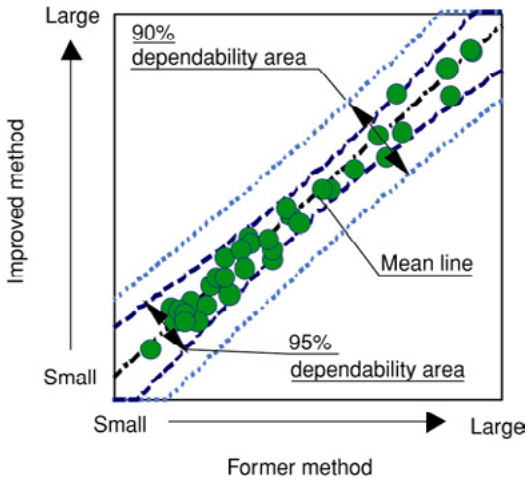


Fig. 11 Scatter diagram comparing measurement methods

Figure 12 shows a comparison of the configurations of curves obtained using the two methods.

Solid lines represent results obtained from the cutting and expansion method, and broken lines results from the divided measurement method. Both methods reproduce extremely similar configurations of curvature demonstrating the ability of the method of overlapping and combining data to provide an accurate rendering of the configuration.

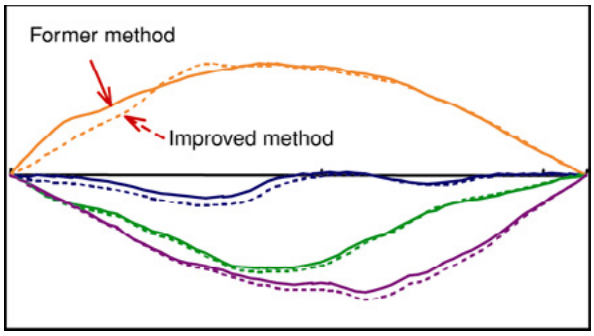


Fig. 12 Comparison of configurations generated by different measurement methods

4. Use in Mass Production

Figure 13 shows a machine for high-speed automatic measurement of the lateral curvature of rings that applies the principles discussed in this paper.

As Fig. 14 shows, when a ring is placed in this machine it undergoes the following operations:

Operation 1: Clamping
Operation 2: Measurement
Operation 3: Unclamping
Operation 4: Moving
Operation 5: Reclamping.

Figure 15 shows the procedures the system automatically applies to the data obtained from measurements:

Procedure 1: Collation of divided measurement data
Procedure 2: Combination of data obtained from over-lapping sections to reproduce configuration of lateral curvature
Procedure 3: Shift of starting point to calculate degree of lateral curvature.

The significant reduction in the number of procedures involved in measurement achieved by this system has enabled it to be utilized in mass production quality control.



Fig. 13 Machine for automatic ring curvature measurement
[Made by: Honda Engineering CO., LTD.]

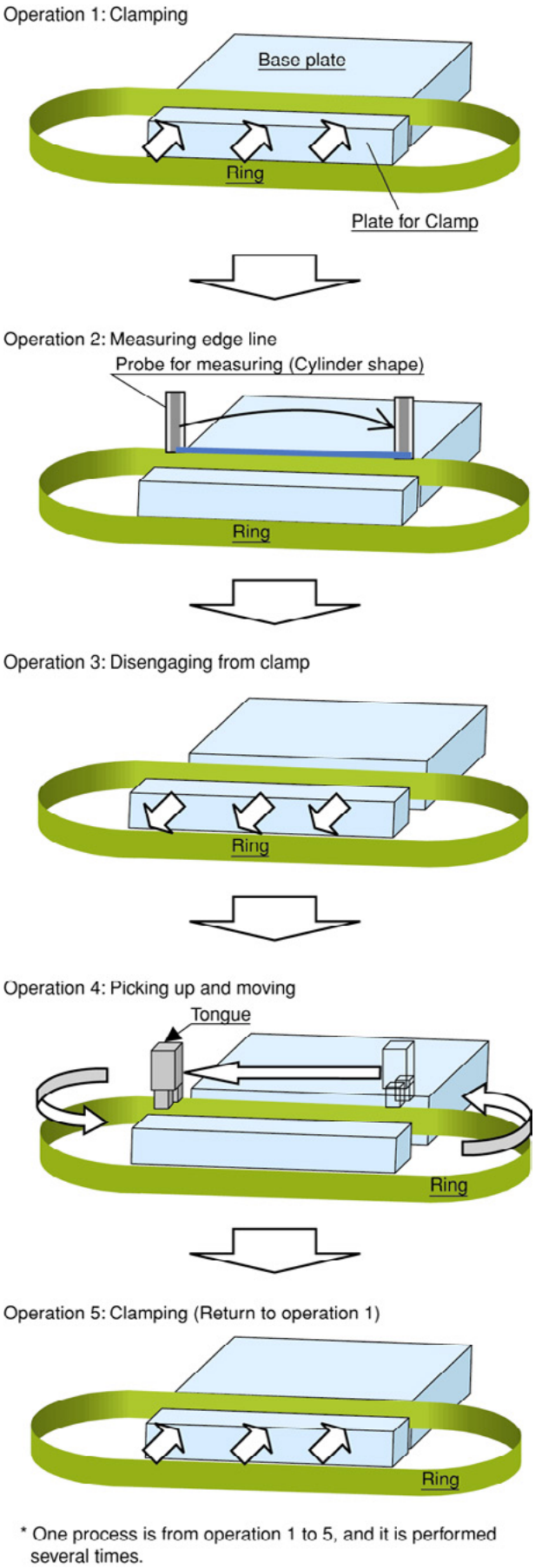


Fig. 14 Conceptual image of operation machine for automatic curvature measurement

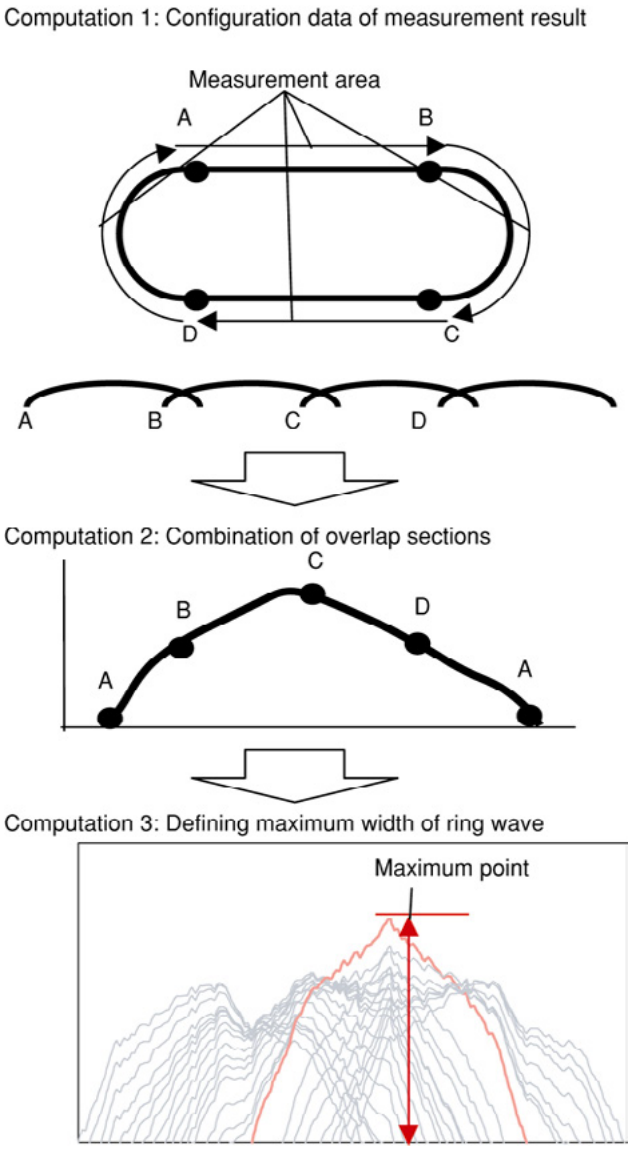


Fig. 15 Image of automatic machine process of computation

5. Conclusion

Honda R&D has developed a method for more accurately measuring the lateral curvature of rings utilized in metal pushing belts for CVT, a factor directly affecting the durability and life of these belts. The salient characteristics of this method are as follows:

1. The method enables measurement over the entire circumference of the ring without cutting, by dividing the circumference into overlapping segments. This makes it possible to apply this method before strength tests.
2. In the conventional cutting and expansion measurement method, values obtained for curvature differ for the same ring depending on the relative positions of the starting point for measurement and points of curvature change making accurate evaluation less possible. Calculations in the newly developed divided measurement method are made on the basis of new starting points for each measurement segment and the maximum value for curvature over the entire circumference is taken as the measured lateral curvature enabling a more accurate evaluation.

6. Afterword

Deformation of components affects the performance of the metal pushing belts utilized in CVT. To provide more accurate measurement of the form of these components, in addition to the ring curvature measurement method discussed in this paper, Honda R&D has developed an original technique for the evaluation of deformation in belt elements.

Research into the ideal form of components and the ability to evaluate production consistency in relation to that ideal is important to the future evolution of metal pushing belts for CVT. The authors will continue their efforts to advance technologies for evaluation of components and enhancing their performance.

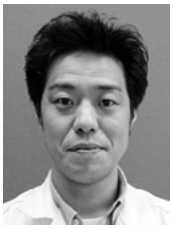
In closing, the authors would like to offer their sincere thanks to all who contributed to the success of this development project.

7. References

(1) Yagasaki, T., et al.: Development of Metal Pushing V-Belt for Continuously Variable Transmission, Honda R&D Technical Review, Vol. 14, No. 1, pp. 181-190 (2002)

(2) Patent Application 2000-70230: Method and equipment for measurement of curvature of thin metal rings and method of production

■ Authors ■


Mamoru ARIKAWA


Hirotoshi SHIMA

Development of High-Speed and High-Precision Production Technology for Mock-up Models

Mitsuhiro OKADA* Soichi ANEKAWA**

ABSTRACT

Technologies for 5-axis machining and high-speed machining were developed with the objective of shortening development schedules and achieving higher-precision quality in the Numeric Control (NC) machining of mock-up models, compared to conventional NC machining which consists mainly of 3-axis machining. The conventional NC machining format was thoroughly reviewed in terms of infrastructure, hardware, software, and machining technology. By developing a new system that links CAD/CAM software with the NC machine, 5-axis NC machining and 3-axis high-speed machining technologies have become possible. At the same time, high quality NC data creation time was reduced. As a result of these new technologies, the NC process has become five times faster than the conventional methods.

1. Introduction

The development of mock-up modeling technology has seen considerable improvements in the areas of speed and quality of NC machining on a full-scale model. This was made possible through improvements in machining technology and the increasing experience of engineers.

It was possible to enhance the efficiency by simply upgrading the older tools to the latest available tools. However, performance could not readily be demonstrated if balance was not maintained among the latest tools, computer technologies, and those who handle them. It is important, therefore, to set ambitious goals, and implement them by carefully going over the plans. We have set the development goal for NC machining to be three times the speed and ten times the accuracy than before. As a result of thorough study of the issues to achieve the goal, we recognized the need for high-speed and high-precision NC machines as well as improvement in NC data creation speeds.

In the past, the design surface was finished by hand after machining. For this reason, we were not able to verify the CAD data against mockup models. As a result, it was necessary to produce verification models frequently.

First, we began the development by trying high speed and accuracy in order to improve the processing speed of mock up models. And then, we transitioned to 5-axis machining from 3-axis machining with 5-axis machining technology, as shown in Fig. 1. Thereafter, we were able to achieve our goal, along with the multiplier effect of improved NC machine performance. As a result, we were able to guarantee verification of mockups through CAD data with no need to produce verification models. This paper discusses these results and related technologies.

* Wako R&D Center
** Tochigi R&D Center

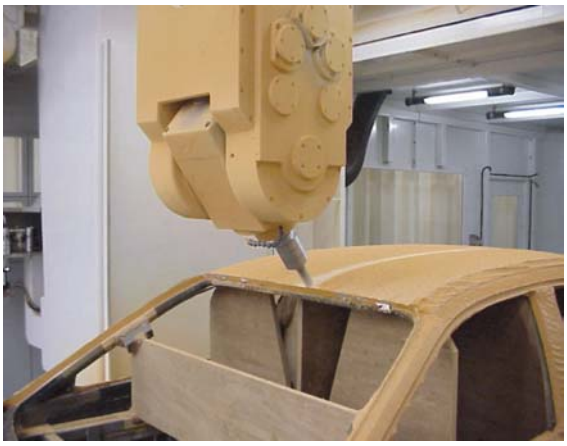


Fig. 1 View of 5-axis machining

2. Development Targets

We focused mainly on the following development areas to achieve the goal of enhancing NC machining speed by three times.

- Develop a high-speed, high-precision 5-axis NC machine
- Develop software for 5-axis NC data

The development goal of the high-speed, high-precision 5-axis NC machine was as follows:

1. Shorten rough machining time by 1/3
2. Shorten finish machining time by 1/3

The development focus of 5-axis NC data software was as follows:

1. Develop 5-axis machining software and its implementation
2. Shorten NC data creation time by 1/2

The main issue was to achieve these requirements.

3. Development of a High-speed, High-precision 5-axis NC Machine

3.1. Specifications

The NC machine has a long Z axis, and is large enough to accommodate one full-scale mock-up, as shown in Fig. 2. When compared with horizontal-type and small machines, it was unfavorable in terms of accuracy and machining conditions. However, we have come up with a structure to maintain the required accuracy. One of the most important units of this machine was the 5-axis head, which was newly designed to improve machining accuracy, rigidity, and machining speed over the previous design. The NC controller was developed with the basis of controlling the Rotating Tool Control Point (RTCP). The cast-iron structure was adopted in order to maintain the stability and strength to withstand the stresses of high-speed machining as well as the resonance during machining.

Hollow Shaft Kegel (HSK) taper was adopted in a built-in spindle in order to handle high-speed rotation.

The machining speed was based on the linear axis 20 m/min (the rotating axis was synchronized), with durability equivalent to existing machines, and full consideration was given to the maintenance of the NC machine. On the hardware side, zero backlashes for each rotating axis was an essential requirement. Although positioning accuracy of each rotating axis was guaranteed through scale feedback, the precise position of the tool tip could not be guaranteed, and errors were not completely eliminated. One issue was eliminating errors of several μ m when the coordinates of the axis were reversed.



Fig. 2 5-axis NC machine

3.2. RTCP and 5-axis NC Machine Actions

As shown in Fig. 3, it is very important to note that NC actions changed completely, depending on whether the RTCP function was ON or OFF. Previously, this function was not available and so was set as RTCP OFF as shown in the diagrams. In creating NC data, head simulation and actions of the NC machine differed. This is why it requires certain expertise in creating data. Although initially there were numerous problems with the NC controller software, immediately after RTCP was implemented those problems were resolved and automated actions are now possible. During NC data creation, the head simulation display matched the real actions of the NC machine, which made it possible to check the data before machining with that data. In operating the NC machine, head actions became faster than the speed of the F command value, thereby necessitating a more balanced speed control.

3.3. 5-axis Machining Test

As the 5-axis machine consists of numerous moving

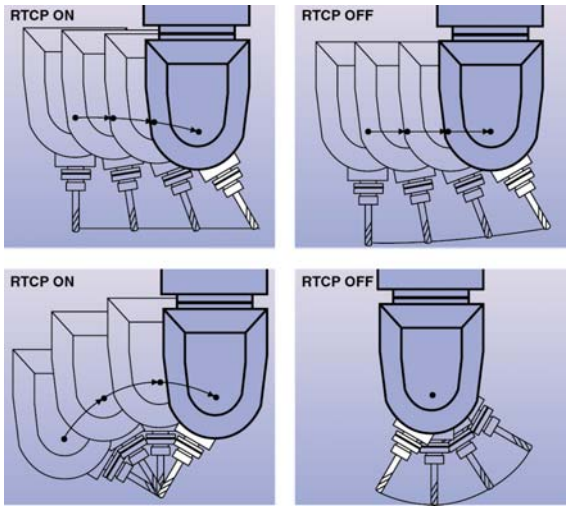


Fig. 3 Movement of RTCP on/off

parts, the static accuracy guaranteed by NC machine manufacturers is not sufficient. It is important, therefore, to guarantee dynamic accuracy at the time of trials. There is no standardized dynamic testing method by the NC machine manufacturers; thereby tests consist of machining spherical surfaces, tapered cones, and machining actual products.

When 5-axis machining was not common in the past, testing through trial and error was repeated. A pair of samples, shown in Fig. 4, confirm different results when RTCP is ON and OFF. These samples specify flat surface machining to simplify measurements. This was aimed at confirming overall precision of the way the NC machine is assembled and basic dynamic actions of the 5-axis control as well as verifying the relationships between 5-axis head and each axis.

Machining produced a washboard appearance when RTCP was OFF, as shown in Fig. 4. This test piece was machined with a ball end mill, which B-axis (C-axis) was rotated +45 degrees to –45 degrees in longitudinal direction.

The machining conditions were as follows:

- Tolerance :0.005 mm
- Machining step :0.4 mm
- Tool :ϕ 20 ball end mill
- Spindle speed :10000 rpm
- Feed rate :1500 mm/min

It is unique for NC data to produce different results depending on whether the NC machine is turned ON or OFF, even though exactly the same NC data is used. Needless to say, RTCP ON is the basic state. However, some pieces could be machined with RTCP OFF, depending on the shapes being machined and the quality of the NC data. The results of machining were measured, and static positioning accuracy of the X, Y, Z, B, and C axes were checked and determined whether any errors in the shape of the workpiece was being made. Static movements were also confirmed by making synchronous adjustments of the NC controller at the same time.

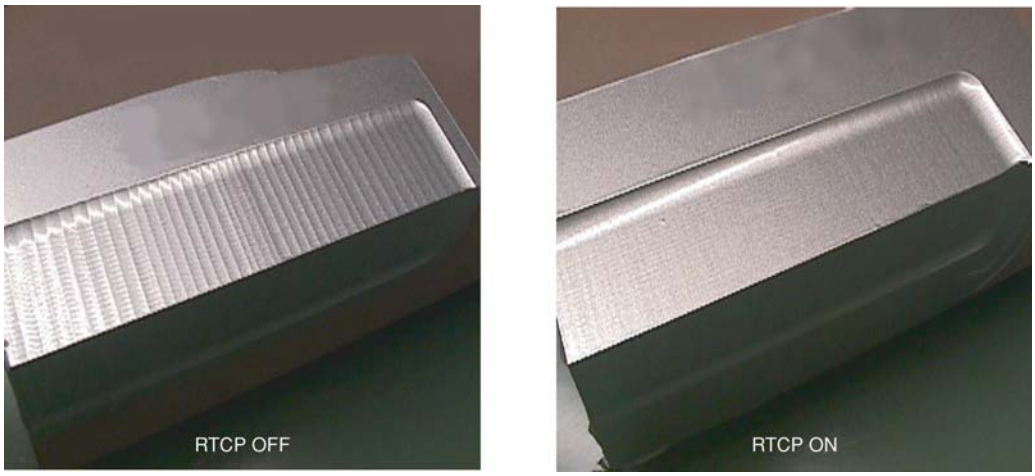


Fig. 4 Result of RTCP on/off

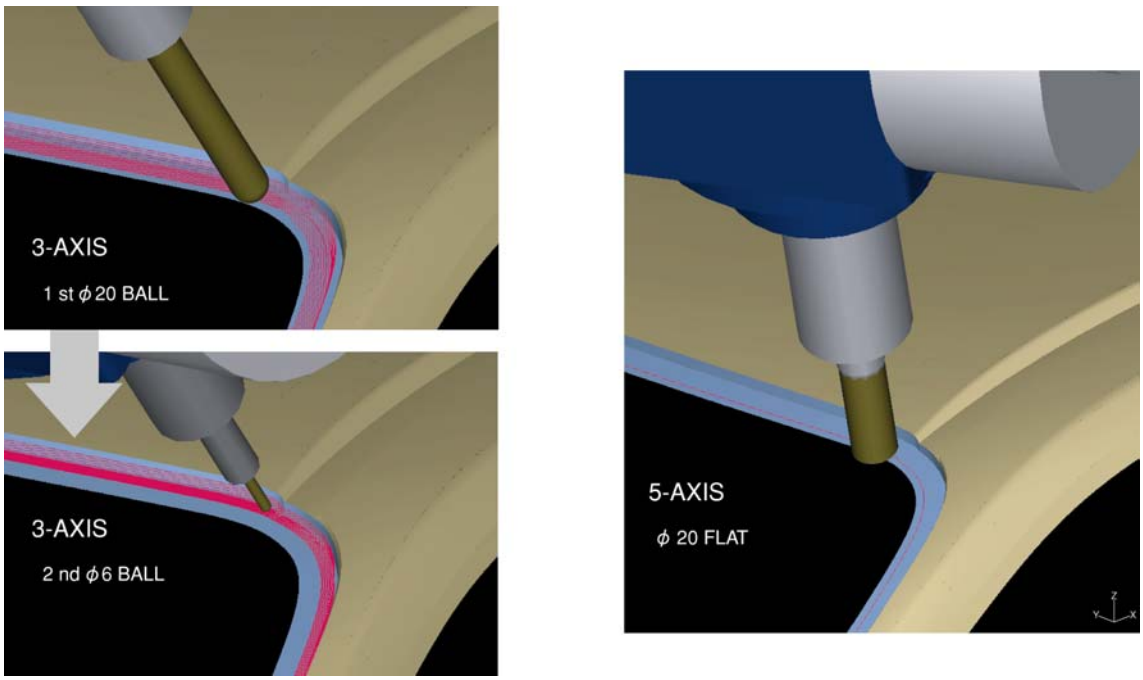


Fig. 5 Difference between 3-axis machining and 5-axis machining

When problems arose through this inspection, we had to explore whether there were problems with the way the NC machine was assembled while re-verifying how the 5-axis head was retrofitted to solve these problems. Next, we verified accuracy and movements of each part through machining.

It was necessary, therefore, to exert effort in making adjustments to guarantee accuracy of the 5-axis NC machine besides the time spent on the basic 3-axis, at the time of its' implementation.

4. Development of 5-axis NC Data Software

4.1. 5-axis NC Data Software

While most of the personal computer CAM software currently available on the market offers sufficient capabilities for 2-axis and 3-axis machining, they are generally not very user-friendly for fixed 5-axis machining, and some do not even support it at all. Furthermore, functions of creating NC data for 5-axis machining are limited, and there are few that are suitable for machining mock-up models. Therefore, we developed software that was suitable for model machining.

4.2. NC Data Creation for 5-axis Contour Machining

In the past, contours of mock-up models were machined with a ball end mill using 3-axis NC data, as shown in Fig. 5. This process was the most common practice with conventional NC machining. Also, this function is essential for mock-up model machining. This section compares machining methods of the NC machining process for window areas as shown in Fig. 5.

The 3-axis machining process was as follows:

Process 1 ϕ 20 ball Rough machining Multiple paths
Process 2 ϕ 20 ball Finish machining Multiple paths
Process 3 ϕ 6 ball Rough machining Multiple paths
Process 4 ϕ 6 ball Finish machining Multiple paths

The machining in processes 1 through 4 takes longer time due to multiple paths and thus, some un-machined areas remain.

The 5-axis machining process was as follows:

Process 1 ϕ 20 flat Rough machining one path
Process 2 ϕ 20 flat Finish machining one path

As a result, the number of processes was cut in half and the machining time was reduced to 1/3. In addition, the quality of machining was improved without un-machined areas.

The 5-axis machining enabled the use of a flat-end mill, and it offered an innovative method of reducing machining processes.

The 5-axis machining features were as follows:

- Reduced machining time
- Improved machining quality
- Reduced tool cost
- Shortened NC data creation time (fewer processes)
- Reduced time to create CAD models of contoured shapes

Recently, we have seen much progress made in machining by high speed and high precision of NC machines. However, these results indicate that in some instances, it is more effective to implement 5-axis machining instead of trying to make the NC machines faster.

4.3. NC Data Creation for 5-axis Surface Machining

The surface machining is one of the most important functions in the 5-axis machining. It performs machining of design surfaces (multiple surfaces) with a flat or corner radius end mill along surfaces.

Normally, 3-axis machining is more accurate and stable than 5-axis machining. However, for a mock-up model, it is more effective to process on a large surface through 5-axis machining with a corner radius end mill rather than faster and finer machining with a ball end mill. In the past, there was a problem of remaining grind marks with the 5-axis machining software. Because of the poor quality on fillet shaped parts, the only alternative was machining faster and finer with 3-axis machining as shown in Fig. 6. The grind marks were caused by the direction of machining in the NC data. However, the primary cause was the increased head movement and the quality deterioration of the 5-axis data at the shape change point. 5-axis surface machining became possible for fillet-shaped parts by minimizing the 5-axis head movement.

The machining conditions for the pieces shown in Fig. 6

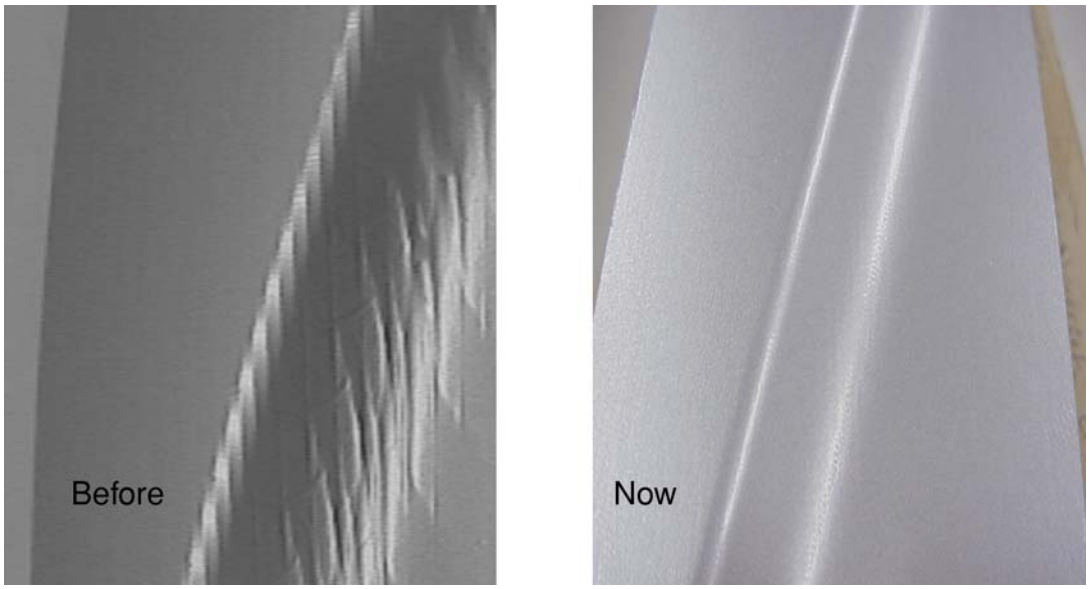


Fig. 6 Result of fillet on part using 5-axis machining

were as follows:

- Tolerance :0.005 mm
- Machining step :Basic setting, 2 mm
- Tool :ϕ 20 R3 corner radius end mill
- Machining direction :Before – Axial direction + fixed stepping
  Now – Direction along surface + variable stepping

It shows the resulting quality affected by the variable stepping.

4.4. New Functions Successfully Implemented Through Joint Development

5-axis NC data with constant machining step left grinding marks where the shape changes, as shown in Fig. 7. It was necessary to have variable step machining to eliminate this problem, as shown in Fig. 8. This was a very important function particularly when using a flat end mill with the 5-axis machining. This function, called “constant scallop height,” is essential for high-quality machining of design surfaces. This function was developed in conjunction with the 5-axis attitude change control.

The 3-axis machining with a ball end mill produced a fairly high-quality surface by making the machining step narrower and setting the grinding mark amount to scallop height 0.005 mm or less, as shown in Fig. 9. This principle was applied in developing the 5-axis machining.

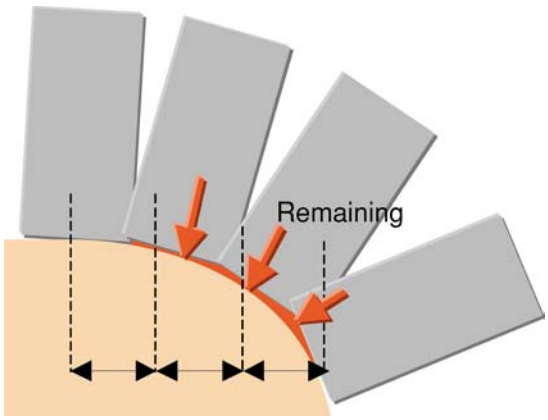


Fig. 7 Constant step over 5 mm

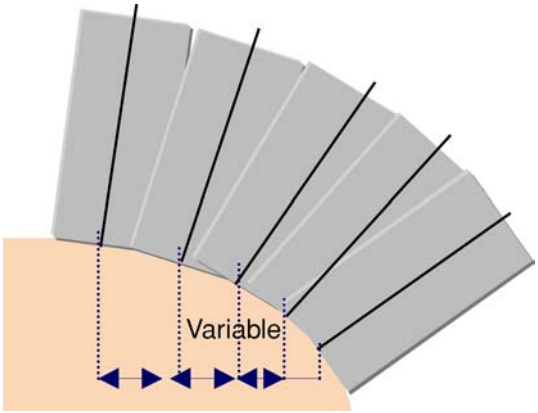


Fig. 8 Variable step over 3-7 mm

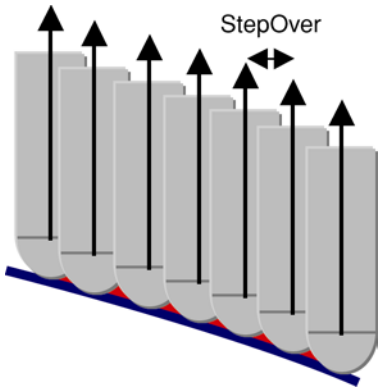


Fig. 9 3-axis milling with step over 0.77 mm

As an example, Fig. 10 shows a simulation using the 5-axis machining on a roof. It was made easy to create the optimal NC data by simulating the 5-axis head and the rotating axis. There was no interference of the 5-axis head in this simple example. However, it becomes extremely useful in complex shapes.

The machining conditions for this simulation were as follows:

- Tolerance :0.005 mm
- Machining step :Specified by scallop height of 0.005 mm
- Tool :ϕ 40 flat end mill
- Machining direction :Direction along surface + variable stepping
- Feed rate :20 m/min.

A smooth design surface and large machining area, such as a roof, was an optimal shape for 5-axis machining. The machining time was reduced to 1/10 in 5-axis machining with the use of a large flat end mill, compared to 3-axis machining. Furthermore, the quality of the machined results with 5-axis machining was quite different from that obtained with 3-axis machining, as shown in Fig. 11. However, it was very difficult to reduce the amount of time needed for creating data. Even though the NC path calculation is quick, it takes longer to verify the NC data in simulation for 5-axis machining than for 3-axis machining because of a need to check the head movement.

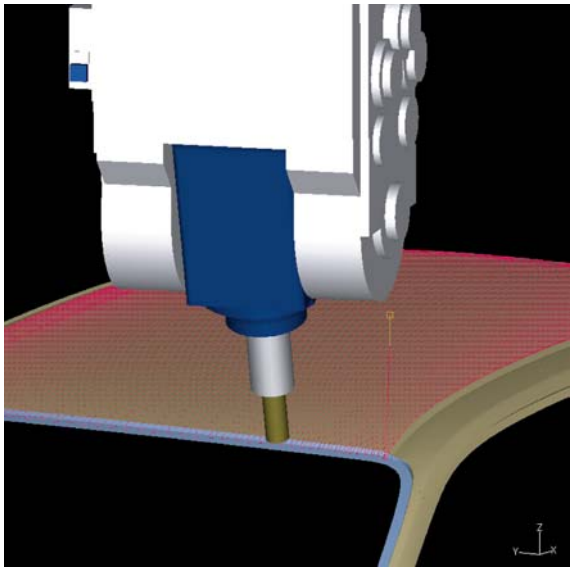


Fig. 10 Simulation by 5-axis machining with flat endmill

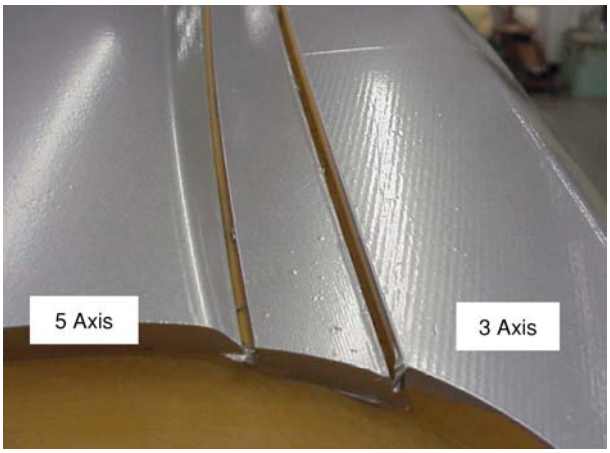


Fig. 11 Difference between 5-axis machining and 3-axis machining

The machining conditions for the ball end mill were as follows:

- Tolerance :0.005 mm
- Machining step :0.65 mm
- Tool :ϕ 30 ball end mill
- Machining direction :Direction of X axis (machining axis: 45 degree tilt)
- Feed rate :30 m/min.

The entire roof surface after 5-axis machining is shown in Fig. 12.

The 5-axis machined surface reflects the fluorescent lights more clearly than the 3-axis machined surface, which indicates the higher quality.



Fig. 12 Result of 5-axis machining

5. Results of Development

The objective of shorter mockup model development time was achieved by shortening rough machining time, NC data creation time, and finish machining time. The software for 5-axis machining was also developed and implemented. Furthermore, the development of 5-axis machining technology demonstrated the capability of reducing machining times not only by increasing machining speeds, but also by optimizing the machining methods. Also, it confirmed improvement in machining quality.

As a result, the machining speed was increased by five times, which far exceeded the original objective.

6. Conclusions

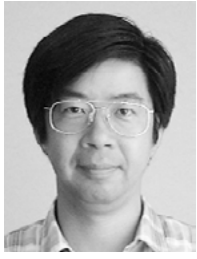
5-axis machining technology had been developed as a core technology for mock-up model NC machining, as opposed to the conventional 3-axis machining. The proprietary technology was developed, because there were few general-purpose hardware and software machining technologies available in this field.

As a result, the capability of practical 5-axis NC machining technology was demonstrated, and machining times were greatly reduced by the multiplier effect from the increased 3-axis machining speed. Furthermore, the system was developed to supply high quality NC data, confirmed by simulation, in a timely manner. This resulted in increasing the NC machining speed by five times.

The authors wish to extend their appreciation to those who cooperated in perfecting this new technology.

■ Authors ■


Mitsuhiro OKADA


Soichi ANEKAWA

Development of a Low Heat-Capacity Exhaust Manifold for SULEV

Kazuo ISHII* Takeshi MUNEMURA* Nobuyuki YOSHIDA*

ABSTRACT

A dual-wall exhaust manifold was developed that has low heat capacity in order to reduce the time taken to reach the catalyst activation temperature. An austenitic stainless steel with significantly improved high-temperature strength and oxidation resistance was developed by optimizing the composition design so that the inner tube could be made as thin as possible. The use of this material made it possible to increase the buckling strength at high temperatures and to make the inner tube wall 0.4 mm thick. In United States emission modes, a dual-wall exhaust manifold with an inner tube having a wall 0.4 mm thick is able to reach the catalyst light-off temperature 3 seconds faster than an ordinary single-wall manifold that is 2 mm thick. This achieved a reduction of approximately 22% in hydrocarbon (HC) emissions. The combined application of air-fuel ratio (A/F) control technology and catalyst technology together with the developed exhaust manifold made it possible to reduce the amount of precious metals used in an under-floor converter by approximately 20% compared to a 2001 model vehicle with SULEV specifications.

1. Introduction

In recent years, as the focus has remained on the effect automobiles have on the global environment, various local regulations are being enforced in many regions. One area of concern is air pollution due to exhaust emissions, and many countries are tackling the early creation of emissions regulations, such as those in California, USA. This has lead to a continuing increase in commercial vehicles that meet ULEV (ultra low emission vehicle) and SULEV (super ultra low emission vehicle) regulations, which had been thought of as almost impossible to meet. In these engines, by combining technologies for improved combustion, more precise air-fuel ratio control, improved catalytic converter conversion performance, and a modified exhaust system, there are fewer and fewer pollutants in exhaust emission[(1), (2)].

Among these technologies, the catalytic converter plays a large role in conversion. Therefore, accompanying the stronger exhaust emissions regulations, there has been an increase in the amount of precious metals used in catalytic converters. From the point of view of preserving precious metal resources, it is necessary to reduce the amount used, while at the same time it is increasingly necessary to develop technology to improve conversion performance.

* Tochigi R&D Center

2. Development Aims

By giving the exhaust manifold thin walls and a low heat-capacity, it is possible to restrain the drop in exhaust gas temperature at engine start, and improve catalyst temperature rise properties. Working for these effects, a dual-wall exhaust manifold, with the inner tube 0.6 mm thick, was developed, and the emissions reduction effects reported[3), 4)]. Making the exhaust manifold a low heat-capacity manifold, in this way, is almost standard technology that contributes to reducing exhaust emissions. In order to contribute to further exhaust emission reductions and a reduction in the amount of precious metals used in catalytic converters, an even lower heat-capacity technology has been pursued. However, when using ferritic stainless steel, the conventional material, for the inner material, the strength limit is 0.6 mm. In the new development project, a high-strength austenitic stainless steel was developed, and with its application, a dual-wall exhaust manifold with an inner tube thickness of 0.4 mm was developed with the aim of thinner walls and lower heat capacity. The goals were a reduction in the amount of precious metals used and contributing towards meeting SULEV regulations.

3. Structure

Figure 1 shows the overall structure of the exhaust manifold developed in this project. Table 1 gives the applied material for each part. Both the tubes and chambers use a 4-1 connecting configuration, with an insulated dual-wall structure. Because the inner tube contributes greatly to heat-capacity, in order to aim for the absolutely lowest heat-capacity that doesn't compromise strength, it was made 0.4 mm thick using a newly developed material that is stronger than conventional materials.

A dual-wall structure was adopted for the chambers in order to give low heat capacity. The chamber is a structure that supports the exhaust gas flow downstream end through a stainless steel mesh. As for the inner chamber, because a slide stabilized by the mesh can be expected and buckling is difficult due to the shape, a conventionally used 0.8 mm ferritic stainless steel has been employed. With the above spec, in comparison with the conventional dual-wall exhaust manifold with an inner tube of 0.6 mm thick and inner chamber of 0.8 mm thick[3], there is a heat-capacity reduction of 15%.

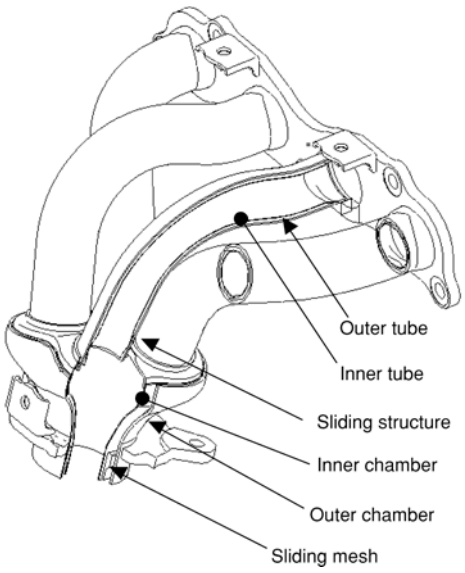


Fig. 1 Structure of exhaust manifold

Table 1 Applied material for each part

Part	Material	Thickness
Outer chamber	JIS SUH409L	2.0mm
Inner chamber	14Cr-Nb stainless steel	0.8mm
Outer tube	14Cr-Nb stainless steel	1.5mm
Inner tube	Developed stainless steel	0.4mm

Next, this paper turns to two of the most important technological elements in this development project – inner tube material and slide structure.

4. Material

In the conventional dual-wall exhaust manifold, an example of the thinnest inner material would be the 0.6 mm thick ferritic stainless steel[3), 4)]. With these conventional parts, the main emphasis lay with durability, from the point of view of thermal fatigue[8], and so ferritic stainless steel was used because it has little thermal expansion. However, in the development of dual-wall exhaust manifolds, technology has been established that avoids thermal fatigue through the use of a slide structure that absorbs thermal expansion[3), 4)]. This creates an environment where the use of austenitic stainless steel with large thermal expansion can be used. In addition, by giving the inner parts of the dual-wall exhaust manifold thinner walls, the main damage figuration has been changed to high temperature, high cycle fatigue from thermal fatigue[4]. In this development project, in order to aim for the greatest thin-walled low heat-capacity, and to achieve the target for an inner wall thickness of 0.4 mm, a study was made of the use of austenitic stainless steel which is very advanced in terms of high temperature, high cycle fatigue.

4.1. Material Concept

At high temperatures austenitic stainless steel is advanced in terms of strength. But because work hardening is great and because there is repeated application of normal to high temperature heat cycles that is peculiar to an automotive exhaust manifold, there are the following concerns in the use of austenitic stainless steel.

(1) When strain induced martensite grows, work hardening is large, and machinability worsens. In addition, concerning strain induced martensite, reverse transformation occurs at approximately 800 °C, so deformations, etc., occur.
(2) Due to repeated thermal expansion and shrinkage, the oxide film breaks away, and there is a drop in cyclic oxidation resistance.

Because of these issues, the development concept adopted was a stable austenitic stainless steel that could

withstand cyclic oxidation. Furthermore, a study was made to combine these characteristics with high-temperature strength so that it would be possible to have an inner thickness of 0.4 mm.

4.2. Composition Design

From the results of study of all properties, the decision was made to use 23Cr-11Ni-N-REM (rare earth metal element). The material concepts and the methods of achieving them based on this decision are shown in Fig. 2. Details of the various studies and their results are discussed below.

4.2.1. Stabilization of austenite structure

Generally, stainless steel structure can be estimated from the Ni equivalent: Ni_{eq} and Cr equivalent: Cr_{eq} calculated from the alloy components, using the Schaeffler diagram. However, when full consideration is given to N, the DeLong diagram shown in Fig. 3 is used[5]. In restricting strain induced martensite transformation, the basic idea is to avoid the martensite growth range (bottom left in Fig 2), and use the austenite range components. In addition, to avoid solidification cracking when welding, it is best to have composition design that gives a certain level of δ ferrite precipitation, meaning a composition design that tends to the ferrite.

4.2.2. Improvements to cyclic oxidation resistance

The reason austenitic stainless steel cyclic oxidation resistance is worse than that of ferritic stainless steel is that, due to repeated thermal expansion; the oxide film tends to break away, whereby protection against oxidation is lost. Accordingly, with improvements to oxide film adhesion, it is possible to improve resistance to cyclic oxidation.

A Ni-based alloy is generally used as an alloy with high resistance to cyclic oxidation. This has a smaller substrate thermal expansion than austenitic stainless steel, and because the difference with the oxidation layer's thermal expansion is small, there is no damage to the oxide film due to repeated thermal expansion. Because of this, it is possible to improve, to a certain extent, resistance to cyclic oxidation by the addition of a large quantity of Ni. However, because Ni is an expensive alloy element, it is not economical. In contrast, it is known that REMs precipitate at the grain boundary of the oxide film, improving adhesion[6, 7]; due to this structure, it is also very effective as an additive even in minute amounts. Accordingly, it was decided to improve resistance to cyclic oxidation using the REM additive, which is economically superior to Ni additives.

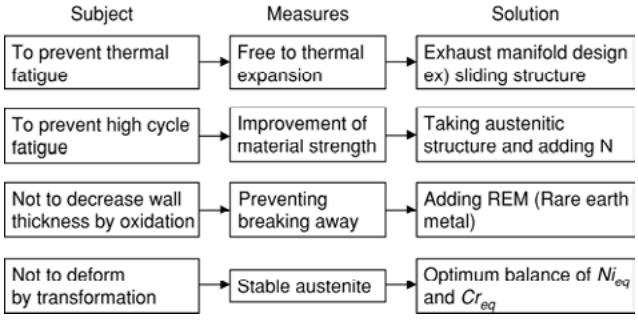


Fig. 2 Subject and solutions for thin inner wall exhaust manifold

4.2.3. Improvements to high temperature strength

As a hard structure that can maintain strength without the effects of re-crystallization at high temperatures, or of recovery, hardening is limited to solid solution hardening whereby solute atoms are a uniform solid solution on the substrate and harden, and to precipitation hardening whereby a foreign precipitated deposit is finely distributed on the substrate and hardened. Considering the requirements of automotive exhaust system materials and welding, and to it being un-tempered, the application of precipitation hardening is difficult to accomplish. Therefore, it is necessary to make effective use of solid solution hardening. Elements having good effect in solid solution hardening are invasive C and N[8]. However, under high temperature conditions, C forms the carbide $Cr_{23}C_6$ which is a cause of embrittlement. Therefore, it is not appropriate for maintaining long-term, stable strength in high temperatures. In addition, oxidation resistance also worsens because Cr is consumed in the above reaction. In comparison, it is difficult for N to form nitrides even under high temperature conditions, and it is possible to maintain long-term, stable strength even in high temperatures. In addition, because there is also a benefit in improving oxidation resistance[9], it was decided to harden with an N additive.

4.3. General Properties of the Applied Composition

Table 2 gives the typical chemical composition of the developed stainless steel. Next, this paper will introduce the properties of these components.

4.3.1. Structural stability

Stainless steel is generally supplied to working in the annealed state. Figure 4 shows the metal structure changes due to cold working of the annealed material. As can be seen in the diagram, the initial austenite crystal grains deform, but strain induced martensite is not generated. The ferrite rates in each working level are less than the measurement lower limits when measured by the ferrite scope (Fischer MP30). From this it is known that it is a stable austenite structure.

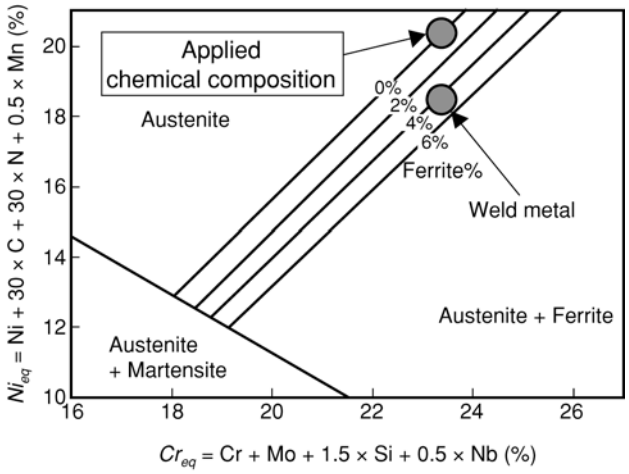


Fig. 3 DeLong diagram[5]

Table 2 Typical chemical composition of the developed stainless steel

(mass%)

C	Si	Mn	Cr	Ni	N	REM
0.07	0.31	0.79	22.86	11.68	0.20	0.03

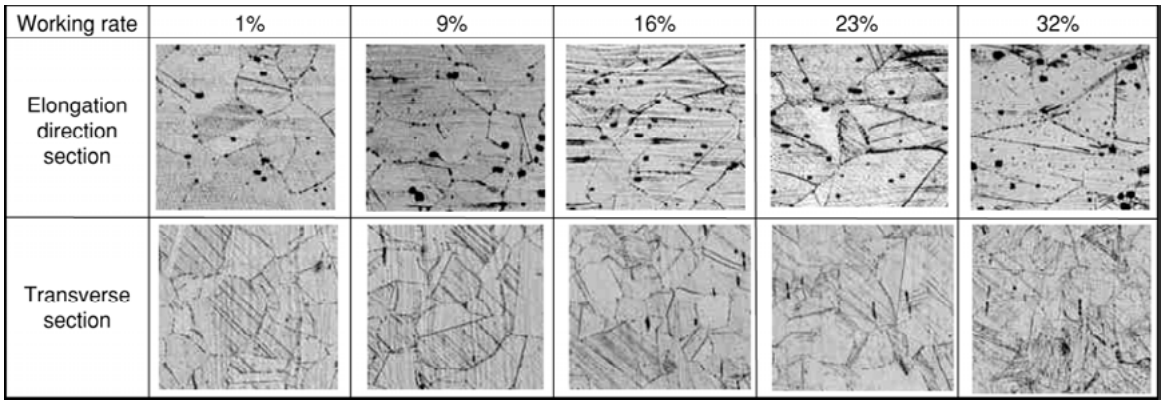


Fig. 4 Change of metal structure by cold working

The TIG weld metal structure is shown in Fig. 5; it is clear that it is an austenite dendrite crystal. In order to avoid weld cracking in austenitic stainless steel weld metal, it is effective to have precipitation of 5% ferrite[5]. Measuring the ferrite rate of weld metal using a ferrite scope, it is stable at approximately 5%. Analyzing the weld metal's nitrogen, it is 0.14%, and the Ni equivalent becomes Ni_{eq} = 18.38, so as shown in Fig. 3, ferrite rate is approximately 5%. In this way, by reducing the amount of nitrogen according to the weld, the ferrite rate can reach its optimum value.

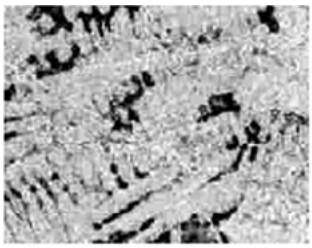


Fig. 5 Structure of weld metal

4.3.2. Oxidation resistance

Figure 6 shows the results of the continuous oxidation test carried out at various temperatures in the air. In continuous oxidation, weight increases due to oxide film growth, and the material that has the least growth is superior in continuous oxidation resistance. From these results it was learned that the developed material has resistance to continuous oxidation that is equal to or better than conventional austenitic stainless steel.

Figure 7 shows the weight changes due to cyclic oxidation in the case of heat cycle applied in air. In this type of cyclic oxidation, a weight reduction can be seen due to the separation of the oxide film, and the material that has the least reduction is superior in cyclic oxidation resistance. From these results it was learned that the developed material has no reduction in weight, so there is almost no break away of oxide film, meaning that it is superior in resistance to cyclic oxidation to conventional stainless steel.

4.3.3. High temperature strength

Among the various high temperature strength properties, Fig. 8 shows proof stress. The developed material achieved strength, at 800 °C, approximately three times that of SUS444, which has the best high-temperature strength of the ferritic stainless steels. In addition, it is 1.2-1.5 times stronger in comparison with conventional austenitic stainless steel.

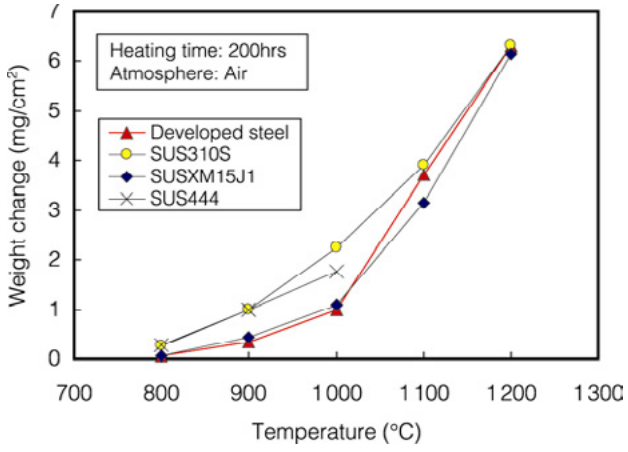


Fig. 6 Weight change by continuous heating

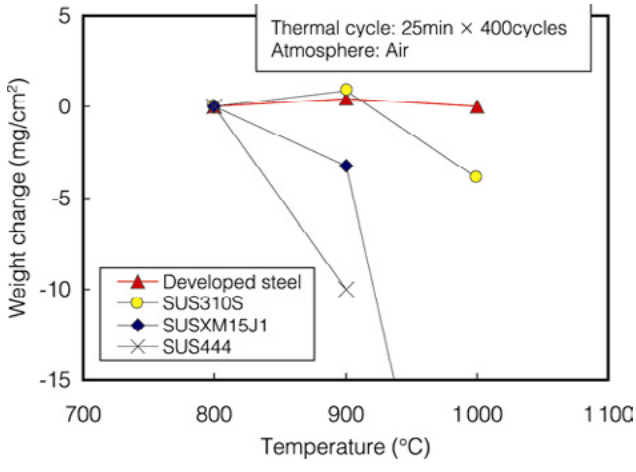


Fig. 7 Weight change by thermal cycles

5. Study of Port Structure

5.1. Evaluation of Buckling Strength in the Dual-wall Tube

In the dual-wall structure, the inner tube comes directly in contact with the exhaust gas and has a higher temperature than the outer tube. Therefore, the inner tube has relative expansion to the outer tube so that when the inner tube high temperature yield strength is insufficient buckling deformation occurs. Therefore, a comparison of conventional material and newly developed material buckling strength was made using an exhaust gas simulation tester. The exhaust gas temperature was 1,020 °C, higher than the actual engine, for the acceleration test. The test was the application of 40 thermal cycles, as shown in Fig. 9, and then inner tube buckling deformation was monitored. Figure 10 shows the results of the buckling test. With conventional ferritic stainless steel, even at 0.6 mm thickness, there is buckling deformation, the inner and outer tubes adhere to each other, and it is not possible to maintain the insulated dual-wall structure, which is the actual purpose. In comparison, with the newly developed material, even at 0.4 mm thickness, there is no buckling deformation.

In order to analyze this buckling deformation behavior, relative thermal expansion was measured as shown in Fig. 11. Figure 12 shows a typical example of relative thermal expansion curve obtained through this test. In this case, the theoretical relative thermal expansion value was calculated using the following equation.

$$\Delta L_{cal} = \alpha_{in} L_{in} \Delta T_{in} - \alpha_{out} L_{out} \Delta T_{out} \quad (1)$$

ΔL_{cal} : Calculated relative thermal expansion
α_{out} : Linear thermal expansion coefficient of outer material
α_{in} : Linear thermal expansion coefficient of inner material

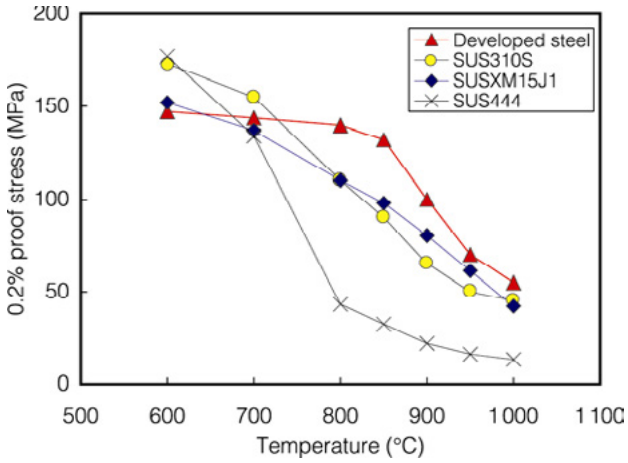


Fig. 8 Proof stress under high temperature

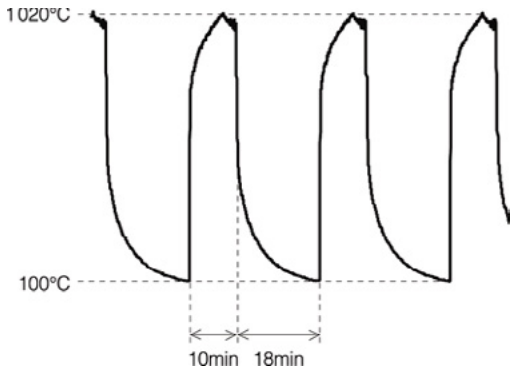


Fig. 9 Thermal cycle pattern for buckling test

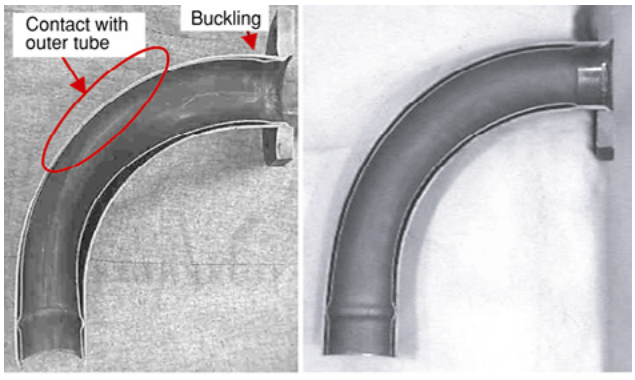


Fig. 10 Buckling deformation of the inner tube after thermal cycles

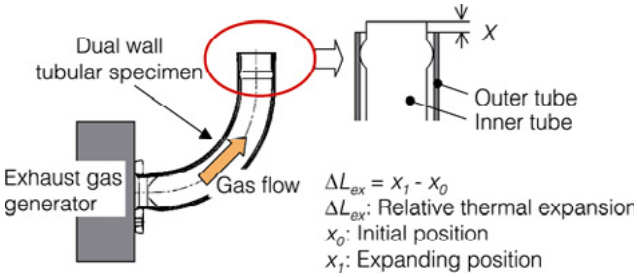


Fig. 11 Test method to measure the relative thermal expansion of inner tube

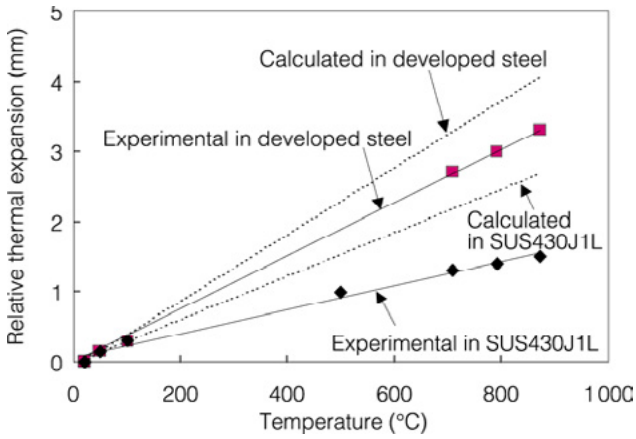


Fig. 12 Thermal expansion behavior

L_{out} : Length of outer tube
L_{in} : Length of inner tube
ΔT_{out} : Temperature vary of outer tube
ΔT_{in} : Temperature vary of inner tube

As can be seen from these results, with the ferritic stainless steel SUS430J1L, relative thermal expansion amount is small, but dissociation from the calculated value is large, and it is clear that thermal expansion restraint is large. In contrast, with the newly developed steel – an austenitic stainless steel – the relative thermal expansion is large, but dissociation from the calculated value is small, and it is clear that thermal expansion restraint is small. Examining these differences, it is thought that when the thermal stress generated by the restraint exceeds the material's proof stress, it is a cause of buckling. Accordingly, when used in parts with this sort of structure, it is necessary to consider restraint levels in the design parameters.

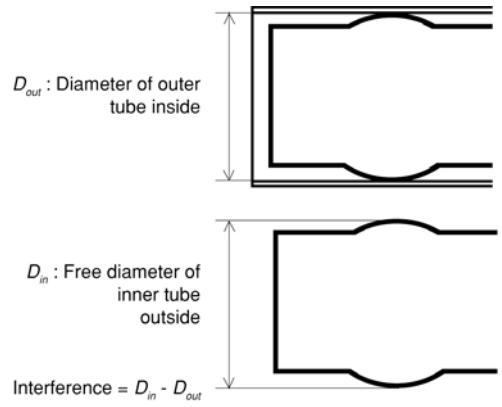


Fig. 13 Structure of sliding port

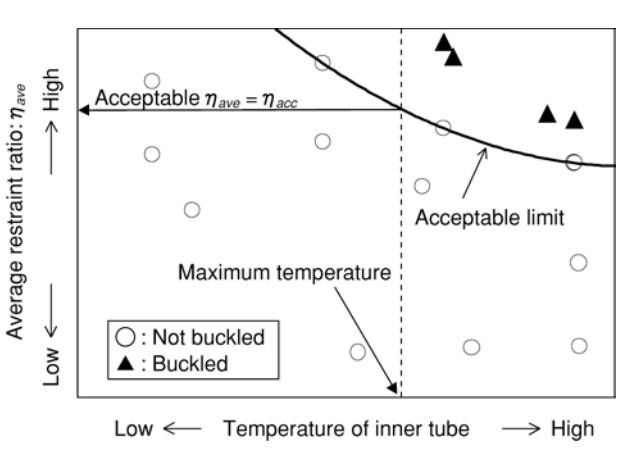


Fig. 14 Acceptable average restraint ratio

5.2. Quantitative Evaluation of Buckling Limits

As for thermal fatigue in exhaust system, it has previously been verified that restraint ratio is the optimum evaluation parameter[10]. Enlarging on this, as a parameter to quantitatively evaluate buckling limits against thermal expansion, average restraint ratio over tube length η_{ave} is defined.

$$\eta_{ave} = \frac{\Delta L_{cal} - \Delta L_{ex}}{\Delta L_{cal}} \quad (2)$$

η_{ave} : Average restraint ratio
ΔL_{ex} : Experimental relative thermal expansion

Average restraint ratio depends on the interference of the slide part. Here, interference is defined as illustrated in Fig. 13. From buckling generation state when average restraint ratio and temperature are changed, the buckling limit graph when the newly developed material is used is as shown in Fig. 14.

5.3. Design of Slide Structure

Exhaust gas flow upstream end of inner tube and outer tube is welded to the flange on the cylinder head side. The downstream end, as shown in Fig. 13, is a sliding structure. Here, setting the exhaust manifold usage design temperature makes it possible to determine acceptable average restraint ratio η_{acc}, from Fig. 14. In order to guarantee inner tube buckling strength, it is necessary to set the interference so the sliding structure slides with no more than the average restraint ratio η_{acc}. Examining the relationship between this interference and average restraint ratio using actual shape samples with three bending points, Fig. 15 shows the test results according to the behavior analysis shown in Fig. 11. From this relationship, in order to keep average restraint ratio within η_{acc}, it is clear that slide part interference should be kept at no more than $\boldsymbol{I}_{max}$, and this was set as the design maximum interference.

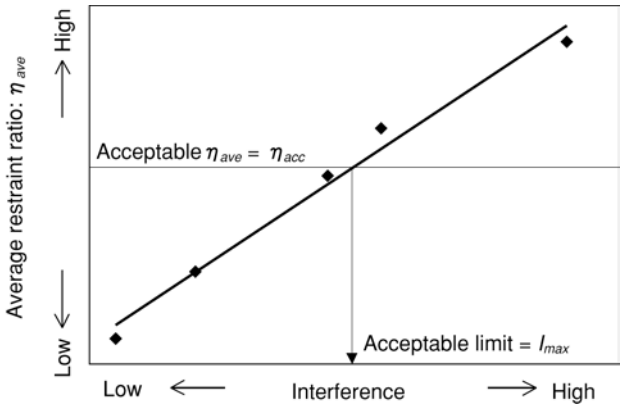


Fig. 15 Relationship of interference and average restraint ratio

6. Part Performance

A comparative test was carried out, using the newly developed exhaust manifold and a 2 mm thick, conventional, single-wall one. Table 3 gives the specifications of each exhaust manifold.

6.1. Emission Performance

6.1.1. Temperature rise properties

The differences in catalytic converter temperature rise properties in US FTP (federal test procedure) cycle at engine start are shown in Fig. 16. After start, the catalyst temperature difference gradually appears, and 20 seconds after start there is a 40 °C temperature difference, and the catalyst's light-off temperature of 400 °C is achieved 3 seconds earlier with the newly developed part. Due to this effect, by using the newly developed exhaust manifold, it is possible to reduce emissions that are discharged before light off.

Table 3 Specification of the exhaust manifold for comparison test

	Tube		Chamber	
	Outer	Inner	Outer	Inner
Conventional	2mm	–	2mm	2mm
Developed	1.5mm	0.4mm	2mm	0.8mm

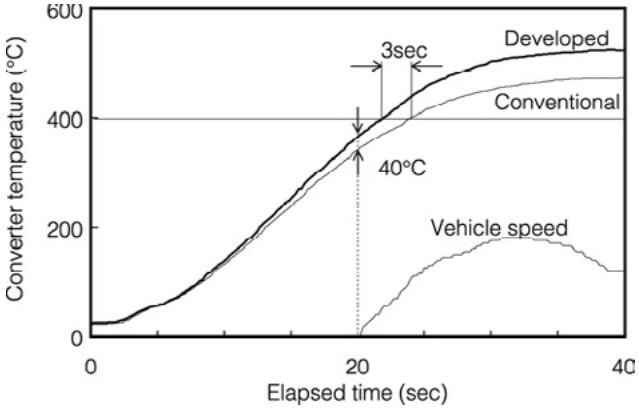


Fig. 16 Converter heat-up behavior on FTP cycle

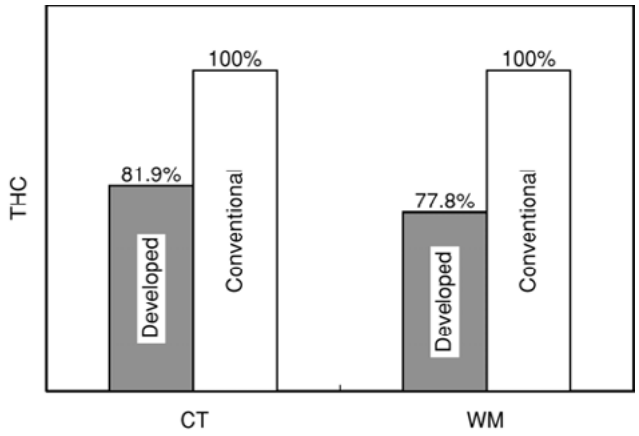


Fig. 17 Effect for emission decrease

6.1.2. Level of emissions achieved

In order to examine the effect on emissions, as a representative value Fig. 17 shows the differences in HC emission amount. By using the newly developed exhaust manifold, with its ability to have early activation of the catalyst at cold start, there is a large effect in reducing emissions at CT (cold transient) – a reduction of approximately 18%. In addition, even with the mode total weighted mean value WM, there is a 22% reduction. In the same way, there is a 10% reduction in NO_x, and a 12% reduction in CO. It is possible to verify a large emission reducing effect.

6.2. Noise Properties

Figure 18 shows a comparison of the differences in noise level due to differences in exhaust manifolds. The newly developed exhaust manifold shows a slight worsening in the high frequency range in comparison with the conventional single-wall product; however in the low frequency range it is superior, and overall it is roughly equivalent. In general, the dual-wall exhaust manifold has worse noise properties than the single-walled one[3]. But, it is believed that with this newly developed manifold, because the inner tube is a completely cylindrical shape, stiffness is comparatively high and there is little noise property worsening.

7. Summary

Development of an exhaust manifold with an inner tube 0.4 mm thick, working to make it as thin-walled and low heat-capacity as possible, was a success. In combination with air-fuel ratio control technology and catalyst technology, it was possible to reduce by approximately 20% the amount of precious metals used in the under-floor converters, in comparison with the 2001 model SULEV spec vehicle. As a result of this development project, the following facts have become clear.

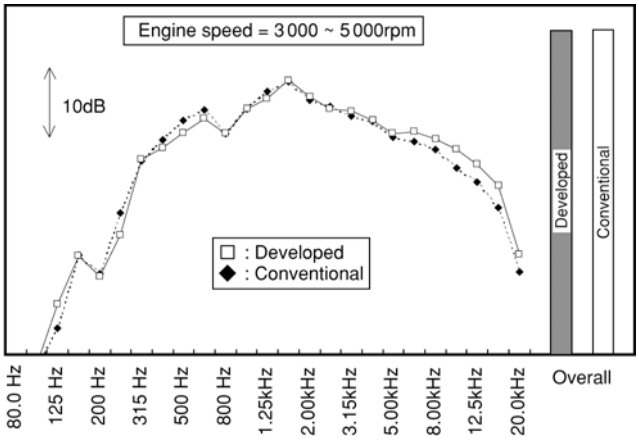


Fig. 18 Comparison of sound pressure level

(1) In order to actualize thinner walls than conventional exhaust manifold for the inner material of the dual-wall, a highly heat resistant stainless steel was developed that had improved high temperature strength and oxidation resistance, by N additives, REM additives, and improving Ni_{eq}-Cr_{eq} balance.
(2) When using the newly developed highly heat resistant stainless steel for the inner tube of a dual-wall exhaust manifold, it was verified, in the unit thermal cycle test, that there is greater strength against buckling deformation than with the conventional material.
(3) The acceptable average restraint ratio was determined according to the buckling evaluation using the unit thermal cycle test. Quantitative evaluation is possible using this acceptable value, and even with a thickness of 0.4 mm, it is possible to have a design that satisfies durability requirements.
(4) The dual-wall exhaust manifold with the inner tube 0.4 mm thick can reach catalyst light off, in the FTP mode, three seconds earlier than the conventional one.
(5) The dual-wall exhaust manifold with the inner tube 0.4 mm thick has a radiated noise level equivalent to that of the exhaust manifold with a thickness of 2 mm (single wall).

The exhaust manifold developed in this project has begun mass production in 2002, and is fitted to the 2003 Accord series, the US SULEV spec vehicle.

8. Acknowledgments

The authors would like to thank the many people involved in this development project, particularly those at Sumitomo Metal Industries, Ltd. and Yutaka Giken Co., Ltd. for their understanding and cooperation, and to thank this magazine for the opportunity to present this paper.

References

(1) Kishi, N. et al.: Development of the High Performance L-4 Engine ULEV System, SAE paper, SAE980415 (1998)

(2) Kitagawa, H. et al.: Super Ultra Low Emission System for "ACCORD SULEV", HONDA R&D Technical Review, Vol. 12, No. 2, pp. 37-44 (2000)

(3) Kishi, N. et al.: Development of the Ultra Low Heat Capacity and Highly Insulating (ULOC) Exhaust Manifold for ULEV, SAE paper, SAE980937 (1998)

(4) Hashimoto, H. et al.: Development of a Low Heat-capacity, 4-2 Connection Exhaust Manifold for High Output Engines, HONDA R&D Technical Review, Vol. 11, No. 1, pp. 85-92 (1999)

(5) Long, C.J. et al.: The Ferrite Content of Austenitic Stainless Steel Weld Metal, The Welding Journal, Vol. 7, pp. 281-297 (1973)

(6) Ishii, K. et al.: Effect of Ti, Zr and Hf on High-Temperature Oxidation Resistance of Fe-20Cr-5Al-0.1La Alloy Foiles, Materials Transactions, JIM, Vol. 39, No. 10, pp. 1040-1045 (1998)

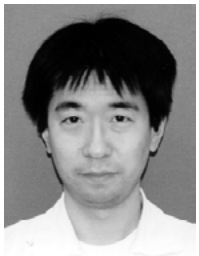
(7) Fukaya, M.: Material Properties of Fe-Cr-Al Alloy Foil for Metal Support, SAE paper, SAE970790 (1997)

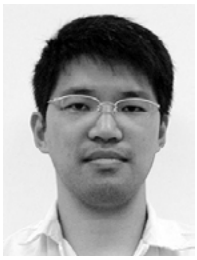
(8) Irvine, K.J. et al.: High-strength austenitic stainless steels, Journal of the Iron and Steel Institute, vol. 199 (2), pp. 153-175 (1961)

(9) Hosoi, Y. et al.: The Effect of Nitrogen Additives on High Temperature Oxidation of Austenite Stainless Steel, The 119th Corrosion Prevention Symposium material "High Nitrogen Stainless Steel – The Current Situation and Problems", pp. 43-49 (1998)

(10) Ishii, K. et al.: Evaluation of Thermal Fatigue Life on the Exhaust Manifold by Analyzing Restraint Ratio, Seoul 2000 FISITA World Automotive Congress, F2000G295 (2000)

■ Authors ■


Kazuo ISHII


Takeshi MUNEMURA


Nobuyuki YOSHIDA

Development of Electronic Throttle Control Utilizing Adaptive Control Method

Eiji HASHIMOTO* Tetsuya ISHIGURO*
Yuji YASUI* Shusuke AKAZAKI*

ABSTRACT

Electronic throttle control has been focused upon in recent years as a measure to provide greater accuracy for idling air control and to help reduce emissions. For this reason, it is necessary to achieve greater robustness in throttle control performance, to cope with variations between individual units and degradation of parts over time. Up to the present, it has been difficult for PID control systems to recognize unspecified disturbances, and this has been an impediment to achieving a balance between robustness and responsiveness. To perform robustness, an adaptive control system has been constructed which utilizes sliding mode control and contains an identifier to perform sequential calculations. This technology has realized previously unavailable levels of robustness, accuracy, and responsiveness in an electronic throttle control.

1. Introduction

Electronic throttle control has been used in recent years to coordinate vehicle traction control and automatic transmission to improve vehicle stability and ride comfort. However, environmental measures such as fuel economy and reduced emissions are also demanded, and electronic throttle control has come to be widely used in the control systems of new engines such as for direct injection engine vehicles, hybrid vehicles, low emission vehicles (LEV) and so on.[1]

However, when electronic throttle control is closely and complexly intertwined with multiple other control systems, the dynamic characteristics fluctuate due to dynamic characteristic variance caused by variation in the throttle angle sensor, drive gear, drive DC motor and other components, changes in the operating environment such as temperature, and degradation over time, etc. This made it difficult to maintain stable control system characteristics, so control system stability was ensured by reducing the control performance.

For example, when PID control is used as the throttle angle drive control, changes in the dynamic characteristics due to the throttle angle and disturbances can be coped with by scheduling the feedback gain according to the throttle angle. However, variation or changes in the dynamic characteristics due to variations in individual components or degradation over time is difficult to observe with PID control. This means that the feedback gain cannot be changed to an appropriate value, which led to a drop in tracking performance and stability with respect to the throttle angle target value. Application of adaptive control[2] using an on-board identifier that successively estimates dynamic characteristic variation, fluctuation and disturbances was considered as a means for resolving these problems.

* Tochigi R&D Center

Therefore, this study applied a new adaptive control capable of adapting even to changes in the dynamic characteristics caused by rapid changes in the throttle angle to electronic throttle control, and realized both high robustness and excellent control performance. This paper reports these results.

2. System Concept

As shown in Fig. 1, this technology aims to create an electronic throttle control system that achieves a high degree of balance between performance, reliability and smartness.

In terms of performance, the system aims to realize a response and control resolution that can emphasize driving enjoyment and satisfy the required safety and environmental performances.

For reliability, the hardware was designed with durability equal to or greater than systems combining a mechanical throttle and idling air control valve. Also, using adaptive control for throttle angle control made it possible to compensate for variance and changes over time in each hardware property, and maintained control system stability even when the properties change such as when the hardware breaks down. This realized the same reliability as a mechanical throttle.

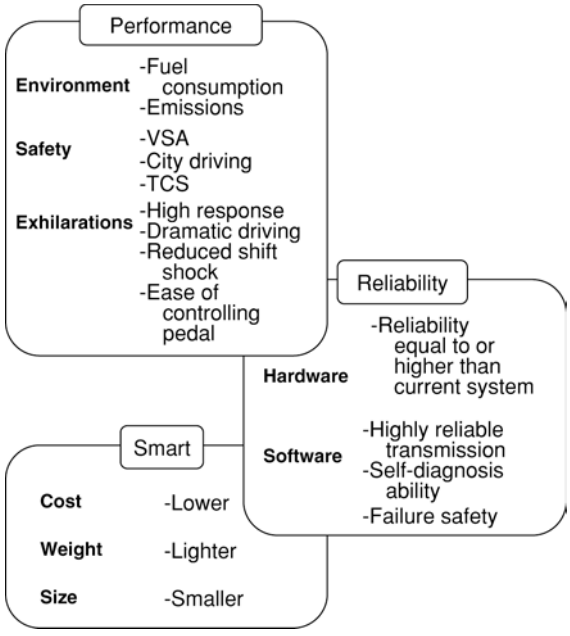


Fig. 1 Electronic throttle control system concept

In the area of smartness, the application of adaptive control improved response and reliability, which reduced the maximum motor torque and eliminated the clutch mechanism for separating the motor from the throttle in the event of a breakdown. This realized size, weight and cost reductions.

2.1. System Layout

Figure 2 shows the on-board layout of the throttle body, accelerator pedal and throttle driver for an engine that uses electronic throttle control.

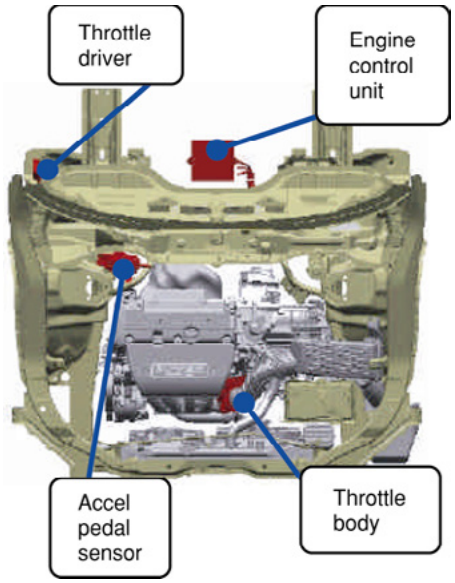


Fig. 2 Layout of electronic throttle control system

As shown in Fig. 3, this system is a dispersed function type architecture that connects the engine control unit and the electronic throttle control using a master-slave system. The electronic throttle control driver is separated from the engine control unit, so the system can be added to the engine control units of multiple models without altering the existing hardware.

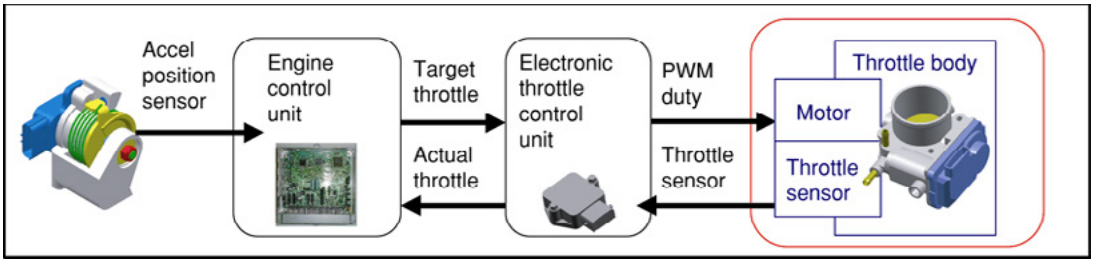


Fig. 3 Electronic throttle control system outline

2.2. Default Angle

The limp-home concept aims to allow a vehicle to move to a service center under its own power when a particular device breaks down, even if normal cruising is not possible.

In order to realize this concept with an electronic throttle control system, the throttle angle is maintained at a certain angle (hereafter “default angle”) by only the force of a spring when driving force is not generated on the engine as shown in Fig. 4. Therefore, the direction of the spring force applied to the throttle valve is inverted near the default angle as shown in Fig. 5. This causes the throttle angle to exhibit nonlinear behavior relative to the motor driving force, which results in lower control performance near the default angle.

3. Adaptive Control Algorithm

When the source voltage is low such as during engine startup or at low air temperatures, the motor drive control feedback gain must be increased at the throttle angle position where the spring tension is not constant near the default angle as shown in Fig. 4 and Fig. 5. However, if this setting is inappropriate, the throttle angle exhibits vibratory behavior.

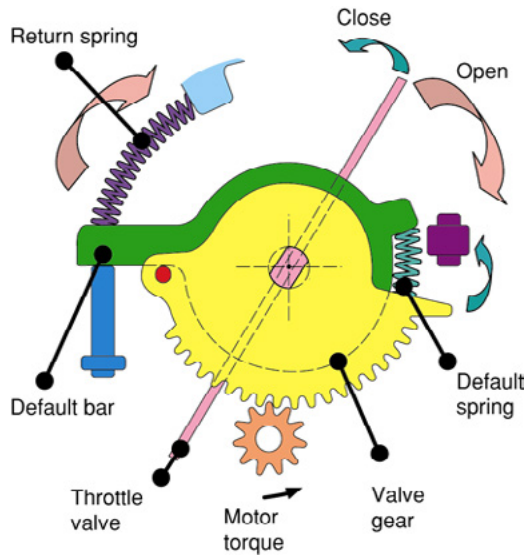


Fig. 4 Outline of default mechanism for electronic throttle

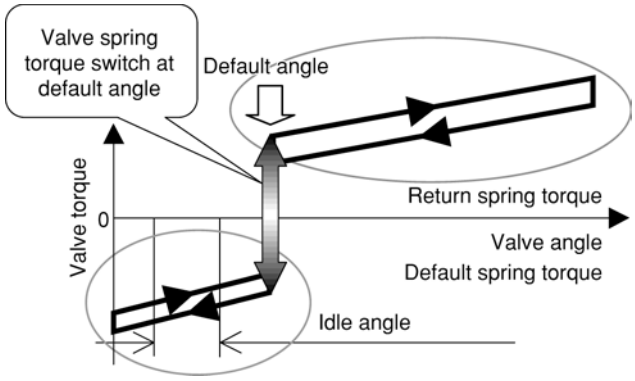


Fig. 5 Valve spring torque characteristic

Therefore, when performing motor drive control by PID control, the control performance must be suppressed to ensure stability by presetting a low feedback gain.

In addition, engine oil, suspended carbon, EGR and other various foreign substances pass through the vehicle throttle, and these foreign substances adhere to the shaft, bearing and valve and cause component wear. This means that changes in friction occur which are difficult to predict, that is to say changes in the dynamic characteristics occur.

However, PID control cannot preset the feedback gain for these immeasurable changes in dynamic characteristics, so the control performance deteriorates even further.[3] PID control with a disturbance observer[4] and I-PD control systems[5] have been constructed as means to deal with this issue, but these systems also suffer drops in control performance when the dynamic characteristics change significantly.

Therefore, this study constructed a new adaptive control and applied it to the motor drive control. This new adaptive control combines a model parameter scheduler that compensates for rapid changes in the dynamic characteristics according to the throttle angle, an on-board identifier for adapting to variation and changes over time in the dynamic characteristics, and a sliding mode controller that realizes rapid response to the throttle angle target value and excellent control performance near the default angle. (Fig. 6) This system successively identifies the optimum control parameters and calculates the proper feedback gain based on these parameters. Therefore, stability with respect to changes in the dynamic characteristics can be ensured while maintaining excellent electronic throttle control performance even when the dynamic characteristics change in a manner that would reduce the control performance of PID control equipped with a disturbance observer, etc. This control algorithm is described in detail below.

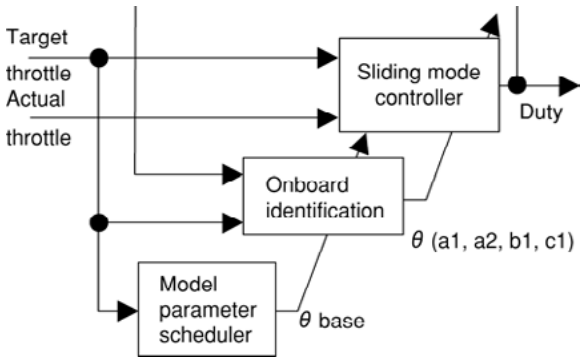


Fig. 6 Block diagram of electronic throttle control

3.1. Modeling

The electronic throttle control dynamic characteristics, fluctuations, and disturbance information related to these dynamic characteristics are converted to numeric form and used to calculate the feedback gain of the controller. Therefore, electronic throttle control was modeled using the ARX model (auto-regressive exogenous model) shown by

Eqs. (1) and (2). In this model, a1 and a2 which are related to the control subject output DTH, b1 which is related to the input DTH, and c1 which reflects disturbance and modeling error are set as the model parameters. These model parameters are calculated successively by the on-board identifier described hereafter.

$$DTH(n+1)=a1' DTH(n)+a2' DTH(n-1) +b1' DUT(n-d)* Vbat+c1' \quad (1)$$

$$DTH(n)=TH(n) - TH_DEF \quad (2)$$

DTH(n) : Deviation between throttle angle and default position
TH(n) : Throttle angle
TH_DEF : Throttle default angle
DUT : PWM drive duty
Vbat : Source voltage
d : Wasted time
a1', a2', b1', c1' : Model parameters

Figure 7 compares the frequency responses for this model and the control subject of the electronic throttle control. This figure shows that the model closely expresses the frequency response of the control subject. This indicates that the appropriate control input can be determined according to changes in the dynamic characteristics of the control subject and disturbances by successively calculating the feedback gain based on the model parameters of this model.

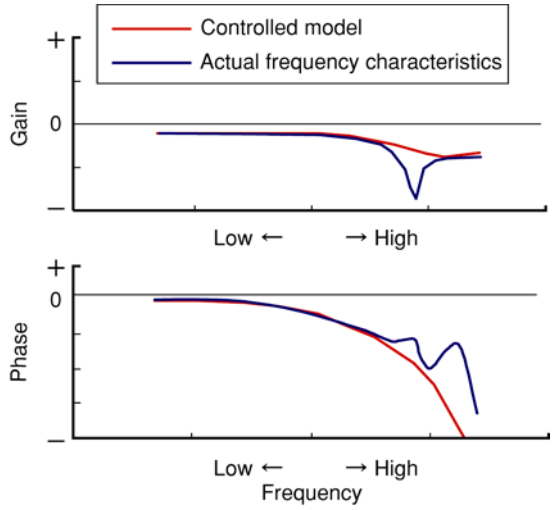


Fig. 7 Frequency characteristics

3.2. On-board Identifier

The on-board identifier identifies the above model parameters using the identification algorithm indicated in Eqs. (3) to (7). This algorithm calculates the model parameters by adding the model parameter update components calculated based on the error eid between the model output DTHHAT and the control subject output DTH to the reference model parameters calculated by the parameter scheduler described hereafter. At this time the reference model parameters are set according to the throttle opening which has a correlation with the changes in the dynamic characteristics of the control subject. This solved the issue of the delay in model parameter identification[3] when the dynamic characteristics of the control subject change rapidly for general adaptive control, that is to say when the throttle angle changes rapidly.

Furthermore, parameter c1 is the model parameter signifying nonlinear control subject characteristics and disturbance, and this absorbs constant disturbance and steady-state error. This ensures high robustness with respect to changes in the dynamic characteristics of the control subject due to source voltage fluctuations and deterioration over time, etc.

$$DTHHAT(n+1)=a1\ DTH(n)+a2\ DTH(n-1)+b1\ DUT(n-d) *Vbat+c1 \quad (3)$$

$$\theta(n) = \theta base(n)+d\theta(n) \quad (4)$$

$$d\theta(n) = d\theta(n)+ KQ(n)*eid(n) \quad (5)$$

$$eid(n) = DTH(n) - DTHHAT(n) \quad (6)$$

$$KQ(n) = P\zeta(n)/1 + \zeta^{T}(n)\ P\zeta(n) \quad (7)$$

θ base: Model parameter reference value determined by the model parameter scheduler according to the throttle angle
ζ(k): [DTH(n-1) DTH(n-2) DUT(n-1) 1]^{T}
a1, a2, b1, c1: Model parameter identification values

3.3. Model Parameter Scheduler

The model parameter scheduler calculates the reference model parameters a1base, a2base and b1base according to the control subject output DTH. These reference model parameters are set as the values of model parameters a1, a2 and b1 which represent the dynamic characteristics of the electronic throttle control near each DTH. Therefore, when variation or change over time occurs in the dynamic characteristics of the electronic throttle control, the on-board identifier corrects only the error between the reference model parameters and the model parameters which is produced by changes in the dynamic characteristics. This makes it possible to reduce the parameter correction amount at each DTH, which minimizes the model parameter identification delay.

3.4. Scheduling Mode Controller

The sliding mode controller[6] calculates the input DUT to the control subject using the model parameters identified by the on-board identifier. Labeling the control time of the controller as n, the proportional function $\sigma(n) = 0$ called the switching line is defined on the phase plane having as axes the current value e(n) and previous value e(n-1) of the deviation between the throttle angle target value and the actual angle as shown in Fig. 8. At this time the sliding mode controller performs control to keep the combination of e(n) and e(n-1) (hereafter "status level") to the switching line, and this status level is then converged toward the origin of the phase plane unaffected by disturbances or control subject modeling error. Also, the control input DUT is calculated as the sum of the three inputs shown below.

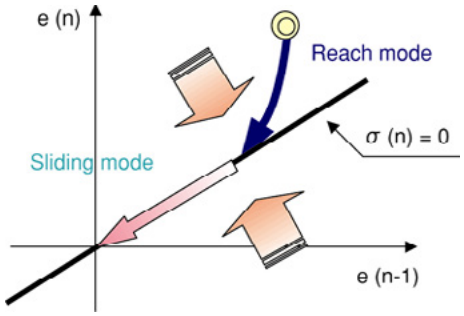


Fig. 8 Sliding mode control outline

Equivalent control input Ueq(n): Input to keep the status level on the switching line

Reach input Urch(n) : Input to converge the status level onto the switching line

Damping input Udump(n) : Input to prevent overshoot of the throttle angle target value

The combination of model parameter operations by the on-board identifier described above and this sliding mode realized rapid response, high control precision, and robustness with respect to modeling error, gear backlash and source voltage fluctuation.

4. Test Results Using a Discrete Unit Tester

4.1. Response Variation during Source Voltage Fluctuation

Figure 9 shows the results of comparing the variation in the response time with PID control at stepped target throttle values under conditions of a source voltage from 10.5 V to 16 V which is the normal control range for electronic throttle control.

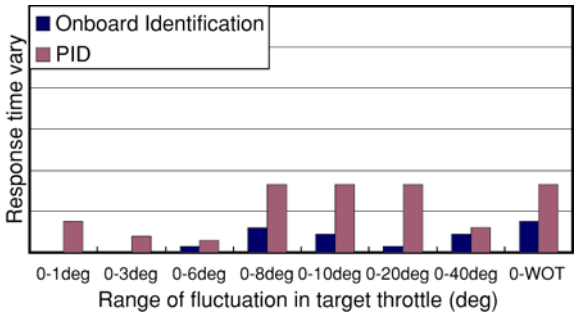


Fig. 9 PID and onboard identification method response time Max – Min varies between 10.5 V – 16 V input voltages.

This figure shows that the variation in the response time when using adaptive control is smaller than that for PID control at all target value fluctuation amounts. This confirmed the control performance stability relative to source voltage fluctuations caused by changes in the air temperature or battery deterioration, etc.

4.2. Response during Voltage Fluctuation

Figure 10 shows the results of comparing the response time with PID control for stepped target throttle values. This figure shows that the response time for adaptive control is shorter than for PID control which reduces the feedback gain due to concerns of producing vibratory behavior.

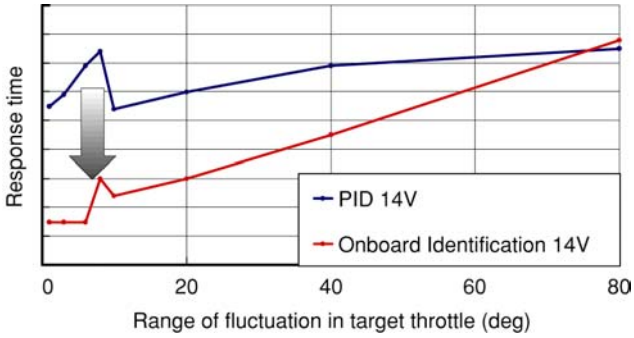


Fig. 10 Difference in response time for PID and onboard identification method.

4.3. Response Changes due to Variation in the Physical elements of the Throttle Drive System

Figure 11 and Fig. 12 show the response time variation and the response waveform relative to the stepped target values when using four types of electronic throttle control with different throttle body characteristics. These figures show that even when the friction fluctuates, the adaptive control response time and fluctuation amount are less than for PID control, and the response behavior is also smaller.

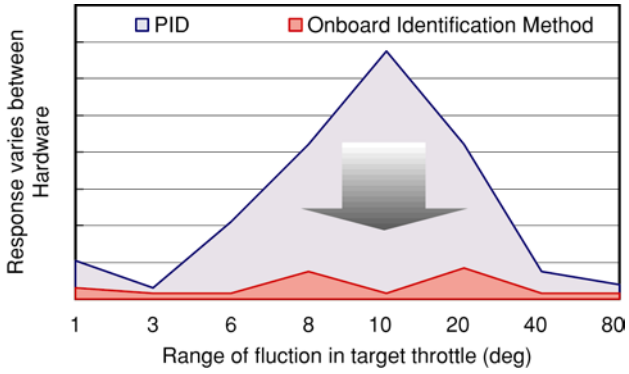


Fig. 11 Difference in response time for PID and onboard identification system with different throttle body characteristics.

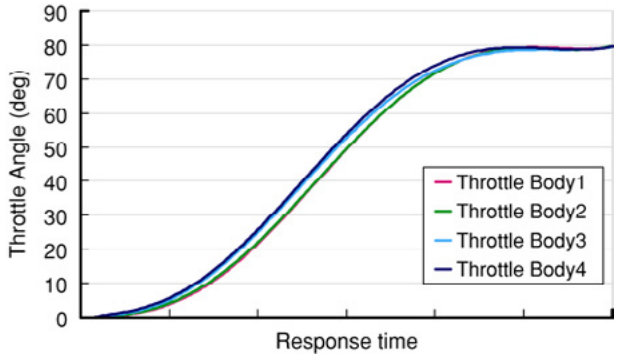


Fig. 12 Response chart graph of different throttle body characteristics.

5. Actual Vehicle Test Results

Running tests were conducted using test vehicles on a test course under hypothetical conditions of cruising at high speed, low speed, normal speed, and congested roads. During these tests the throttle angle was confirmed to be within ±0.2 degrees of the target angle 80% or more of the time, indicating that the system has sufficient performance as a vehicle control device. In addition, idling control performance was equal to or better than the engine speed control performance using a conventional air idling control valve device.

6. Conclusions

The following effects were obtained by applying adaptive control comprised of an on-board identifier, parameter scheduler and sliding mode controller to an electronic throttle control system.

(1) Rapid response and robustness were simultaneously achieved, which was difficult for PID control.
(2) Stable control performance was ensured not only with respect to changes in the environment, deterioration over time and parts variance, but also with respect to source voltage fluctuation and other disturbances.
(3) The results of tests using actual vehicles confirmed that the throttle angle was within ±0.2 degrees of the target angle 80% or more of the time during idling control and throttle control while cruising.

References

(1) McKay, D., et. al.: Delphi Electronic Throttle Control Systems for Model Year 2000; Driver Features, System Security, and OEM Benefits. ETC for the Mass Market, SAE 2000-01-0556 (2000)

(2) Yasui, A., Ueno, I.: Adaptive Sliding Mode Control for Secondary O_2 Feedback (Part 3), Honda R&D Technical Review Vol. 13, No. 2, pp. 59-66 (2001)

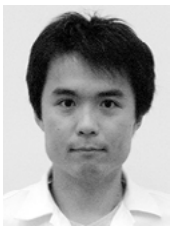
(3) Terao, K.: Introduction to Robust Adaptive Control, Tokyo, Ohm Publishing, pp. 9-11 (1989)

(4) Kunifuda, Nakamura, Matsuyama: Development of a Robust Electronic Throttle Control System, Automotive Technology, Vol. 52, No. 9, pp. 37-42 (1998)

(5) Oguni, Mita: Introduction to System Control Theory, Tokyo, Jikkyo Publishing, pp. 121-132 (1979)

(6) Nonami, Den: Sliding Mode Technology, Tokyo, Corona Publishing, pp. 41-54 (1994)

■ Authors ■


Eiji HASHIMOTO


Tetsuya ISHIGURO


Yuji YASUI


Shusuke AKAZAKI

Development of an Intelligent Power Unit for the Civic Hybrid

Kazuhiko AITAKA* Masaharu HOSODA* Takuya NOMURA*

ABSTRACT

The Intelligent Power Unit (IPU) utilized in Honda's Civic Hybrid Integrated Motor Assist (IMA) system was developed with the aim of making every component lighter, more compact and more efficient than those in the former model. To reduce energy loss, inverter efficiency was increased by fine patterning of the Insulated Gate Bipolar Transistor (IGBT) chips, 12 V DC-DC converter efficiency was increased by utilizing soft-switching, and the internal resistance of the IMA battery was lowered by modifying the electrodes and the current collecting structure. These improvements reduced the amount of heat generated by the unit components and made it possible to combine the previously separate Power Control Unit (PCU) and battery cooling systems into a single system. Consolidation of these two cooling circuits into one has reduced the volume of the newly developed IPU by 42% compared to the former model.

Introduction

One major issue for the automotive industry in recent years is the reduction of CO_2 emissions by lowering automotive fuel consumption. One response to this issue has focused on hybrid systems that combine an engine with an electric motor. In 1999 Honda began to market the Insight, a vehicle installed with a newly developed, compact, lightweight IMA (Integrated Motor Assist) system. Now, Honda has developed an IPU (Intelligent Power Unit) for the IMA system fitted to the Civic Hybrid that entered the market last year, with the aim of further market penetration by hybrid cars. This paper introduces the various component technologies developed in order to achieve the lightweight, compact components necessary to make possible IMA installation in a 4-door sedan.

* Tochigi R&D Center

1. Development Aims of IPU for the Civic Hybrid

Development of the IPU to be equipped to the Civic 4-door sedan had as its goal being able to fit the IMA system while at the same time maintaining ease of vehicle use, including cabin comfort and trunk space of a conventional sedan. The basic concept was "maintaining seating room for five people and the appropriate amount of trunk space." In order to achieve these aims, the target was to compactly store the IPU – which is 40% smaller in volume than that of the Insight – behind the rear seats.

1.1. Smaller IPU

Figure 1 shows the IPU installed in the Insight. The previous mode's IPU volume was 138 L, the breakdown of which is shown below.

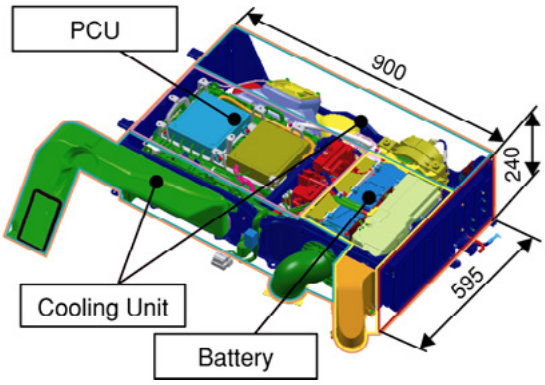


Fig. 1 Dimensions of Insight IPU

- Power Control Unit (PCU) 33 L (24%)
- Battery 43 L (31%)
- Cooling System 62 L (45%)

The target for the Civic Hybrid's IPU volume was set at 80 L, and the following targets were set for reducing components size.

- PCU 20%
- Battery 30%
- Cooling System 60%

1.2. Cooling System Integration

Focusing particularly on making the cooling system more compact, studies were made into integration of the cooling circuit, which conventionally are two separate systems, and integrating the battery and the PCU cooling. Giving consideration to the battery control temperature, the temperature of intake air, which is the coolant for battery cooling, must be at normal temperatures. Therefore, with the Civic Hybrid, the assumption is that cooling intake will be taken from inside the cabin and exhaust back to the cabin. In addition, the increase in air-conditioning load accompanying in-vehicle intake and exhaust and noise inside the vehicle were considered, so cooling airflow target was set at 90 m^3/hr or lower. The cooling system required airflow for the Insight was as follows.

- Inverter 138 m^3/hr
- 12 V DC-DC Converter 120 m^3/hr
- Battery 60 m^3/hr

With the integration of the cooling systems, it was necessary to reduce the inverter and 12 V DC-DC converter required airflow to no more than 90 m^3/hr. With the previous model, because the PCU cooling air was taken from outside the vehicle, giving full consideration to high temperature environments such under a blazing sun, it was necessary to estimate a high intake air temperature. However, because intake air is taken from inside the vehicle when the cooling systems are integrated, a drop in cooling intake air temperature can be expected. That is to say, it is possible to reduce the amount of required airflow. At the same time, it is of course also necessary to reduce the amount of heat generated, by improving the efficiency of each PCU component. Therefore, a study was made, investigating whether or not it would be possible to integrate the two conventional cooling systems into one, by reducing intake air temperature and improving device efficiency.

1.3. Measures to Increase in Assist and Regeneration Power

It was necessary to make additional changes from the Insight including measures to increase by 30% in assist and regeneration power with an increase in vehicle weight and the addition of a cylinder idling system (CIS). In this aspect, improved efficiency in each IPU component device was required, and was an important issue in this development project. In particular, heat generated by an increase in battery input and output was an issue. Therefore, in response, at the same time as maintaining the target maximum airflow amount with the aforementioned cooling system integration, measures were taken to increase the cooling airflow by 50% and to reduce the amount of heat generated by reducing battery internal resistance by 20% over the previous model.

2. Power Control Unit

In order to actualize the installation of the IPU behind the rear seats, it was necessary to reduce the size of the PCU by approximately 20% and to reduce the inverter and 12 V DC-DC converter loss. The following actions necessary to resolve these technological issues are listed below.

- Integration of inverter and pre-driver into one small component
- Reduction in loss by fine patterning of the Insulated Gate Bipolar Transistor (IGBT) chips inside the inverter
- Size reduction through reducing capacitor loss and a high heat-radiation structure
- Size reduction with reduced loss by adopting a soft switching 12 V DC-DC converter control method.

As a result of the above technological developments, the PCU volume was 26.8 L, in comparison to the Insight's 33 L, and a 20% reduction was achieved. Figure 2 shows the Civic Hybrid's PCU.

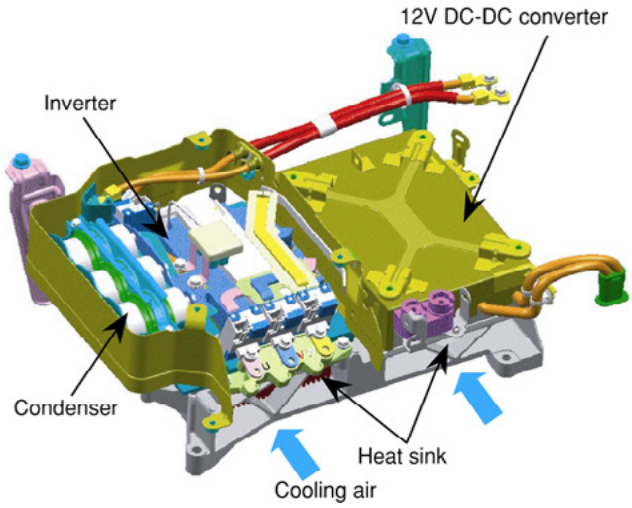


Fig. 2 Power Control Unit

2.1. Inverter

In order to achieve a smaller, lighter-weight inverter with reduced loss, development was carried out with the introduction of various new technologies for each inverter component device. Details are explained below.

2.1.1. Integration of inverter and pre-driver

The following modifications were made to the inverter that controls motor drive.

(1) Custom IC for IGBT element drive circuit
(2) Software processing of the safeguard function with the installation of a high-performance microcomputer
(3) Simplification of interface circuit by allowing motor ECU communication through a serial interface.

With these new technologies a 39% size reduction and 28% weight reduction was achieved in comparison with the previous model. Figure 3 shows the inverter units in the Insight and the Civic Hybrid.

In addition, conventionally, protection against chip excessive heat is carried out when temperature is detected by a thermistor placed near the IGBT chips. However, with this newly developed product, there is a temperature sensor above the IGBT chips increasing temperature detection responsiveness.

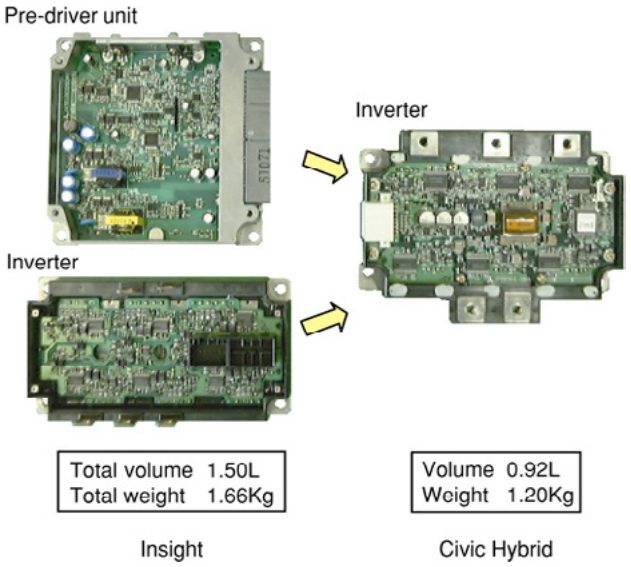


Fig. 3 Inverter unit

2.1.2. Reduction in loss with IGBT chip fine patterning

Figure 4 shows the cell pattern of the IGBT chips that are inverter power elements. By making the cell pattern finer than on the conventional model, approximately three times the number of cells can be mounted in the same chip area, thereby reducing the channel resistance Rch for each unit area. Therefore, IGBT ON voltage drops and there is a maximum reduction in loss of 25% in comparison with the conventional.

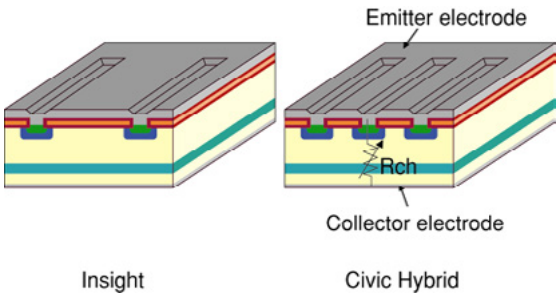


Fig. 4 Model of IGBT fine patterning

2.1.3. Smaller capacitor

Conventional electrolytic capacitor elements are held with resin thereby vibration resistance is maintained and heat is radiated. However, with this newly developed product, element heat radiation is promoted by direct contact between the bottom of the element and the aluminum case (Fig. 5) giving a 20% improvement in heat radiation in comparison with the previous model. In addition, due to a reduction in resistance from electrolyte and electrode foil etching modifications, element characteristic ESR (Equivalent Series Register) are improved and element generated heat is 18% less than the previous model. With the above modifications, a 30% size reduction and a 27% weight reduction were achieved in comparison with the previous capacitor.

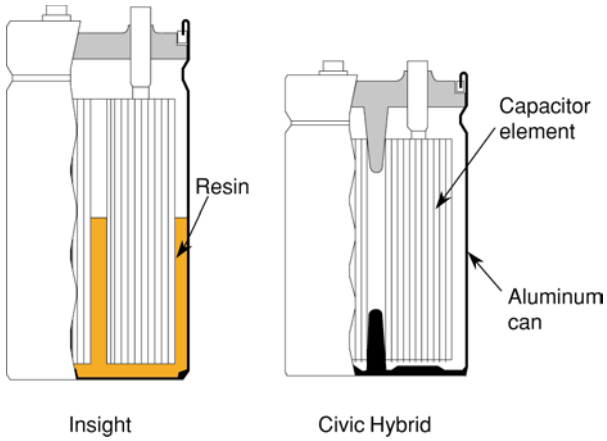


Fig. 5 Capacitor structure

2.1.4. Improvements to inverter efficiency

With the above technologies, inverter efficiency is improved in the total motor drive condition range and loss is reduced. Figure 6 is a graph showing inverter efficiency in relation to motor speed.

In addition, Fig. 7 is a map of inverter efficiency against motor speed and torque. It is clear from plotting on this graph the motor speed and torque sampling data from actual driving that it is the inverter high efficiency range that is mainly used. Energy loss reduction due to efficiency improvements will also contribute to improved fuel economy.

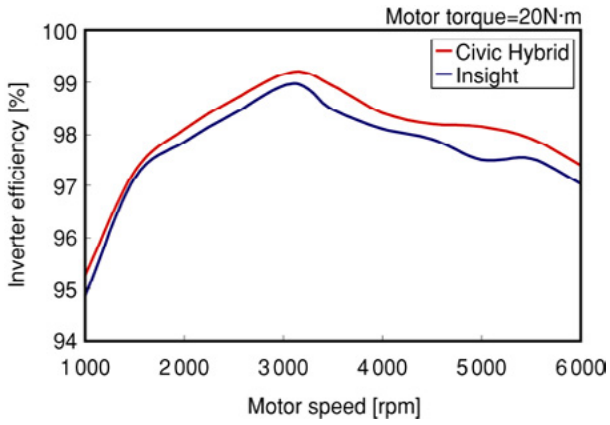


Fig. 6 Inverter efficiency

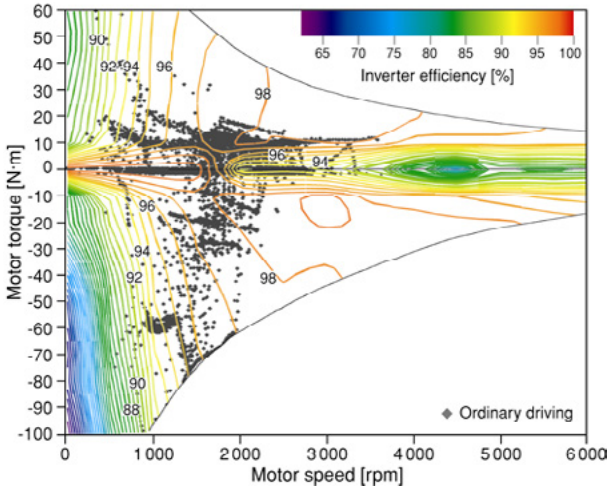


Fig. 7 Inverter efficiency map

2.2. 12 V DC-DC Converter

By adopting, for this 12 V DC-DC converter, a soft-switching system rather than the conventional hard-switching system, loss is reduced. Figure 8 is an outline operation diagram.

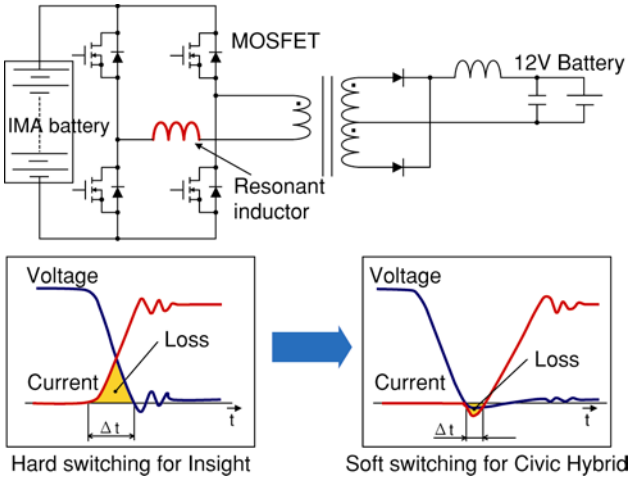


Fig. 8 12 V DC-DC converter circuit

In the switching operation of the MOSFET (Metal Oxide Semiconductor Field Effect Transistor) that drives the transformer, a resonant inductor is added to the path of the current that flows to the transformer through MOSFET from the IMA battery when MOSFET is ON. By controlling switching timing, voltage between MOSFET drain sources and drain current overlap time is shortened, thereby reducing switching loss. As shown in Fig. 9, the adoption of the above soft-switching circuits actualizes an average efficiency improvement of 2% over the previous model. In addition, accompanying this technology, it is possible to simplify the parts inside the converter, achieving a 22% size reduction over the Insight, and a 9% weight reduction.

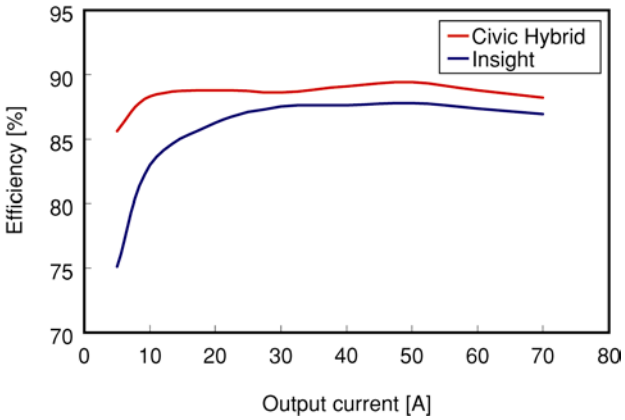


Fig. 9 12 V DC-DC converter efficiency

Figure 10 shows a map of 12 V DC-DC converter efficiency against input voltage from the IMA battery and output current to the 12 V battery. By making modifications to raise the actual use range efficiency shown on this graph, there is a reduction in loss during actual use. Accordingly, cooling with a smaller amount of airflow than required for the Insight is possible, and because there is a reduction in consumed energy, the device achieved a size reduction as well as improved fuel economy.

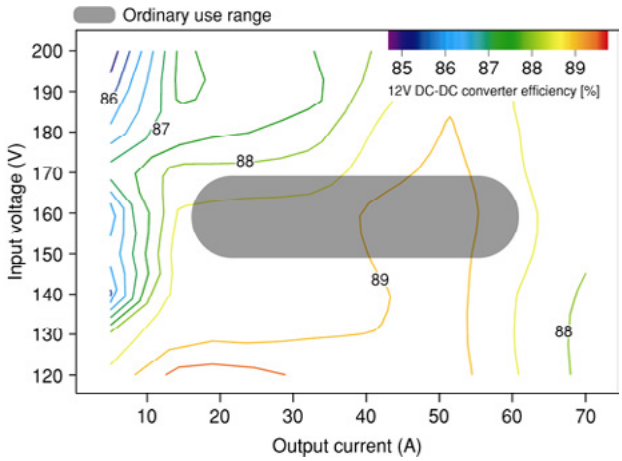


Fig. 10 12 V DC-DC converter efficiency map

3. IMA Battery

Changes from the Insight include an increase in vehicle weight and an engine cylinder idling system (CIS), meaning there is an increase in energy during regeneration. Because of the resulting increase in assist and regeneration power, that is to say, because the average battery input and output levels are larger during driving, it is expected that there will be an increase in battery-generated heat. Therefore, the following countermeasures were studied.

(1) Reduce battery module internal resistance by approximately 20%
(2) Increase battery cooling airflow by 50% of the previous mode.

Figure 11 shows the amount of heat generated and the heat balance during Insight and Civic Hybrid actual driving.

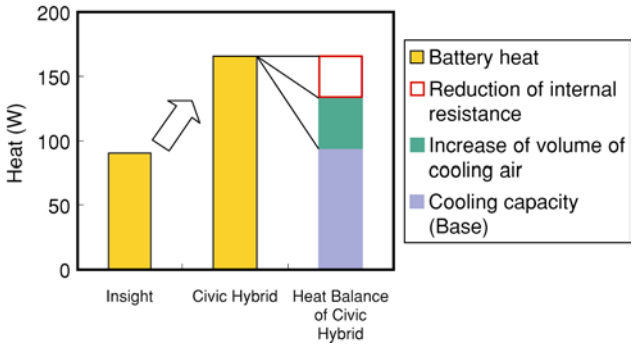


Fig. 11 Battery heat balance

The amount of heat generated was approximately 1.8 times that of the Insight, but with a battery internal resistance reduction of 20% and a cooling airflow increase of 50%, it is possible to keep battery temperature rise to the level over the previous model.

3.1. Battery Module

Modifications unique to the Civic Hybrid were made to the battery module, electrodes and current collector structure were revised, and in particular, a change to the shape of the current collecting plates reduced internal resistance. Figure 13 gives a comparison of current collecting plate shapes.

By changing the shape of these plates, there is an increase in the number of welds to the electrodes, and there is a leveling of collecting plate current density. Together with other internal battery modifications, there was a reduction in resistance of 19% compared with parts fitted to the Insight.



Fig. 12 IMA battery module

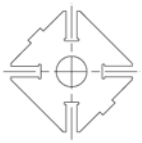
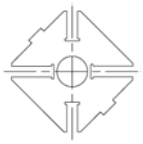
	Insight	Civic Hybrid
Positive current collector		
Negative current collector		
Number of welding points	84	118
Internal resistance	21mΩ	17mΩ (-19%)

Fig. 13 Current collecting plate

3.2. IMA Battery Box

With the aims of weight and size reduction, battery box component parts were revised.

(1) By optimizing the layout of related parts around the battery box (battery ECU, harnesses, etc.), the box unit was made smaller.

(2) Connecting part shapes were given optimum design and made smaller and lighter for the Civic Hybrid maintaining battery box strength the same or better than the previous model.

As a result of the above measures, in comparison with the Insight's battery box, box volume is 29.5% smaller, and weight is 5.6% lighter.

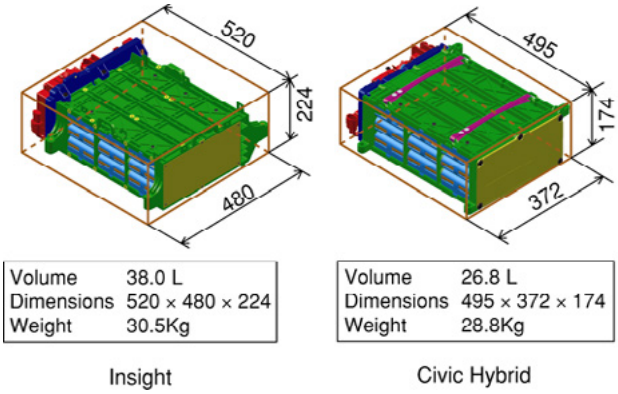


Fig. 14 IMA battery box

4. Integration of Cooling System

The Insight's IPU and its cooling circuit are shown in Fig. 15. In the previous model, the PCU cooling circuits were separate for the PCU and the battery system. The PCU system had cooling air taken from outside the vehicle, cooling the inverter and 12 V DC-DC converter, and then the air was exhausted outside the vehicle cabin. For the battery system, air was taken from inside the vehicle, the battery was cooled, and the air was exhausted back inside the vehicle. The cooling system occupied a large volume – almost 45% – of the total IPU. In contrast, with the Civic Hybrid a study was made of integrating the cooling circuits in order to achieve a cooling system that is 60% smaller.

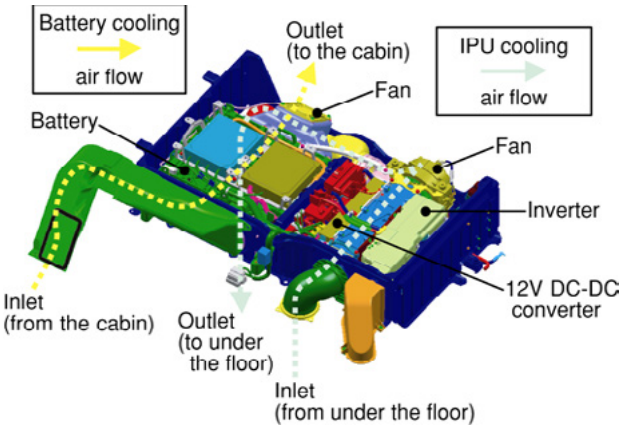


Fig. 15 Cooling air flow in Insight IPU

The cooling circuit of the Civic Hybrid IPU is shown in Fig. 16. With the Civic Hybrid, the IPU is located behind the rear seats, and the cooling air circuit is constructed so that the cooling air is taken in through an inlet placed on the rear tray in the vehicle cabin, the battery is then cooled, and the exhausted air is re-used to cool the PCU, and then the air is exhausted into the trunk space. In addition, there is no duct from the battery outlet to PCU inlet; instead one part of the IPU case is used as the cooling air circuit, which reduces the number of parts. The following were the major issues with this cooling system.

(1) Feasibility of cooling the PCU with exhausted battery cooling air
(2) Noise in the vehicle due to IPU cooling air
(3) Battery temperature rise when the vehicle is left out in the blazing sun, with the battery box located vertically behind the rear seats

The verification results concerning the first issue – feasibility of cooling – are given here. Issues two and three are discussed later.

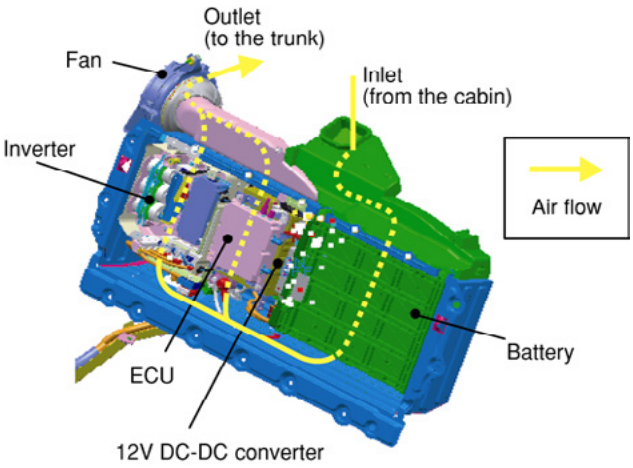


Fig. 16 Cooling air flow in Civic Hybrid IPU

4.1. Study of IPU Cooling Air Temperature

With the Insight, the PCU cooling air is taken from outside the vehicle, and under the assumption of a high temperature environment such as under a blazing sun, the highest PCU cooling intake air temperature was set at 60 °C. With the Civic Hybrid, in order to reduce the intake air temperature, the cooling systems are integrated and the battery cooling exhausted air, taken from inside the vehicle, is used, for PCU cooling. Figure 17 shows shifts in Civic Hybrid battery and PCU intake air temperatures when driving after the vehicle has been left out under a blazing sun. The rear tray intake air temperature (battery intake air temperature) drops as driving begins, and in a steady state is approximately 35 °C. This air temperature rises to approximately 50 °C due to the battery cooling and is used for PCU cooling. From these results, the PCU cooling air maximum temperature was set at 50 °C and a cooling feasibility study was carried out.

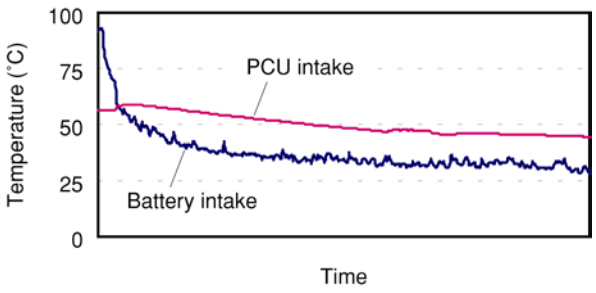


Fig. 17 Cooling air temperature when driving in hot weather

4.2. Study of Reducing the PCU Cooling Airflow Rate

By using the air after battery cooling to cool the PCU, it was possible to lower the intake air maximum temperature by 10 °C (to 50 °C) compared to the Insight. A study was carried out to investigate how much the required airflow rate could be reduced with this and the reduction in each component's loss mentioned earlier. As an example, Fig. 18 shows the relationship between inverter temperature and cooling airflow rate.

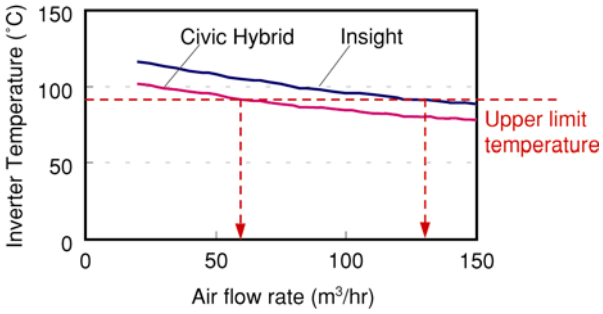


Fig. 18 Characteristics of cooling inverter

Due to a maximum loss reduction of 25% from increasing the inverter efficiency and due to a reduction in intake air temperature, the required airflow rate became 60 m^3/hr, meaning that cooling is possible with an airflow rate 57% less than the previous model. In the same way, the results of studies of the 12 V DC-DC converter show that the required airflow rate is 60 m^3/hr, meaning that cooling is possible with 50% less airflow than the previous model. In addition, concerning the battery, although efficiency is improved by reducing internal resistance, it is necessary to increase required cooling airflow rate by 50% to 90 m^3/hr because of the increase in battery input and output accompanying the increase in vehicle body weight and regeneration energy. The results of cooling airflow rate reduction are shown in Fig. 19. As shown in this graph, against the target maximum cooling airflow rate of 90 m^3/hr, all the maximum required airflow levels for battery, inverter, and 12 V DC-DC converter are at that level or less. Accordingly, it is feasible that the cooling system can cool all component parts at the maximum airflow or less which is set considering the increase in air-conditioning load and noise level inside the vehicle, etc. accompanying in-vehicle air intake and exhaust.

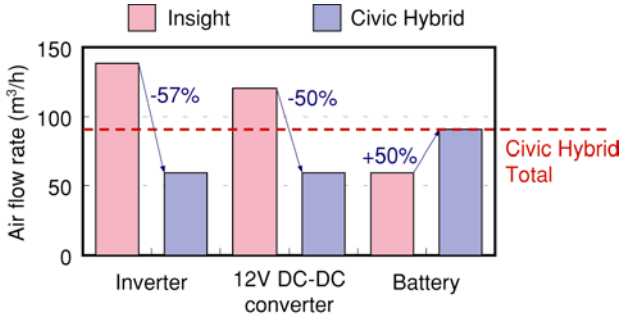


Fig. 19 Air flow rate

In this way, each component's required airflow rate is at or below the target value, and as a result of making the component devices smaller, it was possible to integrate the previous cooling circuits into one. The number of cooling fans and duct parts were also reduced, meaning that the IPU volume occupied by the cooling system was reduced by 62% over the previous model.

5. Cooling Fan Noise Reduction

Together with IMA cooling circuit integration, a PWM control type IPU cooling fan was newly developed for the Civic Hybrid. This fan can be finely controlled with no steps.



Fig. 20 IPU cooling fan

A simple method of improving cooling capability is to increase cooling airflow rate, but doing so invites the possibility of a drop in vehicle marketability due to a worsening of noise and vibration from the increase in intake airflow inside the vehicle. With the Civic Hybrid, in order to balance cooling performance and marketability at a high level, a new fan control method was developed. The larger of the following two values is selected as the fan control duty factor.

(1) Value determined from battery temperature and input/output current value
(2) Value determined by the difference of temperature between each battery module

In order to further reduce fan noise, control is applied according to the upper limit duty factor determined by the vehicle speed at that time. Utilizing the fact that background noise inside the vehicle changes according to vehicle speed, the fan noise discernible by the passengers must be kept to a minimum and at the same time cooling performance maintained. With the Civic Hybrid, the fan noise target value has been established to be at least 8 dB lower than the background noise inside the vehicle. Figure 21 shows vehicle speed and noise levels and Fig. 22 is a fan operation upper limit duty graph.

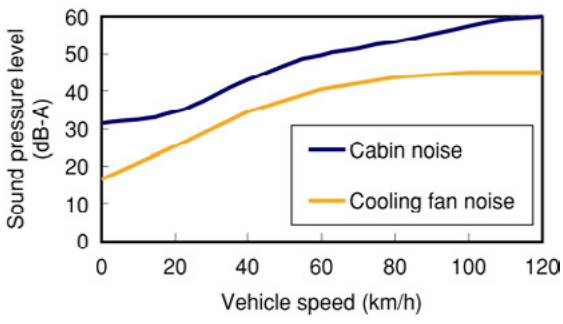


Fig. 21 Cooling fan noise

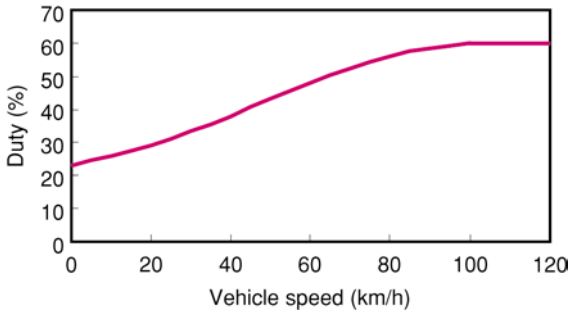


Fig. 22 Cooling fan control

By introducing the above cooling fan control, it is possible to have a cooling system that gives the necessary cooling performance while maintaining quietness.

6. Battery Module Temperature Rise Protection

By locating the IPU behind the rear seats, the battery box is placed vertically, and when the vehicle is left out in the blazing sun, the battery module at the top of the battery box is heated due to solar radiation. There can be a concern if temperature rises excessively. Therefore, with the Civic Hybrid, a heat insulator is applied around the battery box to prevent excessive battery module temperature from rising when the vehicle is left out in the blazing sun.

The major countermeasures are given below.

(1) Place heat insulating material around the battery box
(2) Make the intake duct out of formed resin, having insulating function, and place a hot air insulating rubber valve inside

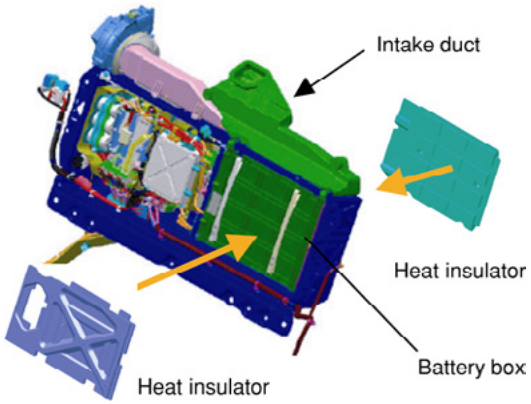


Fig. 23 Heat Insulating device for IMA battery

Through the above countermeasures, battery temperature rise during hot sun exposure is reduced by approximately 10 °C and further temperature rise at high temperatures is prevented. In addition, because these pieces are foaming expandable polypropylene beads, they provide some impact absorption and can provide some additional protection to the battery box in the event of a collision.

7. Summary

As outlined above, with the introduction of new technologies for each component, it has become possible to reduce the amount of heat generated by improving efficiency and to make each part smaller. In particular, by improving inverter and 12 V DC-DC converter efficiency, although electrical load has increased, the amount of heat generated has dropped, and for the IPU as a whole, a simplified cooling system has become possible. The two cooling circuits on the Insight IMA system were made into one. This had the effect of reducing IPU volume by 42% in comparison with the Insight. By locating the compact IPU behind the rear seats, cabin area and comfort equivalent to a conventional sedan have been maintained and it has become possible to fit the new IMA system with minimal loss of trunk space convenience.

References

(1) Matsuki, M., Wakashiro, T., Kamiyama, T., Sato, T., Kaku, T., Kanda, M.: Development of a New Power Train for the Civic Hybrid, Honda R&D Technical Review, Vol. 14, No. 1 April 2002

■ Authors ■



Kazuhiko AITAKA



Masaharu HOSODA



Takuya NOMURA

Development of High-Capacity MgMH Alloy for Hydrogen Storage

Izuru KANOYA* Mitsuya HOSOE* Takanori SUZUKI*

ABSTRACT

A method of mechanical grinding using nanoparticle catalyst was applied to create hydrogen-absorbing magnesium alloy with a chemical composition of Mg-0.33 Ni-0.17 Fe (at%). The use of nanoparticle catalyst made it possible to achieve a 15-minute process time that was one-fortieth or less in comparison with the conventional method with an acceleration of 13.3 G. The synthesized hydrogen storage magnesium alloy possessed a microstructure with catalyst metal distributed uniformly across the powder surface and throughout the matrix. As a result, the alloy yielded significantly improved hydrogen storage capacity, achieving a maximum capacity of 7.49 wt%. This rate of hydrogen absorption places it in the world's top level of hydrogen-absorbing alloys that are currently being reported.

1. Introduction

There are many hydrogen absorbing alloys that function at or below 50 °C, typical examples being $LaNi_5$ and $MmNi_5$. Of these, the largest amounts of hydrogen absorption range from 1.0 to 1.4 wt%. A familiar example of the use of hydrogen absorbing alloys is an Ni-MH battery, in which a hydrogen absorbing alloy is used for the negative electrode. Furthermore, the large amount of research that has been conducted in the field of fuel cells for automobiles in recent years has been accompanied by a great deal of research activity in BCC-type alloys (with a maximum absorption amount ranging from 1.8 to 2.4 wt%) composed of V, Ti, etc[(1)].

Hydrogen-absorbing magnesium alloy (MgMH) is classified as a high-temperature hydride since it functions at temperatures in excess of 300 °C. A feature of MgMH is that at a hydrogen desorption temperature of 290 °C at 0.1 MPa and the generation enthalpy of MgH_2 is high at 74.5 kJ. But the hydrogen storage capacity is extremely large (theoretical value of pure Mg: 7.6 wt%)[(1)]. However, the initial activation of the pure Mg requires that extreme conditions, such as a temperature of 350 °C and a hydrogen pressure of 5 MPa, be maintained for a week. In addition, the rate of hydrogen absorption/desorption is markedly slow. Because of these obstacles, there are hardly any examples of practical application of this material[(1)].

Two conventional methods of producing MgMH with a high absorption amount are mechanical grinding (MG) using ball milling, and mechanical alloying (MA)[(2) - (7)]. Particles of catalyst metal that were on the order of tens of micrometers when added are distributed throughout the matrix in the form of small grains ranging from tens to hundreds of micrometers in size. Additionally, there are reports of absorption amounts being improved in the case of nanosized grain particles[(2) - (7)]. However, the MG and MA processes require tens or hundreds of hours, making them impractical. In addition, in order to improve rates of absorption/desorption by switching from micron-sized catalyst to nanoparticle catalyst metal and achieving a microstructure in which the catalyst metal is distributed uniformly, the MG and MA processes require acceleration well in excess of tens of gravity (G). As a result, energy input will be increased as to make this approach impractical. In order to create a practical MH alloy through MG with ball milling or through MA, the time required for production needs to be greatly reduced, and the required acceleration needs to be reduced.

In light of this situation, the purpose of this research was to bring the absorption amount of MgMH alloy as close as possible to the theoretical value, and to produce the alloy by a method that required less time and less linear acceleration than conventional methods.

* Wako R&D Center

2. Aims

As a means of achieving the objectives, attention focused on moving from micron-sized catalyst metal to nanoparticle catalyst metal at the catalyst introduction stage, so the MG process was performed using nanometer-sized catalyst metal particles ("nanosized") as the introduced material. For the catalyst metal, the decision was made to use a combination of Ni, which has a large catalytic effect on the reaction between Mg and H_2, and Fe, the most inexpensive of the group VIII transition metals, the same group to which Ni belongs. Even with the MgMH alloy, reducing the amount of catalyst metal is directly linked to improving the absorption amount and reducing the cost. However, because reducing the amount of catalyst metal too much will lead to a clear decreasing of the rate of hydrogen absorption/desorption, it is essential that the storage capacity be increased while maintaining a fast rate of absorption/desorption. This research assumed a base composition of Mg-2Ni-1Fe (at%) (maximum amount of absorption: 6.5 wt%, theoretical absorption content = 7.17 wt%), and studied the reduction of the catalyst metal fraction from that base composition.

3. Experimental Procedures

3.1. Production Method

The alloy was synthesized using the MG process, since it permits uniform distribution of the nanosized metal catalyst. Synthesizing MgMH by a conventional MG process requires tens or even hundreds of hours, therefore reduction of the process time is an extremely important issue from an industrial standpoint. Energy consumption can also be reduced by reducing the amount of energy required in the MG process. Therefore, MG range of 1 minute to 10 hrs was studied. Also, an optimization study was conducted, substituting the acceleration of gravity on the pot wall varying from 0.5-23.7 G for the energy input into MG. Fritsch P-5 planetary ball milling apparatus was used for the MG. The MG pot is a gas replacement type with a capacity of 80 cc.

Each metallic element was weighed out at a total mass of 2.5 g in order to produce the target composition in the MG process. After the material was set in the MG pot, a vacuum was created in the pot at room temperature. Then the pot was filled with H_2 at 1 MPa, and the MG process was performed.

3.2. Material Powder

Metal powders of the purity and diameter shown in Table 1 were used. The nanosized catalyst particle powders were checked for O_2 impurities through composition analysis by the inert gas fusion - infrared absorption method. Because Fe more readily oxidizes than Ni, there were more O_2 impurities in the Fe powder. The metal powders that were used had granular diameters of less than 180 μm in the case of Mg and of approximately 20 nm in the case of Ni and Fe. The Ni and Fe powders were produced by the evaporation method in inert gas, and oxidized slowly in the air in order to prevent combustion.

FeNi alloy nanoparticle catalyst powders were used in order to study reduction of the MG time when using nanoparticle catalysts. The composition of the FeNi nanoparticle catalyst powders were Fe-20Ni (wt%), with a diameter of 20 nm.

Table 1 Purity and diameter of each material

Material	Mg	Ni	Fe
Purity	3N	O: 6.9wt%	O: 18wt%
Diameter	<180 μm	26nm	20nm

3.3. Analysis Method

The composition of the MgMH powder that was synthesized was checked using X-ray diffraction measurement (XRD). Transition Electron Microscope (TEM) was used to observe the microstructure of the MgMH powder, the morphology, location and diameter of the catalyst metal. The powder was also analyzed using a Scanning Electron Microscope (SEM) and an Energy Dispersive X-ray Spectrometer (EDX) in order to check the surface condition of the MgMH particles and distribution of the component elements. Pressure-Composition Isotherms (PCT) measurement equipment was used to evaluate the hydrogen absorption characteristics of the powder. For the PCT measurement, samples weighing from 0.25 g to 0.30 g were tested, with a convergence time of 15 minutes and a convergence judgement time of 5 minutes.

4. Test Results

4.1. Reduction of MG Time

4.1.1. Results of absorption amount measurement

Figure 1 shows the relationship between MG time and the maximum hydrogen absorption amount of Mg-3FeNi alloy that was synthesized with an MG acceleration of 23.7 G. This graph shows that the majority of this alloy's theoretical capacity to absorb hydrogen is achieved after 15 minutes of MG. This is likely to be due to two major factors. The first is that the nanoparticle catalysts used are highly activated as a catalyst from the start. The second is that, Fe and Ni surface oxides are easily reduced and the MG process is performed within hydrogen atmosphere, so that the surfaces of the nanoparticle catalysts become highly activated after a short period of time.

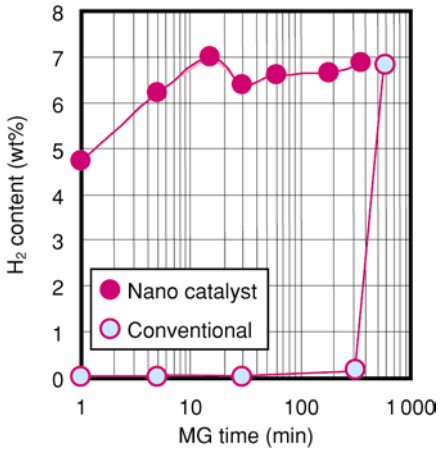


Fig. 1 Relationships between MG time and H2 contents of Mg-3FeNi alloy

Figure 2 shows the PCT property of the Mg-2Ni-1Fe alloy at 310 °C. Figure 3 shows the PCT property of the MgMH alloy produced by the conventional method, with a 10-hour MG process and a catalyst metal particle diameter of less than 150 μm. The 2:1 ratio of Ni to Fe results from retaining the composition which previous studies have found to be effective in terms of both absorption amount and plateau properties. Even if the MG time shown in Fig. 2 is reduced to 15 minutes (1/40 or less of MG time conventionally required), the hydrogen desorption amount exceeds 6.3 wt%, and has an absorption amount that is roughly equivalent to that of conventional materials.

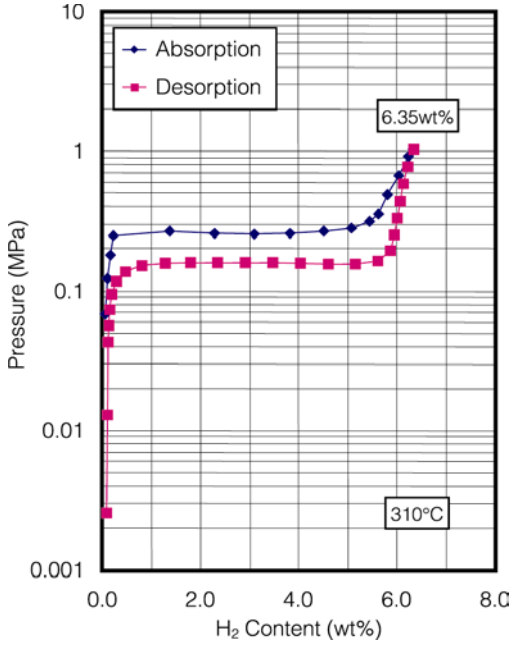


Fig. 2 PCT property of Mg-2Ni-1Fe alloy using nano meter sized catalyst (MG time 15 min)

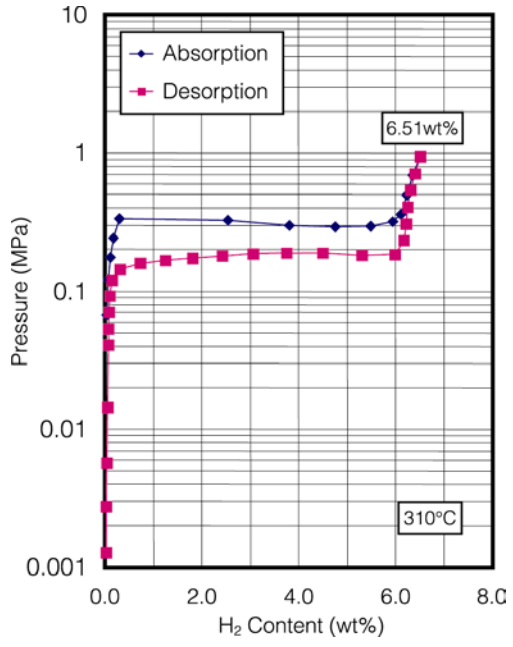


Fig. 3 PCT property of conventional method (10hr, 150 μm cat.)

In addition, the alloys shown in Fig. 2 and Fig. 3 were collected in a controlled glove box with an Ar gas atmosphere. Then, in order to reduce the danger of ignition of the Mg metal powder in air and to improve the safety of the material while handling it in the air, the material was left exposed to the open air for more than 24 hours. After its controlled oxidation, its PCT property was measured. The PCT property confirmed that there was practically no reduction of the hydrogen absorption/ desorption properties even if the material was handled in the open air. This PCT measurement also clearly indicated that, as shown in Fig. 4, it was still possible to obtain approximately the maximum absorption amount even if initial activation was not performed. This demonstrates that the extreme initial activation treatment that was typically performed for conventional alloys is not needed when using nanoparticle catalysts.

Based on the above, using nanoparticle catalysts permitted a reduction of the MG time using planetary ball milling from the conventional 10 hours to 15 minutes (1/40 the previous amount of time). It also became clear that initial activation was no longer necessary, and that once the material had become oxidized there was no reduction in the hydrogen absorption/desorption properties even when the material was handled in the open air.

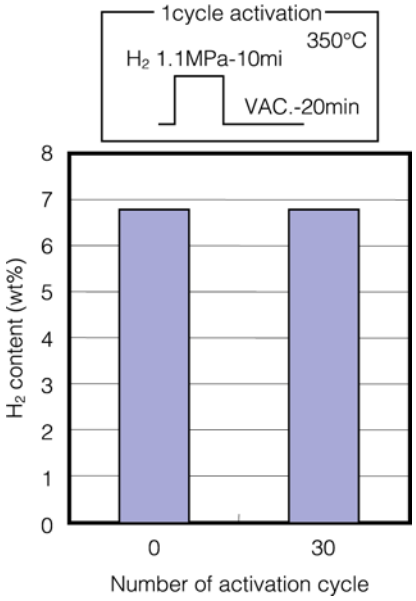


Fig. 4 Relationship of H2 contents and Number of activation cycle

4.1.2. Results of identification of component phases of the Mg-2Ni-1Fe alloy

An XRD measurement was performed in order to identify the component phase of the MgMH powder that was produced. Figure 5 shows the XRD diffraction pattern of the Mg-2Ni-1Fe (at%) that was collected after MG using nanoparticle catalysts. In the conventional method, MG was performed for at least 6 hours to generate MgH_2, but in this method, using nanoparticle catalysts, MgH_2 was generated after 15 minutes.

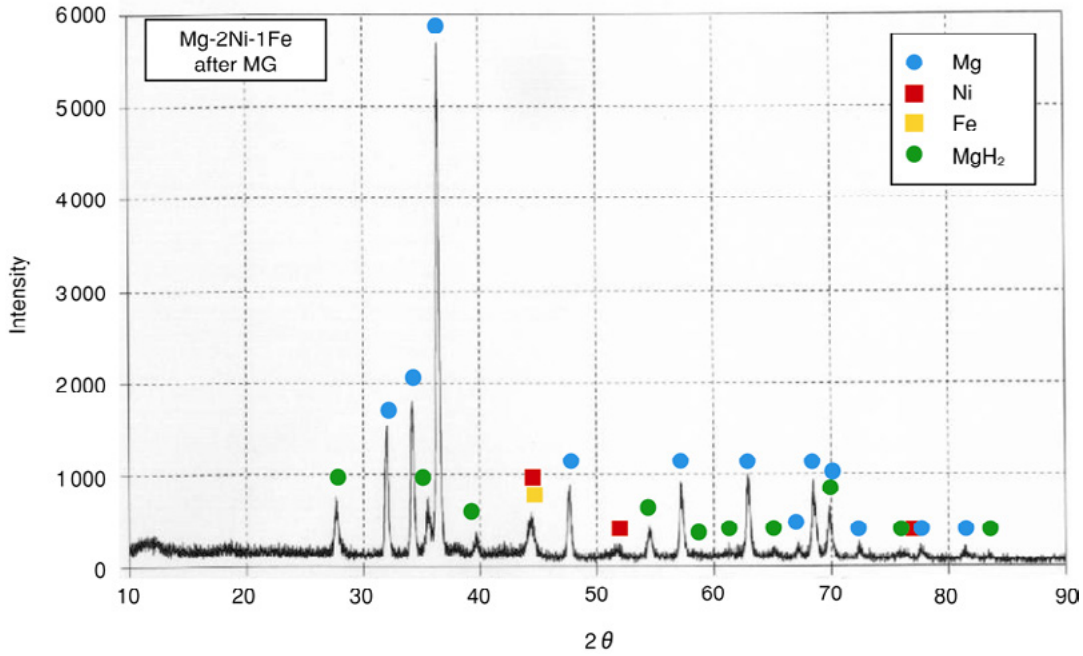


Fig. 5 XRD pattern of Mg-2Ni-1Fe alloy using nano meter sized catalyst (after MG)

As described earlier, the mechanism that renders initial activation unnecessary is likely as follows, based on the results shown in Fig. 5. Because MgH_2 is already synthesized in the MG process, the hydrogen in the alloy is released by heating over 300 °C. As a result, the released hydrogen removes the adsorbed gases and part of the oxidation layer on the surface of the MgMH powder. This puts the surface of the MgMH powder in a state equivalent to post-activation treatment state. Because the above phenomenon occurs continuously, initial activation is completed simply by desorbing hydrogen and maintaining the temperature at over 300 °C.

4.2 Reduction of MG Acceleration

4.2.1. Absorption amount measurement results

The reduction of MG acceleration reduces the amount of energy that is input into the process, which contributes to lower product cost. In addition, large acceleration requires equipment that is larger and that produces greater output. Therefore, methods for decreasing MG acceleration were studied for the purpose of reducing energy requirements.

The reduction of acceleration was studied by changing the acceleration generated on the inner wall of the pot in the planetary ball milling equipment; this was accomplished by changing the rotational speed of the pot. Applied accelerations in this research were 0.5 G, 13.3 G, 21.8 G, and 23.7 G. The MG time was established as 15 minutes, based on the study results described in section 4.1, “Reduction of MG time.” For the purposes of comparison, an MgMH powder that was synthesized by mixing Mg powder and catalyst metal particles with an agate mortar was also studied. Specifically, the Ni and Fe metal particles (diameter = less than 150 μm) that were used in the conventional material were mixed together for five minutes with an agate mortar as the “Coarse As Mix,” while nanoparticle particle metallic powder was used as the “Nano As Mix.”

Figure 6 shows the relationship between the PCT desorption property and the acceleration. It became clear that

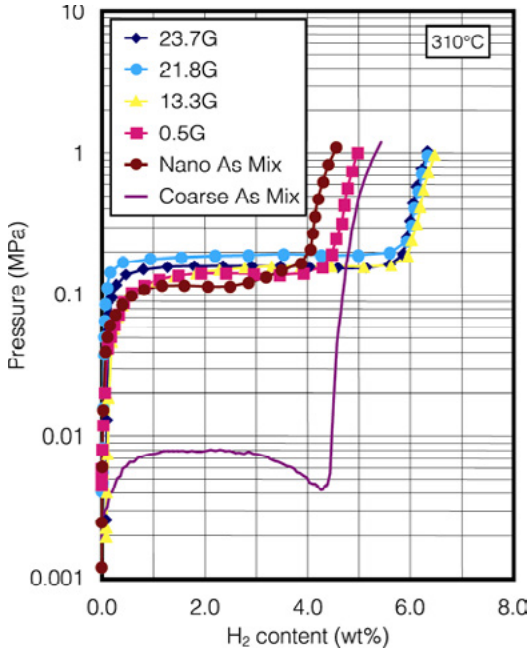


Fig. 6 Relationships between PCT desorption property and MG acceleration

even though the nanoparticle catalyst MG process was reduced to 15 minutes the hydrogen desorption property and the plateau property for 10 hours MG treated conventional material at 23.7 G were achieved with nanoparticle catalysts at 13.3 G to 23.7 G. These results show that the MG acceleration can be reduced by 44%, from 23.7 G to 13.3 G when using nanoparticle catalysts.

It is also clear that the “Nano As Mix” that was synthesized using an agate mortar has a plateau pressure that is equivalent to that of a sample produced by the MG process. The fact that the “Nano As Mix” material has a plateau pressure equivalent to that of the MG material means that the rate of desorption of the “Nano As Mix” is equivalent

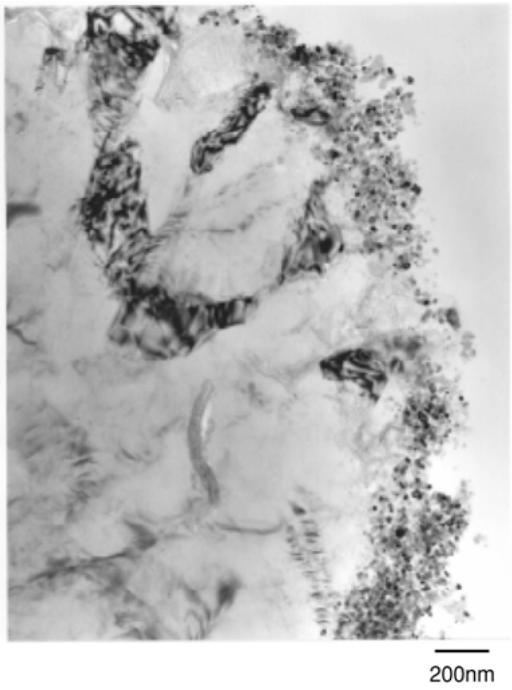


Fig. 7 TEM image of Mg-2Ni-1Fe after MG-0.5G

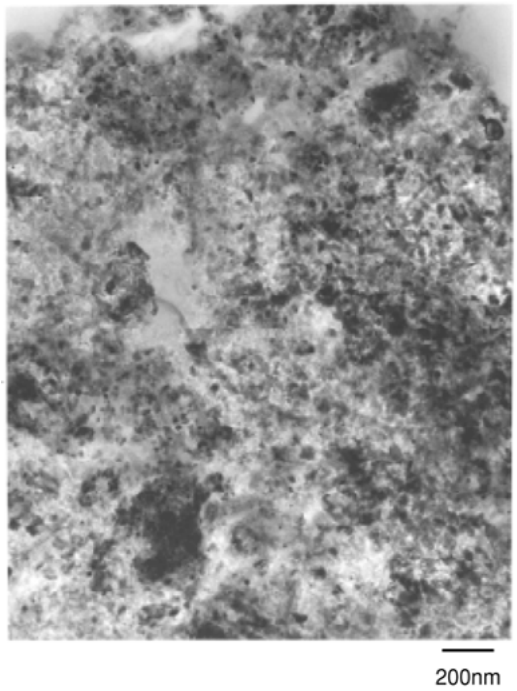


Fig. 8 TEM image of Mg-2Ni-1Fe after MG-13.3G

to that of the MG material. Given these results, it is likely that even simple mixing with nanoparticles easily increases the hydrogen activation at the periphery of the powder where the nanoparticle catalysts have adhered, although the activation towards hydrogen is low within the Mg grains where no nanoparticle exist. As a result, it was possible to measure the amount of hydrogen desorption in the highly activated region near the surface of the Mg powder.

Based on the above, when using nanoparticle catalysts it is possible to reduce the MG acceleration by 44% compared with conventional materials, and the rate of reaction is able to be greatly increased by even simple mixing with nanoparticle catalysts.

4.2.2 Results of microstructure observation

Observation by TEM was used in order to gain a clear understanding of the microstructure of the MgMH powder that was produced. Among the samples shown in Fig. 6, observation by TEM was made on the 0.5 G and 13.3 G samples immediately after the MG process. Figure 7 and 8 show typical TEM images of the 0.5 G and 13.3 G samples, respectively.

It is believed that, in a normal MH alloy, catalyst metal on the surface promotes the dissociation of the atoms in hydrogen molecules, or the reverse reaction. In other words, when hydrogen is absorbed, the catalysts promote the dissociation of the atoms in hydrogen molecules; when hydrogen is desorbed, it has the effect of bonding hydrogen atoms to form molecules.

As Fig. 7 clearly shows, the nanoparticle catalysts in the 0.5 G material are only present on the outermost surface, and do not exist within the matrix of the Mg powder. On the other hand, in the case of the 13.3 G material that is shown in Fig. 8, the nanoparticle catalysts are distributed both within the Mg matrix and on the surface. The nanoparticle catalysts are distributed within the matrix, and this is a likely reason why the MgMH powder overall has a high rate of absorption/desorption, and exhibits a large absorption amount in excess of 6 wt%, similar to 23.7 G material.

These results clearly indicate the importance of uniform distribution of nanoparticle catalyst on the surface of the MgMH powders and within the matrix.

4.3. Reduction of Amount of Catalyst

After studying Mg-xNi two-element alloys (x = 0.5, 1.0, 2.0, 3.0 at %), the results were fed back into Mg-Ni-Fe alloys, and alloys with compositions based on that feedback were created and the amount of hydrogen absorption was measured. As it was considered difficult to stably obtain the

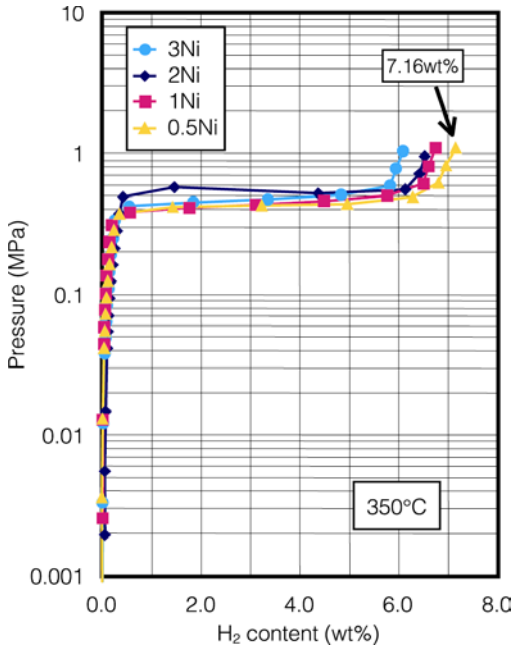


Fig. 9 Relationships between PCT desorption property and contents of Ni catalyst (x=0.5, 1.0, 2.0, 3.0)

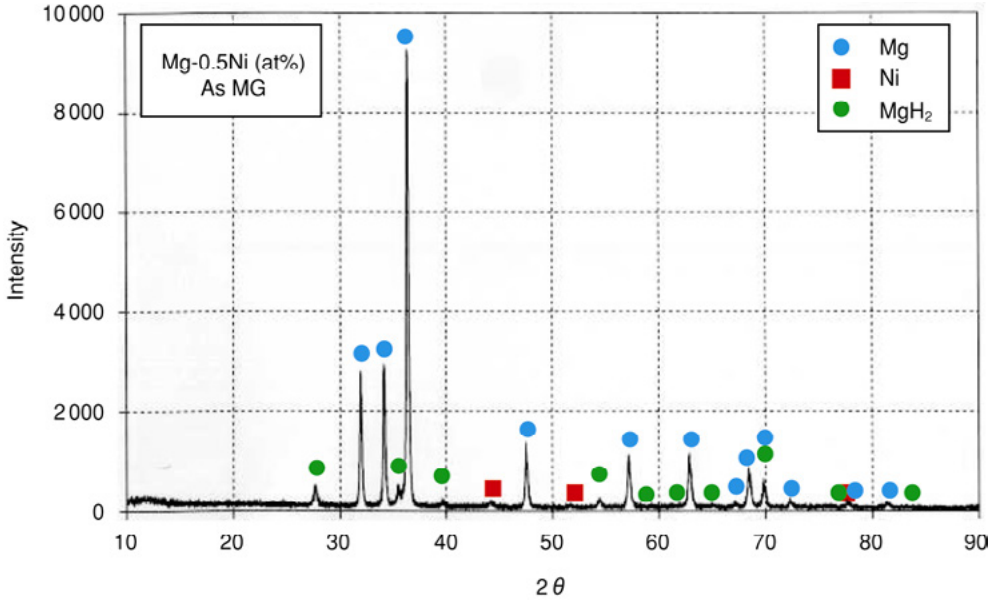


Fig. 10 XRD pattern of Mg-0.5Ni alloy after MG using nanometer sized catalyst

target composition in the range below 0.5 at%, this range is excluded from the study.

Figure 9 shows the results of PCT property measurement in Mg-xNi binary alloys that were produced with different amounts of catalyst. In the case of the alloy using the nanoparticle catalysts reduced the amount of catalyst as low as 0.5 at% which did not accompany decreasing of the hydrogen storage capacity; the maximum amount of desorption exceeds 7 wt%. The hydrogen desorption rate did not drop even when the amount of the catalyst was 0.5 at%. So the amount of hydrogen desorption increased with the decrease in the amount of the catalyst.

4.3.1. Results of XRD measurement

Of the two-element alloys, XRD observation was carried out of the Mg-0.5 Ni (at%) alloy (which exhibited an absorption amount in excess of 7 wt%) immediately after MG (As MG). Figure 10 shows the XRD diffraction pattern. Because the MG process was short, Mg exhibits no broad peak; instead, the pattern is very peaky with high crystallization. Regarding Ni, only small peaks are observed, since the amount that was added was 0.5 at%.

A chief characteristic of the conventional method is that, once MgH_2 is generated after six or more hours of the MG process in a hydrogen atmosphere, the MgH_2 peak is observed in XRD measurement after MG. In the case of the new alloy, the generation of MgH_2 was confirmed even with only 0.5 at% Ni and just 15 minutes of MG. In addition, hydrogen storage capacity in excess of 7 wt% was confirmed for the series of alloys regardless of whether the initial activation treatment was performed or not, just as described in section 4.1.2, “Results of identification of component phases of the Mg-2Ni-1Fe alloy.”

4.3.2 Expansion to Mg-Ni-Fe alloys

It was decided to apply that amount of catalyst to Mg-Ni-Fe alloys (Ni:Fe = 2:1), and a chemical composition of Mg - 0.33Ni - 0.17Fe (at%) was selected, as it became clear that hydrogen storage capacity in excess of 7 wt% could be reached with catalyst amounts of 0.5 at%. Similar to the MG conditions described previously, a vacuum was created in an 80 cc pot, then 1 MPa of H_2 was added, and the MG process was performed for 15 minutes. After a series of MG process, the MgMH powder was collected in the open air and the PCT property was measured. Figure 11 shows the PCT property at 310 °C under convergent conditions for 15 minutes. Figure 12 shows the PCT property at 350 °C under convergent conditions for 5 hours.

In Fig. 11, the maximum hydrogen storage capacity reaches 7.33 wt%, and it clearly exceeds the previous data that has been reported[8]. In Fig. 12, the hydrogen storage capacity reaches 7.49 wt%; although this doesn’t reach the theoretical value (7.57 wt%) for this alloy composition, the difference is a mere -0.08 wt%. Figure 13 shows a comparison of the absorption amount of this alloy compared with other types of alloys and an MgMH alloy produced by industrial melting methods[1], [8], [9]. Although the working

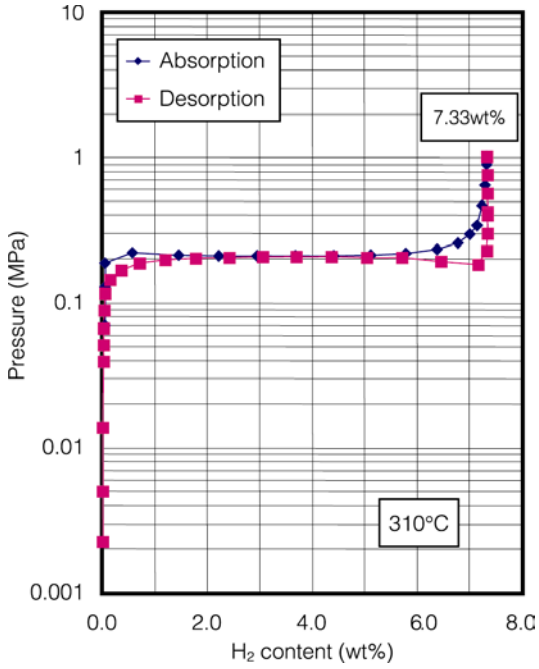


Fig. 11 PCT property of Mg-0.33Ni-0.17Fe alloy

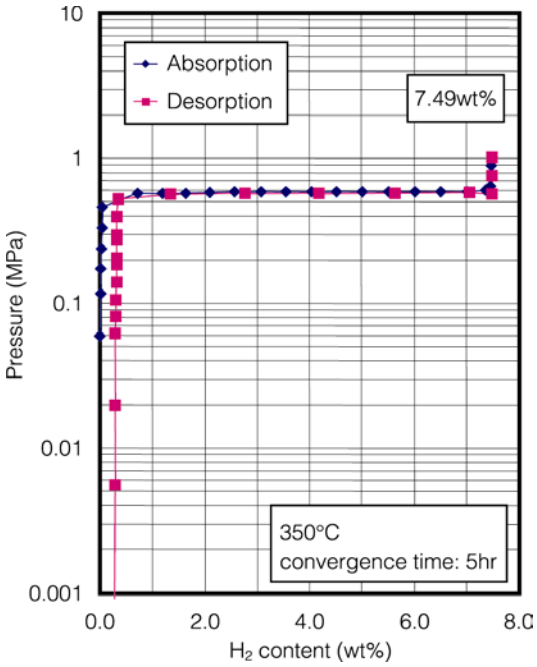


Fig. 12 PCT property of Mg-0.33Ni-0.17Fe alloy with 5 hr convergence time

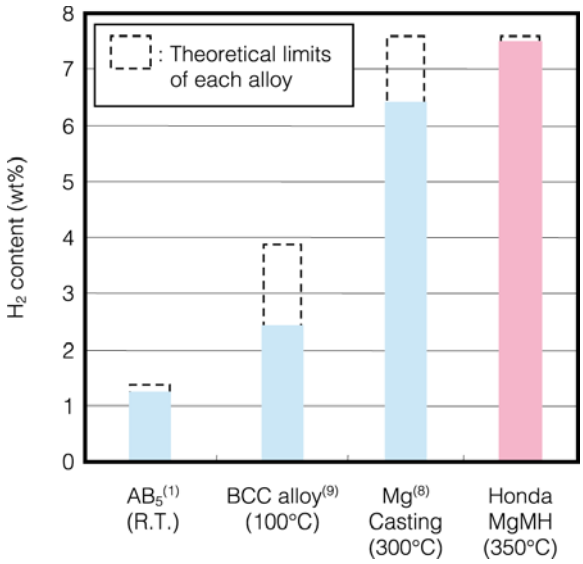


Fig. 13 Comparison of H storage capacity between MgMH in this research and another MH alloy

temperature is higher than that of low-temperature alloys, these graphs show that an absorption amount that is 99% of the theoretical value has been reached, and that this alloy has a hydrogen storage capacity that far exceeds that of other hydrogen absorbing alloys.

4.3.3. Results of component phase identification of Mg-Ni-Fe alloys

Figure 14 shows the XRD diffraction pattern for a dehydrogenated Mg - 0.33Ni - 0.17Fe alloy after PCT measurement. Recrystallization occurs and a Mg peak is observed with extremely high degree of crystallization, as the PCT measurement was performed at 310 °C. And, it is clear that the Ni catalyst now exists in the form of aMg_2Ni compound. Even if the Ni existed in the Mg_2Ni state, it would not reduce absorption/desorption properties as the MgMH have maintained its absorption/desorption properties. Fe is thought to exist in independent domains within the MgMH powder, as Fe does not synthesize a compound with Mg. Although the XRD diffraction pattern of MgMH powder immediately after MG, the generation of MgH_2 has been confirmed in the MgMH powder, initial activation is unnecessary for this alloy.

4.3.4. Results of microstructure observation

TEM observation was carried out in order to clarify the microstructure of the Mg - 0.33Ni - 0.17Fe alloy that was produced. Figure 15 shows a TEM observation image of the dehydrogenated MgMH powder after PCT measurement of the Mg - 0.33Ni - 0.17Fe alloy. Introduced dislocations and defects during MG and hydrogen absorption/desorption disappear and clear crystal grains are formed, as the PCT measurement is performed in a high temperature range around 300 °C. The diameter of the crystal grains likely ranges from several hundred nanometers to several

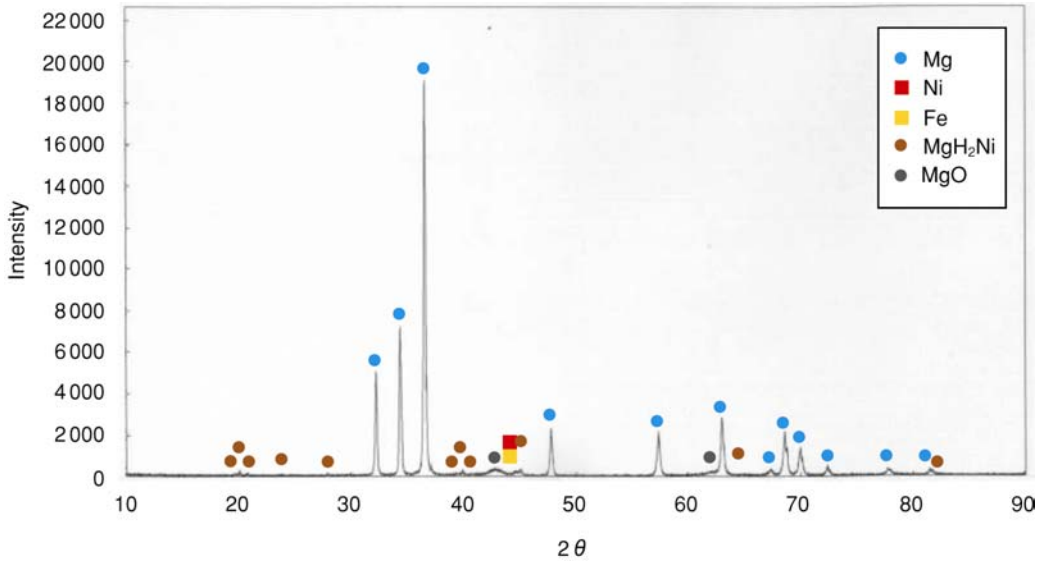


Fig. 14 XRD pattern of Mg-0.33Ni-0.17Fe after PCT measurement

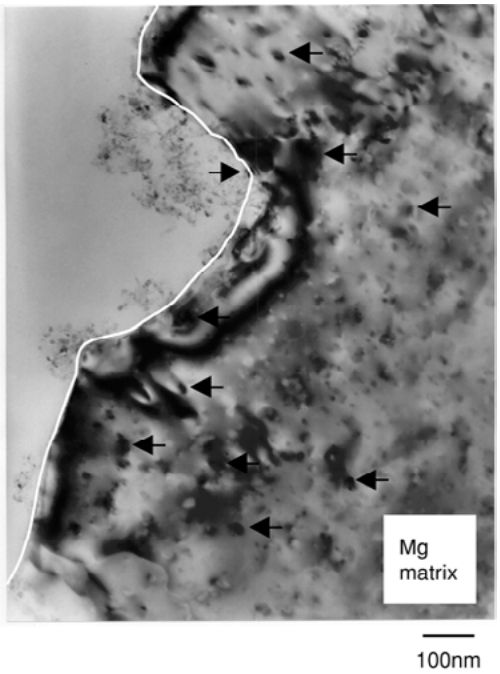


Fig. 15 TEM image of Mg-0.33Ni-0.17Fe after PCT measurement (Arrows indicate some catalysts and white line is a surface of Mg particle)

micrometers. Metallic images that are thought to be nanoparticle catalysts were confirmed in the matrix. It became clear that even though most of these are less than 100 nm in diameter and the PCT measurement was made at high temperature, most of the catalyst particles are distributed uniformly as nanoparticle on the surface of the MgMH particles and throughout the matrix. Regarding the Ni particles, their existence in Mg_2Ni was confirmed as described earlier in section 4.3.3, "Results of component phase identification of Mg-Ni-Fe alloys." In addition, the results of EDX also confirmed that the particles are composed of Mg and Ni.

These TEM observation results clearly indicated that the microstructure that achieves an absorption capacity in excess of 7 wt% in MgMH consists of under 100 nm sized catalyst particles distributed uniformly on the surface of the Mg powder and within the crystal grains.

5. Conclusion

The goal of this research was to produce a practical, easily manufactured Mg hydrogen absorbing alloy with the greatest possible hydrogen storage capacity.

As a result of this research, MgMH alloy was synthesized using nanoparticle catalysts with a chemical composition of Mg - 0.33Ni - 0.17Fe (at%) and 15 minute MG process with an acceleration of 13.3 G. And, it was shown that initial activation was completed through the first hydrogen desorption at 300 °C. In addition, the hydrogen storage capacity approached its theoretical value thereby greatly increasing the rate of hydrogen absorption/desorption. The maximum hydrogen storage capacity of this alloy achieved in this research was 7.49 wt%. This value is among the highest in the world for currently known practical hydrogen absorbing alloys.

This research enabled a simple and effective utilization of nanoparticle catalysts, a type of nanotechnology.

References

(1) Osumi, Y.: Hydrogen Storing Alloy – Physicality and Application, Tokyo, Agne Gijutsu Center, p. 587 (1999)

(2) Orimo, S., Ikeda, K., Fujii, H. and Yamamoto, K: Structural and Hydriding Properties of the Mg-Ni-H System with Nano-and/or Amorphous Structures, Acta Mater., Vol. 45, No. 6, pp. 2271-2278 (1997)

(3) Orimo, S., Fujii, H. and Ikeda, K.,: Notable Hydriding Properties of a Nanostructured Composite Material of the Mg2Ni-H System Synthesized by Reactive Mechanical Grinding, Acta mater., Vol. 45, No. 1, pp .331-341 (1997)

(4) Zaluski, L., Zaluska, A. and Strom-Olsen, J., O.: Hydrogen Absorption in Nanocrystalline Mg2Ni Formed by Mechanical Alloying, J. Alloys and Comp., vol. 217, pp. 245-249 (1995)

(5) Orimo, S., Fujii, H.: Unique Hydrogenation Property of Nanostructured Mg2Ni-H Alloy, The Japan Institute of Metals Report, Vol. 60, No. 7, pp. 685-692 (1996)

(6) Orimo, S., Fujii, H.: Hydrogenation Property of Amorphous Monolayer Mg-Ni-H (D) Alloy, The Japan Institute of Metals Report, Vol. 63, No. 8, pp. 959-964 (1999)

(7) Zaluski, L., Zaluska, A. and Strom-Olsen, J., O.: Nanocrystalline Metal Hydrides, J. Alloys and Comp., Vol. 253-254, pp. 70-79 (1997)

(8) Akiba, Y.: Alloy Having the Largest Amount of Hydrogen Absorption, Materia, Vol. 35, No. 11, pp. 1191-1194 (1996)

(9) Ezaki, K.: Current Status and Issues with Hydrogen Storage Alloy Tank for Automobiles, MH Utilization and Development Study Group, Material for 4th Conference in 2001, pp. 1-14

■ Authors ■


Izuru KANOYA


Mitsuya HOSOE


Takanori SUZUKI

Application and Utilization of HILS for the Development of an Automatic Transmission Control System

Yohei TAKEDA* Ko YODA* Satoshi TERAYAMA*
Kenji HAGIWARA* Yoshiharu SAITO* Tsutomu KAMIYAMAGUCHI*

ABSTRACT

In connection with development of an automatic transmission electronic control unit (AT ECU), a development aid technology known as hardware in the loop simulation (HILS) was introduced for testing with the objective of improving AT control reliability and shortening the time required for development. In order to realize the HILS technology, it was necessary to assure the calculation accuracy in AT shift feeling simulation models and to perform real-time simulations using the existing digital signal processors (DSP). The present development improved the method of modeling the AT hydraulic pressure control system. HILS implemented multi-rating, reducing the scheduler overhead, thus making it possible to lighten the calculation burden on the central processing unit (CPU). As a result, it became possible to perform real-time simulations with assured calculation accuracy, which allowed HILS technology to be utilized during the development of the AT shift control system.

1. Introduction

A new version of a development aid technology called hardware in the loop simulation (HILS) was developed and incorporated into current automatic transmissions (AT) simulation technology [(1)] to see whether it would be effective in improving the control reliability and reducing development time as part of the development of an electronic control unit (ECU) for AT.

In the flow of development of an AT control system incorporating HILS, the control system parameters are set using HILS before actual vehicle testing begins. HILS is necessary in order to achieve sufficient calculation accuracy to replace part of the testing with actual vehicles.

Real-time simulations have not been traditionally possible even when using the most sophisticated commercial digital signal processors (DSP) because HILS places huge calculation loads on the central processing unit (CPU). However, a new HILS was developed which maintains calculation accuracy in real-time simulations and can be run on an existing DSP. It is described in this paper.

An example of development of a new AT shift control system using the HILS is also described.

2. Outline of HILS System for AT

2.1. System Configration

The developed HILS system is made up of 6 components, as shown in Fig. 1: A host computer, a DSP system, an interface box, a relay box, an On-board Diagnostic Systems Stage II (OBD II) monitor, and an AT control ECU. The host computer is used for modeling, downloading the model to the DSP system, inputting parameters for the simulation, analysis and displaying the results.

The DSP system performs the real-time simulation on an Alpha CPU for model calculation, a C40 CPU for I/O processing, and a signal processing board. Here, the Alpha was a trademark for COMPAQ, and the C40, for Texas Instruments.

* Tochigi R&D Center

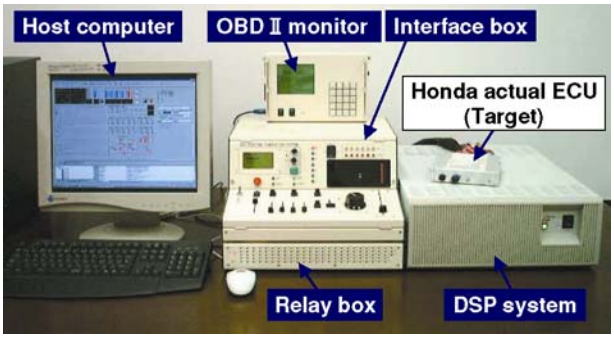


Fig. 1 HILS system overview

The interface box electrically combines the input and output signals from the DSP system line with the signal corresponding to the vehicle connected to the ECU line, and handles processing of the signals corresponding to control actions during manual or automatic driving such as operation of the shift lever, the acceleration pedal, or the brake.

The relay box gives failure conditions of any of the circuits in all the other units.

The OBD II monitor is connected to the ECU and detects failure and failsafe action conditions. The AT control ECU receives the signals from the interface box and performs shift control every 10 ms.

As shown in Fig. 2, the DSP system and ECU are connected via the interface box and relay box.

2.2. AT HILS Model

2.2.1. Model configuration

As indicated in Fig. 3, AT can be divided into the torque transmission system, which is part of the power plant, the hydraulic control system, and the ECU, which is part of the AT electronic element control.

In this HILS, the torque transmission system and the hydraulic control system were mathematically modeled[(1)], and the HILS was connected to an actual ECU through the

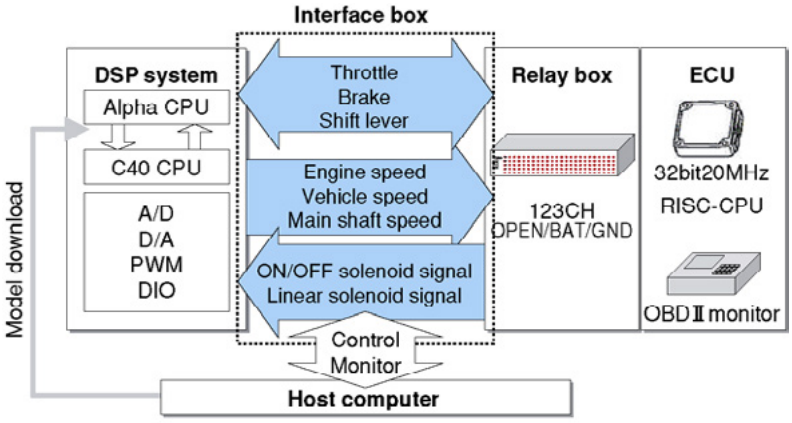


Fig. 2 HILS system schematic

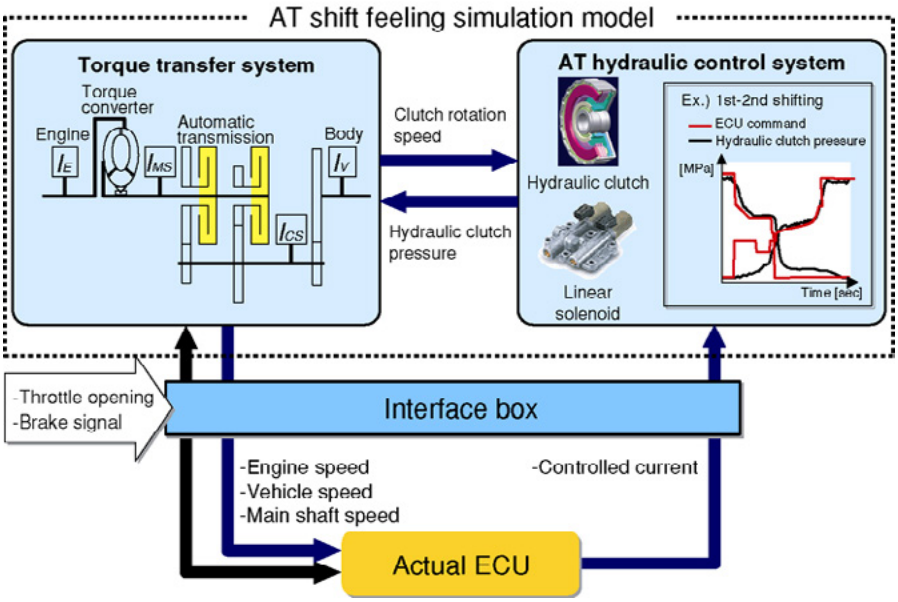


Fig. 3 AT electronic control system schematic

interface box. The following section describes the mathematical models of the torque transmission system and the hydraulic control system.

2.2.2. Model of torque transmission system

Figure 4 illustrates the power flow. Engine torque is supplied by the crankshaft and transmitted through the torque converter to the main shaft. Next, it passes through each gear clutch to the countershaft, and through the final speed reduction gear to the drive shaft. It is possible to calculate the characteristics of the torque transmitted and the rotational speed of each shaft with numerical integration like the Runge-Kutta method.[1), 2)] The expressions for this method are shown below:

Crank shaft	$T_E - T_{MS}/t - I_E \cdot \omega_E = 0$	(1)
Torque converter	$T_{MS} = t \cdot c \cdot (\omega_E/1000)^2$	(2)
AT Main shaft	$T_{MS} - T_L - T_H - I_{MS} \cdot \omega_{MS} - 0$	(3)
AT Counter shaft	$T_L \cdot i_L + T_H \cdot i_H - T_{CS} - I_{CS} \cdot \omega_{CS} = 0$	(4)
Drive shaft	$T_{CS} \cdot i_F - T_{LOSS} - I_V \cdot \omega_V = 0$	(5)
Hydraulic clutch	$T_{CL} = \mu \cdot n \cdot r \, (P_{CL} \cdot A_{CL} - F)$	(6)

Nomenclature

I	: Inertia [N · m · s^2]
i	: Gear ratio
ω	: Angular velocity [rad/sec]
T	: Torque [N · m]
t	: Torque ratio of the torque converter
c	: Pump capacity coefficient of the torque converter
μ	: Clutch disk friction coefficient
n	: Number of clutch disk
r	: Clutch disk effective radius
P	: Hydraulic clutch pressure
A	: Hydraulic clutch piston bearing area
F	: Clutch return spring load

Subscripts

E	: Engine
MS	: Main shaft
CS	: Counter shaft
V	: Body
H	: High gear
L	: Low gear
F	: Final gear
CL	: Hydraulic clutch
$LOSS$	: Running resistance

2.2.3. Model of hydraulic control system

Figure 5 represents the structure of the hydraulic control circuit for the AT. The pressure from the oil pump is supplied through the regulator valve to the shift valves, linear solenoids, etc. to control the pressure at the clutches for each shift stage.

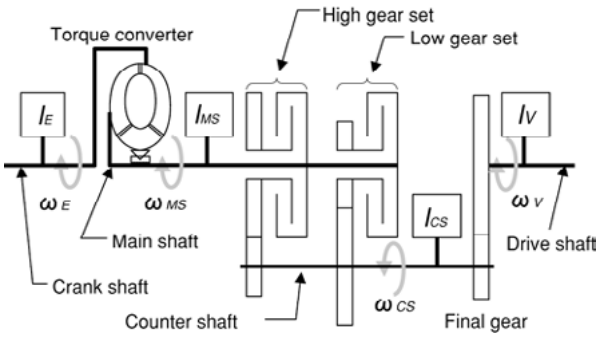


Fig. 4 The parallel shaft type AT schematic

Since applying this hydraulic control circuit within the HILS lightens the calculation load for the model, the transfer function for the hydraulic pressure (Fig. 6) was adopted. As shown in Fig. 7, this transfer function predicts the control pressure at each clutch, in accordance with the hydraulic control command. It defines the settling time, which is the period from the starting time of a control command to the time when the oil in the clutch is completely filled, leaving the deviation with respect to the command within the standard range.

The hydraulic pressure transfer function consists of the adjustable delay time and the variable first-order time-lags. The coefficients for adjustable delay times and the first-order time-lags were each expressed with AT fluid temperature, clutch speed and clutch control pressure in two types of 4-dimensional maps, one for release and one for engagement. The first-order time-lag coefficient maps were determined using a general maximum likelihood estimation method, taking into account the experimentally revealed characteristics of AT oil during transmission shifting.

Figure 8 displays the results of a simulation of the clutch control pressures during 2nd – 3rd upshift, obtained with the model incorporating the hydraulic pressure transfer function. This shows a good match with the experimental results in an actual transmission. The predictions of the clutch control pressures with this simulation method closely reproduce the influence of the dynamics of the hydraulic control system. Also, using the hydraulic pressure transfer function reduced the CPU calculation load to just 1/30 of that necessary with the conventional detailed model at the same level of accuracy.[1)]

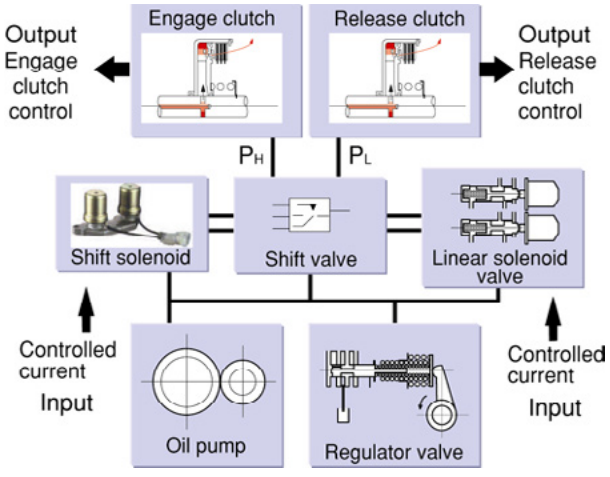


Fig. 5 AT hydraulic control system

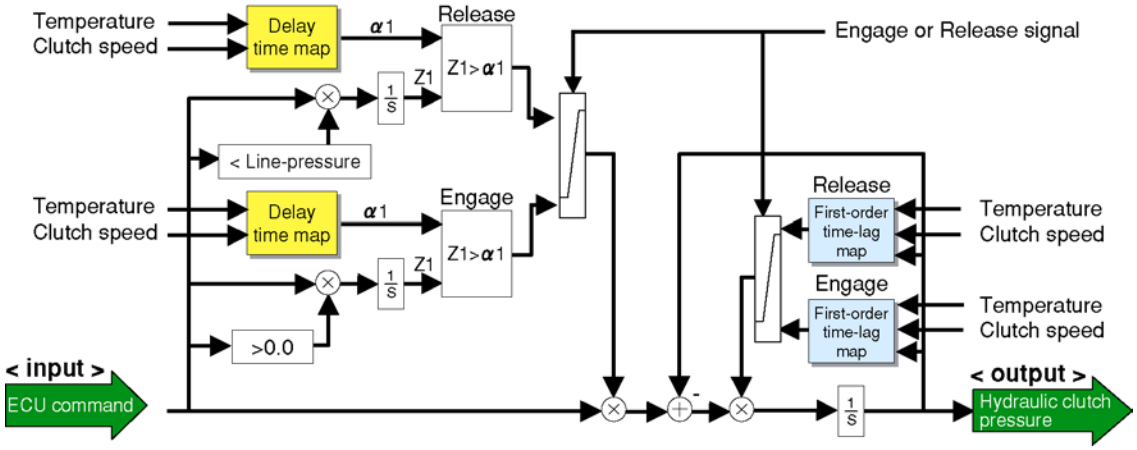


Fig. 6 The transfer function hydraulic pressure

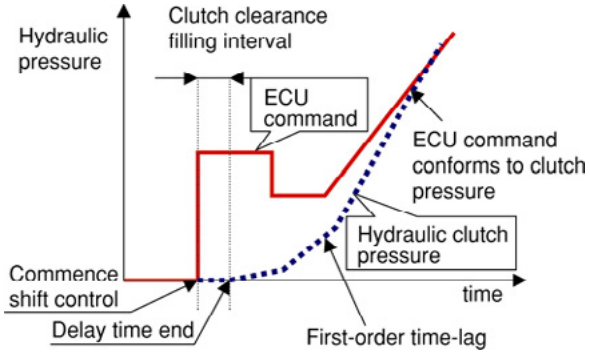


Fig. 7 Delay time and first-order time-lag

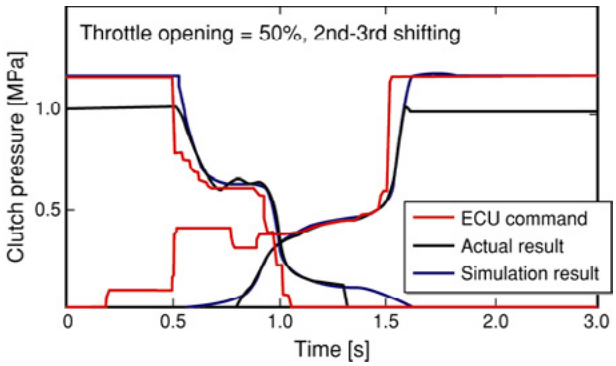


Fig. 8 Verification results of simulation accuracy

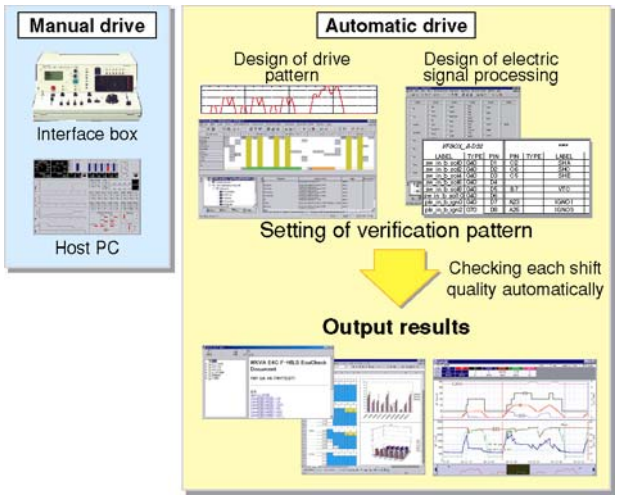


Fig. 9 Environment of HILS test

Table 1 HILS parameters

Classification	Element
Engine	Engine torque irregularity
Clutch	Coefficient of friction
	Clutch clearance
Condition	Vehicle weight
	Grade resistance
Mechanical trouble	Electronic circuit (Short circuit, Broken wires)
	Hydraulic circuit valve

2.3. Environment of HILS Test

This HILS system allows both manual drive tests and automatic drive tests, as shown in Fig. 9.

In the manual drive test, the operator controls the HILS by setting the levers and switches in the interface box, directly operating the interface on the host computer.

In the automatic drive test, the HILS is controlled by activating pre-written programs which set the parameters listed in Table 1 and others, including those of the cruise mode. No further action by the operator is necessary.

In this test mode, the AT shift control system is automatically assessed according to the items in Table 2. The test results are outputted in an HTML-format test report file including tables and graphs.

A data analysis tool was developed which was capable of processing large numbers of data channels with high sampling rates. The analysis tool helped streamline the

Table 2 HILS evaluation method for AT control system

1	The engine speed must not flare while shifting.
2	Heat of the clutch must be lower than standard.
3	Shifting time must be shorter than standard.
4	Change of drive shaft torque must be smaller than standard.
5	The trouble should be able to be judged accurately.
6	It must be able to run.

process, allowing HILS to analyze and process the results from a huge number of tests in a short time.

Verification of the OBD II must use the same automotive situation under many driving conditions. Failure of the ECU must be detected under a large variety of types and patterns of failure, including various combinations in double failures under various timing patterns.

It was confirmed that HILS was an effective development aid technology for conducting tests that would be difficult to create in an actual vehicle. The automatic testing and analysis environment provided by HILS shortened development time and improved control reliability.

3. Adapting Simulation for Real-time Testing

3.1. Issues in Real-Time Simulations

In order to realize a real-time simulation, it is necessary for the CPU execution time to be less than the sampling rate.

The existing torque transmission system model described in section 2.2 was used. The results of a non-real time simulation of a 1st – 2nd upshift are shown in Fig. 10.

The characteristics of the hydraulic pressure observed in a real car were used as the input for this simulation and the output variable was the drive shaft torque. The sampling rate was first set at 20 μs to obtain the same level of precision as in a test of an actual vehicle; for comparison purposes, it was also set at 200 μs, one-tenth the precision.

At the sampling rate of 200 μs, the drive shaft showed a large oscillation in torque, indicating that this sampling rate did not yield enough precision in the calculations.

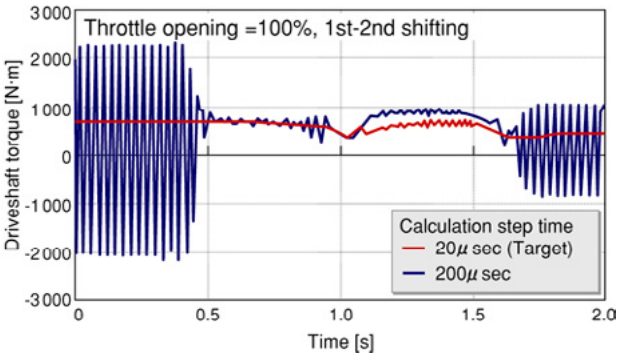


Fig. 10 Non-real-time simulation result

It is notable that when the same test was performed at a single rate in an AT HILS system using a commercial DSP system (Fig. 1), the CPU execution time, corresponding to the sampling rate, was 140 μs.

These results show that fast CPU execution times are necessary in order to observe the AT shift feeling in real time. Therefore, two improvements were performed; multirating of the HILS model and reduction of the scheduler overhead.

3.2. Multirating

Multirating is a well-known, effective method for obtaining the maximum performance from a CPU with limited execution speed.

The HILS model (2.2) was analyzed in detail to examine the practicality of multirating.

This analysis showed that the time constant of a component consisting of a combined λ function and an integrator was the smallest component of all, and was about 20 μs. In other words, this component was the dominant factor in the necessity for the very short sampling rate necessary to obtain an accurate reproduction in this model of tests in an actual vehicle.

The reason that a very short sampling rate is required is the component consists of a combined λ function and an integrator representing the rotational inertia of the main

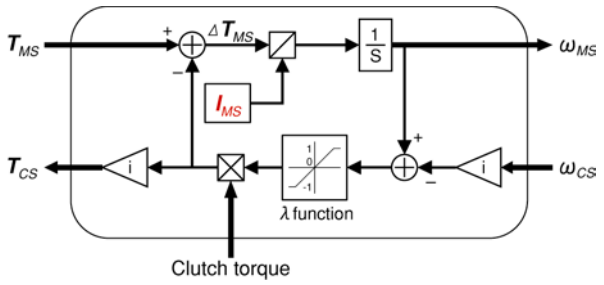


Fig. 11 λ function model for AT torque transfer model

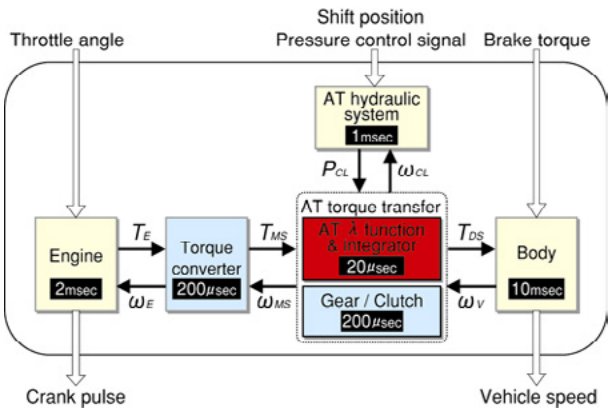


Fig. 12 Multi-rating AT HILS model

shaft (I_{MS}), which is 7.0×10^{-3} N· m· s^2 which is much smaller than the inertia of the engine and vehicle body. Since there were no other such factors influencing accuracy in the rest of the model, the sampling rate was increased to longer than 200 μs. Figure 12 shows the layout of the multirated HILS model and the sampling rates in the other parts of the model.

3.3. Reduction of Scheduler Overhead

Generally, the scheduler overhead must be increased during multirating.

After the multirated HILS model had been actually downloaded and the CPU execution time of the entire model had been measured, it was found to be 108% of the sampling rate of the entire model (upper portion of Fig. 13). This was attributed to the very large fraction of execution time taken up by the scheduler overhead.

The following steps were taken to reduce the scheduler overhead.

As shown in the lower portion of Fig. 13, the only part of the system consisting of the combined λ function and integrator (Fig. 11) which requires minimum sampling rate was programmed to take a certain number of repetitions of sampling; namely 10 times in 200 μs, as necessary for this component within sampling rate. A user code block was used for this.

When the version of the HILS model with the user code block was downloaded and the CPU execution time for the entire system was measured, it was found to be a maximum of 135 μs, including the scheduler overhead. The CPU execution time was 68% of the sampling rate for the entire model, which was judged to leave a sufficient margin.

Thus, a high-speed HILS, capable of approximating a sampling interval of 20 μs, was developed using multirating and by reducing the scheduler overhead.

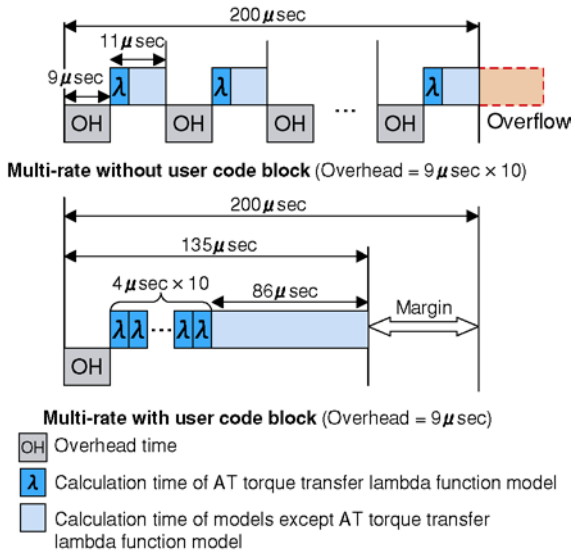


Fig. 13 Measuring results of actual CPU execution times

3.4. Verification of Precision of AT HILS Calculations in High-Speed Simulation

Figure 14 shows the results of a simulation of a 1st - 2nd upshift, as in section 3.1, by the new HILS with multirating and reduced scheduler overhead.

It is clear from the results of the non-real-time simulation using the 20 μs sampling rate, that this simulation method can be used in place of actual vehicle testing. Actual vehicle test data matches well with the results from the HILS model. This means that a real-time simulation for AT shift feeling incorporating a real ECU is accurate enough to replace testing in an actual vehicle.

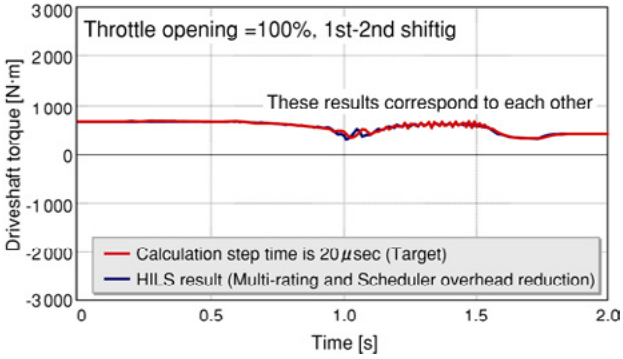


Fig. 14 HILS result

4. Example of Applications

A case of application of HILS in development of an automatic transmission control system is introduced here. Both shift feeling and durability were maximized in optimizing ECU data for this product.

In the conventional development flow shown in Fig. 15, i.e., the pre-HILS process, the durability testing was performed in actual transmissions after the desired data had been preferentially obtained for shift feeling. When malfunctions became evident during durability testing, testing was stopped and ECU data was reset for another round. Testing was repeated so as to find the optimal ECU settings for the product.

In contrast, in the new developmental flow incorporating HILS, ECU data is set by HILS to maximize the reliability of the results in terms of durability after shift feeling tests, prior to the durability tests. A single, final test is then required to verify durability.

Figure 15 shows an example of how the optimized ECU data was identified with HILS after the higher-priority tests of shift feeling had been run to set the data, in the new development flow.

Figure 16 displays the results of the test for a 2nd – 3rd upshift with the throttle opening set at 50%; ECU data had been set to prioritize shift feeling. Figure 17 displays the same results, except that both shift feeling and durability had been given high priority.

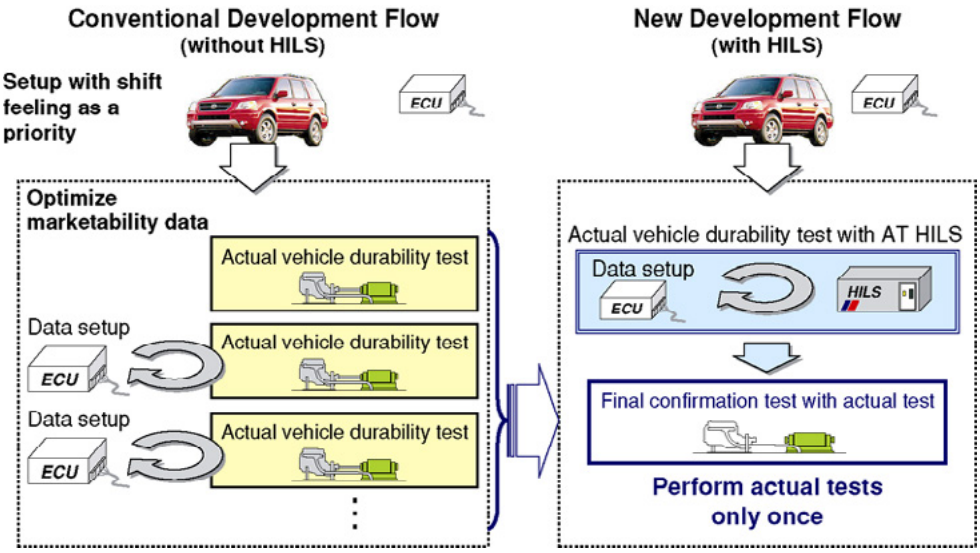


Fig. 15 Optimum data setup balancing shift feeling and durability

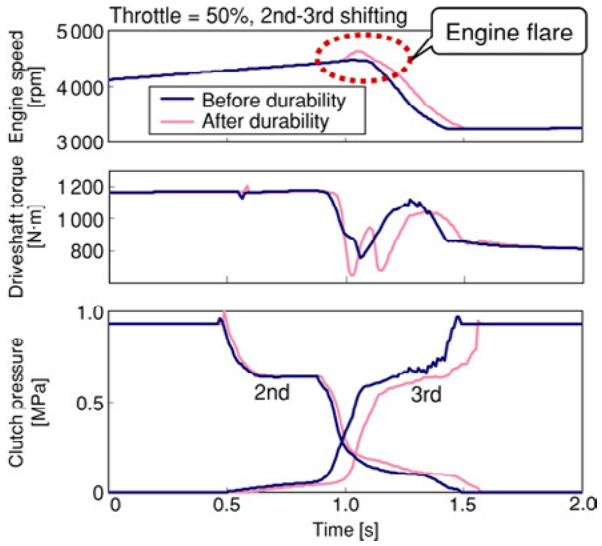


Fig.16 HILS results with initial ECU data

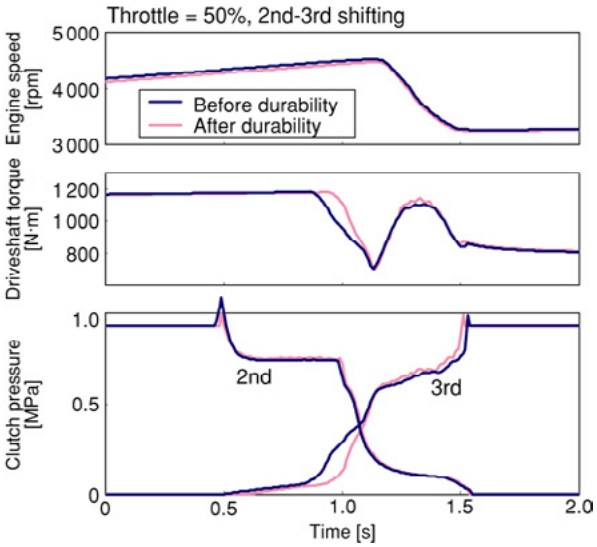


Fig.17 HILS results with refined ECU data

The figures show that the predicted variation in performance after the effects of use had changed the factor of clutch clearance, according to the ECU settings and analysis with HILS.

A good shift feeling was initially obtained, but this deteriorated with use and there was eventually an engine flare during shifting, as shown in Fig. 16. The ECU data were reset, because of this malfunction; specifically, the feedback gain of the 2nd and 3rd hydraulic clutch pressure control was optimized.

As a result, the shift feeling was good both initially and after wear (Fig. 17).

The durability test of an actual transmission was run after the ECU data had been optimized with HILS. This confirmed the maintenance of good shift feeling.

Thus, it has become possible to develop optimized product ECU data in a short time, without waiting for a time-consuming durability test of an actual transmission.

5. Summary

(1) A transfer function of hydraulic pressure composed of an adjustable delay time and variable first-order time-lags was created in order to reduce CPU calculation load in transmission modeling; CPU load was found to be 1/30 that in conventional detail modeling methods.

(2) Multirating and reduction of the scheduler overhead were accomplished in order to attain a high-speed 20 μs execution time, which allowed use of a commercial DSP to carry out real-time simulations of AT shift feeling with

sufficient accuracy to replace testing with actual transmissions.

(3) By applying HILS to the development of the AT control system, it has been proved that real model testing can be replaced with desktop testing, which in turn can shorten development time while simultaneously improving AT control systems.
The HILS method will be applied in all types of AT control system development because it shortens the development times for reliability improvements in AT control systems.

References

(1) Ishikawa, K., et. al.: The Development and Utilization of ACTASS, AVEC '94, pp. 224-229 (1994)

(2) Sakuraba, T., et. al.: The Unification of Simulation Model between Fuel Economy and Acceleration Performance, HONDA R&D Technical Review, Vol. 7, pp. 79-86 (1985)

■ Authors ■


Yohei TAKEDA


Ko YODA


Satoshi TERAYAMA


Kenji HAGIWARA


Yoshiharu SAITO


Tsutomu KAMIYAMAGUCHI

Establishment of Design Method for Transmission by 3D Media

Hiromi SHIMADA* Yoichiro ISHIHAMA*
Nagomu KUBOTA* Takanao UCHIDA*

ABSTRACT

Design trials with 3D media in the product development of transmissions revealed that increased design times became an issue. Consequently, research was performed on measures to resolve this issue, including the building of a 3D design process, development of the necessary 3D CAD functions needed for such a process, establishment of 3D drawing rules, and review of the development process. Design methods were then built that utilize 3D media consistently from layout to product drawing. With use of the newly built 3D design methods, design time was reduced to the level of design using conventional 2D media or even less. This made it possible to build a highly efficient development system for use from design to manufacture.

1. Introduction

In recent years, the use of 3D media in product development has quickly become widespread among automobile developments in the hope that it will improve their efficiency. Improvements in the following are expected from the introduction of 3D media throughout the process from design to manufacture:

(1) Improvement in analyses of design by application of 3D modeling to CAE.
(2) Improvement in analyses of interference between neighboring parts in 3D model layout.
(3) Analysis of the shapes of parts using rapid prototyping of real shapes.
(4) Reduction in die production times due to use of 3D models in CAM (prototypes, mass production) for dies.

To achieve the above effects in transmission development, design with 3D media (3D design) was used in a trial design of a transmission case, a basic transmission part. The case is shown in Fig. 1. However, the test result was anything but promising, as illustrated in the bar graph in Fig. 2: the 3D design trial took 3.3 times as much design time as it would have required while using conventional design with 2D media (2D design). The following countermeasures were established, but did not result in much reduction in design time:

(1) Thorough re-training of designers in use of 3D design.
(2) Improvement of 3D CAD functions.

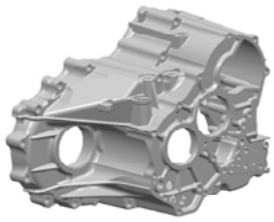


Fig. 1 3D model of a transmission

* Tochigi R&D Center

Accordingly, it was concluded that a fundamental review of design methods would be necessary in order to reduce the 3D design time and to establish 3D design, and this study was instituted.

2. Aim of Study

The aim of this study is to draw about appropriate methods of measures and to conceive a highly efficient design method, based on an analysis of the factors causing the increase in design time during the 3D design trial. The target was set of reducing 3D design time below 2D design time.

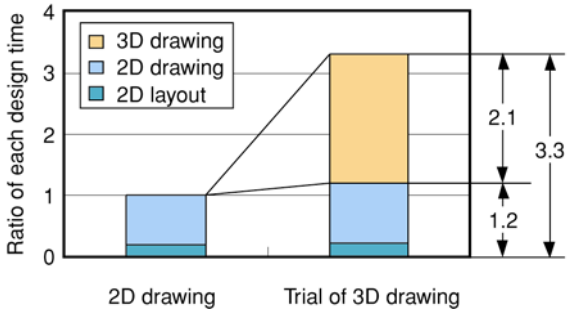


Fig. 2 Comparison of design times

3. Analysis of Factors in Increase in Design Time During the 3D Design Trial

3.1. Analysis of the Design Work

The first step in analysis of the factors increasing design time was to study the design works. These are shown in Fig. 3.

(a) 2D layout:
The transmission is laid out in 2D in accordance with the basic specifications.

(b) Creation of 2D drawings:
Product shapes are studied on the basis of the 2D layout, and 2D drawings are made.

(c) Creation of 3D drawings:
3D product shapes are studied on the basis of the 2D drawings, and 3D drawings (the formal designation for the 3D models at the drawing issuance) are made.

In the above process, the 2D design process consisting of (a) the 2D layout and (b) creation of the 2D drawings in 3D design process was assumed to be a factor increasing design time.

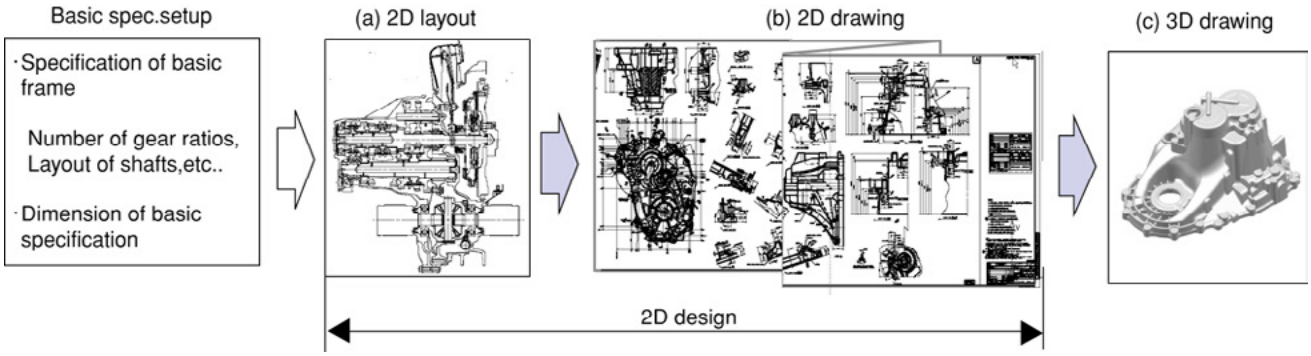


Fig. 3 Design work with the trial of 3D design

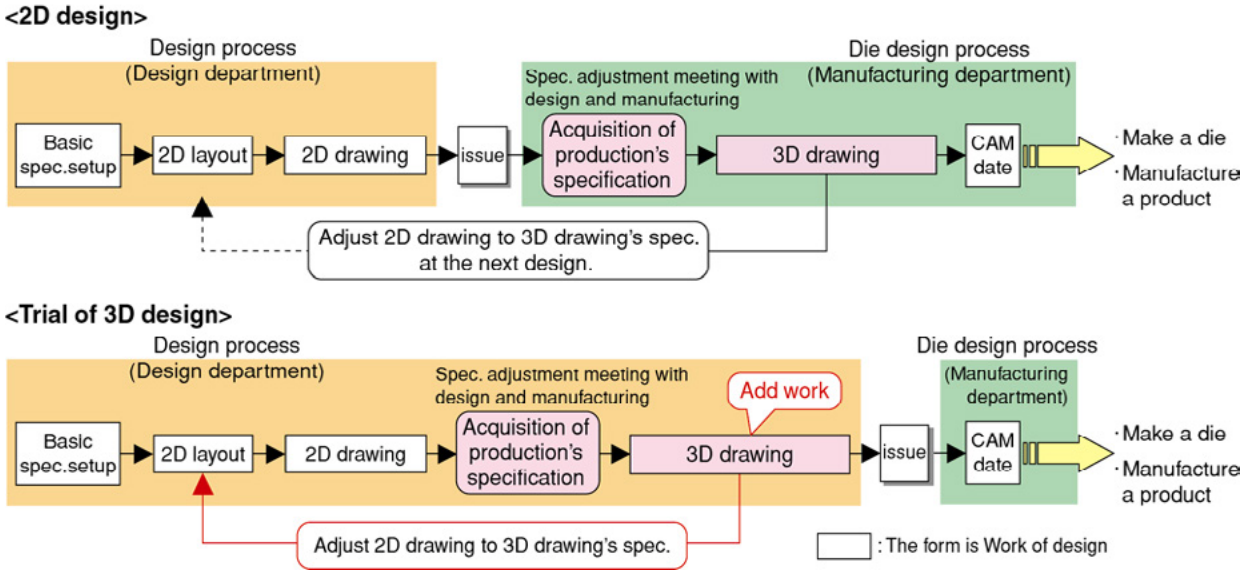


Fig. 4 Comparison of development process with 2D design, and the trial of 3D design

3.2. Factors Due to Design Process

The 3D design trial and the 2D design process were compared to examine the design time in the various design processes and works. As shown in the design process in Fig. 4, the largest factor in design time increase was the addition of 3D drawing creation to the process of 2D design. It was also noted in Fig. 2 that the design time for 3D drawing made up 2/3 in the total time of the 3D design trial.

3.3. Factors in Work of Creating 3D Drawings

3.3.1. Analysis of shares of design time for works in creation of 3D drawings

The work times necessary for the various works in 3D design of the transmission case shown in Fig. 6 were analyzed for the reasons causing 3D drawing to consume 2/3 of the design time during the 3D design trial. As shown in the pie chart in Fig. 5, creation of the 3D drawings of the product shape accounted for only 23% of the work time. Other than this factor, simply waiting for the calculation processing necessary for 3D CAD (computer-aided design) accounted for about 1/2, and corrections to the product shapes in the 3D drawings, about 1/4, of the time.

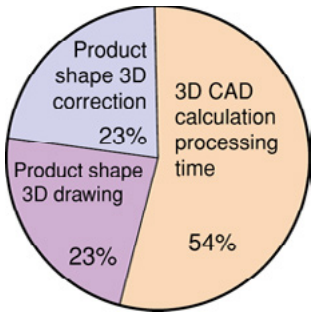


Fig. 5 Percentage of each time taken by 3D drawing work

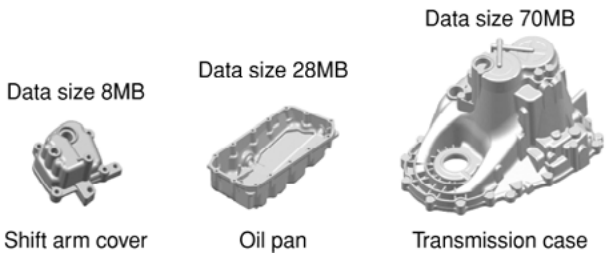


Fig. 6 Cases of various shapes

3.3.2. Factors in time required for calculation processing of 3D CAD

As shown in Fig. 6, there are a variety of shapes in the transmission cases. The relation between the data size of 3D drawing and calculation processing time in 3D CAD was examined. The results are graphed in Fig. 7; it is clear that the processing time increases in what resembles a curve of 2nd-order relation with the data size of 3D drawing. The transmission case used for this factor analysis has 70 MB of data size; that is why calculation time took up 54% of 3D drawing design time.

3.3.3. Factors in time required to correct product shapes

Creation and correction of the product shape 3D drawings were the works performed in die design; analysis of these works showed that the most time-consuming portion was setup of part thickness during drawing corrections. The results of this analysis are given below, with reference to Fig. 8.

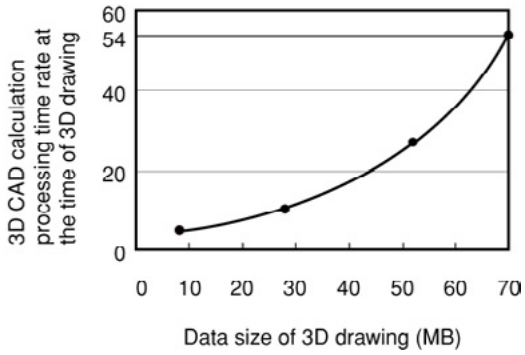


Fig. 7 Relation between data size of 3D drawing and 3D CAD calculation processing time

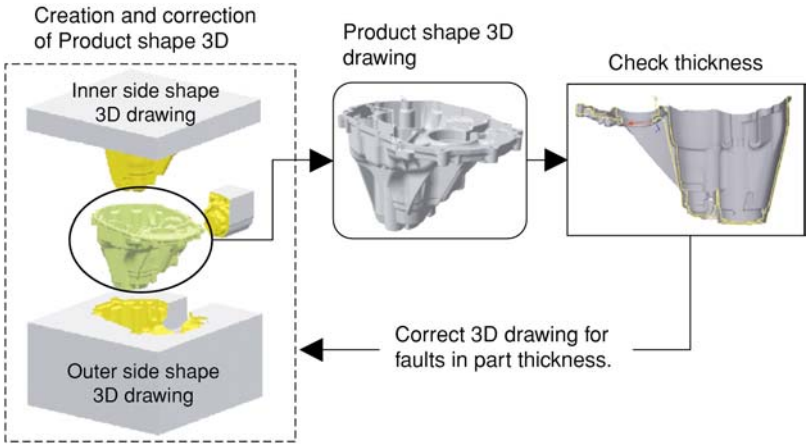


Fig. 8 “Product shape 3D drawing” and “Product shape 3D correction” work

(1) Creation of the product shape 3D drawings
3D drawings of both the exterior shape and the interior shape of the case were made from 2D drawings. The interior shape was deleted from the exterior shape, a process resembling casting a product by die, in order to make the 3D drawing of product shape.
(2) Correction of the product shape 3D drawings
The part thickness was verified on the product shape 3D drawings and the locations with the wrong thickness were identified. Mismatches between the exterior and interior drawings turned out to be factors in these locations, so these mistakes were corrected to complete the drawings.

3.4. Factors Due to Development Process

In order to create 3D drawings of the product shapes in the course of actual use of the die manufacturing CAM data created by the design department, it is necessary to obtain information of production's specification from the Manufacturing department such as the location and shape of the die parting line (see Fig. 9), draft angle, and corner roundness[(1)]. In the development process in the trial of 3D design shown in Fig. 4, after the 2D drawings had been made, there was a specification adjustment meeting performed by the 2D drawings between Design and Manufacturing. Once the information of production's specification had been obtained, the 3D design was initiated. At the same time, it was necessary to reconcile differences in specifications between the 2D and 3D drawings during this part of the process. As a result, there was an increase in design time for creating the 2D layout and drawings, 1.2 times that required in conventional 2D design, as shown in Fig. 2. By the way, the specifications for 2D design were adapted to those of the 3D drawings of the Manufacturing department in the next design cycle, as shown in Fig. 4.

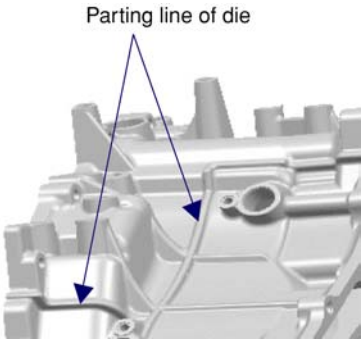


Fig. 9 Parting line of die

3.5. Summary of Factors in Increase of Design Time

As a result of this analysis of the factors affecting design time, the increase in time was attributed to the following items:
(1) The work of creation of 3D drawings was added after 2D design.
(2) Calculation processing time in 3D CAD accounted for about half of work time in creating 3D drawings.
(3) Part thickness setup accounted for 1/4 of work time in creating 3D drawings.
(4) Acquisition of production's specification information was late.

4. Methods for Reducing 3D Design Time

4.1. Issues in Establishing the Method for Reducing 3D Design Time

In consideration of the above factors in increased design time, the following issues were identified for establishing a method for reducing the design time.
(1) Establishing a 3D design method
- 3D design process
- Method for creating 3D drawings from 3D layout

(2) Development and application of 3D CAD functions
- Development of 3D CAD functions offering convenient thickness setup
- Reduction in 3D CAD calculation processing time by dividing 3D drawings
- Improving functionality of automatic creation of 2D drawings from 3D drawings

(3) Obtaining information of production's specification at the layout stage
- Reconsidering development process

4.2. Establishment of 3D Design Method

4.2.1. 3D design process

A fundamental of the design process is that product shapes are investigated in the layout stage, then manufacturing drawings are made. Therefore, this was also a fundamental of the 3D design process, as shown in Fig. 10; layouts were made using 3D media, the shapes of the products were verified, and then, 3D drawings were created. Also, a method was established for creating 2D drawings automatically using the 3D drawings at the same time.

4.2.2. Method of creating 3D drawings from 3D layouts

In order to create 3D drawings from the 3D layouts and to furnish a convenient method for creating walls with uniform thickness in the drawing, the method and system using 3D CAD functionality shown in Fig. 11 and described below were established.

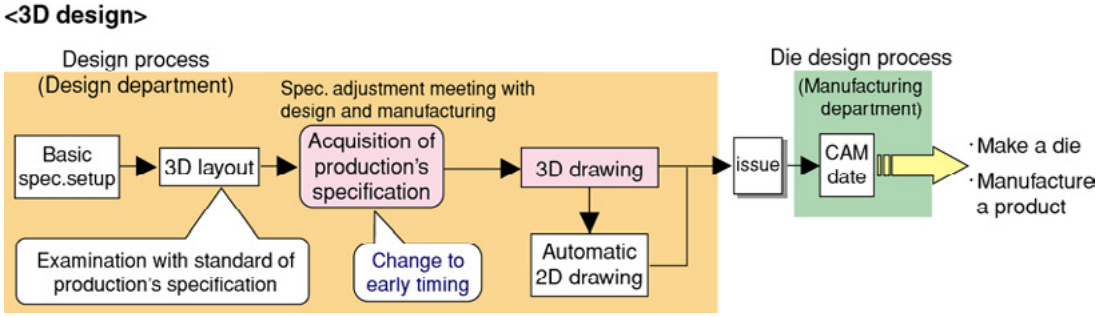


Fig. 10 Change of a development process

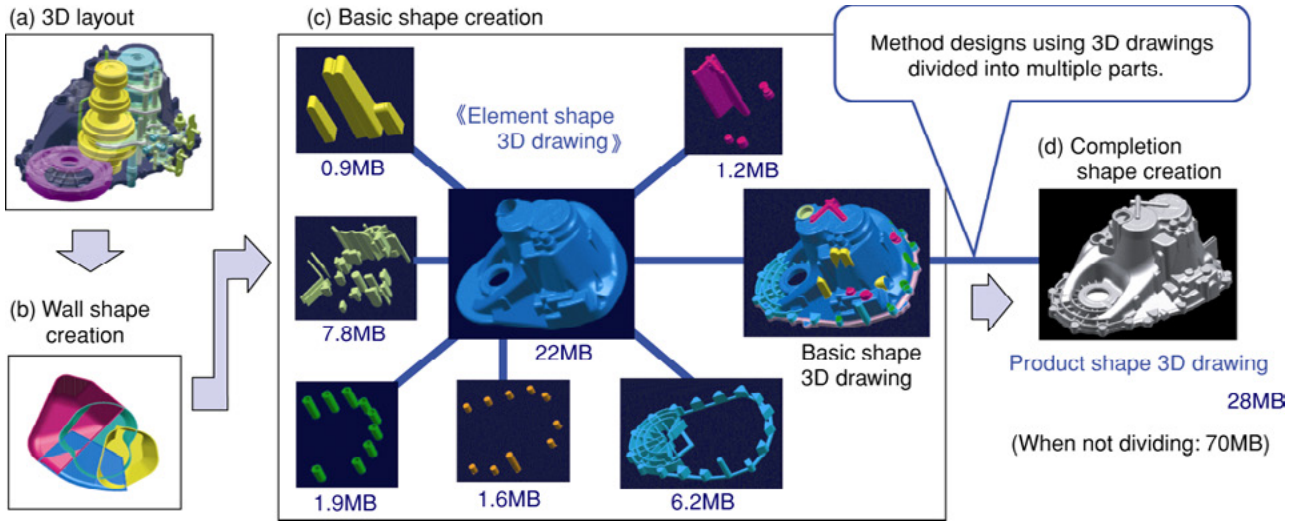


Fig. 11 From the 3D layout to the 3D drawing method

(a) 3D layout:
A 3D layout of the transmission case was made based on the basic specifications.

(b) Creating wall shape:
Using the 3D layout, the wall shape was created by indicating the wall thickness, considering clearances from inner components. (a 'shell' functionality was developed).

(c) Creating the basic shape:
Bosses and other features were added to the wall shape, then, unnecessary portions were removed, and a 3D drawing of the basic shape was made (a 'trim' functionality was developed).

(d) Creating the final shape:
Corner radii (fillets) were added to the basic shape to complete design of the product.

4.3. Development and Application of 3D CAD Functionalities

4.3.1. Development of 3D CAD functionalities offering easy creation of uniform thickness wall

The new 3D CAD functionalities described below were developed for creating the 3D drawings from the 3D layouts. The functionalities are described in Fig. 12.

(1) 'Shell' function
A clearance is defined from the outer shape of internal components. Then, the wall thickness is indicated, instantly creating a wall shape with a uniform thickness.

(2) 'Trim' function
Unnecessary portions of bosses added to a wall are selected and deleted.

These 3D CAD functionalities were requested to a software maker and developed in a joint effort; a method and system for turning 3D layouts into 3D drawings and for the easy creation of uniform thickness walls were established.

4.3.2. Reduction in 3D CAD calculation processing time by division of drawings

In order to reduce the amount of 3D drawing data and thereby reduce calculation processing time, each drawing was divided into multiple, independent 3D drawings. The advantage offered by this division function is explained below with reference to Fig. 11. When a 3D drawing occupying 70 MB was divided into seven element- shape 3D drawings and a product-shape 3D drawing, the total data size was reduced to 28 MB. As a result, the load on the computer posed by calculation processing was relieved; as shown in

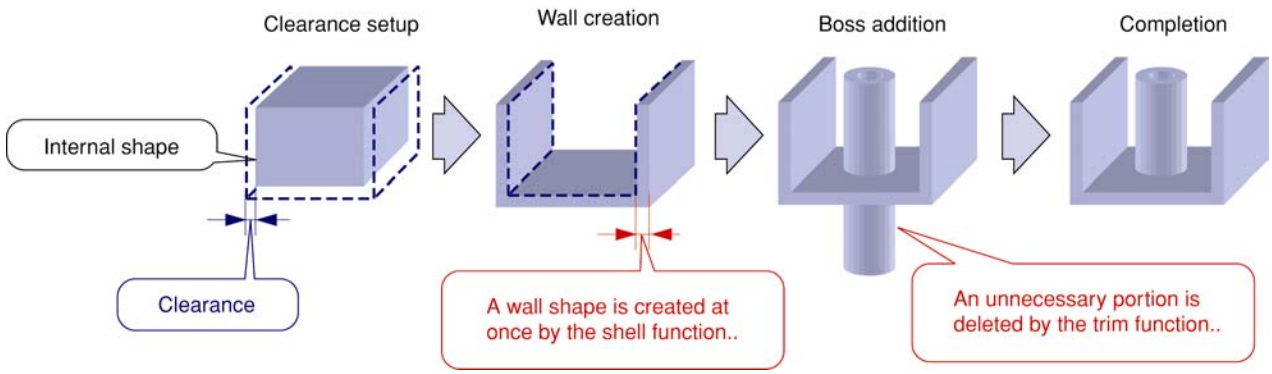


Fig. 12 Shell function and trim function

Fig. 13, calculation processing time was cut from 54% of the total design time to 10%.

4.3.3. Improvement of automatic functionalities to create 2D drawings from 3D drawings

It became necessary to expand 3D CAD function to improve efficiency of creation of 2D drawings. As shown in Fig. 14, the software included automatic functions to create a 2D view from a 3D drawing and to create sectional views, but these functions were somewhat prone to the errors shown in Fig. 15; one line was duplicated, while another is only partially shown. Authors and a 3D CAD software maker cooperated in correcting the errors for these functions, resulting in correctly working functions and a greatly reduced labor time for creating the 2D drawings from the 3D drawings.

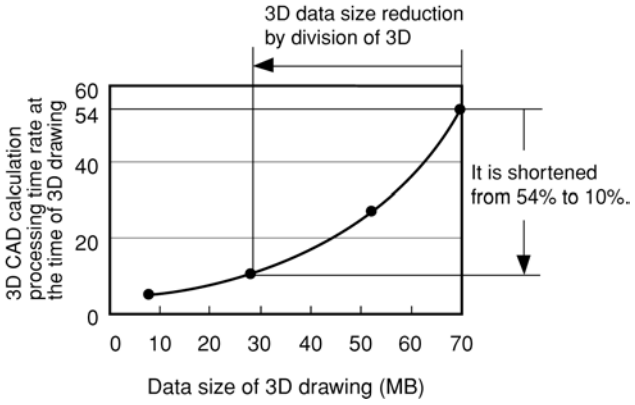


Fig. 13 The shortening effect on 3D CAD calculation processing time

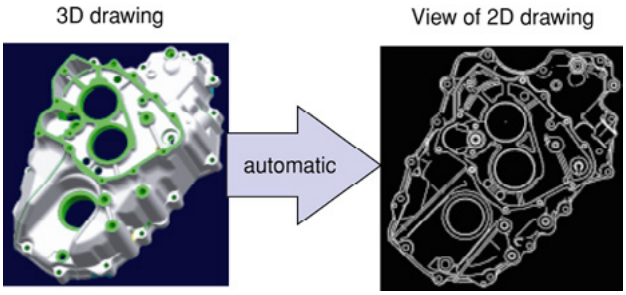


Fig. 14 Automatic drawing of 2D view

4.4. Obtaining Information of Production's Specification at the Layout Stage

As shown in Fig. 10, the development process was revised, with moving forward the specification adjustment meeting between the Design and Manufacturing departments, to enable publication of information of production's specification during the layout stage. This enabled the Design and Manufacturing departments to cooperate in the following issues:

(1) Specification adjustment meeting between Design and Manufacturing should be held with already-completed 3D layouts.
(2) Listing of production's specification action items that should be arranged.
(3) Standardize those items in (2) which can be standardized and apply them in the Design stage before the specification adjustment meeting.
(4) Train all technical staff in charge of production's specification to operate 3D CAD software.
(5) Installing 3D CAD in all departments in charge of examinations over production's specifications.

As a result of these measures, although it was necessary to review the layouts for products whose shapes would be affected by information of production's specification, they obtained drawing corrections after layout preparation, including those necessary to reconcile 2D drawings with 3D drawings (see Figs. 4, 10). The advance examinations in the Design department over production's specifications also contributed to reducing the labor time on the layouts.

4.5. Increasing Efficiency of Manufacturing Department by Revising the Development Process

Owing to revision of the Development process from Design through Manufacturing, it has taken a firm hold to create 3D drawings in the Design department. As a result, labor time for creating drawing in the Manufacturing department was reduced. Furthermore, labor time spent on consultations in Manufacturing was reduced as well since the standardized production's specifications were examined in advance in the Design department.

4.6. Establishment of 3D Drawing Forms

3D drawing forms were established as a part of the institution of 3D design methods. Transmission case drawings require specifications from its manufacturing methods to indicate on material shape and to machining dimensions. Since 3D CAD has no functions to indicate machining dimensions, tolerances, geometric tolerances, or finish instructions, in 3D drawing, it was decided to indicate these on the 2D drawings. As shown in Fig. 16, drawing forms which combines 2D drawing and 3D drawing with material shape definition were established, designated as "3D drawing + 2D drawing"(see Table 1). The labor time for preparation of 2D drawings in the "3D drawing + 2D drawing" was reduced by the time it had previously taken to write the instructions for the shape of the material.

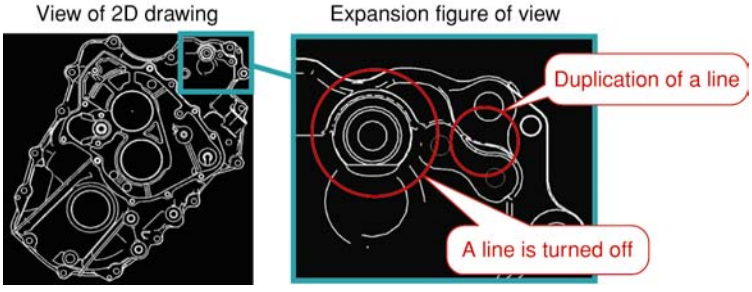


Fig. 15 Shortcomings in function of automatic 2D drawing

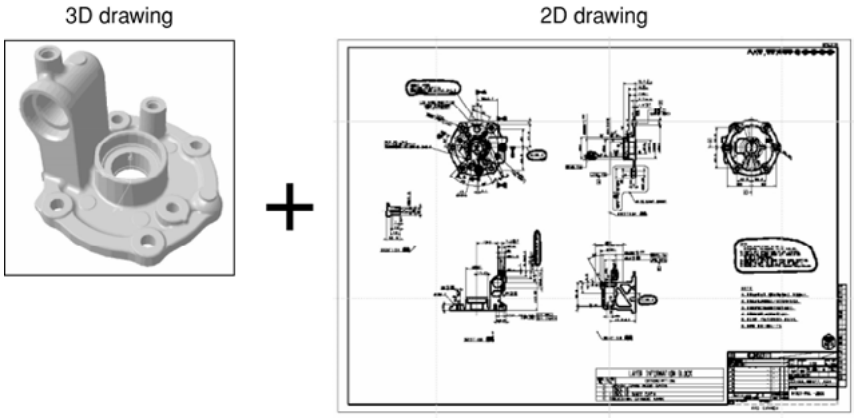


Fig. 16 3D drawing + 2D drawing

Table 1 Drawing rule of "3D drawing + 2D drawing"

Item		3D drawing + 2D drawing		Conventional 2D drawing
		3D drawing	2D drawing	
Material surface dimension		○		○
Machine work dimension			○	○
Tolerance, Geometrical tolerance			○	○
Finish specification			○	○
NOTE	Material, Heat treatment, Pressure leakage standard, hardness, etc..		○	○

4.7. Summary of Methods for Reducing 3D Design Time

The following methods were established for reducing the design time in 3D design:

(1) The process shown in Fig. 17, where 3D drawings are made from 3D layouts; then, 2D drawings are automatically made from 3D drawings.
(2) Functions to create 3D drawings from 3D layouts and to easily create wall with uniform thickness (shell and trim functions).
(3) Division of 3D drawings in order to reduce their data size, shortening the calculation processing time for 3D CAD.
(4) High-efficiency 2D drawing method using automatic creation function from 3D drawings.
(5) Obtaining production's specification information at the layout stage (revising the development process).
(6) Establishment of drawing forms for 3D drawings.

The labor time for the works involved in creation of design drawings with the newly created 3D design method takes about 1/4 the time required in creation of 3D drawings and about 1/3 the time required in layout and 2D drawings compared to the 3D design trial program. As a result, as shown in Fig. 18, the design time with 3D design method is reduced less than that of the 2D design method, which was our goal.

5. Summary

The primary factor of increasing design time during the 3D design trial was the simplistic creation of 3D drawings after 2D design. In order to solve this issue, the transmission design method was fundamentally revised and the following procedure was established for application of 3D media throughout the design course:

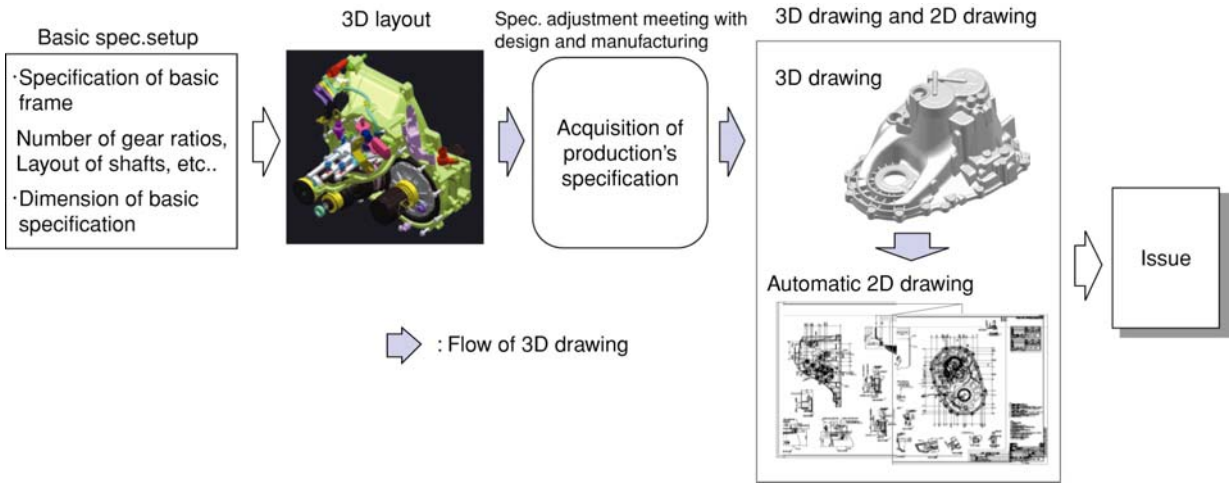


Fig. 17 Design method for transmission by 3D media

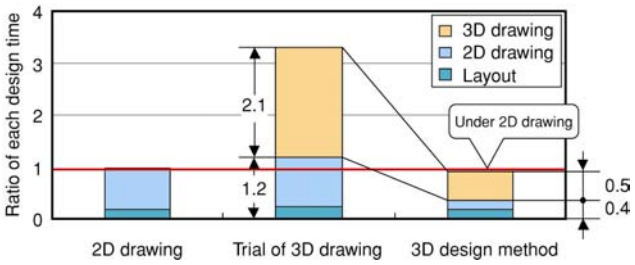


Fig. 18 Effect of the 3D design method

(1) A design process of creating 3D drawings from 3D layouts.
(2) Development of 3D CAD functions for establishing the design process.
(3) Establishment of 3D drawing forms.

The design time under the newly established 3D design method requires less time than that under the 2D design method. A large improvement in design efficiency was realized.

In addition, due to the changeover to a 3D design development process, the work of creation of 3D drawings, which used to be done by the Manufacturing department, has been passed back to the Design department, without labor cost. This has resulted in a highly efficient development system, from Design through Manufacturing.

The authors extend their deepest appreciation to Dassault Systemes, which added and upgraded the 3D CAD functionalities necessary to create this new 3D media-based design method.

References

(1) Kirishima, H., et al.: The Development of Digital Manufacturing Methods in Powertrain Casting Die Department, Honda Engineering Technical Review Vol. 9, pp. 142-147 (2001)

■ Authors ■


Hiromi SHIMADA


Yoichiro ISHIHAMA


Nagomu KUBOTA


Takanao UCHIDA

Development of Stiffness Analysis Technology for Transmission Housing

Masami HIRAOKA* Kouichi TOMITA* Satoru SUZUKI*
Yasutomo IIJIMA* Chikae SASAHARA*

ABSTRACT

A technique was developed for simulating the stiffness and strength of a transmission housing by reproducing the behavior of the housing contact surface. This technique uses non-linear modeling methods to reproduce bolt tightening, positioning with dowel pins, the behavior of contact surfaces with consideration to gasket material and the stiffness of inner parts such as the differential case. The predictive accuracy regarding behavior in an actual transmission increased greatly as a result, and the discrepancy with test results fell to 15% or better. This made it possible to conduct evaluations by simulating the housing stiffness and strength in bench torsion testing at the stage of design. Specialized pre- and postprocessing tools were also developed for widespread dissemination of this simulation technique among designers, shortening the calculation time and labor to the amount of one-third of what it had been.

1. Introduction

Recently, there has been increasing demand lighter and more compact transmissions as well as for improved efficiency in the development of automotive transmissions. Developmental efficiency will require reductions in the number of prototypes; techniques for high-precision predictions of the behavior of the machines are desired for that purpose. The transmission housing in a front wheel drive car typically consists of two parts, left and right halves, joined at large contact surfaces through which the drive reaction forces are transmitted. Since large drive reaction forces of differing directions are applied to the halves of the housing, which are bolted together, the halves slip with respect to each other at the contact surfaces, and it is impossible to predict the stiffness and strength of the housing at the design level with any accuracy with conventional linear analysis. Therefore, it has been necessary to expend much labor time performing repeated tests with prototypes in order to develop mature specifications.

The objective of this study was to construct a versatile, high-precision simulation technology for predicting the stiffness and strength of housings in transmission housing assemblies containing contact surfaces. Special pre- and post-processing tools were also developed to ease use by designers.

2. Behavior in Actual Transmissions

Figure 1 shows the main section of the automatic transmission used for this study. Figure 2 provides the shaft layout and the directions of bearing loads during forward motion. The mating structure where the transmission housing (TM housing) joins with the torque converter housing (TC housing) contains large contact surfaces. The bearing load occurs due to gear reaction forces, which are applied in different direction upon the two housings on each side of those surfaces. The deformation and behavior of the two housing bodies are assumed to be determined not only by the housings themselves but also by the behavior of the contact surfaces.

* Tochigi R&D Center

Deformation and behavior of the housings have been observed under peak load conditions in bench torsion testing of a transmission. Specifications of the test transmission are provided in Table 1. Since the primary concern in a housing is the stiffness at the bearings, displacement was measured at each bearing. A mark was made at the edge of each bearing and the displacement of this mark was recorded with a camera during torque loading (see Fig. 3). The results of these observations are given in Fig. 4. Displacement by every TM housing bearing was, regardless of load vector, in the same direction as the displacement of the differential case support bearing. This indicates that the load on the differential case support bearing of the TM housing dominated the behavior of the housing as a whole. The relative displacement between the TM and TC housings was observed in the vicinity of the differential case support bearing, which carries the highest load of all the bearings (see Fig. 5)[(1)]. The results of those behavioral observations are presented in Fig. 6. Slipping occurred on the contact surfaces around the differential case due to the bearing loads on both halves of it; this confirmed the above assumption that this slipping affected the bearing displacements.

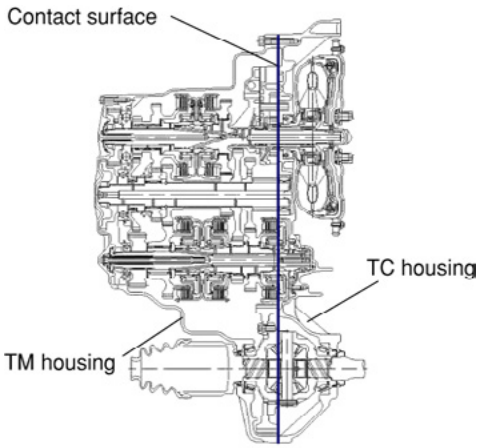


Fig. 1 Main section

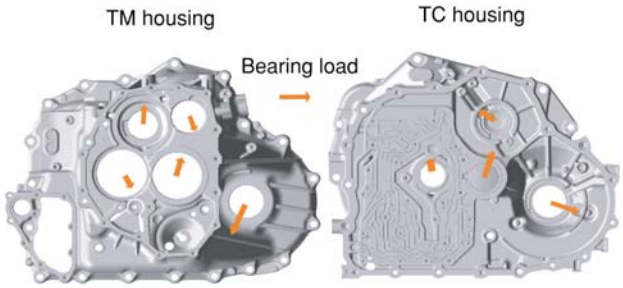


Fig. 2 Direction of bearing load

Table 1 Specification of transmission used in experiments

Type	Transmissible torque	Total gear ratio	Drive system
Type-A	196Nm	12.2	2WD

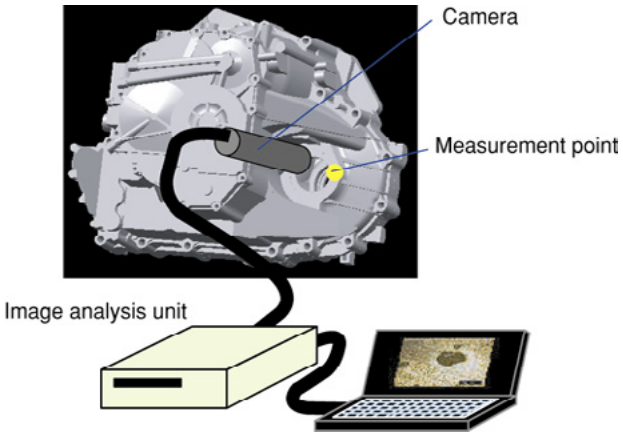


Fig. 3 Measurement method for displacement of bearing

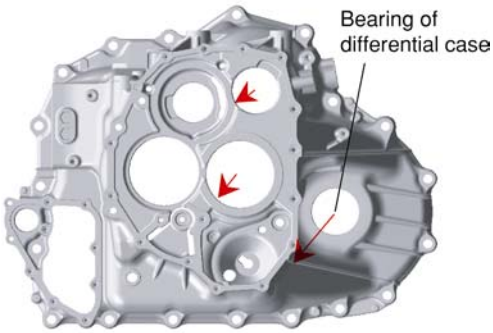


Fig. 4 Result of measurement of displacement of bearing

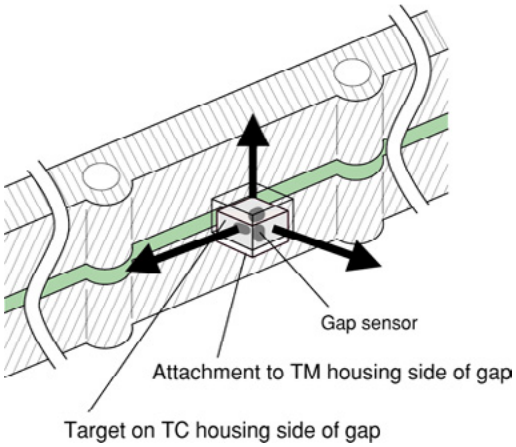


Fig. 5 Measurement method for slip behavior of housing

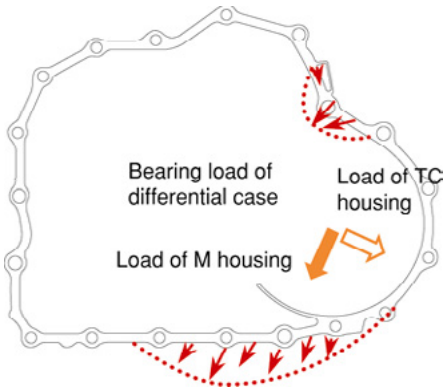


Fig. 6 Result of measurement of relative displacement of housing

3. Establishment of Nonlinear Modeling Technology

Figure 7 shows a graph of the coincidence between the actual observed bearing displacements and the calculated displacements according to conventional linear method relations. Two points were quite inconsistent with the calculation, indicating that linear relations were not accurate enough to be usable. As shown in Fig. 8, these points were on the opposite side of contact surfaces from the standard surface of constraint, and are thus assumed to be affected by the contact surface behavior. It then follows from the above observed behavior that the behavior of the contact surfaces and the loads from the differential case must be reliably reproduced in order to predict housing behavior. Non-linear methods were used in order to reproduce the behavior in the actual transmission. The items incorporated in the model are shown in Fig. 9 and explained in detail below.

3.1. Reproducing Contact Surface Behavior

Slipping on these contact surfaces is believed to occur due to the following factors: the difference in contact pressure between locations immediately under tightened bolts and locations between bolts, and also the application to the contact surface of a shearing force, which is greater than the frictional force caused by the pressure due to the tightening of bolts. Because the shearing force is transmitted from the bearings carrying the loads in the housings via the ribs and the wall surface to the bolt flange, the slip varies with the shapes of these components. The dowel pins and bolts inserted to fasten the housings together also constrain slipping behavior. In other words, in order to reliably reproduce the behavior of the contact surface, it is necessary to reliably reproduce the surface pressure distribution due to bolt tightening, the slipping behavior of the contact surface, and the load transfer path of the housings. In order to reproduce the surface pressure distribution, a separate model of each housing was made and the models were connected to each other with surface contact elements which had been given soft contact properties corresponding to those observed in pressure tests of real gaskets (see Fig. 10). Bolt tightening was modeled as a multi-point constraint at the bolt surfaces and the screw parts using the axial tensions as the loads. The precision of the pressure distribution was confirmed by testing a component. This test piece and the test results are

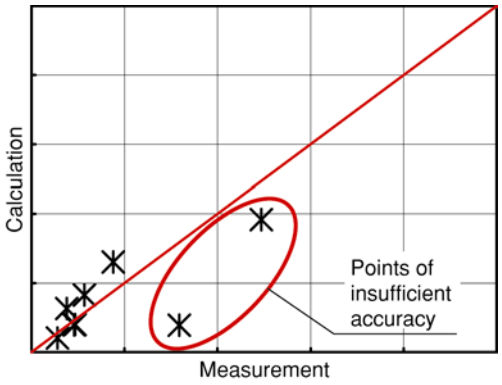


Fig. 7 Comparison of bearing displacement with linear method

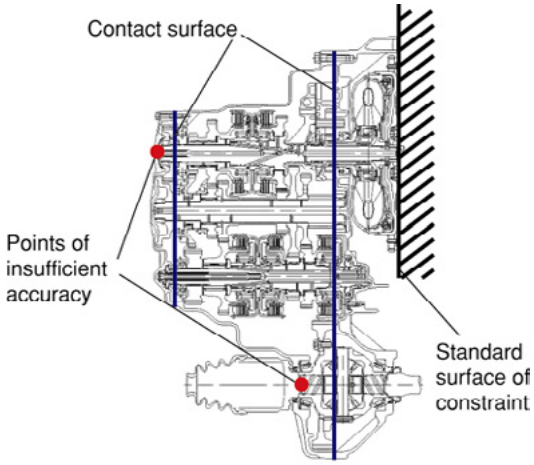


Fig. 8 Point of insufficient accuracy

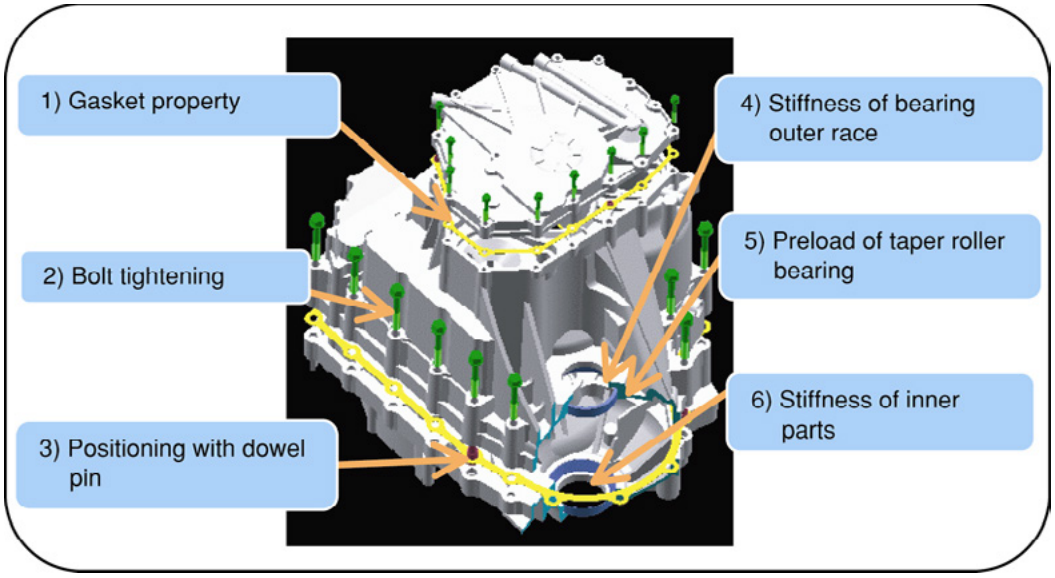


Fig. 9 Items reflected in FE model

shown in Fig. 11. It was found that using the properties of the gasket material enabled good reproduction of the pressure distribution. Next, the following modeling procedure was used to reproduce the behavior of the contact surface. The coefficient of friction of the contact surface was measured and the median of the scattered values was defined as the coefficient of friction. Positioning with dowel pins was modeled using non-linear spring elements possessing backlash and bending stiffness of the bolts was modeled using linear spring elements. The spring constant of those elements was calculated using beam bending theory. Non-linear contact FEM analysis confirmed that this approach was appropriate (see Fig. 12).

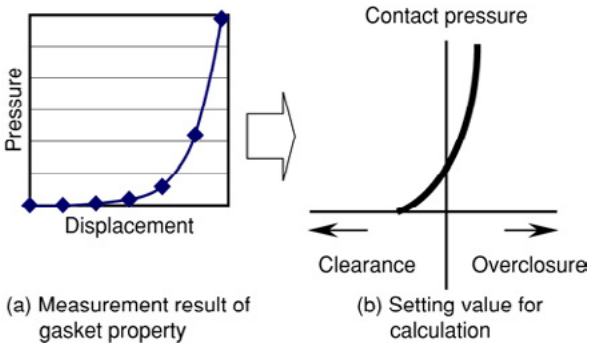


Fig. 10 Softened contact property of gasket

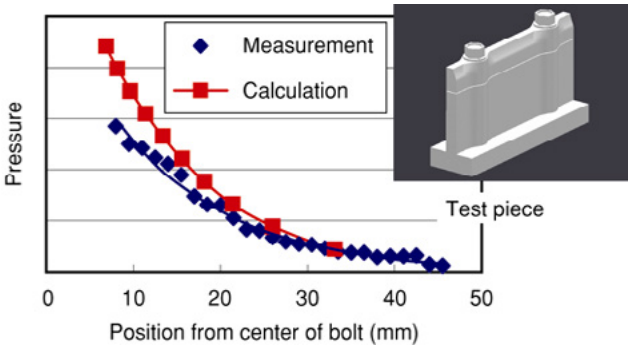


Fig. 11 Comparison of pressure in test piece

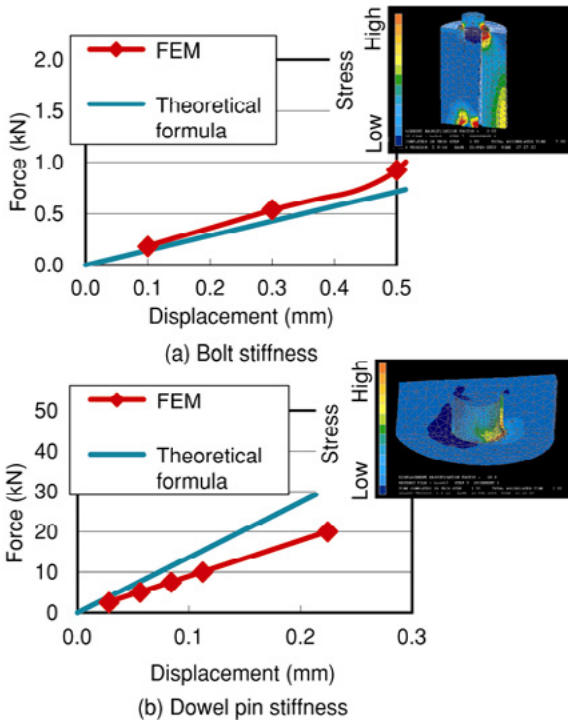


Fig. 12 Verification of stiffness of spring element

3.2. Reproducing the Form of the Load Input from the Differential Case

Modeling the actual shape of the outer races of the bearings and connecting these to the housing with surface contact elements simulated the loads applied by the differential case. The preloads on the tapered-roller bearings were accounted for. The differential case itself was modeled with beam elements, which allowed consideration of the stiffness of components inside the case (inner parts) while reducing the increase in calculation time (see Fig. 13). Figure 14 presents the mesh model of the entire housing.

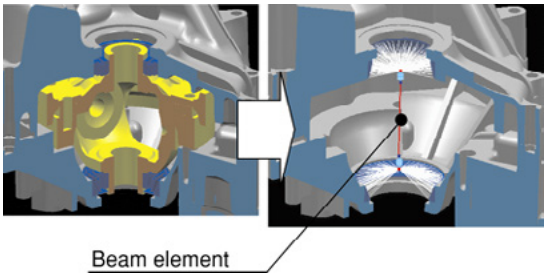


Fig. 13 Modeling of stiffness of differential case

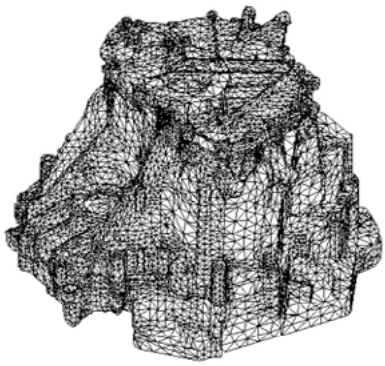


Fig. 14 FE model of transmission housing

4. Improving Precision of Simulation Analysis

Figure 15 shows the contrast between the results of the above non-linear modeling method and the linear simulation. Inclusion of the behavior of the contact surface and of the stiffness of the inner parts in the non-linear model caused a considerable change in predictions of deflection throughout the housing. The reproduction of the input form of the load from the differential case has helped improve the accuracy of predicting the stress state adjacent to the bearings. The previous simulation had inadequately predicted tensile

stresses on the opposite side of the bearing to where the load was applied. The results of this simulation were compared for coincidence with the results of the bench torsion test. As shown in Fig. 16, the calculated pressure distribution on the contact surface due to bolt tightening was quite consistent with that observed, both directly underneath the bolt locations and halfway between the bolt locations. Figure 17 provides measured values of the slipping behavior at the contact surface during application of torque. This displays non-linear hysteresis caused by frictional phenomena; these results show that modeling based on friction theory enables reproduction of gasket slipping properties at the contact surface of real housings. As presented in Fig. 18, the simulation results for slipping match well with measured values. This indicates that the slipping behavior of the contact surface was reproduced, since the slip is a product of a balance between the shearing forces transmitted through the housing and the frictional forces at the contact surface. The results for the bearing displacement are presented for comparison in Fig. 19. Since the behavior of the contact surface was well reproduced in the non-linear model, the difference with the measured values of bearing displacement was kept within 15%, an improvement in precision over the result with the conventional method.

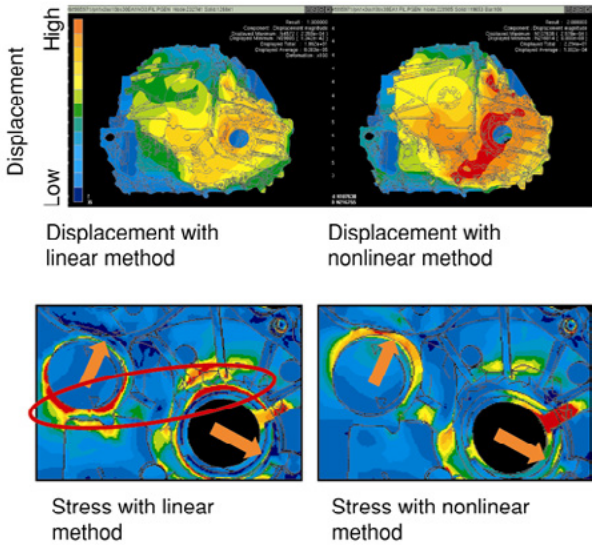


Fig. 15 Comparison of calculation methods

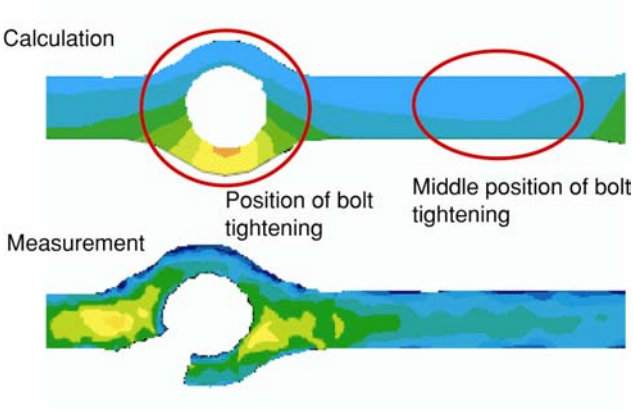


Fig. 16 Comparison of pressure in transmission housing

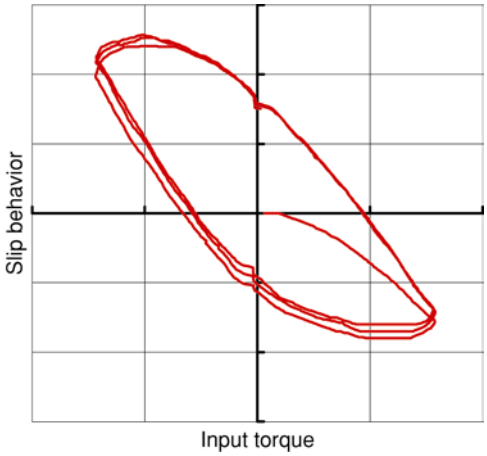


Fig. 17 Result of measurement of slip behavior

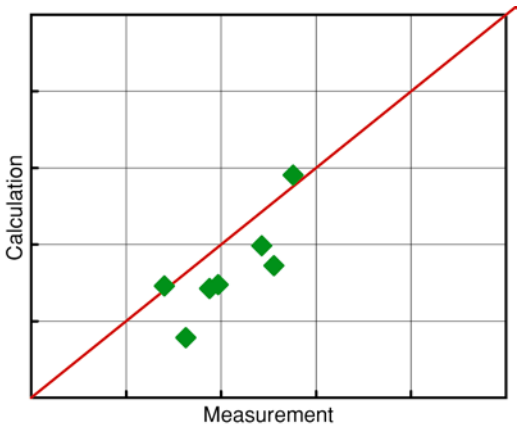


Fig. 18 Comparison of slip behavior

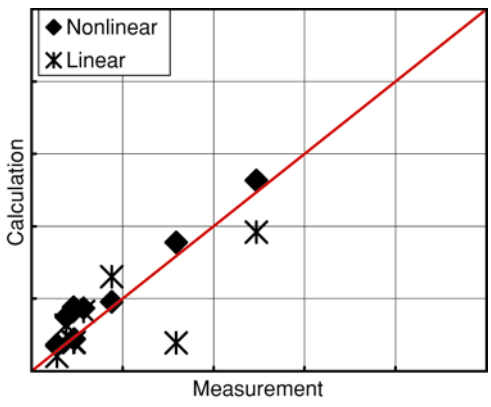


Fig. 19 Comparison of bearing displacement

5. Proof of Applicability

Models of other transmission housings with different shapes, load input paths and torques were created using this simulation technology and their results were compared with measured observations to verify the wider applicability of this method. Specifications of the other models used are presented in Table 2. Coincidence of the results with the bearing displacement is shown in Fig. 20. Predicted strength was also compared with measured strength (see Fig. 21). As shown in these figures, the predictions were quite consistent with the measured values; the model was found fully usable for estimating stiffness and strength of transmission housings. Here, the effect of stiffness of inner parts will be considered. Figure 22 shows the predictions of bearing displacement by the simulations while taking account of or ignoring the stiffness of inner parts, for comparison with the actual measured values. The simulations where the stiffness of inner parts was not considered showed growth in the bearing displacement in the housing types on the right side of the graph. This indicated that the housing stiffness in resistance to input torque was lower among the types on the right side of the graph. There was a glaring difference between the observed displacement and the displacement calculated without stiffness of inner parts in the three types on the right side (Types F, B, E), but when the inner parts were considered, the displacement values matched well. The influence of the stiffness of inner parts was more marked in models with lower stiffness; thus, in those models, it is even more important to account for this factor. Besides the differential case, mentioned before, these key inner parts were found to be the shafts supported by the three bearings.

Table 2 Specification of transmission used in comparison

Type	Transmissible torque	Total gear ratio	Drive system
Type-A	196Nm	12.2	2WD
Type-B	196Nm	12.0	4WD
Type-C	315Nm	12.1	4WD
Type-D	196Nm	11.7	2WD
Type-E	196Nm	15.5	2WD
Type-F	196Nm	14.4	2WD

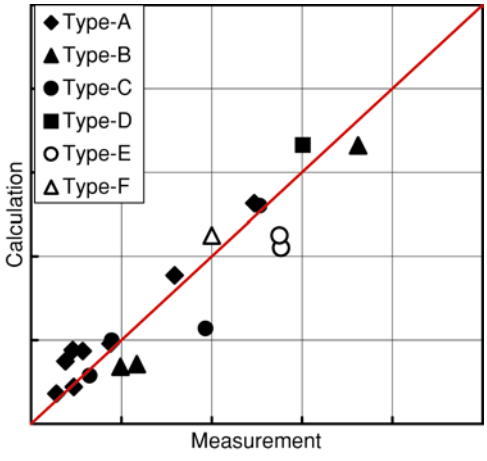


Fig. 20 Comparison of bearing displacement

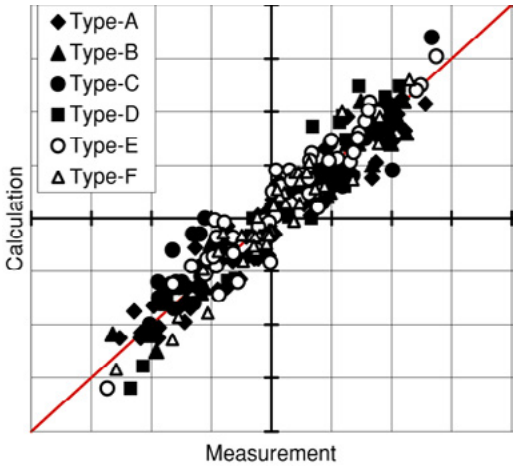


Fig. 21 Comparison of stress

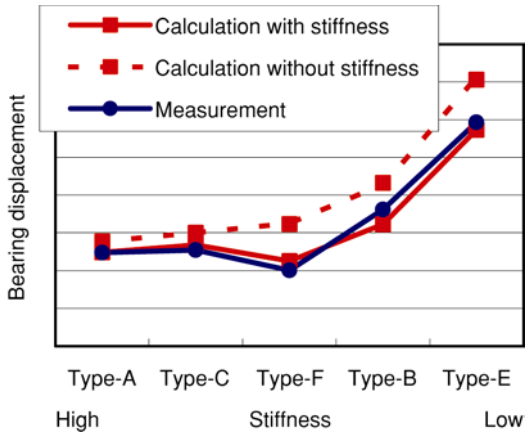


Fig. 22 Influence of stiffness of inner parts

6. Development of Design Tools

6.1. Development of Simulation Tools

In order to encourage wide use of this simulation at the design level, a special pre- and post-processing tool was developed for use on a 3D CAD system. It includes automatic tools for defining contact surfaces and bolt placement. This has proven very practical, and has decreased design labor time to 1/3 of the previous time (see Fig. 23).

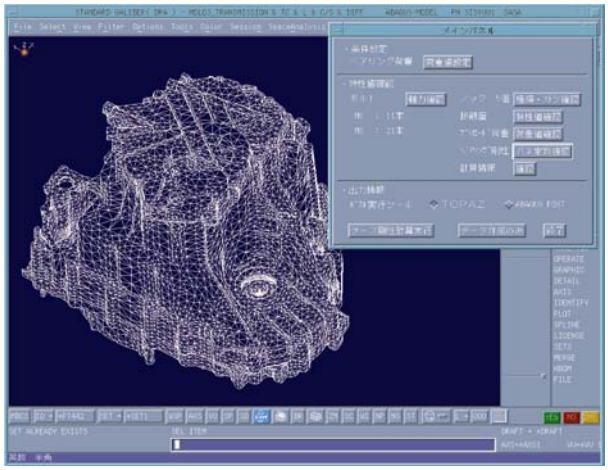


Fig. 23 Simulation tool

6.2. Example of Application

The re-design of a housing on a large transverse automatic transmission is shown below as an example of how this tool was practically applied. This enabled quantitative analysis of the improvement in stiffness and strength thanks to re-design of the shape of the TM housing at the design level (see Fig. 24).

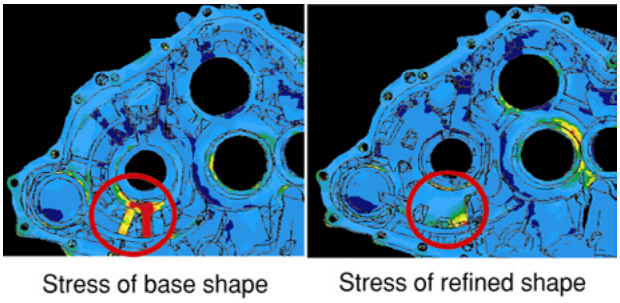


Fig. 24 Application example

7. Summary

A versatile, high-precision simulation technology was constructed for predicting the stiffness and strength of housings in transmission housing assemblies containing contact surfaces. This technology used non-linear modeling to successfully reproduce the behavior described below in actual assemblies. As a result, the difference between results in tests of actual and simulated transmissions was lowered to 15% or less, enabling predictions of bench torsion testing for stiffness and strength at the design level:

(1) For reproduction of contact surface behavior, input of parameters of gaskets, bolt tightening and positioning with dowel pins.
(2) For reproduction of the load input from the differential case, input of parameters of stiffness of inner parts of the differential case, bearing outer race stiffness, and taper roller bearing preload.

Also, in order for maximum practicality and acceptance of this tool among designers, pre-processor and post-processor analytical tools were specially developed for this simulation. These reduced design time to 1/3 of the previous time.

8. Acknowledgements

The authors extend their deepest appreciation to the personnel of Nihon System Gijutsu for their generous assistance in the construction and operation of various tools.

References

(1) Sakurahara, K.: Analysis of Sealing Behavior of Fluid Sealant in Steel plate made Engine Oil Pan: HONDA R&D Technical Review Vol. 10, pp. 106-112 (1998)

■ Authors ■


Masami HIRAOKA


Kouichi TOMITA


Satoru SUZUKI


Yasutomo IIJIMA


Chikae SASAHARA

Development of a High-Filtration-Ratio Automatic Transmission Fluid Strainer

Masaharu SUZUKI* Kouichirou INUKAI* Takeo FURUTA*
Yoshitaka NISHIO** Kazuki MATSUBARA**

ABSTRACT

This development project approached the objective of maintaining automatic transmission ("AT") functionality by focusing on the filtration ratio of the automatic transmission fluid ("ATF") strainer with respect to contaminants that are primary factors in reducing the operating accuracy of the oil pressure control valve. First, a filter medium was developed that raised the one-pass filtration ratio for contaminants 10 - 40 μm in diameter to twice the ratio achieved by the current nonwoven fabric used. Next, the filter medium was made with pleats so that it would prevent both the increase in pressure loss and the reduction of dust holding capacity in the filtration area required. In order to prevent the pleats from adhering, a lattice-shaped net was bonded to the front of the filter medium, the molded plastic element was clamped inside a plastic case that fits over the top and bottom, the outer edges were vibration welded, and the filter was put in place. The results from application showed that this ATF strainer was able to achieve a 50% increase in the quantity of contaminants that the oil pressure control valve for an AT can tolerate while maintaining its normal operating accuracy.

1. Introduction

In response to the market demand for improvements to automatic transmission function, an effort has been made to be more accurate than conventional models by means such as the use of multiple linear solenoids in the gearshift or lock up clutch volume controls. At the same time, it is necessary to take measures to prevent function deterioration, which leads directly to customer complaints. One of the causes for deterioration is a drop in operating accuracy of the oil pressure control valve due to contaminants. Considering that at present it is extremely difficult to completely prevent contaminants from being mixed in during manufacture or generated during operation, it is important to effectively trap the contaminants with an ATF strainer.

In this project, a filter medium has been developed with an improved filtration ratio against contaminants that have a negative effect on the oil pressure control system. In addition, technology has been developed to hold the filter medium in an ATF strainer case that can be fitted in the current layout space. Furthermore, the effectiveness of this ATF strainer application was verified.

This report provides an outline of the technologies above.

2. Understanding the Current Situation

2.1. Analysis of Contaminants Causing the Problem

A breakdown analysis was made of actual linear solenoid valve bodies that caused concerns in oil pressure control

* Tochigi R&D Center
** Toyoda Boshoku Corporation

valve operation. Figure 1 shows the results of totaling the number of incidents for each particle size of those particles causing problems. With the current non-woven fabric, 100% of particles with a particle size of 100 μm or more are trapped in one pass. Therefore, contaminants with a size less than 100 μm were totaled. The results show that those contaminants with a particle size of 10 - 40 μm, that is to say those that are roughly the size of the valve clearance, give the highest incidence rate due to contaminant entrapment. The necessity of increasing the filtration ratio against this particle size was very clear.

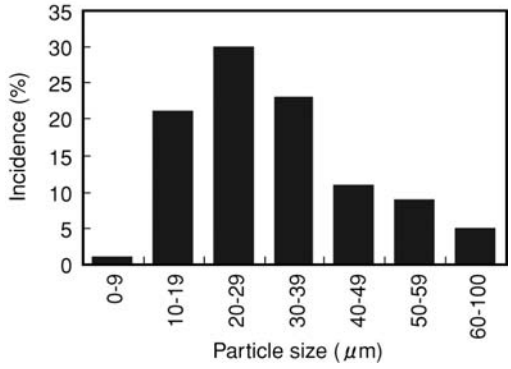


Fig. 1 Incidence of occurrence

2.2. Selection of Test Dust

In order to confirm the effect of countermeasures, it is necessary to select the test dust in advance. It is best if the selected test dust resembles the contaminants actually found in automatic transmissions as closely as possible.

Making a breakdown analysis of automatic transmissions driven in the normal market, the results of contaminant particle size distribution are given in Fig. 2. These results are the total of only those cases concerning automatic transmissions that were not reported as being caused by mechanical problems such as gear damage, etc. Even with new parts or after traveling long distances, there is no significant difference, and it was learned that contaminants were most closely approximated by the market test dust ACCTD (AC Coarse Test Dust).

For these reasons, ACCTD was selected as the market test dust.

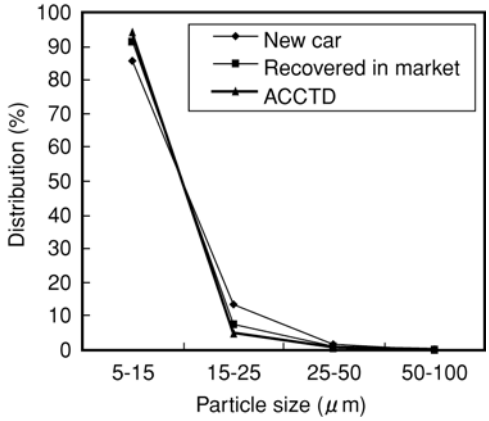


Fig. 2 Particle size distribution

2.3. Current Filter Medium and Filtration Ratio

Figure 3 shows the results of a one-pass filtration ratio test of the current non-woven fabric filter medium, using ACCTD. Focusing on the particles with a particle size of 10 - 40 μm, with one pass there is a filtration ratio of approximately 10 - 45%. It was clear that a new filter medium had to be developed, with a better filtration ratio against this particle size.

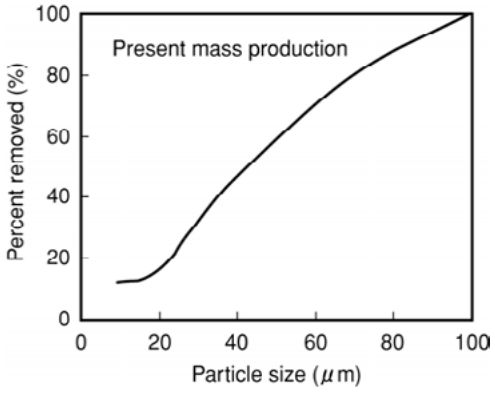


Fig. 3 Particle removal efficiency of filter medium

3. Basic Structure and Basic Performance

3.1. Development Aims

In this project, a filter medium was developed, and a method developed for holding the filter medium in the ATF strainer case.

The specific aims were as follows.

(1) In comparison with the current non-woven fabric, increase the filtration ratio of contaminants having particle size of 10 - 40 μm.

(2) As an ATF strainer, keep pressure loss to that with the current part, and maintain dust holding capacity to that of the current part or even better.

3.2. Composition of Filter Medium

The filter medium developed in this project has, in comparison with the current non-woven fabric, a mixed structure of four types of fiber with different components and fiber diameters.

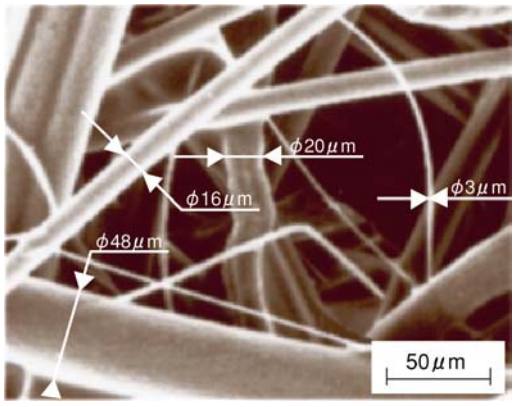


Fig. 4 Fiber composition of new filter medium

(1) The filtration ratio is increased by making the filter openings smaller by using finer fiber.

(2) Bulkiness is maintained with thicker fibers while at the same time, fluid passageway surface area is maintained with fine fibers, keeping down any increase in pressure loss.

Fiber composition of the new filter medium is shown in Fig. 4.

3.3. Improving the Filtration Ratio of the Filter Medium

Figure 5 shows the one-pass filtration ratio of the filter medium against the test dust with a particle size of 10 - 40 μm. The filtration ratio is twice that of the current non-woven fabric, and it is possible to reduce the amount of dust going through in one-pass by 40%.

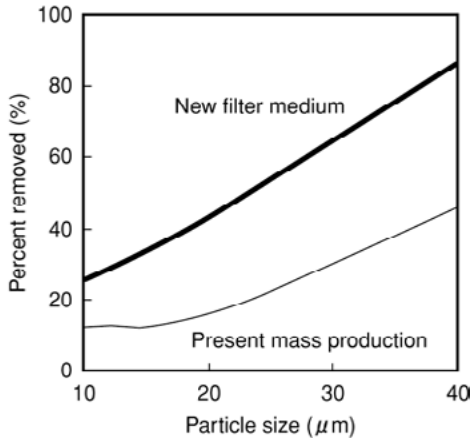


Fig. 5 Particle removal efficiency of filter medium

3.4. Required Effective Filtration Area

An increase in pressure loss and a drop in dust holding capacity, accompanying filter medium filtration ratio increases, will cause a drop in function. Therefore, it is necessary to maintain the required effective filtration area.

An ATF strainer jig was prepared having the same internal shape as the current product. Measurements were made of the relationship between filter medium effective filtration area and pressure loss, and the results are shown in Fig. 6.

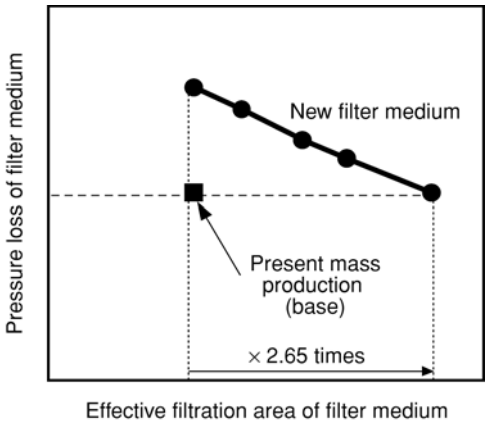


Fig. 6 Pressure loss of filter medium

From these results it is clear that in order to have pressure loss for the ATF strainer as a unit equivalent to that of the current product, the effective filtration area must be increased 2.65 times.

Figure 7 illustrates the concept of holding the filter medium.

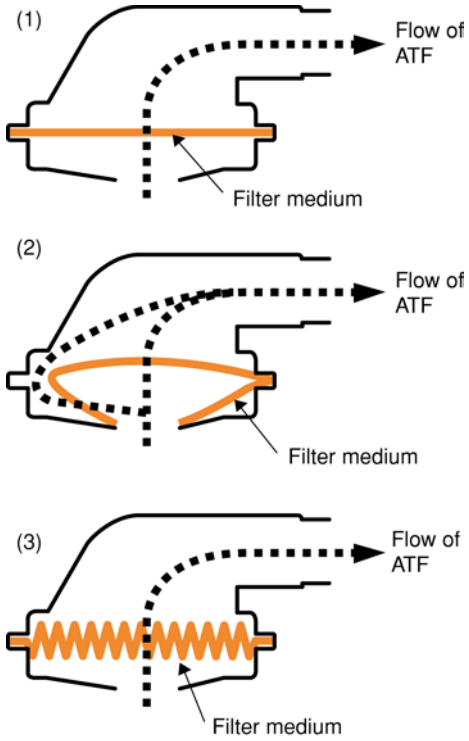


Fig. 7 Cross-sectional view of ATF strainer

In order to maintain an effective filtration area that is 2.65 times that of the current product, it is found that both (1) a single plate and (2) a folded bag shape as with the current part are not feasible. It is necessary to have (3) a pleated shape.

3.5. Maintaining an Effective Filtration Area

If the filter medium is simply pleated and held, when the ATF flow is large, or at low temperatures when viscosity is high, the resistance of the filter medium to the fluid flow

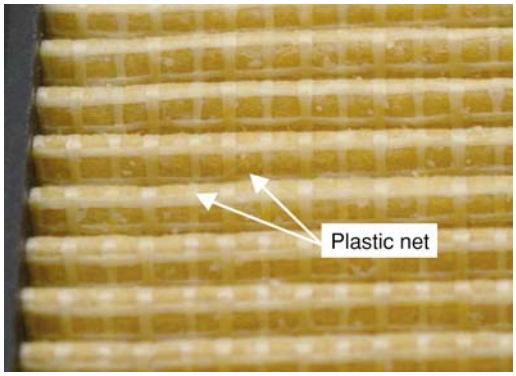


Fig. 8 Surface of new filter medium

becomes high, and there is adhesion of the pleats. If pleat adhesion occurs, the actual effective filtration area decreases, and there is pressure loss in the areas where pleat adhesion occurs, so it is not possible to adopt this type of high filtration ratio filter medium. In order to reliably maintain the pleated shape and prevent pleat adhesion, measures were taken to maintain the strength and stiffness of the filter medium itself, and to maintain the stiffness of the parts supporting the filter medium.

Concerning the filter medium, a plastic, lattice-shaped net was bonded to the surface on the ATF outlet side, and integrated with the filter medium. The filter medium surface appearance is shown in Fig. 8. The lattice pattern is the bonded plastic net.

Figure 9 shows how the filter medium strength is greater by bonding the plastic net. The results of a bursting strength test using a Mullen low-pressure tester, after the filter medium was immersed in 150 ºC ATF for 100 hours, show that strength is increased by 5.13 times over what it was before the net was bonded. In addition, an increase of 19 times more than that of the current non-woven fabric filter medium was displayed.

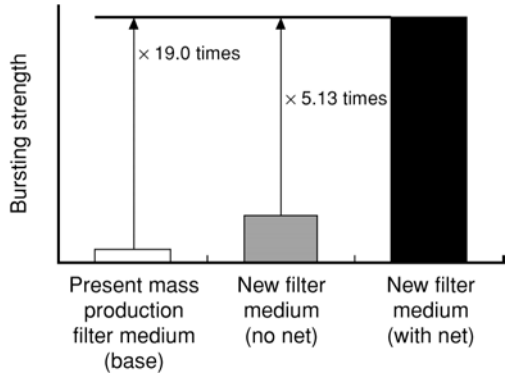


Fig. 9 Bursting strength of filter medium

To support the filter medium, an edging was created for the filter medium and a reinforcement rib was added perpendicularly through the ridges of the pleats. These form an integrated, molded plastic element. This plastic molded element is shown in Fig. 10. In the center, the reinforcement rib that is perpendicular to the filter medium ridgelines can be seen.

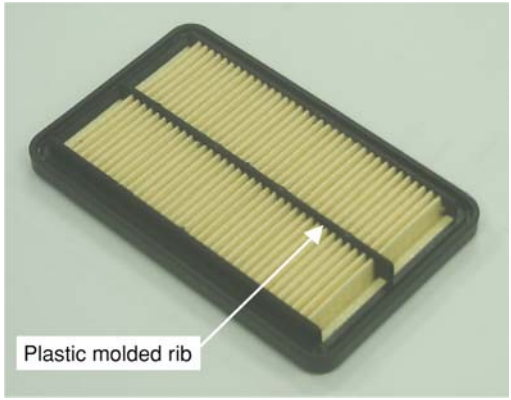


Fig. 10 External view of plastic molded element

3.6. Filter Medium Holding Method

The plastic element created is clamped in place by the plastic top and bottom cases, and the edging is vibration welded, holding the filter medium. This holding method is the first of its kind in the world for an ATF strainer.

The ATF strainer's structure is shown in Fig.11.

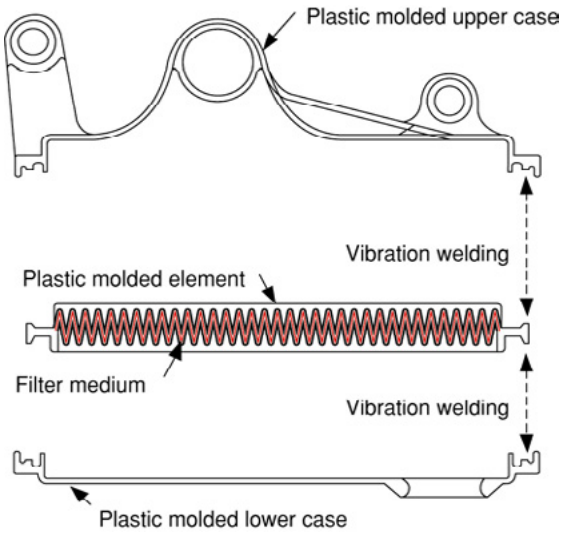


Fig. 11 Structure of new ATF strainer

The ATF strainer's appearance is shown in Fig. 12.



Fig. 12 External view of new ATF strainer

3.7. ATF Strainer Performance

Figure 13 provides pressure loss testing results, with ATF temperature parameters. The ATF strainer unit performance itself is equivalent to the current product. With the support countermeasures for the filter medium and the filter medium support parts, even when ATF flow is large or when viscosity is high and temperatures low, it is possible to prevent pleat adhesion.

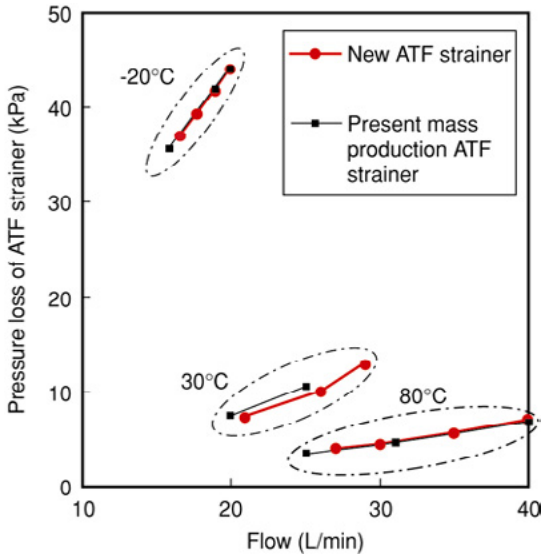


Fig. 13 Pressure loss of ATF strainer

The test results of dust holding capacity, or how much can be held until there is clogging, are shown in Fig. 14. It is clear that the ATF strainer unit can maintain a dust holding capacity that is 3.45 times that of the current product.

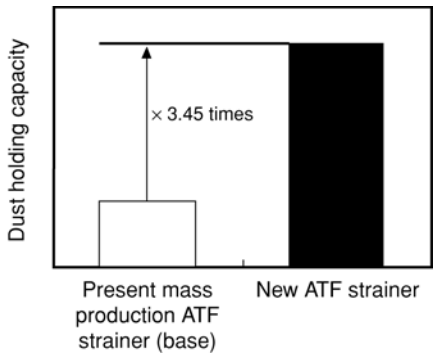


Fig. 14 Dust holding capacity of ATF strainer

From the results above, it was confirmed that a new ATF strainer has been developed with a better filtration ratio, yet having no negative effect on pressure loss or on dust holding capacity.

4. Confirmation of Application Effectiveness on Current Automatic Transmissions

4.1. Improved Multi-pass Filtration Ratio

A multi-pass test was carried out with the new ATF strainer fitted to a current automatic transmission, with all the test dust introduced at the initial stage and the transmission operated. A comparison was made with the existing strainer, examining the drop in the number of particles having a size of 10 - 40 μm that reached the linear solenoid valve. These results are shown in Fig. 15. The effectiveness in reducing the number of particles passing through the filter medium in one pass was 40%, as shown in Fig. 5. As for multi-pass, with elapsed time, the effectiveness in reducing the number is better than with just one pass.

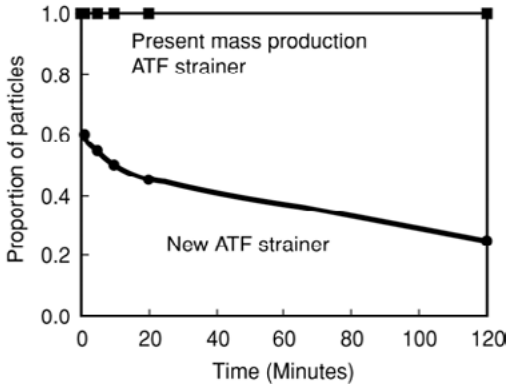


Fig. 15 Decrease of proportion of particles

4.2. Increasing the Tolerated Contaminant Amount

The new ATF strainer was fitted to a current automatic transmission and a certain amount of test dust was introduced at fixed intervals. A comparison was made of the tolerated amount of dust introduced enabling the linear solenoid valve operation accuracy to be properly maintained. The results of this comparison are given in Fig. 16. The amount of contaminants tolerated by the automatic transmission was increased by 50%, and this effect resembles that of the reduction in number of particles that pass through in multi-pass. From these results, the ATF strainer filtration ratio increase proved to be effective in supporting automatic transmission function in an environment with contaminants.

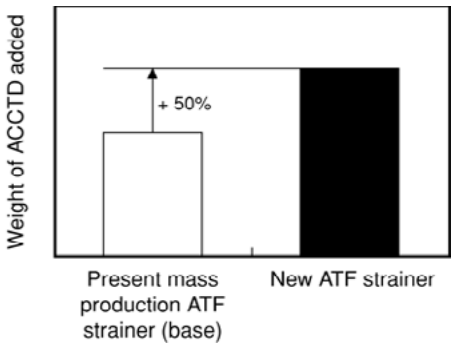


Fig. 16 Effect of lifetime extension by new ATF

5. Summary

By focusing on the ATF strainer's filtration ratio for contaminants and avoiding a drop in ATF strainer oil pressure control valve operation accuracy, the effectiveness of the new strainer in supporting automatic transmission function was verified. The following achievements were observed.

(1) A filter medium was developed having a one-pass filtration ratio against contaminants having a particle size of 10 - 40 μm that was twice that of the current non-woven fabric filter medium. As a result, the number of particles passing through in one pass was reduced by 40%.
(2) While this new filter medium was held in the ATF strainer case that fits in the current layout space, the filter medium was pleated in order to maintain the required effective filtration area. To prevent pleat adhesion, a lattice-shaped net was bonded to the surface of the filter medium, a molded plastic element was clamped by the plastic top and bottom cases, and the edging was bonded using vibration welding. By using this holding method, this ATF strainer, the first of its kind in the world, realized a totally new ATF strainer that has a better filtration ratio without having a negative effect on pressure loss or dust holding capacity.
(3) As a result of the application of this ATF strainer, it was possible to increase by 50% the amount of contaminant tolerated in the maintenance of operation accuracy of the oil pressure control valve. Also, increases in filtration ratio confirmed to be effective in maintaining automatic transmission function in an environment with contaminants.

6. Acknowledgements

The authors would like to take this opportunity to express their deep gratitude to those people at Denso Corporation and Toyoda Boshoku Corporation for their generous cooperation in this development project.

■ Authors ■


Masaharu SUZUKI


Kouichirou INUKAI


Takeo FURUTA


Yoshitaka NISHIO


Kazuki MATSUBARA

Development of Road Friction Coefficient Estimation Logic

Keiyu KIN* Hironobu KIRYU* Osamu YANO*

ABSTRACT

The further development of vehicle stability assist (VSA) and other such forms of vehicle dynamics control requires techniques for estimating the road friction coefficient more accurately and in real-time. The present research integrated non-linear tire characteristics data with vehicle side slip angle estimation logic to develop a new estimation logic that is more accurate and has greater response than the conventional logic. The estimation accuracy of this logic was further verified in tests with actual vehicles, thus demonstrating the validity of the developed logic.

1. Introduction

The authors have continued their research on the further development of vehicle stability assist (VSA) performance using vehicle side slip angle (β) estimation, road friction coefficient (μ) estimation, 4-wheel slip (λ) control and tire characteristic data logics[(1), (2)]. Of these logics, μ estimation logic plays the most important role in providing a more accurate understanding of road surface conditions. This paper discusses the drawbacks of conventional μ estimation logics, and presents details of a newly developed technique for a more accurate, real-time estimation of the road friction coefficient. The validity of this logic has been proven in vehicle tests. In these tests an FR and an on-demand full-time 4WD were run on snow-covered, low-μ wet basalt, and dry asphalt test courses.

2. Issues and Research Goals

As Fig. 1 shows, during turning nonlinear characteristics and road surface conditions cause tire side forces to vary. The higher the tire side slip angle (α) and the lower the road surface μ, the greater the possibility of saturation being reached. This saturation of tire side forces causes the vehicle to deviate from the intended turning path. When this happens,

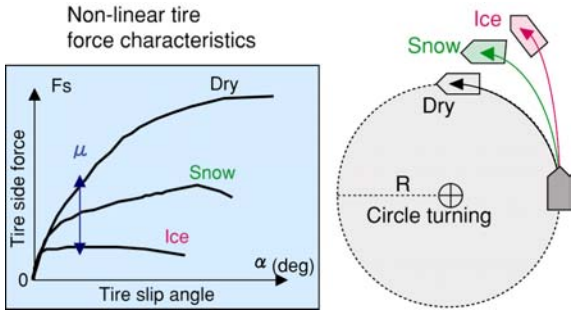


Fig. 1 Tire force characteristic and vehicle dynamics

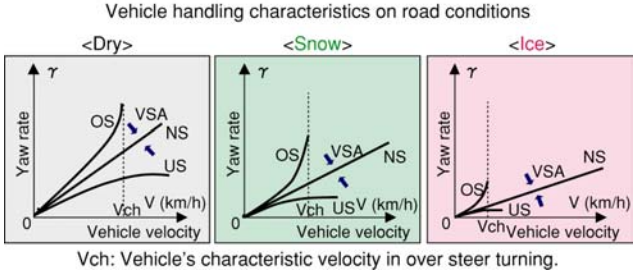


Fig. 2 Vehicle dynamics control

* Tochigi R&D Center

the grip of the tires becomes uneven and the vehicle behavior becomes unstable, demonstrating oversteer (OS) or understeer (US), as shown in Fig. 2. When driving on icy or snowy road surfaces in particular, tire side forces drop drastically, causing the vehicle to more easily become unstable. This necessitates stability control using VSA or a similar technique. Because the effectiveness of this type of control is related to road surface μ, a μ estimation logic becomes indispensable. The purpose of the research discussed in this paper was to develop a logic to estimate μ to an accuracy of ±0.05 (μ within a range from 0 to 1, normalized to 1 on dry road surfaces) using steering angle, acceleration and yaw rate sensors.

3. Conventional Road Surface μ Estimation Logics

3.1. μ Estimation Utilizing Slip Rate

This method is the simplest, calculating vehicle acceleration and deceleration and slip rate from acceleration and deceleration of the tires, and taking gain in these values as changes in road surface μ. As shown in Fig. 3, early ABS and traction control systems (TCS) estimated μ indirectly from the relative λ between tires and road surface at braking and during traction, and selected a corresponding control gain. These simple systems used no sensors other than tire speed sensors. Further development was required to enable estimation during turns.

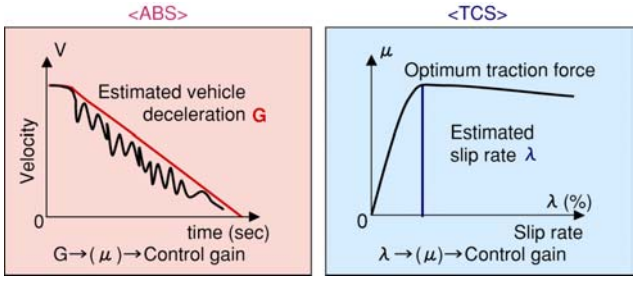


Fig. 3 Primitive slip estimation for ABS and TCS

3.2. μ Estimation Utilizing Yaw Rate

This method adds a steering angle sensor to the system described above. In this system changes in road surface μ are taken as the difference between actual yaw rate and nominal yaw rate (based on a dry road surface) calculated from steering angle and estimated vehicle velocity, providing a logic capable of estimating μ during turns. As Fig. 4 shows, this method judges OS and US, making handling control possible. This method makes road surface μ estimation possible during turning with a minimum of sensors and logics, and has enabled performance improvements in ABS, TCS and 4WS. However, there are some drawbacks to this method which require solution: its high level of reliance on steering angle makes it difficult to establish optimum nominal yaw rates for all road surface conditions, and it is particularly difficult to judge OS when the driver contributes excessive steering input in conditions of low road surface μ.

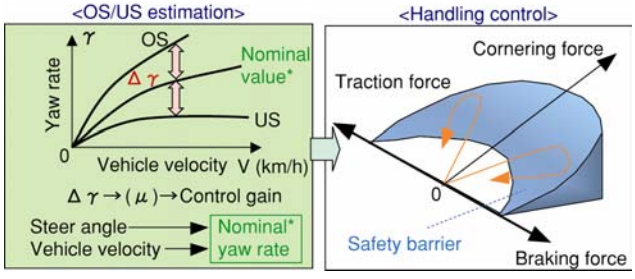


Fig. 4 OS/US estimation for handling control system

3.3. μ Estimation Utilizing Lateral Acceleration

This method utilizes an acceleration sensor in addition to tire speed and steering angle sensors. Estimation of cornering force (centripetal force) is enabled by finding longitudinal and lateral acceleration. The logic utilized in this method estimates direct μ during turning by regarding the vehicle as one tire and calculating tire gripping force from the friction circle of that tire, as shown in Fig. 5. The estimate of μ provided by this method can be used to correct the steering angle nominal yaw rate found using the previous method, and enables improvement of the accuracy of the nominal yaw rate on icy and snowy roads in particular. However, to maintain a stable level of accuracy of estimation when the tire slip control used by more advanced VSA systems and the like is in operation, the tire gripping force for all four wheels must be calculated separately. This makes a μ estimation method indispensable in combination with tire side slip angle (α) and vehicle side slip angle (β) estimation logics. In addition, tire characteristics are not limited to a simple friction circle; it is essential to increase the accuracy of estimated μ values using nonlinear motive force and side force data corresponding to changes in λ and α.

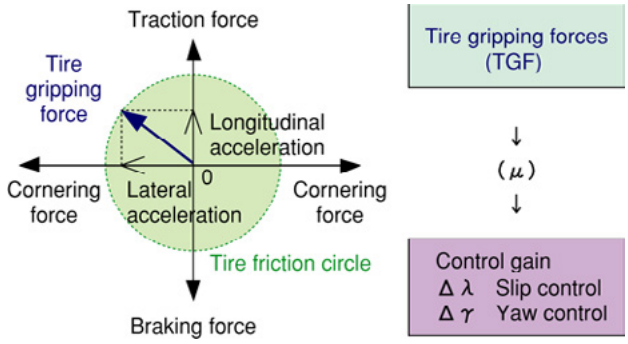


Fig. 5 Estimation of the tire gripping force

4. Newly Developed μ Estimation Logic Utilizing Vehicle Side Slip Angle

To enable road surface μ estimation to be used in vehicle motion control systems like VSA, it was necessary to develop a stable logic which maintained a more accurate target during the operation of λ control. To achieve this, the logic had to estimate α and λ for all four wheels more accurately and in real-time in all conditions, and be able to calculate tire braking and traction force and tire side forces with consideration of dynamic wheel load (Fw).

Figure 6 shows the basic μ estimation logic developed in this project. This logic integrates nonlinear tire characteristic data maps (termed tire data below) reflecting data obtained

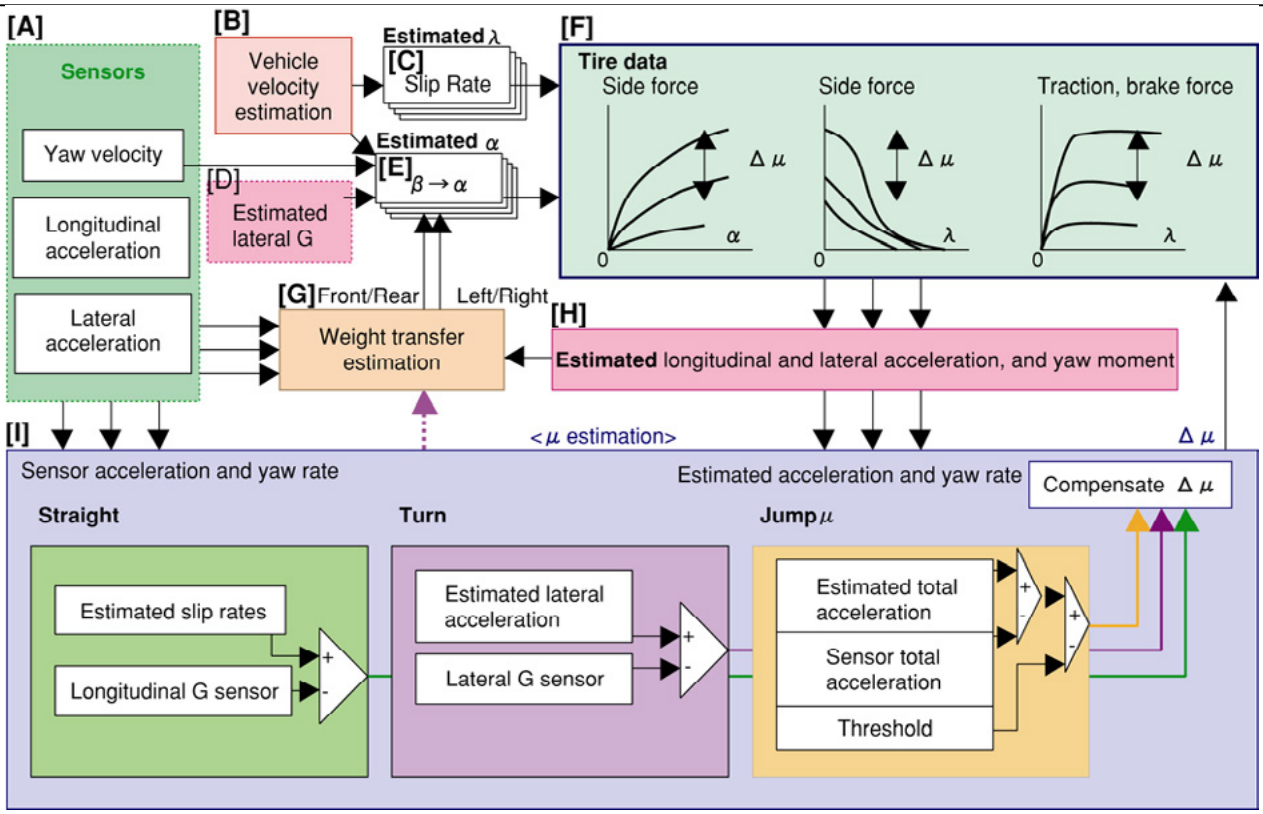


Fig. 6 μ estimation logic

from measurements on actual road and β estimation logic. In addition, it successively corrects the estimated μ values using the three basic parameters of vehicle motion: yaw rate, longitudinal acceleration and lateral acceleration.

Broadly speaking, there are two aspects of this μ estimation logic which are new to these logics. The first of these is that, being combined with a β estimation logic, it estimates yaw rate and acceleration from estimated tire gripping force for each wheel, and provides correction as needed by comparing these estimates with values measured by sensors. The second is that it expresses the basic tire characteristics using nonlinear data reflecting the motion characteristics of actual vehicles.

The remainder of this section will explain the flow of the logic as shown in Fig. 6.

(1) Vehicle yaw rate, longitudinal acceleration and lateral acceleration ([H]) estimated from β estimates ([D], [E]) and nonlinear tire data ([F]) are compared with the output values obtained from vehicle sensors ([A]) and correction values are calculated.

(2) These μ correction values are calculated for three driving modes: Straight, turn and jump μ ([I]).

(3) These μ correction values are applied to the original nonlinear tire data ([F]).

(4) To maintain the accuracy of vehicle yaw rate, longitudinal acceleration and lateral acceleration estimations during the operation of λ control in VSA and similar systems, tire gripping force is calculated for each wheel ([C], [E], [F]).

(5) During turning, estimated α is corrected with estimated front/rear and left/right weight transfer ([G], [E]).
When pitching caused by acceleration and braking or rolling during turning vary the load on the tires, the tire gripping force also varies. To determine the amount of variation under these circumstances, tire side slip angle α estimation is corrected. To take an example: on dry road surfaces (estimated road surface μ close to 1) when there is a greater chance of an effect from weight transfer, the lateral acceleration and yaw rate calculated from estimated tire slip angle for each wheel are respectively compared with values obtained from sensors, enabling correction of estimated α.

(6) To increase the accuracy of estimated tire slip λ, estimated vehicle speed is constantly corrected using nonlinear tire slip data and values obtained from the longitudinal acceleration sensor ([B], [C]).

4. Vehicle Test Evaluations

5.1. FR Vehicle Test Data (Compact Snow Course)

Figure 7 shows data obtained from tests using an FR vehicle on a winding course and a cornering course with a regular 200 m radius. Both courses were covered with compact snow (actual μ value approximately 0.3). Tests on both courses were conducted with closed loop steering input.

These data demonstrate the basic stability of estimated road surface μ and its proximity to actual μ under both dynamic and static conditions. In addition, the estimated vehicle side slip angle β almost exactly corresponds with the side slip angle measured by the sensor, and the estimated lateral acceleration maintains a high level of accuracy, staying close to the values obtained from the lateral G sensor.

These results indicate that the newly developed μ estimation logic satisfies basic performance requirements. However, no slip control, such as provided by VSA, was in operation during this test. The next section discusses a test of road surface μ estimation while slip control is in operation.

5.2. 4WD Vehicle Test Data (Dry Course, Wet Basalt Low μ Course)

The newly developed estimation logic was tested next using a 4WD vehicle with four-wheel slip control in operation on differing road surfaces and under differing driving conditions. Representative examples of the data obtained from these tests are shown in Figs. 8, 9 and 10. Figure 8 shows winding driving on a dry course, Fig. 9 shows slalom driving on a low μ wet basalt course, and Fig. 10 shows a μ jump from a dry course to a low μ wet

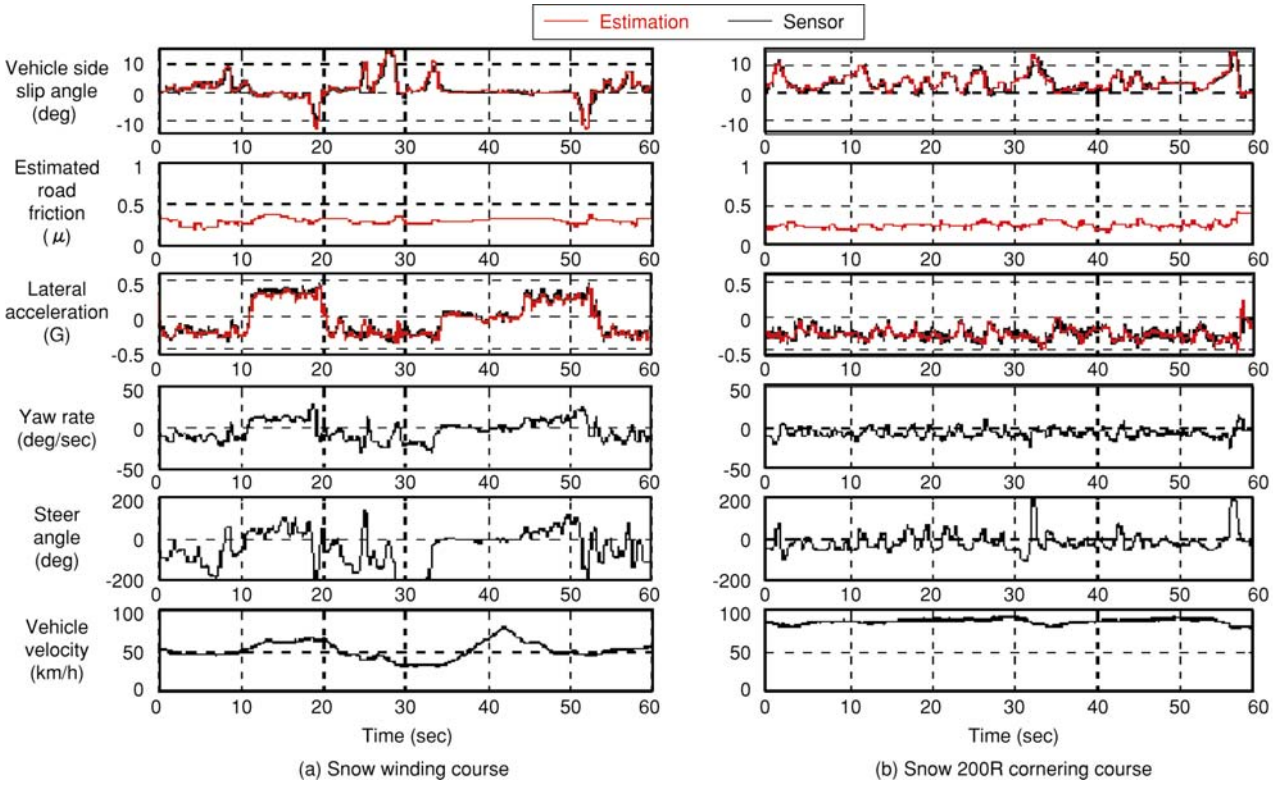


Fig. 7 FR vehicle test data at snow course

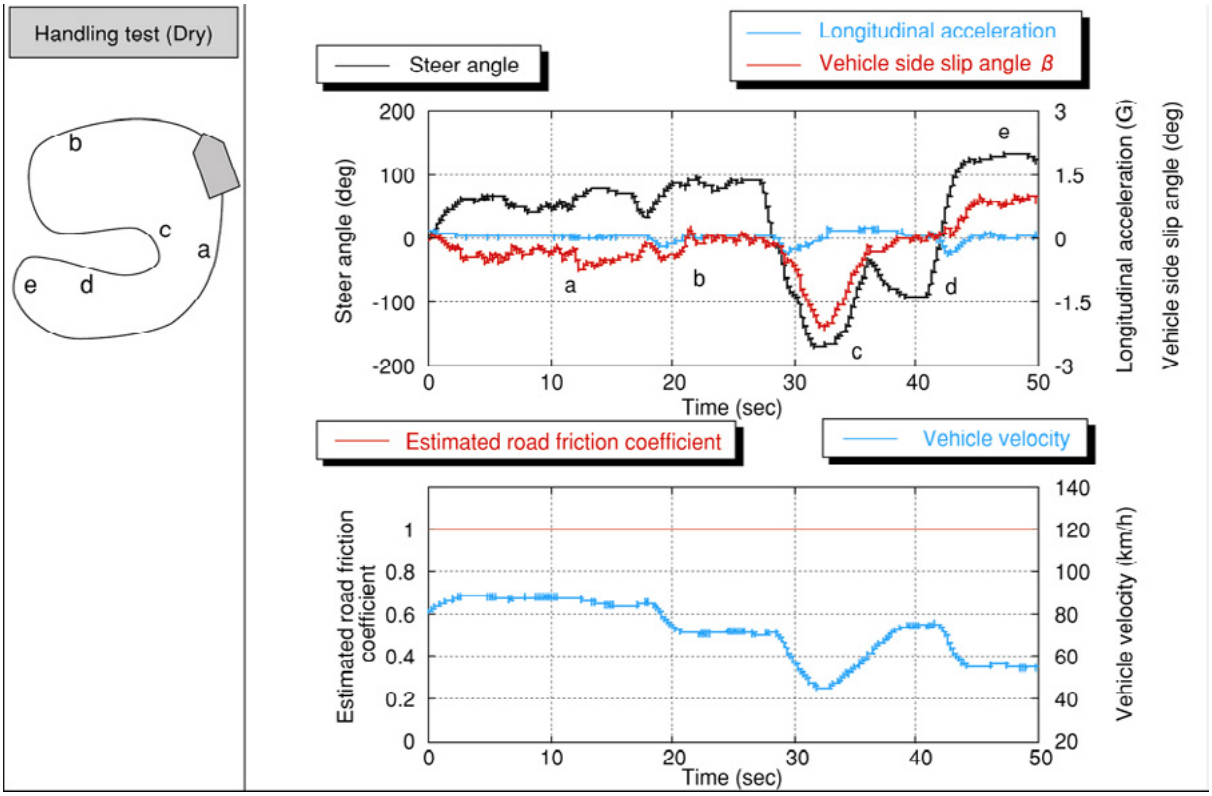


Fig. 8 4WD vehicle test data on dry winding course

basalt course.

As the graphs show, the logic was able to estimate road surface μ more accurately and in real-time, and maintained accuracy under dry, low μ and μ jump conditions. To explain this test data more thoroughly:

(1) Figure 8: Winding driving on dry course

Road surface μ was normalized to 1 for the dry course. As can be seen from the lower graph in Fig. 8, one circuit of the course was sufficient for the logic to determine that the surface was dry. In addition, estimation of vehicle side slip angle β was stable, and road surface μ estimation functioned more accurately during turning.

(2) Figure 9: Slalom driving on low μ wet basalt course

The lower graph in Fig. 9 shows that estimated μ remained close to measured values even during slalom driving on a surface with a low μ value of approximately 0.3 to 0.4. In addition, when the vehicle demonstrated unstable OS behavior and VSA four-wheel λ control was

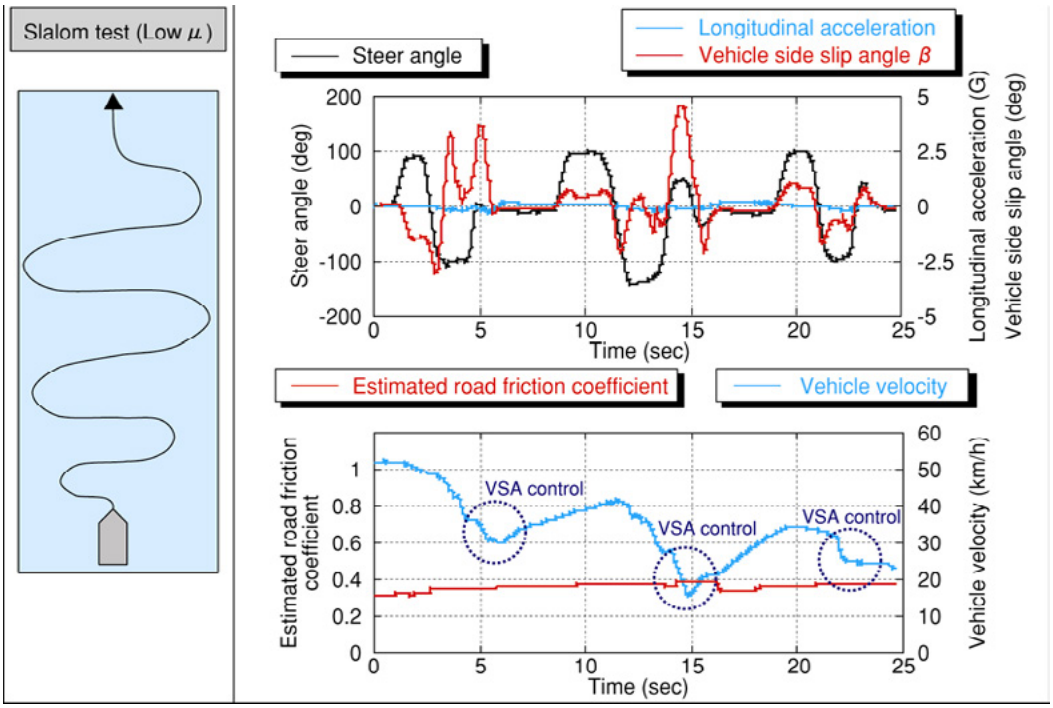


Fig. 9 4WD vehicle test data on low μ slalom course

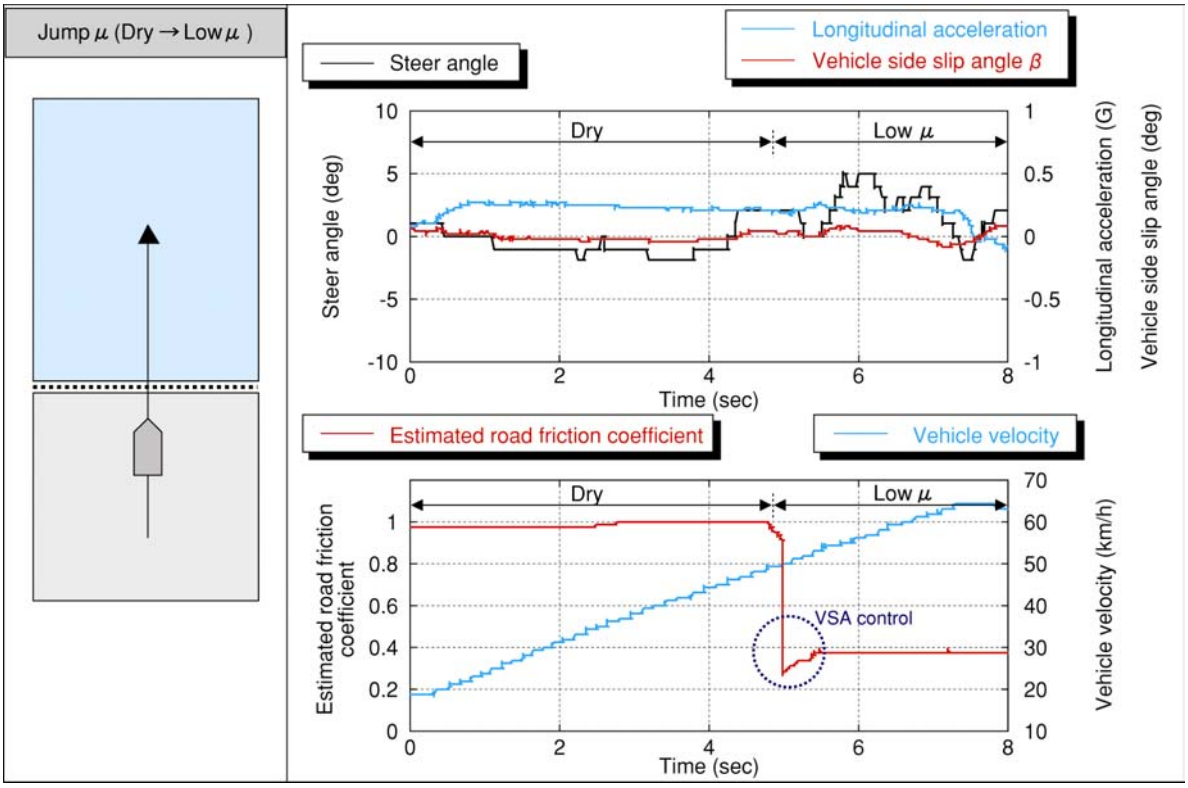


Fig. 10 4WD vehicle test data on jump μ course

in operation, estimation was stable and showed high accuracy. These results show that the new μ estimation logic can be utilized when driving on icy and snowy roads.

(3) Figure 10: μ jump from dry surface to low μ wet basalt course
The lower graph in Fig. 10 shows that the μ change occurring when accelerating from a dry surface to a low μ was accurately responded to within a few 100 msec. Besides, μ estimation was stable although λ control was operating to prevent the drive wheels slipping. These results demonstrate the high level of real-time performance of the newly developed logic.

These tests results demonstrate the capability of the new logic to estimate road surface μ more accurately and in real-time for straight, turning and jump μ driving conditions on all road surfaces. Vehicle tests have therefore confirmed the validity of the newly developed μ estimation logic.

6. Conclusion

The following conclusions may be drawn on the basis of the foregoing discussion:

(1) A μ estimation logic has been developed which is accurate to within ± 0.05 regardless of road surface conditions or driving mode.
(2) This logic enables stable μ estimation even during the operation of tire slip control in VSA and similar systems.
(3) The logic estimates μ more accurately and in real-time when μ jump occurs (in particular from high μ to low μ).

These findings show that the targets of this research project have been achieved.

In the future, the authors intend to further develop the range of applicability of this basic logic by creating a technology enabling real-time self-learning correction for fundamental tire characteristics able to function even when tires with different characteristics are fitted.

References

(1) Kin, K., Yano, O., Urabe, H.: Improvement of Vehicle Stability and Steerability by Slip Control, HONDA R&D Technical Review, Vol. 13, No. 1, pp. 91-98 (2001)

(2) Kin, K., Ikeda, T., Yano, O.: Improvements in Handling on a Slippery Road with VSA, HONDA R&D Technical Review, Vol. 13, No. 2, pp. 83-90 (2001)

■ Authors ■


Keiyu KIN


Hironobu KIRYU


Osamu YANO

Development of a Lightweight Manual Transmission Case of a Heat-Resistant Magnesium Alloy

Hideaki MIYASHITA* Masayuki NAKADA* Masayasu SAKATA*
Yukihiro HAYAKAWA* Sadaharu MATSUMURA*

ABSTRACT

A manual transmission case was developed by using a heat-resistant magnesium alloy that achieves a 24% weight reduction over a conventional aluminum alloy case. AE62-Ca was developed by improving the castability of the Mg-Al-Ca-RE-base heat-resistant magnesium alloy ACM522, which had a history of use in oil pans, and this new alloy was applied. At the same time, with the objective of achieving a more reasonable price, a recycling process was developed that resulted in a recycling yield on a par with general magnesium alloys. A formed-in place gasket was developed that provided adhesive strength without chemical treatment and fluorocation resin coating bolts were also developed to prevent galvanic corrosion at the contact surface.

1. Introduction

In recent years, considering global environmental concerns, vehicle weight reduction in order to improve fuel economy has become a vital issue. One method, adopted particularly in Europe and North America, has been greater application of magnesium alloys.

Honda has used, until recently, general magnesium alloy for engine head covers and steering wheels. In 1999, an oil pan of Mg-Al-Ca-RE heat-resistant magnesium alloy ACM522 went into mass production, but in order to realize even further weight reduction, it is necessary to expand the application of parts using magnesium alloys.

In this project, a heat-resistant magnesium alloy was used for a manual transmission case (referred to as MT case hereafter), subject to the same operating temperatures as the oil pan, achieving a 24% weight reduction over the conventional aluminum alloy case. At the same time, surrounding technologies were also developed to reduce cost.

2. Aims of Development

Figure 1 shows the relationship between engine torque and aluminum alloy MT case weight, for both Honda and other companies. In recent years, as a result of the pursuit of smaller sizes through making the gears and synchros thinner, Honda's case weight is positioned equivalent to other companies or lower. However, the aim of this development project is to secure weight reduction competitiveness through the further application of magnesium alloy.

The authors established the following targets in the development project.

(1) Giving full consideration to the casting of MT cases with complex shapes, at the same time as developing an alloy that has the same level of strength as the current heat resistant alloy ACM522 and that has more advanced castability, one target is to establish a recycling process that actualizes a return rate equivalent to general magnesium alloy.
(2) Maintain a level of durability and marketability that is equivalent to those of the aluminum alloy case.

* Tochigi R&D Center

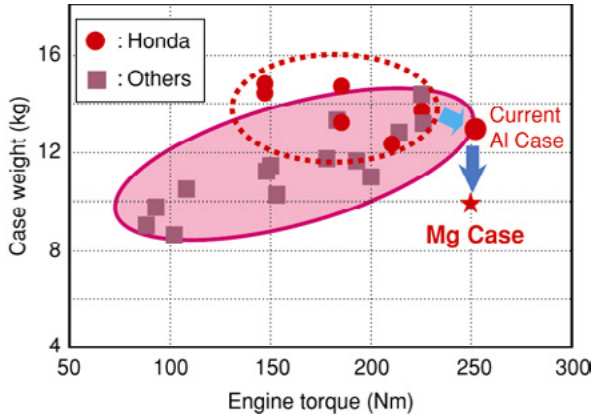


Fig. 1 Relationship between engine torque and manual transmission case weight

(3) Develop a formed-in-place gasket (FIPG hereafter) that gives adhesion strength equivalent to or better than the aluminum alloy case, without chemical treatment.
(4) Develop lower-cost galvanic corrosion countermeasure technology.

3. Material Technology

3.1. Development of Heat-Resistant Magnesium Alloy AE62-Ca

3.1.1. Improved castability

Until now, the heat-resistant magnesium alloy ACM522 was developed with the purpose of application to engine parts and was applied to the oil pan. However, in order to apply it to the MT case, which has an extremely complex shape, it was necessary to further improve castability.

The effects of the amounts of Al and Ca, which are the main components of ACM522, were verified by using the hot-cracking test (by ring-die plate) method[(1)]. This test evaluates total length of cracks occurring in a test specimen that was cast using a ceramic shell mold having a specific ring shape.

As given in Fig. 2, the results show that at 1.2≤Ca≤1.8, 5.0≤Al≤6.0%, it looks like a level equivalent to general alloy AZ91D may be achieved.

However, reducing the amount of Ca causes a drop in creep strength, in comparison with ACM522, and so the amount of rare earth metals (RE) was increased to 2.3% or more.

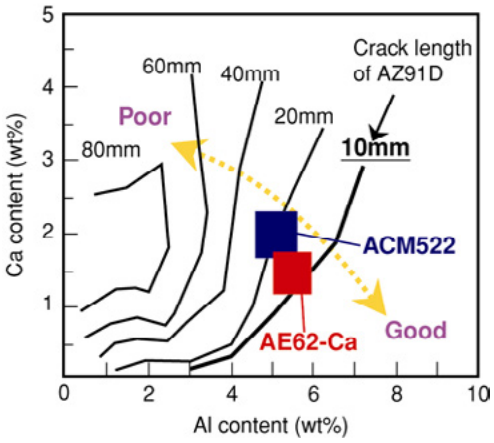


Fig. 2 Effect of Al and Ca content on the total crack length

The results of strength verification of this material, as shown in Fig. 3, confirm that strength equivalent to ACM522 is maintained, and this material was named AE62-Ca.

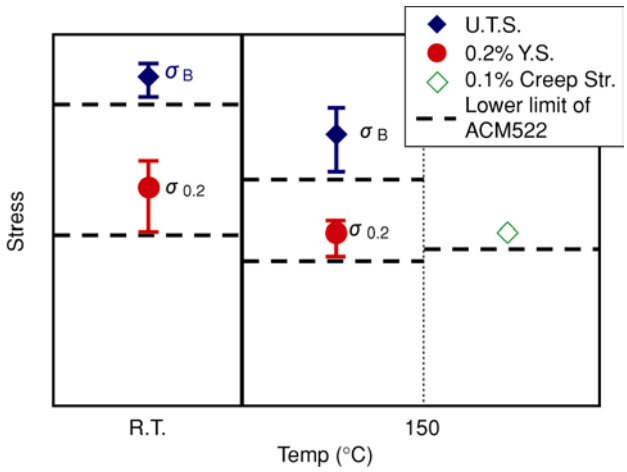


Fig. 3 Strength of AE62-Ca alloy compared with ACM522 alloy

3.1.2. Castability verification with a transmission case

Because magnesium alloy has a lower heat capacity than aluminum alloy, when flow rate drops, fill defects more easily occur. Therefore, with magnesium alloy it is necessary to have casting with high injection speed (high shot speed).

Figure 4 shows the results of verification of the relationship between injection rate, material strength and specific gravity using a metal die.

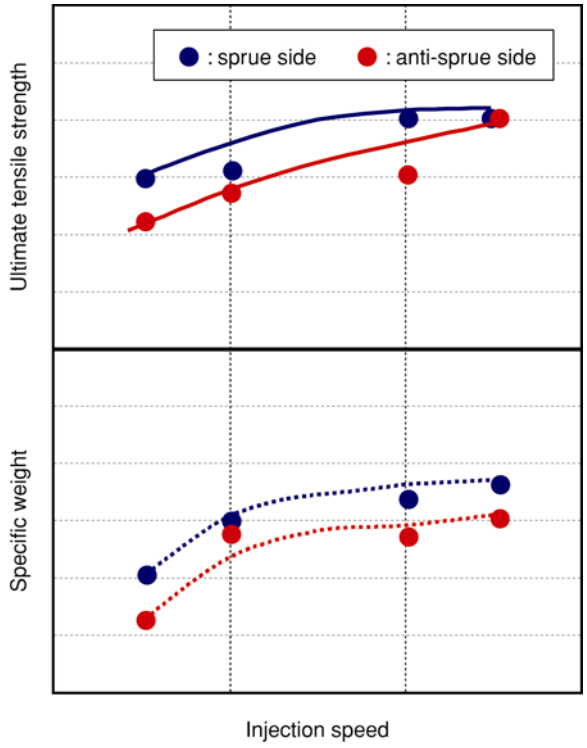


Fig. 4 Effect of injection speed at clutch case

As injection speed drops, there is a noticeable drop in tensile strength and density, and so there is a necessity of maintaining an injection rate at a fixed level or higher.

Implementing further casting simulations, metal die designs were studied. Figure 5 shows an example of analysis using the clutchcase.

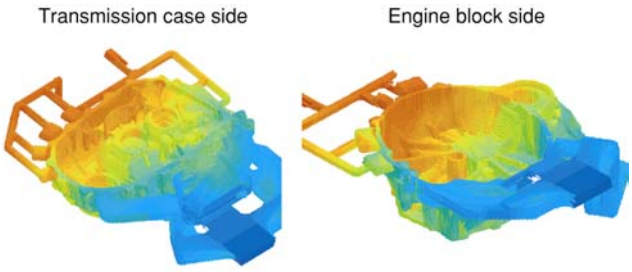


Fig. 5 Flow analysis of molten metal in clutch case mold

Based on the results of these analyses, metal die design was carried out, and the results of continuous casting under uniform conditions confirmed there were good quality parts without cracks.

Figure 6 is a photograph of the outside of a clutch case prototype part.

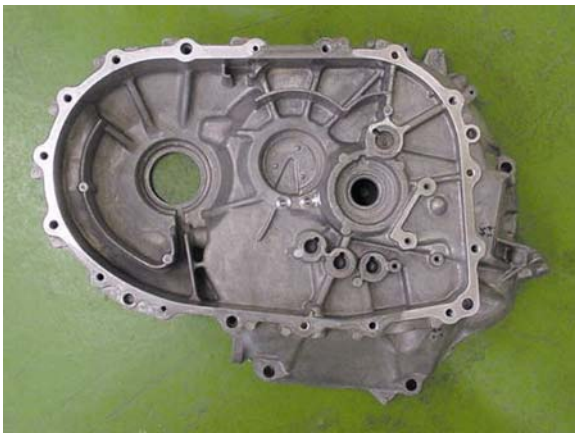


Fig. 6 Appearance of prototype of magnesium clutch case using AE62-Ca

3.1.3. Recycling process

A recycling process using a Cl flux has been established for general magnesium alloys such as AZ91D, but for the heat-resistant alloy ACM522 the drop in major components such as Ca and RE is large so recycling is not implemented. From the cost reduction point of view, the establishment of a recycling process is also an important issue.

In order to understand the causes, samples were taken of molten metal and sludge (sediment and deposits in the container) at each stage of recycling of heat-resistant magnesium alloy under the same conditions as general magnesium alloy and an elemental analysis was performed.

The results show a drop in alloying in the molten metal during the melting and refining processes. Analysis shows that there are oxides incorporating Ca and RE (rare earth elements) as well as Cl compounds in the sludge. From these facts it is clear that the drop in components is caused by the generation of sludge due to “an oxidation reaction between the molten metal and the air” and “a reaction between molten metal and flux components” during the recycling process. The following two countermeasures were implemented.

(1) Prevention of air contact on molten metal surface: The covering flux was changed to an SF_6 (6-fluoride ion) gas atmosphere.
(2) Restrict reaction between molten metal and flux: Change flux introduction and agitation to inert gas bubbling.

The results of carrying out recycling without the use of flux, and through the use of these methods, as shown in Fig. 7, the issue of component part amount drop was resolved.

As shown in Fig. 8, the results of material strength verification show properties equivalent to that of new ingot, and it is possible to use 100% recycled ingot.

In addition, a return rate of 95% was achieved, on a par with general magnesium alloy.

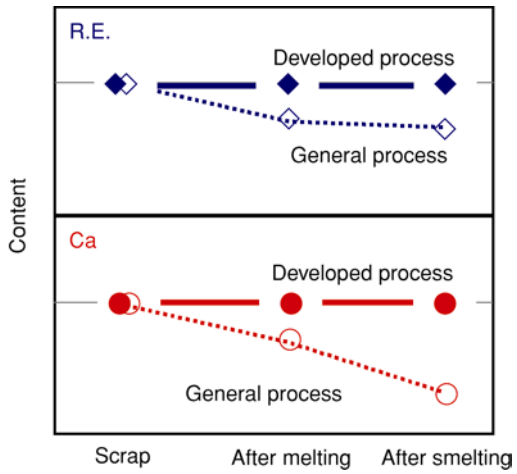


Fig. 7 Loss of R.E./Ca content in recycle process

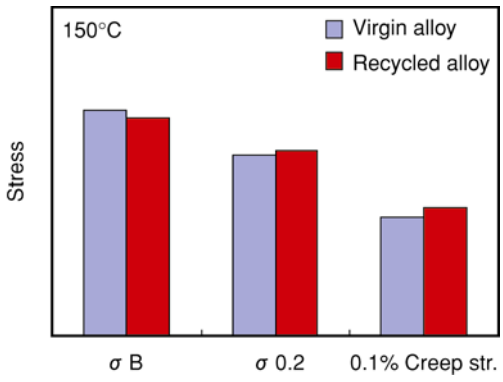


Fig. 8 Strength of recycled AE62-Ca alloy by the developed process compared with virgin alloy

3.2. New FIPG Development

Conventionally, a FIPG has been used to maintain the seal at the contact surface between the transmission case and clutch case. The current FIPG was developed on the assumption of use with aluminum alloy parts, and when used with magnesium alloy parts, there is a drop in adhesion strength. Therefore, with the magnesium alloy oil pan, a chemical membrane was formed with chromic acid treatment to maintain adhesion strength.

Chromate conversion coating increases cost, and because it uses hexavalent chromate, which is a toxic substance, the use of which will be limited in the future, it was vital to develop a new FIPG which does not require a chromate conversion coat.

The drop in adhesion strength with magnesium alloys arises from the fact that there are fewer sites in the magnesium alloy surface compared to the aluminum alloy surface for forming bonds between the OH and silane coupling agent (designated as "AP" agent hereafter), which is the agent supporting adhesion in the FIPG. Figure 9 gives an outline of this.

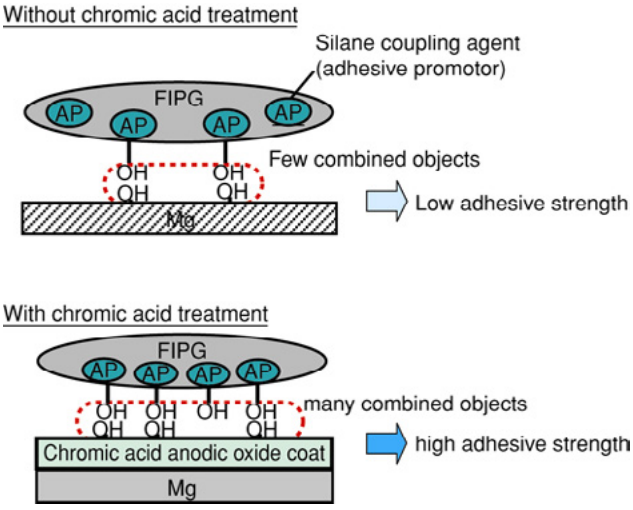


Fig. 9 Adhesive mechanism between FIPG and Mg alloy

The following items were implemented as adhesion strengthening countermeasures, and a performance evaluation was conducted.

(1) New AP agent used:
Add Alkoxy-silane AP

(2) Boundary adhesion strength increase:
Lengthen base polymer chain length

(3) Hardness Increase:
Increase hardening agent amount

(4) Oil resistance increase:
Add swelling restraint filler

The results are shown in Fig. 10.

Combining magnesium alloy with the current FIPG means a drop in adhesion strength to approximately half that with aluminum alloy. But, with the newly developed FIPG, adhesion strength equivalent to aluminum alloy and the current FIPG is achieved, therefore there is no need for a chromate coating.

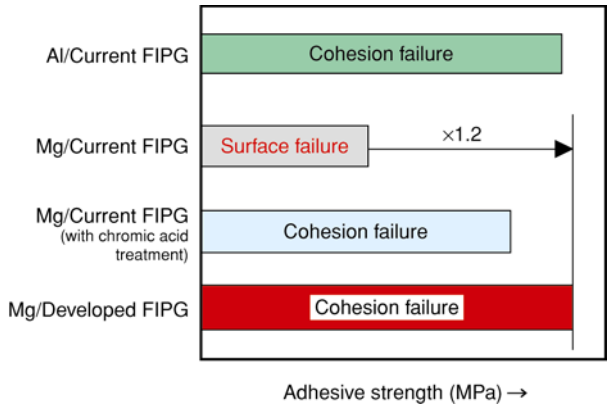


Fig. 10 Comparison of adhesive strength between FIPG and Al/Mg alloy

3.3. Development of Fluorocation Resin Coated Bolt

Because magnesium is the most electronegative structural metal, in comparison with aluminum, when magnesium is exposed to a corrosive environment in a state where there is contact with a dissimilar metal, galvanic corrosion will occur. For parts located under the vehicle body, such as the MT case, water is easily thrown up on it during driving, and particularly in winter, and in regions where de-icing agents are prevalent, there is exposure to an extremely harsh environment, and thorough countermeasures are required.

With the magnesium alloy oil pan, the connection parts were insulated by combining a chrome-plated bolt and an anodized aluminum washer (anodic oxide coating). However, with the MT case, because the number of connection points is quite high, this would mean a large cost increase. Therefore, a new fluorocation resin coating bolt was developed with the aim of reducing cost (Fig. 11).

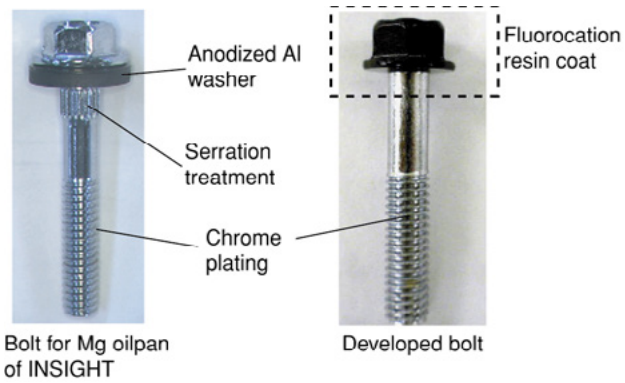


Fig. 11 Galvanic corrosion protection bolt

From the results of the evaluation using the salt spray test, as shown in Fig. 12, it was confirmed that the anti-corrosion performance was at a level equivalent to that of a bolt used with the magnesium oil pan.

In addition, bolt force retention was verified, and it was confirmed that these properties were equivalent to that of existing parts.

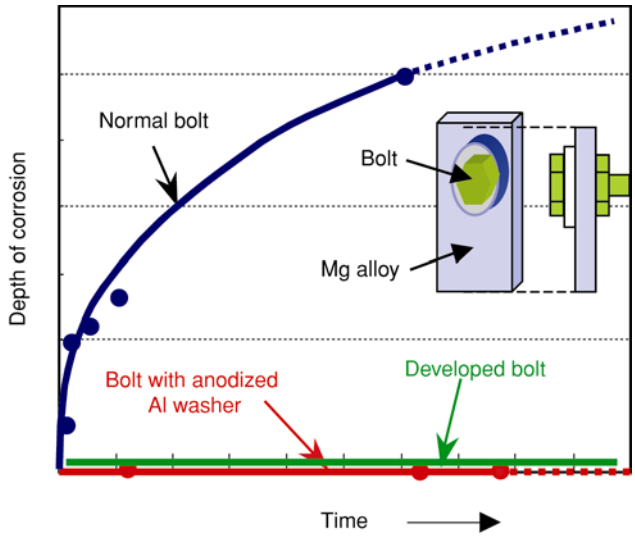


Fig. 12 Performance of anti - galvanic corrosion bolt in salt spray test

4. Design Technology

The Young's Modulus of magnesium alloy is approximately 2/3 that of aluminum alloy, and when the shape is the same, case rigidity is less, seal performance drops, and stress increases, giving rise to the potential issues of insufficient strength and poor NVH properties.

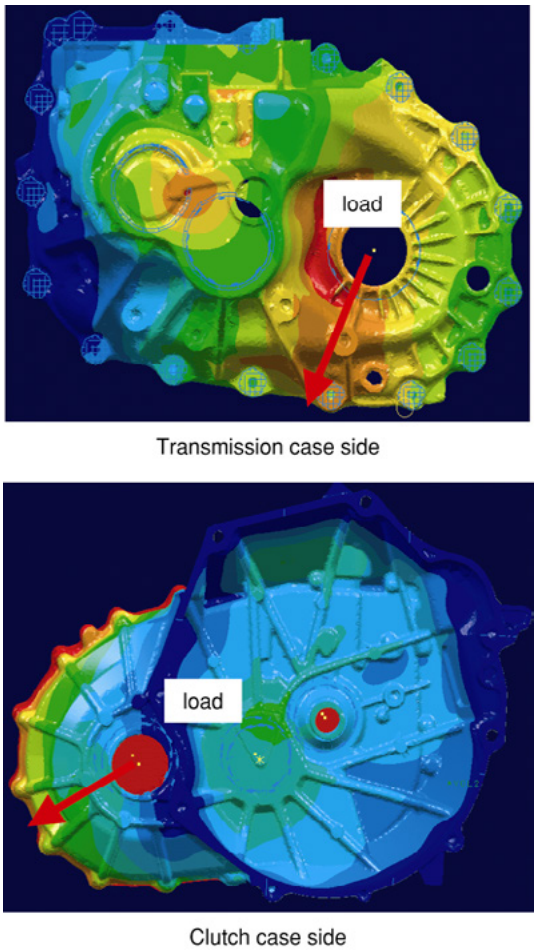


Fig. 13 FEM simulation of deformation of MT case

Because of this, when determining the case structure, shape studies were carried out according to
(1) Analysis of amount of deflection
(2) Stress analysis
(3) Power-train rigidity analysis.
The goal was to maintain rigidity equivalent to the aluminum alloy case, with the minimum amount of weight increase.

4.1. Analysis of Amount of Deflection

Figure 13 shows the results of analysis carried out with the same shape as the aluminum case. Because it is clear that there is a large amount of deflection generated in the contact surface around the differential gear due to input from the final driven gear, as a countermeasure ribs were added focusing on the area around the differential gear and radial thickness was increased.

A prototype part was created that incorporated the countermeasure shape, and using the static torsion test, joining behavior in the locations shown in Fig. 14 where measured. As shown in Fig. 15, the results showed a displacement amount equivalent to the aluminum case and an equivalent level of rigidity was maintained.

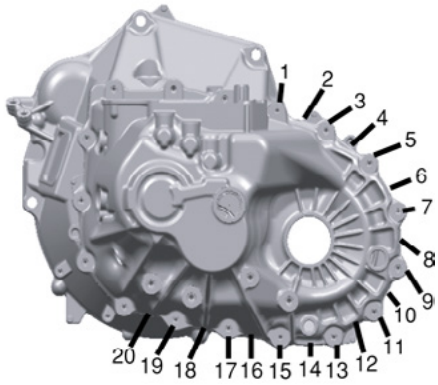


Fig. 14 Measuring points of slip deformation at contact surface between mission case and clutch case

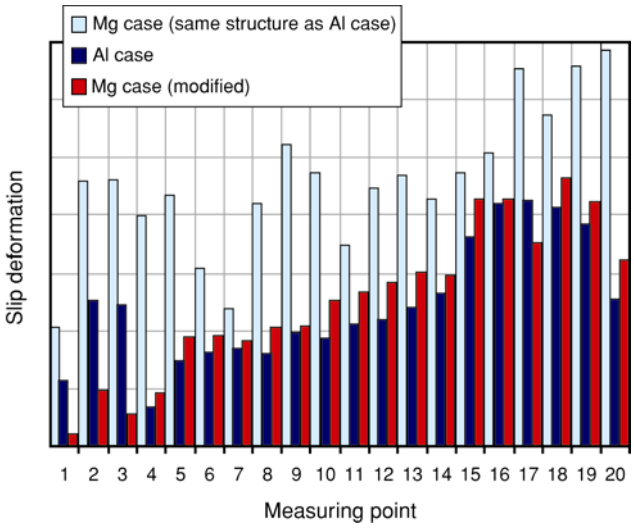


Fig. 15 Comparison of slip deformation at contact surface of case

4.2. Stress Analysis

With the aim of improving the stress analysis simulation of each part, as shown in Fig. 16, analysis was implemented using a model that integrates the transmission case and clutch housing.

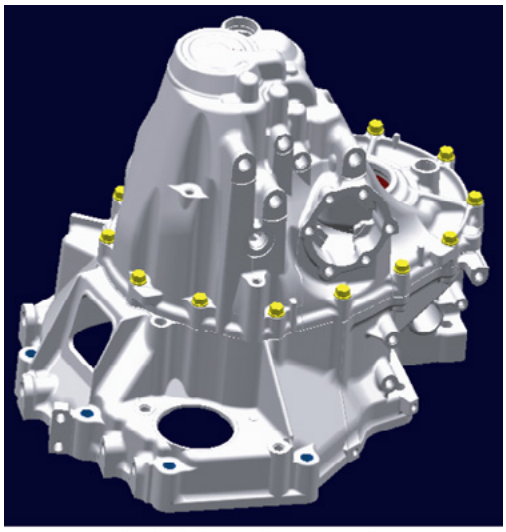


Fig. 16 Image of stress analysis model

Figure 17 shows the results of the analysis. Based on these results, shape countermeasures were applied in areas of high stress, including increasing radii and increasing radial thickness. Therefore, stress levels no more than the target were achieved.

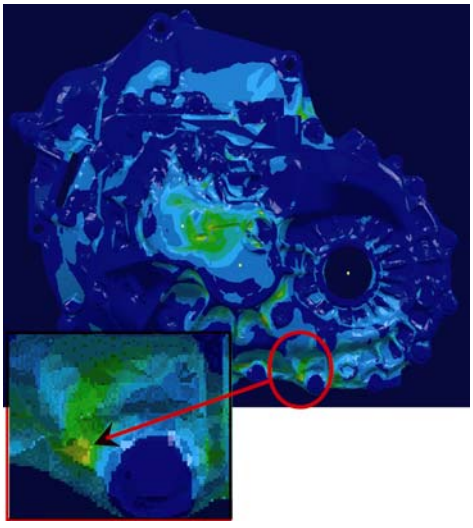


Fig. 17 FEM simulation of stress of MT case

4.3. Power-Train Rigidity Analysis

Because the rigidity of the power train as a whole, when connected to the engine, greatly contributes to NVH properties, further resonance frequency analysis was carried out assuming the engine input state.

Figure 18 gives the results of the analysis in the vertical direction bending mode.

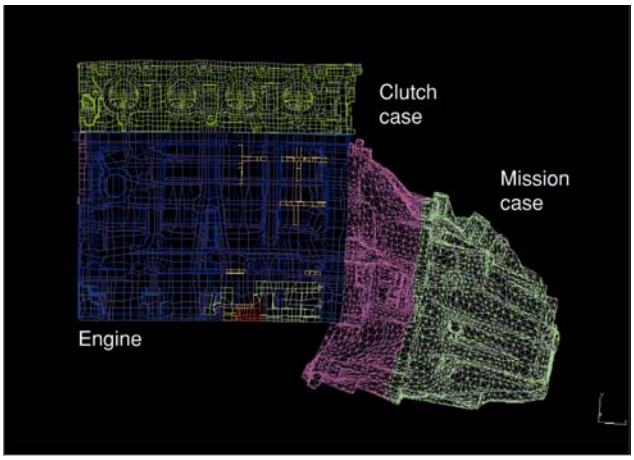


Fig. 18 FEM simulation of resonance frequency analysis at bending mode in the vertical direction

Based on these results, the shape was established so that rigidity would be attained that was equivalent to the aluminum alloy case, focusing on the parts attached to the engine. As shown in Fig. 19 and Fig. 20, NVH performance equivalent to that of the aluminum alloy case was achieved.

In comparison with the aluminum case, the Mg case weight was reduced by 24%.

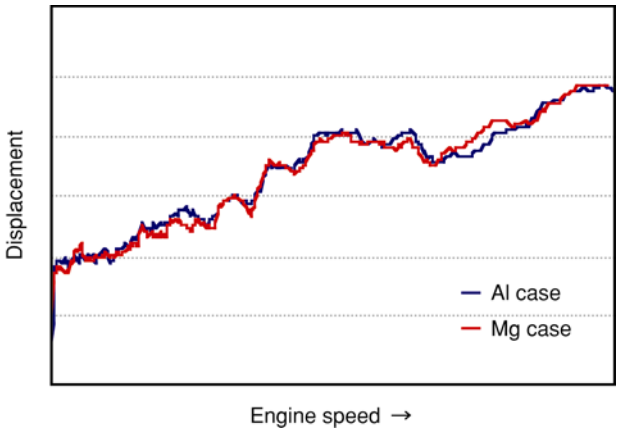


Fig. 19 Displacement of engine rear mount

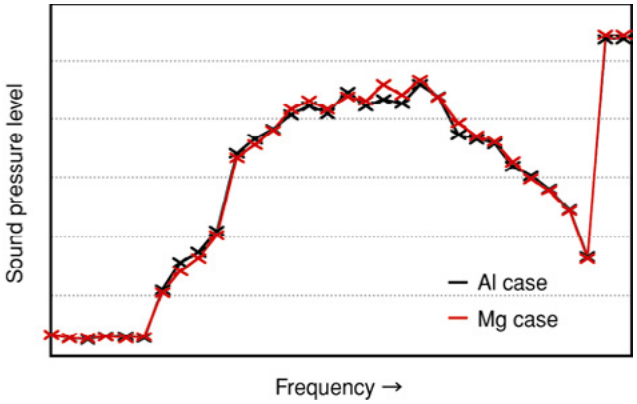


Fig. 20 Sound pressure level from MT case

5. Surrounding Technologies

5.1. Joining Technologies

Generally, when examining bolted joints, it is found that bolt load increases in hot temperatures due to thermal expansion differences between the bolt and the case. This force causes buckling of the flange and threads and creep deformation, which leads to a drop in bolt load. In the case of magnesium alloy, the thermal expansion rate is 20% greater than aluminum alloy, so it is easy for bolt load to drop.

Therefore, for areas where bolt load retention properties are required, such as on the case mating surface, joint specification revisions were made, such as increasing the outer diameter of the bolt flange to reduce stress, and increasing internal thread screw overlap margin.

The results of bolt force behavior at the case contact surface show, as can be seen in Fig. 21, that bolt force is equivalent to that with the aluminum case, or better.

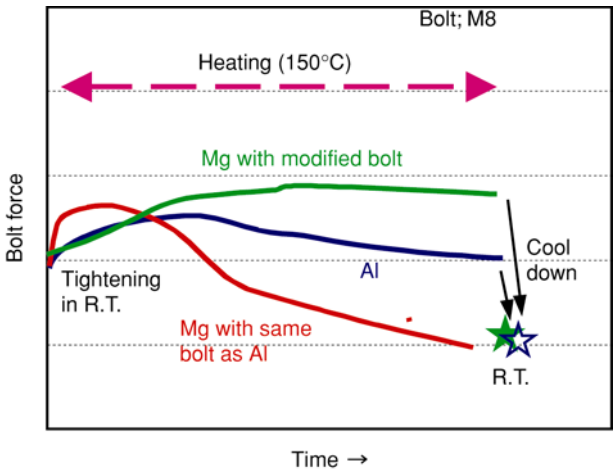


Fig. 21 Comparison of bolt force retention at 150 °C

6. Summary

Using heat-resistant magnesium alloy, a manual transmission case was developed that achieves a 24% weight reduction over the conventional aluminum alloy part.

The technologies used as are listed below.

(1) Development of the AE62-Ca material, giving improved castability over the heat-resistant magnesium alloy ACM522, and establishment of a recycling process that can achieve a scrap recycling rate of 95%, on a par with general magnesium alloy, with the possibility of using 100% recycled ingots.
(2) Development of a FIPG that has adhesion strength at least as good as with the aluminum alloy case, without the use of chemical treatments.
(3) Development of a fluorocation resin coating bolt for the prevention of galvanic corrosion of the connection parts.
(4) Establishment of computer aided engineering to design a magnesium alloy case shape that gives performance equivalent to aluminum alloy parts.

7. Acknowledgements

The authors would like to express their sincere gratitude to the many people both in Honda and elsewhere that gave their generous support and cooperation in this development project.

References

(1) Koike, S., et al.: Development of Lightweight Oil Pans Made of a Heat-Resistant Magnesium Alloy, HONDA R&D Technical Review, Vol. 12, No. 1, pp. 167-174 (2000)

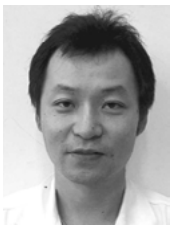
■ Authors ■


Hideaki MIYASHITA


Masayuki NAKADA


Masayasu SAKATA


Yukihiro HAYAKAWA


Sadaharu MATSUMURA

Development of Precoat Adhesive for All Olefin Instrument Panel

Tetsuya ODA* Atsushi KAWATA*

ABSTRACT

To simplify the production process for vacuum-formed instrument panels, adhesive spray coating of the surface of the plastic foundation has been replaced by pre-coating the bottom side surface of the laminated skin, reducing the number of procedures required for spraying and drying. Further, the development of an adhesive with excellent olefin adhesion qualities has reduced the number of pretreatment steps necessary for the foundation and skin. Adoption of this method has simplified the production process, and reduced the required number of procedures from nine to five, thereby resulting in cost reductions.

1. Introduction

The vacuum forming process is widely used to bond polyvinyl chloride (PVC) laminated with soft polypropylene foam (PPF) skins to automotive interior fitting such as instrument panels (I/P). Adhesives are normally used in this process to bond these soft skins to a foundation. Various changes have been made to make the manufacturing process of interior fittings environmentally friendlier: Solvent-free adhesives have been developed[(1)], the I/P can be constructed of all olefin materials[(2)], the olefin skins can be recycled to the foundation[(3)], etc.

The change to all olefin I/P has been achieved by changing skin material from PVC to environmentally friendlier chlorine-free thermoplastic olefin (TPO) resin and foundation material from ABS resin to polypropylene (PP). However, the change to olefin has made numerous additional procedures necessary in the manufacturing process. Among these are flame or plasma pretreatment to increase the wettability of the PP (a low-wettability material) in order to achieve adhesion to the skin. In addition, it is now necessary to conduct primer treatment to the soft PPF layer to achieve adhesion.

This paper describes a method of bonding materials during the production of all olefin I/P using the vacuum forming and fitting process. In this method, an adhesive specially developed to bond olefin materials is precoated on the bottom surface of the PPF. This has reduced the amount of pretreatment necessary for skin and foundation, and has led to an extensive reduction in the number of procedures required in the vacuum forming process.

2. Development Concept

2.1. Construction of I/P

Conventional all olefin I/P are composed of an injection-molded PP foundation, a TPO skin, and a PPF cushion layer. The TPO and PPF are laminated, and the bottom surface is treated with a primer. To bond the skin materials and the foundation, pretreatment (flame treatment, etc.) is conducted on the surface of the PP foundation, and adhesive is applied for the vacuum forming and fitting process. Figure 1 shows the makeup of these IPs; asterisks represent materials or treatments which relate to adhesion.

* Tochigi R&D Center

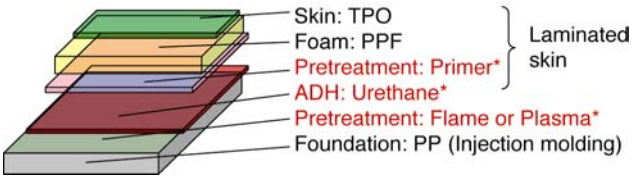


Fig. 1 Construction of instrument panel

2.2. I/P Vacuum Forming Process

Figure 2 shows a representation of the I/P vacuum forming process. The process is made up of nine procedures, as follows:

(1) Injection molding: The PP is formed into the I/P shape.
(2) Pretreatment: Plasma or flame treatment is conducted to promote adhesion to the surface of the PP foundation.
(3) Adhesive coating: Adhesive is sprayed on the surface of the pretreated PP foundation to enable adhesion to the bi-laminate.
(4) Adhesive drying: The solvents (water) in the adhesive are flashed off.
(5) Preheating (Heat activation): The adhesive on the surface of the foundation is reactivated by heating in a convection oven.
(6) Skin heating: The TPO/PPF skin is heated to allow thermoforming into the I/P shape.
(7) Vacuum forming: The heated TPO/PPF is simultaneously molded and bonded.
(8) Trimming: Excess skin is removed after bonding from the foundation.
(9) Curing: The crosslink adhesive is strengthened.

Six of these procedures (2), (3), (4), (5), (7) and (9) are related to adhesion. To further simplify the adhesive-related procedures, this project examined adhesive precoating of the bottom surface of the skin as a method to reduce the required pretreatment of the foundation and skin, thus allowing a reduction in the number of adhesive-related procedures. In this method, precoat adhesive would replace the primer currently applied to the bottom surface of the skin. Because the adhesive would be activated at a high temperature (140 °C+) in procedure (6) above, this could be expected to enable more effective adhesion. By giving this precoat adhesive the role of the former pretreatment and adhesive, three adhesive-related processes (2) – (4) would be eliminated. The possibility of eliminating the curing procedure (9) by using a quick-hardening adhesive was also investigated. In addition, it was expected that the use of a precoat adhesive would increase efficiency by enabling continuous application on the skin production line, rather than the conventional spray coating of the foundation in the forming process. (Fig. 3)

3. Difficulties and Solutions

3.1. Difficulties of Precoating

The following technical challenges were addressed through the development of a precoat adhesive for an I/P vacuum forming process.

(1) Achieving adhesion to PP, a low-wettability and low-adhesion material.
(2) Initial adhesion properties to allow the adhesive to conform to the complex geometry of the I/P.
(3) Cohesion capable of resisting temperatures of 100 °C or more when the I/P is exposed to direct sunlight.
(4) Durability requirements of an automobile interior.
(5) Measures to prevent adhesion to the mold caused by pre-coating the tooling.

A thermal crosslink system, in which a crosslink reaction is commenced by heating, was adopted in addition to the

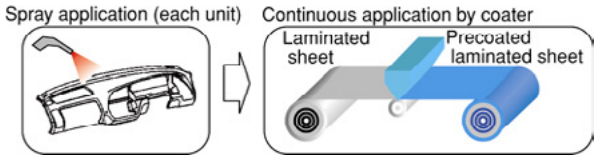


Fig. 3 Change of application system

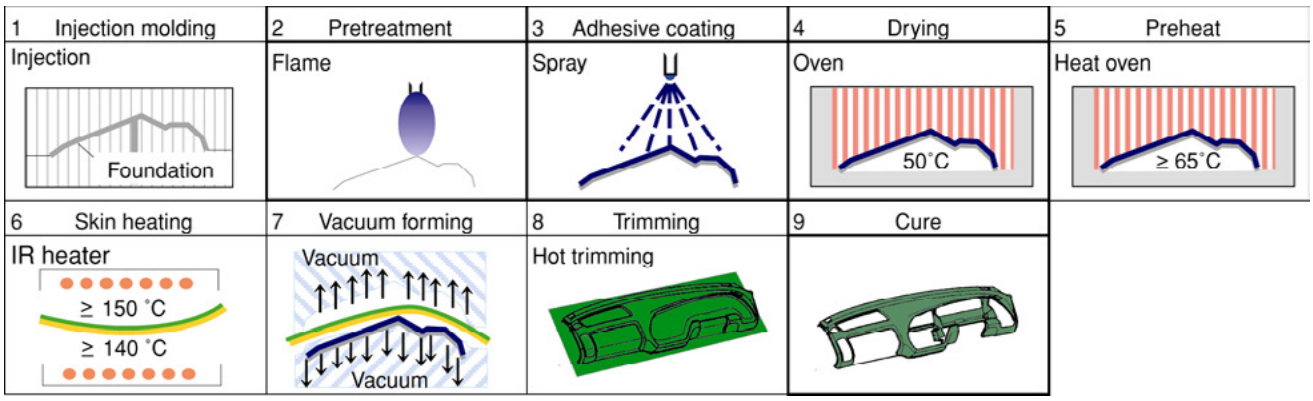


Fig. 2 Vacuum forming process for instrument panel

olefin adhesive which has a high-adhesion property with PP adherent. This made it possible to achieve the required level of heat resistance, durability and reliability. Further reductions in the number of processes involved in the vacuum forming operation were achieved through optimization studies of the adhesive composition and hardening conditions.

3.2. Solutions to Technical Challenges

3.2.1. Adhesion properties to olefin materials (1)

The elements contributing to adhesion to PP were examined at an early stage to enable adhesive precoating.

The following are the most important elements in adhering to PP:

- Wettability of the PP adherent (Adaptability)
- Improving the adhesive's ability to follow minute irregularities on the PP surface (Anchoring effect)

First, to achieve adhesion to the olefin resin, it was important to make the PP (a substance with low adhesion properties) more receptive.

The low surface polarity of olefin (low surface tension: low wettability) surface is a cause of difficulty in adhesion to olefin resin. Adhesion has conventionally been increased through polarization of the olefin surface by coating with a primer, etc., until the surface polarity approached that of the adhesive (rubber, urethane, etc.).

This project examined the feasibility of increasing adhesion performance by developing an adhesive with an olefin structure similar to the base PP.

Solubility parameters (SP value) are an index enabling prediction of the adhesion of two substances.

To ensure adhesion with PP, it is most expedient to select an olefin adhesive with an SP value similar to that of PP. (Table 1). However, olefin adhesives have low SP values and are difficult to dissolve in organic solvents; thereby making the conventional method of spraying, after dispersion in a solvent, unworkable. Olefin adhesives have therefore only been applied in a hot melt type up to the present. Therefore, a functional group was implemented, within the adhesive, with a polarity similar to the base PP to improve adhesion. This functionality enabled dispersion into the solvent while maintaining adhesion to base PP (Fig. 4).

Table 1 Adaptability of adhesive

	Substrate (Plastics)	Solubility parameter (SP Value)	Adhesive (Polymers)	Solubility parameter (SP Value)
↑ Low polarity	Teflon	6.2		
	Silicon	7		
	Polypropylene	7.9	Olefin	8
	Polyethylene	7.9		
	Polystyrene	9.2	CR rubber	9.2
	ABS	9.3	EVA	9.4
	Acryl	9.3	Urethane	10
	PVC	9.6	Epoxide	10.4
	PET	10.7	PET	10.5
	Polyamide	13.2	Polyamide	13

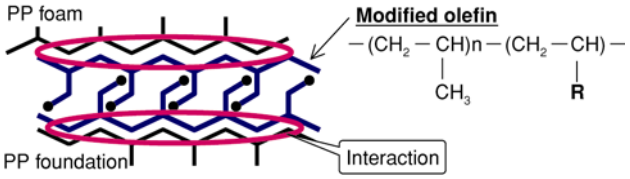


Fig. 4 Adhesion structure model

Adopting a precoating method has made it possible to change the adhesive application method from spraying to the foundation to coating of the skin sheets with a coater. This has increased the degrees of freedom of the application and enabled the use of an olefin adhesive.

3.2.2. Thermal characteristics (2), (3)

Widely varying thermal characteristics are required from the adhesive to enable it to be used in the I/P forming process and resist the temperatures it will be subjected to during use of the vehicle, such as in a closed vehicle cabin in an extremely hot environment. Development proceeded based on hypothetical adhesive temperature characteristics. The adhesive requires flexible characteristics during the pad forming process, in order to improve adhesion (anchoring effect) on minute, uneven, substrate surfaces. On the other hand, for automotive usage it is necessary for the adhesive to have sufficient heat strength (cohesion) to resist high temperatures when the vehicle is left in an extremely hot environment.

Figure 5 shows a thermal history of the skin during the formation process. The laminated skin is raised by heating, and stretched and pressed directly after the temperature required for formation is reached. Figure 6 shows a temperature vs viscosity curve for the adhesive. This data shows that in the 140 °C – 160 °C temperature range, which is required for formation, the adhesive becomes sufficiently soft to follow the uneven contours of the adherend surface.

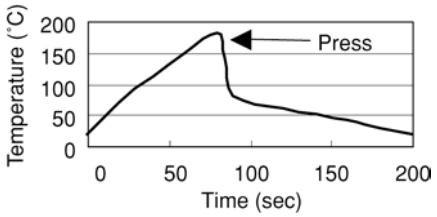


Fig. 5 Temperature of laminated sheet

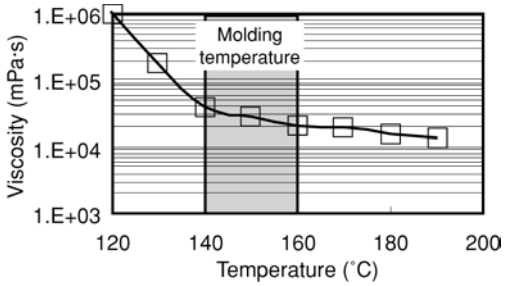


Fig. 6 Temperature vs viscosity curve

In contrast to this, after hardening a high level of cohesion at 110 °C is required of the adhesive in actual use. The modulus is evaluated as an index of cohesion. Figure 7 shows the characteristics of the adhesive from hard to melted

states, and demonstrates that the adhesive is stiff from room temperature up to 110 °C. A reversal of characteristics is required within a temperature difference of only 30 °C (high cohesion at 110 °C, sufficient softness at 140 °C). This is difficult to achieve using the conventional hot melt adhesives, and the thermal crosslinking discussed below was therefore examined.

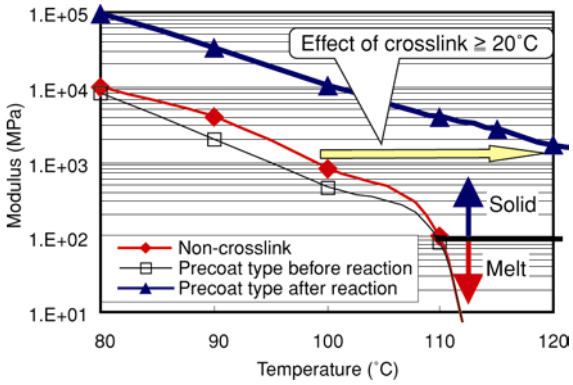


Fig. 7 Temperature vs modulus curve

3.2.3. Mechanism of improved heat resistance (3), (4)

To improve the cohesion of the adhesive when the vehicle is left in an extremely hot environment, a one-component crosslink system was adopted. This system was decided upon, based on the precoating of the bottom surface of the skin and long-term storage post-coating. During storage, it is essential to ensure that adhesion is maintained and that no reaction proceeds. A dormant thermal crosslink system was selected because the reaction will only commence at certain temperatures in this system.

A solvent dispersion system was selected, because heat cannot be applied during the process of production of the skin, due to the characteristics of the thermal crosslink.

Figure 8 shows a model of the mechanism of adhesive curing. At room temperature, solid crosslinking agents are dispersed in the adhesive film. When heat is applied, the base polymer first dissolves, and the crosslinking agents begin to dissolve and disperse. When the reaction commences, a stable three-dimensional structure begins to form. When this structure bonds together, it is impossible to reverse the reaction, and the adhesive will therefore not return to its original state when the temperature drops. In addition, the use of olefin as the base resin has ensured a sufficient level of adhesion with olefin.

The crosslink reaction commences at around the highest temperature reached immediately before the formation process, but the adhesive is still soft during formation, as shown by the temperature vs modulus curve in Fig. 7. After the crosslink reaction is completed, the modulus shows that heat resistance is improved by more than 20 °C compared to performance before the formation of crosslinks. In addition, the use of a thermal crosslink reaction which cannot be reversed has ensured that a high level of strength is maintained after endurance and deterioration.

3.2.4. Sticking to tooling (5)

Next, methods of preventing the adhesive from sticking to the aluminum mold, a typical concern for precoat adhesives, was studied.

Because the bottom surface of the skin makes direct contact with the tooling at the periphery and openings of the foundation, the precoat adhesive can stick to the tooling and be difficult to remove. The application of a surface release treatment was examined as a method of preventing this phenomenon.

Details of these methods of solving the various difficulties outlined above will be presented in the following section.

4. Basic Adhesive Performance

4.1. Adhesion

Figure 9 shows a magnified photograph of a cross-section of the adhesive layer between the PPF and the PP foundation.

Sufficient wettability is essential in obtaining the required level of adhesion. In this photograph, an extremely thin welding layer can be seen at the boundary of the PP and the adhesive. This is thought to give the adhesive strength. Precoating using an adhesive with a modified olefin base polymer has ensured that the adhesive can be heated sufficiently to achieve dissolution; making the adhesive and the PP highly adaptable and enabling the formation of a welding layer.

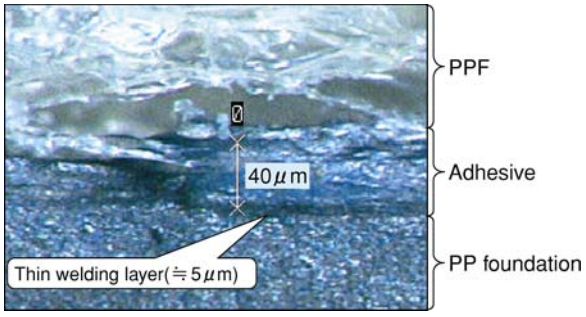


Fig. 9 Section of instrument panel

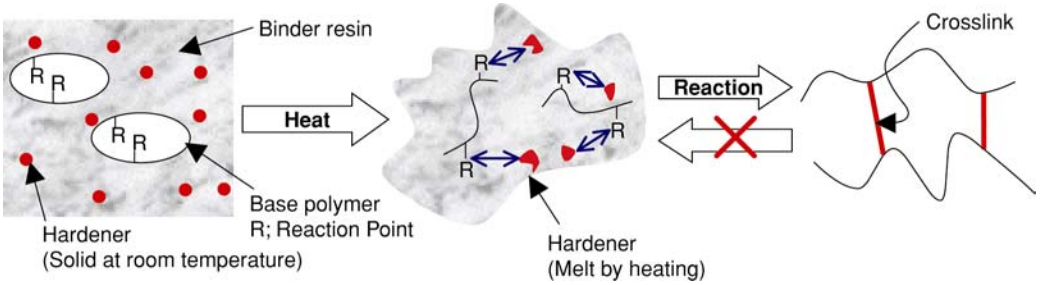


Fig. 8 Increasing toughness

Table 2 Composition of adhesive

Materials			Property	Main purpose
Base resins	Olefin resin	Modified PP A	Low melting point	Adhesion with PP
		Modified PP B	High melting point	↑, Heat resistance
		Modified rubber	——	↑, Flexibility
Additives	Tackifier	Modified rosin	Middle melting point	Initial adhesion
	Hardener	Hardener	Extra high melting point	Reaction with the modified resins
Solvents	Aliphatic	Cyclohexane	bp 81ßC	Viscosity control
	Aromatic	Toluene	bp 110ßC	Dissolution
	Ketone	MIBK	bp 116ßC	Viscosity stability

4.2. Study of Adhesive Composition

The results of the study of adhesive composition conducted in this project are shown in Table 2. The selection of the base polymer is the most important factor in ensuring adhesion. The composition of the adhesive was selected with particular attention to ensuring adhesion with PP. Initial adhesion can be evaluated by measuring initial creep peel length and 180 degree peel strength at 100 °C.

Figure 10 shows the test method. Initial creep is measured by taking a test piece of 25 mm width directly after production and weighting the skin with a 1.96 N load at 90 degree to the foundation. This test piece is left for 30 min. at 80 °C. After this, the length of skin which has peeled from the foundation is measured. 180 degree peel strength is measured by taking a test piece with an identical thermal history to the initial creep test piece and measuring it at the specified temperature in the 180 degree peel strength test specified in JIS K 6829. The heat resistance creep test utilizes the same set-up as for initial creep test, but the test piece is left for 24 hours at 100 °C before peel length is measured.

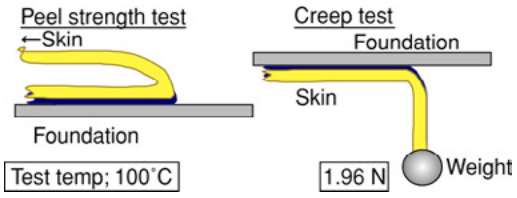


Fig. 10 Adhesion test method

Figure 11 shows results obtained from tests conducted to select a base polymer. The results show an improvement in heat resistance performance obtained by the use of two types of modified PP with different melting points. The resin with a low melting point ensures sufficient softness to allow initial following of the form, while the resin with a high melting point improves heat resistance performance.

Tests also confirmed that using an optimum amount of olefin rubber in the composition of the adhesive has significantly improved peel strength directly after forming. The addition of a rubber component improves ability to follow the form during forming, but an excessive amount of rubber would reduce the modulus in the temperature range in which the I/P will be used. The addition of the correct amount brings the modulus to its maximum value.

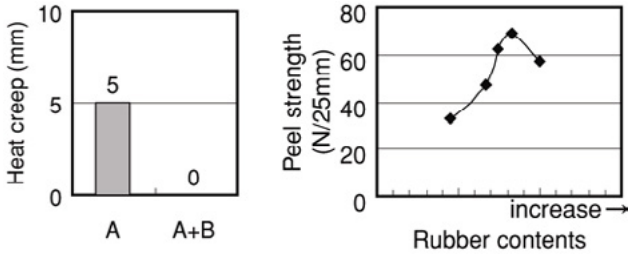


Fig. 11 Base olefin examination

The tackifiers that adjust the adhesive's viscosity were studied next. Making the adhesive viscous increases initial adhesion to the adherent. A functional group was introduced to provide viscosity, leading to a major improvement in peel strength after endurance tests, as shown in Fig. 12.

When introducing a thermal crosslink system, the characteristics of the crosslinking agent must be considered, because they have a significant effect on adhesion. The most important factor in the adoption of thermal crosslinking was the reaction temperature of the crosslinking agent.

Figure 13 shows the relationship between reaction temperature, peel strength and viscosity after storage for 30 days at 40 °C. Because the reaction commences too early when a crosslinking agent with a low reaction temperature is used, the crosslink reaction has already proceeded too far when the materials are bonded, and the adhesive film is too hard to allow sufficient following of the form. This causes adhesion strength to be low. The reaction proceeds slowly if a crosslinking agent which dissolves at room temperature is used, making the adhesive more viscous. These results led to the crosslinking agent with the highest reaction temperature being used.

The results of a study of the mixing ratio of the crosslinking agent are shown in Fig. 14. The relationship between strength and the ratio of crosslinking agent to base resin shown in the figure enabled the selection of a ratio ensuring a sufficient crosslinking effect. This proportion was close to the required proportion theorized from the amount of modification to the resin.

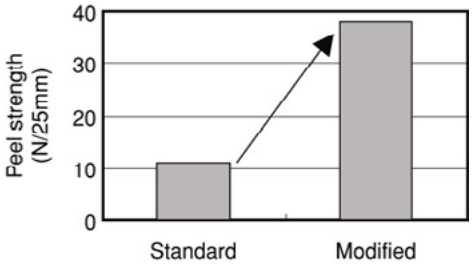


Fig. 12 Effect of modification (after 110°C1000 hr)

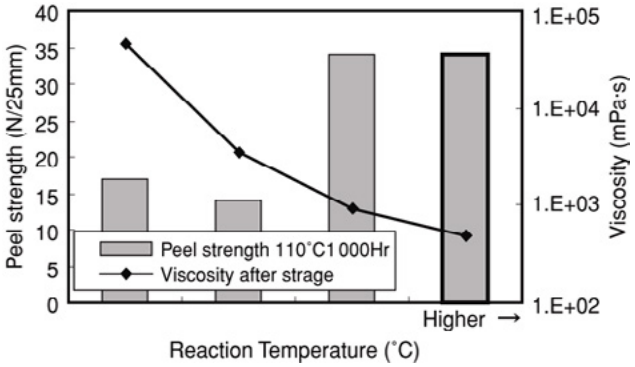


Fig. 13 Reaction temperature of crosslinking agent

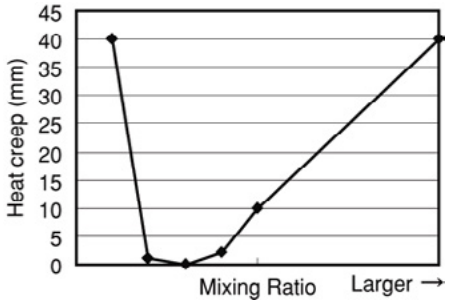


Fig. 14 Mixing ratio of crosslinking agent

The procedures described above made it possible to achieve a basic composition for a pre-coat adhesive with excellent I/P performance. The characteristics of each component were exploited to achieve the performance requirements.

5. Verification of Precoat Characteristics

5.1. Film Thickness Setting

The extensive changes to the forming process entailed by the change to precoating made it necessary to reset various parameters to be controlled at the production site.

The factors, which affect adhesion during the vacuum forming process, are the temperature of the PP foundation, directly before forming, and the adhesive film thickness. The dependence of the adhesion of the new adhesive composition on film thickness and foundation temperature were likewise studied. Figure 15 shows an example of the results of these tests. Creep length was also tested, due to the effect of temperature- and film thickness-dependence. The horizontal axis represents adhesive film thickness, and the vertical axis shows creep length. The smaller the values for creep length, the better the performance.

The example shown is for a foundation temperature of 45 °C, with a minimum film thickness of 17 µm.

Adhesion was studied for various film thicknesses and temperatures. The results of these tests are shown in Fig. 16, and show that the minimum necessary set-up for sufficient adhesion performance are a film thickness of 17 µm and a foundation temperature of 45 °C. This temperature is lower than the minimum temperature of 55 °C for the currently used spray adhesive, leading to benefits for the production process.

Because the skin is stretched to a maximum of twice its size (area ratio) in the vacuum forming process, conditions must be set to ensure that the adhesive film is sufficiently

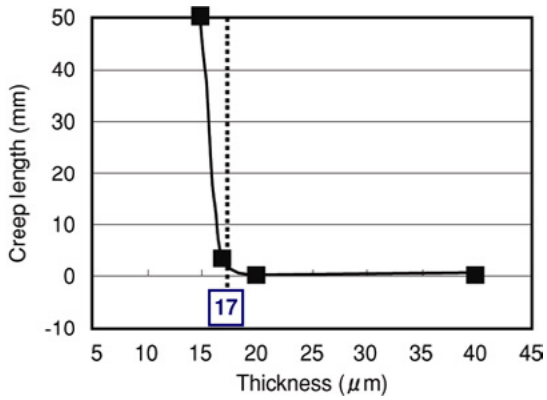


Fig. 15 Initial creep vs adhesive thickness (PP foundation temperature; 45°C)

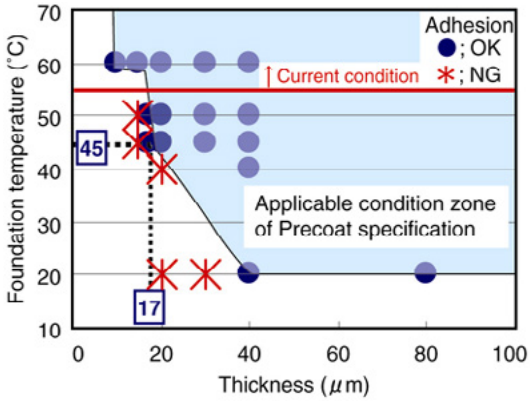


Fig. 16 Foundation temperature vs adhesive thickness

adhesive after stretching. The thickness of the film after stretching is inversely proportional to the degree of stretching the skin, and film thickness therefore halves when the skin is stretched to twice its original area. The minimum film thickness of 17 µm must therefore be doubled to 34 µm for application to the skin during production to maintain adhesion.

5.2. Coating Process

The process of coating the bottom surface of the skin with adhesive was now studied. The skin is coated with precoat adhesive using a conventional coater, and then dried.

It is possible to use various types of conventional liquid coaters, such as roll coaters, knife coaters and gravure coaters.

Figure 17 shows the test results of the accuracy of coating using a roll coater. Film thickness was measured at 516 points for seven production lots. For a target of 40 µm, test results showed a mean value of 40.13, with a standard deviation of 1.49, verifying the performance of this method in actual production. Cp was 1.34 for the lower minimum thickness of 34 µm, demonstrating that the method had achieved the figure of 1.33 required for stability. These results showed that it has been possible to maintain the lower limit of 34 µm, including fluctuation, by establishing a figure of 40 ± 6 µm as the control limit for film thickness on the production line.

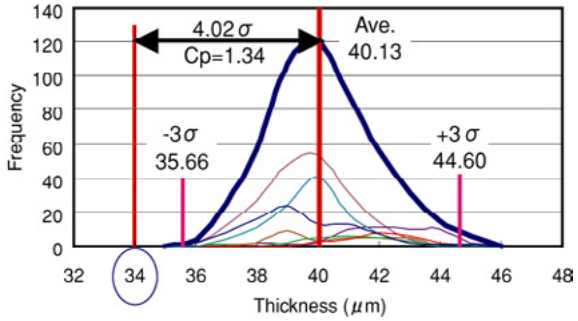


Fig. 17 Range of coating amount

5.3. Durability Performance

Tests were conducted to determine the performance of the adhesive in a finished I/P when applied at minimum film thicknesses. Figure 18 shows the results of tests carried out for the standard film thickness of 40 μm, and a thickness of 30 μm, below the lower limit value. Tests measured the peel strength of I/P formed using specific adhesive film thicknesses after heat aging at 110 °C. The percentages shown in the key represent the degree of stretching the skin was subjected to after formation.

These tests measured heat peel strength under the most severe conditions; results show that high peel strength was maintained even when adhesive thickness was 30 μm, less than the minimum value established by this research, and the sample was aged for 1,500 hrs, 1.5 times the specified time.

It was confirmed that no drop in strength was observed in humidity resistance, thermal cycle resistance, chemical resistance, etc., and all result in PPF break-down.

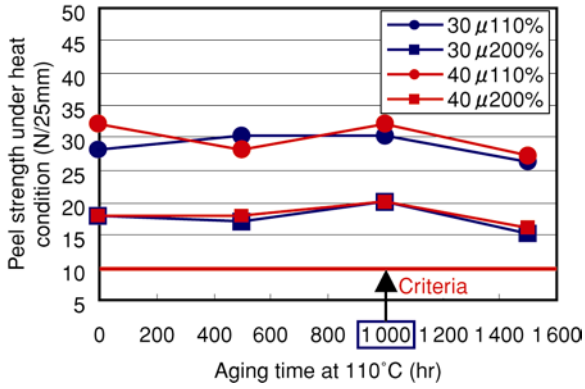


Fig. 18 Heat resistance vs adhesion thickness

5.4. Storage Stability

Two criteria relating to storage were tested to establish the feasibility of the new adhesive for use in I/P production.

One of these was the level of adhesion of the adhesive and the precoated skin after a period of storage. As stated above, precoated skins are often stored for extended periods when the precoating method is used.

To test this, the longest hypothetical period of storage, which would be used during mass production, was established, and test pieces were tested for creep and durability after storage for an extended period.

As Fig. 19 shows, no drop in performance from initial levels was demonstrated in either creep or durability tests, indicating that the new adhesive has good storage characteristics.

In addition to these tests, precoated skins were stacked and stored to test the relation between drying conditions after precoating and the occurrence of blocking, or the adhesion of skins to each other in storage (Figs. 20, 21). When less than 1% of residual solvent remained in the adhesive, blocking did not occur. Drying conditions of more than 80 °C for longer than 60 sec are therefore required to prevent blocking. These results led to 100 °C × 1 min. being established as the drying conditions for the new adhesive.

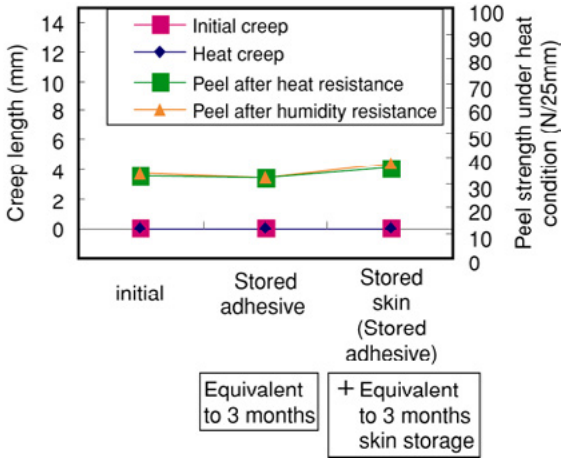


Fig. 19 Adhesion after storage

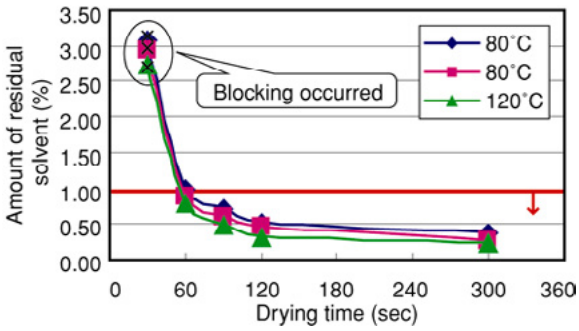


Fig. 20 Drying condition vs residual solvent (blocking)

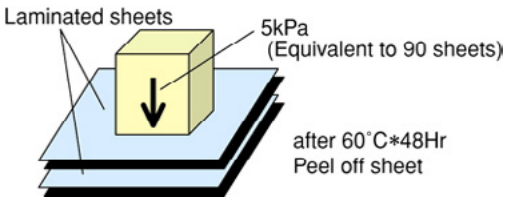


Fig. 21 Sheet blocking test method

5.5. Prevention of Sticking to Tooling

Figure 22 shows the peel strength of the precoat adhesive to aluminum, the material from which the mold is made, at various temperatures. The results demonstrate that peel strength increases with temperature on the untreated aluminum surface. This is because as the temperature of the aluminum adherend increases, the ability of the adhesive to follow the aluminum surface also increases. By contrast, when a silicone surface treatment is applied to the aluminum, desirable peel strength results are obtained not only for 55 °C, the temperature of the mold in the former mass production method, but also for 80 °C. As shown in Table 1, silicone has an SP value lower than that of olefin, ensuring excellent peelability.

A mold releasing composite silicon coating was chosen as the appropriate surface treatment. Silicon resin is the main ingredient of this inorganic coating. The use of a special hardening catalyst has improved dryability at room temperature, and has simplified both the coating operation and maintenance.

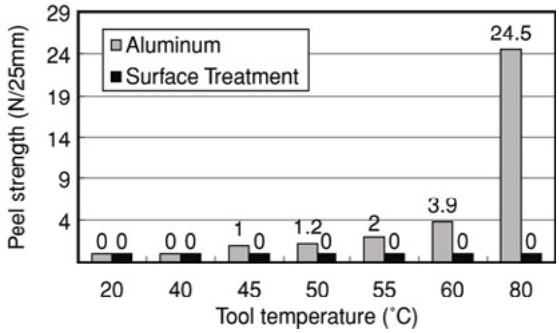


Fig. 22 Sticking to tooling

5.6. Superiority in Actual Production

As previously discussed, the development of a precoat adhesive has enabled a reduction in the number of procedures associated with I/P production, and these reductions have also significantly reduced the number of factors which must be controlled during the formation process. More than ten factors required control in setting conditions for the flame treatment, adhesive coat drying and vacuum forming in the former mass production process. Utilizing a precoat system has reduced these to three: skin storage period, skin heating temperature and PP foundation heating temperature.

Reducing the number of procedures required from nine to five has enabled the space required for production to be reduced from 286 m^2 to 196 m^2, or approximately two-thirds of the space presently required. In addition, the cost of production using the vacuum forming method has been reduced by 50%.

6. Conclusion

This research project used the following methods to develop a precoat adhesive for use in the vacuum forming process. This has enabled the number of procedures and the cost associated with the vacuum forming process to be reduced, while maintaining the quality design of vacuum-formed I/P. This will contribute to the broader use of recyclable all olefin I/P.

(1) A modified olefin resin was used as the base resin to improve adhesion with PP.
(2) A thermal crosslink reaction system was used to achieve heat resistance at 100 °C and above.
(3) A composition of adhesive, coating thickness, production conditions, etc., were optimized to achieve high adhesion with PP and maintain a similar level of productivity found in the former method.
(4) A surface treatment was selected and adopted to prevent sticking to tooling.

The precoat adhesive was developed on the basis of studies of these four factors.

7. Acknowledgments

The authors would like to offer their sincere thanks to everyone, both within Honda and representing other companies, who contributed to the success of this project.

References

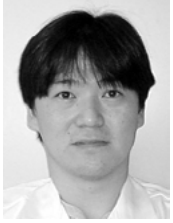
(1) Oyama, M., et al.: Development of a Solvent-free Adhesive for Use in the Vacuum Forming Process, Journal of Society of Automotive Engineers of Japan, Vol. 50, No. 5, pp. 40-45 (1996)

(2) Ito, H., et al.: Development of a 100% Recyclable Instrument Panel, HONDA R&D Technical Review, Vol. 10, pp. 158-165 (1998)

(3) Yamaguchi, T., et al.: A Recycling Technology for Instrument Panel Olefin Skins, Society of Automotive Engineers of Japan 2001 Spring Lecture Series Advance Collection, No. 42-01, pp. 13-16 (2001)

■ Authors ■


Tetsuya ODA


Atsushi KAWATA

Development of a Tubeless Tire Pressure Monitoring System for Motorcycles

Masayoshi ORITA* Tomoyuki HARADA* Toshio YAMAGIWA*

ABSTRACT

A tire air pressure monitoring system for motorcycles was developed. The system informs a rider of low air pressure or an air leak in the tire. High monitoring accuracy was obtained by compensating for the temperature of the air pressure, by measuring air pressure in the tire, by changes in pressure and temperature during running, and by the lowering of air pressure in the case of a flat tire. An air leak is judged by the speed of the air leak converted from an air pressure change and temperature change. The adjustment of the unbalanced revolution of wheels was minimized by mounting a separated tire valve and sensor. Indication of the air pressure and an alarm is for enhancing the rider's recognition during running.

1. Introduction

The recent trend toward larger motorcycle tire sizes and a prevalence toward low-profile tire designs has made it increasingly difficult for the rider to sense underinflated tires or tire air leakage while riding. For safety reasons, it is important for the rider to be aware of any such reduction in air pressure. Thus, a tire air pressure monitoring system for motorcycles has been developed. The system informs the rider of sudden air leaks brought on by tire punctures and helps prevent poor fuel economy caused by driving on underinflated tires by detecting a drop in tire air pressure and notifying the rider of this condition. A tire air pressure monitoring system detects tire air leakage in one of two ways: either by indirect detection, in which the system uses an anti-lock brake system speed detector to detect any differences in the rotation speed of the front and rear tires when a significant leak occurs, or by direct detection, where changes are detected in the tire pressure inside the tire. The indirect detection method is less reliable as there are only two tires for which it is able to draw comparative readings. For this reason, the direct method for detecting changes in tire pressure has been adopted. To accurately detect tire air leakage the system must be able to detect and compensate for the relationship between tire air pressure and temperature changes to determine the cause of the change in tire pressure.

The system also needs to be able to determine the tire temperature allowable limit since increases in tire temperature, due to underinflation, are a leading cause of tire failures. The system must also have an interface display suitable for motorcycles to effectively notify the rider of tire pressure abnormalities. While there are currently tire pressure monitoring systems used in automobiles, this newly developed technology is the world's first motorcycle tire air pressure monitoring system.

2. Targeted Development Goals and Related Issues

In developing a tire air pressure monitoring system for motorcycles, the unique characteristics of motorcycle tires and driving conditions were reviewed and considered before the development targets and topic areas were defined. The developmental goals were to:

(1) Build a system that can detect changes in tire air pressure and temperature while the motorcycle is being ridden and that can accurately inform the rider of tire pressure changes that can possibly lead to tire failure.
(2) Study the relationship between tire damage and temperature changes that occur when the motorcycle is being operated with low tire pressure and have a set temperature at which the system can predict the possible occurrence of a tire failure.
(3) Develop a communication system that incorporates a stable line of transmission within the legal regulations established in Japan, which has adopted the lowest field intensity in the world. The system must also be reliable enough to prevent erroneous data transmission.
(4) Develop a display system that enables the rider to discern failure conditions and system errors.
(5) Develop a sensor that incorporates intelligent assembly design.
(6) Develop a system that preserves battery life from the time of production to the point of sales, in order to provide a transmitter life period of 10 years.

* Asaka R&D Center

3. Analysis of Tire Air Temperature and Air Pressure by Tire Fault Forecasting

To predict tire fault conditions, the relationship between the tire air pressure and the temperature inside the tire was analyzed, and then to what degree these apply to the tire failure was determined. Sudden changes in tire pressure brought on by punctures were also analyzed and the possibility of prediction and precognition of tire failures were discussed.

3.1. Tire Temperature at Tire Damage Occurrence

Continued driving on low inflated tires causes tire chipping and leads to tire damage. An endurance test was conducted while driving on a test drum to record the tire surface temperature and the temperature inside the tire until damage occurred. Air pressures of 50 kPa, 100 kPa, 150 kPa, 200 kPa and 280 kPa were initially set while the tires were still cold. The tire rotation speed was gradually increased from 170 km/h to 280 km/h. Figures 1 and 2 show the respective tire surface temperature conditions recorded with a thermograph.

At low tire air pressure conditions, the left-right block on the tire tread pattern showed an increase in temperature and chipping. Tire air pressure was then set relatively high at 200 kPa, and driven at high speed yielding a high surface temperature at the center part of the tire tread leading to chipping. Figure 3 shows the relationship between the tire air pressure and tire tread surface temperature, tire sidewall

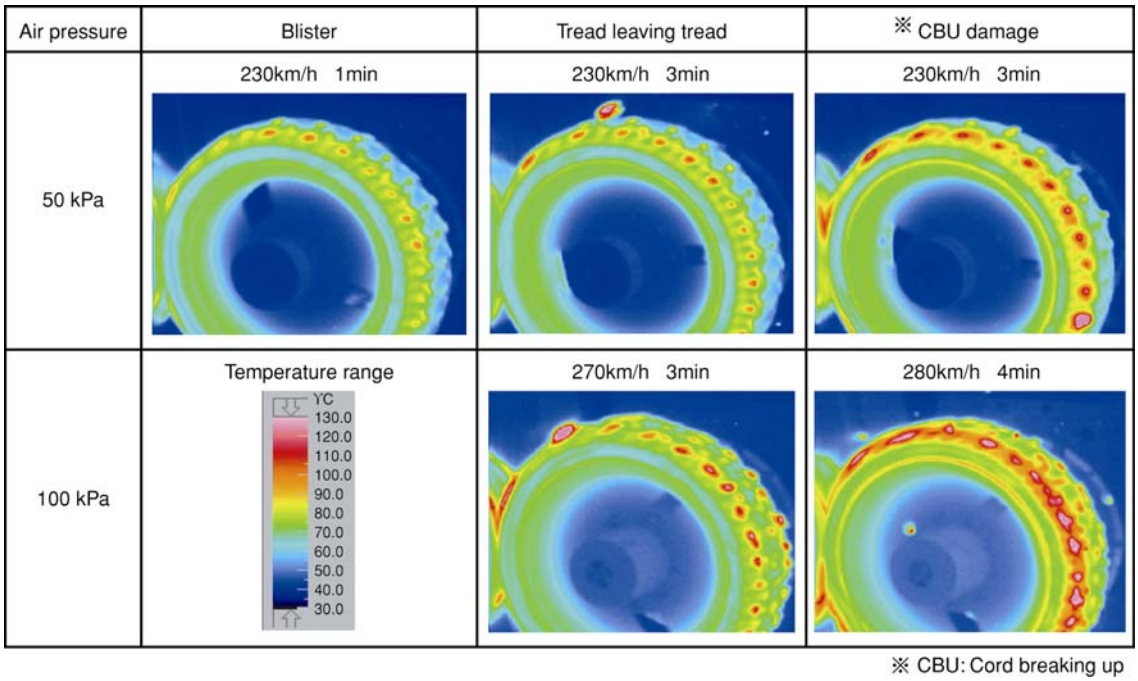


Fig. 1 Temperature images of tire surface: Air pressure 50, 100 kPa

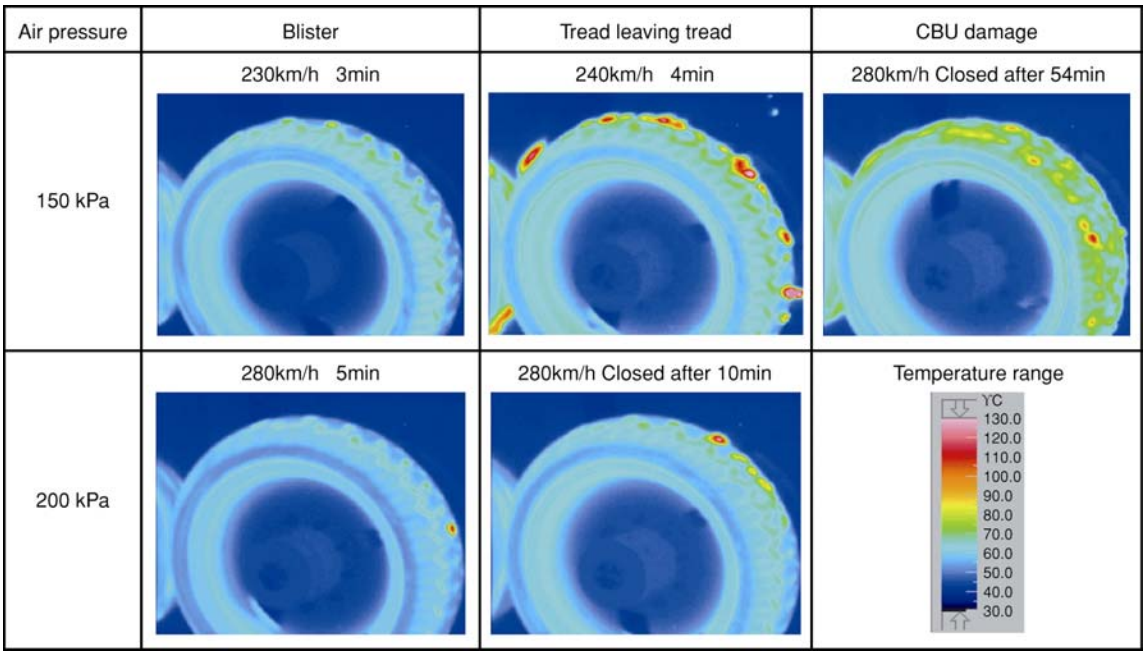


Fig. 2 Temperature images of tire surface: Air pressure 150, 200 kPa

surface temperature, and the temperature inside the tire. These all showed tire failure in the end. The tread surface temperature and the air temperature inside the tire showed a correlation but there was considerable difference in the tread surface temperature and sidewall surface temperature. The higher the tire pressure, the greater the discrepancy became. Furthermore, the lower the tire pressure, the higher the sidewall deflection, which generated more heat and higher air temperature inside the tire. Figure 4 graphically shows a relationship between the air temperature inside the tire and the tire pressure as a parameter. This revealed that the lower the tire pressure, the greater the heat generated from tire flex and the prevalence of chipping and bursting. Figure 5 shows the relationship between the temperature inside the tire and the drum rotation speed, as well as the resulting tire failures. From this, it has been learned that the higher the rotation speed, the easier it becomes for tire failures to occur. Figure 6 shows the relationship between the air temperature inside the tire and the running distance, as well as the resulting tire failures. This has shown that as the temperature inside the tire increases, tire failures tend to occur more readily. Also, the running distance at which the tires can maintain normal conditions tends to decrease at high temperatures.

These three graphs show that tire failures occur more readily with high tire temperature, lower tire pressure and at higher running speeds. Additionally, as conditions like loading force are increased, there is a greater likelihood of tire failures resulting from sudden tire temperature increases. As Figures 4, 5 and 6 clearly demonstrate, the majority of bursting and chipping faults occur in temperature conditions greater than 100 °C. Consequentially, the system temperature warning buzzer has been set at 100 °C. The temperature warning buzzer has a second function to indicate tire failures caused by the tire being driven on low air pressure. Tire deflection caused by over loading and driving beyond the permissible speed range also may cause the tire temperature to increase. The implementation of a temperature warning device has enabled greater accuracy in tire failure identification.

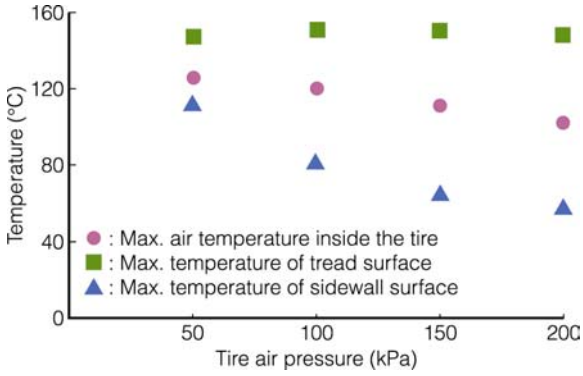


Fig. 3 Relation between temperature of each part of tire and air pressure in tire

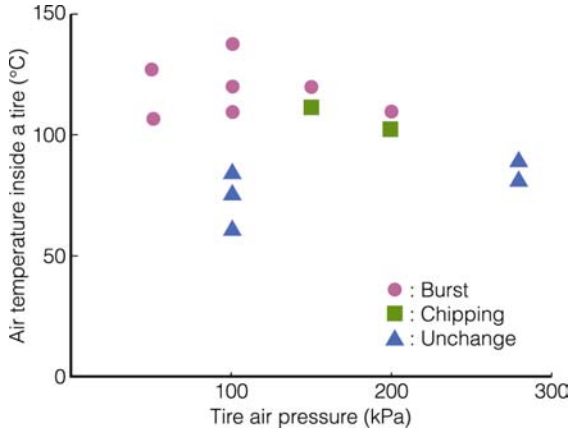


Fig. 4 Relation between air temperature and air pressure in tire at failures

3.2. Verification of Air Leak Speed at Puncture Occurrence

Tire damage frequently occurs as a result of continued running on low air pressure brought on by natural air leakage in rubber tires and by punctures that occur when a foreign object pierces the tire. Most cases of sudden tire pressure deflation occur when an object which has pierced a tire on a local street, suddenly comes out of the tire while travelling at high speed. To detect this occurrence, testing was repeated in which a tire was pierced with a ø 2.8 nail and the test drum speed set to a speed range of 0 ~ 120 km. The tire was run over the test drum as the speed was gradually increased. Figure 7 shows the measurements of air leakage that occurred in the drum test.

For safety, it is important that the rider be notified of any such air pressure leakage. To satisfy this requirement, the system's air pressure measurement interval was set to 7.5 seconds. In the experiment, the nail came out of the tire by centrifugal force causing the tire pressure monitor buzzer

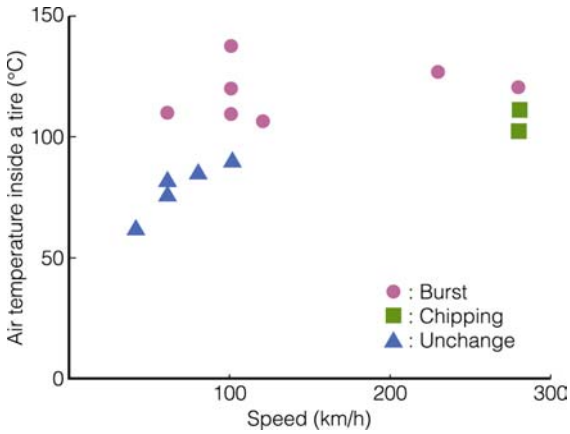


Fig. 5 Relation between air temperature in tire and drum rotation speed at failures

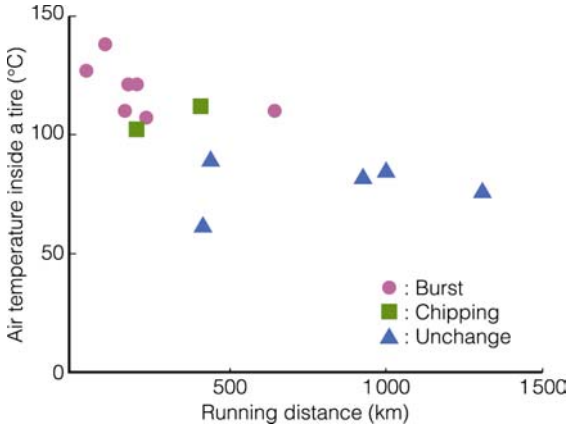


Fig. 6 Relation between air temperature in tire and running distance at failures

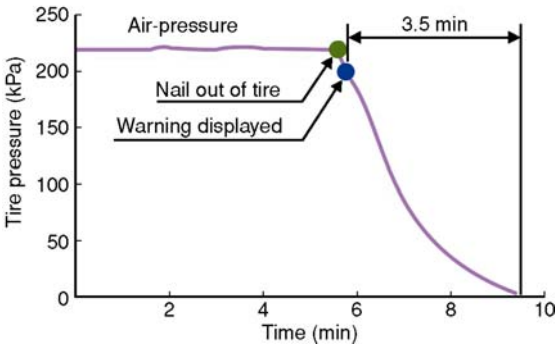


Fig. 7 Result of air leakage by drum test

to sound. It took the air pressure 3 minutes and 30 seconds to drop to zero thereby providing a greater opportunity for the rider to determine an accurate measurement.

3.3. Increasing Detection Accuracy by Temperature Correction

The newly developed air pressure monitoring system works by detecting air leakage according to changes in air pressure. To further increase the level of detection accuracy, the system must also be able to correct for changes in tire air pressure according to temperature changes. Figure 8 shows the changes in air pressure over a period of elapsed time without the application of any temperature correction. As the graph shows, the temperature tends to rise as the air pressure decreases. From this, it can be judged that it becomes increasingly important to adjust changes in temperature with temperature correction as the air pressure decreases. Figures 9 and 10 show the relationship between the changes in measured air pressure according to the temperature inside the tire, and the corrected air pressure following temperature correction. Air pressure adjusted according to temperature can be expressed in the following formula.

$$P = Px - (Tx - 30) \quad (1)$$

P: Corrected air pressure (kPa)
Px: Measured air pressure (kPa)
Tx: Measure temperature (°C) (for conditions where temperatures are greater than 30 °C.)

Formula 1 expresses how air leakage is detected. However, since the formula has been devised for temperatures above 30 °C, temperature correction does not apply to temperature conditions below 30 °C. This is because in low cold temperature conditions, the system misjudges the lower temperature for the standard air pressure and inaccurately concludes the result to be air leakage.

3.4. Increasing Detection Accuracy by Atmospheric Pressure Correction

Prescribed air pressure inside the tire is regulated by relative atmospheric pressure and gauge pressure. As the altitude changes, the air pressure also changes resulting in a variance in tire air pressure even though there is no air leakage. As the altitude increases from 0 m to 3,000 m, the gauged air pressure reading decreases by 30 kPa. This loss represents a 15% reduction in the prescribed standard air pressure setting of 200 kPa and has a large influence on the detection accuracy. Generally, air pressure is regulated according to pressure gauge readings. Once the tire pressure has been adjusted at a high altitude and the motorcycle

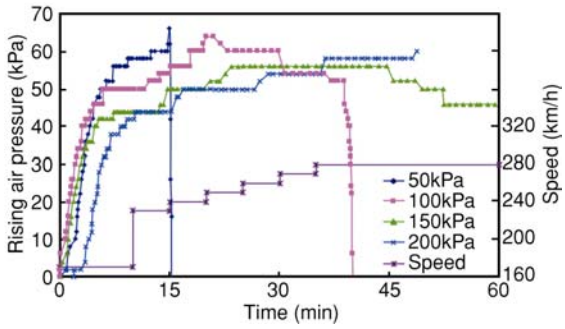


Fig. 8 Relation between air pressure rise and elapsed time during running

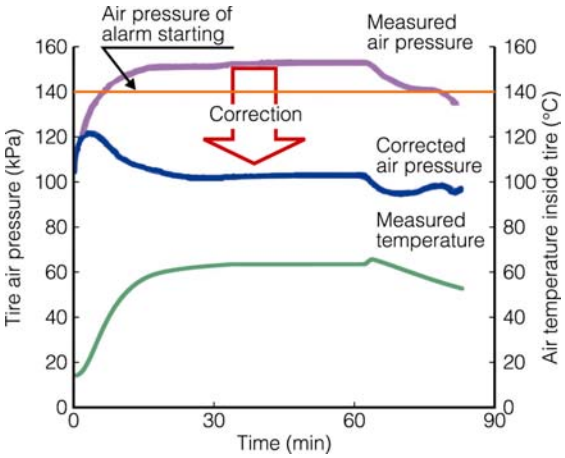


Fig. 9 Example of air temperature rise in tire

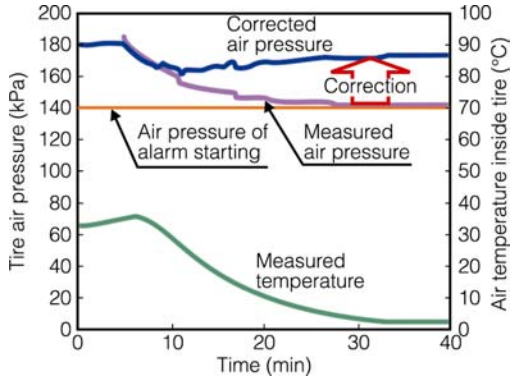


Fig. 10 Example of air temperature decline in tire

descends to a lower altitude, the surrounding atmospheric pressure increases causing the tire air pressure to decrease. Adopting a pressure sensor in the air pressure monitoring system will only measure the absolute pressure but does not measure the difference in atmospheric pressure. There is a concern that as the difference in the absolute pressure measured by the sensor and adjusted gauged tire pressure at high altitude increases, the air pressure monitoring system will increasingly be unable to detect air leakage and low air pressure tire conditions. On the other hand, tires that have had air pressure set at low altitudes show a gauge pressure increase as they move to higher altitudes. Conversely, riders living at high altitudes experience decreases in tire air pressure as they move to lower altitudes. Therefore, effective atmospheric correction will increase the accuracy of the air pressure warning system to respond as the motorcycle moves to higher or lower altitudes.

4. System Configuration

Figure 11 shows the configuration and layout of the air pressure monitoring system. The system is divided into a transmitter, a receiver, and a display unit. The transmitter is fitted to the wheel rim inside the tire and is located on both the front and rear tires. The pressure inside the tire and the temperature are measured in intervals of 7.5 seconds. The measured data is transmitted as radio signals. The signals are transmitted once every 6 minutes if no abnormalities are detected. If a pressure leak occurs, the system detects the leak and transmits the data every 7.5 seconds.

The receiver receives the radio signals from the transmitter, analyzes the data and sends the tire air pressure and temperature information to the display unit. If any abnormality is detected, the receiver sends a warning signal to the display unit as well.

The display unit informs the rider of the current tire condition. To assist the rider in recognizing abnormalities, the system sounds a warning buzzer and displays the information on the display panel. Figure 12 shows the mounting position of the transmitter with air pressure sensor.

Current air pressure sensor transmitters used in automobiles typically consist of a combined valve and sensor transmitter assembly unit. However, air pressure sensor transmitters for motorcycles are designed with separate valve and sensor units. Since motorcycle wheel rims are shaped differently from that of automobiles, the air valves are mounted in different directions. On automobiles, the air valves are usually mounted horizontally while they are mounted vertically on motorcycles. The sensor transmitter is mounted on the inside of the tire wheel and is built separately from the valve. This is to avoid any wheel imbalance caused by the weight of the transmitter. The transmitter mounting is positioned as required to cancel this imbalance. The transmitter is shaped so as to facilitate tire removal and mounting and is mounted on the inside rim opposite the valve. This also allows for less additional weight for wheel balancing. Figure 13 shows the mounting position of the transmitter on the tire wheel.

The sensor transmitter consists of a sensor unit with a semiconductor pressure sensor and a thermo sensor; a circuit unit which determines the air pressure status based on the measured air pressure and temperature conditions and then transmits this data from the built-in antenna; and a small button-shape lithium battery. The circuit unit uses a low frequency radio wave setting of 315 MHz that is applied to keyless entry systems used on automobiles designed for the Japanese market. Transmission signals for each transmitter are allocated unique ID numbers to enable identification of each transmitter. The sensor transmitter achieves reliable durability by adopting a potting processed circuit capable of handling the severe vibration, acceleration, high temperature and humidity conditions, and a power enhanced exclusive lithium battery. Figure 14 shows the configuration of the transmitter with sensor and Table 1 lists the transmitter specifications. The receiver has the same functions and design configuration as the above mentioned keyless entry

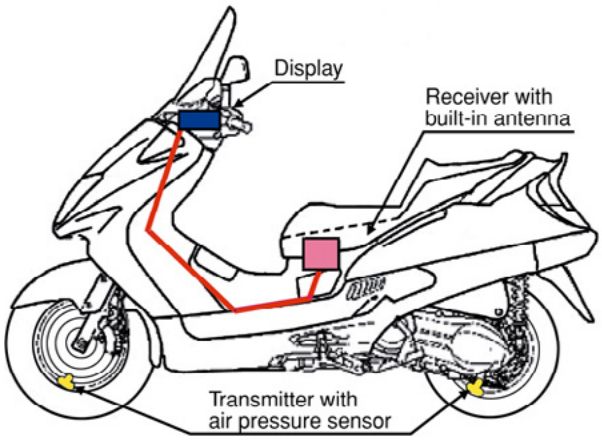


Fig. 11 Configuration of monitoring system of tire air pressure

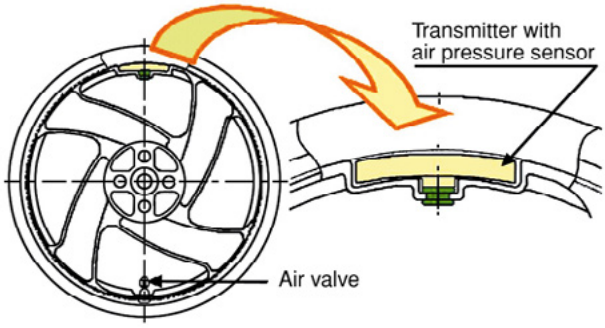


Fig. 12 Mounting location of transmitter with air pressure sensor

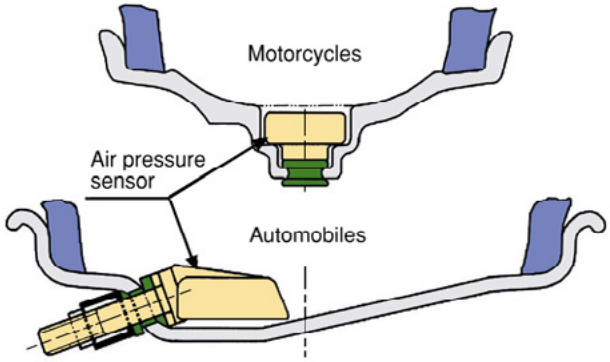


Fig. 13 Comparison of section shape motorcycle's wheel and automobile's wheel

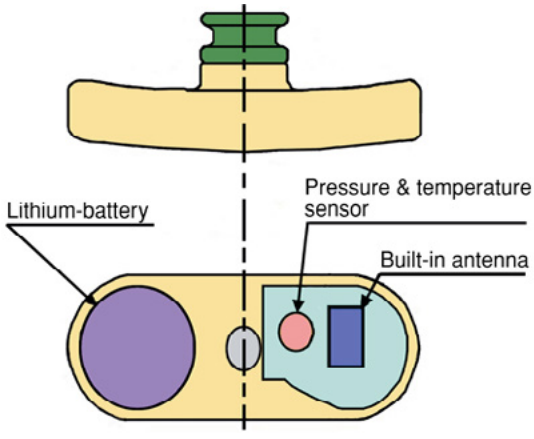


Fig. 14 Configuration of transmitter with air pressure sensor

system. The receiver receives data relating to tire air pressure and temperature from the transmitter and judges whether air leakage, low pressure or abnormal temperatures exist then sends the data to the display unit. Figure 15 shows the receiver unit configuration and Table 2 lists the receiver specifications.

Table 1 Specifications of transmitter with air pressure sensor

Items	Specifications
Mass	50 grams
Pressure sensing element	Semiconductor pressure sensor
Pressure sensing range	0 - 500 kPa
Pressure sensing accuracy	± 2 %
Temperature measuring range	– 40 ~ 120 °C
Temperature measuring accuracy	± 8 °C
Transmitting frequency	314.98 MHz
Modulation formula	FM modulation
Power supply	Coin shaped lithium battery

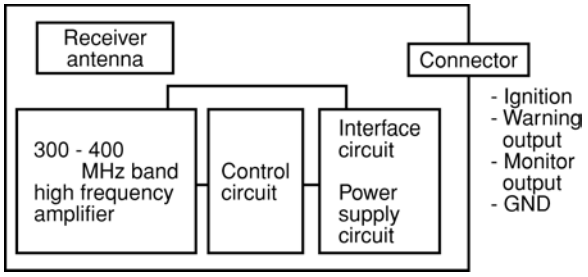


Fig. 15 Configuration of receiver

Table 2 Specifications of receiver

Items	Specifications
Receiving band	300 kHz
Receiving sensitivity	3 dBμV
Mass	60 grams
Antenna	Built-in type
Power source	In-vehicle battery

5. Differences in Field Intensity According to Radio Law and Systemic Variation

Figure 16 shows the allowable ranges of transmitter field intensity defined by respective radio laws in Japan, USA, and Europe. As shown in the figure, Japan imposes the most stringent standard level set at 54 dB μ V/m, the lowest intensity level shown in the comparison.

Existing automobile specifications applied in the USA and Europe position the respective antennas close to the transmitter unit. On the other hand, this system receives radio waves transmitted from the individual units mounted on the front and rear wheels with antenna integrated into one receiver. This configuration sets the receiver at a considerable distance from the transmitter resulting in a weakening of receiver field intensity. This system applies a unique ID to each transmitter and uses FSK type wave transmission. The receiver's single built-in antenna enables reliable transmission even in weak field intensity settings and conforms to domestic radio law standards.

6. Warning System

6.1. Warning Fundamentals

American automobile regulations set by the National Highway Traffic Safety Administration (NHTSA) have

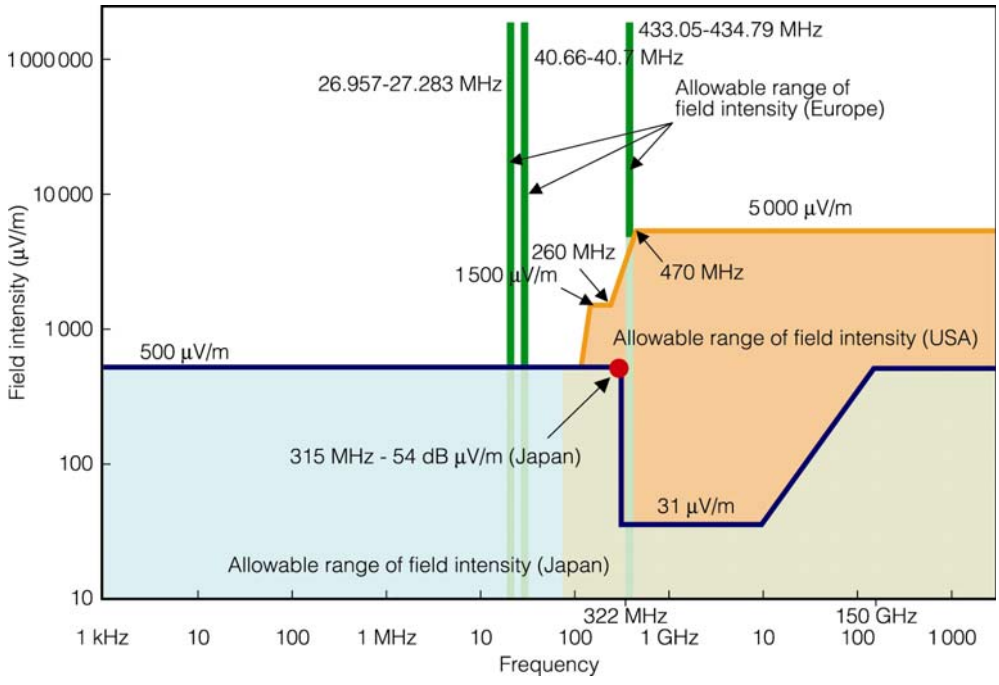


Fig. 16 Radio Laws in Japan, USA, and Europe

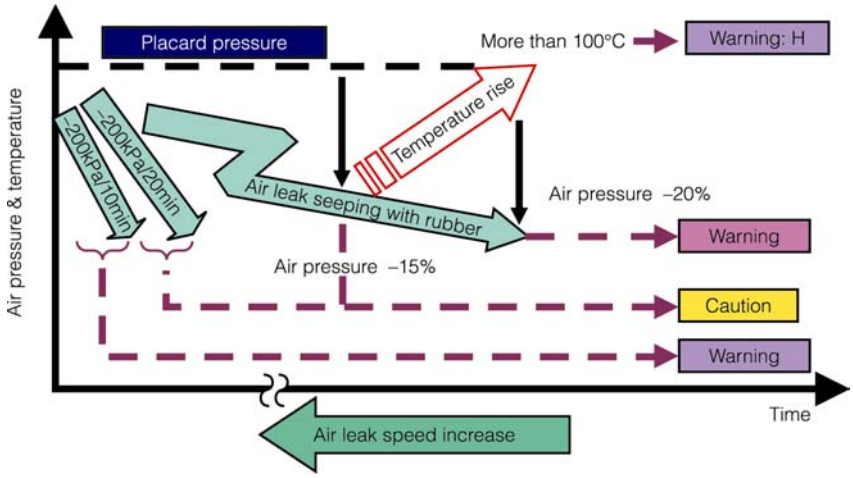


Fig. 17 Operation flow of alarm system

specified warning setting levels to respond when the air pressure level falls by –25%, or –30% below the specified air pressure in cold conditions. The new air pressure monitoring system has set the following warning specifications for detecting abnormal conditions.

(1) Caution Warning
- When the tire air pressure drops from 200 kPa to 0 kPa within a 20 minute period in cold conditions
- When the tire air pressure drops 15% below the specified pressure level in cold conditions

(2) Warning Alert
- When the tire air pressure drops from 200 kPa to 0 kPa within a 10 minute period in cold conditions
- When the tire air pressure drops 20% below the specified pressure level in cold conditions
- When the tire air temperature is greater than 100 °C

Figure 17 shows the operation flow of the alarm system developed for the new tire air pressure monitoring system.

6.2. Rider Display

The method of displaying abnormal status information to the rider is an important element in the design. The system display must be easy to read to enable immediate rider response at infrequent occurrences of abnormal conditions. Figures 18 and 19 show the display setting when detecting abnormal conditions. When a warning or caution condition is displayed, the system also sounds a buzzer to ensure rider is aware of the displayed warning. The buzzer indicates the degree of urgency by changing the buzzer sound interval.

6.3. System Diagnostics and Warnings

The newly developed air pressure monitoring system includes system error diagnostic functions for better reliability. Displaying the location of the system error helps the rider discern the exact nature of the system error and has been designed to enhance tire failure warnings. Table 3 lists the display information for the system error occurrences.

7. Trigger Device for Improved Battery Life

The life of the battery on the air pressure monitoring system transmitter maintains stable battery voltage and will continue to transmit data until the vital voltage level is depleted. To ensure a longer battery life, it is important to ensure that the battery is not tapped until the date of purchase. A trigger device with an ON/OFF battery transmission control setting has been incorporated to ensure the longest battery life possible. Table 4 lists the required conditions for the ON/OFF settings on the trigger device for controlling radio wave transmission from initial factory stock



Fig. 18 Alarm indicator

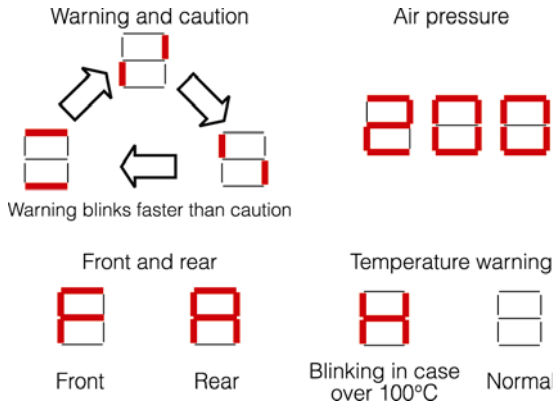


Fig. 19 Indication form

Table 3 Indication of system error

Failure modes	Indications
ID failure	FE00 or RE00
Status failure	FE01 or RE01
Receiver counter failure	FE02 or RE02
Receiver system failure	E03
Transmitter battery voltage failure	FBAT or RBAT

F: Front tire R: Rear tire

Table 4 Management for transmitting radiowave in physical distribution

		Manufacturer	Factory					Carrier	Dealer	
Process flow		Delivery	Assemble	ID registration	Inspection	Stoppage	Shipment	Distribution	Stock	Delivery
State of radiowave	Transmission ON	—	—	O	O	—	—	—	—	O
	Transmission OFF	O	O	—	—	O	O	O	O	—
Trigger device		Unrequired		Required				Unrequired		

to the point of delivery. The device has also been designed to enable dealers to set the transmission ON by increasing tire air pressure temporarily.

8. Efficiency of Tire Air Pressure Monitoring System

According to the NHTSA's recent announcement regarding tire pressure monitoring specifications, the following negative conditions have been observed when tire air pressure drops below the prescribed level. As the following list indicates, there is a reduction in safety, a decrease in wear longevity and a reduction in fuel economy.

(1) Reduction in Safety
- Tire failures by increased bending of tire sidewalls and increased air temperature inside the tire
- Reduction in handling performance resulting from reduced horizontal traction
- Increase in breaking distance on wet roads (Data Source: Goodyear)

(2) Decrease in Wear Longevity
- Reduction in tire wear longevity by 1.78% for every 1 psi drop in tire pressure (Data Source: Goodyear)

(3) Reduction in Fuel Economy
- Poor fuel economy resulting from increased driving resistance.

A report released in 1978 indicates that there is a 1% reduction in fuel economy for every 3.3% drop in tire pressure.

Data recently released by Goodyear indicates that there is a 1% reduction in fuel economy for every 2.96% drop in tire pressure

The purpose behind the proposed legal requirement in America for the air pressure monitor is to prevent tire failures caused by driving on low pressure tires.

According to estimations released by the NHTSA, by fitting tire air pressure monitoring systems (direct monitoring types) to automobiles in the US, there would be 8,722 fewer injuries and 124 fewer deaths a year. The motorcycle tire air pressure monitoring system is expected to bring effective results in reducing the number of road injuries and deaths as well.

9. Conclusion

The newly developed motorcycle tire air pressure monitoring system has achieved effective tire failure forecasting and preventative functionality and more accurate monitoring capability in a systematized mode of delivery.

(1) The tire air pressure monitoring system is reliable and has brought increased accuracy in detecting low tire pressure and air leakage through temperature correction.
(2) The system responds to sudden air leakage due to tire puncture by reducing the time required to measure changes in air pressure conditions.
(3) In addition to temperature monitoring, the system has also achieved dual forecasting functionality.
(4) The system offers system diagnostic functionality by analyzing abnormalities such as decreases in battery voltage and error occurrences in system functions.
(5) The system satisfies low radio wave field intensity regulations prescribed in Japan and adopts a transmitting system that does not require a separate antenna.
(6) The system achieves the decrease in balancing weight used in wheel balancement and a conventional tire assembly by adopting two separate structures of transmitter and tire valve.
(7) The system achieves a battery life of 10 years by adopting an ON/OFF sensor transmission control function and regulating the interval of data transmission.

10. Acknowledgments

The authors would like to express their deep appreciation and gratitude to everyone at Pacific Industrial Co., Ltd., Denso Corporation, Bridgestone Corporation and Inoue Rubber Co., Ltd. for their support and assistance in helping make the development of the motorcycle air pressure monitoring system a success.

References

(1) U.S.DOT/NHTSA: Federal Motor Vehicle Safety standards: Tire Pressure Monitoring Systems; Controls and Displays: Docket No. NHTSA 2000-8572-28 (2000)

■ Authors ■


Masayoshi ORITA


Tomoyuki HARADA


Toshio YAMAGIWA

A Combined Experimental-Numerical Approach for Motorcycle Crank Noise

Masahiko SEKITA* Hiroshi TAMURA*

ABSTRACT

Riders prefer comfortable crank noise levels as they do for handling and riding vibration. A simulation modeling method for a single-cylinder motorcycle engine was established to identify the mechanism that is the cause of unpleasant crank noise. The combined approach of experimental and numerical analysis was applied to evaluate a design change's effectiveness in determining a cause of crank noise. An experiment is effective to identify an important engine behavior parameter when modeling the engine. The result of numerical analysis by using the established model was verified using experimental data from the prototype.

1. Introduction

Crankshaft noise is an unpleasant noise arising when the engine is under load. This is a noise occurring over a relatively wide spectrum, from 900 Hz to 2,000 Hz, according to the findings taken with a sound quality system, as shown in Fig. 1. Objectively, since this noise gives the impression of something rolling inside the engine, it is called a 'rattling' noise.

The purpose of this study was to gain some insight into the mechanisms that generate crankshaft noise and to offer specification improvements that will bring about an objective reduction in the noise. Essential pre-conditions were that the specifications could not involve changes in combustion or output power of the engine.

2. Process of the Generation of Crankshaft Noise

The process of crankshaft noise occurrence consists of three stages as shown in Fig. 2. These are called the 'source', the 'transfer', and the 'emitter'. They are typical elements of crankshaft noise detected at the rider's ear. The approach to reducing noise can involve any of these stages.

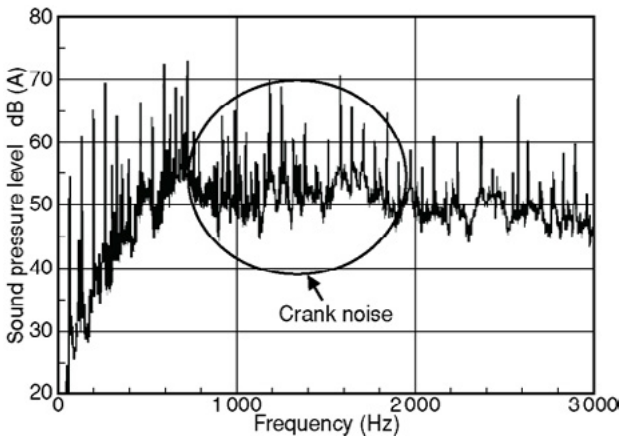


Fig. 1 Frequency range of crank noise

* Asaka R&D Center

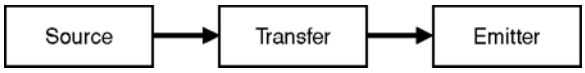


Fig. 2 Process of crank noise generation mechanism

In the present case, the source involved dynamic behavior of the crankshaft in an operating engine. The forces on the bearings are the sum of inertial forces, combustion forces and dynamic properties of the crankshaft. They act on the crankcase and cause it to vibrate, giving rise to the radiation of noise.

In order to reduce crankshaft noise, the following interactions between the stages must be suppressed:

- Source: Changes to the dynamic characteristics of the crankshaft assembly.
- Transfer: Changes of bearing type.
- Emitter: Changes to the dynamic characteristics of the crankcase in order to reduce radiation noise.

The simulations for the investigation of dimensional revisions were mainly carried out for the transfer stage, but simulations of the other noise generation processes were also performed; for example, some changes were suggested in the dimensions for the crankshaft itself.

3. Modeling

It is necessary to model the mechanisms of each of the noise generation stages with the maximum possible precision. This is required in order to obtain a preliminary assessment of the effectiveness of performing an investigation into noise generation mechanisms and dimensional changes. The dynamic characteristics of the crankshaft and crankcase are important parameters for the source and emitter. Therefore, experimental excitation data for these components were used to update the FE models. The dynamic transfer characteristics of the bearings had to be identified for modeling of the transfer stage.

Certain assumptions are necessary in order to create a simulation model. The limitations posed by these assumptions must be taken into account. The model was verified in testing of an actual motorcycle. This enabled verification that the ultimate simulation model was precise enough to run qualitative comparisons with varying dimensions of the components.

3.1. Update of Modal Model

It is clear that the dynamic characteristics of the crankshaft play a key role in noise generation in the source, while the dynamic characteristics of the crankcase are equally important in the emitter; therefore, the dynamic behavior of these components must be well reflected in the model. In order to obtain precise results in the dynamic region, it was necessary to use methods based on experimental data from an actual engine while creating the model. This was particularly important for components with an uncertainty, such as press-fit components, which are often used in crankshaft assemblies in single-cylinder engines. Methods to update existing FE models with experimental data are key to this process. Since it is rare to have physical models available that can actually be used during development under limited conditions, updating is often difficult. However, it is quite effective to build, during the final development stage of a machine, a virtual model of the next-generation machine in order to carry out updated investigations of that next model. This is because actual models exist at this stage and the reliability of the FE model can be assured with the updates.

Experimental modal analysis (EMA) was performed on an actual crankshaft (Fig. 3) and crankcase assembly (Fig. 4). Since experimental errors would influence the updates, special care was essential during these experiments; for example, the mass of the acceleration sensor is itself one of the influences on the crankshaft. The experimental modal parameters were compared with FE simulation parameters using correlation and update techniques. The FE model was divided into different sections in order to identify sections with modeling errors. A sensitivity analysis was done in order to update the material characteristics and connection characteristics of each component or connection (for

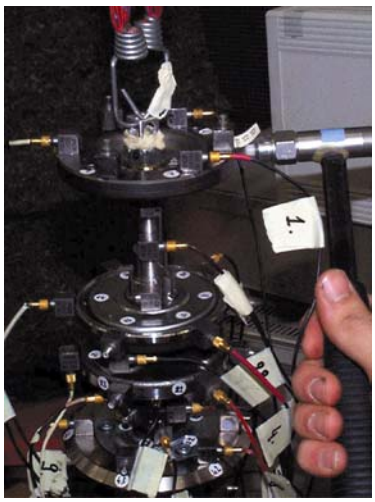


Fig. 3 Modal analysis of crankshaft

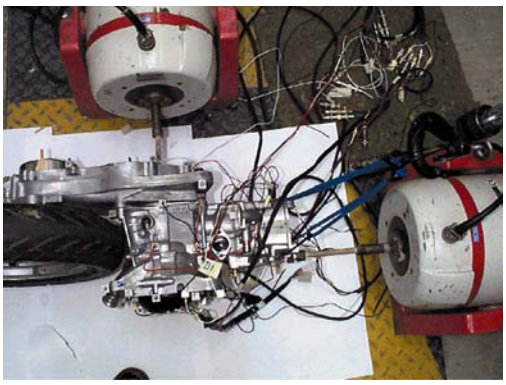


Fig. 4 Modal analysis of crankcase assembly

example, the press-fit connections in the crankshaft). Using these techniques, a good correlation was obtained between the modal parameters of the physical model and those of the FE model in the global modes of both the crankshaft and the crankcase assembly. The results are shown in Fig. 5 and Fig. 6.

3.2. Determination of Bearing Dynamic Stiffness

The inertial forces due to crankshaft rotation and the combustion forces are transmitted through the bearings to the crankcase. The bearing dynamic stiffness must be known in order to obtain the correct response in the crankcase to these excitation forces. A special tester was built to get these parameters. The inner race was placed on the test jig and the outer race was vibrated with an electromagnetic shaker under a random signal at frequencies up to 5 kHz. Figure 7 shows the testing apparatus. The dynamic stiffness of the ball bearing was extracted from the relative displacement between the races and from the reaction forces in the test jig. It was designed to measure both the stiffness in the radial direction and that in the axial direction. A bearing internal clearance is set to provide a balance of low noise and low friction during engine operation. This clearance resulted in noise during dynamic stiffness measurements that was the same as crank noise. It stopped immediately when the clearance was cancelled. This indicated that ball clearance is one of the key noise generation mechanisms.

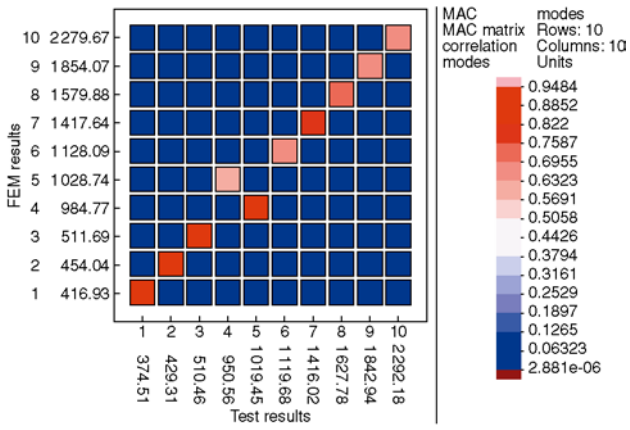


Fig. 5 MAC correlation matrix for crankshaft

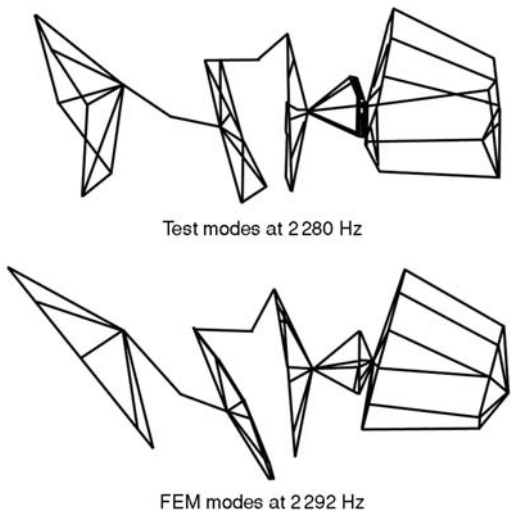


Fig. 6 Comparison of experiment and FEM mode

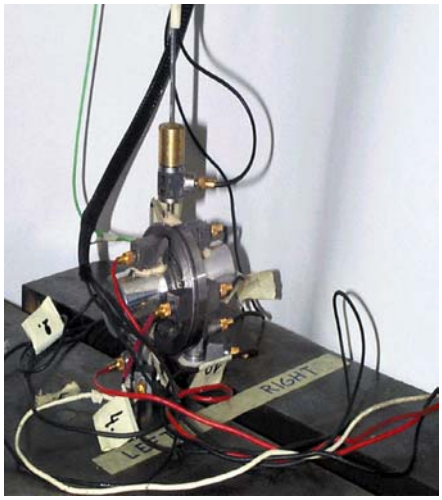


Fig. 7 Test setup for identification of dynamic bearing stiffness

In an engine like that in this study, where the outer races of the crankshaft ball bearings are press-fit into the crank case during assembly of the engine, nearly all of the clearance is cancelled at room temperature. However, this clearance increases with temperature and is significantly larger at the engine operating temperature. This occurs because the coefficient of thermal expansion of the aluminum crankcase is higher than that of the steel bearings. This clearance increase has been confirmed through experiments. Crankshaft noise worsens with an increase in temperature.

3.3. Conditions and Limits in Virtual Model

The purpose in the present virtual model was to observe how changes in various dimensions affected crankshaft noise in an attempt to elucidate noise generation mechanisms. To do this, it was necessary to create models that allow qualitative assessments of changes in various dimensions. For this reason, conditions for certain unknown parameters were set according to the following assumptions:

- The bearing clearance during engine operation is dependent on temperature, but in the simulation, the clearance was fixed. This clearance corresponded to some engine temperature.
- The CVT exerts a force on one end of the crankshaft; this was approximated as the belt tension when the engine is stopped.

- The effect of magnetic forces in the AC generator rotor, which is mounted directly on the crankshaft, was ignored. The excitation forces from the valve train were also ignored.
- The monolithic engine-transmission combination is attached to the frame with a bushing. The frame was assumed rigid and conditions for the engine-frame connection were chosen to avoid causing problems in the model.

Some limitations can be expected in the results due to the method of bearing modeling. If a bearing is perfect with no surface defects (flaws), it will show random noise due to the rolling motion over a wide spectrum of vibrations. However, when there are flaws or other defects in the outer or inner race or in the balls, noise of particular frequencies will be generated, as shown in Fig. 8. These frequencies and their harmonics will be seen in the vibration spectrum of the bearing. It has been reported that these frequencies will appear not only when there are defects in components, but also when the inner and outer races are tilted in relation to each other during operation. In a 4-stroke engine, the combustion forces exert a bending moment on the crankshaft once every two revolutions. This causes the outer races of the bearings to take a periodic tilt with respect to the inner races, as shown in Fig. 9. Thus, even if the bearings are perfect, a harmonic is generated at 0.5/rev, due to the combustion process. These effects were not considered in the present bearing model, so they were not reproduced in the frequency response obtained here.

3.4. Modeling

The virtual dynamic model of the engine is composed of the updated FE models of the crankshaft and the crankcase and the dynamic stiffness models of the bearings. This was subjected to assumptions and limitations described in section 3.3. Next, the internal pressures in the combustion cylinder were measured with in-cylinder sensors on a completed motorcycle mounted in a chassis dynamometer. These pressures were used for the combustion cylinder in the simulation with the virtual model. The completed virtual model is shown in Fig. 10. In this model, the engine and transmission are supported on a rigid frame through bushings.

3.5. Credibility of Model

For the purpose of confirming the model, a completed vehicle was installed on the chassis dynamometer with an acceleration sensor embedded in the crankshaft to measure the acceleration of the crankshaft journal, and a non-contact displacement pickup in the shaft top to observe its displacement in the radial and axial directions. Figure 11 shows the test setup. The measured data were compared with the results of the simulation to verify whether they showed the same trends. Figure 12 provides an example, a comparison of the measured radial acceleration in the vicinity of the crankshaft journal bearing and the simulation. In view of the limitations and assumptions mentioned above, these graphs show quite a good match. This indicates that this virtual model can be used for qualitative comparisons with

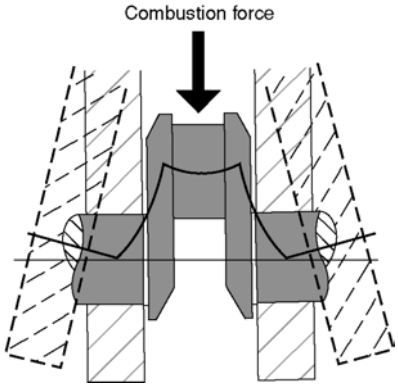


Fig. 9 Periodic bending of crankshaft due to combustion forces

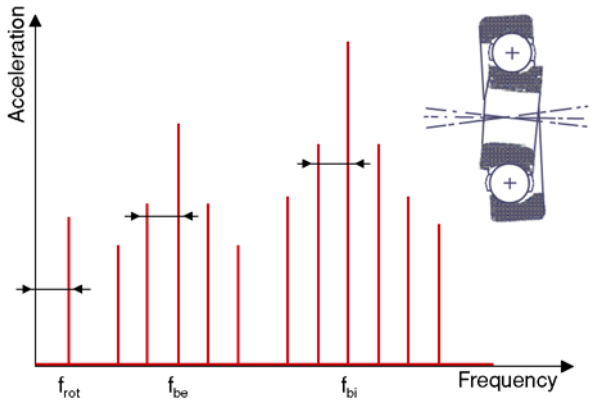


Fig. 8 Characteristic frequencies caused by tilting of inner and outer race

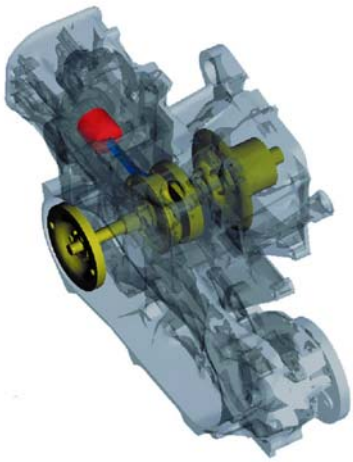


Fig. 10 Virtual mechanical model of engine with transmission

dimensions changed. Figure 13 displays the Lissajoux figure of the displacement of the crankshaft tip. The behavior is plainly visible, including the once-per-two-revolution pressure peak in the combustion cylinder.



Fig. 11 Fixed motorcycle on roller bench

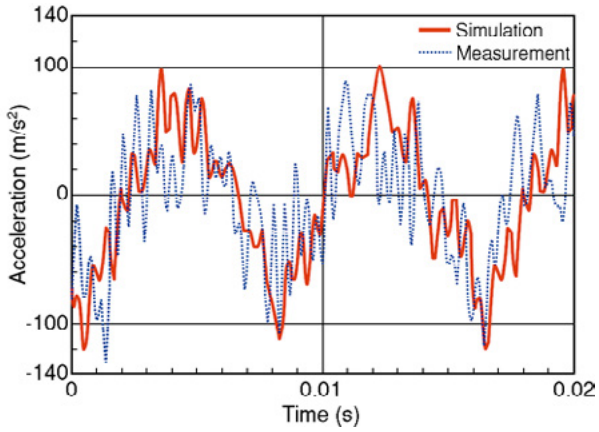


Fig. 12 Virtual acceleration on bearing

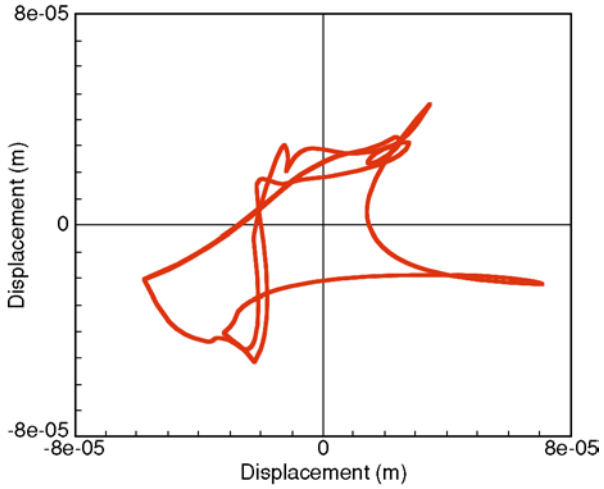


Fig. 13 Lissajoux figure of crankshaft displacement at bearing

3.6. Assessment of Changed Dimensions

The effect on noise from changes to dimensions was calculated with the qualitative virtual engine model. The changes were applied to all three stages of the noise generation mechanism.

- Source: Changes in crankshaft dynamic characteristics due to changes in inertial moment, addition of mass, and change in crankshaft type.
- Transfer: Changes in bearing clearance and bearing type.
- Emitter: Augmented stiffness of crankcase.

The first list of changes applies to the initial noise generation process in other words, to the source. The dynamic characteristics of the shaft were revised by changing the crankshaft dimensions. The post-revision crankshaft incorporated a smaller generator rotor 40% lighter than the previous rotor. Figure 14 shows that this change affected the frequency band of interest, in other words, the spectrum from 900 Hz to 2,000 Hz. The other two changes made in this study had to do with the transfer level of the noise generation process. One was to double the bearing ball clearance, and the other was to change to hydro bearings (plain bearings). Figure 15 and Fig. 16 show the results. As expected, increasing the clearance increased the impact force on the bearings, increasing vibration. Sufficient reductions in the noise level in the spectrum of interest were only obtained by switching to plain bearings.

4. Experimental Verification

All the specification changes were checked in chassis dynamometer tests of a completed motorcycle. Two stages of the noise generation process will be covered here, the source and the transfer stages. Two meaningful sets of information were gained from the results of the study on the virtual model simulation. The dynamic stiffness of the crankshaft is an

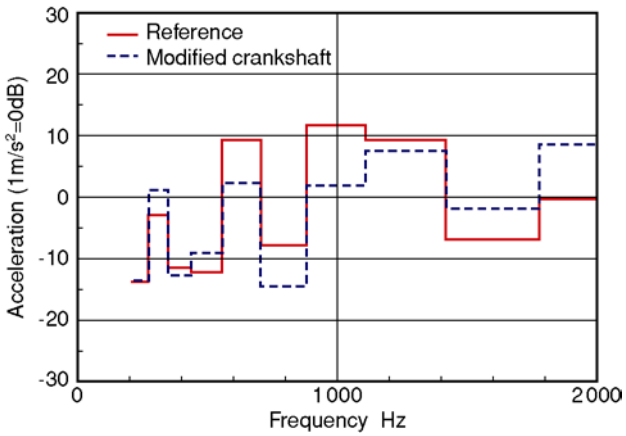


Fig. 14 Simulated comparison of reference acceleration in third octave between reference model and modified crankshaft

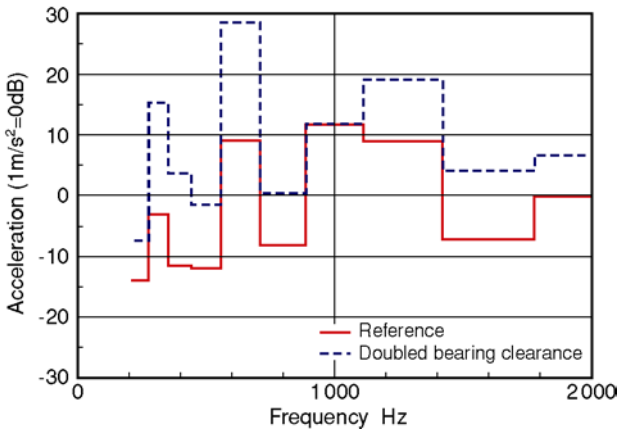


Fig. 15 Simulated comparison of reference acceleration in third octave between reference model and doubled clearance

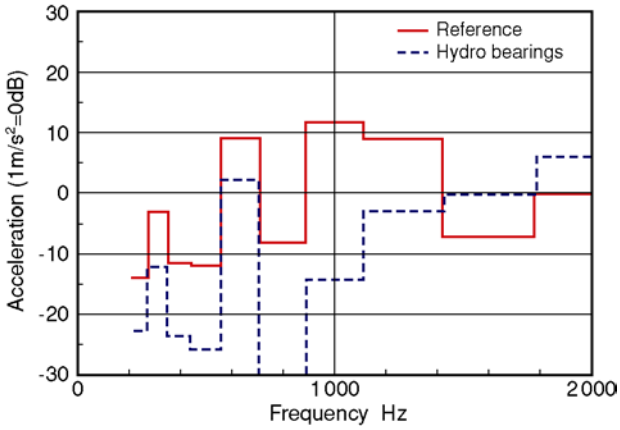


Fig. 16 Simulated comparison of reference acceleration in third octave between reference model and hydrobearings

important element in noise in the source stage, and the ball bearing clearance is an important element in the transfer stage.

4.1. Changed Dimensions at Source Stage

4.1.1. Change in crankshaft dynamic characteristics

In order for a better understanding of the effect of changes in the dynamic characteristics of the crankshaft, rather than designing and creating a whole new crankshaft, a radical modification (removal of large masses at each end) of the original crankshaft was carried out. The generator rotor was completely deleted and the CVT pulley radius and thickness were greatly reduced. Figure 17 shows the original and modified crankshafts. As a result, the resonant frequencies of the shaft were increased. The first torsional resonant frequency was increased from 511 Hz to 849 Hz, and the second, from 1,128 Hz to 1,728 Hz. As shown in Fig. 18, these dimensional changes greatly reduced the crankshaft noise measurement results at the rider's ear in the frequency band. The following is a simplified explanation of the mechanisms of reducing noise. Reviewing the spectrum of combustion cylinder pressures, it is easy to see, as shown in Fig. 19, that the energy is considerably damped at higher frequencies. Due to this effect, if the crankshaft resonant frequencies are raised, the transfer efficiency of the excitation force will be suppressed.

4.2. Change in Dimensions at Transfer Stage

4.2.1. Reduction of ball bearing clearance using limitation on thermal coefficient of expansion

Because the ball bearing outer race is pressed into the aluminum alloy crankcase, after assembly, the clearance is smaller than in the free condition. But during operation, due



Fig. 17 Comparison between original and modified crankshaft

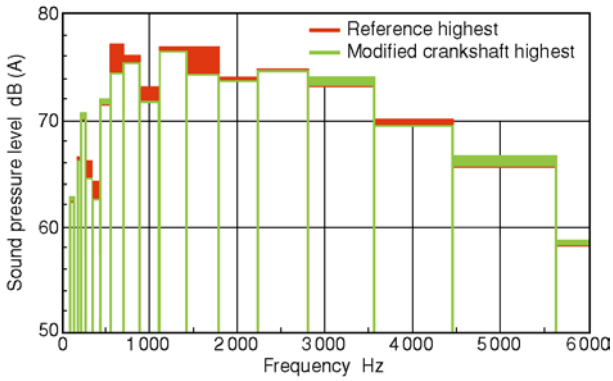


Fig. 18 Frequency analysis result by modified crankshaft

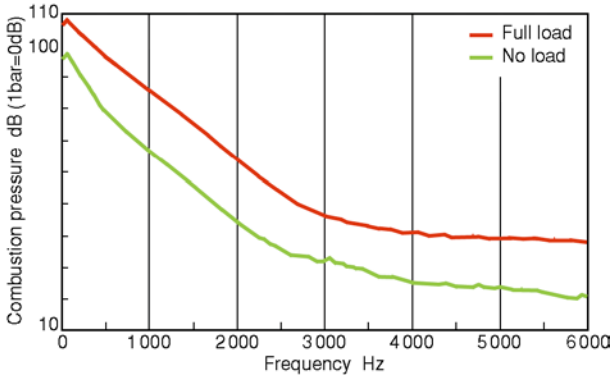


Fig. 19 Combustion pressure per one cycle

to the difference in thermal expansion coefficient between the aluminum alloy crankcase and the steel bearing, the clearance increases together with the oil temperature. In an attempt to prevent excessive clearance, a steel water jacket ring was placed around the outer race, as shown in Fig. 20.

4.2.2. Replacement of ball bearings with plain bearings

Another method to reduce the excitation force due to high bearing clearance is to change the bearing specification. As in Fig. 21, the bearings were changed from the ball type to the plain (hydro) type. Since the oil film damping is larger than that in a ball bearing, these bearings are expected to provide higher damping of the impact forces excited due to the clearance of the bearings in the crankcase.

Both versions showed reductions in noise, as indicated in Fig. 22 and Fig. 23.

These three tests proved the validity of this virtual model for qualitative comparisons of designs with varying specifications. Similar levels of noise reductions were seen in the simulation and experimental results for all the versions. However, sufficient objective noise reduction was only seen from the change of bearings to the plain type. Noise levels dropped in the other versions, but not enough, from the point of view of the rider.



Fig. 20 Crankshaft with water-cooled bearing

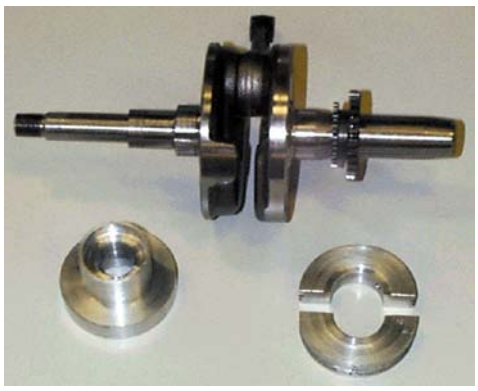


Fig. 21 Crankshaft with hydro bearing

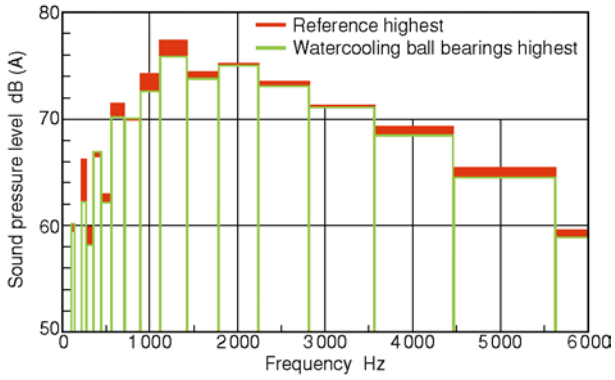


Fig. 22 Frequency analysis result by water-cooled bearing

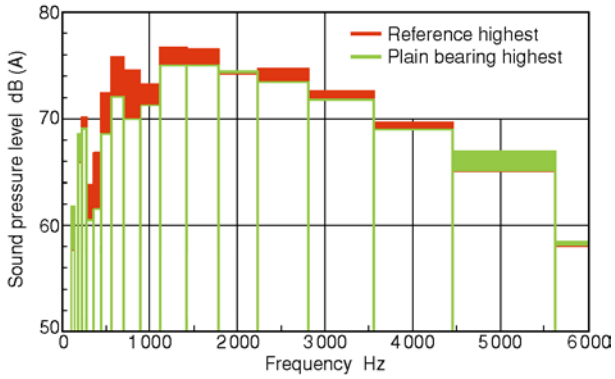


Fig. 23 Frequency analysis result by hydro bearing

5. Summary

A virtual model of an engine was constructed for qualitative assessment of designs for improved crankshaft noise characteristics and for relative comparisons of components with varying specifications. The model was shown valid in experimental tests using a completed motorcycle with components of altered dimensions.

- Crankshaft noise is caused by resonance of the crankshaft assembly.
- Excessive ball bearing clearance exacerbates crankshaft noise and causes the typical rattling noise.
- Noise is diminished by revising the design of the crankshaft.
- Noise is diminished by reducing bearing clearance.
- An objective improvement is obtained only by replacing some ball bearings with plain bearings.
- A combined approach of numerical analysis and experimental analysis contributes much to explaining the mechanisms of noise generation.

In future studies, it is necessary to develop a more precise model of bearings in dynamic mechanical simulation software.

References

(1) Vandenplas, B., Hendrix, W., Sekita, M., Tamura, H.: A combined experimental-numerical approach for motorcycle crank noise: Modeling, ATT 2002, Paris

(2) Mas, Pl, Vandenplas, B., Kuwahara, H., Fukui, Mas, P., Vandenplas, B., Kuwahara, H., Fukui, Y.: A numerical substructuring approach to motorcycle vibration prediction, SETC 2001 01 1849/4267

(3) Schonherr, C.: Schwaderlapp, M.: Schmillen, K.: Beachtung des axialen Bewegungsverhaltens für akustisch günstige Kurbelwellen. In: MTZ 57, Nr. 9 pp. 520-526 (1996)

(4) Kunzel, R.: Essers, U.: Die Lastabhängigkeit des mechanisch verursachten Motorgeräusches. In: MTZ 54, Nr. 9 pp. 452-459 (1993)

(5) Schwadderlapp, M., Wolschendorf, J.: Akustische Verbesserung von Pkw-Dieselmotoren durch Strukturmassnahmen. In: MTZ 54, Nr. 12 pp. 634-641 (1996)

(6) Werkmann, M., Essers, U.: Untersuchung und Beeinflussung rauher Geräuschkomponenten von Verbrennungsmotoren. In: MTZ 57, Nr. 10 pp. 586-590 (1996)

(7) Kampichler, G.: Der neue luftgekühlte Industrie-Dieselmotor von Hatz. In: MTZ 57, Nr. 5 pp. 266-273 (1996)

(8) Wilhelm, M., Strohe, M.: Körperschallanregung der Motorstruktur durch axiale Bewegungen der Kurbelwelle. In: MTZ 53, Nr. 11 pp. 548-555 (1992)

(9) Spessert, B.: Geräuschreduktion von ViertaktDiesel- und Ottomotoren: Rückblick und Stand der Technik Teil 1. In: MTZ 60, Nr. 7/8 pp. 508-517 (1999)

(10) Spessert, B.: Gerauschreduktion von ViertaktDiesel- und Ottomotoren: Rückblick und Stand der Technik Teil 2. In: MTZ 60, Nr. 9 pp. 612-619 (1999)

■ Authors ■



Masahiko SEKITA



Hiroshi TAMURA

Development of a Silent Drive Chain System for Motorcycles

Haruomi SUGITA* Masahiko SEKITA* Tomohiro FUSE*

ABSTRACT

Chain noise, which is one of the influential factors to motorcycle pass-by noise regulation, can be classified into two categories: low frequency noise from the rear wheel originated from cordal action according to the second order component of chain meshing and high frequency noise generated by the impact when a chain roller contacts the sprocket bottom. A shape improvement using a urethane resin damper mounted on the drive sprocket and a steel roller drive chain with a urethane resin roller were effective for noise reduction, respectively. The new chain system that combined these new ideas has been proven to be capable of reducing the chain noise to half that of a conventional system.

1. Introduction

Generally, a chain, shaft or belt is adopted in the drive systems for motorcycles. As shown in Fig. 1, a roller chain (hereafter referred to as “chain”) is widely used for driving the rear wheel from the engine on large sport-type motorcycles. The chain drive is the only method that enables the kind of maneuverability required by a sport motorcycle while offering cost and weight advantages on a high dimension level. Due to advances made to reduce the primary source of motorcycle noise, i.e., air suction and exhaust, to cope with ever more stringent environmental noise regulations that will come into practice within a few years, the concern of chain noise is becoming a larger issue. To reduce motorcycle chain noise and at the same time retain the reliability of the chain drive system has been a difficult goal to achieve. An analysis on the mechanism of chain noise was conducted to show the different causes of the noise conditions. Based on the results of this study, a new chain system was developed in which the chain noise energy was reduced to half that of conventional system designs.

1.1. Chain Noise in Large Sport Models

The main sources of noise in a large chain-driven sport model motorcycle include the exhaust system, intake system, engine, and the drive system. Among these, as shown in Fig. 2, most of the noise from the drive system is attributable to the drive chain. In large sport model motorcycles, the drive chain noise (hereafter referred to as “chain noise”) contributes to as much as 20% of all the noise from the vehicle. Chain noise is usually caused when the chain roller impacts the bottom of the sprocket between the sprocket teeth thereby generating an impact noise. Figure 3 shows attaching a cushioning material (hereafter referred to as “damper”) made of hard rubber or the urethane resin on

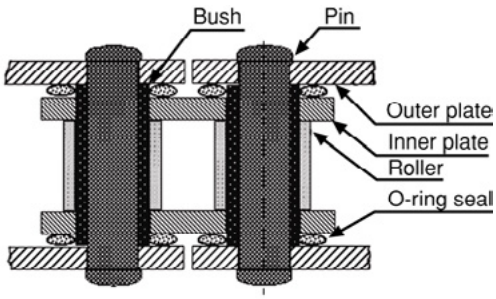


Fig. 1 Structure of conventional drive chain for motorcycles

* Asaka R&D Center

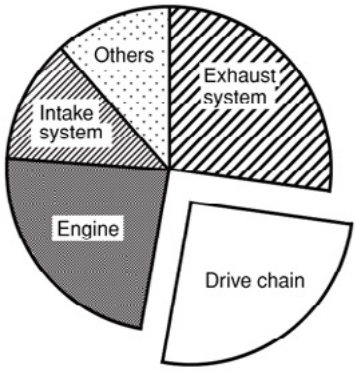


Fig. 2 Ratio of drive chain noise to others

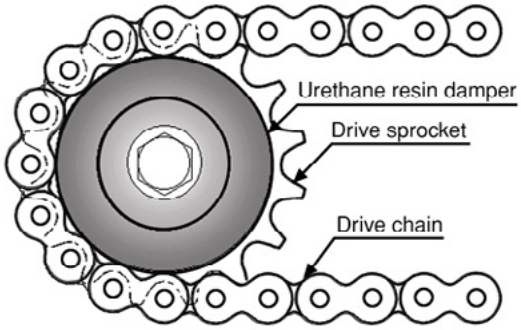


Fig. 3 Conventional drive sprocket and chain for motorcycles

the side of the iron sprocket. This serves to reduce the impact rate and impact noise between the chain roller and the bottom of the sprocket teeth. Also, a cover has been fitted over the drive sprocket assembly to prevent the direct noise radiation.

2. Analysis of Roller Chain Force

2.1. Chain Separated Test Equipment

It is difficult to accurately separate chain noise from all other noises being generated from an actual motorcycle. However, evaluation of the chain noise on the actual vehicle doesn't allow an analysis with high reproducibility due to the effects from other noise sources such as engine or exhaust system. Figure 4 shows the separated sprocket and chain assembly test equipment. This assembly has been devised to test the chain noise in conditions approximating actual vehicle driving conditions. The motor drives the drive shaft and the dynamometer absorbs the driving force. To block the noise generated from these auxiliary machines such as the motor, the drive assembly has been incorporated into a separate soundproof chamber.

2.2. Results of Impact Noise

Figure 5 shows the equipment used to measure the excitation force exerted on the sprocket by the chain. The acceleration pickup was attached to the drive sprocket and the linear acceleration generated by the drive sprocket driven under actual vehicle driving conditions of 1,186 r/min and the driving force 137 N·m was measured. Measurements

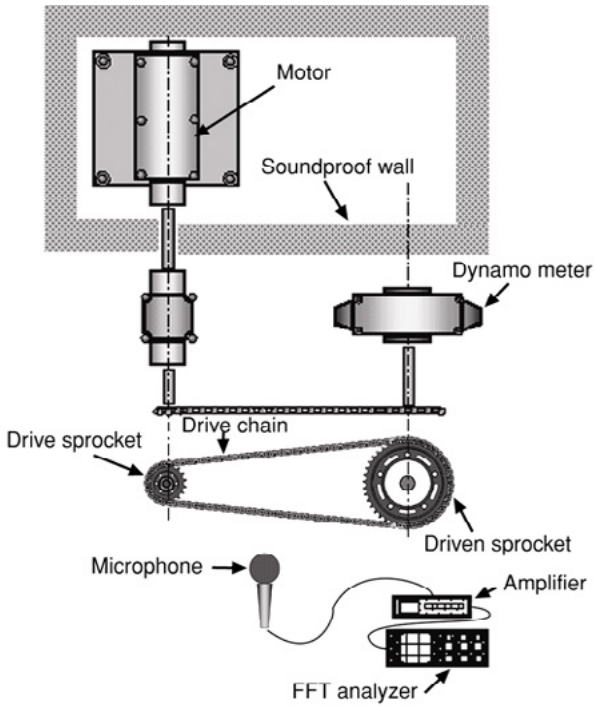


Fig. 4 Chain-separated test equipment

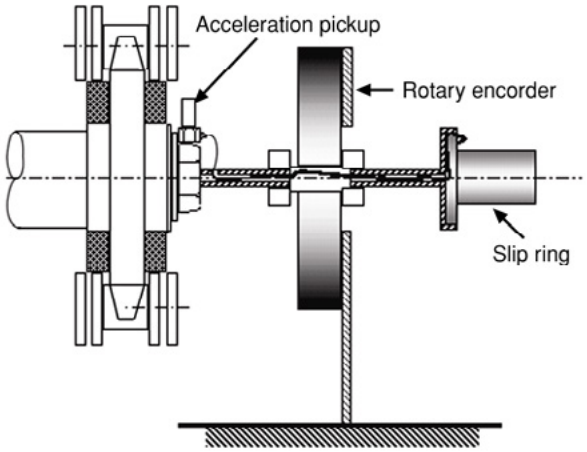


Fig. 5 Measurement equipment of drive sprocket acceleration

were also conducted without the application of a urethane resin damper and with a damper of Hs84 (Shore hardness) and Hs95 degrees of shore hardness respectively. As Fig. 6 shows, impact noise is generated whenever the roller meshes with the drive sprocket. Furthermore, the noise level decreased progressively as tests were conducted without a damper, and with a Hs84 and Hs95 damper respectively. The linear acceleration with a Hs84 and Hs95 damper was confirmed decreasing up to 1/10 compared to that without a damper. Measurement of noise within 1.5 m away from the side of the test equipment was conducted simultaneously, and a maximum noise reduction of 7 dB was confirmed. Thus, it has been confirmed that the cushioning effects of the resin damper have a remarkable influence on the chain noise level.

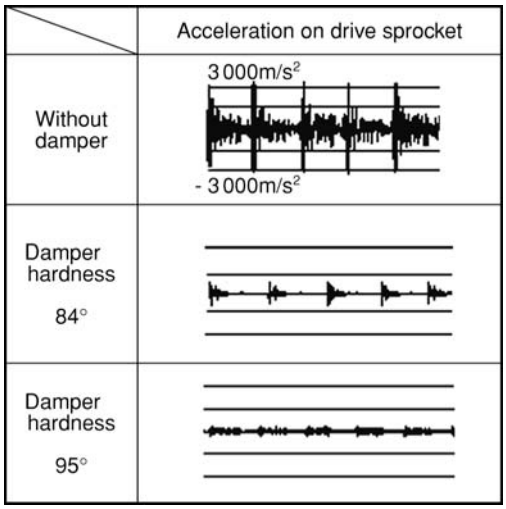


Fig. 6 Acceleration of time domain and frequency domain

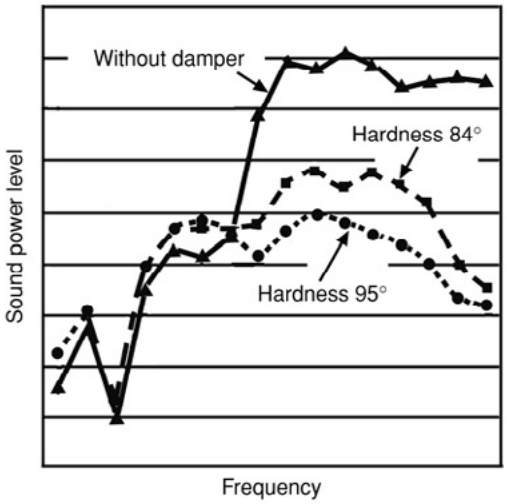


Fig. 7 Frequency analysis of noise from chain-separated test device using three types of urethane resin damper

3. Effectiveness of Impact Noise Reduction in the Actual Vehicles

The result of the chain separated test equipment, that the hardness of the urethane resin damper has significant influence on the degree of acceleration and noise generated, was verified on an actual vehicle. Figure 8 shows that noise generated on an actual vehicle with an applied damper hardness of Hs84 significantly reduces noise occurrence compared with testing conducted without the application of any resin damper. On the other hand, measurements of noise generated with the application of a damper with a Hs95 hardness unexpectedly showed an increase in noise which is actually different from the chain separated test device. Figure 9 shows the frequency analysis of noise generated from the chain-separated test devices. According to the frequency analysis results, it has been shown that the Hs95 damper increased the noise level to a high of 630 Hz compared with that generated by the Hs84 damper. This

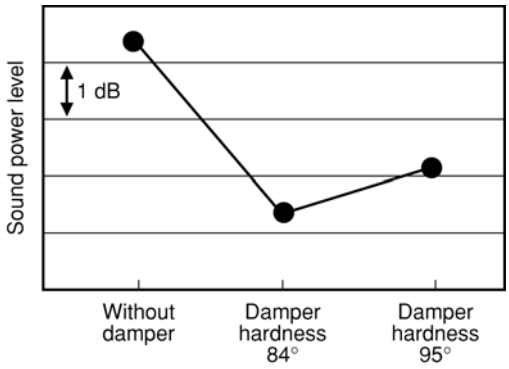


Fig. 8 Noise level of complete motorcycle using three types of drive sprocket

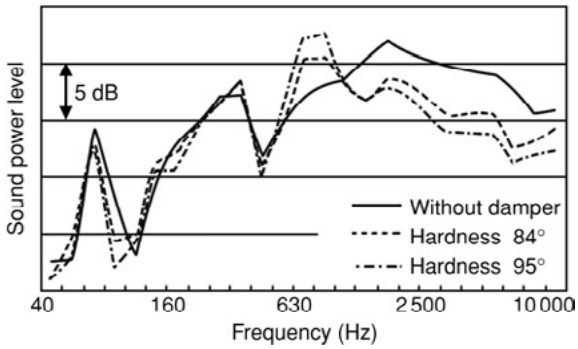


Fig. 9 Frequency analysis of noise from chain-separated test device with rear wheel using three types of urethane resin damper

clearly demonstrates that an increase in noise level exerts influence on the overall noise level and that there is a difference in noise levels generated in component testing (Fig. 7) and noise levels generated on the actual vehicle (Fig. 9).

4. Source of Noise from the Actual Vehicle

Noise measurements were taken from the actual vehicle to determine the source of the 630 Hz sound that did not occur with the test unit. The possible causes were assumed to be coming from the engine, swing arm, rear wheel, etc. Lead masking was applied to these respective locations in testing for noise sources on the actual vehicle. Figure 10 shows the effectiveness of the lead masking application to the rear wheel. These measurements clearly show that the urethane resin damper attached to the drive sprocket exerts influence on noise radiation generated from the rear wheel and that this has an effect on the overall noise from the actual vehicle.

5. Measurement of Rear Wheel Transfer Function

Currently, aluminum die-cast is widely used in the rear wheel component of modern sport type motorcycles. To verify this commonly held view, the rear wheel transfer function on the actual vehicle was measured. Using an impact hammer, force was applied from the driven sprocket

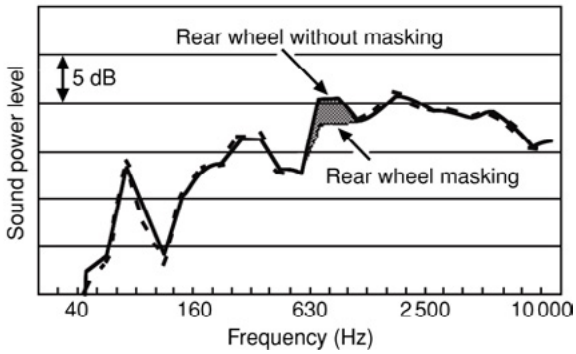


Fig. 10 Effectiveness of lead masking in rear wheel from the actual vehicle

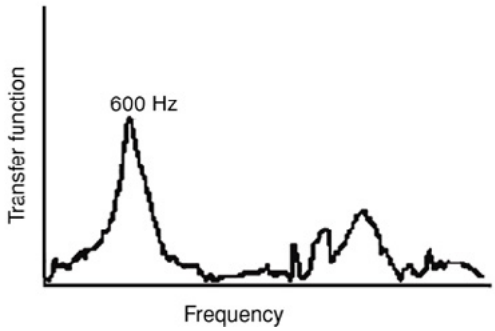


Fig. 11 Transfer function of rear wheel

tooth flank and the rear wheel transfer function was then measured. Figure 11 shows a resonance frequency of 600 Hz generated by the transfer function of the aluminum alloy die-cast rear wheel on the actual vehicle. This shows how easily frequency resonance is generated from the rear wheel. The location at which the resonance occurs is situated on the reduced rim area where lead masking has been applied on the actual vehicle. This proves that a rear wheel generating approximately 600 Hz of natural frequency creates a resonance from the similar level of resulting excitation.

6. Unit Tests Conducted with the Rear Heel Attached

To clarify the cause and effect relationship between the specifications for urethane resin damper on the drive sprocket and the rear wheel radiation noise, the chain-separated testing equipment shown in Fig. 4 was used on the rear wheel. It was attached and fitted to an actual vehicle as shown in Fig. 12. The equipment was used to measure noise occurrences with differing urethane damper configurations: first without the use of a damper and then with Hs84 and Hs95 dampers, respectively. At the same time, to clarify the contribution of the drive and driven system, each system was masked in a wooden box covered with lead and acoustic material and measurements were conducted respectively. Figure 13 shows the results of this test. The following points were learned from the tests conducted on the rear wheel mounted chain drive system.

The noise generated from the drive system showed the

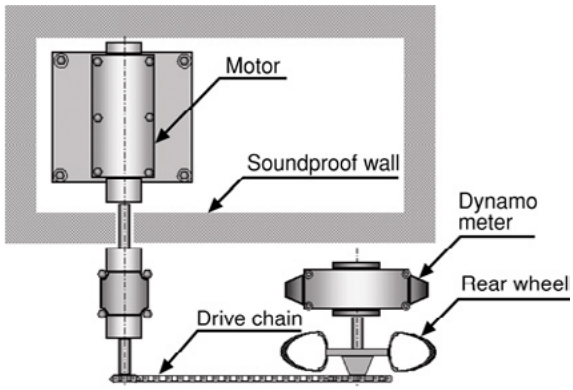


Fig. 12 Chain-separated testing device with rear wheel

following results: noise from testing conducted without a damper was greater than that in which an Hs84 damper was applied, and this in turn showed greater noise than testing in which an Hs95 damper was applied. This result confirms that the change of impact noise greater than 1.6 kHz has an effect. While the noise generated from the driven system showed the following results: noise from testing conducted in which an Hs95 damper was applied was greater than that in which an Hs84 was, and this in turn showed greater noise than testing without a damper, which is the opposite to the result with a drive system. The driven system noise exerted a frequency of 630 Hz. Putting these results together in accounting for the total level of the noise produced revealed that the noise tended to diminish first without a damper and then, with a Hs95 damper and finally with a Hs84 damper. The chain noise on the actual vehicle occurred in the high frequency components causing impact noise between the drive system roller and sprocket teeth bottom, and also in the comparatively low frequency levels of noise emanating from the wheel surface in the rear wheel mounted drive system. The trade off difference in the relationship of these two types of noise showed that they both determined the level of chain noise that occurred on the actual vehicle. This has resolved the question why there was an unexpected change in frequency level of 630 Hz and 800 Hz by modification of the resin damper.

7. Difference of Winding Radius

In testing conducted on the wheel components and the actual vehicle it was shown that while there was a reduction in the level of impact noise generated by the urethane resin damper attached to the drive sprocket, there was an increase in the wheel radiation noise frequency. The testing also confirmed the mechanisms in which this noise occurred. In principle, the roller chain has a variation in the winding radius. As the roller winds around the sprocket, the winding radius on the roller position shifts from position R to position r as shown in Fig. 14. The change in winding radius causes vertical shifting, called cordal action, on the chain line. The following formula expresses the difference in winding radius.

$$r = R \cos(\pi / N) \quad (1)$$

N: the number of sprocket teeth

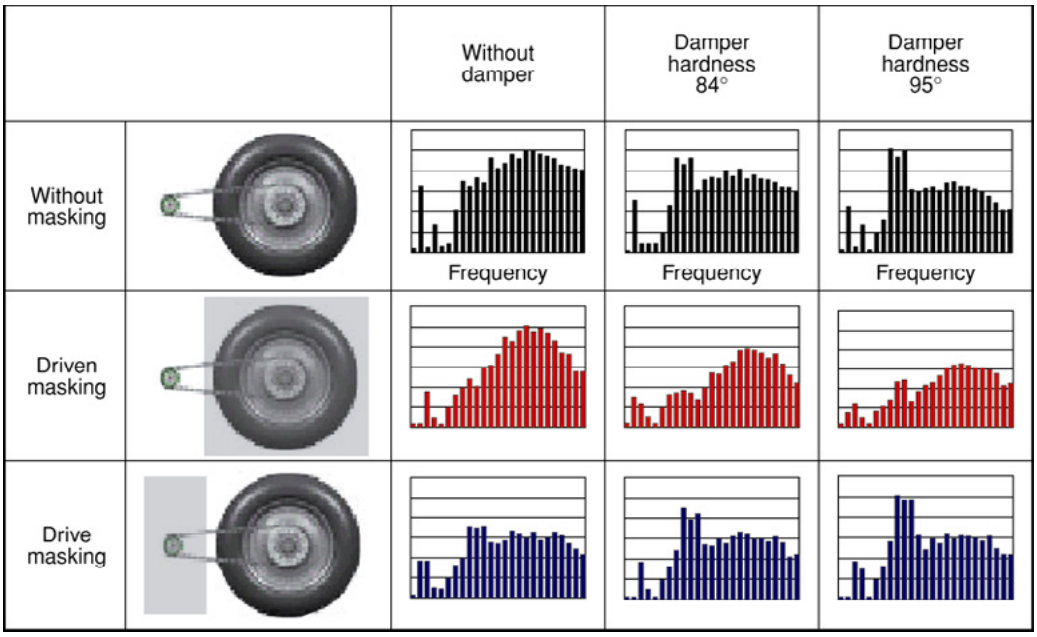


Fig. 13 Comparison of sound frequency from chain-separated testing device using three types of urethane resin damper

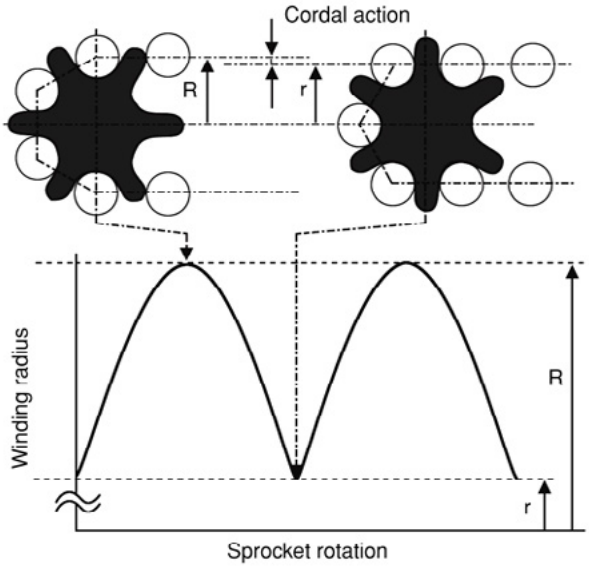


Fig. 14 Relation between winding radius and rotation of sprocket

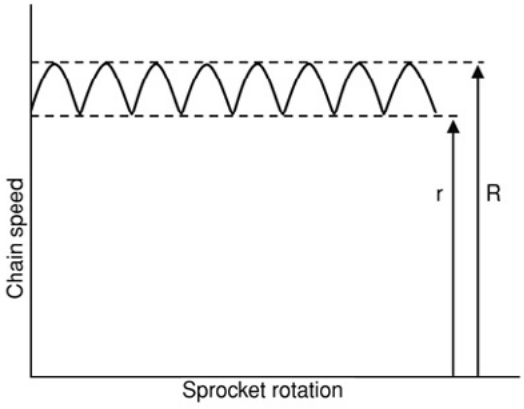


Fig. 15 Fluctuation in chain speed

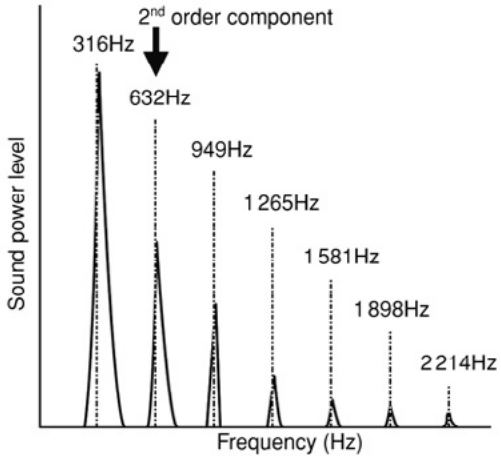


Fig. 16 FFT output of fluctuation in chain speed

The cordal action causes the chain speed to fluctuate even if the drive sprocket's angular velocity remains constant. Figure 15 shows the fluctuation in chain speed for a drive sprocket with 16 teeth that rotates at 1,186 r/min in an actual vehicle condition. Figure 16 shows the FFT output results of the fluctuating chain speed. The fluctuation of the drive sprocket winding radius causes the cordal action which then leads to a fluctuation in chain speed. Consequentially, this will cause a fluctuation in angular velocity flowing from the orderly component of meshing of the driven sprocket. The angular velocity fluctuation exerts an excitation force on the driven system and contributes to chain noise.

8. Why Does the Sprocket with the Resin Damper Increase the Changes in the Winding Radius?

The reasons are to be verified why the resin damper, used for reducing impact noise, was shown to cause greater deterioration in the orderly component of meshing than when no damper was used.

Figure 17 and Fig. 18 show the respective chain winding radius conditions on the resin damper fitted drive sprocket. At the initial winding position of the roller, indicated by the mark (•) in Fig. 17, the plate is positioned in the resin damper tooth indent. At this point, the roller does not sit completely over the bottom of the sprocket between the teeth. As Fig. 18 shows, the winding is continued so that the chain is wound completely over the sprocket. The winding radius is shown by r. The roller point, indicated by mark (•), is completely meshed over the bottom of the sprocket between the teeth. The winding radius R is increased only for the associated tooth indent portion of the resin damper. The difference in winding radius, expressed by R-r, is greater for a chain winding radius associated with a resin damper than that without the application of a resin damper. That is, it has become clear that with the combination of the round urethane resin damper and the gourd-shaped chain plate, the fluctuation of the winding radius becomes larger than when there is no damper. The fluctuation of angular velocity of the driven system increases and the velocity order component also increases. The result shows an increase in excitation force on the wheel and an increase in chain noise, which causes deterioration in the radiation noise level.

8.1. Countermeasures for Two Noise Types

Since there is a relationship between the trade off of the drive and driven system in relation to chain noise, it was believed that there must be a way of reducing noise for the total chain system including the drive and driven systems. It has now been shown that countermeasures are required for two different types of noise: for the impact noise on the drive system and for the wheel radiation noise on the driven system. The noise radiated from the driven system will be dealt with first.

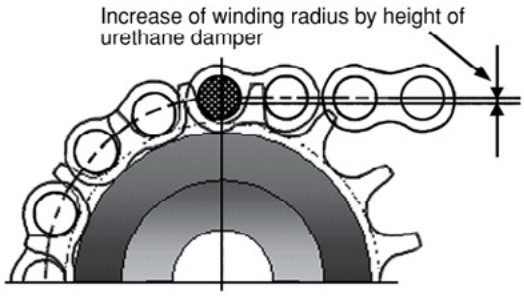


Fig. 17 Condition of meshing start

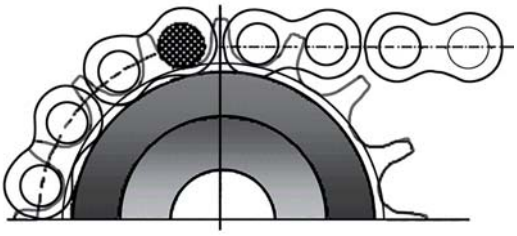


Fig. 18 Condition of completely meshing

8.2. Urethane Resin Damper for Reducing Winding Radius Fluctuation

Winding radius fluctuations approaching conditions close to those in which a resin damper was not used and meshing that enabled a reduction in impact noise were verified. Since fluctuations in winding radius increase the orderly component of meshing, attention was directed to reducing variations in winding radius. Improvements in the meshing between the chain and sprocket were attempted with the resin damper. As can be seen from Fig. 14, as the peak on the graph indicating the winding radius is decreased, the meshing of the roller and sprocket teeth becomes increasingly shallow leading to a greater potential for the chain to become disengaged while the vehicle is being driven. Further attention was then directed to lifting the low point between the peak winding radius points of chain penetration. To raise the low point of the winding radius to align with the chain plate's side view pattern shape, the sprocket protrusion was aligned with the resin damper wherever low points of contact occurred in the winding radius. Changing the winding radius decreased the chain's propensity to sag at those low points on the winding radius. To adjust the sprocket protrusions to avoid disruption to the original power transmission function, the height of protrusion was adjusted to approximate the indent points on the resin damper. Figure 19 shows the resultant resin damper with protrusions that was designed according to the test results.

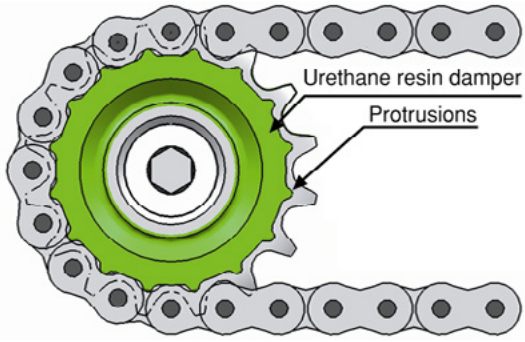


Fig. 19 New form urethane resin damper with protrusion attached

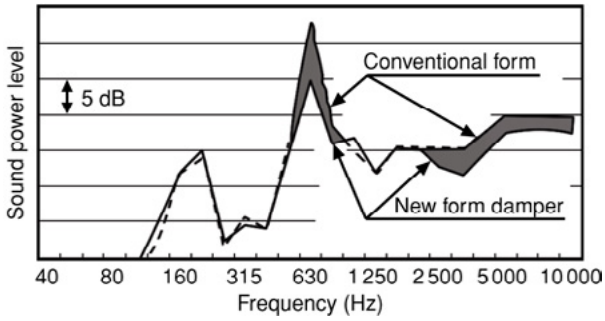


Fig. 20 Effectiveness of new urethane resin damper by chain-separated testing device

8.3. Verification of the Effectiveness of the Protrusion in the Resin Damper

Figure 20 shows the measured performance results of the newly designed urethane resin damper with protrusions including the reduction in impact noise and power transmission frequency. In the wheel connected unit testing and actual vehicle testing, it was shown that there were no significant increases in the previously measured 630 Hz sound level. It was also shown that the reduction in impact noise levels greater than 1.6 kHz was the same as that achieved with the conventional resin damper. Furthermore, by combining the newly devised resin damper with the chain plate, the resin helped to disperse the exaggerated force exerted during meshing, while preserving the qualities associated with the original damper and successfully improving the durability of the silent chain configuration. Also, reducing the irregular movement pattern of the drive sprocket greatly reduced the rockiness experienced by the rider and contributed to the overall improvement in vibration during operation.

9. Reduction of Impact Noise

9.1. Silent Chain

Reducing persistent chain noise requires an effective means for reducing impact noise. However, by attempting to further reduce impact noise with a resin damper attached to the drive sprocket, there was a concern that this would lower drive transmission reliability and bring on deterioration through the previously described trade off in winding radius. Therefore focus was shifted from the sprocket to the drive chain in developing a means for effectively reducing impact noise. However, it was not possible to develop a function capable of servicing the dual requirements for drive transmission while softening impact. This was resolved by separating the drive transmission function and the noise elimination on the chain roller to devise a roller chain with newly enhanced functionality.

9.2. Silent Chain Structure

Figure 21 shows the structural configuration of the newly devised silent chain. This newly developed chain adopts a urethane resin roller (hereafter referred to as resin roller) segment on the steel roller for supporting power transmission. Approximately 15% of the steel roller is constructed with a urethane resin roller segment, which is fitted along a cylindrical direction. The outer dimensions of the resin roller measure about 1.2 times that of the steel roller. This enables the resin roller to sit firmly on the bottom of the sprocket between the teeth and aligns the steel roller with the elastic deformation portion of the resin roller. This structural design successfully reduces chain noise by reducing the impact speed of the steel roller. The structural characteristics provide alternate positioning of the resin roller that is set on single sides while countering chain line shifting and wear imbalances on the steel roller. In determining a suitable width for the resin roller, both the silent characteristics and durability were taken into account in relationship to measurement restrictions defined by the steel roller. In determining the outer diameter dimensions for the resin roller, it was known that larger dimensions for the resin roller would provide greater reinforcement to the silent chain characteristics. By incorporating the driven sprocket resin damper in the newly devised resin roller chain, a greater reduction in impact noise was achieved. By the alternate positioning of the resin roller, even numbered toothed sprockets experienced the tooth flank wear. This was countered by recombining the drive chain along a half circle. The newly developed silent chain design has successfully been applied to 530 size chains that can be used on large scale motorcycles.

9.3. Effectiveness of the Silent Chain

Figure 22 shows the effective reduction in noise achieved by the newly developed silent chain. The measured results show a frequency reduction of more than 1.6 kHz. Also, no increase in the 630 Hz orderly component of meshing has been verified. The effectiveness of chain silence has also been tested and verified for up to 20,000 km of driving with assured durability. This has been made possible by addressing the requirements for the drive force transmission function and the silent chain function within a single roller assembly made up of steel and resin components. Additionally, applying this impact noise countermeasure to the main chain component has been an effective means in reducing chain noise generated from the driven sprocket.

This new chain system comprised of a new drive sprocket resin damper and silent chain has not only resolved the long studied roller impact noise but has also resolved the noise radiating from the drive system by isolating its origins to the orderly component of meshing mechanism. By successfully incorporating the described two results, this research has achieved a greater than 50% reduction in chain noise energy compared with that in conventional drive chain systems.

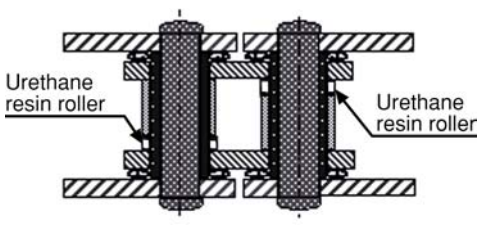


Fig. 21 Structure of developed silent chain

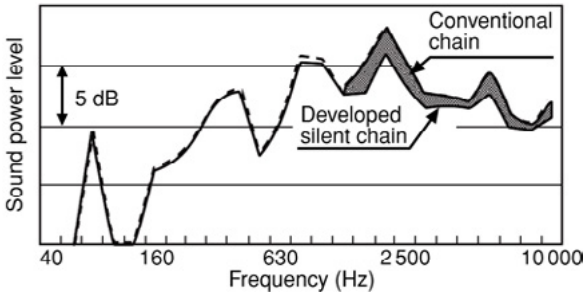


Fig. 22 Effectiveness of developed silent chain

10. Conclusion

In reducing the roller chain drive noise on rear wheel drive systems adopted by large scale sport type motorcycles, attention was focussed on the excitation force emanating from the chain noise, cordal action and the radiation noise generated by the drive system. The results gained from testing conducted on the unit equipment and on the actual vehicle are given below.

(a) Two different types of noise were discovered: one is an impact noise greater than 1.6 kHz on the roller chain and the other noise is generated by the excitation force resulting from angular velocity fluctuations on the chain.
(b) The noise from a rear wheel generated by the excitation force on the chain's angular velocity fluctuation was shown to cause the cordal action experienced by the roller chain.
(c) In reducing the level of noise from the rear wheel, it was discovered that the attached drive sprocket resin damper actually worsened the cordal action.
(d) By combining the newly developed silent chain and the resin damper in the new system, the chain noise energy level was reduced to less than half that in conventional system configurations.
(e) By conducting testing on rear wheel assembly unit equipment, an analysis of the high chain noise was able to correlate these noises to the actual vehicle.

11. Acknowledgments

The authors would like to express their deep appreciation and gratitude to all those people within the company and all others for their assistance with this research into the reduction of drive chain noise. In particular, we would like to thank employees of Daido Kogyo Co., Ltd. for their close cooperation in research activities related to the resin roller silent chain assembly.

References

(1) Nakagome, M.: Safe roller chain design, Tokyo, Yokendo, p. 111 (1989)

(2) Shimura, Y.: Mechanical element application manual for chains, Tokyo, Kogyo Chosakai Publishing Co. Ltd., p. 242 (1995)

■ Authors ■


Haruomi SUGITA


Masahiko SEKITA


Tomohiro FUSE

Development of Interior Sound for a Medium Coupe with Sportiness as an Objective Evaluation Index

Masashi IWAI* Yasuo ISHII* Koji ITO*
Tomoyuki NUMATA* Kazuya KUTSUZAWA* Hidenori SEIKE**

ABSTRACT

A new model medium size coupe was developed with consideration of a sporty interior sound. Subjective evaluation of competitor vehicles was correlated with measured objective results to establish a target interior sound index. The target values on this index were determined at the concept stage of development with respect to relative position of competing cars. As a result of subjective evaluation of artificial interior sounds that represented candidate target values, a target sound was established. The air intake system from the base sedan was modified exclusively for the coupe. Adjustments to intake tube diameter, length, and intake inlet position resulted in an exclusive coupe intake sound. This yielded an interior sound with the sportiness and linear feeling that was desired under acceleration.

1. Introduction

Interior sound is one of the major factors that contribute to the product appeal of a vehicle. Each new car concept has different demands for the interior sound: a luxury car requires a quiet interior, while a sports car must allow the driver to hear more sound. In the case of a vehicle where it is desirable to hear more sound, it is important to match the sound with the vehicle and specific driving conditions. In recent years, much has been written about concepts and approaches to sound design[(1)]. However, because such vehicle development proceeded primarily on the basis of subjective evaluations with certain assumptions about the vehicle and without establishing specific numeric targets, a large number of man-hours were expended in a process of trial and error.

Therefore, as previously reported by one of the authors, a “sportiness” index was developed to quantify target interior sound target values. This paper describes how sportiness was applied in the development of a new medium coupe in order to achieve a sporty sound suited for the new car concept.

* Tochigi R&D Center
** Tigers Polymer Corporation

2. Method of Objective Evaluation of Interior Sound

"Sportiness" is an expression by objective parameters, that is, values that can be measured by instruments, of a subjective rating of the degree to which a person feels the interior sound of a vehicle during acceleration as "sporty". The ratings range from 0 ("not sporty at all") to 50 ("extremely sporty"), and are calculated by the following formula:

$$\text{Sportiness} = A \cdot (ONR) + B \cdot (TP) + C \cdot (ESP) - D$$

A, B, C, D: Positive constants ONR: Order to noise ratio
TP: Tonality ESP: Engine speed increase rate

The basic concept of sportiness is defined as follows. Sounds of the engine speed order components are regarded as sound components, which work positively to create a sporty feel. Components other than the order components are negative components that are regarded as noise.

The order to noise ratio (ONR) expresses the extent to which the sound components exceed the noise components, weighting each order frequency for each speed, giving some effect to the size of the sound components. Effectively increasing the ONR means increasing the absolute value of the sound components in actual interior sound.

The tonality (TP) is a psychoacoustic parameter that expresses the degree to which a pure sound stands out; in this case, it expresses the degree to which the sound components stand out relative to the noise components. Effectively increasing TP means reducing the noise components in actual interior sound. Unlike ONR, TP is not necessarily affected by the absolute value of the sound components.

Engine speed increase rate (ESP) is expressed as "rpm/sec". Increasing the ESP means selecting an engine with good pickup.

Accordingly, based on the formula above, in order to increase sportiness it is necessary to effectively increase each parameter (ONR, TP, and ESP).

Although an earlier article reported on the development of this new evaluation index this article describes the incorporation of two objective evaluation methods based on sportiness into the development of a new car.

In order to objectively evaluate the positioning of the interior sound of the development vehicle one of these methods uses a map that shows the positioning of the interior sound by comparing two values, representing sportiness and loudness (volume). The two values are expressed as an average over a range from 2,000 to 6,000 rpm. Figure 1 shows such a map using current major cars; as seen in this figure, the cars can be grouped into four areas: pure sports cars, sporty cars, exclusive sporty cars, and featureless cars. By using this map, the development vehicle positioning can be estimated relative to competitor vehicles. This method is useful when determining the directionality of the target interior sound. It is important to realize, however, that the groupings shown on this map are named for convenience according to the types of cars that fall in those areas; there are no clear-cut boundaries delineated between the areas.

The second method expresses the change in sportiness versus the engine speed as a characteristic in order to objectively evaluate the sensory expression of linearity during acceleration. This method permits an understanding of the positioning of the development vehicle on the sportiness/loudness map as an even more detailed characteristic. By comparing the results with the target characteristics, it is possible to clearly determine the range of engine speeds that requires improvement, and to what extent.

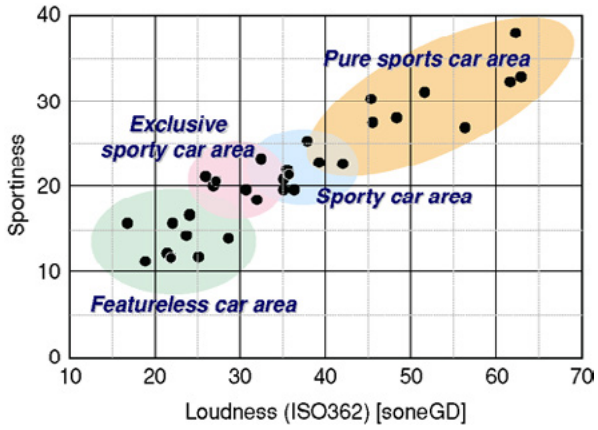


Fig. 1 Sportiness/loudness map

3. Setting the Target Sound

3.1. Target Setting on the Sportiness/Loudness Map

In setting the target for the interior sound of a new coupe based on the concept, the set target was replaced with information on how the user would drive the car and a sensory expression of the sound when the car was being driven in that manner. The decision was made to emphasize quietness while cruising, with a linear sporty sound that matches the driver sensations during acceleration for merging or passing on the American highway. In other words, while cruising, the quietness of the base sedan would be targeted, but during acceleration, the car would feature a sporty interior sound unique to the coupe.

Next, four vehicles (the base sedan and comparative vehicles A, B, and C) were driven by experts, who provided subjective evaluations of the interior sound. For the comparative vehicles, three medium size sedans/coupes with 6-cylinder/3-liter engines were selected, since they were thought to be likely competitors to the new coupe. First, the interior sound of these vehicles during acceleration was measured and their positioning on the sportiness/loudness map was clearly determined. These objective evaluations were then verified by cross-referencing them with the subjective evaluations that were made during the test drives. The correlation between these objective and subjective evaluations was extremely high. The target area on the map for the objective evaluations was then established, based on the index value for comparative car A, which was closest to the targets for the new car in the subjective evaluations by the expert drivers, as shown in Fig. 2.

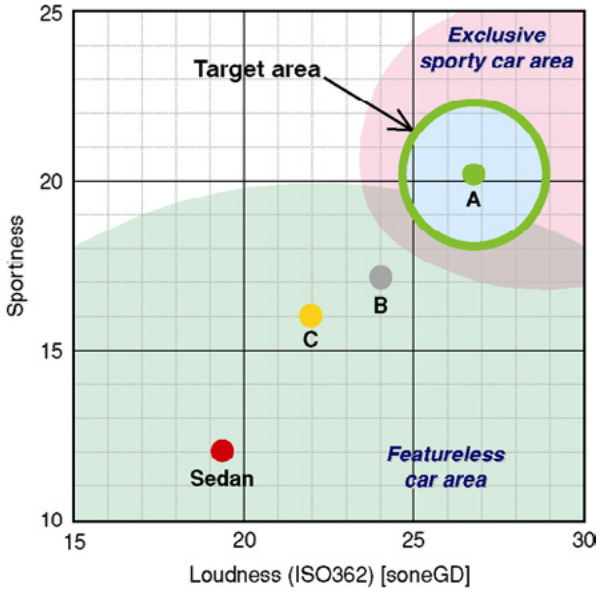


Fig. 2 Target area of sportiness/loudness map

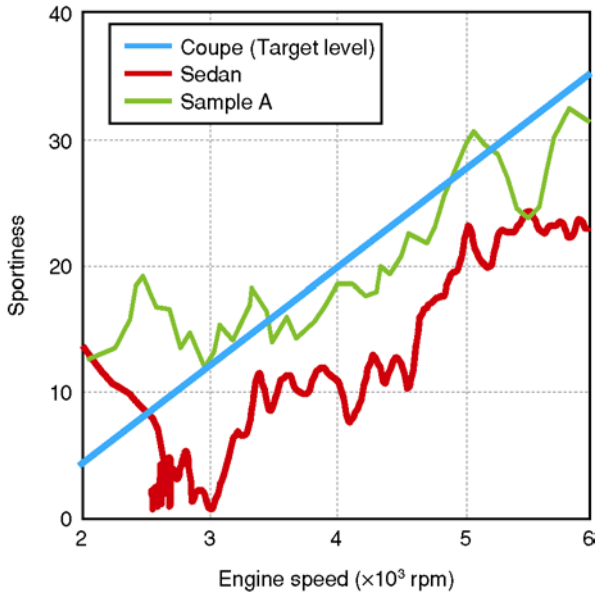


Fig. 3 Target sportiness characteristics

3.2. Setting the Target Sound Based on Subjective Evaluation of Artificial Sounds

Once the target area was established on the sportiness/loudness map, the target sound was studied. First, the sound of the base sedan was measured. A sound editor was then used to process the data and create several types of target sounds that would be positioned in the target area on the map. Next, the expert drivers listened to these candidate target sounds; on the basis of their subjective evaluations, the target sound was selected. Figure 3 shows the characteristics (sportiness versus engine speed) of the target sound that was ultimately selected. The sportiness of the target sound for the coupe was about ten units higher than that of the base sedan, and rose in a linear fashion as the engine speed increased. Figure 4 shows the results of an order tracking analysis accumulated for each engine speed. As shown in Fig. 4, the sound of the third order component of the engine speed was highest. This indicates that this sound component, which contributes positively to creating a sporty sensation, was high.

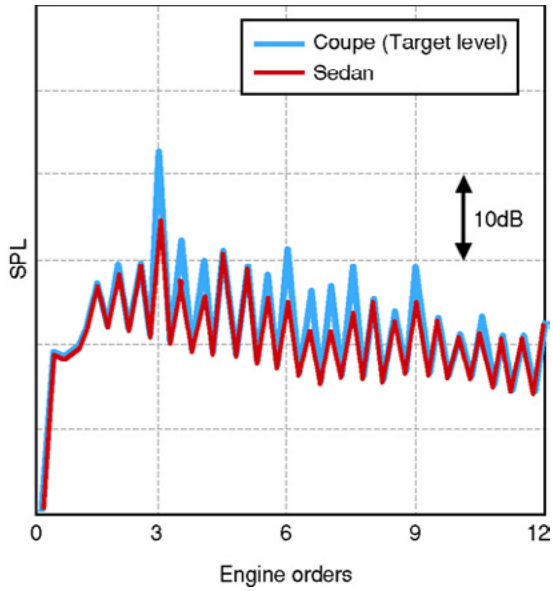


Fig. 4 Target interior sound characteristics

3.3. User Verification of the Target Sound

Next, the target interior sound selected by the expert drivers was played for typical users to verify how they would react to the sound. 55 test subjects who currently own a car in the same category were selected at random from the region where the car is to be sold. For this subjective evaluation, recordings of the target sound for the new car as well as the interior sound of the four vehicles that were used for the subjective evaluation by expert drivers (as described previously) were prepared. The test subjects were then asked about the following three items in regards to each interior sound:

(1) Is the sound appealing or not
(2) Is the sound sporty or not
(3) Does the sound fit the subject's impression of the car design

The test subjects were each allowed to view design sketches in order to determine whether the sound fit the design of the car.

The test subjects were asked to respond to each question on a scale from 0 (negative response) to 50 (positive response). The results were then subjected to a cluster analysis. Figure 5 shows the average ratings for the largest clusters. The target sound for the new car attained high ratings in response to each question. The highest mark was attained in regards to the question of whether the sound was sporty or not. The car that received the next highest rating was the car that had the interior sound that was established as the target for the new car from among the four vehicles for which the experts gave their subjective evaluations.

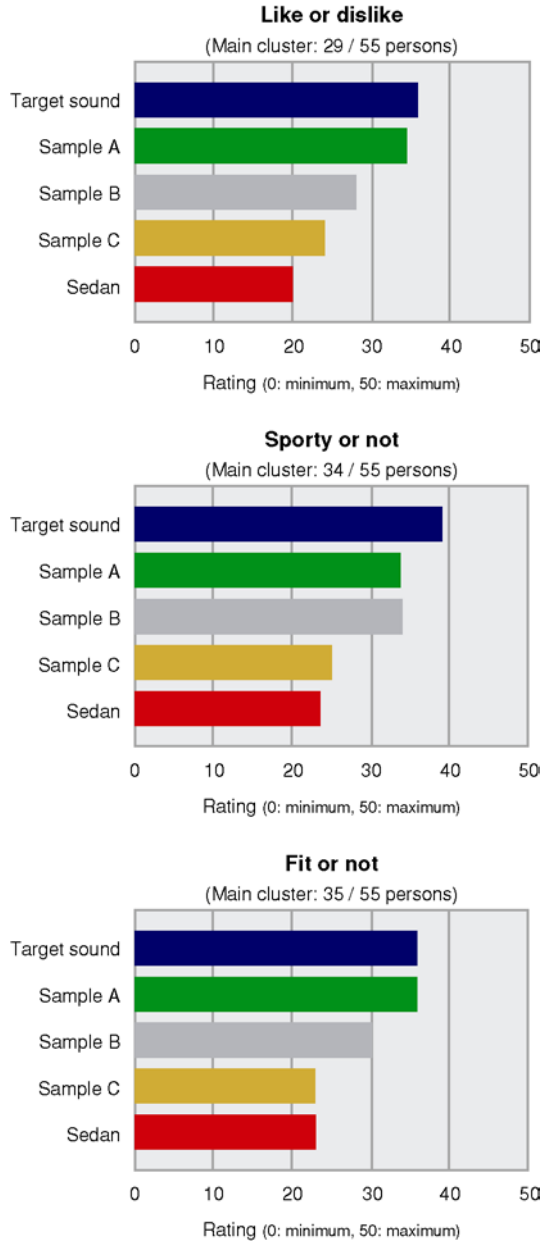


Fig. 5 Results of subjective evaluations

4. Study of Measures to Achieve the Target Sound

Once the target sound was determined, it was necessary to study the means for attaining that target sound. It was decided that the goal would be to maintain a quiet sound equivalent to that of the base sedan while cruising, but to obtain a sporty, linear sound during acceleration. From that standpoint, it would be necessary to emphasize the third order component of the engine speed order frequency in the interior sound of the coupe during acceleration compared to the sedan. Therefore, the decision was made to control the sound during acceleration by using the intake noise that is generated according to how far the throttle is opened.

4.1. Air Intake Location

When using the intake noise to control the interior sound, the intake noise characteristics and the air-borne transfer characteristics of the car body become very important factors. Because the air-borne transfer characteristics are determined by the location of the air intake, the location of the air intake was studied first. As shown in Fig. 6, a comparison was made between two locations: at the front left side of the engine bay (the same location as in the base sedan), and in the left fender panel at a location that allows space for air intake system tubing. Figure 7 shows the transfer functions for both locations. The transfer coefficient for the location in the fender panel is greater than that of the location in the engine bay (the same location as the sedan). In other words, this location demonstrates characteristics that make the intake noise mode audible in the interior of the car. Therefore, in order to make the intake noise during acceleration stand out, the decision was made to locate the air intake inside the fender.

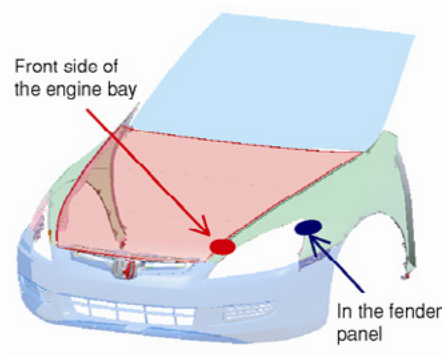


Fig. 6 Location of the intake orifice

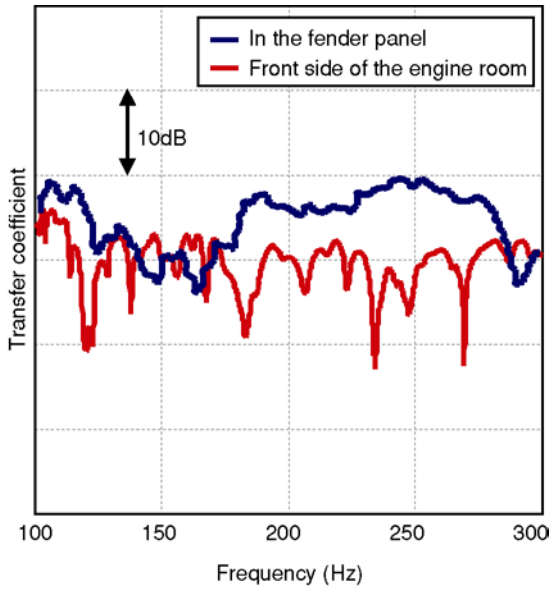


Fig. 7 Air-borne transfer characteristics

4.2. Intake Noise Characteristics

By setting the air intake inside the fender, it was possible to use the intake noise to control the interior sound. First, the target intake noise was calculated on the basis of the target interior sound and the air-borne transfer characteristics against the air intake. Figure 8 shows the difference between the target intake noise for the coupe and the intake noise of the base sedan. These results indicate that the third order component of the intake noise at high speeds needs to be increased by approximately 20 dB.

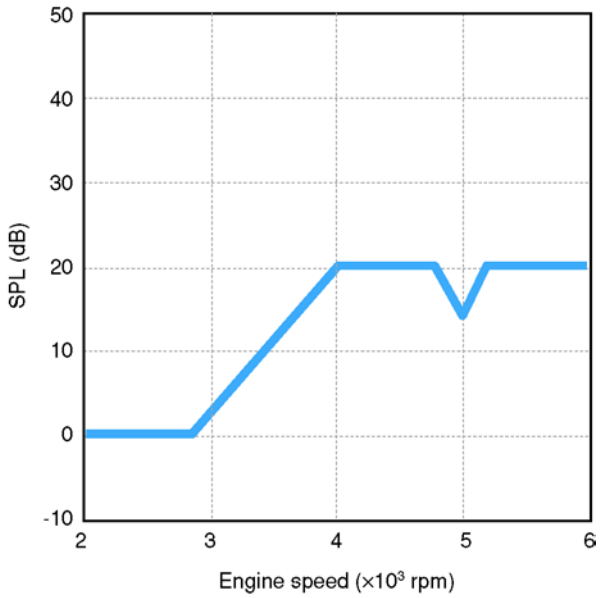


Fig. 8 Difference of intake noise target (3rd order)

In studying the specifications for the intake system, it was assumed that the base engine and the same intake system air cleaner and air flow tubes from the sedan would also be used in the new coupe. Therefore, careful attention was given to the intake tube. The inner diameter of the intake tube in the sedan is 80 mm, the length is 1,000 mm, and it has a 7 L resonator and multiple side-branches, resulting in high noise reduction performance. The study of the intake tube specifications for the coupe was performed by calculating the intake system attenuation, and setting the target value so that the intake system attenuation would be reduced by 20 dB in the range of the third order component compared to sedan's intake system attenuation. The calculations indicated that an intake tube that would satisfy the coupe's target value for the attenuation would have an inner diameter of 90 mm, a length of 700 mm, and 195 Hz branch tubes. Figure 9 shows the

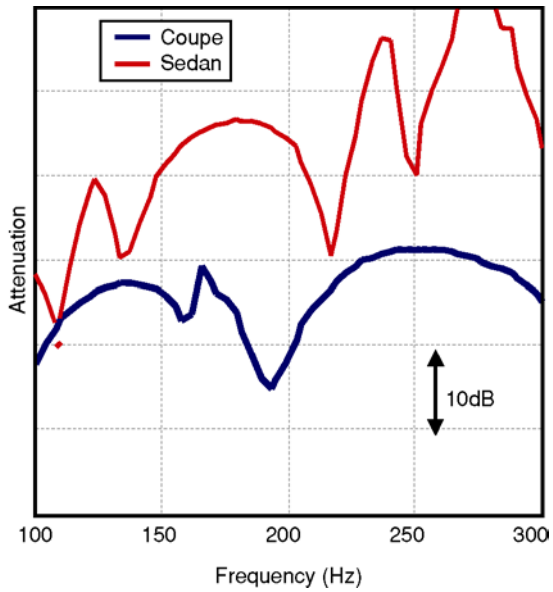


Fig. 9 Intake attenuation characteristics

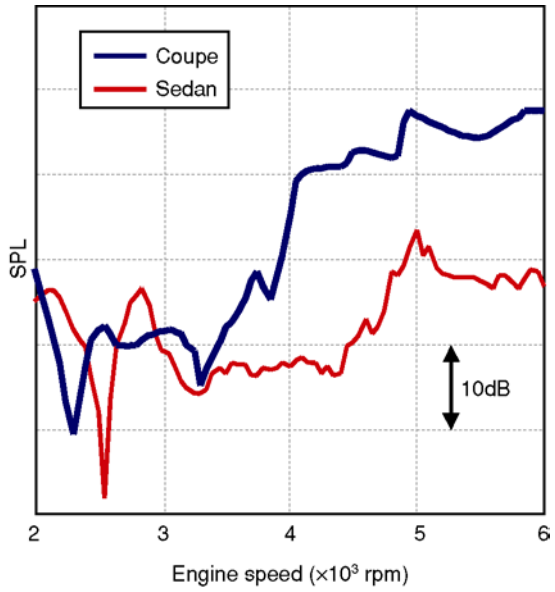


Fig. 10 Result of intake noise (3rd order)

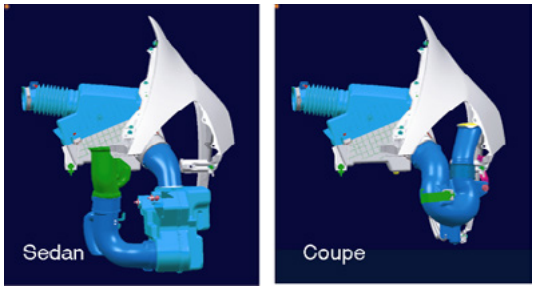


Fig. 11 Intake system layout

results of the calculated attenuation with these specifications. In addition, a prototype of the coupe with an intake tube that met these specifications was produced, and the intake noise was measured. As shown in Fig. 10, the measured results satisfied the target intake noise characteristics with a 20 dB increase in the third order component at high speeds over the sedan.

Based on these results, the intake system for the new coupe was specially adapted, and differed from the intake system of the base sedan as shown in Fig. 11.

5. Confirmation of Results in an Actual Car

An intake system meeting the specifications that resulted from the preceding study of the intake system was installed in a prototype of the new coupe, and the interior sound was measured. Figure 12 shows the positioning of the measured results and the target interior sound as sportiness versus engine speed. This graph indicates that the results produced by the current proposed specifications are very close to the target interior sound. In addition, as shown in Fig. 13, these results fall in the target area on the sportiness/loudness map.

Finally, subjective evaluation by expert drivers also yielded positive results for the sound during acceleration as being sporty and linear, in accordance with the concept for the new coupe.

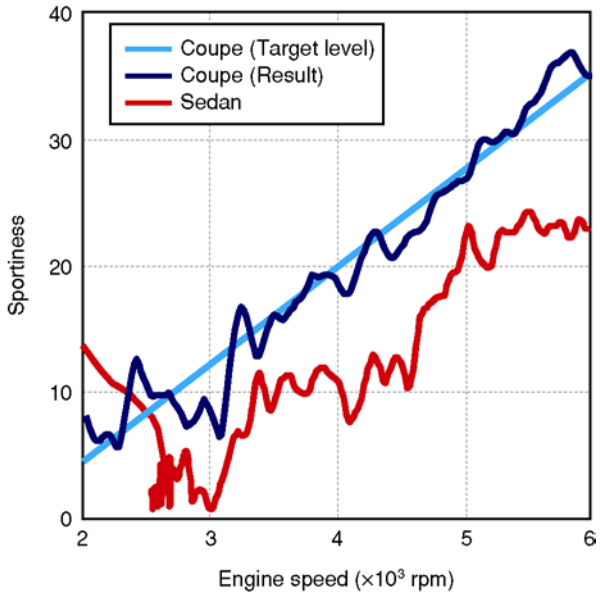


Fig. 12 Result of sportiness characteristics

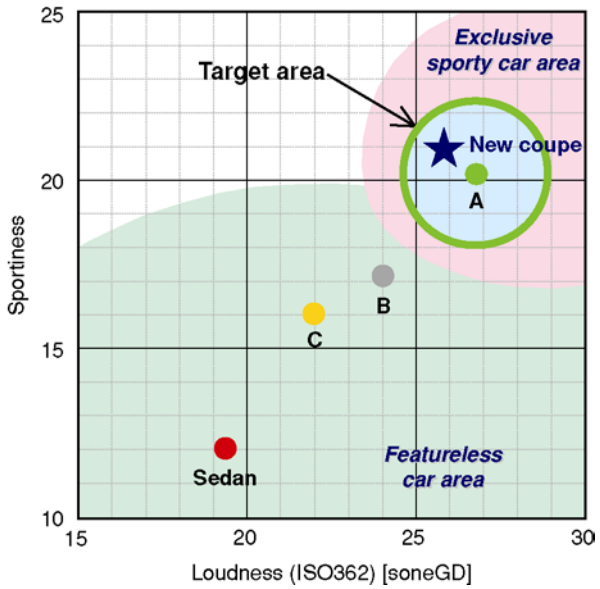


Fig. 13 Result of sportiness/loudness map

6. Conclusions

The development of interior sound for the new medium coupe yielded the following results:

(1) Using subjective analysis based on comparative vehicles along with the “sportiness” method of objective analysis, it was possible at the beginning of the development process to clarify the positioning of the sound and quantitatively express the target values for the new vehicle that were being aimed at in development.

(2) By using artificial sounds positioned in the target area on the sportiness/loudness map to create candidates for the target sound and then conducting subjective evaluations through listening tests, it was possible to narrow in on the desired target sound at the beginning of development.

(3) By considering the sound sources to be controlled and the air-borne transfer characteristics of the car body in relation to the target interior sound, it was possible to quantitatively determine the target values for the sound source and efficiently develop a design suited to those sound source characteristics.

By introducing an interior sound index as described above, it was possible to achieve the aim for the new car, an interior sound that was linear and sporty during acceleration, while simultaneously achieving a major reduction in development man-hours.

References

(1) Lindner, U.: Sounddesign-the BMW Inline Six-Cylinder Engine in Different Vehicle Applications, SAE Paper 2001-01-1428

(2) Ishii, Y., et al.: Development of a Software Tool for Objective Evaluation of Sport Car Interior Sound, Honda R&D Technical Review, Vol. 13, No. 1, pp. 131-138 (2001)

■ Authors ■

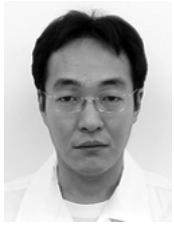

Masashi IWAI


Yasuo ISHII


Koji ITO


Tomoyuki NUMATA


Kazuya KUTSUZAWA


Hidenori SEIKE

Sensory Evaluation of Road Noise with Physiological Reaction using Electroencephalogram

Yasuo ISHII* Tsuyoshi YAMASHITA* Yutaka ARAGA**

ABSTRACT

A method for direct measurement of organic reactions (brain waves) was used to evaluate interior road noise. This was used in addition to the conventional, indirect method of descriptive sensory evaluation. The results showed that the annoyance factors in perception of sample sounds that included road noise could be divided into an active pleasant-unpleasant factor and a passive comfort-discomfort factor. The use of brain wave measurement for the passive comfort factor demonstrated the possibility of obtaining objective descriptions that are statistically significant.

1. Introduction

There has been much research presented on the perception of interior road noise based on descriptive sensory evaluation[(1), (2)]. The tone factors that are referenced in regards to road noise include power, muffling, and comfort-discomfort. While a large body of research and case studies concerning this sort of psychological evaluation of noises based on sensory evaluations exist, conventional sensory evaluations may suffer from limitations in how faithfully they can capture the subjective responses of human test subjects. These limitations stem from the fact that it is impossible to completely avoid any bias that may creep into the results via the subject's thought processes as those subjects record their responses to audio stimuli. This sort of perturbation can be avoided if it is possible to directly measure subjective evaluations. In response to recent demand for results that are very correlated to human responses, there has been tremendous interest in evaluation methods that focus on response to physiological signals[(3), (4)]. One such example is conducting a psychological evaluation of auditory stimuli by measuring heart rate and electric potential across the skin. These signals convey little information, however, and have been found to be of limited use when attempting to estimate complex mental activity, such as experiencing comfort-discomfort.

This research, intended to clearly define "comfortable" road noise, consists of brain wave testing conducted while exposing the test subjects to noises, which included actual vehicle noises. Objective analyses and evaluations of responses to road noise (such as comfort-discomfort) are then conducted by focusing on the analysis of brain wave responses that electrically reflect the activities of the central nervous system and brain; both of which govern complex mental activities. Other objectives are to precisely specify the comfort response and to create a formula for estimating the comfort-discomfort of road noise based on the correlation of comfort response with the physical characteristics of certain noises. If these objectives could be achieved, it would be possible to indicate specific targets for the development of comfortable road noise. This article describes this attempt and the results that are derived.

2. Brain Wave Measurement and Evaluation Methods

Feelings of comfort or discomfort that arise from exposure to road noise are the result of brain activity, and it is likely that the effects of such activity manifest themselves in the brain waves. The road noise is a binaural recording made from the passenger seat in a vehicle that is driving on a rough road surface, and is played for the subjects through headphones. However, because the magnets in the headphones introduce noise in the brain wave measurements, the playback signal is passed through a high-pass filter (40 Hz).

Brain waves are measured using an ESA-16 Emotion Spectrum Analysis System manufactured by Brain Functions Laboratory Inc. and the 12 electrodes are placed according to the international 10/20 placement system, using monopolar derivation with the reference electrode on the right ear.

The following three methods for evaluating brain waves are used in this research:

(1) Emotion spectrum analysis
(2) Alpha wave band power percentile analysis

* Tochigi R&D Center
** NF Corporation

(3) Beta wave band PCA (Principal Component Analysis)

Because these methods of brain wave analysis are not commonly known techniques, they are briefly described below[5], [6].

2.1. Overview of Emotion Spectrum Analysis

Although some research is conducted on the classification of emotions produced by brain activity, this research will only consider four elementary emotion factors: joy, anger, sadness, and relaxation. Figure 1 shows the scalp electric potential when each of these emotion factors is expressed.

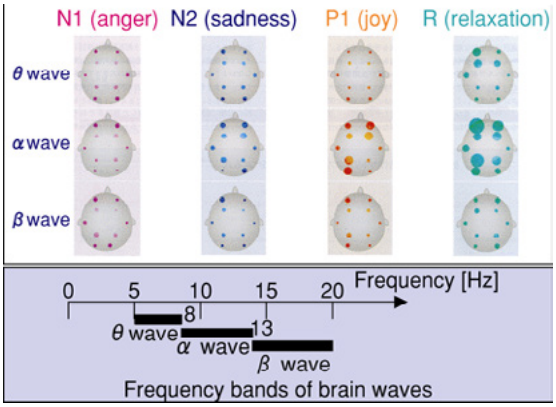


Fig. 1 Contribution of brain wave data for each emotion factor

In emotion spectrum analysis, after eliminating the effects of individual differences in scalp electric potential levels, the cross-correlation coefficients of the electric potential between each electrode position are used as a means of recording in a time series the phase relationship and positional relationship between each electrode potential, and then these coefficients are input to derive the four emotion factors. Figure 2 shows an overview of this process. Because the ten electrodes can be paired up in 45 different combinations (${}_{10}C_2$), and the brain wave measurement bands are the three bands of the theta wave, the alpha wave and the beta wave, the cross-correlation coefficients for the electric potential between electrodes that are input is a vector of which elements are 135 (45 factors multiplied by 3 bands). The four emotion factor vectors are then derived by multiplying these vectors by a 4 × 135 coefficient matrix called the “emotion matrix”. Emotion spectrum analysis is a method of expressing these changes over time numerically. This emotion matrix is calculated beforehand by other statistical means.

$$Z_1 = C_{1,1}Y_1 + C_{1,2}Y_2 + \cdots + C_{1,135}Y_{135} + D_1$$
$$Z_2 = C_{2,1}Y_1 + C_{2,2}Y_2 + \cdots + C_{2,135}Y_{135} + D_2$$
$$Z_3 = C_{3,1}Y_1 + C_{3,2}Y_2 + \cdots + C_{3,135}Y_{135} + D_3$$
$$Z_4 = C_{4,1}Y_1 + C_{4,2}Y_2 + \cdots + C_{4,135}Y_{135} + D_4$$
$$Z = C * Y + D$$

Y_1~Y_{135}: cross-correlation coefficients between potentials of two electrodes

Z_1: anger Z_2: sadness Z_3: joy Z_4: relaxation
parameters indicating emotional levels (Z: emotion vector)

$C_{1,1}$~$C_{4,135}$: coefficients (C: emotion matrix)

D_1 ~ D_4: constants (D: constant matrix)

Fig. 2 Calculation method to derive emotion factors from brain wave data

The joy, anger, sadness and relaxation emotion factors that are derived express the respective emotions that their names indicate. Other emotions are also expressed.

(1) N1 (anger/stress): Although this value is naturally high when the test subject is angry, it is also high when the test subject is under stress or excited.
(2) N2 (sadness/down): Indicates that the subject is sad or feeling down.
(3) P1 (joy/accomplishment): Indicates that the subject feels happy or is otherwise feeling positive, after achieving some goal, for example.
(4) R (relaxation): Indicates that the subject is comfortable and relaxed.

2.2. Overview of Alpha Wave Band Power Percentile Analysis

The power percentile of the alpha wave band among the brain waves indicates the degree of nonalertness. When this value is high, it usually indicates a decrease in brain activity or awakening.

Alpha wave band power percentile = $W\alpha/(W\theta + W\alpha + W\beta)$
$W\alpha$, $W\beta$, $W\theta$: Power of each respective band

2.3. Overview of Beta Wave PCA (Principal Component Analysis)

This method applies principal component analysis to the beta wave band of four points on the forehead, where higher mental activity occurs, and calculates the contribution rate of the first principal component. When this value is high, it can be assumed that the brain cells in the vicinity of the frontal lobe are working in concert with each other; therefore, this contribution rate indicates the concentration or diffusion of mental activity.

3. Preliminary Experiments

The first thing to be confirmed is whether or not changes in brain waves can be elicited through audio stimuli. To determine this, the brain waves of subjects are measured while they listened to sample noises through headphones. Because it is also necessary to study the emotions of each subject, a sensory evaluation using the Semantic Differential method with the same sample noises is also conducted.

3.1. Brain Wave Test

For the sample noises, three recordings (a, b, and c) of road noise are made while driving on a rough road surface. These recordings are used to create five minutes of continuous noise and thirty seconds of intermittent noise. The four test subjects (S1, S2, S3, S4) are all males.

Figure 3 shows the results of the brain wave measurements for subject S2 when listening to the continuous noise. These results show the changes in the values of each emotion factor, the alpha wave band power percentile, and PCA while the noises are played and the subject opened and closed his eyes. The relaxation value is clearly increased before the start of the test, during the breaks, and after the test, showing that the subject felt at ease when testing is not actively in progress.

However, from these results it is difficult to directly discern any differences in the indicated values in response to

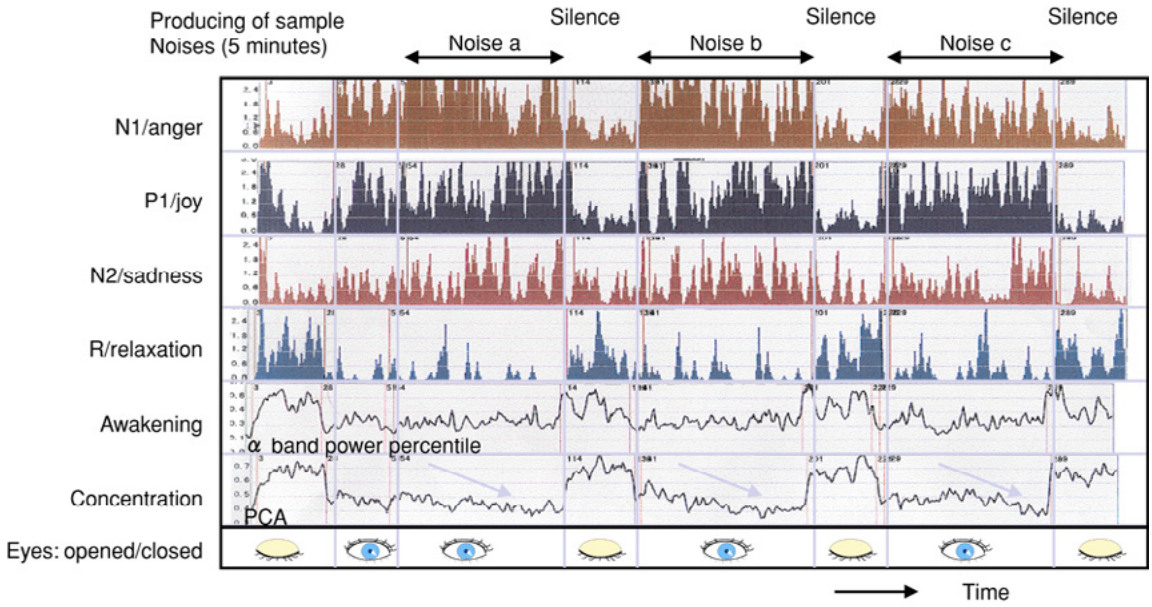


Fig. 3 Variations of emotion spectra for continuing noises

Table 1 Average emotion spectra during one term for each subject

Color of number shows consistency of order between states of eyes opened or closed;

Agree perfectly, Agree partly, Disagree

	Ranking of average emotion spectra							Ranking of average emotion spectra					
Sub.S1	Eyes opened			Eyes closed			Sub.S3	Eyes opened			Eyes closed		
	a	b	c	a	b	c		a	b	c	a	b	c
N1/anger	2	1	3	1	2	3	N1/anger	2	3	1	1	3	2
P1/joy	1	3	2	1	3	2	P1/joy	3	1	2	3	1	2
N2/sad	1	2	3	2	3	1	N2/sad	3	1	2	3	2	1
R/relax	3	2	1	2	1	3	R/relax	1	3	2	1	3	2
Sub.S2	Eyes opened			Eyes closed			Sub.S4	Eyes opened			Eyes closed		
	a	b	c	a	b	c		a	b	c	a	b	c
N1/anger	3	2	1	3	1	2	N1/anger	3	1	2	1	3	2
P1/joy	1	2	3	1	3	2	P1/joy	2	1	3	2	1	3
N2/sad	2	1	3	3	1	2	N2/sad	2	3	1	2	3	1
R/relax	2	1	3	1	3	2	R/relax	1	2	3	3	1	2

the different samples. Table 1 shows the average values produced while each sample is played, and the comparative ranking of each.

In this table, those cases where the ranking of each sample noise is the same whether the subject's eyes are open or closed are shown in red. Looking at these results, it is easy to see the differences in ranking when the eyes are open versus when the eyes are closed for the same individual subject. Looking at the results for joy, the rankings of the three noises when the eyes are open matched the rankings when the eyes are closed in the case of three of the four subjects (S1, S3, and S4). Even so, the rankings for each subject differed from those of the others, and the differences between subjects are considerable, making it difficult to find a common trend. It is possible that each individual's evaluation axis in regards to noise is different, and there is a need for a study that cross-references these results with the sensory evaluation results. Regarding the alpha wave band power percentiles (indicating the degree of nonawakening), Table 2 shows that noise c caused a decrease in alertness. Regarding PCA, the differences between the sample noises are small, making this method unsuitable for the evaluation of audio stimuli.

Table 2 Result of a band power percentile

Color of number shows consistency of order between states of eyes opened or closed;

Agree perfectly, Agree partly, Disagree

	Ranking of average value					
	Eyes opened			Eyes closed		
	a	b	c	a	b	c
Sub.S1	2	3	1	2	1	3
Sub.S2	1	3	2	3	2	1
Sub.S3	3	2	1	1	2	3
Sub.S4	3	2	1	1	2	3

3.2. Sensory Evaluation

A sensory evaluation is conducted with the same four test subjects, using a procedure similar to that used in the brain wave test. Each subject is asked to evaluate three sample noises. As shown in Table 3, a principal component analysis is performed using the Semantic Differential method with seven grades and 15 different adjectives for noise evaluation. Three principal components are extracted, based on the results; however, because principal components 1 and 2 had a cumulative contribution rate of 80%, principal components 1 and 2 are sufficient for describing the tone structure of the road noise for these four subjects. (Refer to Fig. 4.)

Principal component 1 consists of:

- Positive noise parameters in the positive direction
- Negative noise parameters in the negative direction

Those parameters with large factor loading are “fresh” and “smooth”, supposed “aesthetic clarity” indicating comfort-discomfort. (Refer to Fig. 5.)

Principal component 2 indicates a muffled feeling.

Figure 6 shows how each of the four subjects scored each sample noises according to the two principal components. The only area in which the four subjects scored the sample noises in the same order is in the relative positioning of intermittent noises a and b (a1 and b1), a and c (a2 and c2) and b and c (b3 and c3), expressed by principal

Table 3 Condition of sensory evaluation

Sample noise	Subject	Adjective		
1 Continuing noise a 2 Continuing noise b 3 Continuing noise c 4 Alternate noise a&b 5 Alternate noise a&c 6 Alternate noise b&c	1 S1 2 S2 3 S3 4 S4	1 fresh 2 high-pitched 3 unpleasant 4 annoying 5 alive	6 stagnant 7 rough 8 offensive 9 bright 10 loud	11 powerful 12 rich 13 dry 14 smooth 15 booming
Grade for estimation				
1 2 3 4 5 6 7 agree neutral disagree				

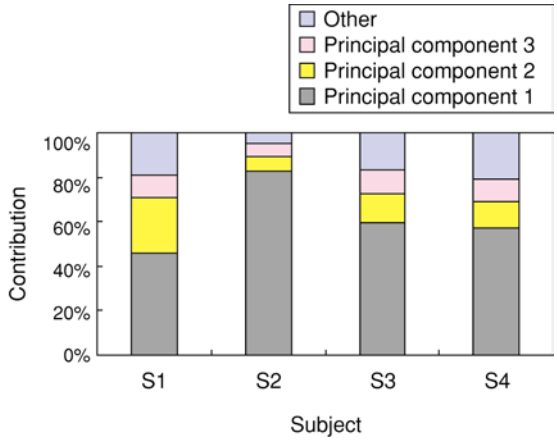


Fig. 4 Component contribution of each subject

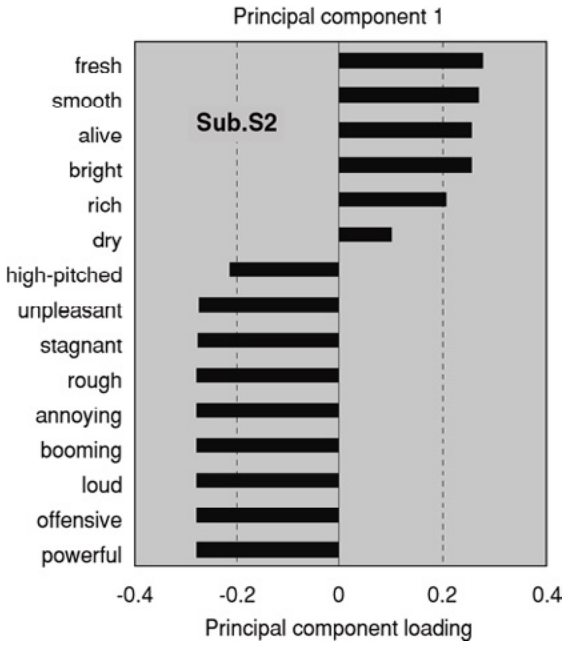


Fig. 5 Principal component loading for principal component 1 (subject S2)

Sample noise	notation	Sample noise	notation
Continuing noise a	a0	Alternative noise a&b	a1&b1
Continuing noise b	b0	Alternative noise a&c	a2&c2
Continuing noise c	c0	Alternative noise b&c	b3&c3

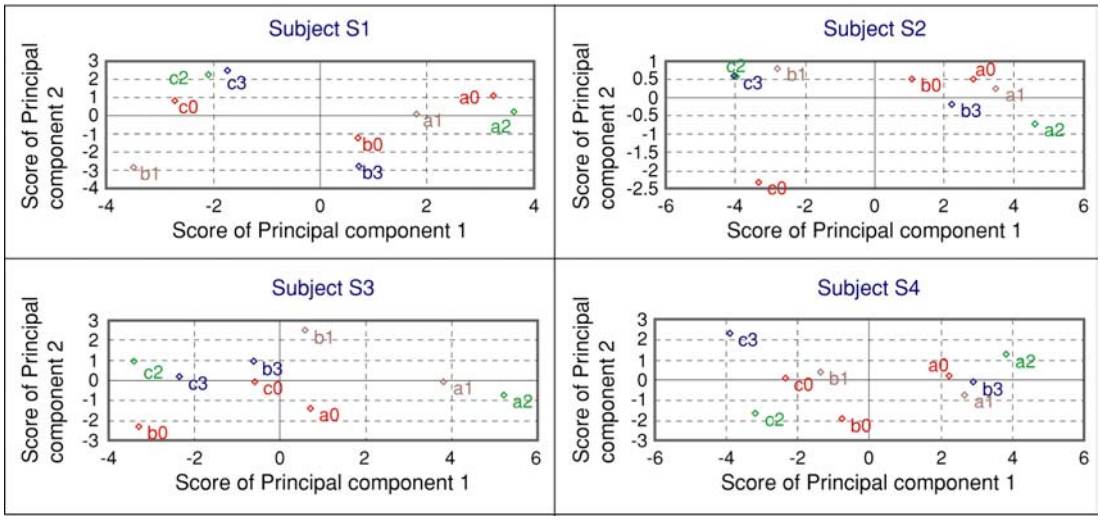


Fig. 6 Principal component score for each sample noise; horizontal: principal component 1, vertical: principal component 2

component 1 (aesthetic clarity). Accordingly, the results of principal component 1 testing using intermittent noise are deemed suitable for comparison with organic response tests.

3.3. Comparison of the Brain Wave Measurement Data with the Sensory Evaluation Results

Because the purpose of this research is to define comfortable road noise, the focus is placed on principal component 1, and a comparison is made between the brain wave measurement data and sensory evaluation results for subject S2, for whom principal component 1 accounted for 80% of his response. Figure 7 shows the results.

For subject S2, for whom principal component 1 determined 80% of his response, the sensory evaluation results and emotion spectrum measurement results for intermittent noise have correlation with the emotion vector that shows comfortableness ([P1 + R] – [N1 + N2]) which is composed by subtracting the emotion vectors that indicate discomfort (anger/N1 and sadness/N2) from the emotion vectors that indicate comfort (joy/P1 and relaxation R).

The importance of the results obtained from these preliminary experiments is that there are significant differences in brain wave measurements when subjects are exposed to road noise, and that the emotional state of subjects can be identified by measuring their brain waves in response to audio stimuli.

In addition, because there is a need for a detailed analysis of comfort and discomfort, four more adjectives are added for a separate sensory evaluation in order to emphasize and draw out comfort-related emotions: vigorous, sweet, gloomy, and composed. All adjectives are for emotional emphasis. Based on the results of the factor analysis shown in Fig. 8, it is possible to identify “active” “pleasant” with high factor loading for “bright” and “sweet”, and “passive comfort” with high factor loading for “composed” and “smooth”.

(1) Active pleasant (an active comfort, an excited, vigorous comfort)

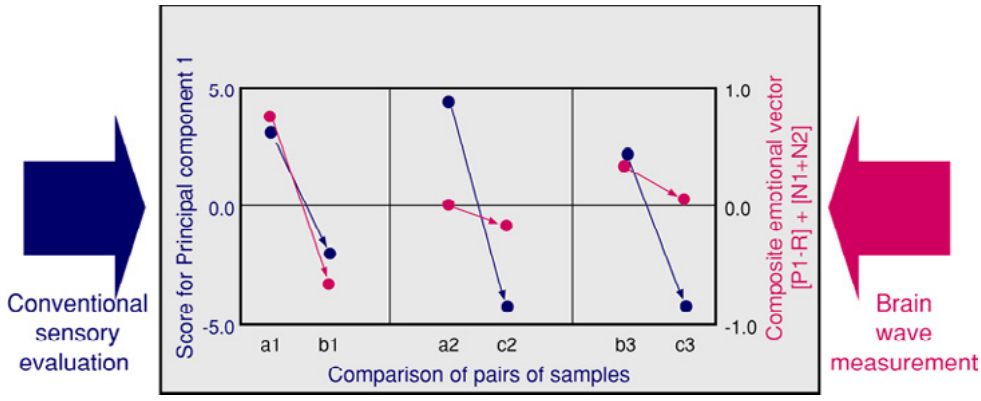


Fig. 7 Comparison between conventional results and results from brain wave measurement

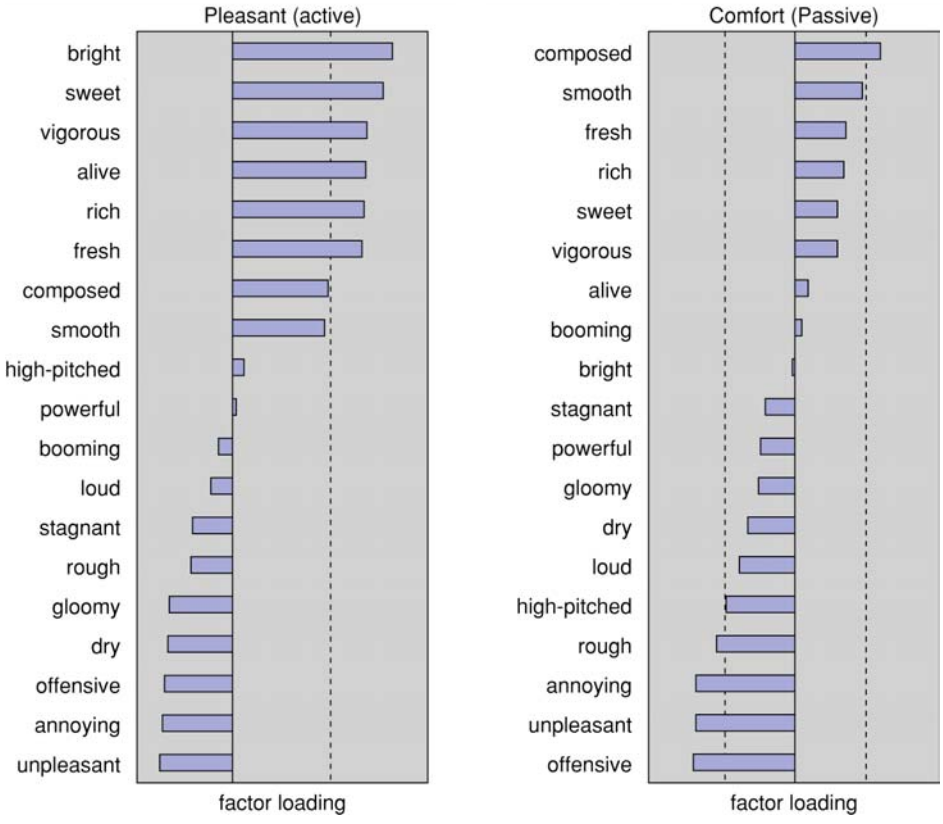


Fig. 8 Differences between active pleasant and passive comfort

(2) Passive comfort (a quiet comfort, a relaxed, pleasant comfort)

Because passive comfort is deemed to be important in addressing road noise, the analysis of the main tests focused on passive comfort.

4. Main Tests

4.1. Method

In order to understand passive comfort through brain wave measurements, the results of the preliminary tests formed the basis of the main tests. A total of 21 subjects (average age: 23.6) are tested. The brain wave measurement method that is used in the preliminary tests is used without modification in the main tests, and the analysis is conducted by calculating the emotion spectrum and the composite values. In addition, typically pleasant noises and uncomfortable noises that are not road noises are added to the sample noises.

The sample noises are all binaural recordings that are played back to the subjects through headphones. A breakdown of the sample noises follows:

(1) Road noise samples: Recordings made from the passenger seat in ten stock cars while driving on a rough road surface
(2) Reference noises for discomfort: Recordings made from the passenger seat while driving on an extremely rough road surface, the roar of a waterfall at Nikko Yutaki, the sound of scratching on frosted glass
(3) Reference noises for comfort: A gentle breeze in the woods in Kirifuri Kogen, a small stream, the sound of a waterfall with the sound pressure reduced and with AM modulation applied to produce a more calming effect
(4) Reference noise for each stage: Pink noise

A total of 18 noises are used. (Refer to Table 4.)

Sample noises are played back in the following manner: ten seconds of pink noise (for stabilization), 45 seconds of the sample noise, ten seconds of silence. In order to eliminate any possible effect caused by the sequence of the sample noises, the noises are played in a random order.

Table 4 Sample noises

No.	group	content	
1	Road noise	A	Medium
2		B	Medium
3		C	Compact
4		D	Compact
5		E	Medium
6		F	Entry
7		G	Compact
8		H	Entry
9		I	Executive
10		J	Executive
11	Criteria noise	K	Rough road
12		Waterfall	
13		Waterfall AM	
14		A gentle breeze in wood	
15		Stream	
16		Scratch of a nail on frosted glass	
17		Pink noise	

The following the four emotion spectrum composite values:

(1) N1 + P1: Combines an increase in mental alertness and an increase in good feeling, and is interpreted as a pleasant feeling
(2) N2 + R: Combines a decrease in mental activity and a decrease in good feeling, and is interpreted as a gloomy feeling
(3) N1 + N2: Combines an increase in mental activity and a decrease in good feeling, and is interpreted as an irritated feeling
(4) P1 + R: Combines a decrease in mental activity and an increase in good feeling, and is interpreted as a comfortable feeling

After the measurement of brain waves is completed, a sensory evaluation is conducted using the same sample noises. Passive comfort is then evaluated by the Semantic Differential method using a seven grade scale for each of 16 tone factors.

As shown in the analysis flow in Fig. 9, the validity of each of the brain wave measurement results and sensory evaluations is verified and then each pair is compared.

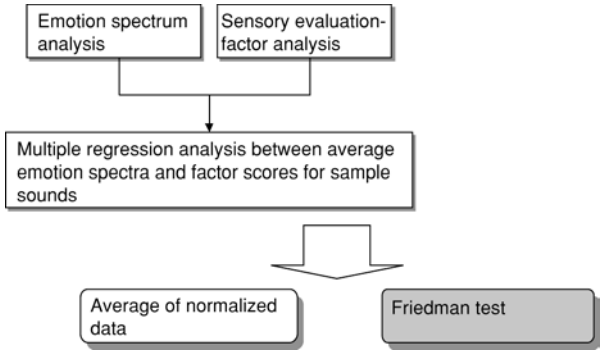


Fig. 9 Analysis flow

4.2. Results of Emotion Spectrum Analysis

Table 5 shows the results of statistical verification of the emotion spectrum and the composite values calculated from the brain wave measurements taken during the playback of the sample noises for all of the subjects. Verification is accomplished by using the Friedman test to determine the significance of the ranking of the 21 subjects for the 18 sample noises; those items with 1% significance are marked by ** in the table. Aside from a few cases, such as N1 Anger, the table shows that the emotion vectors demonstrate significant response to the sample noises. Figure 10 shows the results for R Relax for each sample noise.

Table 5 Significant difference of emotion spectra for sample noises **expresses 99% reliable

Emotion spectrum	Significant difference
N1 Anger	—
P1 Joy	**
N2 Sadness	**
R Relaxation	**
α band power percentile	**
PCA Concentration	**
N1+P1	—
N2+R	—
N1+N2	**
P1+R	**

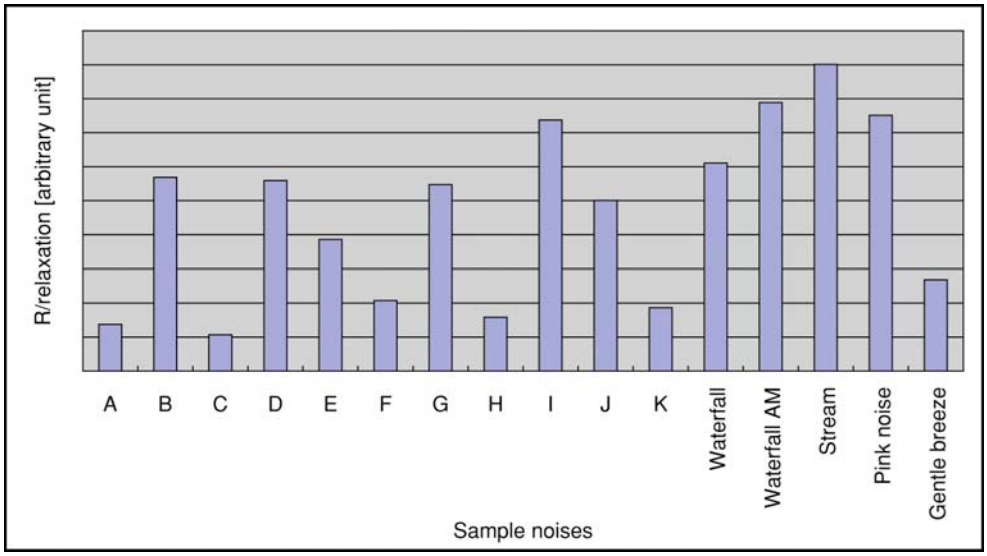


Fig. 10 Emotion spectra of sample noises

4.3. Results of Factor Analysis

After the brain wave measurements, the same sample noises are used in a sensory evaluation using the Semantic Differential method with a seven grade scale for 16 adjectives. Table 6 shows the factor analysis of the results. As shown in the table, three factors are derived: comfort-discomfort, roughness-smoothness, and silence-noise.

Of these, comfort-discomfort expressed passive comfort (feeling comfortable and at ease) and active discomfort (irritated and uncomfortable), a pairing that demonstrated its usefulness for the evaluation of road noise in the preliminary tests. In addition, in this factor analysis the comfort-discomfort factor (passive comfort factor) has a high contribution rate of 42.6%, so that the passive comfort component in this sensory evaluation should have high reliability and be expressed vividly. Figure 11 shows the passive comfort factor scores for each sample noise.

Table 6 Results of factor analysis

No.	Name	Factor contribution rate (%)	Factor cumulative contribution rate (%)
1	Comfort	42.6	42.6
2	Roughness	13.4	56.0
3	Silence	10.9	66.9

4.4. Comparison of the Emotion Spectra and the Passive Comfort Factor

The emotion spectra that are derived from the brain wave measurements demonstrated significant response to the sample noises. In addition, the first factor for the same sample noises is the passive comfort factor. In regards to how to express comfort-discomfort in response to the road noise through the brain wave measurement results, the passive comfort factor score for each sample noise is set up as the criterion variable, and a multiple regression analysis is performed for each subject with the emotion spectra N1, P1, N2, and R for that sample noise as the explanation variables. However, the coefficients of the emotion spectra in the multiple regression equation differ considerably for each subject; the correlation coefficient for all of the subjects is only 0.2, making it difficult to specify consistent coefficients. The decision is made to reflect the results of the brain wave

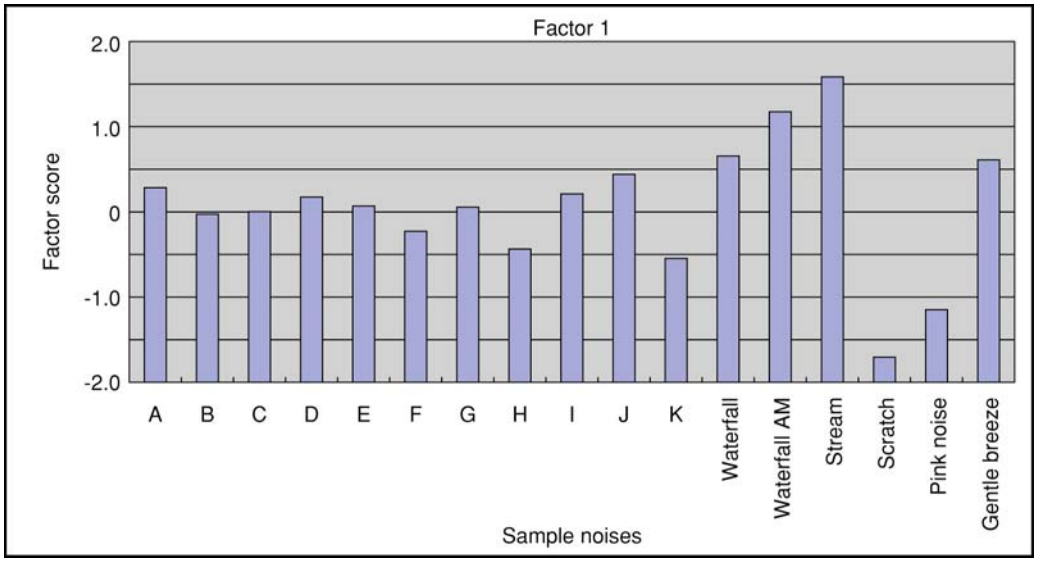


Fig. 11 Factor score of sample noises

measurements by averaging the individual multiple regression scores for all of the subjects. That the average passive comfort score for all subjects, calculated by a multiple regression equation based on this emotion spectrum primary linkage, is significant for the playback of each sample noise is made clear by the Friedman test. (Refer to Table 7.) In other words, it is confirmed that it is possible to use the measured results of brain waves, a physiological response, to express passive comfort in response to noise, including road noise. However, because all of the emotion spectra for joy, anger, sadness and relaxation are used, the interpretation of the regression equation itself is difficult due to individual differences.

Table 7 Significant difference of multi-regression correlation scores **expresses 99% reliable

Factor	Significant difference
Comfort (Factor 1)	**
Roughness (Factor 2)	**
Silence (Factor 3)	**

5. Comparison with Objective Measurements

The multiple regression scores (refer to section 4.4) that reflect the organic response (the results of the brain wave measurements) to each sample noise are expressed through a first order polynomial of physical values and of objective values for psychoacoustic parameters. When deriving the regression equation, the following conditions are maintained:

1. No sign inversions or multi-colinearity.
2. Multiple correlation coefficients of at least 0.9.
3. In analysis of variance of regression fluctuations, a P value of 0.05 or less is significant.
4. In determining the significant difference for partial regression coefficients, significant difference probabilities of 0.05 or less are ignored.

The regression equation that is derived is as follows:

Passive comfort-discomfort = – A * Loudness + B * Kurtosis + C * Tonality + D

A, B, C: Partial regression coefficients D: Constant

Multiple correlation coefficients: 0.901

The passive comfort regression equation and the factor scores have a high correlation. (Refer to Fig. 12.) Furthermore, according to the regression equation, the sample noises that are used in these tests are comfortable sounds that have low volume, have small changes in amplitude, and only a few frequency components that stand out.

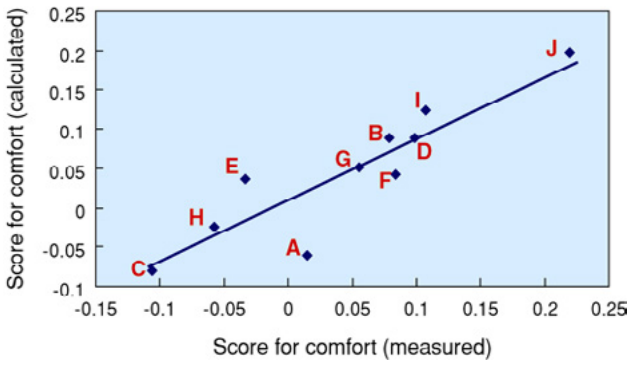


Fig. 12 Comparison of measured and calculated comfort scores

6. Conclusions

The following are the results of this research on objective evaluation of noise through the measurement of organic response (brain waves):

(1) It was possible to obtain significant results by measuring brain waves in response to the playback of sample noises, including road noise.

(2) It was discovered that passive comfort, which expresses the comfort-discomfort of road noise by conventional means, can be expressed by emotion vectors determined through brain wave measurement.

(3) It was possible to derive a regression equation that objectively expressed the multiple regression score that was calculated from the passive comfort of individual subjects using emotion vectors.

An issue that requires further research:

(4) It is difficult to say definitively that the passive comfort regression equation based on emotion vectors will apply to everyone, due to large individual differences.

The authors wish to acknowledge the assistance of Brain Functions Laboratory Inc. in the measurement and analysis of brain waves.

References

(1) Yamashita, T., Ishii, Y., Nakamura, M., Kitamura, O.: A Study on Evaluation of Cabin Noise Feeling, The Society of Rubber Industry, Japan No. 63 pp. 122-130 (1990)

(2) Murata, H., Osasa, Y.: Sound Evaluation of Cabin Noise During Regular Cruising, Society of Automotive Engineers of Japan, Inc. Preprint 942 No. 95, pp. 145-148 (1994)

(3) Mizuno, Y., Sugisaki, M.: A Study of Evaluation Method for Driving Fatigue Using Electrocardiogram RR Interval, Society of Automotive Engineers of Japan, Inc. Preprint No. 951, pp. 165-168 (1995)

(4) Hirosawa, Y., Kitagawa, A., Maruyama, G., Nakahara, T.: Influences of Exposure to Idling Noise on Organic Information, Society of Automotive Engineers of Japan, Inc. Preprint No. 983, pp. 197-200 (1998)

(5) Musha, T.: Measuring Emotions, Nikkei Science April, vol.26 No. 4, pp. 26-29 (1996)

(6) Musha, T., Terasaki, Y., Haque, H., Ivanitsky, G.: Feature extraction from EEGs associated with emotions, Artif Life Robotics, vol. 1, pp. 15-19 (1997)

■ Authors ■


Yasuo ISHII


Tsuyoshi YAMASHITA


Yutaka ARAGA

Development of Pass-by Noise Analysis Technology with Utilization of Engine Control Data

Jun KITAHARA* Jason RAY** Mark PAFUMI**

ABSTRACT

The purpose of this paper is to introduce the new pass-by noise analysis technology with utilization of engine control data. This newly constructed measurement system obtains comprehensive engine control data while measuring vehicle pass-by noise levels with real-time data analysis capability. The measurement system combines two different data acquisition systems into one. The first system converts digital values obtained from an engine control unit into an analog signal output, while the second system obtains multiple channel analog signals. By performing pass-by noise testing with this system, the relationship between environment induced fluctuating engine control parameters, such as charging efficiency and ignition timing, and the effect on noise levels is determined. Furthermore, by normalizing obtained data to standard environmental conditions, vehicle noise levels and the amount of change in noise levels resulting from specification changes are accurately evaluated.

1. Introduction

Pass-by noise regulations place legal limits on the exterior noises, which may be emitted by an automobile. These are composed of the ‘Regulation on exhaust proximity noise’, which limit noise when the automobile is stationary, the ‘Regulation on constant-speed pass-by noise’, applying when the automobile is moving at a steady speed, the ‘Regulation on acceleration pass-by noise’, applying when the automobile is accelerating, and others. The testing methods for all these standards are specified. Of these, quite strict conditions are posed on permissible noise during acceleration, when the automobile is emitting a large amount of acoustic energy.

An example is given in Fig. 1, which shows the testing method specified in Japan for determining acceleration noise. The test vehicle enters the noise measurement area at a steady speed of 50 kph, accelerates at full throttle from Begin Acceleration Line A–A’ to the End Acceleration Line B–B’, and coasts thereafter. The sound pressure level during acceleration is measured by a microphone placed 7.5 m from the centerline of the car’s path. The car is assessed by the maximum level recorded.

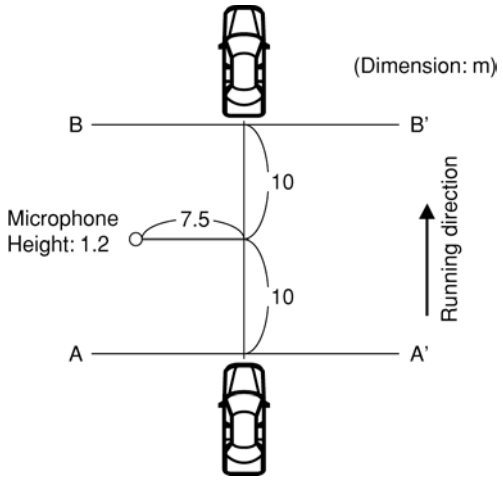


Fig. 1 Japan pass-by noise regulation method

* Tochigi R&D Center
** Honda R&D Americas, Inc.

Since the pass-by noise testing must be conducted outside throughout the year, it is greatly influenced by varying environmental conditions. Sound pressure levels recorded from the same vehicle will fluctuate with different environmental conditions. For example, changes in acceleration will result from an increase or decrease in intake charging efficiency, which has direct impact to ignition timing as commanded by the ECU (Electronic Control Unit). Therefore, in order to correctly assess the sound pressure level emitted by the test vehicle, it is essential to specify the parameters affecting these fluctuations and to obtain a quantitative assessment of their influences on the sound pressure level.

In the present study, a new pass-by measurement system was constructed to simultaneously measure and analyze all fluctuating parameters: sound pressure level, environmental conditions and ECU data This system was successful in identifying relations between these variables, and is presented below.

2. New System for Measuring Pass-by Noise

The ECU continuously performs fine optimization of the engine in response to the vehicle driving conditions. Therefore, monitoring of the engine control data is critical for accurate assessment of pass-by sound pressure level. Fundamental engine performance data is obtained from the ECU using the ECU Monitor Card System (EMCS). This information is processed using a D/A convertor and streamed to a second computer, which combines all measured noise, weather and ECU information; MBBM PAK system. The overall configuration of the system is shown in Fig. 2. The signals output by the ECU including ignition timing and intake air temperature are digitized into hexadecimal format. It was necessary to convert the signals from the ECU to analog in order to synchronize them with the sound pressure level measurements, so a digital/analog convertor was incorporated into the EMCS.

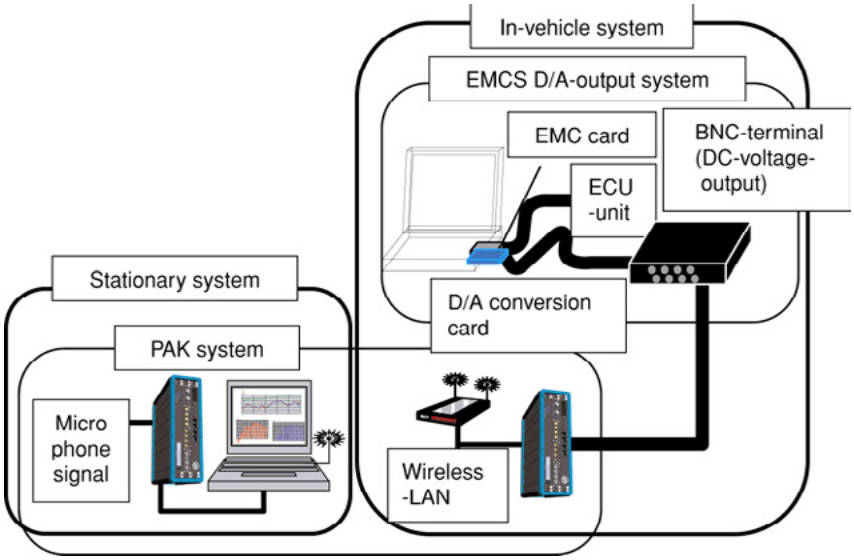


Fig. 2 System configuration

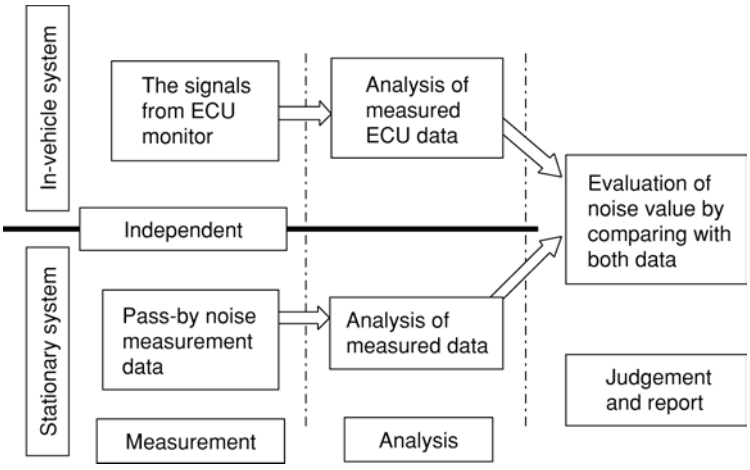


Fig. 3 Old system for analysis: Flow chart of ECU data and pass-by noise data

The conventional system was as shown in Fig. 3; the onboard engine control data monitoring system and stationary noise monitoring system were completely independent, making it very difficult to synchronize the information for analysis. The new system, shown in Fig. 2, contains the onboard and stationary modules in the 'front end'; the onboard system transmits the data to the noise measurement system over a radio telemetry link. Thus, the engine control data in the vehicle are input directly into the stationary system, allowing analysis of those data with sound pressure level data in real time (see Fig. 4).

The new system is therefore able to make comprehensive observations of the engine control data and sound data for comprehensive, real-time processing and analysis.

The PAK system provides for processing of observation results for user-specified visual output of data. The format for displayed data can be set in advance, which allows increased efficiency in data analysis and processing.

3. Analytical Results

The sources of pass-by acceleration noise are the engine and power train, air intake, exhaust, exhaust radiation noise, tires, and others. These all combine to generate the pass-by acceleration sound pressure level. Engine noise accounts for most of this, as shown in the chart of noise contributors in Fig. 5. Accordingly, the authors investigated the relationship of pass-by sound pressure level with charging efficiency and ignition timing, the chief engine parameters strongly influenced by the environment and therefore key parameters in noise.

3.1. Influence of Charging Efficiency

Since the charging efficiency fluctuates with temperature, humidity and atmospheric pressure, and causes fluctuations in engine output, acceleration characteristics change and have significant impact to overall SPL in the noise measurement area. To correct for this phenomenon, an 'engine power correction coefficient' is provided in the Japan Industrial Standards to estimate engine output in varying atmospheric conditions. The following equation shows how to calculate the correction coefficient (K):

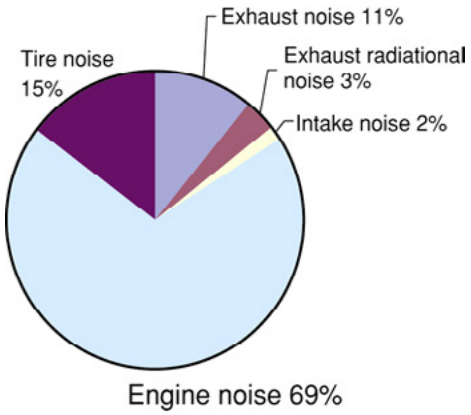


Fig. 5 Example of contribution analysis for pass-by noise

$$K = \left(\frac{Po}{P}\right)^{1.2}\left(\frac{\theta + 273}{\theta o + 273}\right)^{0.6}$$

Po :Standard dry atmospheric pressure (= 99 kPa)
θ o :Standard atmospheric temperature (=25 °C)
P :Observed dry atmospheric pressure (kPa)
P = Pa – Pw
Pa :Observed atmospheric pressure (kPa)
Pw :Observed partial pressure of water vapor (kPa)
θ :Observed intake air temperature (°C)

To confirm the accuracy of the engine power correction coefficient, it was compared to acceleration performance within the measurement area. Results can be seen in Fig. 6 with the corresponding acceleration values graphed as percentages of the acceleration corresponding to an engine power correction coefficient of 1. Clearly, the relation was linear. In other words, the acceleration can be standardized using the engine power correction coefficient, and a course

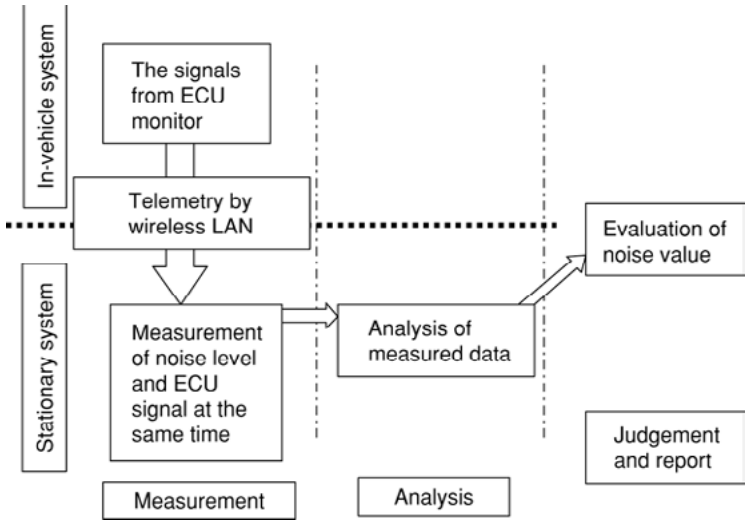


Fig. 4 New system for analysis: Flow chart of ECU data and pass-by noise data

exit speed can be calculated by adding the averaged acceleration rate to the initial course entry speed When the ignition timing and other conditions are identical, the sound pressure level has an approximately linear regression relationship with the final speed, as shown in Fig. 7. Using the engine power correction coefficient, a standardized final speed can be calculated which allows calculation of a standardized pass-by sound pressure level based on the charging efficiency.

3.2. Influence of Fluctuations in Ignition Timing

The value set for engine ignition timing is modified according to intake air temperature, coolant temperature and the detection of knocking. The inlet air temperature varies in proportion with exterior air temperature (Fig. 8), so ignition is retarded in order to prevent abnormal combustion, or "knocking", when the inlet air temperature is high (Fig. 9). Also, in the case where a vehicle sits at idle between test runs, the under hood temperatures may be raised and cause ignition retard during noise measurement, because the air intake is often located inside the engine compartment. Thus, the ignition timing may fluctuate during pass-by noise measurements even when the atmospheric conditions are uniform. Figure 10 presents fluctuations in engine RPM and ignition timing during actual pass-by noise measurements. The engine noise fluctuates with ignition timing even at constant RPM (Fig. 11), which affects pass-by noise. As a

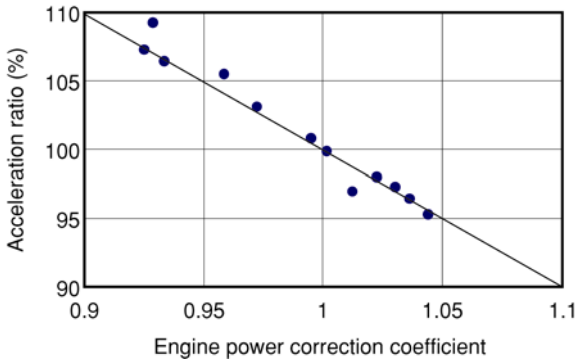


Fig. 6 Relationship between correction coefficient of engine power and acceleration ratio

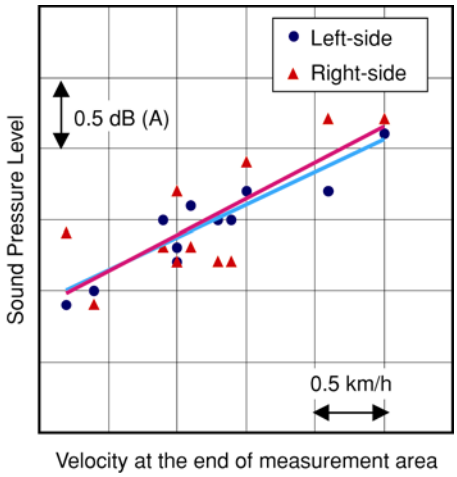


Fig. 7 Relationship between velocity at the end of measurement area and sound pressure level

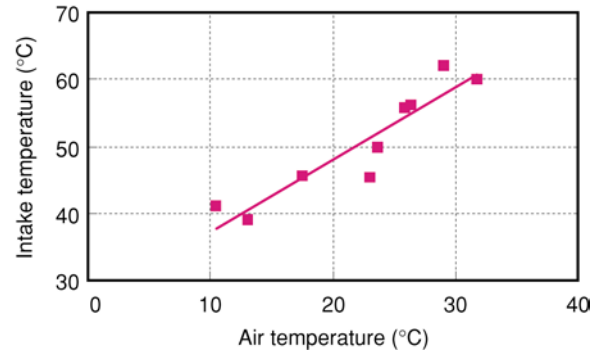


Fig. 8 Relationship between air temperature and intake temperature

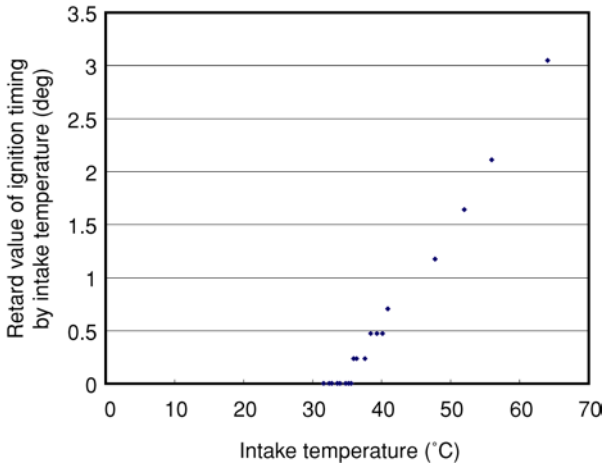


Fig. 9 Relationship between intake temperature and retard value of ignition timing by intake temperature

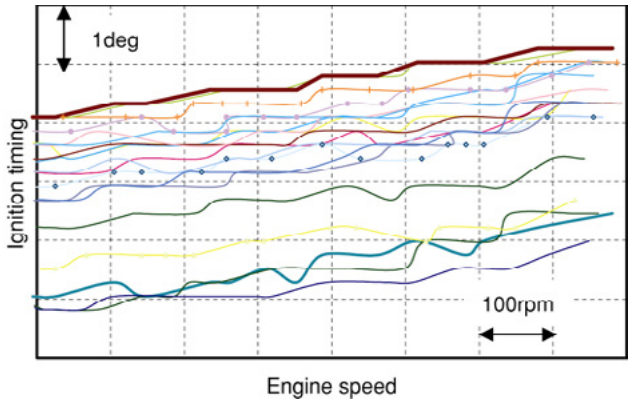


Fig. 10 Change of ignition timing while measuring pass-by noise

result, the sound pressure level may vary even when the final speed, i.e. the engine RPM, is the same, weakening the correlation of sound pressure level with speed, as shown in Fig. 12. This relation cannot be assessed with these data alone.

However, if data at nearly constant ignition timing are selected, the trend of noise with respect to final speed and the changes in sound pressure level with respect to ignition timing can be specified (Fig. 13). On closer examination of changes in sound pressure level due to variations in specifications, it was possible to make precise comparisons of sound pressure level at constant ignition timing under varying environmental conditions.

Furthermore, ignition timing retard will increase with temperature rise, so that the control value is increasingly delayed from the regular timing; as a result, the sound pressure level decreases. This relationship is shown in Fig. 14. Finally, by monitoring the difference between the ignition timing and the control value and comparing the change in sound pressure level corresponding to the ignition timing, it is possible to make more precise predictions of the sound pressure level from the commanded ignition timing.

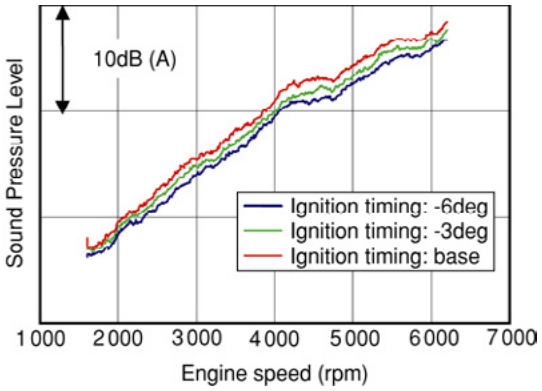


Fig. 11 Influence of ignition timing on engine noise

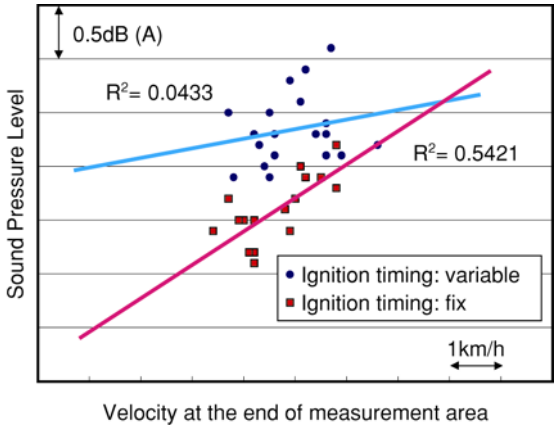


Fig. 12 Influence of ignition timing change on pass-by noise

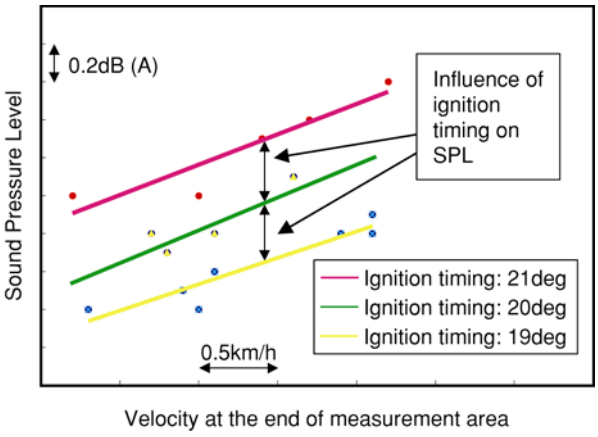


Fig. 13 Sound pressure level due to the difference of ignition timing

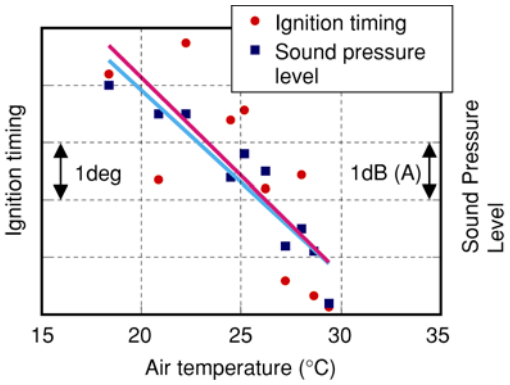


Fig. 14 Relationship of ignition timing and sound pressure level with air temperature

4. Summary

Technology was developed for real-time measurement and analysis of sound pressure levels and engine control data, which are key parameters in assessing pass-by noise from automobiles. Charging efficiency and ignition timing are key engine control parameters, which fluctuate greatly with environmental conditions and influence the overall engine noise. The following results were obtained while investigating the influence of fluctuating atmospheric conditions on sound pressure levels:

(1) Charging efficiency, influences engine output, and sound pressure level during acceleration through the noise measurement area. It was possible to estimate a standard sound pressure level as a function of charging efficiency, by correlating exit speed and sound pressure level, in combination with the standardized engine power correction coefficient, which is determined by the atmospheric conditions during acceleration.

(2) A quantitative relation between ignition timing and sound pressure levels was determined, allowing estimation of the change in sound pressure level from ignition timing.

A method for standardizing sound pressure level was established on the basis of the relationship between the

measured sound pressure level and parameters causing fluctuations. The method enabled precise measurements of sound pressure levels and changes in levels with changes in specifications.

This technology was developed as a joint effort of the Tochigi R&D Center and the Ohio R&D Center. Authors believe that the fruit of this combination of approaches and know-how on systems and noise measurements from the two large institutions for research on automobiles holds great promise for future development of automobiles.

References

(1) Kanemaru, K., Uno, M.: Development of Computer System for Vehicle Exterior Noise Analysis, Journal of Society of Automotive Engineers of Japan, Vol. 44, No. 10, pp. 38-42 (1990)

(2) Road vehicles-Engine power test code, JIS D 1001

(3) Nagashima, K., Maeda, Y., Kimura, Y., Takaoka, N., Tadaka, K., Hatakeyama, K.: Development of Engine Performance Data Acquisition System, HONDA R&D Technical Review, Vol. 12, No. 2, pp. 55-60 (2000)

■ Authors ■


Jun KITAHARA


Jason RAY


Mark PAFUMI

Development of the Exhaust System Radiation Noise Simulation Technology Using Exhaust Pulsation

Hiroshi NAKAGAWA* Hideyuki YOSHIMOTO* Masaki ENDO**
Yuji SHIRAHIGE* Masamichi FUJISHIRO* Masato SAKURAI*

ABSTRACT

The purpose of this paper is to propose a simulation method using Finite Element Model in order to predict exhaust radiation noise. This newly developed method predicts the radiation noise in a sound field located away from the vibrating surface of structure by coupling calculation between fluid exhaust gas and exhaust parts. By applying measurement values to boundary conditions, accurate radiation noise from the exhaust system is obtained, and the noise causing parts and the mechanism are clarified. This method allows for the investigation of exhaust radiation noise at an early stage in development. Also, the accuracy of measurement values using boundary conditions is improved by introducing semiconductor pressure sensors with 1-MHz sampling and a laser Doppler velocimeter. Furthermore, the measurement results showed the existence of a shock wave during an exhaust pulsation.

1. Introduction

As public consciousness continues to be aroused to environmental issues, there have been increasing demands for quieter automobiles.

Exhaust radiation noise is part of the noise from automobiles. Its main cause is the pulsation of the exhaust gas, which excites vibration of the surfaces of the exhaust piping and muffler. This vibration is finally transmitted as radiation noise.

Meanwhile, another key goal in automobile development is weight reduction, in order to reduce CO_2, but weight reductions tend to exacerbate radiation noise.

It is essential to further develop technologies for simulation and prediction, key components of Computer Aided Engineering (CAE). In the pursuit to balance reduced radiated noise and weight reduction, CAE has been instrumental in improving noise and vibration (NV) reduction in the exhaust system.

Below, the authors describe a method we developed for predicting radiation noise with good precision. It is based on determining the appropriate inputs by measurements taken of the exhaust-pulse. These inputs were then applied to the numerical model to find surface vibrations of the exhaust piping and muffler, yielding radiation noise.

2. Outline of Experimental Technology

2.1. Measurements of Exhaust-pulse

The exhaust-pulse emitted by the engine was the input applied to the numerical model. Since it is presently difficult to directly calculate the exhaust-pulse with any precision, it was measured directly and applied to the numerical model as a boundary condition.

The following were the measured items and procedures:

(1) Flow velocity measurements inside the exhaust piping:

* Tochigi R&D Center
** Tokyo Denki University

laser doppler velocimeter (LDV)
(2) Pressure measurements inside the exhaust pipe: semiconductor pressure sensors, manometer
(3) Temperature measurements inside the exhaust piping: thermocouple

These measurements were also taken in an anechoic room in order to verify the correlation between them and the radiation noise, as described later. Also, an isolated exhaust system was constructed, as shown in Fig. 1, in order to observe exhaust-pulse due only to the exhaust system. A flexible joint was inserted between the engine outlet and the pipe to eliminate vibration input from the engine.

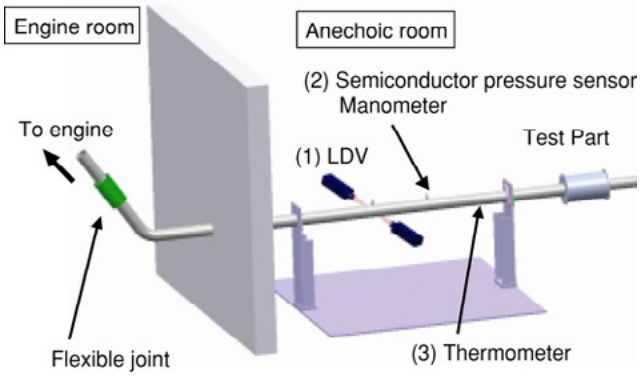


Fig. 1 Exhaust pulsation measurement conditions

2.2. Exhaust-pulse in Pressure Measurements

In order to increase the resolution of the exhaust-pulse waveforms, semiconductor sensors with a highly responsive sampling rates of 1 MHz were used. The results are shown in Fig. 2. Discontinuities are seen in the results; these show the presence of shock waves.

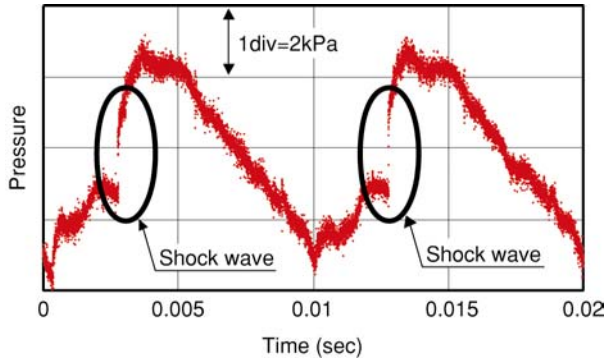


Fig. 2 Pressure of the exhaust pulsation

It was necessary to model the behavior of these shockwaves in order to take precise measurements of the exhaust system phenomena.

2.3. Observations with Shock Wave Generator

For this research, it was only necessary to create a shock wave of a certain level. The shock tube generator shown in Fig. 3 was used to simulate one exhaust process from a single-cylinder of the engine. This apparatus released compressed air from a pressurized tank at a maximum of 1 MPa through a valve down into the exhaust system. The valve was calibrated to mimic the speed of the engine exhaust valves. The chamber behind the shock wave

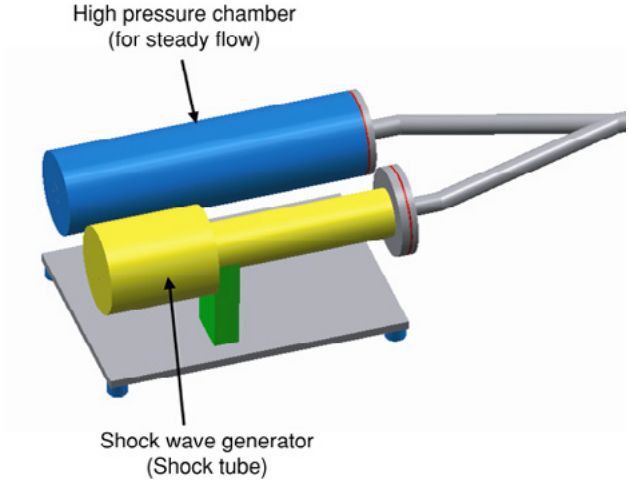


Fig. 3 Shock tube device

generator supplied a constant flow of air to smooth the flow from the compressor and enable measurements of flow velocity with the LDV.

The layout of the entire measurement system is shown in Fig. 4.

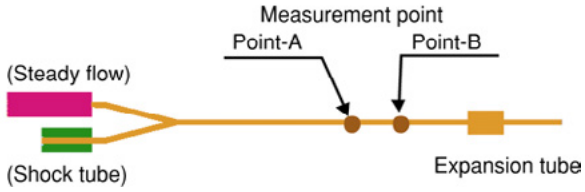


Fig. 4 Block diagram of the whole measurement

The shock wave grows as it proceeds down the exhaust pipe. The Mach number of the shock wave can be calculated by taking pressure measurements at two separated points in the pipe.

The shock wave was discontinuous and contained steady components over a wide spectrum, from low to high frequencies. Therefore, the output signal was processed to remove noise due to sensor resonance and other sources. The pressures were calculated using Eq. (1).

$$\frac{P_2}{P_1} = 1 + \frac{2\gamma}{\gamma + 1}(M^2 - 1) \tag{1}$$

(P_1 : Pressure before passage of shock wave P_2 : Pressure after passage of shock wave γ : Ratio of specific heat M : Mach number)

The obtained pressure waveform is shown in Fig. 5.

The flow velocity in the air can be approximated using Eq. (2), assuming that the flow occurs only after passage of the shock wave generated by a traveling wave[1].

Figure 6 compares the pressures observed with the LDV to the approximation.

$$\Delta u = \frac{20.05\sqrt{T_2}\,\Delta P}{\gamma \cdot P_2} \tag{2}$$

(T_2: Temperature after passage of shock wave)

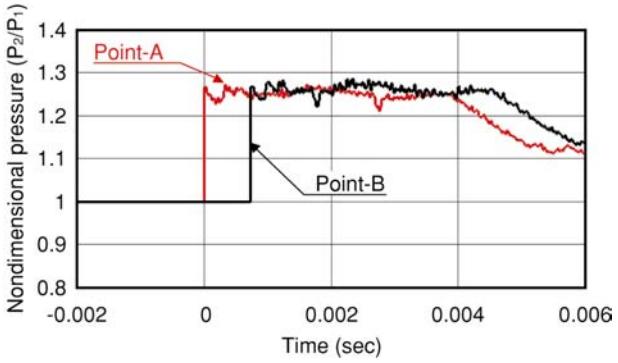


Fig. 5 Pressure wave form

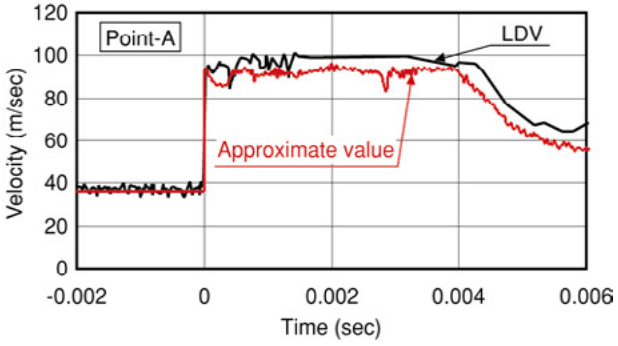


Fig. 6 Velocity comparison between the LDV and approximate value

The above methods enabled generation and measurement of shock waves to obtain a correlation with the calculations. It was also found that the calculations were reasonably precise approximations of the measured velocities with the LDV.

3. Outline of Calculation Technologies

3.1. Procedure of Numerical Calculation

RADIOSS-CFD, a package capable of the structural coupling calculations for fluids undergoing shock waves, was used for these calculations. Arbitrary Lagrangian Eulerian (ALE) coupling analysis was used for the fluid and structural system[3].

The following section explains the procedure for verifying the correlation between the calculations and the observations.

The authors verified the results of the fluid analysis, structural analysis, and acoustic analysis first; and then the precision of the coupling analysis for the fluid, structural, and acoustic results were verified.

3.2. Fluid Analysis Precision Verification

3.2.1. Verification of shock wave pressure and flow velocity precision of shock wave

An investigation of the measurements in Fig. 4 taken at Point A in the shock wave tube was carried out. The numerical model had about 120,000 elements (mesh size under 2 mm).

Figure 7 shows the waveforms of the calculated and observed pressure waves, and Fig. 8, a comparison of the flow velocities of the calculated and approximated value from the pressure wave.

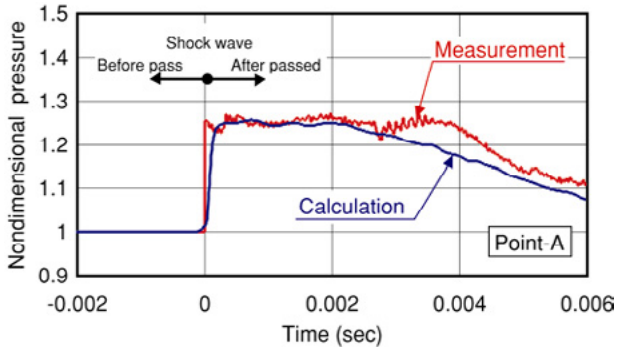


Fig. 7 Pressure comparison

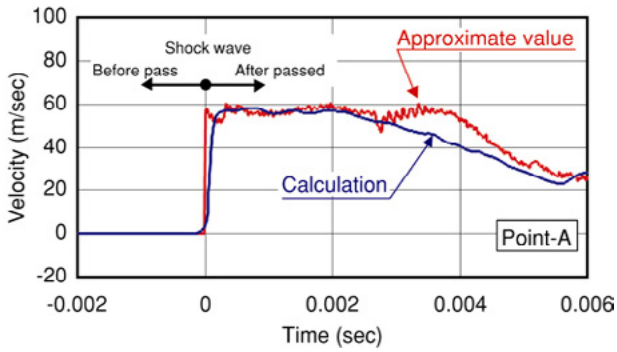


Fig. 8 Velocity comparison

A steady flow was added to allow measurement of the flow velocity; this was subtracted from the results in the figures stated.

Zero seconds on the time axis of each figure represents the time of the surface of discontinuity in the shock wave. That represents the border between the pressure or velocity at times before passage of a shock wave, on the negative time side, and after, on the positive side.

The calculations showed very low error, within 3% for the maximum pressure ratio and the flow velocity of the surface of discontinuity in the shock wave. The pressure ratio after passage of the shock wave also had a low error.

These results indicated that the shock wave component and the exhaust-pulse component in a single exhaust process could be simulated with sufficient precision.

3.2.2. Exhaust-pulse pressure and flow velocity precision verification

It is possible to construct a complete model of the exhaust system, but at the development stage, in order to save time, components are modeled by themselves, as if cut out of the system.

As shown in Fig. 9, a targeted test piece is placed in the middle of exhaust systems. It is confirmed that either pressure or velocity should be set as outlet boundary condition of the test piece.

In other words, components can be analyzed by themselves in succession down the exhaust stream and the same final result will be calculated as if all the system were analyzed simultaneously.

The physical quantities of the input (exhaust-pulse), were calculated from energy, density and flow velocity because it was a compressible fluid.

The flow velocity could be directly measured with the LDV. The energy and density of the flow was calculated using the measured pressures and temperatures as follows:

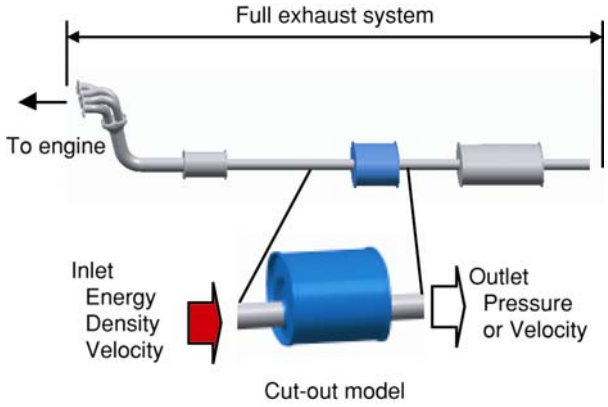


Fig. 9 Calculation model

Generally, the flow was assumed to be isentropic, in which energy exchange is in equilibrium. If pressure and ratio of specific heats are represented by P and γ, respectively, the energy E is calculated with the following equations:

$$E = \frac{P}{\gamma - 1} \tag{3}$$

$$P \cdot \upsilon^{\gamma} = Constant \tag{4}$$

$$P\upsilon = RT \tag{5}$$

(υ : Specific volume R : Gas constant)

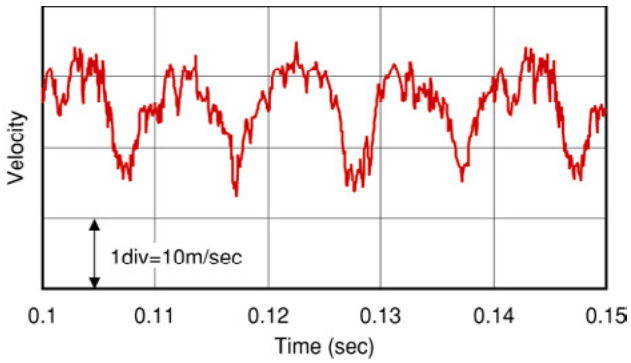


Fig. 10 Measured velocity inside of the exhaust pipe (3,000 rpm WOT)

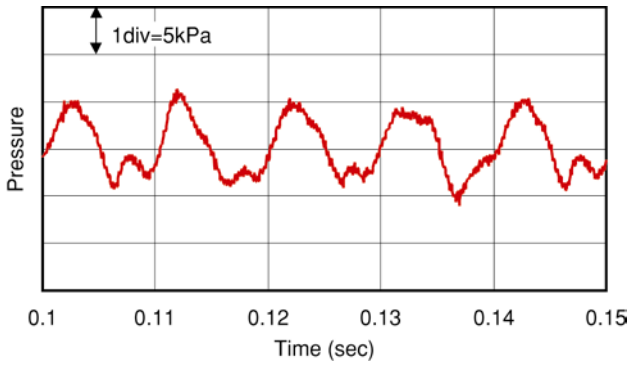


Fig. 11 Measured pressure inside of the exhaust pipe (3,000 rpm WOT)

Equation (6) is derived from Eqs. (4) and (5), and the density was calculated with Eq. (7).

$$P \cdot \left(\frac{RT}{P}\right)^{\gamma} = Constant \tag{6}$$

$$\rho = \left(\frac{P}{Constant}\right)^{\frac{1}{\gamma}} \tag{7}$$

The value of the constant in Eq. (6) was estimated using average values for the measured pressure and temperature. A test piece was placed at the end of the exhaust system in this experiment. The correlation between experimental and numerically predicted conditions was verified using a mass production engine motored with a dynamo. For reference, Fig. 10 and Fig. 11 show the results for flow velocity and pressure, respectively, in the exhaust pipe. The location of measurements here was the entrance to the muffler.

Figure 12 shows a numerical model of a simple muffler.

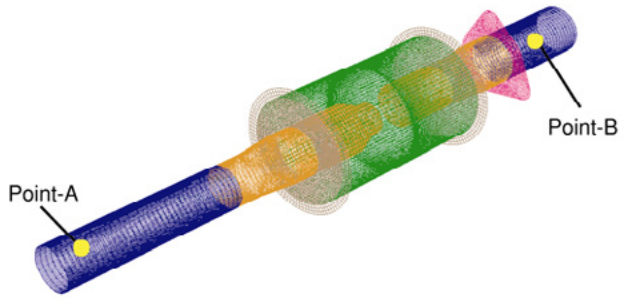


Fig. 12 Simple muffler calculation model

This contains about 450,000 elements (mesh size less than 2 mm). The pressure and temperature were used to find the energy and density, which were used as inputs to this model with the flow velocity.

Figures 13 and 14 show comparisons of the calculated and measured pressure waves upstream and downstream, respectively, of the muffler.

It is clear that the progress of the exhaust-pulse from the mouth of the muffler through the internal structure to the exit is a relatively precise prediction.

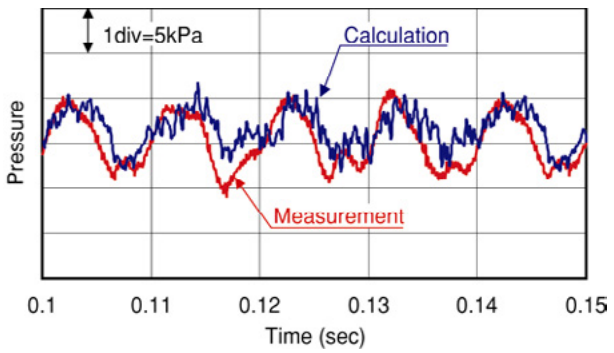


Fig. 13 Comparison of the pressure within the pipe (Point-A)

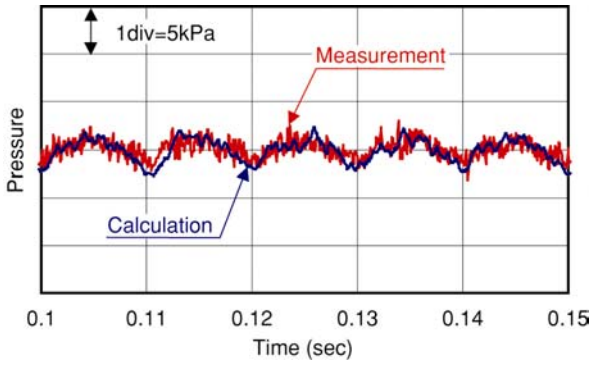


Fig. 14 Comparison of the pressure within the pipe (Point-B)

3.3. Structural and Acoustic Analysis Precision Verification

Figure 15 shows the FE model of the structure and how measurements were taken.

Hammering excitation, a previously established method, was used for comparison to verify the validity of this model.

The mass of each component in the numerical model was checked; then, all components were combined simply into a model, including the welding beads holding them together. For the comparison examination, the Frequency Response Function (FRF) of the surface, the level of response velocity of the surface vibration on a muffler to a unit load, was calculated. The results of that test are shown in Fig. 16.

Hammering excitation was chosen over acoustic analysis as a method of verifying radiation noise generated from surface vibration of the muffler because it is difficult to carry out an acoustic analysis alone, and since the results of the above structural analysis were so accurate.

The numerical model is shown in Fig. 17. This consists of the model of the interior air within the muffler structure and also a volume of the air surrounding the muffler.

The comparison test used a unit load and the resulting radiated noise measured at 100 mm from the muffler surface. The results are shown in Fig. 18.

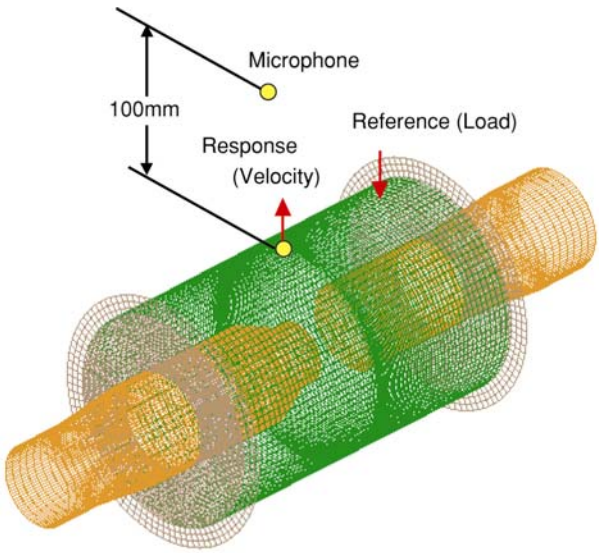


Fig. 15 FE model and measurement condition

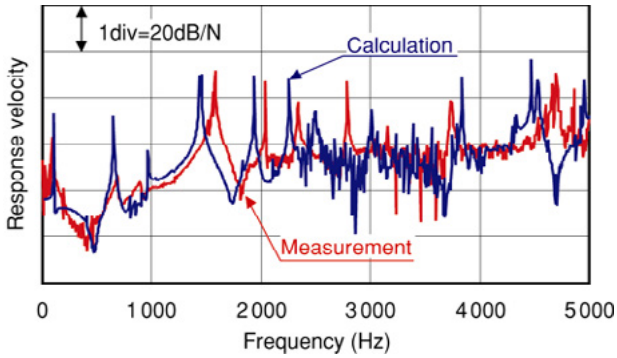


Fig. 16 Comparison of surface vibration on the muffler

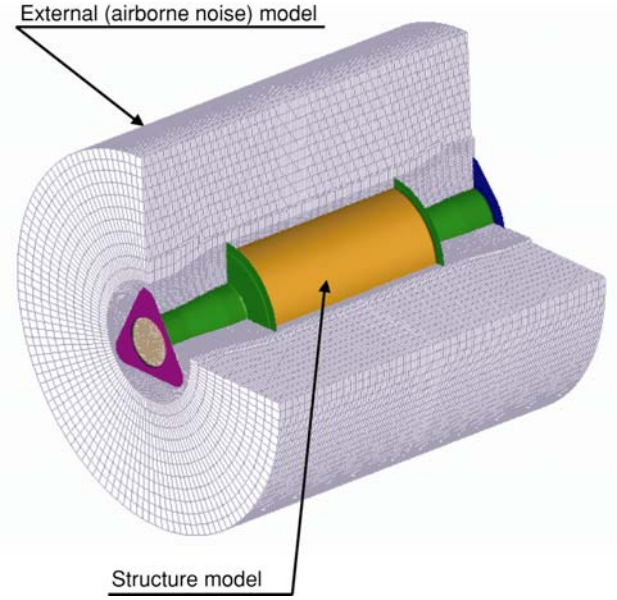


Fig. 17 Airborne noise model

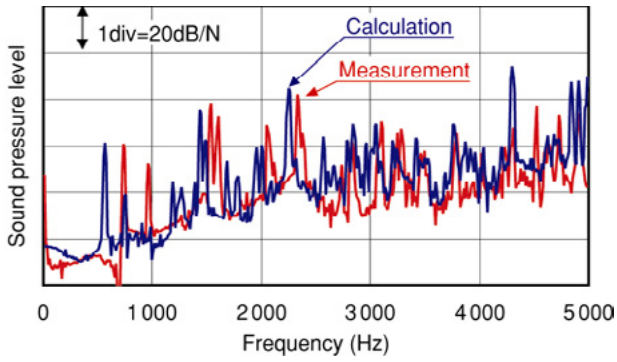


Fig. 18 The result of the radiation noise level

In Fig. 16, the peak frequency shows an error of about 70 Hz.

The reason for this was that the model used simple models of the weld beads; if the shapes and material properties of the weld beads had been more accurate, the results would probably have been closer to measured results.

However, this model, with simple welds, still provides a fairly accurate prediction of the response waveform trends. In consideration of the difficulty of modeling the welds correctly, this modeling method seems to have a lot of potential for further development.

As shown by the results in Figs. 16 and 18, simulating the exterior airborne noise and simultaneously taking into account the welding bead stiffness in the structure, a very accurate prediction of radiation noise was achieved using the FE model.

3.4. Exhaust Radiation Noise Precision Verification

Exhaust-pulse from motoring was applied to the obtained boundary conditions and fluid, structural model. Calculations for the fluid conditions and structural vibration in the exhaust pipe and radiation noise at the exterior were executed in the model.

Figure 19 shows the FE model, radiation noise calculations and the location for measurements. The calculated and measured results are in Fig. 20.

It is clear that the predicted exhaust radiation noise matches with the observed noise quite precisely.

These results will allow analysis of many phenomena causing radiation noise, including exhaust-pulse and structure-borne ones.

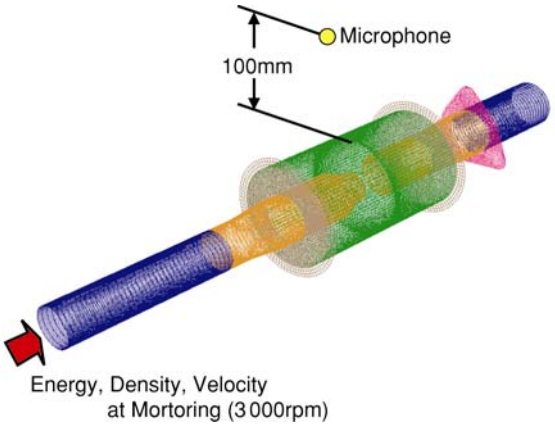


Fig. 19 Radiation noise measurement by the motoring

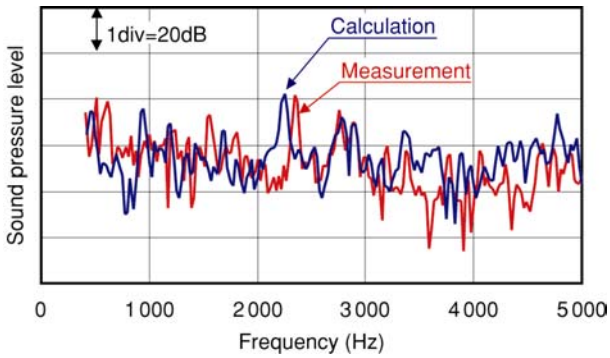


Fig. 20 The result of the radiation noise by the motoring

4. Application to Development

4.1. Example of Analysis of Phenomena

An analysis was carried out using the present method to examine the mechanisms of emission of a 1,400 Hz noise from the simple muffler surface when it is subjected to a steady flow in flow test.

The calculated and observed surface vibrations at Point-A in the simple muffler shown in Fig. 21 are provided in Fig. 22.

Since the trends of the waveforms of the peak surface vibrations are similar, it follows that the fluid behavior of the input source is being well reproduced.

Therefore, the focus was shifted to the fluid phenomena within the muffler; these were examined with a numerical model. Pressure contours within the muffler are shown in Fig. 23, and the fluctuations of the pressure at Point-B in Fig. 23 are given in Fig. 24.

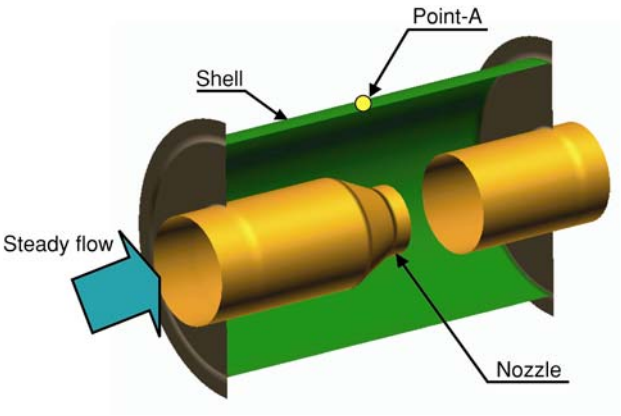


Fig. 21 Inside structure of the simple muffler

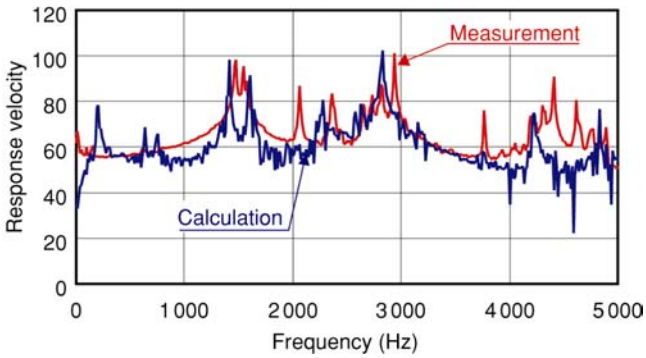


Fig. 22 The result of the surface vibration (Point-A)

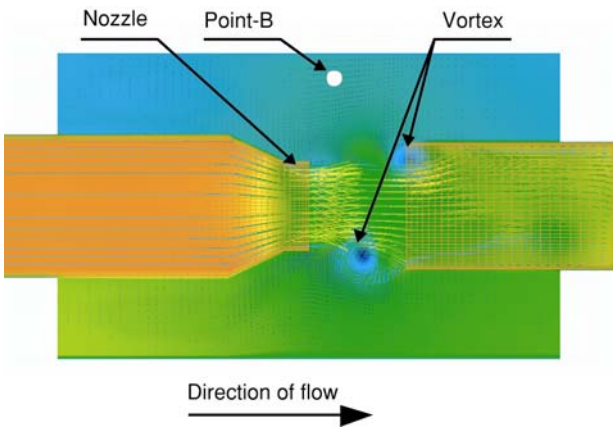


Fig. 23 Pressure contour inside of the muffler

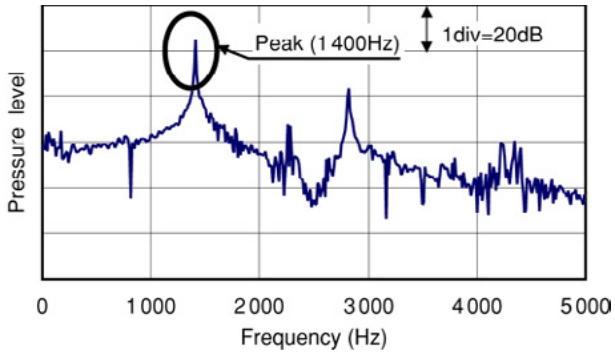


Fig. 24 Pressure inside of the muffler (Point-B)

The results indicate that vortices occur at the narrow end of the funnel portion and disperse in the downstream tube. Furthermore, the rate of pressure fluctuation can be seen here as approximately 1,400 Hz.

Thus, it was determined how to model the fluid behavior inside a muffler, which has been considered difficult to reproduce by experiment, and causative factors in the behavior have been identified.[4]

4.2. Application of Procedure to Reduce Exhaust Radiation noise

It was attempted to reduce the exhaust-pulse with an upstream sub-muffler in order to reduce the radiation noise from an actual main muffler. As shown in Fig. 25, modifying the volume of the expansion chamber of the sub-muffler, making it larger, attenuated the exhaust-pulse. The calculated fluctuations in exhaust-pulse at the exit from the sub-muffler (Point-A) are shown in Fig. 26.

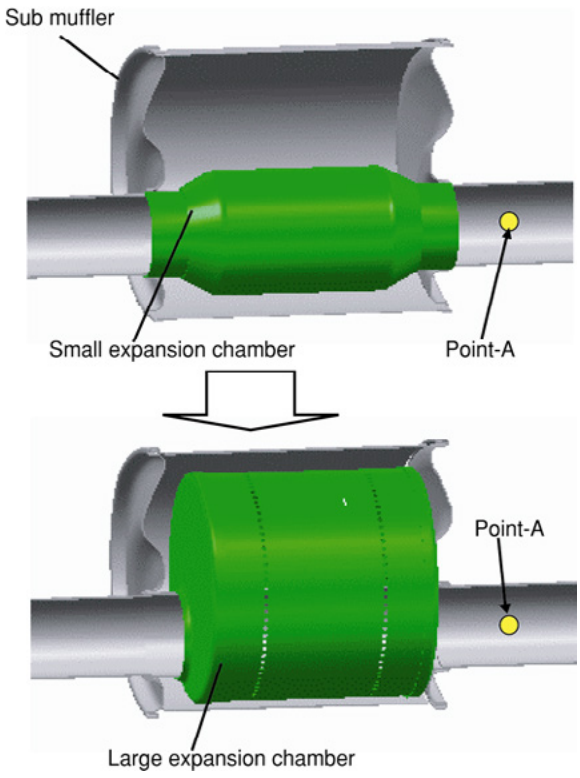


Fig. 25 Expansion chamber inside of the sub muffler

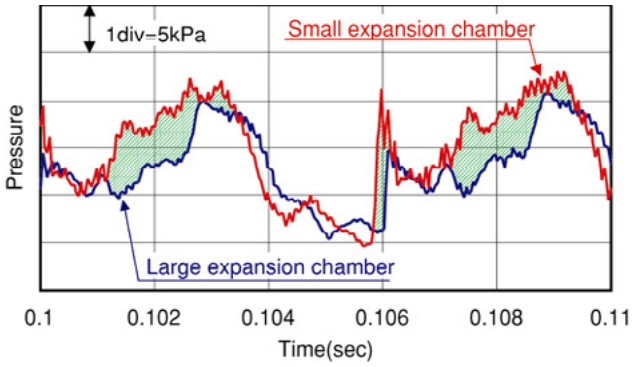


Fig. 26 Comparison of pressure at the sub muffler exit (Point-A)

As indicated by the shaded area in the above graph, the exhaust pressure has been decreased.

A test sub-muffler was constructed on the basis of these results and the radiation noise from the main muffler of a bench-mounted engine was observed. Figure 27 shows the layout of the test including the location of noise measurements, and Fig. 28, the observed results.

The shaded area in Fig. 28 shows how much the sound pressure level was reduced by the addition of the sub muffler.

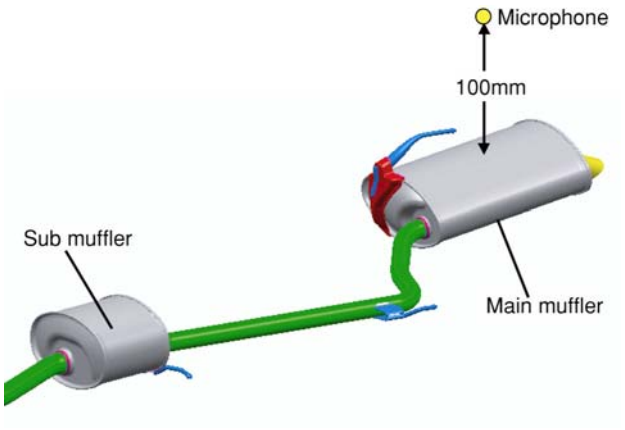


Fig. 27 Measurement of radiation noise from the main muffler

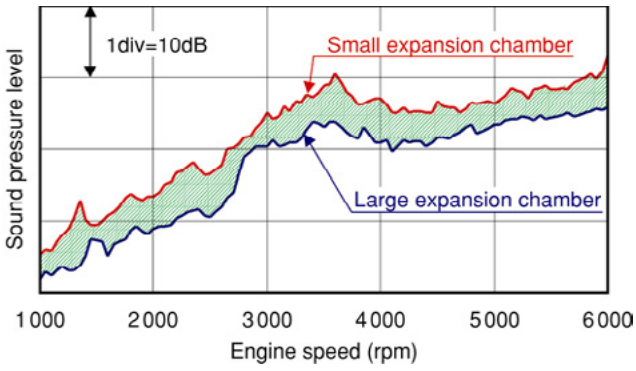


Fig. 28 Comparison of radiation noise from the main muffler

5. Conclusion

A technology for predicting the acoustic energy radiated from the exhaust piping and muffler was developed by the following processes:

(1) Fluid analysis of the interior of the exhaust system requires accounting for three factors: Exhaust gas energy, density and flow velocity. The energy and density can be calculated using measurements of the pressures and temperatures in the piping, and the velocity can be found with a LDV.
(2) Structural analysis of the exhaust system was carried out, including verification of the FRF, mode shape, and modeling of welds.
(3) For acoustic analysis of the exhaust system, a precise prediction of radiation noise was made by creating a FE model which included exterior air surrounding the muffler,

The three processes above made it possible to analyze the complicated phenomena of exhaust radiation noise.

6. Afterword

The tools described above, which allow comparatively quick analysis of noise parameters, from exhaust pipe vibration to radiation noise calculations, were supplied to developers in order to encourage the spread of this technology.

References

(1) Iwamoto, J.: Example and Drill-Compressible fluid dynamics, Tokyo, Kyoritsu Shuppan Co., Ltd., p. 156 (1980)

(2) Takekawa, H., Yoshida, N.: FFT processing on random data of exhaust gas flow pulsation, Ono Sokki Technical Report, No. 14, pp.45-49 (2001)

(3) Donea, J.: Arbitrary Lagrangian-Eulerian Finite Elements Methods, Computational Methods in Transient Analysis, Vol. 1, No. 10 (1983)

(4) Perie, F., Nakagawa, H., Yoshimoto, H., Sakurai, M., Yoshida, N., Fukui, Y.: Prediction of Aeroacoustic Noise in Exhaust Systems, The 29th FISITA World Automotive Congress, F02E150 (2002)

(5) Endo, M., Iwamoto, J.: Numerical analysis of pulsatile jet from exhaust pipe, JSAE Review, Vol. 20, No. 2, pp. 243-249 (1999)

■ Authors ■


Hiroshi NAKAGAWA


Hideyuki YOSHIMOTO


Masaki ENDO


Yuji SHIRAHIGE


Masamichi FUJISHIRO


Masato SAKURAI

Study of Noise Reduction for an Overdriven Compact Oil Pump

Koji HIRANO* Hisayuki HASHIMOTO* Masakazu KINOSHITA*
Yasunori ONO** Yoshiaki SENGA**

ABSTRACT

An issue involving noise reduction due to an abnormal noise from the oil filter arose during the development of an overdriven compact oil pump. This issue was approached by focusing on the amplitude of the oil pressure fluctuation at the pump discharge side (hereafter oil pressure fluctuation amplitude) which was the excitation force. Noise reduction was implemented using technology to reduce the oil pressure fluctuation amplitude. This involved revising the number of teeth in the rotor and changing the characteristics of the opening of the relief valve.

A small-diameter, multi-toothed compact rotor was developed to take full advantage of compactness and low friction for the 2003 Accord. The number of teeth in the inner rotor was increased from four to eight, thus reducing the oil pressure fluctuation force. The relief valve was also given additional pre-relief holes in order to improve the response at the valve opening timing, with the objective of improving the product's marketability with respect to noise and vibration.

1. Introduction

The emphasis on environmental issues in recent years has prompted efforts to greatly improve fuel consumption in automobile engines. Weight reduction, lean-burn combustion and the reduction of mechanical friction in respective parts are sited in support of technologies for improving fuel consumption.

In seeking ways to build more compact engines, the reduction of the overall length has contributed to the improved degree of freedom in vehicle installations.

Overdriven compact oil pumps are an effective technology for realizing reduction of mechanical friction and compact design. However, there are many issues with noise stemming from high speed driving and the small number of teeth on the rotor.

In this development project, abnormal noise radiating from the oil filter occurred at a certain level of engine speed after the engine was completely warmed up. This abnormal noise was transmitted to the vehicle cabin and significantly reduced the marketability of the vehicle.

In seeking countermeasures to resolve this issue, the mechanisms generating the abnormal noise were clarified and a technology was developed to reduce the noise.

2. Aim of Research

To highlight the main topics, Fig. 1 illustrates a block diagram of the oil circuit and Fig. 2 lists the assumptions regarding the mechanisms that generate abnormal noise around the filter.

Since the abnormal noise is a phenomenon unique to the overdriven compact oil pump and it was observed at a particular speed range, it was believed that associated responses such as the oil pressure fluctuation amplitude as excitation forces and resonance mechanism generated at a particular speed range contributed to the abnormal noise.

Regarding excitation forces, in comparison with conventional crankshaft direct drive type uniform speed pumps (hereafter, called coaxial drive pumps), the rotor size for overdriven compact oil pumps is smaller and the changes

* Tochigi R&D Center
** Yamada Seisakusho Co., Ltd.

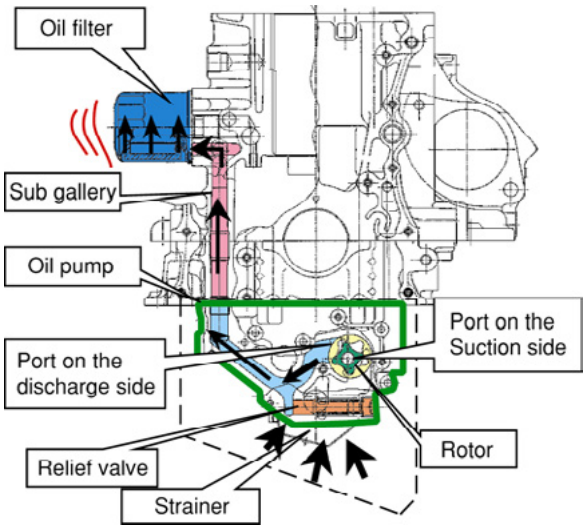


Fig. 1 Block diagram of the oil circuit

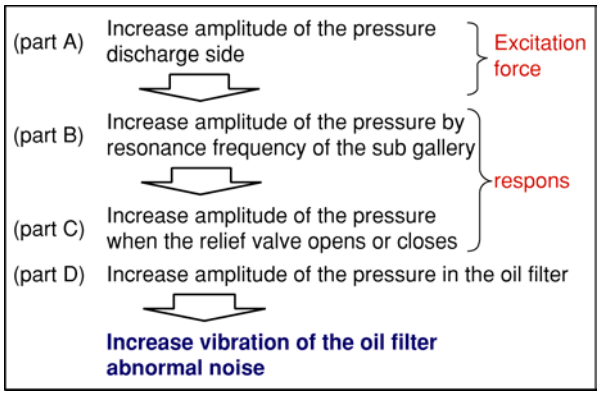


Fig. 2 Assumptions regarding the mechanism of abnormal noise from the oil filter

in pressure are bigger for each unit time. In effect, this means that the pressure fluctuation amplitude is larger than on conventional configurations.

The next issue regarding such influential responses drew attention to the oil pressure resonance and response characteristics of the relief valve. An oil pressure resonance occurred inside the flow passage from the oil pump to the oil filter and caused the oil pressure fluctuation amplitude to increase. When the peak pressure in the flow passage reaches the opening valve pressure, the relief valve begins to stroke. The relief valve is a valve for adjusting pressure. Therefore, the valve opens and closes repeatedly to adjust the pressure inside the flow passage in close proximity to the relief pressure. Particularly, when the valve closes, an oil hammer occurs due to the sudden stop of oil flow. This, it is believed, leads to a further increase in pressure fluctuation amplitude inside the flow passage and excites the filter and thus leads to the generation of abnormal noise.

This topic seeks to verify these described assumptions and develop a technology for reducing noise by taking advantage of the low friction merits embodied in the overdriven compact oil pump.

3. Basic Structure

The developed overdriven compact oil pump, which is attached to the lower engine block, uses an internal gear trochoid type rotor similar to that used in typical coaxial type drive pumps. Whereas the outer dimensions of the coaxial outer drive rotor is approximately 80 mm, the dimensions of the rotor for the overdriven compact oil pump have been reduced to 40 mm to achieve compactness.

The crankshaft coaxial type drive rotor is driven at the same speed as the engine. However, because the theoretical oil discharge per single rotor turn for overdriven compact oil pumps is small, the theoretical discharge per engine rotation has been adjusted to approximate that of the crankshaft coaxial pump by increasing the rotor speed. This results in a rotor speed increase of 1.6 to 2 times over the crankshaft by silent chain.

Figure 3 shows a comparative view of the described compact overdriven pump and a conventional pump. Table 1 lists the comparative oil pump specifications. Figure 4 illustrates the oil circuit system including the overdriven compact oil pump.

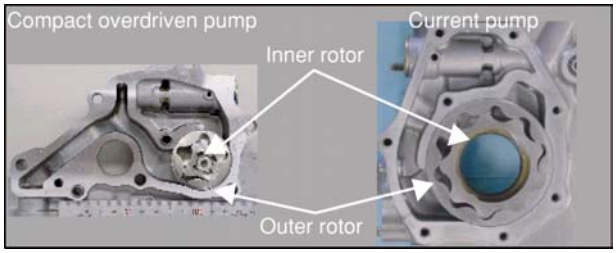


Fig. 3 Comparison of the structures

Table 1 Specification of the oil pump

	Overdriven compact oil pump	Current oil pump
Over driven ratio	Double speed	Single speed
Number of the teeth	Inner 4 / outer 5	Inner 9 / outer 10
Rotor size	Φ40 × 15.0t	Φ80 × 6.0t
Delivery oil (cc) (at round pump)	6.12	12.2
Delivery oil (cc) (at round crankshaft)	12.2	12.2

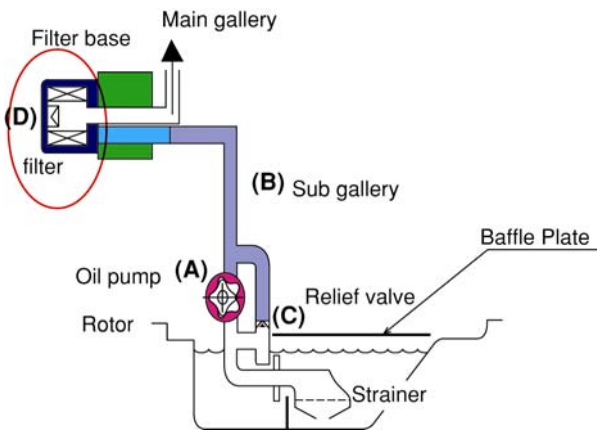


Fig. 4 Oil circuit system of the engine

This oil pump is attached to the lower engine block and is situated in the oil pan. The chain driven rotor conveys the oil to the sub gallery from the strainer via the discharge side port. The oil, which has passed through the sub gallery, is filtered through the oil filter and is then supplied to the journal and cylinder head via the main gallery. When the pressure on the discharge side, including the sub gallery, exceeds the set pressure value, the relief valve begins to operate and the excess oil is returned to the intake controller port via the relief valve passage.

4. Verification of Mechanisms Causing Abnormal Noise

4.1 Understanding the Issue

The abnormal noise occurs at particular engine speeds once the engine has been warmed up and the oil temperature exceeds 90 °C. The abnormal noise radiates mostly from the filter.

Figure 5 shows the measured results of the abnormal noise level measured near the filter.

From the measured results, it was learned that the main cause of the noise was attributed to the oil pump meshing order components and the total order frequency unexpectedly increased. Figure 6 shows the measured results of the pressure fluctuation amplitude on the discharge side of the oil pump, which was thought to be the source of the excitation force.

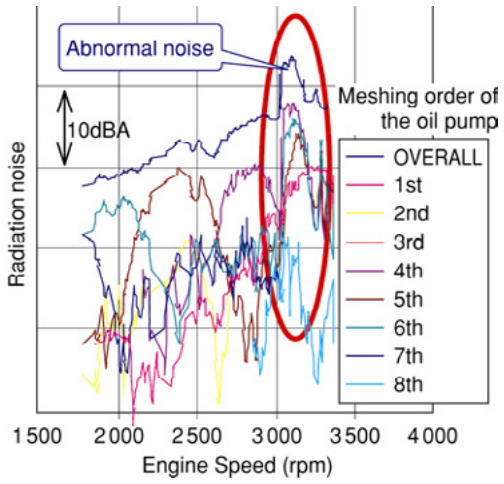


Fig. 5 Sound pressure level nearby filter

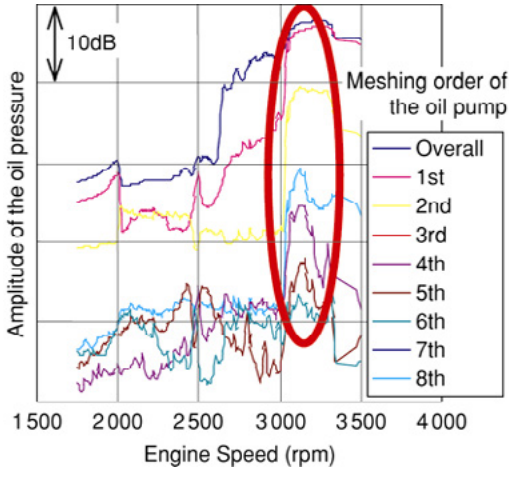


Fig. 6 Oil pressure fluctuation on the discharge side

This also showed the same results as the filter radiation noise. The noise on the filter occurs at particular engine speeds and oil temperature. Therefore, the noise can be caused not only by the excitation force due to oil pressure amplitude on the discharge side of the oil pump but also by the total response system which creates resonance. In verifying the mechanisms that cause the noise, the following points needed to be investigated:

- Excitation forces effect – oil pressure fluctuation amplitude caused by the discharged oil from the rotor
- Responses system effect – effect by resonance that occurs inside the sub gallery flow passage and effect by the relief valve operation.

4.2 Introducing Unit Test Bench Analysis

Once it was known that the abnormal noise radiated only from the filter surface, the next step was to verify the mechanism. However, since it would be difficult to conduct testing by unit engine test to evaluate only the mechanisms at issue, shown in Section 2, a new unit test bench was devised to satisfy the following three conditions while monitoring the noise that occurred near the filter.

(1) To verify resonance inside the oil flow passage, the passage shape can be changed.
(2) Relief valve motion can be verified.
(3) Pressure fluctuation amplitude on the oil circuit can be easily measured.

Figure 7 outlines the unit test bench. The unit test bench consists of an oil pump attached to a jig which is configured to the sub gallery and filter base shapes. The motor then drives the pump and the pressure within the flow passage is set with the regulating valve configured to the filter after flow.

To measure the excitation force caused by pressure fluctuation, and the resonance inside the oil flow passage, a pressure sensor was fitted to the oil pump and inside the flow passage while a gap sensor was fitted to measure the motion of the relief valve. The results gained from the unit bench test verified the same abnormal noise occurrence as the test on the actual vehicle.

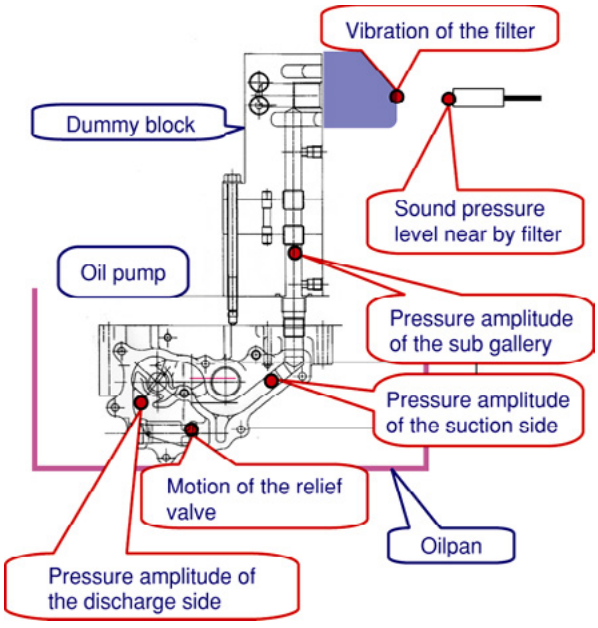


Fig. 7 Test bench

4.3 Effects of Excitation Force

The first thing to be thought of as the excitation force is the oil pressure fluctuation amplitude brought on by the oil discharged from the rotor. This is based on the supposition that this is affected by the theoretical discharge volume per rotor tooth. Note here that this value is the theoretical discharge volume per engine rotation divided by the number of teeth on the oil pump rotor that mesh in a single engine rotation.

Specifically, to diminish the oil pressure fluctuation amplitude, it was believed necessary to increase the number of rotor teeth on the pump producing a large volume of discharge flow.

The unit analysis bench test shown in Fig. 7 was applied to measure the excitation force first. Figure 8 shows the comparative results of respective oil pressure fluctuation amplitudes on the overdriven compact oil pump and the coaxial drive pump. The oil pressure fluctuation amplitude on the overdriven compact oil pump generates what is thought to be a peak resonance level at around 3,000 rpm. However, the amplitude on overdriven compact oil pumps is approximately twice as large over that on conventional coaxial drive pumps in the speed range below 2,000 rpm which was not included in the range affected by resonance. As shown in Table 2, the overdriven compact oil pump generates 13% more oil discharge volume per rotor tooth in comparison with that generated by the conventional coaxial drive pump which naturally leads to an estimated increase in pressure fluctuation amplitude. However, it was difficult to predict that the pressure fluctuation amplitude would actually be twice that of the test results indicated.

Based on these test results, the pump's drive speed, in addition to the theoretical oil discharge volume per rotor tooth, is also believed to cause the increase in pressure amplitude which is the excitation force on the pump.

To verify the actual measurement results, the pressure fluctuation amplitude of the oil discharged from the rotor was estimated by calculation.

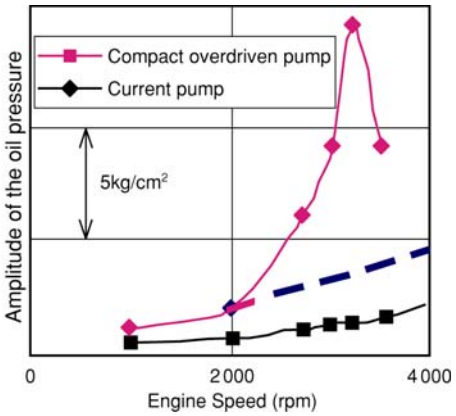


Fig. 8 Result of the pressure fluctuation amplitude measured on the discharge side

Table 2 Delivery oil per rotor tooth

	Overdriven compact oil pump	Current oil pump
Over driven ratio	Double speed	Single speed
Number of the teeth	Inner 4 / outer 5	Inner 9 / outer 10
Delivery oil (cc) (at round crankshaft)	12.2	12.2
Delivery oil (cc) (at rotor tooth)	1.53	1.35

As shown in Fig. 9, the cell located between the inner rotor and outer rotor is filled with oil. As the rotor turns, the cell volume changes which leads to oil being discharged from the cell. To simplify the calculation, it was supposed that the cell was filled to capacity with oil all the time. Also, the oil was treated as a fluid devoid of any pressure influences.

The cell volume is highlighted by the grey area shown in Fig. 9 and is indicated by V. If the rotor's maximum volume rotation angle indicated by θ is zero, the cell's volume changes in accordance with the rotation angle as shown in Fig. 10. The amount of oil flow per rotor tooth discharged from the rotor is expressed by Q, the volume of the rotor cell by V and the rotor rotation angle by θ,

$$Q(\theta) = V_{max} - V(\theta) \quad (1)$$

The amount of oil flow per rotor tooth discharged at the moment from the rotor where $\theta = \omega t$ is expressed by the following formula.

$$\frac{dQ}{dt} = -\frac{dV}{dt} = -\omega \frac{dV}{d\theta} \quad (2)$$

The total volume of oil flow was calculated according to the total number of rotor teeth and then that value is substituted in the formula[1, 2] for pulsation ratio ε.

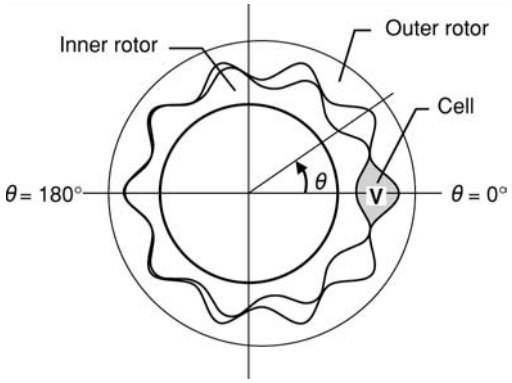


Fig. 9 Model of the oil pump rotor

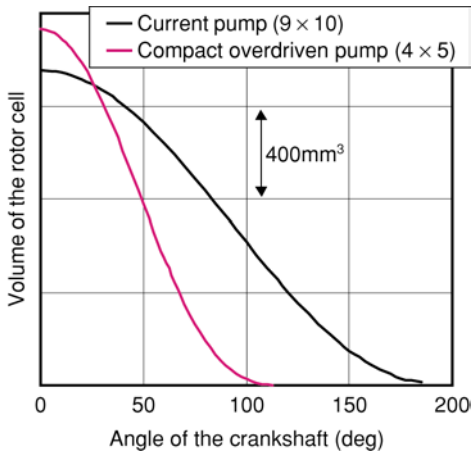


Fig. 10 Rotor cell volume (calculation)

$$\varepsilon = \{(\frac{dQ}{dt})_{max} - (\frac{dQ}{dt})_{min}\} / (\frac{dQ}{dt})_{mean}$$

$$= \sum_{i=1}^{N} [\{(\frac{dV_i}{d\theta})_{max} - (\frac{dV_i}{d\theta})_{min}\} / (\frac{dV_i}{d\theta})_{mean}] \quad (3)$$

Q : amount of oil flow
V : cell volume
V_{max} : maximum value for cell volume
θ : angle of rotor rotation
ω : rotor angular velocity
N : the number of meshed sprocket teeth

The pulsation rate is expressed in formula (3) as the change in cell volume. Figure 11 shows a comparative evaluation of rotor cell volume change per rotor tooth for an overdriven compact oil pump and coaxial drive pump. Figure 12 shows the cell volume change according to crankshaft rotation angle.

In comparing the changes in cell volume, it was shown that the change in cell volume for overdriven compact oil pumps was virtually double. These results also matched the results yielded in the unit analysis bench test. The pressure pulsation ratio, expressed by ε, is calculated in formulas[(1), (2)] using the number of rotor teeth as a parameter. Figure 13 shows the calculation results of the pressure pulsation.

From these calculation results, it was learned that in order to make the pressure pulsation ratio in overdriven compact oil pumps equal to that in coaxial drive pumps, the number of rotor teeth needed to be double that of the current rotor configuration, that is, 8 on the inner rotor and 9 on the outer rotor.

However, with the current method of designing a rotor,

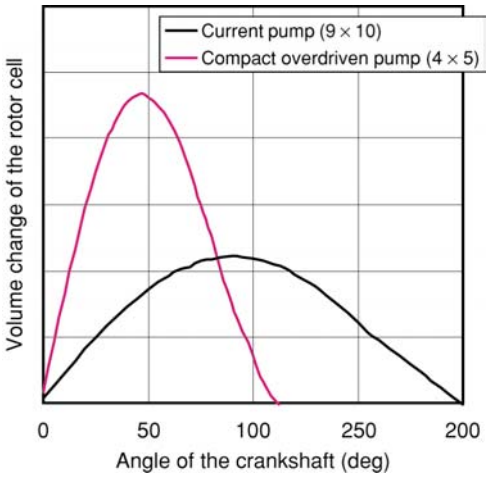


Fig. 11 Volume change of the rotor cell (calculation)

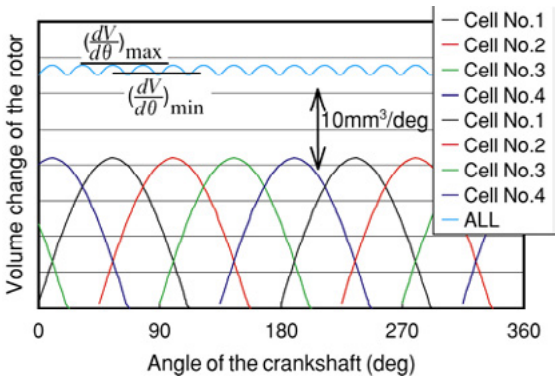


Fig. 12 Volume change of the rotor (calculation)

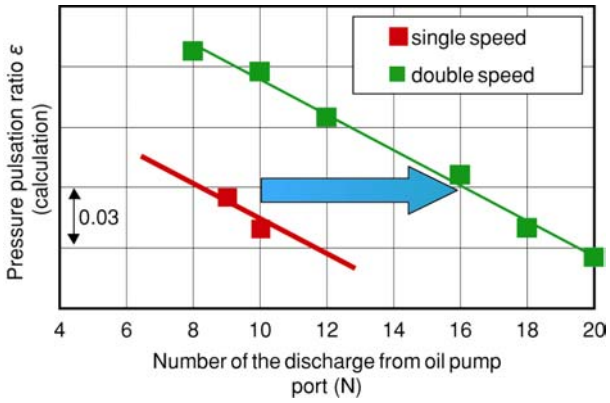


Fig. 13 Result of calculation of the pressure pulsation

which is based on the trochoid curve, the increase in the number of rotor teeth also increased the degree of friction linked to the increase in the rotor's outer dimension.

Figure 14 shows the relationship between the friction of the oil pump and the pressure amplitude. To significantly diminish the friction, a small diameter multi toothed rotor was developed. The developed rotor measures 45 mm in diameter and has 8 teeth on the inner rotor and 9 teeth on the outer rotor. The new rotor was designed to reduce the contact area on the sliding rotor parts to achieve a reduced level of friction. Figure 15 illustrates the structural design for reducing the contact area. Figure 16 shows the effect of the reduced friction on the oil pump.

This design modification has taken advantage of the merits of the low friction characteristics associated with compact rotors while achieving a 60% reduction in pressure fluctuation amplitude.

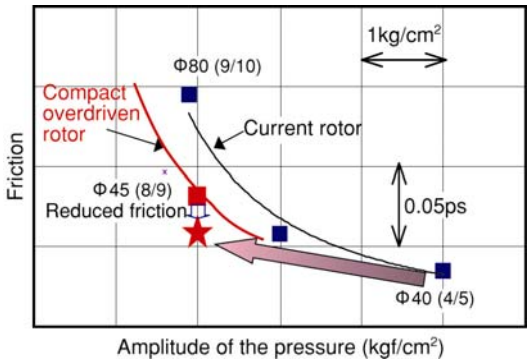


Fig. 14 The relation between pressure fluctuation amplitude and friction of the oil pump

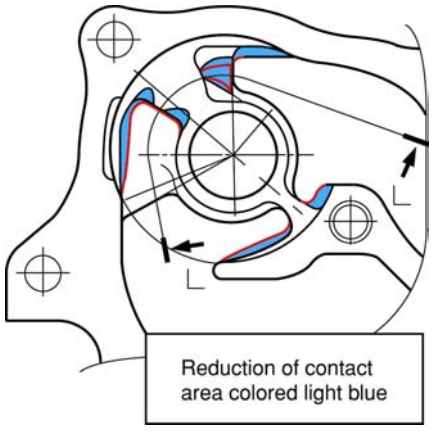


Fig. 15 Effect of reduced friction of the oil pump

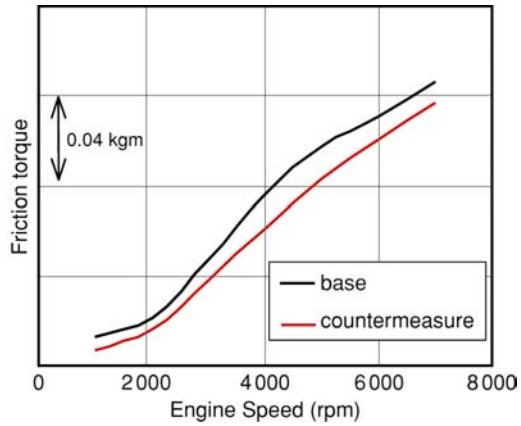


Fig. 16 Effect of reduced friction of the oil pump

4.4 Effects of the Response System

The effect of the response system was investigated by focusing on the resonance occurrences inside the sub gallery flow passage and the influences from the relief valve.

The occurrence of abnormal noise drew attention to the occurrence of resonance on the sub gallery flow passage generated at a certain level of motor speed and at certain oil temperature levels. The sub gallery flow passage length was used as parameter in the unit test bench. Figure 17 shows the pressure amplitude at the sub gallery.

These results showed that by changing the sub gallery passage length, indicated by L, the corresponding change in peak of pressure fluctuation amplitude inside the flow passage also changed and was affected by the resonance on the flow passage.

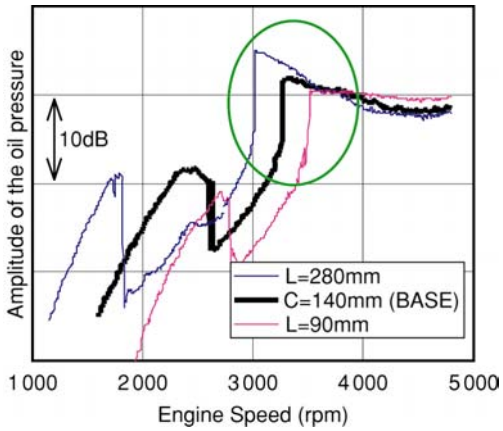


Fig. 17 Amplitude of the pressure at sub gallery

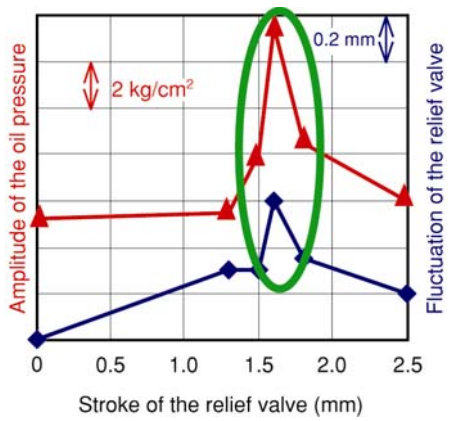


Fig. 18 The relation between amplitude of the pressure and relief valve location

As the graph in Fig. 17 illustrates, the oil pressure amplitude generated as the engine speed approaches 3,000 rpm shows a sudden exaggerated increase. The point at which this exaggerated increase occurs was in proximity to the opening pressure of the relief valve and it was estimated that the oil hammer occurred when the relief valve opened and closed. To verify the correlation between the increase in oil pressure amplitude and the opening and closing of the relief valve, a gap sensor was used to measure the relief valve motion. Figure 18 shows the results of the relationship between the oil pressure amplitude and the relief valve location.

As estimated, the relief valve motion amplitude and oil pressure fluctuation amplitude showed a sharp increase at the point where the relief valve opened. The oil pressure amplitude was greater for the overdriven compact oil pump than that for the conventional coaxial pump. Furthermore, the amplitude on the relief valve motion tended to increase along with the oil pressure amplitude increases brought on by the resonance inside the flow passage.

When the maximum value of oil pressure inside the flow passage exceeds the pressure level of the opening valve, the relief valve, being a pressure controller, vibrates in response to increased oil pressure. The valve maintains the pressure level from the pump to the filter by releasing oil excess to the suction port. In this respect, the positioning of the relief valve has presented a concern. In particular, the oil hammer tended to occur as a result of the valve passage movement associated with the relief valve closing. Figure 19 shows the relationship between the relief valve stroke and the open area of the relief passage. The highlighted area indicates the location of the relief valve when the oil pressure fluctuation amplitude measured by unit test bench increased sharply. As can be seen in Fig. 19, the relief valve vibrates at the point where the opening area of the relief passage changes sharply. These results can be summed up as follows.

(1) The relief valve operates in response to the pressure amplitude inside the flow passage near the relief opening.
(2) When the relief valve opening position exceeds 1.5 mm, the oil begins to flow and the pressure inside the flow passage is reduced.
(3) The relief valve closes to maintain the set pressure.
(4) For the relief valve to stop the sudden flow of oil, an oil hammer occurs and the pressure inside the passage is temporarily increased.

As the processes described in the previous four steps are repeated, the pressure fluctuation amplitude inside the flow

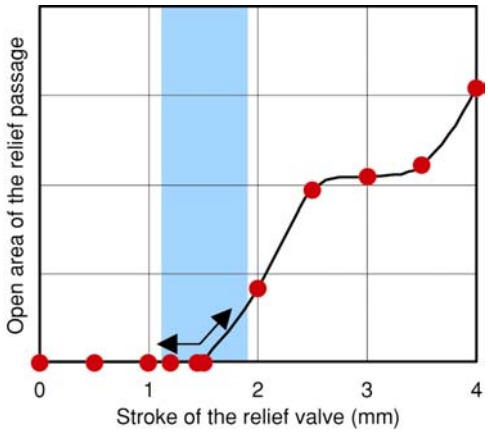


Fig. 19 The relation between relief valve stroke and open area of the relief passage

passage sharply increases causing the oil filter to resonate, which is thought to lead to the abnormal noise. To countermeasure this condition, the relationship between the relief passage opening area and the stroke volume were modified to improve the opening characteristics of the relief valve. Figure 20 shows this relationship. As shown in Fig. 21, the countermeasure was achieved by adding two relief holes to change the original relief open area configuration. This made it possible to diminish the sudden change of cross section area.

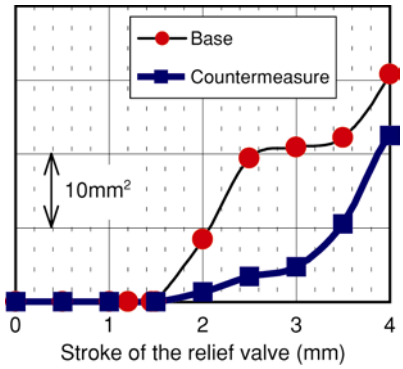


Fig. 20 The relation between area of the passage and stroke of the relief valve

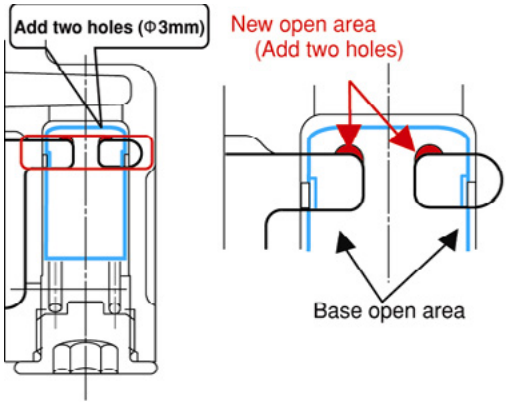


Fig. 21 Remove open area of the relief passage

5. Countermeasure Details

In consideration of the mechanisms outlined in Section 2, the following were discovered to be the cause of the abnormal noise. The size and number of rotor teeth was a contributing factor to the increase in the excitation force compared with the conventional pump. Also, resonance inside the sub gallery flow passage and the shape of the relief valve passage contributed to the sharp increase in oil pressure fluctuation amplitude brought on by relief valve response characteristics.

As shown in Table 3, the oil pump specifications were modified to reduce the excitation force as a countermeasure to the abnormal noise. The number of rotor teeth was increased, from 4 teeth on the inner rotor and 5 teeth on the outer rotor, to 8 teeth on the inner rotor and 9 teeth on the outer rotor. Also, two pre relief holes were added to change the relief valve opening characteristics. Figure 22 shows the results of the countermeasures in reducing oil pump noise and the levels at which the abnormal noise ceased to occur.

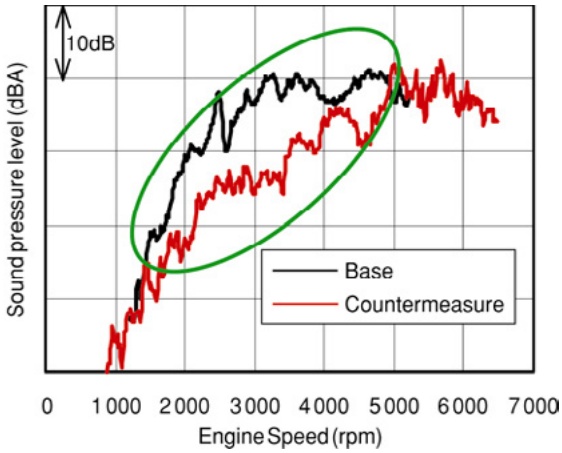


Fig. 22 Results of the countermeasures to reduce oil pump noise

Table 3 Oil pump specification comparison

	Base	Countermeasure
Over driven ratio	Double speed	Double speed
Number of the teeth	Inner 4 / outer 5	Inner 8 / outer 9
Rotor size	Φ40 × 15.0t	Φ45 × 14.3t
Delivery oil (cc) (at round pump)	6.12	5.94
Delivery oil (cc) (at round crankshaft)	12.2	11.9

6. Conclusion

A unit test bench was devised to determine the mechanisms that led to the occurrence of abnormal noise. The unit test bench enabled adjustments to the oil passage shape and the pressure inside the flow passage to significantly reduce noise occurrences in overdriven compact oil pumps. By applying the unit test bench and the effective countermeasures described below in the development of the new oil pump design realized the reduction of oil pump noise.

(1) To reduce noise in overdriven compact oil pumps, it was learned that the number of rotor teeth needed to be set in proportion to the drive speed to diminish the oil pressure amplitude. The optimal number of teeth for a compact multi toothed inner rotor was verified and set to 8.

(2) To diminish sudden changes to the relief hole opening surface area, the hole configuration was changed.

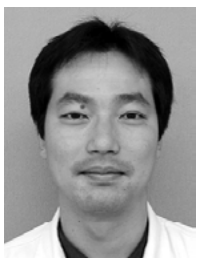
References

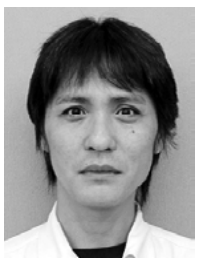
(1) Committee on Editing of Oil Pressure Technologies handbook: Pressure technology handbook, New edition, Nikkan Kogyo Shinbun, p. 267 (1976)

(2) Japan Society of Mechanical Engineers: Mechanical engineering handbook, Edition 6, Tokyo, Japan Society of Mechanical Engineers, pp. 9-86 (1977)

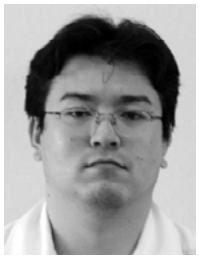
■ Authors ■


Koji HIRANO


Hisayuki HASHIMOTO


Masakazu KINOSHITA


Yasunori ONO


Yoshiaki SENGA

Establishment of a Method for Formability Evaluation on Motorcycle Fuel Tank

Takashi OGINO* Hiroyuki KAMO * Tomoyuki TAGAMI *
Minoru SAITO** Hiroki YOKOTA* Shoji KUWABARA*

ABSTRACT

The “Press map method” for simplicity and high speed and the “Press CAE analysis method” for depth and high accuracy were developed as tools for achieving a press formability of motorcycle fuel tanks. The methods enabling evaluation of press formability in the design stage were established. The effectiveness and reliability of the methods were verified by confirming the correlation of actual measurement data with the analysis result in applying the method to the actual models.

1. Introduction

Fuel tanks are sealed containers that hold fuel. At the same time, the outer tank is also a part that comprises the functional beauty of the overall motorcycle, and various shapes are required depending on the engine and frame shapes. Particularly in recent years, demands for new fuel tank shapes are increasing due to diversifying user needs and support for environmental issues, etc. Therefore, in order to reduce time and cost when manufacturing a new shape fuel tank, development of a method capable of investigating manufacturing requirements in the design stage is required in place of the conventional trial-and-error tool manufacturing method.

2. Formability Evaluation during Product Development

2.1. Press Forming

Figure 1 shows the tool structure when press forming a fuel tank. A panel is clamped between the die and the blank holder, then the desired shape is formed by plastically deforming the panel between the die and the punch. Typical problems occurring at this time include cracks and wrinkles. Forming can be performed well within the stretching and shrinkage tolerance limits of the steel plate, but cracks and wrinkles occur when these limits are exceeded. Figure 2 shows actual examples of these press defects. Cracks and wrinkles have an inverse relationship, and measures to prevent cracking often lead to wrinkles. Wrinkles not only mar the appearance, but can also lead to a drop in the part strength or tool damage. These defects are mainly caused by sudden or uneven changes in the tool shape, and various countermeasures are taken to ease these changes.

These countermeasures are broadly divided into the following two methods.

(1) Changing the press machine settings, adjusting the draw bead height, or otherwise modifying the forming conditions.
(2) Changing the tool shape including the product shape and the die addendum.

Changing the forming conditions and modifying the die addendum have no effect on the product shape, but the product shape may also need to be changed depending on the nature of the trouble. These changes may not be limited to just the fuel tank, and may lead to changes in the design aspects or functional shapes of other parts, resulting in significant modification process time and costs.

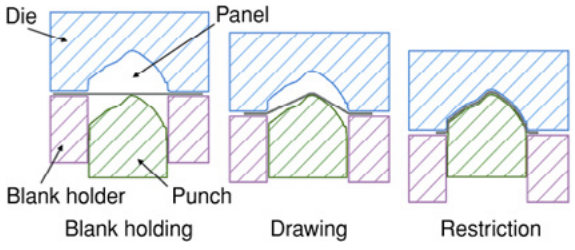


Fig. 1 Press die structure and motion

* Asaka R&D Center
** Honda Enginering Co., Ltd.

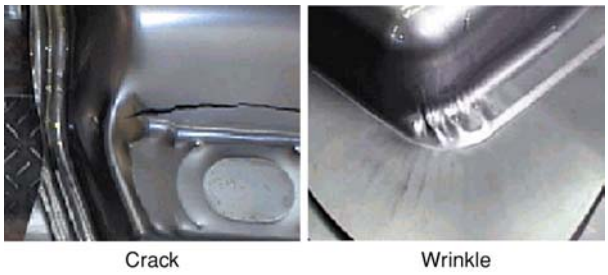


Fig. 2 Press defect

2.2. Formability Prediction Tools and Their Application Timing in Development

When using formability prediction tools in product development, different functions are required in the product design stage and in the tool design stage. In the product design stage, the formability must be investigated simultaneously with the functional design of the tank and related parts. Thus, it is important that the prediction tool be able to easily and quickly investigate the formability of various shapes, and propose measures for major problems regarding formability.

On the other hand, in the tool design stage, the tool shape and forming conditions must be investigated in order to accurately manufacture the product-designed parts in the mass production process. Thus, it is important that the prediction tool be able to simulate and predict the actual press forming process, and accurately evaluate the forming results in detail. Therefore, the simple and high-speed "Press map method" and the in-depth and high accuracy "Press CAE analysis method" were developed as desktop investigative tools that can be used in the product design and tool design stages. Figure 3 shows the position of each design stage and the tool application timing within the development flow.

3. Development of the Press Map Method

As described in section 2, sudden unevenness in the product shape is unfavorable for formability, and taking measures to deal with this in the product design stage reduces subsequent problems. The press map method was developed by applying the difference of the peripheral length method, which had been used as a tool design method that allows easy investigation of various shapes by quantifying sudden unevenness.

3.1. Press Map Method

When press forming a shape such as that shown in Fig. 4, the panel is deformed by the protrusion having the level difference D. Plate A is formed while being pulled toward plate B, and conversely plate B is pulled toward plate A and formed by that reaction. The condition of plate A at this time can be approximated by assuming that the load Pi per unit length in the in-plane direction of the flat plate is applied over the range of length C as shown in Fig. 5. If the load when the plate is stretched to the breaking limit is kept constant, the level difference d_a is proportional to the load application length C, and d_a is also proportional to the length E which uses the deformation start point O as the reference.

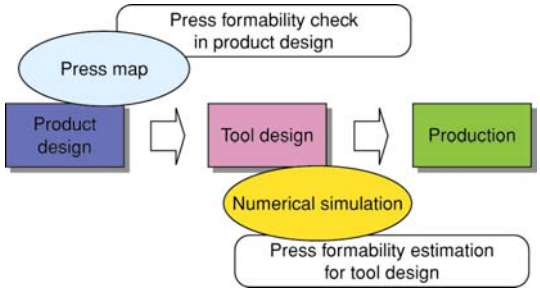


Fig. 3 Simulation map in a product flow

Figure 6 shows a graph of the relationship between length E and d_a. This figure shows three types of deformation patterns (i, j and k). Patterns i and j show the shape at the breaking limit, and pattern k represents the case when a further load is applied to pattern i, and shows the broken condition. When lines a and b are drawn through both shoulders of the deformed shape to divide the graph into the three areas I, II and III, each area has the following characteristics.

- Area I is the area in which deformation of an arbitrary point Q on the plate is possible.
- Area II is the area in which all of patterns i, j and k exist, and deformation may or may not be feasible depending on the loading length C.
- Area III is the area where deformation is impossible.

Based on these characteristics, the feasibility of deformation for an arbitrary point Q on the plate can be expressed by length L and level difference d_a. Next, plate B is also pulled and deformed by the plate A breaking load P_i, and the amount of deformation d_b is proportional only to sectional width W. The maximum deformation level difference D that can be formed can be obtained by combining the displacements of plates A and B.

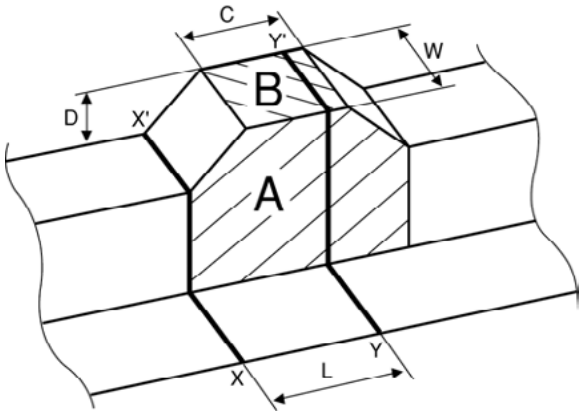


Fig. 4 Typical press shape

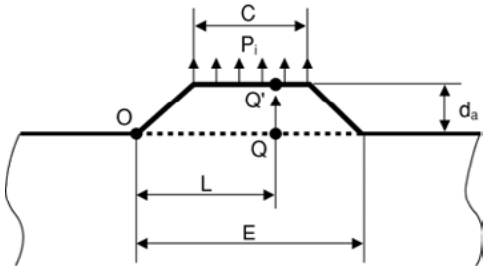


Fig. 5 Deformation of plate A

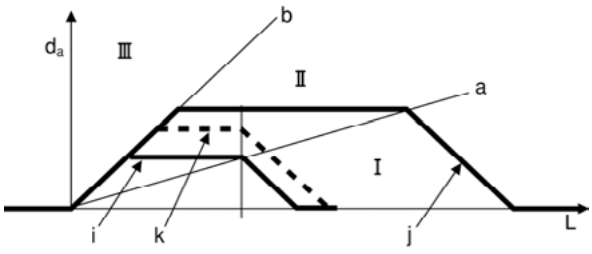


Fig. 6 Relationship between L and d_a

$$D = d_a + d_b \quad (1)$$

In other words, the maximum deformation level difference D that can be formed can be expressed by length L and sectional width W. At this time the difference F (difference of peripheral length) between the length of the two sections X-X' and Y-Y' in Fig. 4 is identical to level difference D, so this level difference can be replaced with the difference of peripheral length. This relationship is shown by L and F in Fig. 7, with W held constant. This relationship is called a press map, and the above-mentioned areas I, II and III are the stability (stable forming), feasibility (production technology investigation) and impossible (forming impossible) areas, respectively.

To judge the formability of the shape shown in Fig. 8, the distance between sections and the difference of peripheral length of sections x, y and z relative to the reference section are measured and plotted on the press map. Figure 7 shows the values for each section. Sections x and z fall within the stability area, but section y lies within the feasibility area where formability may or may not be achieved. However, the level difference stretches to section z, so in this case the level difference is judged to be formable.

Actual products have complex shapes, but this method can be applied by viewing complex shapes as an aggregate of these level difference shapes. Therefore, the differences of peripheral length were measured for an actual formed part, and formability was confirmed for each section. Figure 9 shows these results. The map judgment values match closely with the actual phenomena, confirming that this method can also be applied to actual parts.

3.2. Construction of a Press Map System

A CAD-based press map system was constructed as a tool for efficiently performing press map judgments. This system creates multiple parallel sections passing in the press direction for a product shape such as shown in Fig. 10, and calculates the length (peripheral length) of each created section. When any two optional sections are selected from among the multiple created sections, the difference of peripheral length = *La* - *Lb* and the distance between the sections = *Lc* are obtained.

These values are then plotted on the aforementioned press map to determine whether problems will occur during press forming. The judgment values are displayed as section lines of different colors and thickness. The thickness indicates the formability judgment area, and the color indicates the relative peripheral length. This length distinction provides pointers for shape modification.

When the product shape has large level differences that make forming difficult, the die face portions are generally curved to ensure formability, and these curved die faces are also supported. Conversely, a function for calculating the excess peripheral length in case of flat die faces and creating curved die faces has also been added. The formability judgment takes approximately one to two minutes, so this system is used to investigate shapes or design die faces.

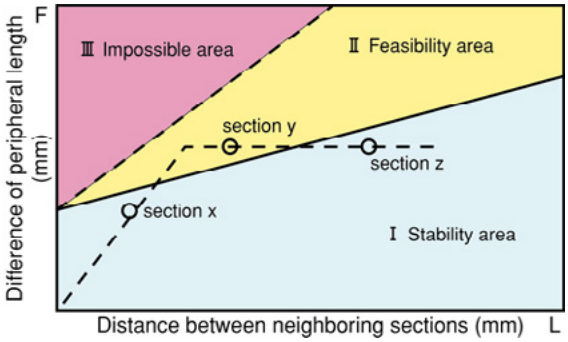


Fig. 7 Press map

3.3. Example of Applying the Press Map System

Figure 11 shows an example of applying the press map system. In this application example, tool specifications with flat die faces were initially considered, but investigation with the press map system showed that there were many impossible areas, so this was changed to curved die face specifications. The red and yellow section lines both show impossible area sections, with red indicating a short peripheral length and yellow a long peripheral length. As a countermeasure, the die face was built up to shorten the yellow sections. The prototype results at this time show that forming was possible without major problems as shown in Fig. 12.

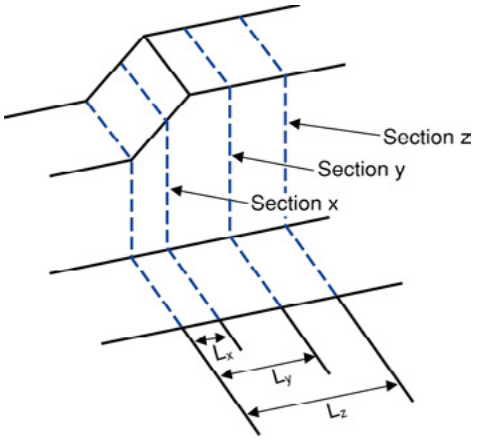


Fig. 8 Sections on a shape

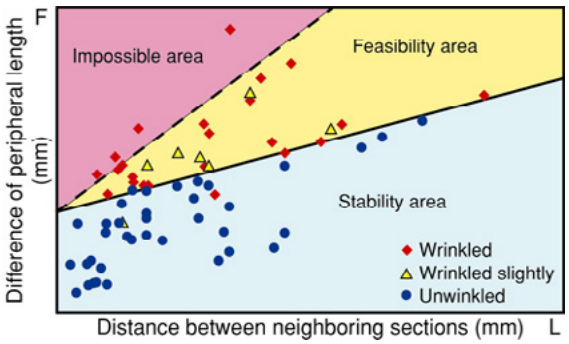


Fig. 9 Measured data on press map

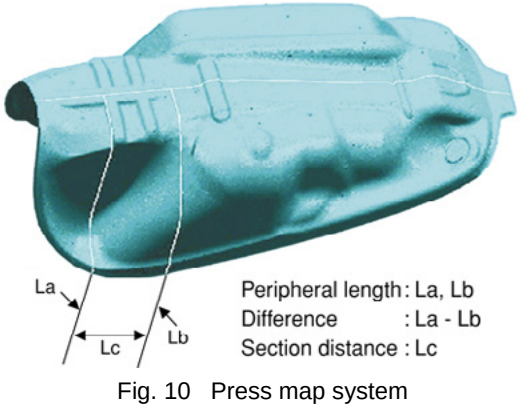


Fig. 10 Press map system

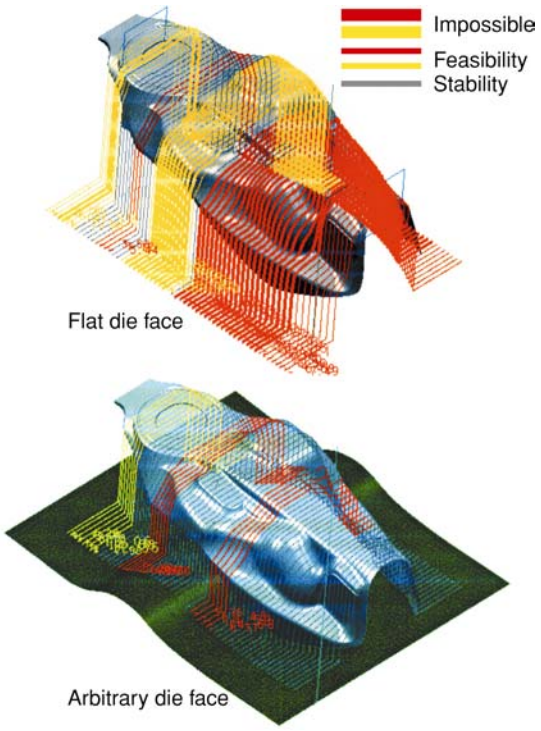


Fig. 11 Example of product shape



Fig. 12 Result of press forming with arbitrary die face

These results verified the effectiveness of the press map system as a formability judgment tool. In addition, using the same curved die faces for the prototype as for mass production made it possible to incorporate countermeasures into the tool specifications based on the prototype results, thus helping to improve the tool design efficiency.

4. Development of the Press CAE System

In the tool design stage, it is necessary to investigate the tool shape including the product shape, and the formability including the forming conditions. Thus, it must be possible to perform simulations under the same conditions as the actual press forming process. In addition, functions capable of evaluating panel cracking, wrinkling and strain in the forming process are also demanded. Elastic and plastic deformation analysis (press CAE) that uses finite element method (FEM) is utilized as a system for achieving these functions.

4.1. Press CAE

The following functions are required to simulate the press forming process.

- Handling of complex product shapes
- Analysis of nonlinear phenomena (large deformation, plastic deformation, contact with the tool) occurring in the materials
- Handling of issues unique to press forming such as the draw bead and trim
- Stable analysis in a practical length of time
- Accurate evaluation of formability

A number of methods using FEM have been proposed as methods that satisfy these requirements, and these can be broadly divided into dynamic explicit analysis and static implicit analysis. Each method has advantages and disadvantages, but dynamic explicit analysis software was selected from the viewpoints of analysis time and accuracy. This method was originally developed for shock analysis and crash analysis simulations. However, it has been adapted to quasi-static press forming analysis and features stable calculation with reliable solutions for nonlinear analysis such as large deformation and contact. On the other hand, this method requires extremely small analysis time steps (approximately 10^{-6} seconds), and an enormous amount of time is required to analyze press processes lasting several seconds. Therefore, some means were needed to allow practical simulations, and this is currently achieved by increasing the forming speed by a factor of 10 to 100 times over the range that does not affect the accuracy of the analysis results.

4.2. Introduction and Customization of the Press CAE System

In order to efficiently predict formability using dynamic explicit analysis, a pre-post system was introduced and customized. This system has the following features.

- This system is designed specially for press forming, and parameter input uses press forming terminology such as single action press, die, punch, bead, and so on to make the system easy to use for press designers. In addition, default values are set for the internal parameters used for analysis, which allows analysis to be executed without having to concentrate on the dynamic explicit analysis software.
- The panel deformation resistance due to the draw bead can be input as a numerical parameter. This greatly reduces the calculation time compared to modeling the draw bead based on the die shape. This parameter value is identified with experiments and analysis to derive the accurate value.
- The system has a material database function, and data unique to the company can be registered. Tensile tests are currently being performed with materials used in products to measure and register stress-strain curves and r values (anisotropic parameters).
- The system has abundant results display functions, and formability can be evaluated from various viewpoints. Display functions include plate thickness reduction rate distribution, forming limit diagram (FLD), scribed circle,

shock line, forming pressure, distribution of contact between the panel and the die, etc.

- A database is constructed within the in-house intranet, and stores the analysis conditions and analysis results. These data are opened to product and tool designers, and used for tool design.

Figure 13 shows the analysis procedure using this system.

(1) 3D model creation
The die addendum and die face shape are added to the product model to create the tool shape. Here, the fillets that are essential for press forming must be faithfully created.

(2) Mesh creation
The die, blank holder, punch and panel are all expressed by polygon using a finite element mesh.

(3) Forming condition setting and analysis
The material characteristics, cushion pressure, friction, draw bead load, stroke amount and other forming conditions are set, and analysis is executed.

(4) Results evaluation
The strain, deformation, plate thickness, stress and surface pressure of the plate during the forming process are output, and the tool shape, the material type, plate thickness, shape and placement of panel, cushion pressure, friction and draw bead parameters are investigated based on these results.

(5) Accumulation of results
These results are saved in the aforementioned analysis database.

Figure 14 shows an example of analysis results. This graph outputs the fuel tank thickness along the symmetrical plane, and shows both the measurement and analysis results. Both results show an excellent correlation over the entire graph, thus confirming that the system can be applied to actual products.

4.3. Example of Applying the Press CAE System

An example of applying the press CAE system to wrinkles and cracks is shown below.

4.3.1 Predicting wrinkles

Figure 15 shows the deformation shape based on the analysis results. The upper figure is before and the lower figure is after the countermeasures. Plate overflow occurred in concave areas before the countermeasures, but this plate overflow could be prevented by changing the die face shape.

The die is a rigid body so the analysis shows less wrinkling at the bottom dead point than for the actual product. Therefore, plate deformation, wrinkle timing, wrinkle height and other phenomena in the forming process are currently used in reference to fuel tank shapes for similar models from the aforementioned database to assist designers in their wrinkle judgments.

4.3.2. Predicting cracks

Figure 16 shows the plate thickness distribution and a graph of the minimum plate thickness for each specification based on the analysis results. Although the initial specifications cleared the cracking judgment value, it is close to the limit value and leaves no forming margin in consideration of variance during mass production. Therefore, in this case the panel placement and shape were modified to increase the forming margin. The minimum plate thickness was compared for the base specifications and improvement proposals 1 and 2. The comprehensive cracking judgment also uses the plate thickness reduction rate, forming limit line diagram and plate thickness reduction history.

5. Future Themes

(1) The next most common forming defect after cracks and wrinkles is surface deformation. This occurs as minute wrinkles or waves on the product shape and leads to a drop in appearance quality. There are methods for judging surface deformation by the deformation shape, stress, strain, and so on, but the accuracy is still insufficient. The number of case examples must be increased and judgment technology established in the future.

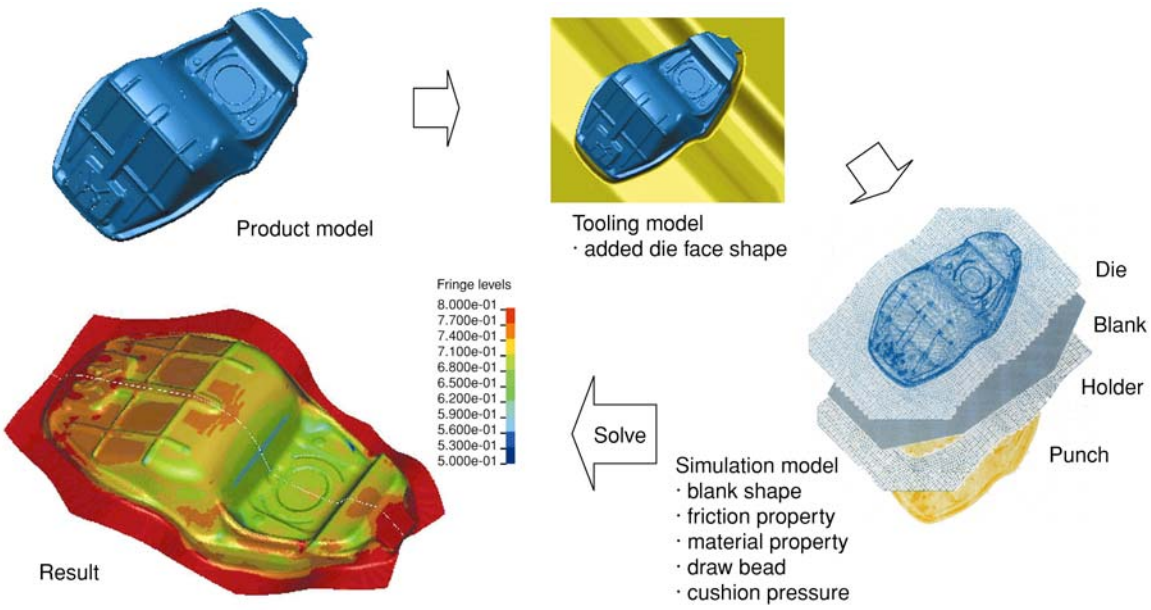


Fig. 13 Simulation flow

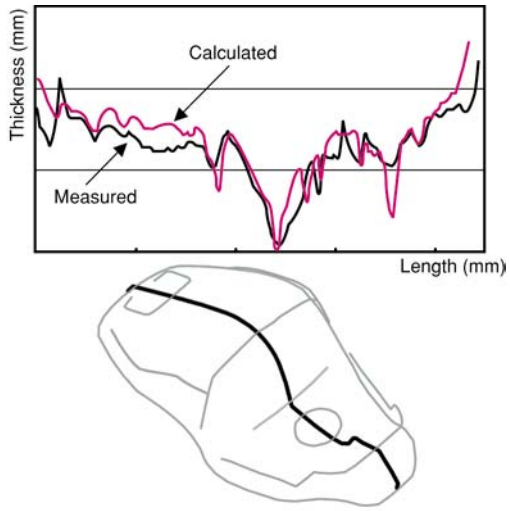


Fig. 14 Measured and calculated thickness distribution on a product shape

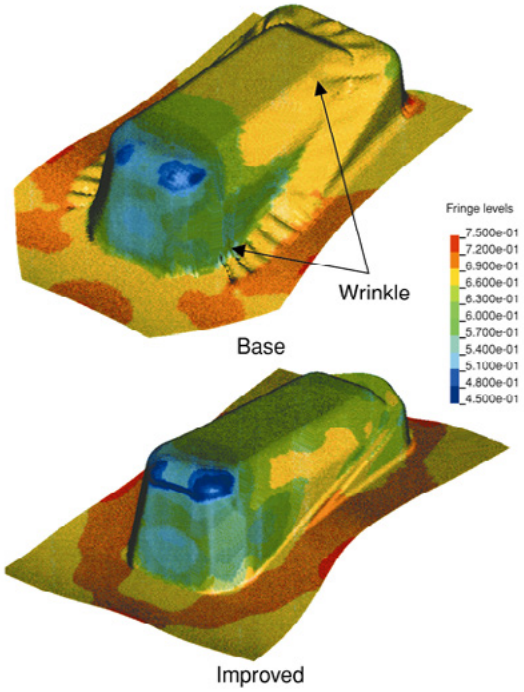


Fig. 15 Countermeasure implementation for wrinkle

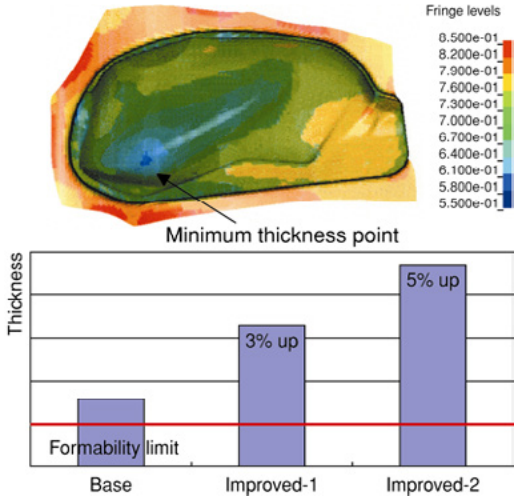


Fig. 16 Countermeasure implementation for crack

(2) Within the tool shape, the die addendum is a part that has a large effect on formability. The difference of peripheral length can be adjusted and plate inflow can be controlled according to the die addendum shape. However, unlike tuning with the analysis parameters such as for the cushion pressure, investigating the die addendum shape requires multiple die addendum models. Simpler tools to create them are currently being investigated.

(3) With the shift to overseas production, press forming is increasingly using local facilities and materials. However, the formability of the materials in each location differs, so the material properties of local materials must be acquired in the future.

6. Conclusion

The following two systems were constructed as methods for evaluating press formability.

(1) Simple and high-speed “press map method”
The press map method was developed focusing on the deformed condition of a plate with level differences. This system is used to investigate shapes in the product design stage and to design die faces in the tool design stage, and its effectiveness was verified.

(2) In-depth and high accuracy “press CAE analysis method”
The press CAE analysis method using FEM was developed. This system is used to investigate tool shape and forming condition settings in the tool design stage, and its effectiveness was verified.

These two systems make it possible to quantitatively investigate manufacturing requirements in the design stage.

References

(1) KUWABARA, S.: Relationship between Difference of Peripheral Length along the Punch Surface and Wrinkles in Thin Steel Plate Press Forming, Honda Engineering Technical Review Vol. 2, pp. 118-124 (1994)

(2) MAKINOUCHI, A.: Current World Trends in Plate Forming Simulations and Related Technology, Plasticity and Forming, Vol. 40, No. 460, pp. 12-21 (1999-5)

■ Authors ■


Takashi OGINO


Hiroyuki KAMO


Tomoyuki TAGAMI


Minoru SAITO


Hiroki YOKOTA


Shoji KUWABARA

Technical Papers Submitted to Out-of-company: January, 2001 to June 2002

(English Papers only)

Date	Conference	Title	Author	Organization
2002/1/1	JSAE/JSAE Review Vol.23, No.1	Development of high fatigue strength ultra-fine grained stainless steel for cylinder head gasket	Takashi Katsurai	Tochigi R&D Center
		Analysis of the accessory belt lateral vibration in automotive engines	Atsuo Fujii	Tochigi R&D Center
			Shogo Yonemoto	Tochigi R&D Center
			Kiyoshi Miyazaki	Tochigi R&D Center
			Seiji Furumata	Tochigi R&D Center
			Hiroshi Miyazawa	Tochigi R&D Center
			Kazuma Okuda	Tochigi R&D Center
		Development of automatic transmission control system using hardware-in-the-loop simulation system	Kenji Hagiwara	Tochigi R&D Center
			Satoshi Terayama	Tochigi R&D Center
			Youhei Takeda	Tochigi R&D Center
			Ko Yoda	Tochigi R&D Center
			Shoichi Suzuki	Tochigi R&D Center
2002/2/1	Japan Society for Fuzzy Theory and intelligent informatics/ Journal of SOFT	The Pareto Archived Evolution Strategy : A New Baseline Algorithm for Pareto Multiobjective Optimization	Tatsuya Okabe	Honda R&D Europe
			Bernhard Sendhoff	Honda R&D Europe
2002/2/14 ～15	Magna Steyr/3rd All-Wheel drive congress in Graz/New dynamics of 4WD vehicles (Graz, Austria)	Development of a 4WD System for SUVs	Shouji Tokushima	Tochigi R&D Center
			Kazuhiro Nakano	Tochigi R&D Center
			Koji Kuroda	Tochigi R&D Center
2002/3/4 ～7	SAE World Congress 2002/ (Detroit, USA)	A Study of Oil Film Pressure Distribution on Connecting Rods Big Ends	Kenji Sato	Tochigi R&D Center
			Kyoichi Machida	Tochigi R&D Center
			Katsunori Makino	Wako Research Center
		All Clutch to Clutch 5 Speed Automatic Transmission	Hideki Wakamatsu	Honda R&D Americas Inc. OHIO Center
			Tatsuyuki Oohashi	Tochigi R&D Center
			Shouji Asatsuke	Tochigi R&D Center
			Yoshiharu Saitoh	Tochigi R&D Center
		Application of HIL Simulations for the Development of Vehicle Stability Assist System	Takeshi Ohba	Tochigi R&D Center
			Ichiro Takema	Tochigi R&D Center
			Yukimasa Minami	Tochigi R&D Center
			Hiroki Yokoyama	Tochigi R&D Center
		Development of a 4WD System for SUVs	Shouji Tokushima	Tochigi R&D Center
			Kazuhiro Nakano	Tochigi R&D Center
			Koji Kuroda	Tochigi R&D Center
			Yoshikazu Konishi	Tochigi R&D Center
			Kazunori Kobayashi	Tochigi R&D Center
		The Development and Utilization of HILS for the Development of an Automatic Transmission Control System	Kenji Hagiwara	Tochigi R&D Center
			Satoshi Terayama	Tochigi R&D Center
			Ko Yoda	Tochigi R&D Center
			Youhei Takeda	Tochigi R&D Center
		A study on a Metal Pushing V-Belt type CVT (A novel approach to characterize the friction between blocks and a pulley, and shifting mechanisms)	Ryuhei Kataoka	Doshisha Univ.
			Toru Fujii	Doshisha Univ.
			Kazuya Okubo	Doshisha Univ.
			Shigeru Kanehara	Tochigi R&D Center
		Development of a Magnetic Coupling Water Pump for a Four-Stroke 50cm3 Scooter Engine	Yutaka Miyake	Asaka R&D Center
			Tadashi Niino	Asaka R&D Center
			Masatoshi Fukamachi	Asaka R&D Center
			Shin Nabeya	Asaka R&D Center
			Osamu Satou	Yamada Seisakusho Co.,
2002/3/21	The American Physical Society/APS March Meeting 2002 (Indiana , USA)	Hydrogen Storage on SWNTs produced by HiPCo process	Bhabendra K. Pradhan	Pennsylvania State Univ.
			A.R.Harutyunyan	Pennsylvania State Univ.
			Hajime Goto	Wako Research Center
			Yoshiya Fujiwara	Wako Research Center
			Peter C. Eklund	Pennsylvania State Univ.

2002/4/1	Nature Vol.416 (18 Apr 2002)	Green revolution：A mutant gibberellin-synthesis gene in rice	Akie Sasaki Motoyuki Ashikari Miyako Ueguchi Hironori Itoh Asuka Nishimura Datta Swapan Kanako Ishiyama Tamio Saito Masatomo Kobayashi Hidemi Kitano Gurdev S.Khush Makoto Matsuoka	Nagoya Univ. BioScience Center Nagoya Univ. BioScience Center Nagoya Univ. BioScience Center Nagoya Univ. BioScience Center Wako Research Center International Rice Research Institute RIKEN TSUKUBA Institute Bioresource RIKEN Plant Molecular Biology Laboratory RIKEN TSUKUBA Institute Bioresource Nagoya Univ. Graduate School of Bioagricultural Science International Rice Research Institute Nagoya Univ. BioScience Center
2002/5/8 ～10	ACC (American Control Conference)/American Automatic Control Council (Anchorage, USA)	Automated steering control system design for passenger vehicle in consideration of steering actuator dynamics	Yukihiro Fujiwara Masakazu Yoshii Shuichi Adachi	Tochigi R&D Center Utsunomiya Univ. Utsunomiya Univ.
2002/5/12 ～17	201st Meeting of The Electrochemical Society / Electrochemical Society,Inc. (Philadelphia , USA)	MICRO FUEL CELL BASED ON THICK PHOTORESIST	Suk-Won Cha Sang-Joon J. Lee Ryan O'Hayre Yong-Il Park Yuji Saito Fritz B. Prinz	Stanford Univ. Stanford Univ. Stanford Univ. Stanford Univ. Honda R&D Americas Stanford Univ.
2002/5/22 ～24	National Institute for Materials Science / The First International Conference on Advanced Structural Steels/Proceedings P269-270 (Tsukuba)	High Strength Steels for Automobile Application	Taku Kitayama	Tochigi R&D Center
2002/5/29 ～31	Hibbitt, Karlsson & Sorensen, Inc./ 2002 ABAQUS User's Conference (Newport, Rhode Island USA)	Application of Metal Pushing V-belt Stress Simulation with CVT Pulley stiffness	Toshihiro Saito Takemasa Okano	Tochigi R&D Center Tochigi R&D Center
2002/5/31	ICCN 2001 / Proceeding of the conference	To compute face detection of cross-modal integration by spatiotemporal attention	Takamasa Koshizen Bernd Heisele Hiroshi Tsujino	Wako Research Center Honda R&D Americas Wako Research Center
2002/6/2 ～7	2002 FISITA World Automotive Congress (Helsinki, Finland)	Development of a new compact gasoline engine "i-DSI" for the small category vehicle	Yukio Nakayama Makoto Suzuki Yoichi Iwata Junji Yamano	Tochigi R&D Center Tochigi R&D Center Tochigi R&D Center Tochigi R&D Center
2002/6/10	Studies in Fuzziness and Soft Computing	Advanced Fuzzy Systems Design and Applications	Yaochu Jin Bernhard Sendhoff	Honda R&D Europe Honda R&D Europe
2002/6/15	ISC2002/International Supercomputer Conference (in HEIDELBERG/ University of Mannheim, University of Tennessee)	Construction of PC-Cluster for CFD applications (TOP500 CERTIFICATE Self-made Pentium4 Cluster Honda R&D is ranked No.412)	Keiichiro Takato	Wako Research Center
2002/6/16 ～21	Metal Power Industries Federation/2002 World Congress on Powder Metallurgy & Particulate Materials (Orlando, USA)	Development of a rotor core of motor for a hybrid-car by means of sinter diffusion bonding	Kazuo Asaka Toshiyasu Komatsu	Hitachi Powdered Metals Co., Ltd. Tochigi R&D Center
2002/6/24	20th AIAA Applied Aerodynamics Conference and Exhibit (St. Louis)	NLF Airfoil Development for Honda Jet	Michimasa Fujino	Wako Research Center

Editor's Postscripts

The *Honda R&D Technical Review* has made steady progress since its inaugural issue, moving to twice-yearly publication, public access on the Web, and an English-language edition among others. It is now much better both quantitatively and qualitatively. As a result, we are being put to active use at Honda research centers inside and outside Japan, and are hearing from people who are eager to see the next issue. I believe this shows widespread acceptance of the *Technical Review* as a tool for technical communication.

Meanwhile, in order for Honda to hold its position as “a company whose existence will be welcomed by society” and to realize our “spirited independence” goal, all of us at Honda R&D Co., Ltd. will have to continue constantly creating new values. This means that our mission is to continue supplying the world with products that let us share the joy with our customers, and also to contribute to society by means of the original, innovative technology that supports such products.

Given these circumstances, the *Technical Review* will play an increasingly important role as a tool for technical communication with the world outside the company, which has in fact been our purpose from the very beginning. I want us to go on creating technology that embodies the dreams originating from our untiring spirit of exploration, and sending the technology out into the world together with our products. I cannot help but hope that the *Technical Review* will become a publication that is greeted with great anticipation not only by the automobile industry but by other industries and the academia, as well, and that someday it will become the authoritative source on advanced technology.

(Takado)

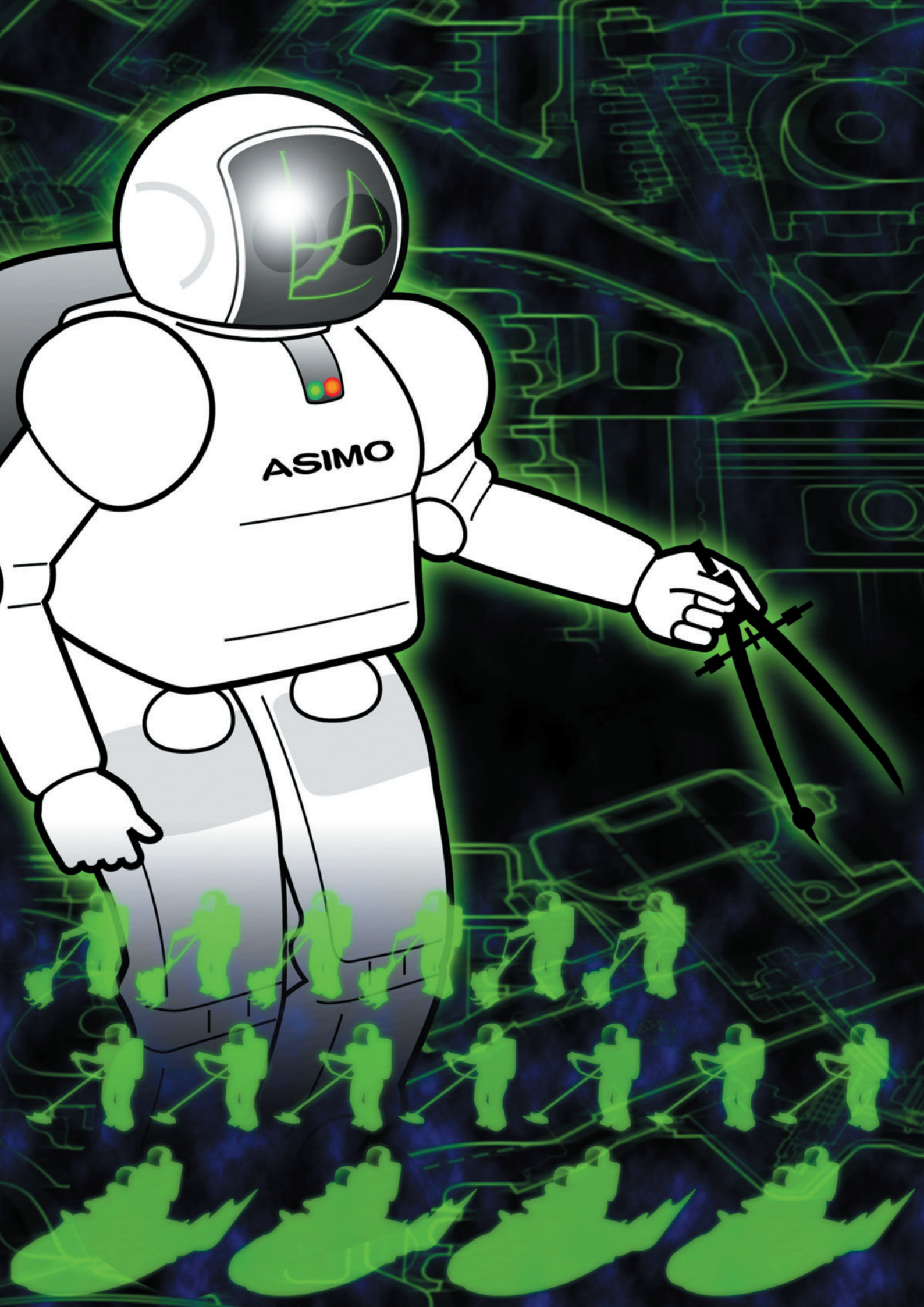
I read a newspaper article that said, “Human beings grow lazier as technology advances.” It's true that the world has become so convenient that we can watch television and adjust our air conditioning, as well as hold conversations over the Internet with people on the other side of the world and even see their faces, all while lying on our beds. When we go someplace we're not familiar with, we can receive directions by using devices, and we can buy necessities any time we want at a convenience store. When ASIMO becomes more evolved, we will not even have to spend that time to go to a nearby convenience store ourselves.

If the world keeps going this way, it is more and more going to turn into a pleasant, lazy paradise. However, it is people after all who must think up the devices and make the arrangements, so we have to carry out research in order to progress toward even higher objectives. The *Technical Review* is, in a sense, a crystallization of the efforts made by researchers behind the scenes to realize that lazy society. We will get the better of the lazy society, and with the greatest speed in the world. What an unusual challenge this is!

(Kudo)

Honda R&D Technical Review English Version Vol.14 No.2
The following associates provided us with their cooperation and expertise:

Karen	Arneson	American Honda Motor Co., Inc.
John	Basinger	Honda R&D Americas, Inc. Ohio Center
Bill	Bezilla	Honda R&D Americas, Inc. North Carolina Center
Jeff	Brown	Honda R&D Americas, Inc. Ohio Center
Mary	Christopherson	American Honda Motor Co., Inc.
Dennis	Chung	Honda R&D Americas, Inc. Ohio Center
Chris	Combs	Honda R&D Americas, Inc. Ohio Center
Harry	Freind	Honda R&D Americas, Inc. Ohio Center
Koichi	Funatsu	Honda R&D Americas, Inc. Ohio Center
Charlie	Gagliano	Honda R&D Americas, Inc. Ohio Center
Lee	Goldring	American Honda Motor Co., Inc.
George	Graus	Honda R&D Americas, Inc. North Carolina Center
Adam	Hanes	Honda R&D Americas, Inc. North Carolina Center
Cory	McEnhill	Honda R&D Americas, Inc. Ohio Center
Ashley	Nichols	Honda R&D Americas, Inc. Ohio Center
Bill	Post	Honda R&D Americas, Inc. Ohio Center
Jay	Ray	Honda R&D Americas, Inc. Ohio Center
Noboru	Sannodo	Honda R&D Americas, Inc. Ohio Center
Alan	Seid	Honda R&D Americas, Inc. Ohio Center
David	Thompson	Honda R&D Americas, Inc. Ohio Center
Shunnichi	Tsuzuki	Honda R&D Americas, Inc. Ohio Center
Hideki	Wakamatsu	Honda R&D Americas, Inc. Ohio Center
William	Willen	American Honda Motor Co., Inc.
Masashi	Yamamoto	Honda R&D Americas, Inc. Ohio Center
Yoshio	Yamamoto	Honda R&D Americas, Inc. Ohio Center


ASIMO